STRONG MICROWAVES IN PLASMAS

2000

Volume 2

Institute of Applied Physics
Nizhny Novgorod

RUSSIAN ACADEMY OF SCIENCES
INSTITUTE OF APPLIED PHYSICS

STRONG MICROWAVES IN PLASMAS

PROCEEDINGS
OF THE INTERNATIONAL WORKSHOP

Nizhny Novgorod,
2 – 9 August 1999

Edited by
A.G. Litvak

In two volumes
Volume 2

Nizhny Novgorod – 2000

ISBN 5-8048-0008-6

NONLINEAR PROCESSES IN PLASMAS (THEORY AND MICROWAVE EXPERIMENTS)

INVESTIGATION OF STRONG LANGMUIR TURBULENCE BY ELECTROMAGNETIC RADIATION

L.N.Vyacheslavov, V.S. Burmasov, I.V. Kandaurov, E.P. Kruglyakov, O.I. Meshkov, and A.L. Sanin

Budker Institute of Nuclear Physics, 630090, Novosibirsk, Russia

Results of experiments where high current relativistic electron beam drives strong Langmuir turbulence in a weakly magnetized plasma are presented. An external magnetic field, which governs the dispersion of Langmuir waves in the energy containing bulk of the spectrum, and a non-Maxwellian electron distribution function are the distinguishing features of the experiments. Both these circumstances greatly affect a mechanism of energy transfer from oscillations to plasma electrons. Thomson scattering is the major diagnostic technique for investigation both the w- and k-spectra of Langmuir and ion-acoustic waves and for studying of the dynamics of electron distribution function. Besides Thomson scattering a mesh based monochromator for λ = 470 nm is employed for observation of spontaneous plasma emission near $2w_{pe}$ as well as two versions of the Stark spectroscopy for measurement of turbulent microfields. The detailed k-spectrum of Langmuir turbulence obtained for the first time in beam-plasma systems manifests itself as a broad one. It decreases nearly as k^{-2} and shows that Langmuir oscillations are strongly unstable relative to transverse low frequency perturbations. k-Spectrum of short-wavelength ion-sound and non-thermal fraction of the distribution function of plasma electrons, which stores about half of plasma energy content, are studied. A mechanism of heating of plasma electron is suggested.

Introduction

After the seminal paper by V.E Zakharov [1] strong Langmuir turbulence (SLT) came to the constant attention of researchers in plasma physics. This interesting nonlinear phenomenon plays its role in heating of laboratory plasma by lasers [2, 3] and by electron beams [4, 5], or in experiments on the ionosphere modification by high power microwaves [6, 7]. Electromagnetic emission from active galactic nuclei [8, 9], pulsar magnetospheres [10, 11], solar corona [12], interplanetary plasma [13] and planetary foreshocks [14, 15] are often associated with Langmuir turbulence. Theory and simulation more penetrate to physics of individual element of SLT - caviton in isotropic Maxwellian plasmas (see Ref. 16 and literature therein). In the same time, under practically important conditions of superthermal electrons, which appeared as a direct consequence of SLT, or an external magnetic field, the Langmuir

wave collapse is studied in limited number of specific cases. The Zakharov equations modified in the context of a magnetic field were solved only for packets of Langmuir waves travelling along [17, 18, 19] or normal [20] to the magnetic field direction. A few limiting cases of relatively low level of SLT (adiabatic collapse) [21, 22, 23] or large scale cavitons [24] were studied in a magnetized plasma. High-energy tail of the electron distribution function was approximated in simulations by two-temperature Maxwellian distribution [25]. A self-consistent determination of the electron distribution function was performed only for the one-dimensional Vlasov equation [26] or for 2.5D particle-in-cell simulations carried on a 128x128 grid [27].

The averaged characteristics of turbulence as wave spectra or the electron distribution functions, which are most interesting practically, are much less investigated theoretically. The analytic calculations of SLT spectra was done for one-dimensional case [28, 29]. Besides, such calculations need a number assumptions on the mechanisms of transportation and dissipation of the energy of turbulence. The simulation of steady-state turbulence with inclusion of sufficient number of cavitons is yet far beyond of the capabilities of modern computers and enables just estimations [30].

It is interesting that the experimental investigation of SLT driven by electron beam is in a situation similar to that in theory. The most impressive results were obtained on the dynamics of a single caviton [31], but not in real turbulence. The collapse phenomenon was studied under the special conditions when the region with unstable plasma waves was comparable in size with a single caviton. In those circumstances the cavern appeared in the same location precisely enough to enable the spatial measurements on shot-by-shot basis. Subsequently the experiments [31] were continued at a longer time scale but with the same ratio of the cavern size to the cross-section of the turbulence region [32, 33]. The laboratory experiments where the turbulence region is much larger than all characteristic sizes of non-linear processes are few. The studies of turbulent oscillations were carried out either with electromagnetic plasma emission [34, 35] or using the Stark spectroscopy of spectral line shapes [36, 37, 38]. The spectroscopy of turbulence microfields gives a mere estimation of the turbulence level and sometimes leaves room for ambiguity in data interpretation. In the above mentioned experiments only in Ref. 37 a magnetic field influenced dispersion of the Langmuir waves but it was not taken into account in interpretation of the experimental data.

The present paper describes the results of the detailed investigation of SLT driven by electron beam in magnetized non-Maxwellian plasma. It includes observations of ω- and k-spectra of Langmuir and ion-acoustic waves, which usually accompanies SLT.

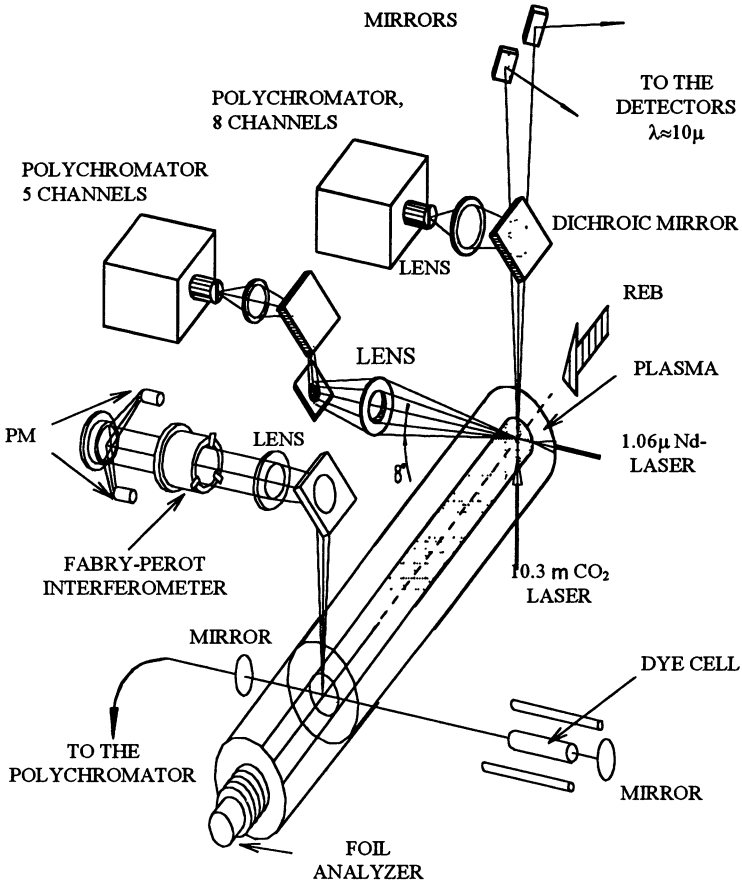

Fig.1.Schematic of the experiment.

Besides, electron distribution function and the microscopic dynamics of the plasma density are observed. The Thomson scattering is chosen as a basic diagnostic technique and associated instruments are developed. Besides, others non-perturbing diagnostics complementary to the Thomson scattering are employed.

Experimental setup

The layout of the experiment and the diagnostics is presented in Fig. 1 and parameters of the experiment in Table. The relativistic electron beam (REB) is injected along the plasma column situated in the longitudinal magnetic field. In the cross-section of the column located at distance of 12 cm from the injection plane the Thomson scattering diagnostics both collective and non-collective are positioned. The collective small-angle Thomson scattering of pulsed CO_2 laser light [39] is employed for observation of plasma waves. The non-collective mode of Thomson scattering is based on 1.06 μ neodymium laser and uses two receiving systems [40]. The first system employs the conventional 90°-detection for measurements of temperature and density of a Maxwellian bulk when the second system uses the 8°-scattering that is peculiar for the observation of high energy tails of the electron distribution function. The Stark spectroscopy measurements are performed at the distance of 95 cm from the plane of the beam injection. Both emission and laser introcavity absorption spectroscopic techniques [41] are applied for observations of turbulent microfields. The electrons with energies higher than 20 keV are detected by the multifoil analyzer at the end of plasma chamber. The diagnostic instrumentation is described in some details in [42].

Table. Parameters of the experiment.

Plasma	Density	n_e=1-2·10^{15} cm^{-3}	
	Initial temperature	T_o=1 eV	
	Final electron temperature	T_e=20-60 eV	
	Magnetic field	B_o=25 kGs	ω_{pe}/ω_{ce}=1/5
Electron beam	Density	n_b=3-5·10^{11} cm^{-3}	n_b/n_e=3-5·10^{-4}
	Energy	E_e=600 keV	E_e/T_e=1-3·10^4
	Duration	τ_b=200 ns	$\tau_b\omega_{pe}/2\pi$=7·10^4
	Diameter	d_b=1.8 cm	$d_b\omega_{pe}/2\pi c$=20

Spectra of Langmuir oscillations

A five-channel ω-spectrometer [39] based on diffraction grating is employed for measurement of a frequency spectrum of the blue satellite in the scattering signal. (An ammonia notch filter rejects the red satellite). The measurements indicate that spectral shift of the satellite varies as the square root of plasma density, which is determined independently in the same shot by non-coherent Thomson scattering [43]. This result

characterizes the observed plasma waves as the Langmuir waves.

Before proceeding to discussion of the results of the wave vector spectra observation it is useful to consider the characteristic regions in a k-space (Fig.2). The triangle cross-section indicates in the Figure the region where waves directly interact with the electron beam due to kinetic beam-plasma instability. The angular divergence θ_b of the electron beam determines the angular width of the section. The superluminal waves with $kc/\omega_{pe} < 1$ do not interact with light and cannot be detected by Thomson scattering method.

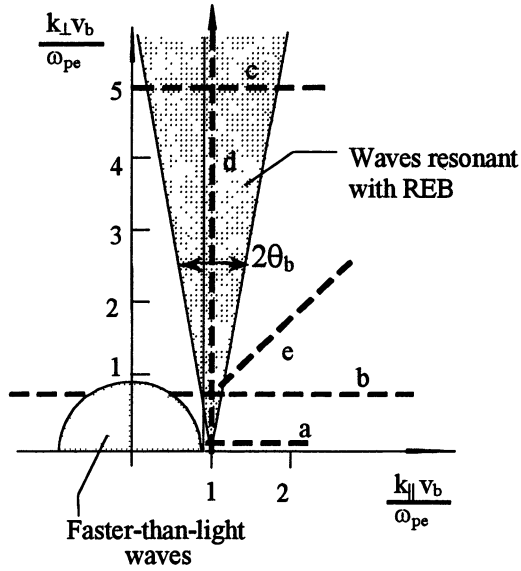

Fig.2. Characteristic regions in a k-space. Dashed lines mark the directions of measurements.

The k-spectrum observed along the direction of magnetic field keeping $k_\perp \approx 1$ (line b in Fig.2) is shown in Fig.3. The error bars indicate here the r.m.s. deviation of the mean values averaged over ten shots. Fig.3 includes spectra both the waves resonant with the REB and non-resonant waves. It is found for $k_\parallel \gg 1$ case that the scaling is ($W_k \sim k_\parallel^{-4.1}$) for waves, which are non-resonant with the REB. The spectrum resolved along the line d where $k_\parallel = 1$ is shown in Fig.4. The results of the measurements are displayed here for two different incident angles of the probe laser beam $\gamma = 90°$ (triangles) and $\gamma = 30°$ (squares). The error bars indicate here the r.m.s. deviation of the mean value over ten and seven shots respectively. The function fitted to the experimental points is given

by solid curve. The spectral energy density of turbulence for $k_\perp \gg 1$ scales as $1 / k_\perp^{3.6}$.

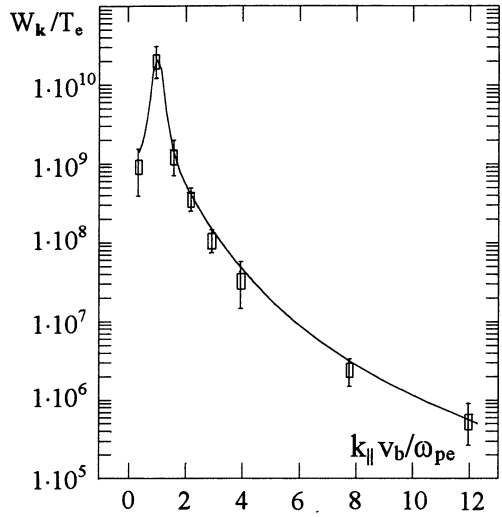

Fig.3. Spectrum measured along the line *b*.

For the angular dependence of non-resonant waves to be examined, we compared a spectral density $W_{\mathbf{k}}$ for wave vectors **k**, which are equal in magnitude, but different in directions. The result of the comparison is represented in Fig.5. The fitting curves of Fig. 3, 4 are re-plotted here versus the magnitude of wave vectors. The new data, corresponding to $k_\parallel < 0$ (cross) and to $k_\perp \sim k_\parallel$ (rectangles) and the spectrum along line *b* ($k_\perp \approx 1$) are close enough to conclude that spectrum of non-resonant waves is approximately isotropic. The curves of Fig.5 are used as approximations of wave spectra in calculations.

The results of measurements of the *k*-spectra enable us to estimate the energy density of turbulence, integrated over *k* [43]. The estimations yield that half of the total energy density of turbulence is contained in the waves travelling within the cone of angle $\varphi = 42°$ about the direction of magnetic field. At the same time, this cone contains almost 70% of the total energy density of the resonant waves. It clearly demonstrates that in our case the *k*-spectrum of Langmuir turbulence in magnetised plasma is broad. The important point is also that the electron beam directly drives waves in a broad region in a *k*-space. This feature found in our experiments is distinctly different to that treated by the most of theories and simulations where usually only one or few pumped modes present in

a magnetised plasma [17-23].

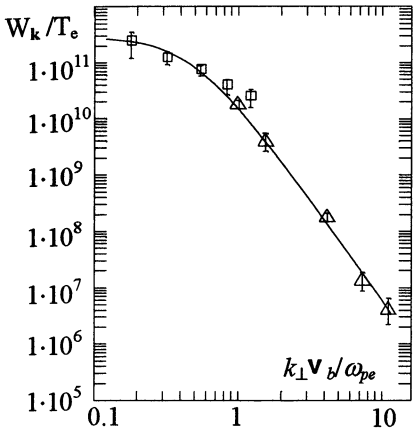

Fig. 4. Spectra along the line *d*.

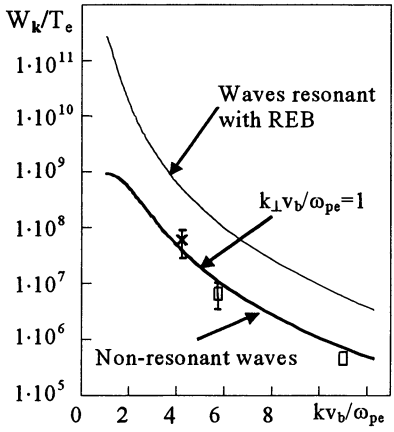

Fig. 5. Isotropy of non-resonant spectrum.

Integration of the curves fitted to the experimental data gives the level of turbulence of 8% for non-resonant waves and 16% for the resonant ones. The limits for integration here are governed by the coverage of our measurements $0.1 < (k_\perp v_b)/\omega_{pe} < 13$; $0 < (k_\| v_b)/\omega_{pe} < 13$. The total energy of turbulence ($W/nT_e = 24\%$) is simply a sum of the quantities for the resonant and non-resonant relative to the REB waves. The accuracy of these values is determined by a precision of the absolute calibration of the receiving system and is about factor of two.

It is of interest to inspect the experimental spectra concerning the excitation of the modulational instability. Criterion of modulational instability for long ($q >> \omega_{pe}/v_b$) perturbations, produced by broad spectra of Langmuir oscillation in a plasma with a weak magnetic field was investigated by Pozzoli and Ryutov [44] They considered the influence of the Langmuir waves on low-frequency motion of the plasma in terms of effective temperature:

$$T_{eff} = \frac{\omega_{pe}}{4n_e} \int \frac{1}{\Omega - \mathbf{q}\mathbf{v}_g} \mathbf{q} \frac{\partial W_\mathbf{k}}{\partial \mathbf{k}} d\mathbf{k}, \qquad (1)$$

where Ω, $\mathbf{q}$ - are frequency and wave vector of low-frequency modulational perturbations; $\mathbf{v_g}$ - group velocity of the Langmuir waves.

The net force produced by the waves and the electron pressure is equal to $(T_{eff} - T_e) \nabla n_e$. The low-frequency modulations grow when $T_{eff} > T_e$. The last inequality determines the criterion of the modulational

instability and, hence, strong turbulence conditions. Numerical calculation [43] shows that the threshold of modulational instability is far exceeded for transversal perturbations $T_{eff}/T_e = 30 \pm 2$. At the same time, the perturbations directed along magnetic field are near the threshold: $T_{eff}/T_e = 1 \pm 0.7$. The errors here are determined by the calculation accuracy only, and do not include an inaccuracy of the experimental data. Thus, in our experiment the steady-state level of Langmuir turbulence exceeds the threshold of modulational instability by more than one order of magnitude.

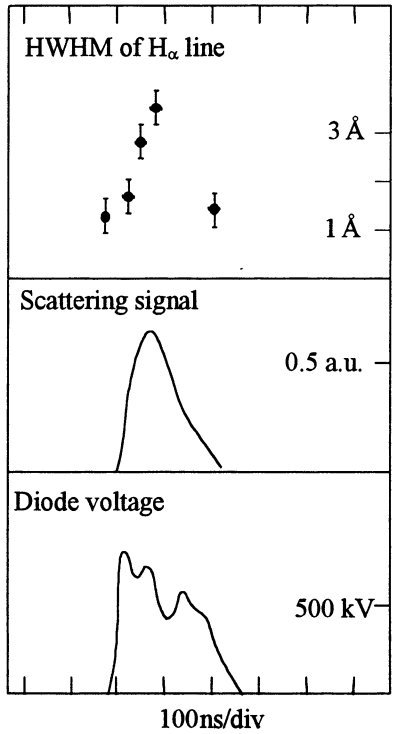

Fig.6. Timing of signals from SLT comparing with the REB current.

The spectroscopic measurements of the H_α line show considerable broadening during injection of the electron beam. The time behaviour of the line width (HWHM) is similar to that of the amplitude of the CO_2 laser scattering signal as it seen from Fig.6. It means that the Stark spectroscopy detects the high level of plasma microfields simultaneously with collective Thomson scattering signal.

Distribution function of plasma electrons

The structure of plasma heating due to absorption of turbulent Langmuir oscillations is observed with non-coherent Thomson scattering.

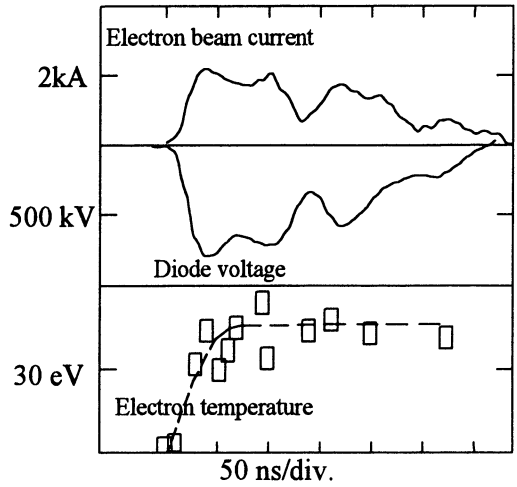

Fig.7. Time behaviour of plasma temperature and the electron beam characteristics.

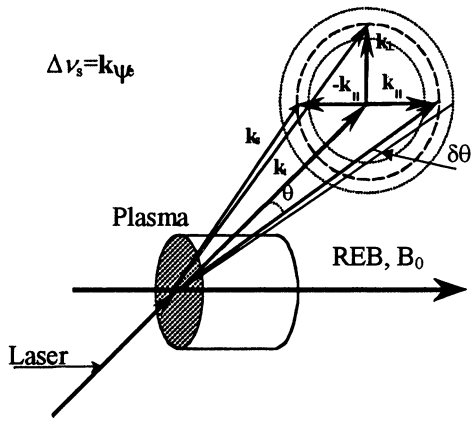

Fig. 8. Geometry of small-angle non-coherent scattering.

The results of 90°-scattering (Fig. 7) show that the temperature of Maxwellian bulk of the electron distribution function rises from 1 eV to 30-40 eV within first 50 ns and then remains approximately constant during the beam injection. Since the characteristic time for ion heating by collisions with plasma electrons is of order of microseconds it follows

that plasma remains non-isothermal during almost all the time of existence of SLT.

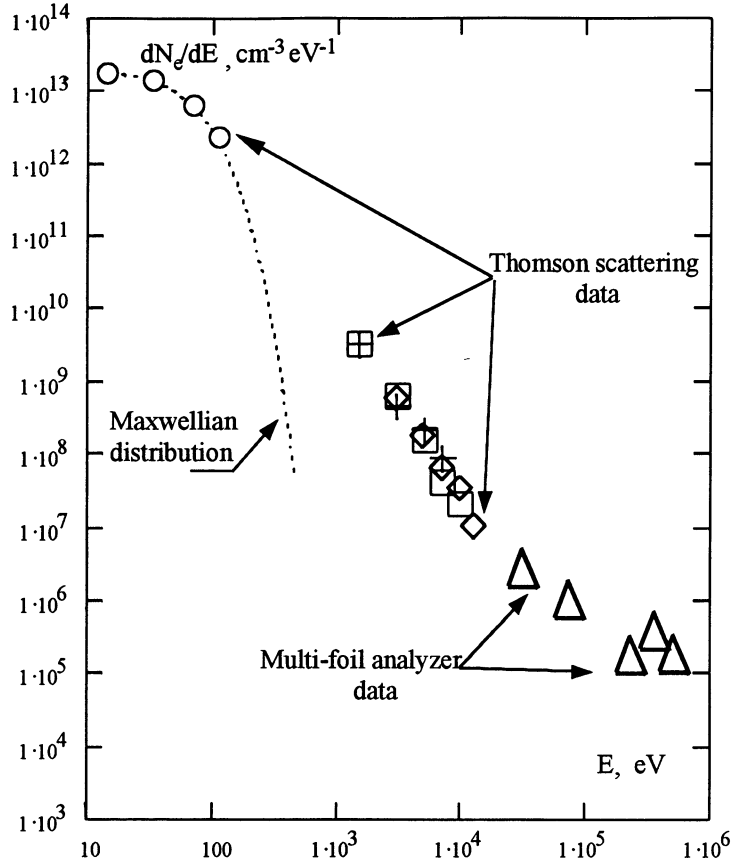

Fig. 9. The distribution function of plasma electrons according to Thomson scattering and end foil analyser data.

The non-Maxwellian tail in plasma electron distribution function was studied with small-angle non-coherent scattering [42, 45]. The small-angle geometry allows for the measurements of the distribution over different components of electron velocity relative to electron beam running direction as it seen in Fig. 8. Besides, ratio of scattering signal to plasma background light increases about two orders of magnitude in small-angle configuration relative to conventional 90°-systems. It is achieved by narrowing of scattering spectrum and by higher ratio of lengths of scattering volume and the ambient plasma along the viewing line. The investigation of the angular dependence of the scattering

spectrum reveals that the distribution of electrons with energies up to 10 keV is isotropic within factor 1.5.

The beam and the fast plasma electrons with energy exceeding 20 keV that escape from the output of plasma chamber, are registered by multi-foil analyser. The electrons traverse successively a stack of four thin aluminium foils and, finally, are stopped by a collector. With the current of absorbed electrons in the foils and the collector one could restore the energy distribution function of fast electrons [46]. The main sources of an uncertainty in the restored function are variability of the foil currents from shot to shot and a lack of the information about an angular distribution of electrons in this energy range. The total electron distribution function is shown in Fig.9. The high-energy tail contains about half of the entire plasma energy.

The experimentally obtained both the electron distribution function and the spectra of turbulent Langmuir oscillations enable evaluation a k-space structure of pumping and damping regions for turbulence. Figure 10 represents the energy density of Langmuir waves

$$W(k) = 2\pi \int_0^{\pi} W_{\mathbf{k}}(k,\theta)\, k^2 \sin\theta \, d\theta , \qquad (2)$$

pumping power

$$P_d = 2\pi \int_0^{\pi} W_{\mathbf{k}}(k,\theta)\, \Gamma(k,\theta)\, k^2 \sin\theta \, d\theta , \qquad (3)$$

where $\Gamma(k,\theta)$ is the kinetic growth rate for two-stream instability [47]. Damping power P_d and energy density absorbed in plasma electrons from Langmuir oscillations E_a were determined as follows

$$P_d(k) = \frac{\pi \omega_{pe}^3}{2k^2} W(k) \left. \frac{df_{ev}(\mathrm{v})}{d\mathrm{v}} \right|_{\mathrm{v}=\omega/k} , \qquad (4)$$

$$E_a(E_e) = \int_{E_e/1\,2}^{1.2 \cdot E_e} f_{ee}(t)\, t \, dt , \qquad (5)$$

where $f_{ev}(\mathrm{v})$, $f_{ee}(E_e)$ experimental distribution functions of plasma electrons. Two abscissa scales used in Fig. 10 are the normalised wave vector of Langmuir oscillations and the energy of electrons with velocities matched the phase velocities of Langmuir waves with given k.

Figure 10 shows that Langmuir oscillations are damped in broad region whereas pumping region looks well separated from the main part of the plasma electrons. In contrast to relative flat dependence of the

damping power, energy absorbed in plasma increases towards lower energies. It can be explained by faster escape of more energetic electrons from the turbulent region in a physical space.

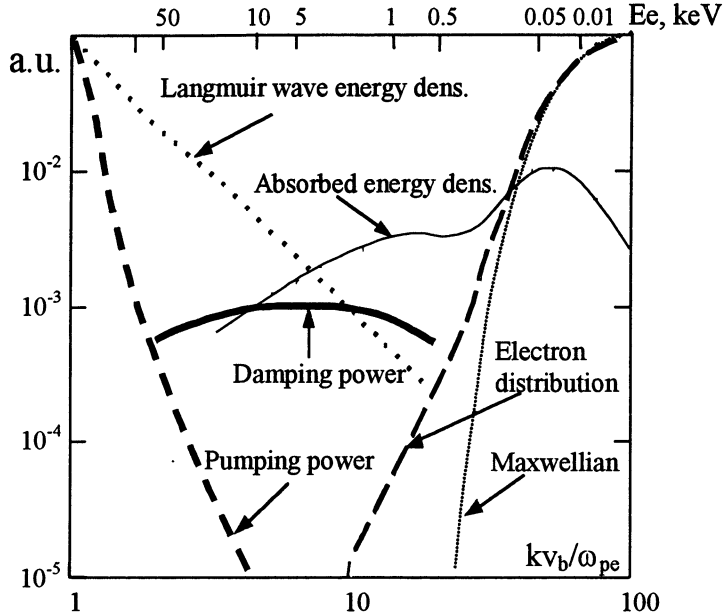

Fig.10. Structure of pumping and dumping of turbulent Langmuir oscillations according to the experimental data.

Mechanism of energy transfer

The Langmuir wave collapse comes first in explanation of energy transfer from turbulent oscillations towards plasma electrons in SLT. The collapsing density depletions confine Langmuir waves inside and translate them towards large wave numbers. The waves moderate in the process according to the dispersion equation unless plasma electrons absorb their entire energy. In our case, however, there are some doubts against this widely accepted picture. Under our conditions of broad spectrum of Langmuir waves in magnetized non-Maxwellian, non-isothermal plasma the theory of collapse is extremely difficult and hence the collapse scenario is weak developed. Still, estimations show that each of the above mentioned complications impede collapse. On the other hand, some time ago other processes are suggested for damping of SLT in weakly magnetized [48] or non-isothermal [49, 50] plasmas where the collapse plays just an ancillary role. Non-thermal low-frequency density

fluctuations are essential in both these processes, which namely are Langmuir waves conversion in the latter case and the elastic scattering of Langmuir waves along the lines of constant frequency in the former. The scattering is the resonant process in contrast to the conversion, which involves the forced Langmuir oscillations, so the rate of scattering for Langmuir waves is faster. In the following, we will show that the scattering mechanism can provide the energy transfer in our case.

The particularities of dispersion for Langmuir waves in a weak magnetic field

$$\omega_L = \omega_{pe} + \frac{3k^2 v_{Te}^2}{2\omega_{pe}} + \frac{\omega_{ce}^2}{2\omega_{pe}} \frac{k_\perp^2}{k^2} \left(1 - \frac{\omega_{pe}^2}{k^2 c^2} \right) \qquad (6)$$

enables moderation of Langmuir waves in the process of elastic scattering by increase of the thermal term in the dispersion equation at the expenses of initially much larger the magnetic term. The lines of constant frequency in a k-space are shown in Fig.11.

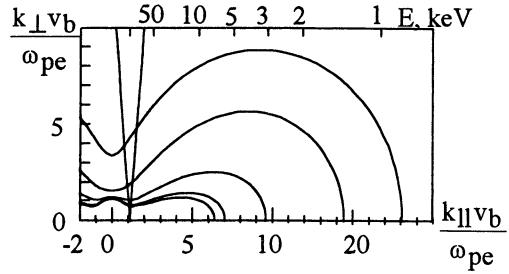

Fig. 11. Lines of ω_L=const that determine the paths for elastic scattering of Langmuir waves from plasma density fluctuations.

As it was mentioned above the plasma is non-isothermal that leads to accumulation of weakly damped ion-acoustic oscillations and greatly increases the scattering effect. The ion-acoustic oscillation can be generated in various ways. One is the weak turbulence decay of Langmuir waves. Others are modulation instability of Langmuir waves and return current, produced in plasma by pulsed electron beam. We have measured low-frequency density fluctuations by the modified CO_2 Thomson scattering techniques (see Fig. 12). Dashed line in the Figure corresponds to the spectrum of ion-acoustic oscillations produced in the process of decay of Langmuir waves. This spectrum was calculated using the equations included the direct and inverse decay rates from Ref. 51.

The dramatic difference between two spectra excludes the decay of Langmuir waves as a possible explanation of the experimentally observed

low-frequency density fluctuations. The experimentally evaluated frequency of the density oscillations [52], which is near 2 GHz, uniquely indicates the ion-acoustic waves. The lower-hybrid waves with about the same frequency ($\omega_{LH} \approx (\omega_{ce}\omega_{ci})^{1/2}$) are excluded because these waves travel nearly normal to the magnetic field direction and cannot be observed in the experimental geometry and with the validity of the thick grating approximation for scattering. There is also good experimental evidence against the return current instability as a source of the observed ion sound oscillations [52].

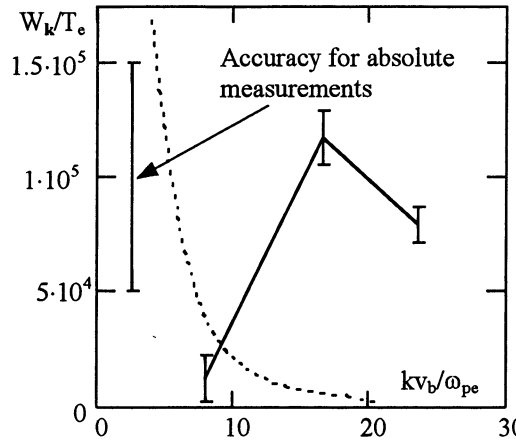

Fig. 12. Experimental spectrum of low frequency density fluctuations. Dashed line indicates spectrum according to decay generated ion sound.

The magnetic term in dispersion (6) is initially small for the Langmuir waves generated at small angles relative to the electron beam travelling direction. Therefore, the moderation of such waves in the process of scattering along the lines $\omega_L = \text{const}$ (see Fig. 11) is not effective enough, whereas the electron beam pumps these waves most strongly as it is seen from Fig. 10. The lines ω_L =const in Figure 11 are plotted for Langmuir wave inverse decay L1+S = L2 with the resonance conditions

$$\mathbf{k}_{L1} + \mathbf{k}_S = \mathbf{k}_{L2}, \qquad \omega_{L1} + \omega_S = \omega_{L2} \tag{7}$$

and under assumption that $\omega_L >> \omega_S$. However, strong excitation of Langmuir waves by the electron beam and still faster dissipation of moderated Langmuir waves in non-Maxwellian plasma decreases the life-time of waves and considerable broad the resonance. In this case the conservation conditions (7) fulfil within accuracy of the resonance

broadening [51]. It expands the range for deceleration of primary Langmuir waves enough to make them resonant with electrons of energies of order of 1 keV as Fig. 13 shows. Here E_{f0} , E_{f1} and E_{f5} indicate the minimal energy of resonant electrons for waves excited at angle θ relative to the beam direction and then moderated in the scattering process.

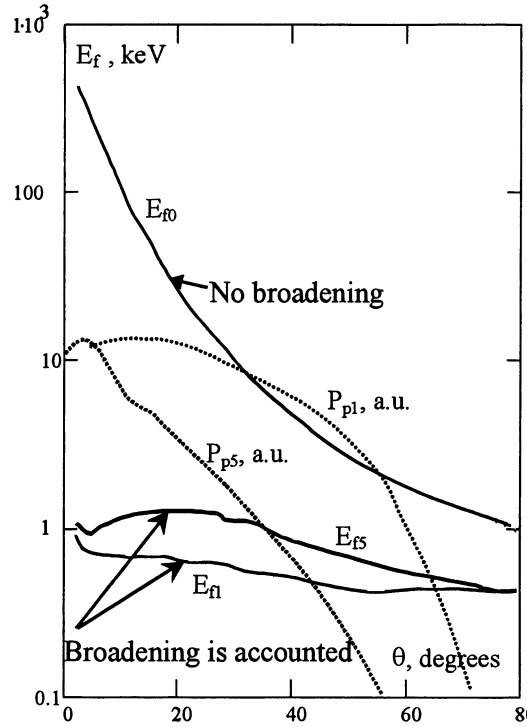

Fig. 13. The role of resonance broadening in the structure of energy deposition into plasma electrons.

In calculation of E_{f0} no resonance broadening is accounted in contrast to E_{f1} and E_{f5}. The diversity between the latter two curves is due to different growth rates for two separate angular divergence of the electron beam of 1 and 5 degrees used in the calculations. We did not measure the actual divergences, but it should be within these values for foil-less REB injection used. The plots P_{p1} and P_{p5} represent the structure of the pumping power for mentioned electron beam divergences. The figure shows a considerable reduction in the energy of resonant electrons when the resonance broadening is taken into consideration.

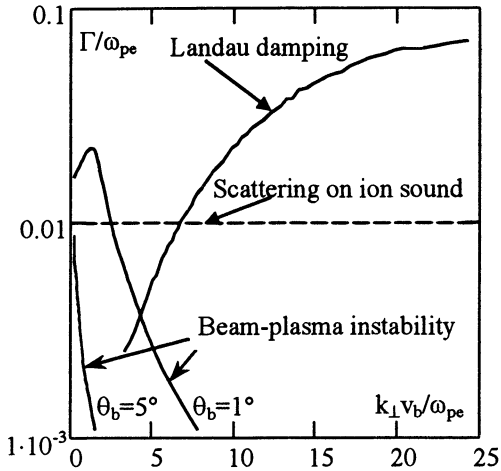

Fig. 14. The growth and damping rates for Langmuir waves.

The scattering rate for Langmuir waves can be estimated in similar way as in Ref. 47 :

$$\frac{\gamma_S}{\omega_{pe}} \approx \frac{W_S}{N_e T_e}\left(\frac{\omega_L}{\Delta\omega_L}\right). \qquad (8)$$

Figure 14 represents the scattering rate together with the Landau damping rate and the linear growth rates for beam-plasma instability. Within the accuracy of qualitative estimations the rates of all processes involved in the energy transfer are comparable. It means that scattering on ion-acoustic oscillations can provide energy transfer in a k-space through the region that contains the main energy density of Langmuir waves.

An observation of plasma emission near $2\omega_{pe}$ [42, 53] shows that measured power is near the spontaneous emission power calculated from the experimental spectrum of Langmuir waves. In case the considerable part of Langmuir waves is compressed in density cavities the emission should be several order of magnitude higher [54, 55]. Hence the observed plasma emission power gives the evidence that the majority of Langmuir waves do not confined in the collapsing cavitons. The additional indication in favor of scattering mechanism are the first results of direct observation of the dynamics of the plasma density [42] those show also no density depletion with relative depth more than 20% detected in the energy containing region for Langmuir oscillations.

Acknowledgements

This work was supported in part by the Russian Foundation for Basic Research, project No 98-02-17788.

References

1 Zakharov V.E. Sov. Phys. JETP, 1972, **35**, 908.
2 Dahmani F., Ghobrini D., EL-Mahdaoni M. Phys. Fluids, 1991, **B3**, 2558.
3 Briand J., Berge L., Gomes A., Quemener Y., Arnas C., Armengaud M., and Dinguirard J. P. Phys. Fluids, 1990, **B2**, 160.
4 Galeev A.A., Sagdeev R.Z., Shapiro V.D., Shevchenko V.I. Sov. Phys. JETP, 1977, **46**, 266.
5 Robinson P.A., Newman D.L. Phys. Fluids, 1990, **B2**, 3120.
6 Cheung P.Y., Wong A.Y., Tanikawa T., Santory J., DuBois D.F., Rose H.A., Russell D. Phys. Rev. Lett., 1989, **61**, 2676.
7 DuBois D.F., Rose H.A., Russell D. J. Geophys. Res., 1990, **95A**, 21,221.
8 Lesch H. IEEE Transactions on Plasma Science, 1989, **17**, 252.
9 Pelletier, G., Royal Astronom. Soc., Monthly Notices, 1992, **254**, 635.
10 Verga A. D., Ferro Fontan C . Plasma Phys. Controll. Fusion, 1985, **27**, 19.
11 Thompson C., Blandford R. D., Evans C.R., Phinney E. S. Astrophys. J., Prt. 1, 1994, **422**, 304.
12 Kontorovich V. M., Pimenov S. F., Tsvyk N. A. Astronomicheskij Zhurnal, 1993, **70**, 571 [in Russian].
13 Kellogg P. J., Goetz K., Howard R. L., Monson S. J. Geophys. Res. Lett., 1992, **19**, 1303.
14 Ho C. M., Strangeway R. J., Russell C. T. Geophys. Res. Lett., 1993, **20**, 2775.
15 Cairns I.H., Robinson P.A. Geophys. Res. Lett., 1992, **19**, 1069.
16 Robinson P.A., Rev. Mod. Phys., 1997, **69**, 507.
17 Krasnosel'skikh V.V., Sotnikov V.I. Sov. J. Plasma Phys., 1985, **3**, 491.
18 Pelletier G., Sol H., Asseo E. Phys.Rev., 1988, **A38**, 2552.
19 Hadzievski Lj.R., Skoric M.M., Rubenchik A.M., Shapiro E.G., Turitsyn S.K. Phys.Rev., 1990, **42A**, 3561.
20 Assalaulov Zh. A., Zakharov V.E. Sov. J. Plasma Phys., 1985, 11, 72.
21 Goldman M.V., Weatherall J.C. Phys. Fluids, 1981, **24**, 668.
22 Rowland H.L. Phys.Fluids, 1985, **28**, 190.
23 Kuznetsov E.A., Skoric M.M. Phys. Rev., 1988, **A38**, 1422.
24 Zakharov V.E. JETP Letters, 1975, **21**, 221.
25 Degtyarev L. M., Zakharov V. E., Sagdeev R. Z., Solov'ev G. I., Shapiro V. D., and Shevchenko V. I. Sov. Phys. JETP, 1983, **58**, 710.
26 Wang J.G., Payne G.l., DuBois D.F., Rose H.A. Phys. Plasmas, 1996, **3**, 111.
27 Newman D.L., Winglee R.M., Robinson P.A., Glanz J., Goldman M.V. Phys. Fluids, 1990, **B2**, 2600.
28 Kingsep A.S., Rudakov L.I., Sudan R.N. Phys. Rev. Lett., 1973, **31**, 1482.
29 Komilov K., Khakimov F. Kh., Tsytovich V. N. Radiofizika, 1979, **22**, 268 [in Russian].
30 Robinson P.A., Newman D.L. Phys. Fluids, 1990, **B2**, 2999.

31 Cheung P.Y., Wong A.Y. Phys.Fluids, 1985, **28**, 1538.
32 Cheung P.Y., Wong A.Y. Phys. Rev Lett., 1985, **55**, 1880.
33 McFarland M.D., Wong A.Y. Phys. Plasmas, 1997, **4**, 945.
34 Baranga A.B., Benford G., Tzach D. Phys. Rev. Lett.,1985, **54**, 377.
35 Karfidov D. M., Rubenchik A. M., Sergeichev K. F., and Sychev I. A. JETP Letters, 1988, 346.
36 Levron D., Benford G., Baranga B.A., James M. Phys. Fluids, 1988, **31**, 2026.
37 Janssen G. C. A. M., Granneman E. H. A., Hopman H. J. Phys. Fluids **B1**, 1989, 2488.
38 Karfidov D.M., Lukina N.A. Phys. Let., 1997, **A232**, 443.
39 Vyacheslavov L.N., Kandaurov I.V., Kruglyakov E.P., Losev M.V., Sanin A.L. Rev. Sci. Instrum., 1993, **64**, 1398.
40 Vyacheslavov L.N., Gurko V.F., Kandaurov I.V., Kruglyakov E.P., Meshkov O.I., Sanin A.L., Zharov V.F. Plasma Phys. Rep., 1998, **24**, 195.
41 Gorbach L.M., Kandaurov I.V., Kruglyakov E.P., Meshkov O.I., Sanin A.L., Vyacheslavov L.N. Plasma Phys. Rep. 1994, **20**, 45.
42 Vyacheslavov L.N., Gurko V.F., Kandaurov I.V., Kruglyakov E.P., Meshkov O.I., Sanin A.L., Zharov V.F. Plasma Phys. Rep., 1998, **24**, 211.
43 Vyacheslavov L.N., Burmasov B.S., Kandaurov I.V., Kruglyakov E.P., Meshkov O.I., Sanin A.L. Phys. Plasmas, 1995, **2**, 2224.
44 Pozzoli R., Ryutov D.D. Phys. Fluids, 1979, **22**, 1782.
45 Vyacheslavov L.N., Gurko V.F., Kandaurov I.V., Kruglyakov E.P., Meshkov O.I., Sanin A.L., Zharov V.F. Plasma Phys. Rep., 1998, **24**, 223.
46 Arzhannikov A.V., Astrelin V.T. Zhurnal Prikladnoi mekhaniki i tekhnicheskoi fiziki (J. Applied Mechnics and Technical Physics) (1979), **118** [in Russian].
47 Breizman B.N. In Review of Plasma Physics, edited by B.B. Kadomtsev, (Consultants Bureau, N.Y., 1987), vol. 15.
48 Breizman B.N., Erofeev V.I. Soviet J. Plasma Phys., 1985, **11**, 223.
49 Kaw P.K., Lin A.T., Dawson J.M. Phys. Fluids, 1973, **16**, 1967.
50 Galeev A.A., Sagdeev R.Z., Shapiro V.D., Shevchenko V.I. JETP Lett., 1976, **24**, 21.
51 Tsytovich V.N. Theory of turbulent plasma, (Consultants Bureau, N.Y., 1977).
52 Burmasov V.S., Vyacheslavov L.N., Kandaurov I.V., Kruglyakov E.P., Meshkov O.I., Sanin A.L. Plasma Phys. Rep. 1997, **23**, 142.
53 Kandaurov I.V., Kruglyakov E.P., Losev M.V., Meshkov O.I., Sanin A.L., Vyacheslavov L.N. Proc. 9th International Conf. On High Power Particle Beams, Washington DC, 1992, **2**, 1037.
54 Freund H.P., Popadopoulos K. Phys. Fluids, 1980, **23**, 732.
55 Akimoto K., Rowland H.L., Popadopoulos K. Phys. Fluids, 1988, 31, 2185.

ELECTRON-ION COLLISIONS IN STRONG MICROWAVES IN PLASMAS

A. A. Balakin, G. M. Fraiman

Institute of Applied Physics RAS, Nizhny Novgorod

The processes of electron-ion collisions in plasma in strong fields are discussed. Some arguments in favour of the determining role of near collisions in such regimes are presented There are demonstrated some effects caused by the focusing properties of the Coulomb potential both numerically and analytically. It is presented that in strong fields the effect of the "Coulomb logarithm" does not take place. Some estimation for effective scattering cross-section in strong microwaves are shown that this one is more than it was accepted earlier and, in particular, the Joulean losses in plasma are not decreasing at the field increase. The additional strong bunching effect is found. The applicability conditions of the experimental observation of the predicted effects are discussed.

The problem of the electron - ion collision efficiency in plasma at the strong electromagnetic radiation is one of the fundamental problems in plasma theory. The having existed lately insight [1-5] are based practically on a simple idea that the general contribution to collisions integral and, consequently, to cross-sections, change of the energy, harmonic generation and so on, is due to far collisions. That is, it was accepted more or less explicitly, that the collisions with large impact parameter and, correspondingly, with negligible variations of not only the scattering angles but exactly of the impact parameters at the scattering process, are determining. Practically, this is the same idea which is the Landau-Balescu-Lenard collisions integral (being quite true for weak fields) based on [6]. In present paper using conclusions of [7-8] we shall expound general reasons in favour of other results based on the knowledge that in quite strong electromagnetic fields the near collisions are determining. To begin with it should be noted that in quite rare plasma for the collisions integral characteristics determination it is enough to use the pair-collisions approximation [6]. This means that instead of the many-particles problem solutions it is enough to answer the task dealing with the collision of the electron beam with one ion in strong field of high frequency. Exactly the details of this problem in the simplest statement for the case of outer microwave with linear polarisation are represented itself the central object of investigation of the present paper. The more so, to be short, the basic features of processes will be demonstrated on the example of the problem of scattering of

electron beam propagating along the outer field (the longitudinal scattering).

The plan of the paper includes: in the beginning (the paragraph 1) we shall discuss namely the strong field conception. It will be shown that the scattering problem depends on two parameters only and the sphere of these parameters according to our interests will be separated. In p. 2 we shall demonstrate some numerical results. Hear the general attention will be paid to effects caused by the focusing properties of the Coulomb potential and mostly to the fact, that after oscillations repeated many times in the vicinity of the ion electron significantly change it impact parameter and, consequently the scattering becomes far more effective. Farther, the p. 3. we shall investigate the process of the energy changing at more remote distances. We shall considerate the impact parameters ρ at which the electron can not to attract itself effectively to the ion and consequently the change of the energy and scattering angles are known to be small values. We mean the range of impact parameters where in case of weak fields the Coulomb logarithm "gains". It will be shown that in strong fields logarithm does not take effect, because of even the negligible variation of the electron drift velocity is enough in order to the dependence of the change of energy upon the impact parameter becomes faster than $1/\rho^2$. So, we shall see that the range of "small" impact parameters causes the general contribution in change of energy. In p.4 we shall fulfilled the estimations for the effective cross-section of collisions demonstrating that the account of focusing properties of the Coulomb potential leads to larger cross-sections than having being accepted ealiar and in particular the Joulean losses in plasma are not decreasing at the field increase. In p.5 more fine effects (caused by the fact that in process of attraction the additional bunching (clustering) of electrons on phases takes place, so at the field increasing the electrons collisions moments (the moments of the very late, the nearest approach to the ion) becomes sufficiently locked to the quite determined outer field phases) are discussed. In conclusion (p. 6) the applicability conditions and some applications of presented effects are under consideration.

1. The strong laser field

Let us examine in more detail the statement of the problem and explain that we mean under the term "strong laser field". On figure 1 the typical trajectory of the electron being scattered are represented. The solid curve corresponds to the true trajectory. The dotted line

corresponds to the drift one, having been calculated by *deduction of the oscillating curve*, which is determined by the movement of electron with the charge e without the account of the Coulomb field of the ion with the charge Ze in the field $\boldsymbol{E}(r,t) = \boldsymbol{E} \cdot \sin \omega t$. The trajectory is described by the nonrelativistic Newton equation

$$m\ddot{\boldsymbol{r}} = -Ze^2/R^3\, \boldsymbol{r} + e\boldsymbol{E} \sin \omega t \,. \qquad (1)$$

For the description of the equation (1) solutions it is convenient to introduce the drift electron coordinate $\boldsymbol{r}(t)$, supposing that its full coordinate $\boldsymbol{R}(t)$ is represented in the next form:

$$\boldsymbol{R}(t) = \boldsymbol{r}(t) - \boldsymbol{r}_{\sim} \sin \Omega t, \quad \boldsymbol{r}_{\sim} = eE/m\omega^2\, \boldsymbol{z}_0 \,. \qquad (2)$$

In such way we can introduce the electron drift velocity before (v.) and after (v_+) the collision:

$$V_-(t) = v_- + v_{\sim} \cos \Omega t, \quad v_{\sim} = -eE/m\omega\, z_0 \,, \; V_+(t) = v_+ + v_{\sim} \cos \Omega t \,. \qquad (3)$$

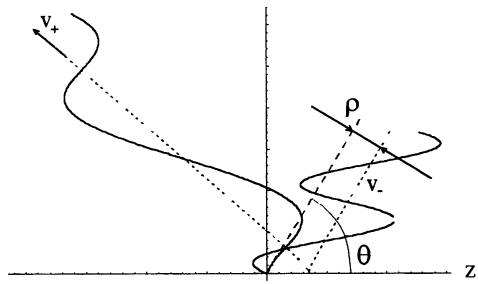

Fig. 1. The typical electron trajectory (solid line), drift trajectory (dotted line) and parameters of the scattered electron (v is the velocity, ρ is the impact parameter, θ – the angle between the velocity and the field $\boldsymbol{E}$)

The knowledge of the drift velocity v_+ dependence upon v_-, the vector of impact parameter and initial distance (or incoming phase) makes it possible to determine all necessary data of scattering. Namely, it is the effective and transport collision cross-section, the probability of transition from the initial state to the final one and so on. For example, the effective differential cross-section of scattering is determined with the expression:

$$d\sigma_{eff}(v_-, v_{\sim}, \rho) = 2 \frac{\langle v_+^2 - v_-^2 \rangle}{v_{\sim}^2} d\rho \,, \qquad (4)$$

and characterizes the non-elasticity of the scattering. Hear $d\rho$ is the square in the plane perpendicular to the direction of the beam

propagation near the vector of impact parameter ρ (fig. 1). Also, the transport cross-section of the scattering

$$d\sigma_{tr}(v_-, v_-) = \frac{\left\langle (v_+)_\perp^2 \right\rangle}{v_-^2} d\rho = \frac{dw_{tr}}{v_-^2} \qquad (5)$$

is causing the drift velocity deviation of particles from the initial direction, as $v_{+\perp}$ is the component of the full velocity at the way-out perpendicular to the beam propagation. Both in (4) and (5) the angular brackets mean the averaging on the field period. The denominator in (4) corresponds to normalisation to the average in time oscillating energy of scattered particles, and in (5) - to the square of the average drift velocity.

Now let us note that the equation (1) is being operated by the only parameter.

$$\Omega = \omega \sqrt[4]{m^2 Z / eE^3} = \omega / \omega_E . \qquad (6)$$

Indeed, after introducing the characteristic scales in form

$$r_E = \sqrt{eZ/E}, \quad \omega_E = \sqrt[4]{eE^3/m^2 Z}, \quad v_E = \sqrt[4]{Ze^3 E/m^2}, \qquad (7)$$

where r_E is the distance from the Coulomb centre, at which the ion field eZ/r_E^2 is equivalent to the amplitude of the external field E; ω_E is the characteristic frequency at the movement along the ceplerian orbit of radius r_E, $v_E = r_E \cdot \omega_E$ is the characteristic velocity at this orbit, one can get the next dimensionless equation:

$$\ddot{\boldsymbol{R}} = -\boldsymbol{R}/R^3 + \boldsymbol{n} \cos \Omega t . \qquad (8)$$

So, characteristics of the scattering of electrons on ions (such as cross-sections and frequency of collisions) are determined with only two dimensionless parameters: the relation of the initial drift velocity of electron beam to its oscillating one $v_- / v_\sim = \Omega v_-$, and the only dimensionless parameter of the equation $\Omega = \omega / \omega_E \equiv \sqrt{r_E / r_\sim}$. The first from them is the usual accepted parameter, characterising the oscillating behaviour of electron in the external microwave. The second (new one) is the condition of that the electron during its transit past the ion stays mostly wide apart from the last. In the field of large drift velocities $v_- >> v_\sim$ electrons are moving merely along the direct line without any significant oscillation, so the methods of weak electric field expansion (Born approximation, straight-line approximation) are acceptable. In inverse case of small drift velocities the electron movement proves

sufficiently modified, - it represents itself oscillations with range $r_{\sim}$, and drifting slowly with the "heat" velocity of electron. If amplitude of this oscillations ($r_{\sim}$) is small in comparison with the interaction field region (r_E) then, seemingly, the pondermotive description is appropriate. In case of large range repeating electron oscillations at the passing through the interaction field may lead to its anomalous strong attraction to ion.

Exactly this case will be interesting for us in present work mainly. Later we shall call such regimes ($\Omega << 1, \Omega\nu << 1$) like regimes with strong field (fig. 2).

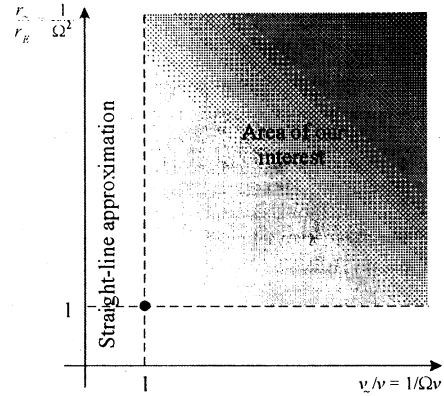

Fig. 2. The dimensionless parameters plane

During the numerical experiment the calculations has been fulfilled for free dimentionless frequency values (Ω=0.1, 0.32, 1). The electron beams with drift velocities from 10^{-2} to 10^{4} and impact parameters ρ (depending on the drift velocity) in range from 10^{-2} to 10^{3} distributed homogeneously on all phases of the fly into having been investigated. The initial distance from the Coulomb singularity to the leading particles centre was equal to $10 \cdot r_{\sim}$ ($10/\Omega^2$); the particle was considerate as having lost the interaction field if the distance between the leading centre and the Coulomb singularity becomes more than $10 \cdot r_{\sim}$. The special attention having been paid to the choice of sufficient particles number on the field period. So in separate calculations at investigation of non-elastic interactions the number of particles on the period run up to 2000.

2. Numerical results

During numerical investigation it was found that electron in the process of repeated oscillating attracted itself adiabatically to the ion from large distances (fig. 3) merely like with "parachute". As a result

separate electrons fall to small vicinity of the ion and undergo the strong scattering with large gain of energy (of the order of the oscillating energy of electron).

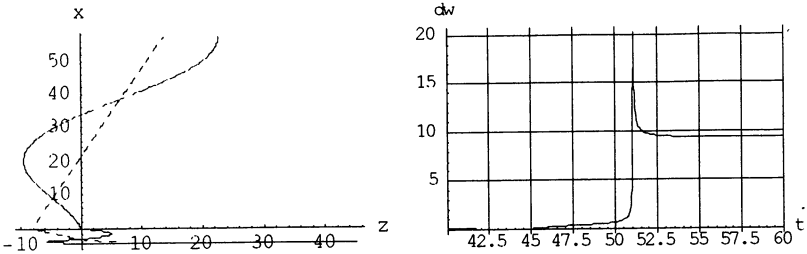

Fig. 3 On the left is the trajectory of particle (the full line) and of the drift centre (the dotted line), on the right is the dependence of the energy change from the time for Ω=0.32, ν=1

The result of such attraction is the non-monotony dependence of the energy exchange, averaged on incoming phases of many electrons, on impact parameters (fig. 4). The position of the former two maximums may be easily found analytically. So the nearest maximum coordinate is equal to $\sqrt{2\pi}r_E$. This corresponds to the electrons hit to small vicinity of the ion for half-period (one return to ion). Qualitatively the explanation of this peak consists in the next. Electron travelling past the ion undergoes the small-angle scattering and gains small transverse velocity and for the time of the half of oscillation period (due to gained transverse velocity) to pass the ion at the distance comparative to the Ruserthord radius $r_{rez}(v_\sim) = Ze^2 / mv_\sim^2$, having been estimated on the oscillations velocity. Respectively, the second peak appears for two returns (small-angle collisions) of the electron to the ion and so on. In all the number of such returns can not exceed $N \sim v_\sim / v_T$.

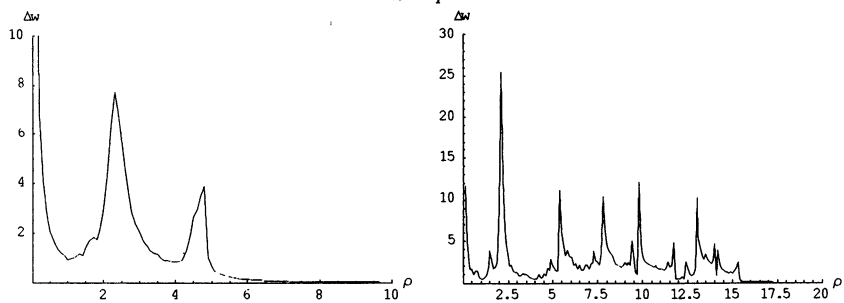

Fig. 4. Value of the energy change from the impact parameter for the longitudinal collision, averaged on the incoming phases at Ω=0.32, ν=1 (left) and Ω=0.1, ν=1 (right)

The same essential attraction exists also at the scattering of electrons beam propagating under the angle to the polarisation vector of the electric field of the laser wave. A sufficient increase of the effective cross-section and collision frequency on a factor of the order of $\nu_{\sim}/\nu_T$ is the result of this modification of attraction. Numerical calculations agree with this result (fig. 5).

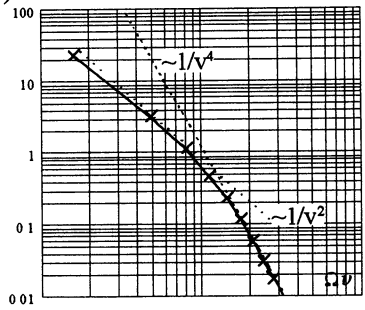

Fig. 5. The dependence of the gained energy upon velocity at the transverse scattering (double logarithmic scale) Ω=0.32; the dotted line is the dependencies $\Delta w \sim 1/v^2$ and $\Delta w \sim 1/v^4$.

The other important feature of collisions of this type is the separation from all interacted electrons the small part of electrons gaining very large energy. We named such electrons "representative". In other words the electrons distribution function becomes of two scales. One part is narrow (cold), including the most of particles, the other is wide (the width is about of oscillations velocity) and including a little of particles (fig. 6).

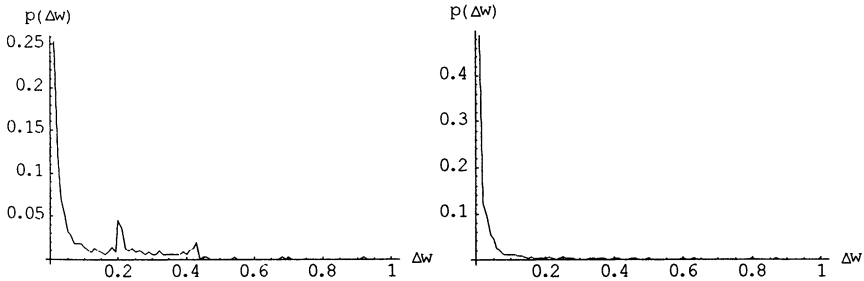

Fig. 6. The electron distribution function depending on their energy change at Ω=0.1, v=1.

This effect may be used for the effective generation of high harmonics of radiation. Indeed, as the number of "hot" particles is small and collision frequency for them after the scattering is small then they may be easily "removed" from plasma merely without variations of the distribution

function of the bulk of cold electrons. At the same time the spectrum of radiation of representative electrons is very wide which gives a possibility to construct a gear for the radiation generation on the base of Markuse effect [9], but using all plasma electrons in capacity of the beam.

At last it is necessary to consider the very important new effect - the electrons bunching at the passing the ion. This bunching is the more unusual because it take place the scattering of different electrons on different occasionally placed ions with the only synchronising mechanism - the microwave electric field. The bunching means that, instead of the homogeneous initial distribution of electrons on the field phases, quite all electrons as a result of adiabatic attraction passing the ion merely at the same field phase (fig.7). It represents the dependence of the field phase at the moment of the "last" collision (the moment of the nearest passing the ion by the electron) upon its initial (incoming) phase. All electrons begin the movement along the field from the impact distance ρ=3.2. It may be seen that the energy change with field occurs in the narrow belt of the field phases. "Steps" on this dependence corresponds to the collisions moments shift on the field half-period. With the increase of the drift velocity the electron bunching on the phases loses i.e. collisions begin to occur at occasional, not depending on the outer field phase moments of time. From another side if the microwave intensity increase the width of steps will decrease. The such phase bunching mechanism seems to be similar to the mechanism being used in electronics for the generation of electromagnetic radiation (reflecting klystron) and represents itself its distributed analogue.

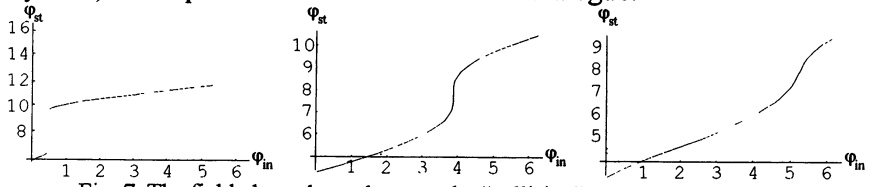

Fig. 7. The field phase dependence at the "collision" upon the initial field phase for free velocity values $v = v_{\perp}/2$, $v_{\perp}$, $3\,v_{\perp}/2$ at Ω=0.32

The such phase bunching mechanism seems to be similar to the mechanism being used in electronics for the generation of electromagnetic radiation (reflecting klystron) and represents itself its distributed analogue.

The presence of such effect leads to the possibility of appearance of quasi-discrete spectrum of the coherent braking radiation along the

propagation of the laser wave! The additional increase of the braking radiation is caused by representative electrons having initially impact parameters far more larger than Ruserthord radius established on electron oscillations velocity and being scattered intensively. The bunching degree and correspondingly the narrowness of maximums in the spectrum increases at the heat velocity decrease or the decrease of the outer field frequency or the outer field amplitude increase.

3.Why do the "Coulomb logarithm" disappear in strong fields?

One of the most untrivial results of the solution of the problem of energy exchange with the strong field consists in the absence (even at large impact distances) of the range of parameters corresponding to the so called Coulomb logarithm [6]. Let us remind how to arises such range of parameters in weak fields. If the electron oscillations radius is smaller in comparison with the distance to the Coulomb centre, i.e. impact parameters are rather large, than to solve the problem it is enough to expand the potential in the equation for the drift centre (2) on powers of the oscillations radius and to take into account the first correction term corresponding to the dipole approximation. Then actually the static ion field determines trajectory of the drift center, and energy change with the field is determined by the oscillating dipole field work along this trajectory. This problem can be easily solved [6] at impact parameters corresponding to the sphere of the sufficiently non-adiabatic interaction $\rho<v/\Omega$. One can satisfy oneself that beginning from comparatively small impact parameters, corresponding to Ruserthord radius Ze^2/mv^2, estimated on drift velocity, and right until distances corresponding the limit of the non-adiabatic zone v/Ω the estimation

$$\Delta w \sim m\tilde{v}^2 \frac{r_{rez}^2(v)}{\rho^2} e^{-\Omega\rho/v} \qquad (9)$$

is true for energy change with the field averaged on incoming phases and depending on the impact parameter. The exponent in the right part corresponds to adiabatic electron flying through the interaction field at impact parameters larger than the non-adiabatic field size. So, one can see that at integrating on impact parameters a logarithmic factor, corresponding to the energy change "cut" on this limit, occurs.

Now let us discuss how this picture changes in strong fields. The first of all one should remind that in the range of impact parameters, corresponding to "parachute" effect, the impact parameter changes

sufficiently and this range as if analogue to small impact parameters in weak fields. It is essentials that in this range drift trajectories deviate strongly in dependence from the field phase unlike weak field case. At drift velocities smaller than one (in dimensionless variables) the attraction zone limit occurs farther than the adiabatic zone limit. Because of this directly after it the exponential cutting begins.

At large drift velocities $1<v<1/\Omega$ the decrease law other from the capture zone is the power series, gradually converting to $1/\rho^2$. That is with the increase of the velocity in this zone we passing gradually to the regime with the Coulomb logarithm.

4. The effective scattering cross-section

In this paragraph there are will be fulfilled the effective scattering cross-section estimations, showing that the account of focusing properties of Coulomb potential leads to larger cross-sections than it has been accepted earlier and, in particular, the Joul losses in plasma do not decrease with the field increase. As we have seen earlier the basic contribution to the energy change the impact parameters range, from which electrons manage to attract themselves to ion, gives. The fig. 4, on which the dependence of the averaged on entrance phases electrons energy change from the impact parameter being demonstrated, shows it numerically Peaks correspond to electrons which for the integer number of half-periods from finite impact distance hit to the "zero", having the maximum velocity (kinetic energy).

It is interesting to note that at $v<<v_*$ the first peak (nearest to $\rho=0$) radius is determined only r_E and is equal to:

$$\rho_1 = \sqrt{2\pi} r_E . \qquad (10)$$

Indeed, taking into account that the oscillations radius is large in comparison with rE and, consequently, the scattering is small-angle, one comes to this estimation proposing that electron covers for half-period the distance equivalent to the initial impact parameter.

The similar estimation for electron, having possibility to attract itself to the zero for half-period, leads to the next limit of the zone of "strong collisions".

$$\rho_{st} \sim \frac{1}{\Omega v} = \frac{v_*}{v} r_E . \qquad (11)$$

It is essential that the size of this zone increase with the field increase (i.e with the oscillation velocity).

The effective scattering cross-section can be calculated by the integration of dependencies (of the type of the one being shown on fig. 4) on impact parameters and by dividing (according to (4)) on electron oscillations energy. In case of longitudinal electrons scattering for this value

$$\sigma_{eff} \approx \frac{4\pi\Omega^2}{\nu^2} \tag{12}$$

is true with good accuracy.

Let us stress once more that exactly electrons with impact parameters in the range $0<\rho<\rho_{at}$ provides the general contribution to this value. Outer from this range the energy change becomes exponentially weak, so the effect of the type of the Coulomb logarithm is absent*.

The angle dependence for the effective cross-section may be determined in the same way. For more details see [7-8]. Let us just note hear that for small drift velocities the effective cross-section sign always corresponds to damping and its value is lightly anisotropic on the angle between the beam and outer field. The dependence of the full effective cross-section (after the integration on angles) is represented on fig.5. It may be approximated with good accuracy by the expression (in dimension form):

$$\sigma_{eff} \approx \frac{4\pi\left(Ze^2\right)^2}{m^2\nu^2 v_{\sim}^{\ 2}}. \tag{13}$$

From the point of view of applications one of the most interesting consequences of this dependence consists in the obvious conclusion that the energy contribution to plasma (the Joule heating) does not damp with the field increase but goes into saturation. Really, accounting, energy contribution being $Q_{eff} = \nu_{eff} W_{\sim} = \sigma_{eff} N \nu W_{\sim} = \frac{2\pi\left(Ze^2\right)^2}{m\nu}$, we can see that this value does not depend at large oscillations energies upon field and is determined only by the pure drift characteristics.

---

* It should be noted, the absence of the energy change averaged on phases means that the part of electrons increases its energy and other part decreases the one on the same value. That is, it may means the diffusion energy spreading of the monoenergetic beam and consequently the arise of diffusion in velocities space. Detailed analysis of this question is out of frames of the present paper.

5. Strong correlation at e-i collision

The main feature of radiation in super strong fields is a significant increase of radiation due to appearing of the representative electrons [7]. They appear as a result of attraction increasing caused by multiple correlated returns of these electrons to the single ion with sequent large angle collision (with large energy change). It is obvious that these electrons also radiate strongly. These effects are demonstrated in fig. 8.

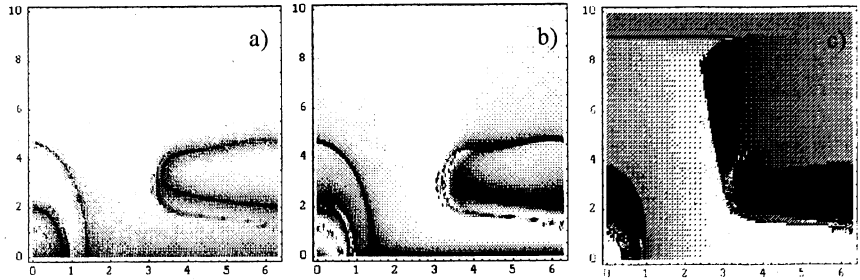

Fig 8 The minimal distance (a), energy change (b) and collisional phase (c) depending on impact parameter and incoming phase for ν=1, Ω=0.32

We had talk above about a) and b) figures. The dark color on these dependencies means more energy exchange electrons and less impact parameters at "last" collision. This is understandable that strong exchange have the particles with less minimal distance. But what is really new: all collisions from the attraction region take place in the same time (fig. 8c). Qualitatively this effect is the consequence of the strong transversal correlation for all elctrons from "parashut" region (11). These effect then stronger then microwave intensity more.

Let us remind that in the framework of classical model of bremsstrahlung the randomness assumption of collision moment is adopted and as a result the coherent component of radiation is absent. In the case of scattering over an UH electromagnetic field the situation changes cardinally.

6. Conclusion

The picture of collision processes of electrons with ions in strong fields undergoes sufficient modifications even in rare plasma. And this caused by not only quantitative effects, demonstrating monotonous increase of energy contribution with the field increase. First of all, the difference from weak fields consists in that the sufficient energy change zone determines itself by not so much the sizes of non-adiabatic

collisions zone $\rho < v/\Omega$ as far smaller size (11). Within this zone strong energy changes are sufficient, then the energy of the order of oscillations one immediately transfers to the heat (not regulated) movement. That is the size of the zone of sufficient energy change is defined with the scale on which the electron can manage to attract itself to the ion at repeated oscillations near the ion. Moreover, since the Coulomb logarithm effect disappears the collision efficiency depends upon the ion charge sign. In case of negative ions the picture and the collisions efficiency should be absolutely different than in case of positive ones.

In definite sense plasma in strong field becomes as if more transparent. The matter is electrons feel the ions field (from the energy change positions) at smaller distances than in weak fields.

Concerning the condition of the adequacy of this consideration it is enough to require that the interaction volume $\sigma_{eff} r_{\sim}$ was smaller than the inverse plasma density. That is in the same collision process not more than one ion takes part. Exactly using of such approach having been good practice beginning from Boltsman. With the account of (13) this leads to the simple estimation

$$r_E << r_d \qquad (14)$$

or in dimension form (where the electrons temperature T in eV, the radiation power P in W/cm^2, electrons concentration n in cm^3)

$$n << 7.44 \cdot 10^{13} \cdot T\sqrt{P} \,. \qquad (15)$$

That is with the field increasing the acceptability conditions becomes more feasible.

One should note that mentioned "transparency" takes place only with regards to energetic processes. The matter is, as it was noted in [7-8], the transport collision cross-section depends on field quite weakly. The discussion of this rather inquisitive effect is out of the present work frames. We shall only note hear that the cross-section of transport collisions, which is in response for the electrons distribution function isotropization, is proportional to v^{-4}, i.e. is sufficiently larger than the energy change cross-section.

The big group of expected effects connects with more fine collision process characteristics. First of all, we have seen that electrons from the "parashut" zone (2) in the process of attraction to the ion is bunching on phase, converging to the field zeroes phases (to maximum oscillations velocity). This means that in strong fields these electrons will undergo strong accelerating at last scattering and then will swiftly quit the ion. But the same means that them will emit far more effective braking

radiation. In particular, at rather strong fields harmonics of falling radiation should demonstrate themselves since their intensity may be proportional to the concentration square, but not to the first degree, as it takes place in weak fields. To discover these effects one should think about the deviation from the background braking radiation, caused by all other electrons. More over, one may try to organise the resonant system for harmonics. At this the laser field will be used in capacity of a pumping field.

Let us formulate now all conditions of correctness of our consideration in convenient for the experiment form (lower the time will be in c, wave frequency - in ω 1/sec; wavelength λ in cm; plasma concentration n in cm^3; electrons temperature T in eV; laser radiation flux density P in W/cm^2):

- the condition of the determining role of pair collisions

$$nV_{int} = nr_{\sim}\sigma_{eff} << 1 \Leftrightarrow r_E << r_d \qquad n << 7.44 \cdot 10^{13} \cdot T\sqrt{P}$$

- the condition of the strong field regime

$$\nu << \nu_{\sim} \qquad T << 1.87 \cdot 10^{-5} \cdot P\lambda^2, \quad T << 6.64 \cdot 10^{17} \cdot P/\omega^2$$

$$\omega << \omega_E \qquad \lambda >> 9.46 \cdot P^{-3/8}, \quad \omega << 1.99 \cdot 10^{10} \cdot P^{3/8}$$

- the condition on the impulse duration

$$\tau_{imp} >> \frac{\nu_{\sim}}{\nu}\frac{2\pi}{\omega} \qquad \tau_{imp} >> 5.11 \cdot 10^9 \sqrt{\frac{P}{T}}\frac{1}{\omega^2}$$

This inequalities show that regimes of electrons-ions collisions, corresponding to expounded ideas, may be comparatively easy realised both in laser and microwave (centimeters and millimeters) wavelengths range. For example at the wavelength 5 cm, $n \sim 10^{11}$ cm^3, $T \sim 1$ eV, it is enough that P>3 кВт/см^2. Similarly in laser range λ=1 mkm it is enough that $P>2 \cdot 10^{13}$ W/cm^2.

At last, let us compare our considerations with the classical ones. Generally speaking, this question already as itself is rather non-trivial. More detail analysis will be fulfilled in the separate paper. Hear we shall note that conditions of such approximation seemingly are rather weak and may be developed from the next considerations. The most interesting for us was electrons scattering with large variations of impulses and consequently in small vicinity of the ion. To the first view, estimating there de-broil wave length and requiring it to be smaller than radius of the scattering zone, estimated on oscillations velocity: we come to the condition $mv_{\sim}^2 >> \hbar\omega$. That is conditions are worse with the field

increase. From the other side, it is widely known [10] that the solution of the quantum problem of scattering in Coulomb field coincides exactly with the classical problem solution. That is the zone, where the Coulomb field is dominating, is the zone of quasi-classical consideration. Therefore we need to satisfy just the condition that the de-broil wave length, estimated on oscillations velocity, is small in comparison with the size of the zone within which outer field influences weakly on the dynamics, i.e. is small in comparison with the Coulomb field $eEr_E = \sqrt{Ze^3E} >> \hbar\omega$. It is clear that with the field increase this condition becomes weaker.

The work has been performed under support of the Russian fund of fundamental investigation (the grant number № 99-02-16443).

References

1 J Dawson and C Oberman Phys Fluids **5**, 517 (1962).

2 V P Silin, Zh Eksp Teor Fiz **47**, 2254 (1964).; V P. Silin, Quantum Electronics **29**, 11-18 (1999)

3 N M Kroll and K. M Watson, Phys. Rev A **8**, 804 (1973); F V. Bunkin A. E. Kazakov and M V Fedorov, Sov. Phys. Uspekhi **107**, 559 (1972); M.H Mittleman, *Introduction to the Theory of Laser-Atom Interactions*, Plenum Press, New York and London, 1993

4 C D Decker, W B Mori, J. M Dawson and T Katsouleas, Phys. Plasmas **1**, 4043, (1994)

5 G Shvets and N.J Fisch, Phys Plasmas 4, 428 (1997).

6 E M Lifshitz and L.P Pitaevski, *Physical Kinetics*, Pergamon, Oxford, 1981.

7 G M Fraiman, V.A. Mironov, A A. Balakin Phys. Rev Lett. **82**, 319 (1999); G M Fraiman, V A Mironov, A.A Balakin, Zh Eksp Teor. Fiz. **115**, 463 (1999) [J Exp Theor Phys **88**, 254 (1999)]

8 G M Fraiman, V.A. Mironov, A.A. Balakin preprint of IAP RAS №442 (1997); G M. Fraiman, V A Mironov, A A. Balakin preprint of IAP RAS №468 (1998).

9 Marcuse D , Bell Syst Techn J. **41**, 1557 (1962); M.V. Fedorov, *Interaction of Intense Laser Light with Free Electrons*, Harwood Academic Publishers, Chur (1991)

10 L D Landau and E.M Lifshitz, *Quantum Mechanics*, Pergamon, Oxford.

RADAR MICROWAVE SCATTERING IN THE UPPER HYBRID RESONANCE A FEASIBLE DIAGNOSTICS OF SMALL SCALE WAVES AND FLUCTUATIONS IN TOKAMAK PLASMAS

D.G. Bulyiginskiy, A.D. Gurchenko, E.Z. Gusakov, V.V. Korkin, M. M. Larionov, K.M. Novik, Yu.V. Petrov, A.Yu. Popov, A.N. Saveliev, V.L. Selenin, A.Yu. Stepanov

Ioffe Physico-Technical Institute, St.Petersburg, Russia

The first results of the RADAR UHR scattering scheme application to study of density and magnetic turbulence in tokamak plasmas as well as the investigation of Lower Hybrid wave propagation and conversion into the Ion Bernstein wave are given in the present paper.

Introduction

Investigation of plasma fluctuations attracts considerable attention at present. A suitable tool for diagnosing density fluctuations or waves in a plasma with modest parameters is microwave Back Scattering (BS) in the Upper Hybrid Resonance (UHR) [1-3]. In this method, the probing is performed by an extraordinary wave, and the signal back scattered off low-frequency electron density fluctuations in the UHR region, given by condition

$$\omega_i^2 = \omega_{ce}^2(x) + \omega_{pe}^2(x), \qquad (1)$$

is detected. When approaching the resonance point, the wave number grows strongly, taking values much larger than the vacuum value $k_0 = \omega_i / c$ (ω_i is the incident wave frequency). This provides a way to observe small-scale fluctuations. The amplitudes of the incident and back-scattered waves increase along with the wave number, thus leading to strongly enhanced BS signals. Moreover, a high spatial resolution can be achieved since this process is localised to the resonance region. A single antenna can be taken to launch the probing wave as well as to receive the scattered signal whereby the spatial distribution of the fluctuations can be scanned by displacing the UHR layer due to the variation of probing frequency or magnetic field.

Due to the strong spatial variation of the incident wave number near the UHR, the Bragg condition for BS can be fulfilled in a wide range of fluctuation scales, which may contribute to the BS signal. Because of this integral feature, less a priori information on the fluctuation phenomena under investigation is generally needed to design the scattering diagnostics.

During the last decade, the BS experiments have been focused on three main problems, the BS diagnostics of spontaneously excited density fluctuations [4-6], the study of lower-hybrid waves [7-9], and the investigation of parametric instabilities [10-13].

In the above experiments, the BS diagnostics was applied both on linear plasma devices and on tokamaks providing information on small-scale plasma phenomena in the inner part of plasma discharges. However, the data obtained were mainly qualitative because of the poor wave number resolution, which is consequence of integration in a wide range of fluctuation wave number spectrum, mentioned above.

To improve the wave number resolution, the time-of-flight technique has been proposed recently [14-16]. It is based on the fact that the time delay of the signal scattered in the UHR depends linearly on the wave number of fluctuations q as

$$t_d = 2q\omega_i \Big/ \left| \frac{\partial \omega_{pe}^2}{\partial x} + \frac{\partial \omega_{ce}^2}{\partial x} \right| \qquad (2)$$

Two versions of the BS time-of-flight technique were developed [17]. The first method uses microwave pulses for the probing and employs a stroboscopic technique for detecting the scattered signal. It was applied to investigate parametrically driven ion acoustic waves [18]; lower-hybrid wave propagation and decay instability [19,20], and small-scale low frequency turbulence [19]. The second modification utilises a frequency-modulated incident wave. It was applied to measure lower-hybrid wave spectra [21].

The BS in the UHR fails to solve the problem of magnetic turbulence diagnostics in tokamak because of low relative level of magnetic fluctuations, compared to the fluctuations of density. The Cross-Polarisation Scattering (CPS) in the UHR, resulting in the extraordinary to ordinary (X→O) mode conversion, can be used for this purpose instead. This approach is based on the suppression of the CPS signal caused by density fluctuations in the experimental geometry utilising microwave probing perpendicular to the tokamak magnetic field [22]. The CPS effect was used on Tore Supra [23], where the X→O conversion was studied under conditions when the O-mode receiving antenna was protected from the higher level X-mode radiation forward scattered from the density fluctuations by the cut off and thick evanescent layer. The level of magnetic turbulence was estimated in this experiment, however the localisation of measurements and wave number resolution there was

poor. The UHR CPS scheme is free from these drawbacks.

The expected merits of the UHR CPS scheme are as follows:

1. Localisation of the CPS from small scale fluctuations by the position of the UHR;
2. Wide fluctuation wave number spectrum available for diagnostics in the simple 1D probing scheme;
3. Possibility of fluctuation wave number measurements using experiments with time of flight resolution [18];
4. X → O and O → X CPS cross-section increase in the UHR [24];
5. Suppression of the CPS caused by density fluctuations due to the perpendicular propagation of the incident wave in the UHR [24];
6. Absorption in the UHR of the parasitic X → X radiation forward scattered from the density fluctuations;
7. Electron cyclotron absorption of the spurious O-mode component of the probing wave.

The first results of the RADAR UHR scattering scheme application to study of density and magnetic turbulence in tokamak plasmas as well as the investigation of Lower Hybrid (LH) wave propagation and conversion into the Ion Bernstein (IB) wave are given in the present paper.

Investigation of density and magnetic turbulence.

The experiment was performed at the FT-1 tokamak (R=62.5cm, a=15cm, B_t=1T, I_p=30kA, $T_e(0)\cong$400eV, $n_e(0)=10^{13}cm^{-3}$) [25]. The probing extraordinary wave at frequency 28.05GHz, power 50W was launched into the plasma from high magnetic field side of the torus. A short (7ns) pulse amplitude modulation of the incident wave was used with repetition time of 70ns. The gate technique was utilized for the scattered signal time delay measurements. The near by standing X-mode receiving horn antenna and the O-mode antenna at the low field side were used to pick up the BS and CPS signals. The antennae diagram angular width was 15°, where as their mode selectivity was better than 10^{-2}.

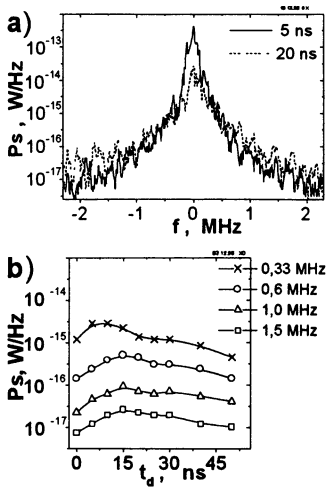

Fig.1. a) The UHR CPS spectra; b) signal dependence on the time delay for different frequency components

The CPS spectra measured with time

of flight resolution at magnetic field 9.9kGs (r_{UH}=13.3cm) are shown in Fig.1a for t_d=5ns and 25ns. These spectra are quasi Lorenzian. The width of the CPS line increases with the time delay of measurements. The maximal amplitude is decreasing with the time delay till saturation, which takes place at t_d=30ns at the level 3×10^{-13}W/Hz. This saturation level is determined by the continuous scattering of the probing wave, suppressed by the modulator to the -20dB level. Unlike the line maximum, the behaviour of the spectrum wings is not monotonic. At frequencies shifted by $|f_s-f_i|$>0.3MHz the CPS signal first increases with time delay and then decreases (Fig.1b).

Quite unexpectedly the X-mode scattered component was also observed at the low field side. The corresponding scattering spectra are shown in Fig.2a. The scattering line amplitude is comparable for this X and O-mode scattering components, where as the spectrum form is much different. Unlike O-mode, the X-mode spectra are triangular in the logarithmic scale and thus depend exponentially on the frequency shift. They are much broader, than those for the O-mode, at small time delays t_d <20ns and thus the level of the X-mode component with big frequency shift is typically a factor of 3 higher. The dependencies of the X-mode scattered signal on time delay are shown for different frequency shifts in Fig.2b. Unlike the O-mode case, these dependencies are typically monotonic. The wide X-mode spectrum observed at the low field side is not likely to be generated by scattering in the UHR. Because of large width of the evanescent region it should be strongly suppressed. Most likely this X-mode is produced by depolarising reflection of the spurious incident O-mode at the wall. Its spectral broadening could be produced as a result of propagation in the turbulent zone between the wall and the X-mode cut-off. This supposition is supported by similarity of spectra observed for the X-mode (Fig.2a) and those, observed in the reflectometry mode in Fig.4a or for the X→O CPS in the absence of the UHR.

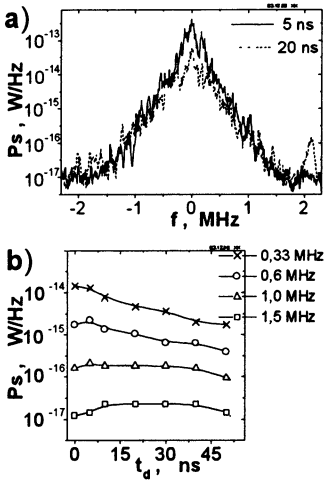

Fig.2. a) The scattered X-mode spectra; b) signal dependence on the time delay

The UHR BS spectra observed at H=9.9kGs are shown in Fig.3a. The amplitude of the BS line is smaller than that of the CPS one (Fig.1a), however its wings are much broader. These wings are very small at small time delay t_d=0ns, but they become much more pronounced for larger time delay, when the central part of the spectrum quickly decreases. The non-suppressed line at the incident frequency corresponds to the continuously acting part of the incident wave, attenuated by the modulator and directly coupled to the receiving horn antenna. When the UHR is not accessible at low magnetic field H=6.9kGs, the BS signal is

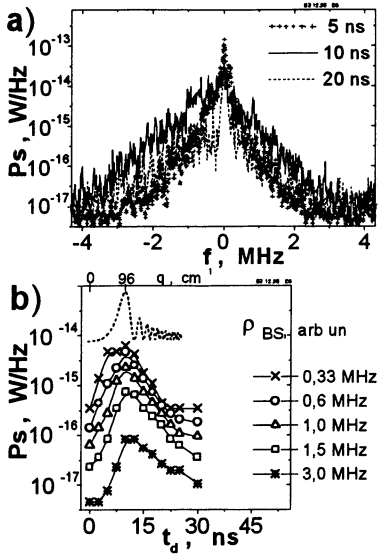

Fig.3. a) The UHR BS spectra; b) signal dependence on the time delay and the dependence of BS efficiency on the corresponding turbulence wave numbers

measured in reflectometry scattering mode. It is a factor of 10dB larger than the signal in the UHR BS mode. The corresponding spectra are shown in Fig.4a. They are triangular, less broad than in Fig.3a, and their time evolution is very different. In the UHR mode the BS signal possess the well pronounced, sharp maximum at t_d=10ns for all, but incident, frequencies (see Fig.3b). More than a 10dB variation of the BS signal is observed there. The maximal values of the BS signal exceed the corresponding values of CPS at the same frequencies by 3 – 10 dB. On contrary, the time delay behaviour of BS frequency components in the reflectometry mode is monotonic (see Fig.4b) and smooth.

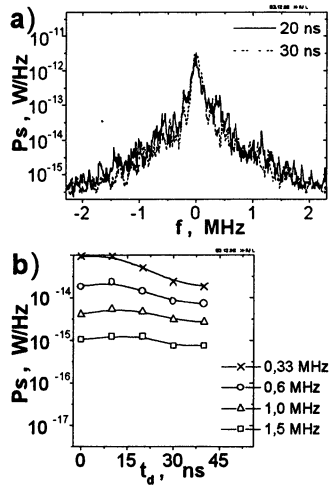

Fig.4. a) The X-mode reflectometry spectra; b) signal dependence on the time delay

The maximum shown in Fig.3b could be explained by the dependence of BS efficiency on the fluctuation wave number, shown in Fig.3b by dotted line, which according to [3] possess a maximum, when $q_x = 2k_{conv} \equiv 2k_c\sqrt{c/v_{Te}}$, and BS takes place in the linear conversion point. For $T_e(r_{UH}) \approx 70$eV, $2k_{conv}=96\text{cm}^{-1}$, close to the wave number $q=104\text{cm}^{-1}$, corresponding to $t_d=10$ns, according to the theoretical dependence (2).

Another interesting peculiarity of the BS, as well as CPS, spectra is strong broadening with the growing time delay or fluctuation wave number. The spectrum width is roughly proportional to the wave number, so that different spectra looks similar after compression of the frequency scale by the factor equal to the ratio of measurement time delays. One of the possible interpretations of the above observations could be given in terms of Doppler broadening of scattering spectra in the turbulent media [26]. The BS spectrum shape in this case should be determined by the distribution function of the turbulence velocity component. However this mechanism fails to explain different width of BS and CPS spectra, measured at the same time delay. Alternative explanation of the above peculiarities of BS and CPS spectra is based on the effect of growth of poloidal wave number of the incident X-mode in the UHR, which is roughly given for FT-1 by $k_\theta=\eta k_{\theta 0}k_r$, where η=0.15cm, $k_{\theta 0}$ is initial value of k_θ in the ray tracing and k_r is the radial wave number. The ray trajectories for the X mode and corresponding dependencies of k_θ on k_r are shown in Fig.5. The BS frequency spectrum width in this model is determined by the Doppler broadening $\delta f=2k_\theta v/2\pi$ and in the case of gaussian antenna pattern $p_i^2 \propto \exp\left[-(k_{\theta 0}\rho)^2\right]$ is given by $p_{BS} \propto \exp\left[-(2\pi\delta f\rho)^2/(\eta q v)^2\right]$,

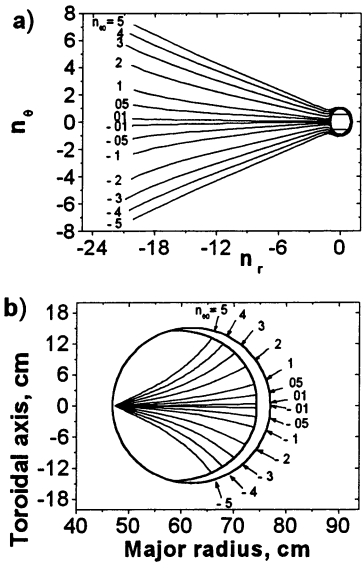

Fig.5. Ray tracing for the incident X-mode. a) Dependence of the poloidal wave number on the radial wave number; b) projections of the ray trajectories to the poloidal cross-section.

where $q=2k_r$, $\rho\approx1.45$cm. The CPS spectrum width in this model is also determined by the Doppler shift effect, but the spectrum is proportional not to the probing wave diagram, but rather to the poloidal distribution of the receiving antenna field in the frontogenetic zone. Supposing it also gaussian $E_z^2 \propto \exp\left[-2y^2/\rho^2\right]$ and using the linear approximation of the ray trajectory poloidal shift dependence on $k_{\theta 0}$ - $y_{UH}(k_{\theta 0}) \approx \beta k_{\theta 0}$, one obtain the CPS spectrum as $p_{CPS} \propto \exp\left[-2(2\pi\beta\delta f)^2/(\eta q v \rho)^2\right]$. Parameter β here is determined from ray tracing as $\beta=7\text{cm}^2$. The ratio of the BS and CPS spectral width in this model is given by $2^{1/2}\beta/\rho^2\cong5$, in rough agreement with the experimental results. The poloidal velocity v, necessary for description of both spectra, $2.5\times10^5\text{cm/s} < v < 5\times10^5\text{cm/s}$ is close to the electron diamagnetic drift velocity, calculated for FT-1 edge plasma parameters [25] $v=5\times10^5$cm/s. The experimental results for both BS and CPS are consistent with fluctuation wave number spectrum decreasing as q^{-3}. The rough estimation of the density and magnetic field perturbation, based on the q^{-3} dependence extrapolation to larger scales and on the turbulence isotropy supposition results in values of $\delta n/n_{UH} \approx 1\times10^{-2}$ and $\delta B/B_0 \approx 4\times10^{-4}$.

Investigation of the Lower Hybrid wave propagation and conversion.

The slow wave linear conversion in the Lower Hybrid Resonance (LHR) was proposed as a promising mechanism of ion heating in a tokamak plasmas in beginning of 70th. Since that time the investigations of this method were performed at different machines, utilizing different frequencies in the range from 300MHz to 2.5GHz [27]. In spite of numerous attempts, the role of the LHR in the slow wave absorption was not clearly demonstrated and effective ion heating was not achieved. Evidences of a rather complicated picture of LH wave interaction with plasma, including nonlinear phenomena, was found instead, appealing for development of new sensitive methods of plasma wave diagnostics in a hot tokamak plasmas. The results of the application of RADAR BS diagnostics to study of LH waves propagation in FT-1 tokamak carried out at different plasma densities and RF powers are given in the present part of the paper.

The experiments were carried out at the FT-1 tokamak in discharges with two density levels $n_e(0)=0.7\times10^{13}\text{cm}^{-3}$ and $n_e(0)= 1.1\times10^{13}\text{cm}^{-3}$, referenced below as low and high density discharge. The LH wave at frequency 360 MHz was excited in plasma by a loop antenna. The

experiment was performed at two power levels 22 and 50kW. The microwave probing at frequency 27.6 GHz and power 50 W was performed both in the cross-section of LH antenna and opposite to it. (These cross-sections are mentioned below as LH and BS.) The X-mode emitting and receiving horn antennae were positioned in the equatorial plane at high magnetic field side of the torus. The amplitude modulation of the incident wave at frequency 10 MHz was used to get the time of flight resolved data. The AM phase delay measurement scheme was discussed in detail in [28]. The time delay of the scattered signal was determined using the value of the phase shift of its modulation in respect to the incident wave. Dependencies of the frequency spectrum, power and time delay of the BS signal in the 60 MHz band on the toroidal magnetic field were studied in the experiment for both the down and up shifted spectrum components, corresponding to LH waves propagating correspondingly into and outside the plasma.

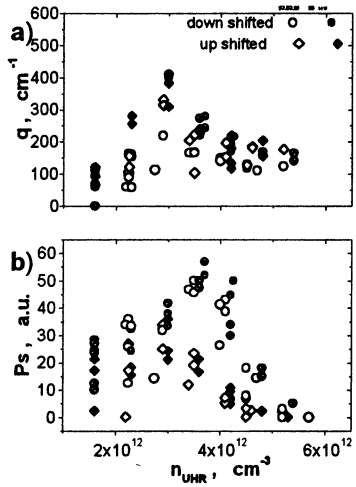

Fig.6. LH wave number (a) and ES power (b) in the ES cross-section versus n_{UHR} (P_{LH}=22kW, $n_e(0)=7\times10^{12}cm^{-3}$). Open and dark symbols correspond to beginning and end of RF pulse.

These dependencies, measured in the BS cross-section are shown in Fig.6a,b for the case of low density and low LH power. The magnetic field is expressed there in terms of n_{UH}, using (1). As it is seen in Fig.6a, the LH perturbation radial wave number increases with increasing n_{UH} for both spectral components. At $n_{UH}=3\times10^{13}cm^{-3}$ the wave number is maximal $q=400cm^{-1}$ and then decreases to the level $q=150cm^{-1}$ when $n_{UH}=5.5\times10^{13}$ cm^{-3}.

At low densities $n_{UH}<3\times10^{13}cm^{-3}$ the BS power is

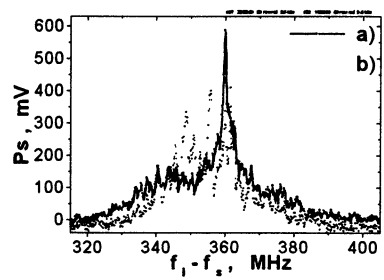

Fig.7. ES spectrum down-shifted component a) P_{LH}=22kW, $n_e(0)=7\times10^{12}cm^{-3}$, B_0=8.5kGs; b) P_{LH}=50kW, $n_e(0)=1.1\times10^{13}cm^{-3}$, B_0=9.6kGs

also comparable for up and down shifted components. However at larger UH densities, as it is shown in Fig.6b, the down shifted component dominates and, thus, the power of the wave propagating inside the plasma is a factor of 3 higher. The 3MHz wide LH line, shifted by 360MHz, is dominant in the spectrum under these conditions (see Fig.7a). The high values of wave number, observed in the experiment, could not be attributed to LH wave and are only possible for Ion Bernstein Waves (IBW). To explain the above observations one could suppose that at $n_{UH}>3\times10^{12}cm^{-3}$ ($H<10kGs$) the UHR is situated in the region of energy inflow, close to the LH resonance layer. Where as at lower n_{UH} (higher magnetic fields) BS takes place far from the LH power stream.

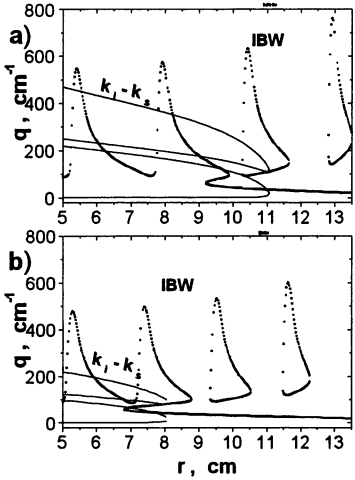

Fig.8. Dispersion curves for LH waves and probing waves (k_i - k_S).
a) B=9.5kGs; b) B=8kGs

In order to check this supposition the dispersion curves of IBW and probing X-mode were analyzed in 1D geometry, only valid after linear wave conversion in the LHR. These curves are shown in Fig.8 by dotted lines for IBW and by solid for the difference of incident and scattered wave number k_i-k_s. As it is seen in Fig.8a at H=9.5kGs, $n_{UH}=3.5\times10^{12}cm^{-3}$ the Bragg resonance conditions for BS – $q=k_i-k_s$ is fulfilled at q=400cm^{-1} . At smaller magnetic field H=8kGs, $n_{UH}=4.7\times10^{12}cm^{-3}$ the Bragg resonance conditions could be fulfilled only at q=150cm^{-1}. Both values are close to the observed in Fig.8b, but nevertheless it is necessary to check if the linear conversion could take place in the BS cross-section at $H\approx$9.5kGs. The φθ projections of the LH wave ray trajectories, calculated at different magnetic fields, confirming this possibility are shown in Fig.9. The ray trajectories are started in the LH antenna cross-section with initial value of parallel

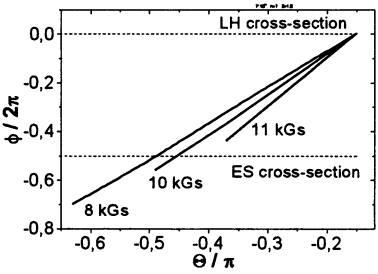

Fig.9. LH wave ray trajectories in the φΘ plane $n_e(0)=1.1\times10^{13}cm^{-3}$

refractive index $N_{//}$=7 and finished after wave absorption in the LHR.

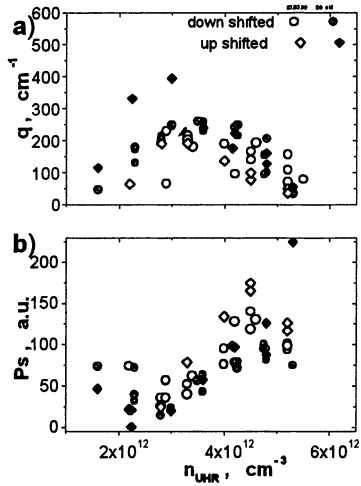

Fig.10. LH wave number (a) and ES power (b) in the LH cross-section versus n_{UHR} (P_{LH}=22kW, $n_e(0)=7\times10^{12}cm^{-3}$)

According to [29], the value of z_{eff}=1.8, which is lower than typical for FT-1, was used in the ray tracing for this low density discharge.

The distributions of $q(n_{UH})$ and $p_s(n_{UH})$, measured in the same discharge in the LH cross-section are shown in Fig.10a,b. The wave number distributions, seen there are similar to those shown in Fig.6a, where as the BS power behavior is different. It increases, when the UHR is approaching the LH antenna, possess a minimum at $n_{UH}=3\times10^{12}cm^{-3}$ and then increases till the highest n_{UH} available in the experiment. Unlike Fig.6b, down and up-shifted satellites are comparable there and no maximum exists in the dependencies. This observation is in qualitive agreement with the ray tracing prediction, that for H>8kGs majority of ray trajectories reachs the LHR before the LH cross-section and only at H<8kGs, at lowest magnetic fields, where BS is possible, the linear conversion takes place in this cross-section.

In the higher density discharge and at higher power the observed BS spectrum is much broader (see Fig.7b), no exact LH line is observed. The wave numbers measured in the BS cross-section in low density discharge at 50kW of LH power are plotted in Fig.11a. The observed q values are much higher than at 22kW. They are increasing from the beginning of the RF pulse to its end following the growth of the plasma

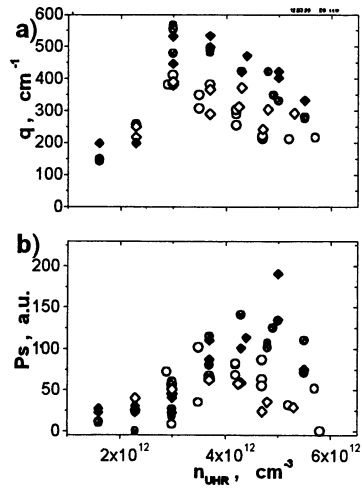

Fig.11. LH wave number (a) and ES power (b) in the ES cross-section versus n_{UHR} (P_{LH}=50kW, $n_e(0)=8\times10^{12}cm^{-3}$)

density from $n_e(0)=0.8\times10^{13}cm^{-3}$ to $n_e(0)= 1.2\times10^{13}cm^{-3}$. The BS power distribution shown in Fig.11b is similar for both spectrum components. The BS signal also increases from the beginning of the pulse to its end for both up and down-shifted components. The observed peculiarities of the BS signal behavior are most likely related to the nonlinear effects, which became more pronounced at higher density and LH power.

Conclusions.

The comparative study of the UHR CPS and BS produced by spontaneous tokamak turbulence in FT-1 have confirmed the feasibility of the diagnostics under development. The CPS effect produced by magnetic turbulence component was observed and the CPS spectra were shown to be different from those produced by BS effect and by reflectometry scattering. The RADAR scheme was shown to be effective tool for carrying out the wave number resolved measurements. The mechanism of CPS and BS spectra broadening in the UHR, related to the increase of the poloidal probing wave number in the UHR was proposed.

Investigation of the LH wave propagation in tokamak plasmas have shown that in the edge plasma, far from the calculated LH resonance cone zone, the LH wave spectrum is very broad, up to 10 MHz and no evident energy flow direction is seen. The typical radial wavelength of 0.06 – 0.12 cm is measured for scattered LH waves in this region. At small LH power and low plasma density, in the LH wave propagation region close to the LH resonance, the frequency spectrum is narrow (2-3 MHz) and propagation direction into the plasma is well pronounced in agreement with linear theory. The LH radial wavelength in this region is 0.03 cm. The small scale high number Ion Bernstein harmonics, which are produced by linear wave conversion in the LH resonance were also observed. There wavelength is shown to be 0.01 – 0.015 cm.

At higher LH power and plasma density the linear propagation picture is no longer observed. The wave numbers increases by a factor of 2, the frequency spectra become broader and no dominant direction of the energy flow is observed.

Acknowledgments.

The paper was supported by INTAS grant 97-11018, RFBR grants 98-02-18348; 96-15-96367, 99-02-17975, by the grant of RF Science Ministry and by the grant of FOM-Institute for Plasma Physics.

References.

1. Piliya A.D., 1966, Zh.Tech.Fiz. **36**, 2195.

2. Fidone I. 1973, Phys. Fluids **16,** 1680
3. Novik K.M. and Piliya A.D., 1994, Plasma Phys. Control. Fusion **35**, 357.
4. Budnikov V.N., Varfolomeev V.I., Novik K.M. and Piliya A.D. 1980, Fiz. Plazmy **6**, 1050.
5. Budnikov V. N., Kaganskaya M. N, Novik K. M., Piliya A. D., Selenin V. L., and Esterkin A.R. 1993, Fiz. Plazmy **19**, 92
6. Aleksandrov V.O., Budnikov V.N., Esipov L. A., Kornienkov V.K., Miroshnichenko V.S., Novik K. M., Stepanov A.Yu., 1989 Pis'ma Zh. Tekh. Fiz. **15**, 40
7. Budnikov V. N., Kaganskaya M. N, Novik K. M., Piliya A. D., and Selenin V. L., 1987, Proc. Inter. Conf. on Plasma Physics (Kiev, 1987) Vol.3, p.137
8. Novik K.M., 1986, Proc. Course Basic and Advanced Diagnostic Technique for Fusion Plasmas (Varenna,1986) Vol II, p.517.
9. Aleksandrov V.O., Budnikov V.N., Dyachenko V.V., Esipov L. A., Novik K. M., Piliya A. D., Stepanov A.Yu., Scherbinin O.N., 1986, Vopr. At. Nauki Tekh., Termoyadernyi Sintez, 1, 30
10. Arkhipenko V.I., Budnikov V.N., Gusakov E.Z., Romanchuk I.A., Simonchik L.V., 1985, Zh. Tech. Fiz. **55**, 298
11. Arkhipenko V.I., Budnikov V.N., Gusakov E.Z.,Saveliev A.N., Simonchik L.V., 1987, Zh. Exper.Teor. Fiz. **93**, 1221
12. Budnikov V.N., Esipov L. A., Irzak M.A., Novik K. M., Stepanov A.Yu. and Aleksandrov V.O., 1989, Proc. 12th Int Conf. on Plasma Phys. and Contr. Fusion (Nice 1989) (Vienna IAEA) Vol.I, p.645
13. Budnikov V.N. 1991, Nuclear Fusion, **31**, 611
14. Gusakov E.Z., Piliya A.D., 1992, Sov. Tech. Phys. Lett. **18**, 325-326.
15. Arkhipenko V.I., Budnikov V.N., Gusakov E.Z., Piliya A. D., Selenin V.L., Simonchik L.V., 1992, Proc. Inter. Conf. on Plasma Phys. (Insbruck 1992) Vol.II, p.1203
16. Brüsehaber B., Gusakov E. Z., Krämer M. and Piliya A. D., 1994, Plasma Phys Control. Fusion, **36**, 997
17. Arkhipenko V. I. et. al. Plasma Phys. Control. Fusion, 1995, **37A** , 347-359.
18. Arkhipenko V.I. et. al. JETP Lett., 1994, **59,** p. 421.
19. Gusakov E.Z. et. al. Tech. Phys. Lett., 1995, **21** (7), 541.
20. Brüsehaber B. and Krämer M., 1997, Plasma Phys. Control. Fusion **39**, 389
21. Brüsehaber B. et. al. Tech. Phys. Lett., 1995, **21**, 508-511.
22. Gresillon D. et al. Proc. 12th EPS Conf. on Contr. Fusion and Plasma Physics, Budapest, 1985, II, 664.
23. Zou X.L. et al. Proc. 20th Conf. on Controlled Fusion and Plasma Physics, Lisbon, 1993, III, 1091.
24. Gusakov E.Z. Proc. 25th Conf. on Controlled Fusion and Plasma Physics, Prague, 1998, V.22C, 39
25. Bulyginsliy D.G. et al. Plasma Physics and Controlled Nuclear Fusion Research, 1984, 1, 491.
26. C.Hanuise et.al. Ann.Geophysicae 1993, 11, 29
27. Golant V.E., Fedorov V.I. RF Plasma Heating in Toroidal Devices. Consultants Bureau New York.
28. Bulyiginskiy D.G. et. al. Proc. 25th EPS Conf. Contr. Fusion and Plasma Phys. 1998, V.22C, 1542.
29. Lashkul S.I. et. al. Sov. Journ. Appl. Spectroscopy, 1991, 54, 887.

EXACT NONLINEAR THEORY OF THE RESISTIVE HIGH-CURRENT PLASMA-FILLED DIODE

K. V. Chukbar, A. A. Ivanov (Jr), A. S. Kingsep

Russian Research Center «Kurchatov Institute» Moscow, Russia

First exact solution has been demonstrated which presents within the frames of 2D and 2-fluid MHD the quasi-steady regime of the current / mass flow in a plasma-filled, high-current [$j \Leftrightarrow B \Leftrightarrow V_i \Leftrightarrow n \Leftrightarrow T$], resistive [$\sigma = f(B,p)\, n^a j^b$] diode with electrodes of an arbitrary shape. Results may be used: to calculate the impedance, to provide tests while simulating such systems, to predict and/or explain the properties of a self-consistent plasma cloud inside the high-current diode.

The paper deals with the quasi-steady solutions of the nonlinear equations of plasma-filled diode. These words imply that the characteristic longitudinal and transversal scales of the problem $l_\parallel, l_\perp >> r_{De}, \rho_{Be}, \rho_{Bi}$. The current in the diode is considered sufficiently high for the main parameters of the problems to be self-consistent: $j \Leftrightarrow B \Leftrightarrow V_i \Leftrightarrow n \Leftrightarrow T$.

The term «resistive» means that resistive dynamics becomes predominating compared to the self-consistent MHD or EMHD dynamics if the heating effect exceeds the initial temperature: $T < \Delta T \cong (l_\parallel / u) j^2 / \sigma \qquad j \approx cB/(4\pi l_\perp), \quad \sigma = (ne^2/m)\tau_e$, or, what is the same, $\omega_{Be}\tau_e \le (l_\parallel / l_\perp) B^2 / (8\pi nT)$.

That is the diode aspect ratio does not allow the self-consistent EMHD electron flow to be established: $nec/\sigma B >> l_\perp / l_\parallel$. Anyway we have $\tau >> l_\parallel / V_i >> l_\parallel / v_e, V << j/ne$.

The essential point in the problem of resistive diode is the expression for resistivity. It is supposed to be of a rather general form, depending on B, p, n and j as $\sigma = f(B,p) n^a j^b$ with f being the arbitrary function of 2 variables. In fact, it includes all the interesting partial cases: Spitzer's, Sagdeev formula $\sigma = \omega_{pe} v_{Te} / (4\pi u)$ etc. We consider plane 2-d geometry $\{x, y\}$ with $\partial/\partial z = 0$. As for the boundary conditions, the conductivity of electrodes is supposed to be infinite: $\sigma_{electrode} \cong \infty$.

Let us first focus at the limit $\omega_{Be}\tau_e >> 1$. The reduced system of basic equations in this case looks as follows:

$$n\frac{M_i}{Z_i}(\mathbf{V}\nabla)\mathbf{V} = -\nabla(B^2/8\pi + p) \quad \text{(quasi-steady flow)}, \tag{1}$$

$$\nabla(nV) = 0 \quad \text{(quasi-steady flow)}, \tag{2}$$

$$\mathbf{E} = \frac{\mathbf{j}}{\sigma} - \frac{1}{ne}\nabla(B^2/8\pi + p) \quad \text{(electron inertia is negligible)}, \tag{3}$$

$$\mathbf{u}\nabla p - \gamma p\,\mathbf{u}\nabla \ln n = (\gamma - 1)j^2/\sigma \quad \text{(equation for energy)}, \tag{4}$$

$$\mathbf{j} = \frac{c}{4\pi}\nabla \times \mathbf{B} = -ne\mathbf{u} \quad ([u >> V \Rightarrow v_e \cong \mathbf{u}, |\partial \mathbf{E}/\partial t| << j/\sigma]), \tag{5}$$

$$\mathbf{E} = -\nabla\varphi. \tag{6}$$

Here and below we put $T_i << Z_i T_e$, i.e., $p = nT_e$. The subsequent procedure is as follows: transition to $\{\varphi, B\}$ co-ordinates, taking into account nonlinear space curvature, solution including Lamé coefficients, reconstruction of the initial geometry, flow patterns and impedance.

The transition to dimensionless variables:

$$p \to PB_0^2/(8\pi) \quad n \to NB_0^2/(8\pi eU) \quad v \to V\sqrt{Z_i eU/M_i} \quad \varphi \to U\Phi.$$

As for curvilinear co-ordinates, current flow lines in the plane geometry coincide with $B = const$ contours, therefore we take $\mathbf{e}_x \| \mathbf{j}$ and $\eta = B/B_0$. With the Lamé coefficients $h_1 = \sqrt{(\partial x/\partial\xi)^2 + (\partial y/\partial\xi)^2}$, $h_2 = \sqrt{(\partial x/\partial\eta)^2 + (\partial y/\partial\eta)^2}$ we obtain the transformed expression for conductivity $\sigma = \frac{cB_0}{4\pi U}\Sigma(\eta, P)N^a\left(\frac{l}{h_2}\right)^b$, where l is the typical space scale. The function $f(B, p)$ transforms to $\Sigma(\eta, P)$.

The important thing one should bear in mind during these transitions is the equation that provides the geometry being plane:

$$\frac{\partial}{\partial\xi}\frac{1}{h_1}\frac{\partial h_2}{\partial\xi} + \frac{\partial}{\partial\eta}\frac{1}{h_2}\frac{\partial h_1}{\partial\eta} = 0. \tag{7}$$

The original basic equations transform in the new co-ordinate system to

$$NV\partial V/\partial\xi = -\partial P/\partial\xi, \tag{8}$$

$$NV^2\partial \ln h_1/\partial\eta = \partial(\eta^2 + P)/\partial\eta, \tag{9}$$

$$\partial(h_2 NV)/\partial\xi = 0, \tag{10}$$

$$\frac{h_1}{h_2}\frac{1}{N^a\Sigma}\left(\frac{h_2}{l}\right)^b + \frac{1}{N}\frac{\partial P}{\partial\xi} = \frac{\partial\Phi}{\partial\xi}, \tag{11}$$

$$(1/N)\partial(\eta^2 + P)/\partial\eta = \partial\Phi/\partial\eta, \tag{12}$$

$$\frac{\partial P}{\partial\xi} - \gamma P\frac{\partial \ln N}{\partial\xi} = (\gamma - 1)\frac{h_1}{h_2}\frac{N}{\Sigma N^a}\left(\frac{h_2}{l}\right)^b. \tag{13}$$

Near the electrodes ($\xi = 0,1$) the tangential component of electric field $E_\eta = 0$, so $\Phi = \Phi(\xi)$ or $\Phi = \xi$ and $\{\xi,\eta\} \leftrightarrow \{\varphi, B\}$.

We expand these near-electrode solutions to the whole area of the diode, thus making the class of solution smaller, but nevertheless we rest in the class of exact solutions. Then we have $\eta^2 + P = f(\xi)$ and due to the boundary conditions on the electrodes at $\eta = \pm 1$ $f(\xi) = 1$ and $P = 1 - \eta^2$. Thus we obtained the so-called Benneth equilibrium (pressure balance).

Now let's discuss the conditions of the existence of solution:

1) if $a + b = 1 : h_1 = l$, $h_2 = l(\xi + \xi_0)\Sigma^{-\frac{1}{a}}(\eta)F^{-1}(\eta)$;

2) if $a + b \neq 1$ the necessary condition is $V \equiv 0$ in the whole volume of plasma filling, and the solution is looking as $N = F(\eta)/(\xi + \xi_0)$, $h_1 = h_2\Sigma(\eta)F^a(\eta)\left(l/h_2\right)^b 1/(\xi + \xi_0)^a$. If we take h_2 in the form of $h_2 = l\,\Xi(\xi)H(\eta)$, we can obtain the exact solution in integral form.

One should emphasize that the resulting solutions give $h_1/h_2 \approx \omega_{Be}\tau_e >> 1$, that is the gap between electrodes essentially exceeds the thickness of the plasma cloud.

The next step in development of our model consists in taking into account the terms with heat transfer and heat flows under then same condition of $\omega_{Be}\tau_e >> 1$. The changing equation are as follows:

$$\mathbf{E} = \frac{\mathbf{j}}{\sigma} - \frac{1}{ne}\nabla\left(\frac{B^2}{8\pi} + p\right) + \frac{\mathbf{R}}{ne},\ \mathbf{R} = -\alpha\frac{n}{\omega_{Be}\tau_e}\left[\frac{\mathbf{B}}{B},\nabla\frac{p}{n}\right], \qquad (14)$$

$$\mathbf{u}\nabla p - \gamma p\ \mathbf{u}\nabla \ln n = (\gamma - 1)(j^2/\sigma - \mathbf{Ru}) +$$

$$+ (\gamma - 1)\,\mathrm{div}\left(-\frac{\alpha p}{\omega_{Be}\tau_e}\left[\frac{\mathbf{B}}{B},\mathbf{u}\right] + \beta\frac{cp}{eB}\left[\frac{\mathbf{B}}{B},\nabla\frac{p}{n}\right] + \delta\frac{cp}{eB\omega_{Be}\tau_e}\nabla\frac{p}{n}\right),$$

$$\alpha, \beta, \gamma \approx 1 \qquad (15)$$

Despite being much more complicated, the new system can be successfully solved by following the same procedure. Finally we have $N = F(\eta)/(\xi + \xi_0)$ again and the solution is the same after substituting $F^a \Rightarrow F^a\left(1 + (\alpha/2)(F/\eta)\,d(P/F)/d\eta\right)$. The qualitative results remain the same. In fact, even numerical results do not change significantly.

As for the turbulent plasma filling of the diode, small-scale turbulence corresponds merely to the proper choice of a, b and f in $\sigma = f(B,p)n^a j^b$. MHD turbulence results in Bohm transport coefficients which, in turn, correspond to $\omega_{Be}\tau_{ei} \sim 1$. EMHD field dynamics on the background of plasma density fluctuating in space and/or time results in $\sigma = nec/B$ which also corresponds to $\omega_{Be}\tau_{ei} \sim 1$. Thus, we choose $\sigma = nec/B$ to model these situations. It is equivalent to $\sigma = f(B,p)n^a j^b$ with $a + b = 1$.

Only two equations of the basic set have to be modified:

$$\mathbf{u}\nabla p - \gamma p\mathbf{u}\nabla \ln n = (\gamma - 1)\left(j^2/\sigma + \alpha n\mathbf{u}\left[\mathbf{h},\nabla T\right]\right) +$$

$$+ (\gamma - 1)\mathrm{div}\left(-\alpha T n\left[\mathbf{h},\mathbf{u}\right] + \beta(nT\tau/m)\left[\mathbf{h},\nabla T\right] + \delta(nT\tau/m)\nabla T\right), \qquad (16)$$

$$\mathbf{E} = \mathbf{j}/\sigma - 1/(ne)\nabla(B^2/(8\pi) + p) +$$

$$+ \varepsilon\, m/(\tau e)\left[\mathbf{h},\mathbf{u}\right] - \varsigma/e\nabla T - \alpha/e\left[\mathbf{h},\nabla T\right],$$

$$\alpha, \beta, \delta, \varepsilon, \zeta \approx 1. \qquad (17)$$

Kinetic coefficients ε, ζ are new parameters. Let us suppose that plasma filling is stable in average, and we may carry out the same calculation procedure. After all operations, instead of

$$\partial\Phi / \partial\eta = 1 / N \partial (\eta^2 + P) / \partial\eta + \alpha / \kappa \ \partial (P / N) / \partial\xi \tag{18}$$

which was the case for $\omega_{Be}\tau_e >> 1 (\kappa = h_1 / h_2)$ one can readily obtain

$$\partial\bar{A} / \partial\eta = 1 / N \ \partial (\eta^2 (1 - \varepsilon) + P) / \partial\eta + \alpha / \kappa \partial (P / N) / \partial\xi + \varsigma \partial (P / N) / \partial\eta . \tag{19}$$

Thus, ε results in renormalization of the first term in the RHS. To feel the effect of ζ, let us put $\alpha, \beta, \delta, \varepsilon = 0$, $\zeta \neq 0$. Reconstruction of the initial co-ordinate system turns out to be simple enough:

$$\left(\partial x / \partial\xi\right)^2 + \left(\partial y / \partial\xi\right)^2 = A^2 (1 - \eta^2)^2 , \tag{20}$$

$$\left(\partial x / \partial\eta\right)^2 + \left(\partial y / \partial\eta\right)^2 = 4\eta^2 (\xi + \xi_0)^2 \tag{21}$$

resulting (e.g., $A = 1$) in

$$x(\xi,\eta) = \pm (l / \sqrt{2})(1 - \eta^2)(\xi + \xi_0) \sin(\ln((1 - \eta^2) / (\xi + \xi_0))) , \tag{22}$$

$$y(\xi,\eta) = \pm (l / \sqrt{2})(1 - \eta^2)(\xi + \xi_0) \cos(\ln((1 - \eta^2) / (\xi + \xi_0))) . \tag{23}$$

This random example of exact solution of 2D and 2-fluid MHD equations seems to be of some interest in the context of general plasma theory.

The work was supported by INTAS grant 97-0021, as well as RFBR grant 99-02-16659.

SHORT MICROWAVE PULSE GENERATION VIA RELATIVISTIC IONIZATION FRONT PRODUCED BY LASER PULSE

T. Higashiguchi, N. Yugami, H. Okabe, T. Niiyama, S. Sasaki, E. Takahashi, H. Ito, and Y. Nishida*

Energy and Environmental Science, Graduate School of Engineering, Utsunomiya University, Utsunomiya, Tochigi 321-8585, Japan
*HITACHI co., Hitachi, Ibaraki 317-8511, Japan

An interaction between a periodic electrostatic field (DC) and a relativistic underdense ionization front generates a short microwave pulse (AC). A capacitor structure for producing an electrostatic field is set in the X-band waveguide (cut-off frequency of 6.6 GHz) for matching the impedance to that of the emitted microwave pulse. A center frequency and a pulse duration observed 9 to 10 GHz and ~ 6 ns (FWHM), respectively. An output power of the emitted radiation is proportional to the applied bias voltage with a power of 2.2.

1. Introduction

A new short microwave pulse source (called the DC to AC radiation converter: DARC) is proposed by Mori *et al.* in 1995 [1]. The DARC has following advantages such as frequency tunability (from GHz to THz), ultrashort pulse (a few cycles) and high power (from W to kW range) [1-3]. In the principle of the DARC using the relativistic underdense ionization front, a phase modulation of the periodic electrostatic field occurs at the ionization front and the transmitted wave is directly radiated in the plasma. In our recent experiment [3], a maximum frequency of the short microwave pulse ranges from 9.5 to 14.1 GHz in the S-band structure (a capacitor array with a period of 1 cm and a cut-off frequency of 1.3 GHz for a TE_{10} mode). In addition, the electric field of the emitted radiation is polarized in the same direction as the expected electrostatic field. However, the plasma density produced by a Nd:YAG laser pulse is unknown and also the argon gas has difficulty in ionization by the ultraviolet light. In this paper, the TMAE (tetrakis-dimethyl-amino-ethylene: $C_{10}H_{24}N_4$) gas [1] is used for easy ionization to the $4\omega_0$ light of the Nd:YAG laser. The frequency of the emitted radiation is measured in detail by a time of flight (TOF) method using a delay waveguide line. Furthermore, the detected signal intensity of the emitted radiation is measured precisely as a function of the applied bias voltage.

2. Principle of the DARC

A radiation principle of the DARC scheme is shown in Fig. 1. An electrode array is alternately biased by a pulsed power supply, and the periodic electrostatic field is given by $E_x \sim E_0 \sin k_0 z$ on the z-axis, where E_0 and k_0 are, respectively, an amplitude and a wavenumber of the electrostatic field at a frequency of $\omega_0 = 0$. The amplitude E_0 of the electrostatic field is approximately equal to V_B/b, where V_B and b are the applied bias voltage and the gap between a top electrode and a bottom one, respectively. A velocity of the ionization front is equal to the group velocity of an ionizing laser in the plasma, i.e., $v_f = c(1-\omega_p^2/\omega_L^2)^{1/2} \sim c$, where ω_p, ω_L and c are a plasma frequency, a laser frequency and a speed of light, respectively. The frequency of the emitted radiation can be directly estimated by using two conditions [1], one is the dispersion relation of the electromagnetic (EM) wave in the plasma: $\omega^2 = \omega_p^2 + c^2k^2$ and the other is the phase continuity equation at the ionization front: $\omega + kv_f = k_0 v_f$. For $\omega_p^2 << \omega_L^2$, the estimated frequency of the emitted radiation is approximately equal to,

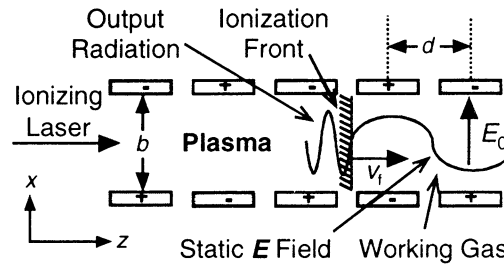

Fig. 1. Radiation principle of DARC.

$$\omega \sim k_0 v_f/2 + \omega_p^2 / 2k_0 v_f. \quad (1)$$

The emitted frequency depends on both the plasma density and the wavenumber of the periodic electrostatic field, and must be higher than the plasma frequency. The radiation from the DARC propagates in the same direction (+z direction) as the ionization front.

3. Experimental Arrangement and Results

In the DARC experiments, the capacitor array for exciting the periodic electrostatic field consists of $N = 6$ periods (i.e., 13 pairs) and a distance, d, of the adjacent electrodes is $d = 2\pi/2k_0 = 1$ cm with a gap of $b =$ 0.6 cm. This electrode structure is inserted in the X-band waveguide (type: WR-90, cut-off frequency: 6.6 GHz). For excitation of the electrostatic field, the electrode array is alternately biased by the high voltage pulsed power supply with a maximum voltage of ~ 5 kV and the pulse duration of ~ 2 μs. One set of electrodes is biased to high voltage and the others and the waveguide wall are connected to the ground. A working

gas is the TMAE (ionization potential: U_i = 5.4 eV). The laser light at a wavelength of 266 nm (photon energy: $h\nu$ = 4.7 eV) is used for the creation of the ionization front. The pulse duration of the ionizing laser is ~ 6 ns (FWHM), the laser total energy is ~ 100 mJ and the spot diameter is 1 cm. A pin-photo diode is used for detecting the Nd:YAG laser light. As the laser energy is fixed, the plasma density is expected to be proportional to the TMAE gas pressure. The plasma density is measured by 24 GHz microwave interferometer. The radiated short microwave pulse is detected by the crystal diode (time resolution of ~ 1 ns).

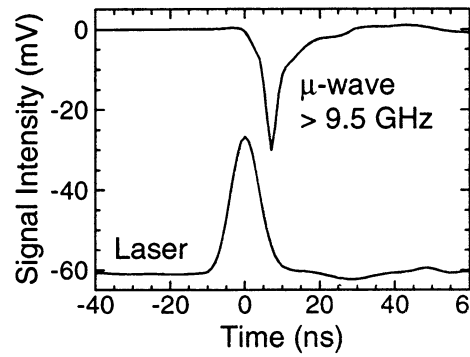

Fig. 2. Typical example of the emitted radiation.

Figure 2 shows the typical example of the emitted radiation from the DARC (top trace) and a laser pulse signal detected by the pin-photo diode (bottom trace). The experimental parameters are the TMAE gas pressure of 5 mTorr (plasma density of 6×10^{11} cm^{-3}) and the applied bias voltage of 1 kV. The waveguide used for detection has a cut-off frequency of 9.5 GHz. The emitted radiation signal delays ~ 10 ns with respect to the laser pulse. This delay time depends on the cable length of the measurement system, although two signals should have no delay. The pulse duration of the emitted radiation is ~ 6 ns (FWHM).

The center frequency of the emitted radiation from DARC is measured by the TOF method. The spectrum analyzer is popularly used for the frequency measurement. However, the wave to be measured is pulsive, and thus, it is not easy to employ the spectrum analyzer for frequency measurement. The TOF method has following advantages, (i) the time response is better than the conventional spectrum analyzer, (ii) the spectrum of the emitted radiation can be observed for 1 shut and (iii) the size is compact for the frequency measurement in the X-band microwave. The principle of the TOF method by the delay waveguide line is that the frequency of the emitted radiation from the DARC is resolved by a dispersion from the group velocity change of the EM wave in the waveguide. The dispersion relation of the EM wave in the waveguide is given by $\omega^2 = \omega_c^2 + c^2k^2$, where ω_c is the cut-off frequency of the waveguide. As the

group velocity in the waveguide is given by $v_g = c(1 - \omega_c^2/\omega^2)^{1/2}$, thus has frequency dependence. The velocities for frequency of 9 GHz and 10 GHz in the present waveguide are equal to $0.68c$ and $0.75c$, respectively. The delay time is given by $t_d(\omega) = L/v_g$ when the EM wave travels in the waveguide for the length L. Thus, the frequency of the emitted radiation can be observed by measuring the delay time. The emitted frequency from the DARC is given by

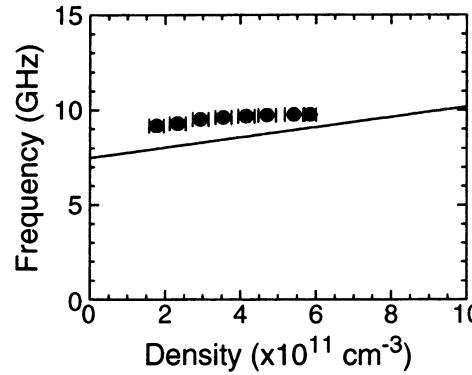

Fig. 3. Frequency v.s. Plasma Density.

$$\omega = \omega_c c t_d/(c^2 t_d^2 - L^2)^{1/2}. \quad (2)$$

In the present experiments, the emitted radiation from the DARC is separated by the directional coupler, one signal corresponds to the radiation and the other to the delayed signal through the delay waveguide line. The delay line consists of the waveguide with a cut-off frequency of 6.6 GHz and its length of 5144 cm. A waveform of the delayed signal shows the resolved frequency components. Figure 3 shows the observed frequency as a function of the plasma density. Here, the frequency of the emitted radiation is converted by the measured delay time and eq. (2).

The plasma density is measured by 24 GHz microwave interferometer as a function of the TMAE gas pressure. The plotted points are the average values of the experimental 5 data. The error bars for the horizontal and the vertical values are the standard deviation of the plasma density and the observed frequency, respectively. The observed frequencies increase with the increment of the plasma density. A solid line represents the predicted frequency given by eq. (1) for $d = 1$ cm. The observed frequencies are in reasonable agreement with the predicted linear dependence of the emitted radiation on the plasma density.

Figure 4 shows the output power of the observed radiation as a function of the applied bias voltage. In the experiment, the output power is measured by the combination of the waveguide with a cut-off frequency of 6.6 GHz, the waveguide-coax converter and the crystal detector. The crystal detector is calibrated to the detected power as a function of the output signal intensity near the frequency of the emitted radiation.

However, the attenuation rate and the pick-up rate of other components such as the horn antenna and the waveguide-coax converter are not precisely calibrated yet. Thus, the exact radiation power of the emitted radiation from the DARC is unknown. The detected power is experimentally proportional to the applied bias voltage with the power of 2.2. The breakdown occurs over the applied bias voltage of ~ 4 kV. Here, the experimental parameters are the TMAE gas pressure of 5 mTorr (plasma density of 6×10^{11} cm^{-3}) and the observed frequency of 9.6 GHz.

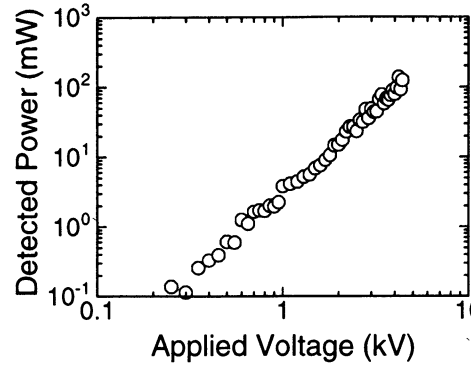

Fig. 4. Detected power versus the applied bias voltage.

4. Discussion and Summary

In this section, the pulse duration and the output power of the observed radiation is discussed. First, the pulse duration is observed much longer than the expected values. The theory predicts that the pulse duration τ is determined by the period of the electrostatic field, i.e., $\tau = 2\pi N/\omega$ for an ideally sharp ionization front with a scale length of $L_f << d$, where N is the number of the electrostatic field periods [1]. The observed pulse duration is much longer than the theoretically expected value of 625 ps for $N = 6$ periods and the emitted frequency of 9.6 GHz (shown in Fig. 3), rather the same pulse duration as the ionizing laser pulse. The plasma is slowly produced during the laser pulse duration of ~ 6 ns, thereafter the plasma density decays for a long time scale of more than ~ μs. When the laser light ionizes the TMAE gas filling the electrode structure, the plasma density increases from zero to maximum density during the laser pulse irradiation. In our experiments, as the scale length of the ionization front is $L_f = c\tau_L = 300$ cm $>> d = 1$ cm, where τ_L is the pulse duration of the ionizing laser, the ionization front boundary is not sharp. The frequency upshift takes place during the time when the ionization front moves around, in other words, once the laser pulse is shut off, the ionization front disappears and the radiation does not occur anymore even if the steady plasma exists. In the present case, the laser power increases with finite time and the radiation takes place while the laser pulse increases in

its intensity. After the laser pulse crosses the maximum intensity, the effects from the weak ionization are hidden away by the dense plasma and no serious radiation takes place. Therefore, we can expect that the radiation intensity might be proportional to the increment of the plasma density, resulting in the output microwave with a pulse shape similar to that of the laser pulse [3].

Next, the output power is estimated. The theory gives the output power of the emitted radiation as follow,

$$P_{out} = \varepsilon_0 E_0^2 v_{gp} A/2 = \varepsilon_0 (V_B/b)^2 v_{gp} A/2, \quad (3)$$

where ε_0, v_{gp} and A are the dielectric constant in vacuum, the group velocity of the emitted radiation in the plasma and the area of the ionization front, respectively [1]. Thus, the output power is proportional to the applied bias voltage with the power of 2. The experimental values of the bias voltage dependence are in good agreement with the theoritical value. The expected theoretical maximum output power of the emitted radiation is estimated to be $P_{max} \sim 4.3$ kW by using eq. (3) with the experimental parameters of $V_B = 1$ kV, $b = 0.6$ cm and $A = 0.6$ cm $\times$ 0.9 cm at the output frequency of 9.6 GHz, with the group velocity of the emitted radiation of $v_{gp} \sim 0.68c$ in the plasma.

In summary, a short microwave pulse (~ 6 ns) is observed by the DARC principle. The observed pulse duration of the emitted radiation could be explained by the increment of the plasma density resulting from the finite duration of the ionization process during the laser pulse irradiation. The emitted frequency (9-10 GHz) measured by the TOF method is proportional to the plasma density. The detected output power is proportional to the applied bias voltage with the power of 2.2, close coincidence with the predicted value of 2.0.

Acknowledgement

We would like to acknowledge useful discussions with Dr. T. Ueki. A part of the present work was supported by a Grant-in-Aid for Scientific Reserch from the Ministry of Education, Science, Sports and Culture, Japan.

References

1. W. B. Mori *et al.*, Phys. Rev. Lett., 1995, **74**, 542; C. H. Lai *et al.*, Phys. Rev. Lett., 1996, **77**, 4764; P. Muggli *et al.*, Appl. Phys. Lett., 1998, **72**, 19; P. Muggli *et al.*, Phys. Plasmas, 1998, **5**, 2112.
2. N. Yugami *et al.*, Jpn. J. Appl. Phys., 1998, **37**, 688.
3. T. Higashiguchi *et al.*, Jpn. J. Appl. Phys., 1999, **38**, L527.

DYNAMICS OF ELECTRICAL DISCHARGES IN A THUNDERSTORM CLOUD

D. I. Iudin[1], *V. Yu. Trakhtengerts*[2]

[1] Radiophysical Research Institute, Nizhny Novgorod, Russia

[2] Institute of Applied Physics, Nizhny Novgorod, Russia

Abstract

Discharge activity inside a thundercloud is investigated on its mature stage. This activity is accompanied by numerous "elementary" discharges of 1 μs duration, which are united, during a lightning flash, into chains with different spatio-temporal scales. Such a discharge dynamics is characterized by the averaged universal power-law frequency spectrum. The phenomenological model is suggested which can explain basic features of this dynamics. The model is based on the interaction of large-scale (DC) and small-scale electric fields which have different origins. DC field is due to the commonly accepted charge separation effects inside a thundercloud, while small-scale cells appear as a consequence of the resistive instability similar to the beam-plasma instabilities in collisional plasmas. The saturation level for the field insidse the cells is higher than for DC field and can locally reach the breakdown value. Initial "elementary" discharges appear between the maximum and minimum of the electric field in electrical waves generated by the instability. These occasionally appearing short-living conducting elements form a charge drainage system (CDS) for the large-scale electric field. Methods of the fractal geometry permit us to find electrical parameters of this CDS and spatio-temporal characteristics of its separate current elements, that can be related to the observed hierarchy of the lightning discharges. The qualitative picture of a lightning flash is discussed with the viewpoint of this model.

1. Introduction

Thunderstorm electricity problem is extremely diverse and includes a number of key questions, beginning from cloud electrification mechanisms and ending with the flash shaping final stage, when a stepped leader arises and a return stroke as the most powerful manifestation of

lightning discharge is established. Nowadays, a considerable progress in understanding and modeling of elementary processes of cloud particles electrification is achieved [1]. There exists an advance in the model development of the flash channel formation, when the channel formation is accompanied by a leader and return stroke progression [2–5].

Posed major difficulty is the situation with understanding of processes defining lightning discharge preliminary stage. This stage on its most developed phase lasts approximately some tenth of a second and consists of numerous (up to 10^5) relatively feeble discharges [4, 6–10]. Experimental investigations demonstrate several preliminary stage peculiarities that reveal it as very complex and puzzle phenomena. One may select two subintervals (with the approximately equal duration) in the preliminary breakdown stage [9]. The first subinterval contains a consequence of the very high frequency pulses (VHF) which appear without visible large-scale (DC) field changes. A graduate DC field change accompanies VHF on the second subinterval and tightly connected with leader progression. Figure 1 shows a typical recording of the ground E-field change and the VHF for one of the cloud-to-ground (CG) flashes in South Florida during the summer of 1981 [9]. The results obtained with the VHF source location systems reveal pulse duration changes, which are connected with Doppler effect under the radiation of a fast (up to 10^7 m/s) moving sources [8, 11]. Sometimes VHF emission is seen as a consequence of coherent signals [12].

A change of DC electric field and lowering of a negative macroscopic charge, which is accumulated in the lower edge of a cloud, take place during the second subinterval of a preliminary stage (Figure 1). The VHF mapping of intracloud discharges shows on this stage appearance of more long trains of VHF pulses, which testify formation of intracloud streamers and a stepped leader [8, 11]. Further activity of intracloud streamers and dart leaders is continued during intervals between strokes and is accompanied by specific K- and J- changes of an electric field with characteristic time scales from 100 μs up to 10 ms [7]. Below we will try to draw the qualitative picture of intracloud electric discharge dynamics, which would permit to unite all above processes. Our model is based on the interaction of a large-scale

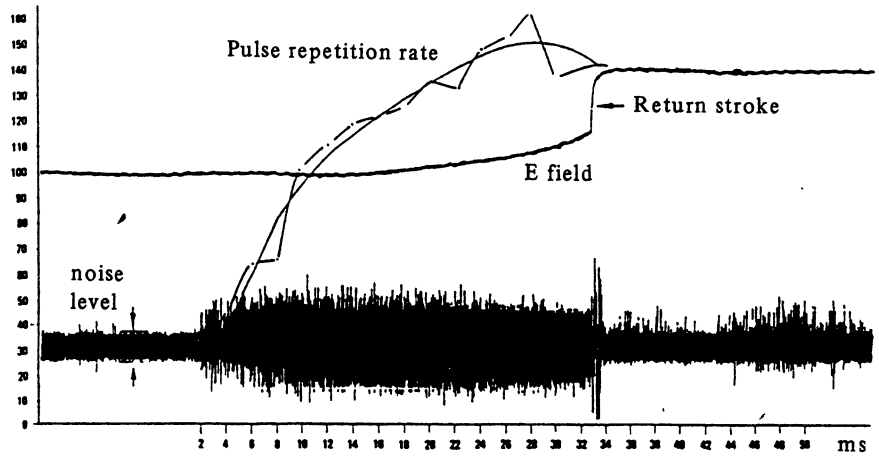

Figure 1. An example of VHF pulse emission (a lower trace) which appears at the preliminary stage of a lightning discharge; dashed-dotted line corresponds to the number of pulses. The electric field behavior is shown by the thick line (in arbitrary units).

(DC) electric field with small-scale electric cells, which appear on the mature stage of a thundercloud development. In section 2 we discuss shortly a physical mechanism, which leads to generation of small-scale electric cells inside a cloud. Formation of a charge drainage system (a cloud metallization) is discussed in section 3. Section 4 describes a spatio-temporal hierarchy of electric discharges inside the cloud. A mechanism of DC electric field amplification in the Earth-cloud gap is considered in section 5. Discussion of the results and conclusion are given in sections 6 and 7.

2. Small-scale electrical structure

The principal aim of our consideration is to bring the idea that lightning discharge preliminary stage is closely related with a thundercloud fine electrical structure. The multilayer cellular electrical structure had been detected practically in all in situ experiments [1, 13], however a spatial resolution of existing experiments does not give the reliable information about the scales 1–10 m. At the same time there is a considerable physical foundation for an existence of such a small-scale electrical structure in a thunderstorm cloud. The idea is that

a mature thundercloud becomes similar to a plasma-like multiflow system. The combined effect of gravity and uprising convective flow creates interpenetrative streams of charged heavy (large drops and hailstones) and light (ice crystals and the fine drops) components. At the observed velocities $u \sim 5$–20 m/s of the uprising streams the large particles (with mass $M \sim 10^{-5}$ kg) are suspended in the stream. They fill the lower part of a cloud, while the light fraction is carried away by the stream into an upper part of the cloud. As it was shown in [14, 15], this multiflow system is unstable to generation of electrostatic waves with the electric field $E \propto \exp(-i\omega t + i\mathbf{kr})$, where $\mathbf{r}$ and t are the space coordinate and time. In the simplest case of monodispersed charged hailstones and ionized air flow the frequency ω and the wave vector $\mathbf{k}$ satisfy to the dispersion equation [14, 15]

$$1 - \frac{\Omega^2}{\omega(\omega + i\nu)} + \frac{4\pi i\sigma}{\omega - \mathbf{ku}} = 0, \qquad (1)$$

where $\Omega^2 = 4\pi q^2 N/M$ is the square of the "large particle gas" plasma frequency, q, N, and M are the charge, density, and mass of hailstones, $\nu \approx g/u$ is the effective collision frequency, g is acceleration due to gravity, $\mathbf{u}$ and σ are the air flow velocity and conductivity; the large particles are supposed to be suspended in the air flow. It is easy to see from (1), that these wave are unstable. The instability threshold is given by condition $(\Omega/\nu)^2 \geq 1$ and the instability increment is derived as $\gamma \simeq 2\pi\sigma(\Omega/\nu)$ for the optimal size of a cell $a \sim \pi/k \simeq \pi u/\Omega$. For particle radius $\sim$0.5 cm and $N \sim 10^3$ m^{-3} the instability threshold is achieved for $q \sim 10^{-10}$ C. According to the experimental data (see, for example, [16]) these values are quite resonable. Putting $u \sim 10$ m/s and $\Omega \approx 2\nu$, we find $\nu \sim 1$ s^{-1}, $a \sim 10$ m, and $\gamma \sim 4\pi\sigma \sim 1$ s^{-1} ($4\pi\sigma \sim \nu$). The further examinations [17] with an account for charge exchange between the particles have shown a considerable universality of such an instability in a wide range of the cloud parameters. At the nonlinear stage a small-scale electric field amplitude is determined by a balance between the electric force and the force of gravity that are superimposed on a large particle $E \sim Mg/q \sim 10^6$ V/m. Hence the small-scale electric field amplitude can considerably exceed the median field amplitude.

3. Cloud metallization

We will concentrate hereinafter on the thundercloud part that is responsible for the cloud-to-ground lightning discharge. It occupies several kilometers L over the altitude and some tens kilometers Λ at the horizontal direction. Packed in it basically are large particles with a negative charge. The macroscopic electric field stipulated by them (its vertical component) is directed opposite to the fair weather field. In the mature cloud the beam-plasma instability develops and gives rise to an alternating electric field $\widetilde{E}$ on the background of the large-scale field E_0. The alternating field $\widetilde{E}$ locally reaches breakdown value. It is obvious, that discharges inside cells arise randomly in space and in time by reason of the condition distinctions in different cloud parts. A size of such an elementary discharge is $a \ll L$ and its lifetime is τ. According to estimations (see section 2) the value a makes about $10m$, $L \sim 3 \div 5\ km$ and $L/a \sim 10^2 \div 10^3 \gg 1$. By analogy with a similar laboratory spark discharge we take the elementary discharge duration (the lifetime) as $\tau \sim 1$–$10\ \mu s$ [18].

We interpret the conductive elements occurrence as emergence of a new phase in an initially homogeneous and poorly conducting medium. The conductive elements give rise to their connected complexes — conductive clusters. The conductive clusters appearance essentially changes the medium properties. In the presence of even a feeble external field the conductive clusters realize the charge transfer that in turn gives rise to strong field fluctuations [19, 20]. An important point is that connection in the conductive elements ensemble appears on scales which far exceed a separate element size. We describe the conductive elements ensemble by application of percolation theory [21–24].

We will assume, that cells are placed in the corners of a prime cubic lattice. When the small-scale electric field amplitude reaches some critical value E_c there is a breakdown between cells and a good conductor appears with a lifetime τ.This breakdown stimulates breakdowns in neighboring cells, if the amplitude of an electric field in them exceeds some fixed magnitude E_a (activation level). The activation level is much less then critical one [25].

In a simple cubic lattice each cell has six nearest neighbors. Choose from all of six pairs that the amplitude of electric field in which is

maximum. We enter a cumulative distribution function of cells $f(E)$ over this maximum amplitude such that $f(E)dE$ characterizes specific fraction of cells being among pairs with magnitude of an electric field amplitude E hitting in an interval $[E, E+dE]$. It is obvious that $\int_0^\infty f(E)dE = 1$, and $\int_0^\infty Ef(E)dE = \bar{E}$ is a median magnitude of the inhomogeneous field amplitude. Fix in the instantaneous cloud photo all cells being among pairs, the electric field magnitude in which exceeds the activation level. Their specific fraction makes magnitude $x = \int_{E_a}^{E_c} f(E)dE$. Essuming that the correlations in allocation of pairs with $E \geq E_a$ are absent, we come to a percolation problem on a cubic lattice. It means that in the vicinity of the critical value x_c the characteristic size R_c of clusters consisting of cells with $E \geq E_a$ increases with x by a power law $R_c \simeq a \left(\frac{x_c - x}{x_c}\right)^{-\nu}$, where ν is the correlation radius critical exponent [21–24]. For three dimensions $x_c \simeq 0.25$ and $\nu \simeq 0.8$.

Single pair breakdown tends to the 'metallization' over the all activated cluster. As this takes place, a cluster metallization time t_m depends on its sizes R [19, 23, 26]:

$$t_m \sim \varepsilon \left(\frac{R}{a}\right)^{D_g}, \tag{2}$$

here ε is a time of interaction, i.e. the time of excitation transmission from a punched cell to the next activated cell, D_g is the fractal geodesic dimension of a percolation cluster. For three dimensions $D_g = 1.37$. In order to prevent misunderstanding we will underline that hereinafter the dimensionalities concerning to percolation cluster will be designated by capital D and for the other fractals dimensionalities we shall use lower case d. The relation between t_m and τ is important. According to (2) the requirement $t_m \sim \tau$ limits sizes of conductive fragments and determines a characteristic metallization front width $h_m \simeq a \left(\frac{\tau}{\varepsilon}\right)^{1/D_g}$. The metallization front spreads from a point of the first breakdown over all activated clusters and at $R_c > h_m$ is divided into a set of unconnected conductive fragments with sizes of the order h_m.

Metallization process is reversible in the absence of a large-scale

field. We have a quasistationary pattern of birth and vanishing of the conductive fragments representing fractal areas with dimension of a three-dimensional percolation cluster $D_f = 2.54$ [23] and sizes not exceeding h_m.

Stipulated by the nonzero volume density of the negative charge the large-scale field brings in an essential anisotropy to metallization process, initiating a potential smoothing currents in conductive fragments. Thus the metallization process is accompanied by the lowering of a negative cloud charge centre. It is obvious that the electrical charge inside a conductive cluster has time to be redistributed on cluster volume, if the cluster conductivity σ is sufficiently large: $\sigma_m \tau > 1$, where σ_m is a maximum value of $\sigma(t)$, τ is a conductive element lifetime. This inequality is fulfilled, if as we suppose there is an electrical breakdown in a cell. At the same time because of the limited lifetime a magnitude of a median current in a separate element is restricted by the value [1] $j_a \simeq q_a/\tau$, where q_a is a macroscopic charge of a separate cell. It means that in the external field E_0 each element of the electric circuit has effective resistance

$$r_a \sim \frac{aE_0}{j_a} \sim \frac{a\tau E_0}{q_a}. \tag{3}$$

A free charge density at the ionization (metallization) front propagated in a charged dielectric grows in time. It corresponds to the current growth with the cluster elongation. The rate of a charge growth is enhanced by the ramification of conductive channels in the actual three-dimensional front. It is natural to assume that as far as a charge grows at the metallization front, its further propagation along electric field gains the self-channelling character. As this takes place, the metallization front goes beyond the limits of a separate activation zone and falls into other zones located mainly along the large-scale field. The occurrence of the self-maintained current channels we connect with existence of some critical current magnitude, since which the ohmic dissipation in the channel is capable to support a high level of channel's conductivity. We enter a scale R^* that corresponds to

[1] When a cell structure arises, together with a median current there naturally exists current of an intra-cell discharge, which is much more (at least for short clusters) then median one, however its lifetime is always restricted by the magnitude τ.

the critical current magnitude. The metallization front has to get over the scale R^* before it passes in the self-channeling regime. We guess, that $a \ll R^* \ll L$, where L is a width of a fissile cloud region. On scales $R^* < R < L$ the self-maintained channels, being united with each other, shape a quasistationary current system. The system's viability is determined by gathering of a charge in metallization process on scales $a < R < R^*$.

Critical current evaluation represents rather difficult problem which goes beyond the frameworks of the present examination. For us the key possibility is important that short-lived conductivity fluctuations caused by discharges in small-scale electric cells can be supported by macrostructural currents induced in conductive clusters by a large-scale field. Being liberated on conductive fragments the negative space charge is transferred during the metallization process to the lower part of a cloud, flowing down over numerous channels to a common 'trunk'. The confluence of fine channels stipulates the current magnification that in turn gives rise to the peculiar kind of hierarchy where the high-order level transfers the greater charge in a unit time.

Basically the scale R^* is a boundary parting fractals with different dimensionalities. When $R \lesssim R^*$ we deal with the percolation cluster with dimension D_f and with peculiar temporal dynamics. For $R \gtrsim R^*$ the cluster-cluster aggregation gets into the act and the fractal aggregate with already smaller dimension d_f (and with an alternative temporal dynamics) appears. To elucidate the key moments of the offered model we have simplified a problem, guessing that R^* is not vastly more then a and basicly we deal with a cluster-cluster aggregation. Qualitatively it also corresponds to the experimental data showing the existence of rather stable current channels of the intracloud electric circuit on scales $l > 3 \cdot 10^2$ m [8].

In the following section we describe the quasistationary behavior of a charge gathering (or charge questioning) system in the light of a hypothesis of a system's spatial-temporal self-similarity.

4. A charge transportation processes in thundercloud

In the previous section we saw that the conductive fragments development tends to the macroscopic charge release with the subsequent lowering of the negative charge centre in the thundercloud. As this

takes place, the hierarchy of current channels appears, whose viability is supported by metallization process. The effectiveness of each channel of the current system is defined by the sizes of its "basin" (influence zone).

Our task is to determine, using outcomes of fractal geometry, following quantitative performances of the current network: the cluster current dependence from cluster's sizes, the lifetime of various sites in the fractal circuit, the spatial distribution of charges flowing down on the lower edge of a cloud. Here we take advantage of the parallels between the electrical charge gathering system and a drainage system of the rivers' basins [27] and polymeric structures in polymeric compounds chemistry [23]. It would be possible to term our fractal circuit as the charge drainage system (CDS). This CDS is a system with the restricted resource and consequently with the limiting lifetime. In our case the quasi-stationarity of the questioning process implies the invariance of a CDS structure. The separate fragment vanishing is compensated by junction of a long-lived CDS trunk with new conductive clusters ensuring the carrier of a fresh charge from yet not questioning regions of a cloud.

We suppose here that on scales $a < R < L$ the instantaneous CDS photo is fractal with Hausdorff dimension d_f. The CDS being created due to junction of conductive fragments, the magnitude d_f should be close to dimension of a cluster originating at a cluster-cluster aggregation [28, 29]. Computer experiments' data [26] testify that the fractal dimension of clusters originating at a cluster-cluster aggregation in three-dimensional space makes magnitude $d_f \simeq 1,8$.

We turn now to searching the CDS complete resistance and CDS current. Conventionally figured on Fig. 2 is a two-dimensional projection of the system. We shall take advantage of analogy with fractal ensemble of monomers in a polymeric macromolecule. Consider a fractal chain of monomers forming the macromolecule [23]]. We remind here the concept of 'chemical' or 'topological' dimension of the fractal aggregate and associated with it cluster geodesic line dimension. Fixing an arbitrary monomer of a cluster we shall count the number M of all monomers located not farther than in n steps from chosen. For the fractal aggregate the magnitude M is power function

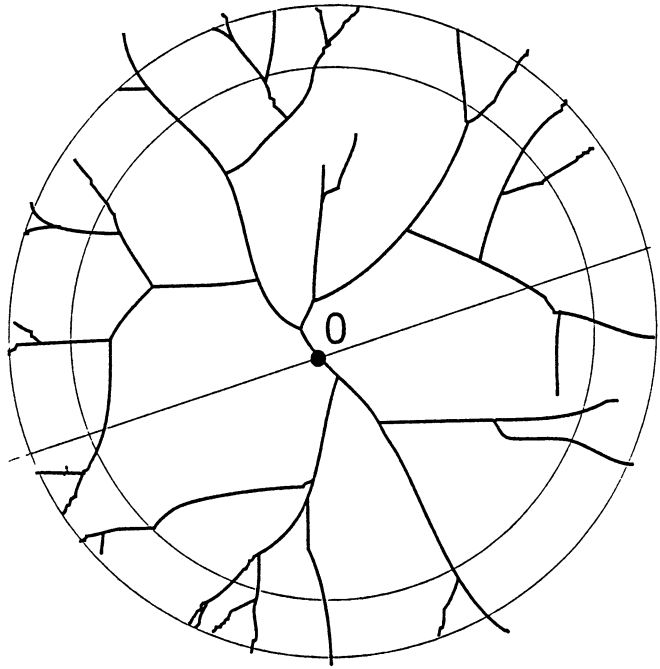

Figure 2. A two-dimensional projection of charge drainage system (CDS).

of the number of steps

$$M \simeq n^{d_c}, \tag{4}$$

where d_c is the cluster chemical dimension. The minimum number of steps n, parting two monomers from one polymeric aggregate, corresponds to the shortest paths on a cluster from one monomer to another. A fractal line representing this path is termed as a cluster geodesic line. Thus

$$n \simeq \left(\frac{R}{a}\right)^{d_g}, \tag{5}$$

where a is a monomer size, R is the 'Euclidean' distance, and d_g is geodesic dimension. Combining (4) and (5) we obtain

$$M \simeq \left(\frac{R}{a}\right)^{d_c d_g}. \tag{6}$$

On the other hand the number of monomers (or mass of cluster elements) made in the Euclidean orb of radius R is defined by the fractal aggregate dimension d_f, i.e. $M \simeq \left(\frac{R}{a}\right)^{d_f}$ and we obtain that $d_c \equiv d_f/d_g$.

In our problem the macromolecules correspond to our conductive clusters, and the original small monomers to the current circuit elements with the electrical resistance given by the formula (3).

Define now the complete resistance $r(n)$ measured between an interior point O of a fractal tree (fractal tree — fractal without loops, Fig. 2) and all knots of n-chemical stratum, that is all peripheral knots of the fractal removed from O on the same chemical distance n. Let $B(n)$ be number of connections in n-stratum of fractal. It is clear, that

$$B(n) \sim \frac{dM\,(n)}{dn} \sim n^{d_c-1}. \tag{7}$$

In essence $B(n)$ is an admittance of n-chemical stratum. To find $r(n)$, it is necessary to integrate resistance of all sequentially connected chemical stratums. In result we shall have:

$$r\,(n) = \int_1^n \frac{dn'}{B\,(n')} \sim n^{2-d_c}. \tag{8}$$

Passing from n-space in actual comprehending space, we obtain

$$r(R) \sim R^{2d_g-d_f}\,. \tag{9}$$

Taking into account the relation $I \sim \frac{U}{r} \sim \frac{E_0 R}{r}$, it is possible to find the current, gathered by the cluster with the length R:

$$I_R \sim \frac{E_0 R}{r} \sim \frac{q_a}{\tau}\left(\frac{R}{a}\right)^{1+d_f-2d_g}. \tag{10}$$

Above all CDS elements were supposed to be identical. In the real chain different CDS branches have different resistances and conduct different currents. These peculiarities can be considered in frame of a multifractal approach. We suppose for simplicity, that a power law is valid for a real CDS but with another power. So, we suppose that

at $R < L$ the CDS current is a power function of CDS scale

$$I_R \sim \frac{q_a}{\tau} \left(\frac{R}{a}\right)^{3-\gamma}, \tag{11}$$

where $3-\gamma$ is a critical exponent of a current, which differs generally speaking from the obtained above value $1+d_f-2d_g$ for a fractal web with a fixed resistance of connections.

The area of a scaling condition (11) is restricted to thickness of an active cloud region L so the CDS structure essentially varies on scales $L < R < \Lambda$, where Λ characterizes a horizontal size of a thunderstorm cell. It is tied directly to modification of the effective "basin"dimension: at $R < L$ basin has three-dimensional character and at $R > L$ — two-dimensional. Besides on scales $L < R < \Lambda$ the effective voltage in the drainage network remains by magnitude about $E_0 L$. All this have culminated in saturation of a CDS current on scales $R > L$.

We reason that on scales $R < L < \Lambda$ the CDS current does not depend on R and coincides by magnitude with I_L. During a flash time t_{flash} CDS gathers some portion of the cloud charge Q_{total} arranged on about $(\Lambda/L)^2$ the L-sized areas. The 'questioning' of each such an area requires a time

$$\tau_L \simeq t_{flash} \left(\frac{L}{\Lambda}\right)^2. \tag{12}$$

The time τ_L is a crossover time or a time of passage from a fractal condition of questioning to homogeneous one. Using the formula (11), we obtain

$$\tau_L \simeq \frac{Q_{total}\,(L/\Lambda)^2}{I_L} \simeq \tau \left(\frac{L}{a}\right)^{\gamma}, \tag{13}$$

where τ is the lifetime of conductive connection of small-scale structure, γ is a lifetime critical exponent. The current (11) results from questioning of newly arrived in CDS small-scale structure's cells provided with a charge

$$q_a \simeq \frac{Q_{total}}{(L/a)^3} \left(\frac{L}{\Lambda}\right)^2. \tag{14}$$

Comparing (11), (12), (13) we discover, that in time τ about $(L/a)^{3-\gamma}$ CDS's elements are substituted on the average . It is obvious that all CDS's elements can not be exchanged at once and thus:

$3-\gamma < d_f$. On the other hand, the number of substituted channels can not decrease with growth of a scale, therefore $\gamma < 3$.

The structural self-similarity of CDS allows to note relation (13) for any CDS's fragment with sizes $R < L$. The fragment's lifetime and the current imported by it in CDS make accordingly

$$\tau_R \simeq \tau \left(\frac{R}{a}\right)^{\gamma}, \tag{15}$$

As the potential variations are proportional to the fragment's scale $U_R \simeq E_0 R$ we can define an effective resistance and capacity of the CDS's fragment using (11), (15)

$$r_R \simeq \frac{U_R}{I_R} \simeq \frac{a\tau E_0}{q_a} \left(\frac{R}{a}\right)^{\gamma-2}, \tag{16}$$

$$C_R \simeq \frac{Q_R}{U_R} \simeq \frac{q_a}{aE_0} \left(\frac{R}{a}\right)^{2}. \tag{17}$$

The product $r_R C_R$ determines a relaxation time of a CDS circuit and $r_R C_R \simeq \tau_R$.

CDS is a hierarchical system and the invariance of its structure requires a constant renewal of each floor of the hierarchy. In the active cloud part besides CDS there is a set of finer current clusters, being united with CDS renew CDS's composition at different structural levels. The set of CDS's channels by a potency $(L/a)^{3-\gamma}$ varies on a time interval about τ. For this time the part of elements goes out of CDS composition other part turns to larger drainage channels joining CDS with other conductive fragments.

The entered current I_L characterizes median magnitude of a charge transferred by CDS for a time unit. Really, a charge carrier in CDS is exercised by discrete portions, which's magnitude and frequency of occurrence are defined by fluctuations of CDS structure. The electric fields fluctuations stipulated by processes of switching CDS with new clusters can be associated with observed so-called K-, J-, M-processes [4].

We estimate the emergence frequency f_R of fluctuations as a function of their scale. It is not difficult for making if to recollect, that we watch CDS renewal happening on a set of connections by a potency $(L/a)^{3-\gamma}$ with fragments of a scale R and lifetime τ_R. Thus,

the frequency of an occurrence of clusters with characteristic spatial R and temporal τ_R scales is equal to

$$f_R \simeq \tau_R^{-1} \left(\frac{L}{R}\right)^{3-\gamma} \simeq \tau^{-1} \left(\frac{R}{a}\right)^{-3} \left(\frac{L}{a}\right)^{3-\gamma}. \tag{18}$$

The largest events — fluctuations of a scale L — occur with the frequency

$$f_L \simeq \tau^{-1} \left(\frac{L}{a}\right)^{-\gamma} \simeq \tau_L^{-1}. \tag{19}$$

The relevant fluctuations of the dipole moment are estimated by magnitude

$$\Delta M_L \simeq Q_{total} \left(\frac{L}{\Lambda}\right)^2 L. \tag{20}$$

The modifications of the dipole moment caused by fluctuations on an intermediate scale $a < R < L$ make

$$\Delta M_L \simeq q_a R^4. \tag{21}$$

Now we estimate modifications of a quasistatic electrical energy $W_R \simeq P_R \tau_R$ caused by current fluctuations, here P_R is a power of low-frequency electrical variations. For fluctuations of a scale R we have

$$P_R \tau_R \simeq \int_0^R q_a \left(R'\right)^3 E_0 dR' \simeq q_a \left(\frac{R}{a}\right)^3 E_0 R \sim R^4. \tag{22}$$

Using (18) and (21) for dimensionless frequency of events we have

$$\ln\left(\tau f_R\right) \simeq (-\gamma) \ln\left(\frac{L}{a}\right) - \frac{3}{4} \ln\left(\frac{W_R}{W_L}\right). \tag{23}$$

The relation (23) reflects the fact of a diminution of events' frequency with magnification of their energy and under the shape coincides with the known empirical law of earthquakes recurrence. At $R = L$ (23) is identical to (19).

5. Fractal mechanism of a field amplification in a cloud-ground gap

Scenario of the lightning development essentially depends on the large-scale field configuration. For intracloud discharge the field is generated by extended and oppositely charged zones inside the cloud. In this case CDS represents a stochastic tree, whose rooted system is discharged on its crone. In the event of a ground discharge CDS is loaded by the ground-cloud discharge gap, and the system works as a pulse current generator. The magnification of a field in the ground-cloud gap up to a critical value is ensured with fractal geometry of CDS. It is associated with the prime geometrical fact: the flat cut of a fractal with a Hausdorff dimension D and topological dimension $d \geq 1$ gives a set with fractal dimension $D-1$ and topological dimension $d-1$. In our case it means, that charges flowing down at the metallization process are localized on a fractal set of cells on the lower cloud boundary. The set has dimension $d_f - 1$.

We estimate the electric field perturbations through the calculation of an electric field of the inhomogeneously charged plane with a charge surface density

$$\rho_\perp(R_\perp) = \begin{cases} \rho_0 & when \quad 0 < R_\perp < a, \\ \rho_0 (R_\perp/a)^{d_f-3} & when \quad a < R_\perp < L, \\ \rho_0 (L/a)^{d_f-3} & when \quad L < R_\perp < \Lambda, \end{cases} \tag{24}$$

where $R_\perp$ is the 'Euclidean' distance along the lower cloud boundary, the central point $R_\perp = 0$ corresponds actually to the starting point for the stepped leader.

Integrating (24) over the low edge of a cloud we obtain (as the first approximation in respect to L/a) magnitude of the charges that flow down

$$Q_\perp \simeq 2\pi\rho_0 a^2 \frac{1}{d_f - 1} \left(\frac{L}{a}\right)^{d_f-1} \left(\frac{\Lambda}{L}\right)^2. \tag{25}$$

If so, the field amplitude near the center can be written as

$$\delta E \simeq 4\pi\rho_0 \simeq 2a^{-2}(d_f - 1) \left(\frac{L}{a}\right)^{1-d_f} \left(\frac{L}{\Lambda}\right)^2 Q_\perp \tag{26}$$

or as

$$\delta E \simeq \frac{4\pi Q_\perp}{\Lambda^2} \frac{d_f - 1}{2\pi} \left(\frac{L}{a}\right)^{3-d_f}.$$

Taking into account, that

$$E_0 \simeq \frac{4\pi Q_{total}}{\Lambda^2} .$$

we obtain

$$\delta E \simeq E_0 \frac{Q_\perp}{Q_{total}} \frac{d_f - 1}{2\pi} \left(\frac{L}{a}\right)^{3-d_f} .$$

The dependence $Q_\perp(t)$ can be presented by the linear law:

$$Q_\perp(t) \simeq Q_{total} \frac{t}{t_{flash}} \simeq Q_{total} \left(\frac{L}{a}\right)^{-\gamma} \left(\frac{L}{\Lambda}\right)^2 \frac{t}{\tau} \qquad (25a)$$

and

$$\delta E \simeq E_0 \frac{d_f - 1}{2\pi} \left(\frac{L}{a}\right)^{3-\gamma-d_f} \left(\frac{L}{\Lambda}\right)^2 \frac{t}{\tau}. \qquad (26a)$$

Hence, the period of generation or the time interval between separate strokes in the flash can be estimated as

$$t_p \simeq \frac{E_c}{E_0} \left(\frac{L}{a}\right)^{d_f+\gamma-3} \left(\frac{L}{\Lambda}\right)^2 \tau, \qquad (27)$$

where E_c is a breakdown field value in the cloud-ground gap.

6. Discussion

Surveyed in the paper charge gathering system implies the existence of a spatial-time intracloud hierarchy. The cell's period a is an elementary spatial scale of the system. We use for estimations $a \simeq 5$ m. This scale is defined by the development of the electrodynamic instability similar to the beam instability in the multicomponent plasma. We relate the nonlinear stage of the instability development with the cloud metallization process, when the growth of a local field in cells tends to the numerous intracloud microdischarges. Simultaneously we introduce the lifetime of a conductive cell τ, which can be choosen by analogy to the spark discharge. In particular estimations we suppose $\tau = 2.5\mu$s for $a \simeq 5$ m.

The first subinterval of a preliminary breakdown stage, which lasts some tens of msec and is not accompanied by DC electric field variations, is connected in our model with a development of trains

of short-scale discharges, when the ionization front runs the distance $R < R^*$, the critical length, corresponding to a train to be transformed to a self-maintained channel. Every microdischarge produces a VHF pulse. The appearance frequency F of these pulses can be estimated from the relation:

$$F = \frac{dn}{dt} = n_{\rm m} x \gamma_b,$$

where $n_{\rm m} = v/a^3$ is the total number of cells in a thundercloud, $n_{\rm m}x$ is the number of activated cells, γ_b is the cell's growth rate (see section 2). To form a developed CDS, x must be close to the percolation critical value $x_c \sim 0.25$. Putting $v \sim L^3 \sim 125$ km, $a \sim 5$ m, $x \sim 0.2$, and $\gamma_b \sim 0.1$ s^{-1}, we find $F \sim 2 \cdot 10^7$ s^{-1}. This magnitude exceeds by the order of value the observed $F_{\rm exp} \sim 10^6$ s^{-1} [8, 9]. Possibly, this description is connected with the calculation method of these pulses. The velocity of a pulse train front, which can be estimated as $V_f > a/\tau \sim 2 \cdot 10^6$ m/s is quite reasonable in comparison with the experimental value ($\gtrsim 10^7$ m/s, see [8]). A cell activation assumes formation of some coherent pulse trains, that can explain qualitatively the Warwick's data [12].

The growth of x and, correspondinly, R leads under $R > R^*$ to appearance of a self-supported current channel, which can be associated with an intracloud leader (the second subinterval of a preliminary breakdown). It is the begining of developed CDS dynamics. On this stage the charge, moving in CDS is exercised by discrete portions, whose magnitude and frequency of occurrence is defined by the fluctuations of the CDS's elements total number. We suppose that these fluctuations correspond to the K- and J-processes.

The J- or " junction "-process takes place in the cloud during the time interval between return strokes. It is identified with an electric field having a relatively steady change on a time scale of tens of milliseconds [7]. The J-processes are stipulated by the largest modifications of the drainage system on a space scale $R \gtrsim L$. It is specified by mainly horizontal transference of a negative charge at the J-processes. Within the framework of the developed approach the crossover time τ_L corresponds to the characteristic temporal scale of J-variations. When $t_{flash} = 0.5sec$, $\Lambda = 25km$, $L = 5km$, $\gamma = 1.3$ the crossover time is estimated by magnitude $\tau_L = 20msec$. The

dipole moment maximum fluctuations make $\Delta M_L \sim 20C \cdot km$. The J-processes correspond to "slow" questioning of large-scale regions on a space scale L. The K-processes have duration less than one millisecond and dipole moment modifications about $0.1 \div 1C \cdot km$ [7]. In our model the intervals between K-variations may be linked to the times τ_R when $R < L$. Characteristic frequencies $1/\tau_L \sim 50Hz$ and $1/\tau \sim 400kHz$ determine the cloud radiation low-frequency band.

The CDS demonstrates scaling properties when $a < R < L$. During a flash CDS's configuration changes $t_{flash}/\tau_L \simeq (\Lambda/L)^2 \simeq 25$ times. The median CDS current makes about $200A$ and transfers the charge $Q_{total} = 100C$. This value is typical for the median magnitude of a stepped leader current. The same value corresponds to the continue current magnitude between strokes.

7. Conclusions

The offered model describes dynamics of the electrical charges in a thunderstorm cloud on its mature stage. Two key assumptions form the model basis. The first one suggests a small-scale electric structure of a cloud. The structure development manifests itself as multiple discharges casually originating in space and in time and filling a central part of a cloud. This structure originates by reason of dissipative beam-plasma instability in a thundercloud. Such an instability is accompanied by a cloud small-scale electrical stratification having the scales $a \sim 1 \div 10^2$ m [14, 15]. The second assumption states, that originating conductive connections generate a fractal structure. This allows the analysis of the large-scale electric field and charge behavior to be reduced to a percolation problem. The problem is similar in many respects to the development of a drainage system with growing inflows number (the number of connections increases). The cluster-to-cluster aggregation plays an important role here. In process of this aggregation the electric current grows induced by the large-scale electric field. The current trunk appears conditioned by association of the conductive clusters. This aggregation conceptually is described by single formula (11) representing the current growth with the cluster scale magnification.

There is a problem of the sharp non-stationarity of the cluster's originating and vanishing. We suppose here that when the electric

current grows, the threshold is achieved, when the ohmic dissipation begins to support the quasi-stationary channelling. Similar effect takes place in an electric arc. When joining the channel, the new-generated clusters connect various volumes with a relevant spatial charge to the trunk, allowing the cumulative current to flow down. The current channel plays a role of an original conductive edge, where the charge accumulates and the large-scale electric field reaches the breakdown value. From this edge, the basic lightning discharge leader develops. The topological similarity with the fractal processes allows to describe quantitatively the effects mentioned above.

It is surprising, that the model based on the relatively small number of parameters (a, L, τ and d_f) allows to describe (qualitatively and sometimes quantitatively) the basic properties of the preliminary stage of lightning discharge and the K- and J-processes; the charge lowering; the current accumulation; particular stroke series in a flash; the ramified structure of the electrical discharges inside a cloud.

The further steps should include at first the sophysticated experimental investgiations of short-scale fields and space charges with good space ($l \leq 1\ m$) and temporal resolution at different stages of a thundercloud evolution. We plan to develop the computational model for a cloud metallization to find the conditions for its critical behavior (when $x \sim x_c$) and to consider transition to the leader formation. It is necessary to develop the physical model of the intercloud beam-plasma instability in a more rigorous approximation.

References

1. MacGorman D.R., Rust W.D., *The electrical nature of storms*, Oxford University Press 1998
2. Labanne G., Richard P., Bondion A., in *Lightning Electromagnetics*, edited by Gardner R.L., 1987 pp. 285–317
3. Dulzon A.A., Noskov M.D., Lopatin W., Shelukin P.V., in *Proc. 10th Intern. Confer. On Atmos. Electricity*, Osaka 1996, 1996 p. 260
4. Rakov V.A., Uman M.A., *J. Geophys. Res.* 1990, **95**, 18631
5. Borovsky J.E., *J. Geophys. Res.* 1995, **100**, 2697
6. Beasley W., Uman M.A., Rustan P.L., *J. Geophys. Res.* 1982, **87**, 4883
7. Uman M.A., *The Lightning Discharge*, vol. 39 of *Internat. Geophys. Series* 1987

8. Proctor D.E., Uytenbogaargt R., Meredith B.M., *J. Geophys. Res.* 1988, **93**, 12683
9. Moreau J.P., Rustan P.L., in *Lightning Electromagnetics*, edited by Gardner R.L., 1987 p. 257
10. Mazur M., Krehbiel P.R., Shao X.M., *J. Geophys. Res.* 1995, **100**, 25731
11. Proctor D.E., *J. Geophys. Res.* 1983, **88**, 5421
12. Warwick J.W., in *Dusty and Dirty Plasmas, Noise and Chaos in Space and in the Laboratory*, edited by Kikuchi H., Plenum Press, N.Y., 1994 pp. 284–293
13. Marshall T.C., Rust W.D., *J. Geophys. Res.* 1991, **96**, 22297
14. Trakhtengerts V.Y., *Doklady Akad. Nauk SSSR* 1989, **308**, 584
15. Trakhtengerts V.Y., *J. Atmos. Terr. Phys.* 1992, **54**, 217
16. Burne C.I., Fen A.A., Stenard M.E., Conrad A.C., Torzon R.L., *J. Geophys. Res.* 1987, **92**, 1017
17. Mareev E.A., Sorokin A.E., Trakhtengerts V.Y., *Fizika Plazmy* 1999, **25**, 289
18. Bazelyan E.M., Raizer Y.P., *Spark Discharge*, CRC Press, New York 1998
19. Visman G., Pietronero L., Mir, Moscow, 1988 pp. 210–220
20. Bownum D.R., Stroud D., *Phys. Rev. B* 1989, **40**, 4641
21. Shklovsky B.I., Efros A.L., *Uspekhi Fiz. Nauk* 1975, **117**, 401
22. Stauffer D., *Phys. Reports* 1979, **54**, 1
23. Sokolov I.M., *Uspekhi Fiz. Nauk* 1986, **150**, 221
24. Feder E., *Fractals*, Mir, Moscow 1991
25. Wang D., Shimada Y., Uchida S., Fujiwara E., Kawasaki Z.I., Matsuura K., Izaka Y., Yamanaka C., in *Dusty and Dirty Plasmas, Noise and Chaos in Space and in the Laboratory*, edited by Kikuchi H., Plenum Press, N.Y., 1994 pp. 313–322
26. Kolb M., *Phys. Rev. Lett.* 1984, **53**, 1653
27. Nagatani T., *Phys. Rev. E* 1993, **47**, 63
28. Witten T.A., Sandera L.M., *Phys. Rev. B* 1983, **27**, 5686
29. Smirnov B.M., *Physics of fractal clusters*, Nauka, Moscow 1991

INFLUENCE OF THE MAGNETIZED PLASMA SHELL ON EFFICIENCY OF RADIATION OF A SHORT ANTENNA

E.E. Dynin, A.V. Kostrov, A.I. Smirnov, M.V. Starodubtsev

Institute of Applied Physics, Russian Academy of Sciences, Nizhny Novgorod, Russia

Experimental investigations of an electric dipole surrounded with a magnetized plasma shell show that the input impedance of such an antenna system could be matched with a feeder in a wide frequency range near the lower-hybrid frequency. As a result, the radiated power in the presence of the plasma shell grew by almost three orders as compared to radiation of the dipole without plasma.

It is known that an electric antenna placed in an isotropic plasma shell has resonance properties at the frequencies close to the plasma frequency, $\omega_0 \leq \omega_p$, which is connected with vanishing of its input reactance. By that, dielectric permittivity of the plasma, $\varepsilon = 1 - \omega_p^2/\omega_0^2$, is negative, since plasma reactance has the inductive character, and the transitional double layer (or an insulating layer near the antenna surface) and the free space are a capacity.

It is evident that the use of plasma shells as matching devices is most promising for short antennas ($k_0 L << 1$, where $k_0 = \omega_0 /c$, and L is efficient size of the emitter) at frequencies below 1 MHz ($\lambda > 300$ m). In the case of isotropic plasma, at such frequencies the resonant conditions can be fulfilled only at very low densities ($n_p < 10^5$ cm^{-3}), for which, under the conditions of a real experiment, the plasma frequency is lower than the frequency of collisions with neutrals ν_{em}. In the magnetized plasma, geometric resonance can be realized at higher plasma densities ($\omega_p >> \omega_0, \nu_{eff}$) [1]. This resonance is connected with the negative value of transverse dielectric permittivity at frequencies below the lower-hybrid frequency, ω_{lh}: $\varepsilon_\perp = 1 + \omega_p^2(1 - \omega_{lh}^2/\omega_0^2)/\omega_c^2$, where ω_c is electron gyrofrequency, and $\omega_p > \omega_c >> \omega_0$.

This report describes an experimental investigation of the influence of a magnetized plasma shell on efficiency of radiation of an electric dipole antenna in the frequency range below the lower-hybrid frequency (30 kHz $< \omega_0 <$ 2 MHz).

Investigations of electrodynamic characteristics of the electric dipole antenna surrounded with a magnetized plasma shell were performed at the set-up being a glass tube 100 cm long and 16 cm in diameter that

contained an electric dipole with $2l = 80$ cm. The working gas was argon under pressure $p \sim 10^{-3}$ Torr. Magnetic field was produced by two Helmholtz coils 50 cm in diameter each. The maximum value of the magnetic field reached $H = 100$ Oe. The plasma was produced by means of a pulse inductance high-frequency discharge. Efficiency of antenna radiation in the plasma shell was studied in the regime of decaying plasma, i.e. after the plasma source had been turned off (see upper curve in Fig.1). Plasma density reached its maximum, $n_p \sim 10^{13}$ cm^{-3} and relaxed with characteristic time $\tau \sim 500$ μs. The emitting antenna was continuously fed with a high-frequency monochromatic signal from the generator. The feeder was equipped with a 50-Ohm reflectometer, which made it possible to measure the amplitude and phase of the signal reflected from the antenna. As the receiving antennas, a symmetric electric dipole with $2l = 2$ cm and a shielded loop antenna were used.

The regime of decaying plasma gave the possibility to determine, during one cycle of set-up operation in the wide range of plasma density variation, the optimal conditions for plasma antenna radiation.

Characteristic oscillograms of the signals from the receiving antenna placed at the distance of 2 m from the emitting one are shown in Fig.1 (middle curve). It is evident that radiation of the antenna surrounded with the plasma shell has the resonance character in time, i.e. exists in a certain range of plasma density variation. There is no radiation in dense plasma and it appears only at some resonant value of density at the moment of the best matching of the antenna with the feeder (lower curve in Fig.1). As the frequency of the signal fed to the antenna grew the minimum of the reflected signal and the maximum of radiation were shifting towards more dense plasma. For example, for $f_0 = 100$ kHz the maximum of radiation corresponds to plasma density $n_{res} = 7 \cdot 10^{10}$ cm^{-3}, and for $f_0 = 1$ MHz, to plasma density $n_{res} = 2 \cdot 10^{11}$ cm^{-3}.

One of the important characteristics of this antenna system is the coefficient of amplification of plasma antenna radiation power as compared to radiation of a similar antenna without plasma. For the frequency $f_0 = 100$ kHz it is, as shown by the experiments, the value of the order of 10^3. A characteristic peculiarity of the plasma antenna system is weak (as compared to conventional short antennas) dependence of the emitted power on frequency: the maximum amplitude of the emitted signal with frequency fall-down from 1 MHz to 30 kHz decreased by not more than three times.

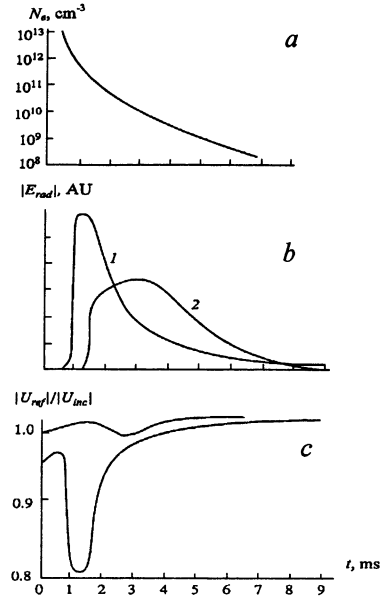

Fig. 1. Oscillograms of plasma density (*a*), amplitude of electric fields at a distance 1 m from the emitter (*b*) and amplitude of reflected signal (*c*):
1 – f_0 = 1 MHz, *2* – f_0 = 100 kHz.

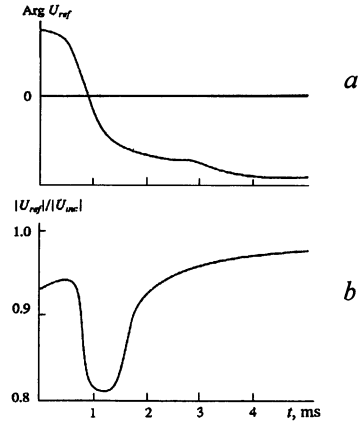

Fig. 2. Phase (*a*) and amplitude (*b*) measurements of the reflected signal. f_0 = 1 MHz.

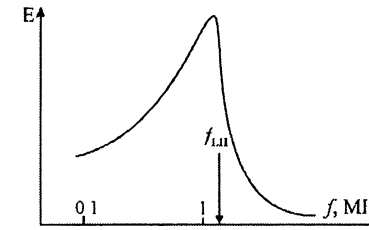

Fig. 3. Electric fields inside the plasma shell as a function of the working frequency.

Phase measurements show that in dense plasma ($n_p >> n_{res}$) the input impedance of the antenna is inductive (there is no radiation). At plasma density corresponding to the minimum of the reflection coefficient (Fig. 2), the input reactance of the antenna vanishes, and the real part of the impedance is strongly dependent on density, n_{res}, at which matching happened, and, thus, is noticeably different at different frequencies (as the result of that, for a greater part of frequencies only partial matching of the antenna with the feeding line is observed).

The high-frequency field within the plasma chamber and in the free space appears at the same time at the moment of matching. Before that moment (at $n_p > n_{res}$) there is no field in the plasma, after that ($n_p < n_{res}$) the field fills the entire plasma chamber uniformly. It should be noted that at the frequencies below the lower-hybrid frequencies significant amplification of the field in plasma took place, as compared to the field in the free space, whereas at the frequencies over the lower-hybrid one there was no such amplification (Fig. 3). One can see that electric fields inside the plasma volume reach the maximum of amplitude near the lower hybrid frequency what prove that there is resonance in the system of oscillator–plasma–free space in the lower-hybrid frequency range.

Thus, the experimental investigation of electrodynamic characteristics of the dipole antenna surrounded with a magnetized plasma shell demonstrate that such an antenna system has matching properties for low frequencies ($\omega_0 < \omega_{lh}$). In the presence of the plasma shell the power radiated by the antenna grew by almost three orders as compared to radiation of the dipole without plasma.

Definitive interpretation of the observed resonance is complicated by the difficulty of analytical description of the emitter even in the framework of a quasi-static model ($\omega_p L/c << 1$, where L is oscillator length). Under the conditions of the experiment described in this paper, the quasi-static approximation may be invalid, therefore explanation of the experimental results requires further experimental and theoretical studies.

The results obtained seem to be sufficiently promising in terms of making efficient small-sized antenna devices in the long-wave range.

This work was supported by RFBR (grants №98–02–17177 and 98–02–17028).

References

1. Kostrov A.V., Pakhotin V.A., Smirnov A.I. et al., Sov. J. Plasma Phys., 1995, **21**, 460

WHISTLER EXCITATION BY ELECTRON BEAMS IN A MAGNETOPLASMA

C. Krafft, M.V. Starodubtsev, A.V. Kostrov**

Laboratoire de Physique des Gaz et des Plasmas,
Universite Paris-Sud, Orsay, France
*Institute of Applied Physics, Russian Academy of Sciences,
Nizhny Novgorod, Russia

Measurements have been performed in a laboratory experiment modeling the interaction of a modulated electron beam with a magnetized plasma under conditions relevant to space experiments. Whistler emission through different mechanisms have been evidenced. Nonresonant whistler excitation is produced by transition radiation from the point of beam injection into the plasma. Whistler emission through Cherenkov and normal Doppler-shifted cyclotron resonances has been characterized as a function of the beam and plasma parameters.

Modulated electron beams can be used as emitters of VLF waves the ionospheric/magnetospheric plasma and radiating on their whole length at the modulation frequency as an artificial antenna, what has been observed in active space experiments with electron beam injection. Recent studies on whistler emission by density modulated beams have been performed in laboratory experiments [1-3]. The linear and nonlinear stages of the interaction of pulsed or modulated beams with magnetized plasmas were also investigated theoretically and by means of numerical simulations [4, 5]. Measurements presented here have been performed in a laboratory experiment modeling the interaction of a modulated electron beam with a magnetized plasma under conditions relevant to space experiments involving beam injection. Depending on the choice of physical conditions, emission of whistler waves through resonant mechanisms of Cherenkov and Doppler-shifted cyclotron radiations could be observed simultaneously or separately from another type of whistler emission, the nonresonant transition radiation from the beam injection point [1-3]. In this report, we present the characteristics of the emission and the propagation of whistlers emitted through different mechanisms and discuss how the beam and plasma parameters govern these emissions.

The experiments are performed in a discharge plasma (argon pressure between 10^{-5} and 10^{-3} Torr) generated by a large negatively biased oxide cathode that provides electrons accelerated by an adjacent grounded grid, which ionize the gas [1]. The plasma (length of 0.7 m, radius of 0.3 m) is immersed in an axial and uniform magnetic field B_0 less than 300 G.

Pulsed discharges are used and the experiment is performed in the afterglow maxwellian plasma where the maximal plasma density reach 10^{12} cm^{-3}. The electron gun, which is a commercially available triode, is located in a separate chamber at the end of the main chamber opposite to the cathode. It consists in an oxide-coated cathode, a grid of command used to modulate and regulate the electron beam as well as an acceleration grid. The injection pitch angle can change between $\alpha_p = 0°$ and $\alpha_p = 45°$. The gun produces a beam of radius $r_b = 5$ mm with a modulated current I_b, an energy E_b and a modulation frequency f_m below 5 mA, 300 eV and 500 MHz, respectively.

The resonant beam-wave coupling is described by the condition $k_z(m) = (\omega + m\omega_c)/v_{bz}$, where k_z and v_{bz} are the parallel wave number and the parallel beam velocity ($m = 0, 1, 2,...$). When the beam injection is oblique, two resonant whistler radiation mechanisms have been evidenced: through Cherenkov ($m = 0$) and normal Doppler shifted cyclotron resonances ($m = -1$). Whistlers are right-polarized electromagnetic waves with frequency ω and wave number $\boldsymbol{k}$ verifying the dispersion relation: $c^2 k^2/\omega^2 \approx \omega_p^2/(\omega(\omega - \omega_c \cos\theta))$ in the cold plasma approximation and for a dense plasma; θ is the whistler propagation angle with respect to the magnetic field B_0 directed along the z-axis. Both for Cherenkov and Doppler radiation, beam-whistler resonant coupling only occurs for plasma densities lower than the plasma density thresholds n_p^{Ch} (for $m = 0$) and n_p^{D} (for $m = -1$). Whistlers excited through Doppler ($m = -1$) resonance propagate opposite to the beam direction, i.e. $(\boldsymbol{v}_{bz}\, \boldsymbol{v}_{gz}^{D}) < 0$ and $(\boldsymbol{v}_{bz}\, \boldsymbol{v}_{pz}^{D}) < 0$, where $\boldsymbol{v}_{gz}^{D}$ and $\boldsymbol{v}_{pz}^{D}$ - parallel group and phase velocities vectors of Doppler radiation. On the contrary, Cherenkov radiation propagates in the beam direction: $(\boldsymbol{v}_{bz}\, \boldsymbol{v}_{gz}^{Ch}) > 0$ and $(\boldsymbol{v}_{bz}\, \boldsymbol{v}_{pz}^{Ch}) > 0$, where $\boldsymbol{v}_{gz}^{Ch}$ and $\boldsymbol{v}_{pz}^{Ch}$ - parallel group and phase velocities vectors of Cherenkov radiation.

As the electron bunches produced by the cathode of the electron gun are traveling in the vacuum inside the gun chamber, then passing through a metallic interface (wall of the chamber) at the gun exit (injection point of the beam) and penetrating inside another medium (plasma), one expects that wave fields associated with the so-called transition radiation phenomenon should exist and be detectable in the plasma chamber. To first approximation, the beam can be modelled as successive point charges moving out of the gun into the plasma, leading to an effective electric dipole formed by the injected electrons and their image charges induced in the conducting wall surrounding the electron gun.

Transition radiation

Experimental measurements have been performed in the afterglow plasma that permits us to study a wide range of plasma densities. Whistler excitation through resonant mechanisms by a modulated beam is only possible for plasma densities below critical densities n_p^{Ch} or n_p^{D}. Nevertheless, the significant whistler radiation at $n_p > (n_p^{Ch}, n_p^{D})$ has been detected. These wave fields have been identified as transition radiation from the region of the beam injection point into the plasma [1].

The nonresonant character of this beam-plasma interaction has been demonstrated owing to the measurement of the parallel wavelengths of the radiated waves. Figure 1 displays interferometric curves of whistlers emitted at plasma conditions preferential to the observation of transition radiation by a beam modulated at the frequency $f_m = 50$ MHz for $B_0 = 60$ G, $E_b = 300$ eV (z_0 is the fixed longitudinal coordinate of the reference point). The waves signals have been measured by shielded and noninsulated loop antennas which were located at $r = 2$ cm radially from the beam axis. One can see that observed waves propagate with different parallel wavelengths λ_z^{tr} depending on the background plasma density, what is contrary to the properties of resonant radiation: the parallel wavelengths of whistlers excited through resonant mechanisms are fully determined by resonant conditions ($\lambda_z(m) = 2\pi v_{bz}/(\omega + m\omega_c)$) and does not depend from the plasma density.

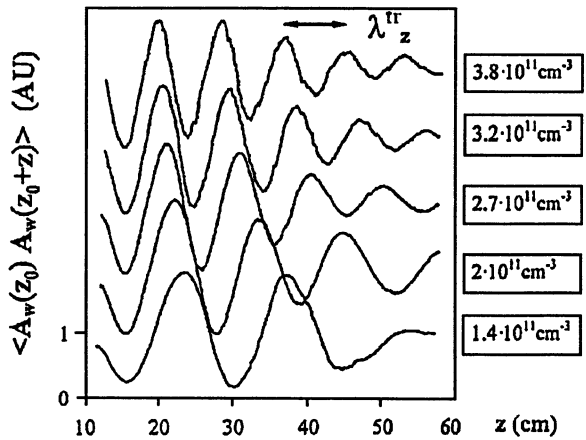

Fig.1. Interferometric measurements of transition radiation at different plasma densities

Cherenkov radiation

Owing to adequate choice of experimental conditions we have separated resonant and nonresonant whistler emissions one from each other [2]. Fig.2 shows corresponding unperturbed interferometric measurements of whistlers excited at frequency $f = 2f_m = 100$ MHz through Cherenkov resonance with a modulated electron beam, for different plasma densities in the afterglow ($E_b = 300$ eV and $B_0 = 50$ G) at parallel beam injection, when Doppler radiation is impossible. One can see that the longitudinal wavelength of Cherenkov radiation does not depend on the plasma parameters but, in accordance with whistler dispersion relation, at high plasma density (Fig.2a) near and below the critical density n_p^{Ch}, the modulated beam excites a quasi-longitudinal whistler propagating with an angle $\theta \approx 4°$ with respect to B_0. For lower plasma densities (Fig. 2b-c), whistlers are propagating with increasing θ. Conical phase surfaces and the directive radiation pattern have been observed, as predicted by theory for whistlers excited through Cherenkov resonance in an infinite magnetized plasma volume. For very low plasma densities, θ tends to the resonance cone angle $\theta_{res} \approx 44°$ (Fig. 2d).

Doppler radiation

When the beam injection is oblique, whistler radiation through normal Doppler shifted resonance ($m = -1$) with the beam has also been observed [3]. Measurements of phase velocities (v_{pz}^{Ch}, $v_{p\perp}^{Ch}$) and (v_{pz}^{D}, $v_{p\perp}^{D}$) of whistlers radiated through Cherenkov and Doppler resonances are shown on Fig.3a-b and Fig.3c-d, respectively. One can see that Cherenkov radiation propagates in the beam direction and the measured phase velocity $v_{pz}^{Ch} \approx 7.4 \cdot 10^8$ cm/s (see Fig.3a) is in a good agreement with the independently measured beam parallel velocity $v_{bz} \approx 7.6 \cdot 10^8$ cm/s; the perpendicular phase velocity $v_{p\perp}^{Ch}$, of the order of 10^9 cm/s (see Fig.3b), is also close to the theoretical value. Figures 3c and 3d show similar measurements performed in the domain of plasma parameters preferable for observations of Doppler radiation. One can see that in this case whistlers propagate opposite to the beam direction as it is the case for resonant radiation at $m = -1$. Moreover, the corresponding phase velocities v_{pz}^{D} and $v_{p\perp}^{D}$, of the order of $2.1 \cdot 10^9$ cm/s and $2.7 \cdot 10^9$ cm/s, respectively, are in accordance with phase velocities of whistlers excited through Doppler resonance. The linear dependence $k_z^D(B_0)$, characteristic of the Doppler radiation, has been found.

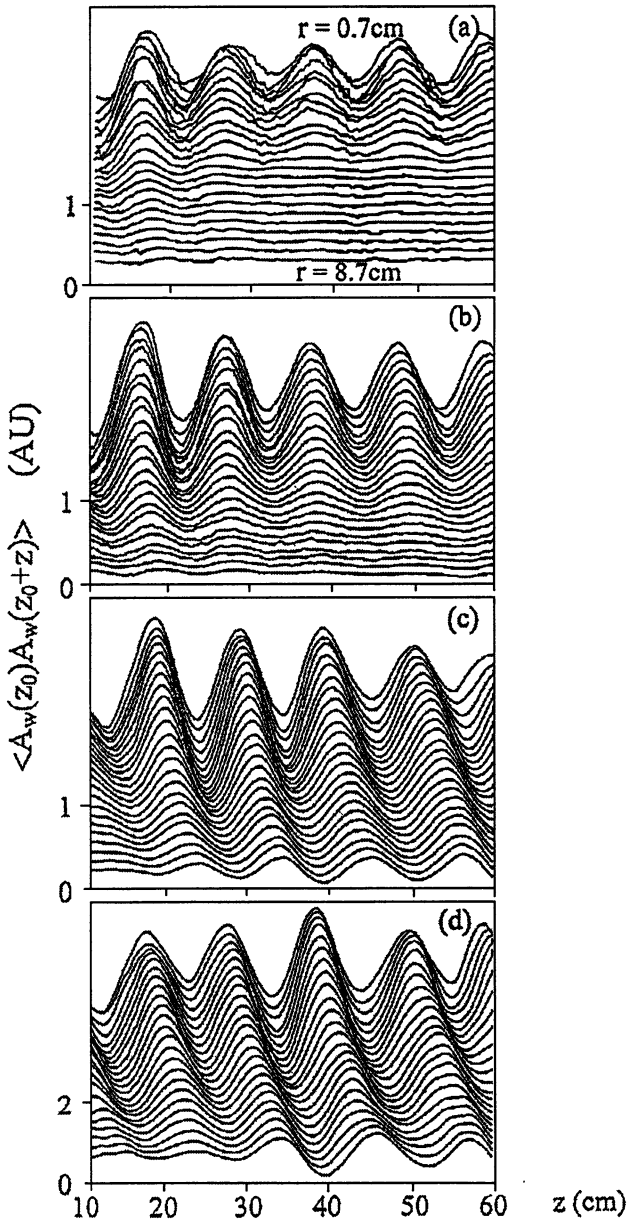

Fig.2. Interferometric measurements of Cherenkov radiation at different plasma densities: $a - 4.2 \cdot 10^{10}$ cm^{-3}, $b - 4 \cdot 10^{10}$ cm^{-3}, $c - 3.4 \cdot 10^{10}$ cm^{-3}, $d - 1.7 \cdot 10^{10}$ cm^{-3}.

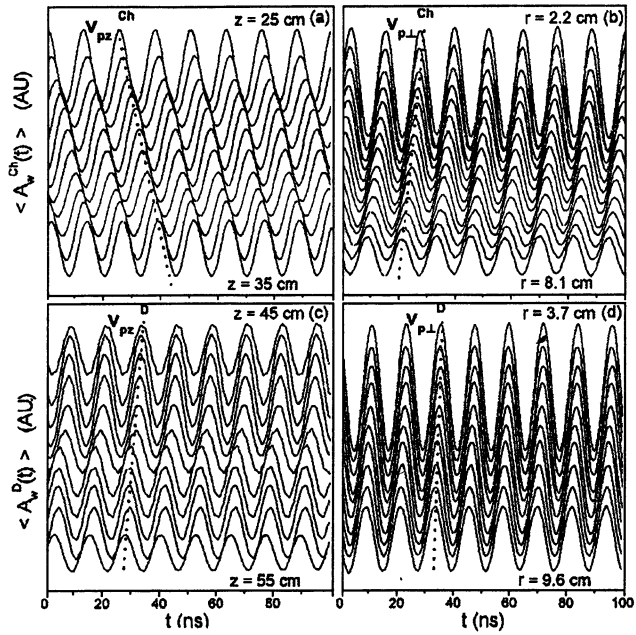

Fig.3. Phase velocities: *a,b* – Cherenkov radiation, *c,d* – Doppler radiation.

In conclusion, first observations of whistlers excited spontaneously by a modulated electron beam through different mechanisms: (i) nonresonant transition radiation, (ii) Cherenkov resonance and (iii) normal Doppler shifted resonance have been observed in a laboratory experiment. The characteristics of the excited waves have been found in a good accordance with theoretical predictions. These results should shed light on mechanisms of whistler waves excitation in space plasmas, either by artificial beams injected from satellites in the ionosphere and the magnetosphere or by fluxes of energetic particles present in many astrophysical and space phenomena.

This work was supported by MENESR (France) and RFBR (grants №98-02-17177 and 98-02-17028).

References

1. Starodubtsev M., Krafft C., et al. Phys.Plasmas, 1999, **6**, 1427.
2. Starodubtsev M., Krafft C., et al. Phys.Plasmas, 1999, **6**, 2862.
3. Starodubtsev M. and Krafft C. Phys.Rev.Lett., 1999, **83**, 1335.
4. Volokitin A., Krafft C., Matthieussent G. Phys.Plasmas, 1997, **4**, 4126.
5. Krafft C. and Volokitin A. Phys.Plasmas, 1998, **5**, 4243.

BLEACHING OF OVERDENSE PLASMA UNDER ELECTRO-MAGNETICALLY DRIVEN LANGMUIR TURBULENCE

*A.V. Kochetov, E. Mjoelhus**

Institute of Applied Physics, RAS, Nizhny Novgorod, 603600, Russia
**University of Tromsoe, Tromsoe, N-9037, Norway*

The parametric Langmuir turbulence drive by electromagnetic field in homogeneous overdense plasma was studied in the framework of the Zakharov system of equations including driven and damped extensions. The modification of real and imaginary parts of the effective (spatially and temporally averaged) dielectric constant due to Langmuir turbulence excitation was investigated. It was demonstrated that the saturation turbulence level corresponded to plasma bleaching and depended on prehistory of drive processes.

Introduction

It was shown in papers [1-4] that the excitation of strong Langmuir turbulence in plasmas could essentially modify of real and imaginary parts of plasma dielectric constant. For example, the interpretation of some spectrum peculiarities of artificial ionospheric radiation (i.e., stimulated electromagnetic emission), strong absorption of light by plasma produced under the radiation of solids targets by laser beams (laser fusion problem) and penetration of incident waves into overdense plasma (plasma bleaching) was based on features of Langmuir turbulence driven by electromagnetic waves. Since the turbulence was driven by electromagnetic wave the wave was self-affected propagating throughout the turbulent region.

The solving of self-consistent problem of wave propagation in plasma with Langmuir turbulence seems to be extremely complicated till today, in particular, due to the large difference between the scales of electromagnetic and Langmuir waves. The basic virtue of productive approach, formulated in [1, 5, 6], is to separate the problem into three parts: the first, investigation of Langmuir turbulence excitation by given electromagnetic source, the second, calculation of the turbulence contribution into the modification of dielectric constant, the third, study of electromagnetic wave propagation.

The particular feature of present paper is the numerical simulations of parametric Langmuir turbulence drive in overdense plasma (e.g., in skin-layer of incident wave). In these conditions Langmuir turbulence drive can change cordially the regimes of interaction: initially reflected wave

get ability to penetrate into overdense plasma due to changing the sign of the real part of modified dielectric constant of plasma.

Basic Equations

Let us consider the drive of Langmuir waves $\boldsymbol{E} = \frac{1}{2}\left[E(x,t)\exp(-i\omega_0 t) + \kappa.c.\right]\boldsymbol{x}_0$ in the Zakharov system of equations [7] with driven and damped extensions:

$$\begin{aligned} &i\left(\frac{\partial}{\partial t} + \hat{\nu}_e\right)E + \frac{\partial^2 E}{\partial x^2} + (\Omega - n)E = nE_0 - \overline{nE}, \\ &\frac{\partial^2 n}{\partial t^2} + 2\hat{\nu}_i \frac{\partial n}{\partial t} - \frac{\partial^2 n}{\partial x^2} = \frac{\partial^2}{\partial x^2}\left|\boldsymbol{E} + \boldsymbol{E}_0\right|^2; \end{aligned} \qquad (1)$$

written in dimensionless variables with the units:

$$t = \frac{3}{2\eta}\frac{M}{m}\frac{1}{\omega_0}, \quad x = \frac{3}{2}\sqrt{\frac{M}{m}}\frac{r_{De}}{\sqrt{\eta}}, \quad \varepsilon = \left(\frac{64\pi}{3}\eta\frac{m}{M}h_0 T_e\right)^{1/2},$$

$$N = \frac{4}{3}\eta\frac{m}{M}n_0, \quad \Omega = \frac{3}{2\eta}\frac{M}{m}\left(\frac{\omega_0 - \omega_{pe}}{\omega_0}\right), \quad \eta = 1 + 3\frac{T_i}{T_e},$$

where $m, T_e, \omega_{pe}, n_0, r_{De}$ is the mass, temperature, plasma frequency, density and Debye-length for electrons, M, T_i is the mass and temperature of ions, $\hat{\nu}_e$ and $\hat{\nu}_i$ is damping operators (for details, see [5, 8]). We consider $E_0 > E_{th}$ for oscillating two stream instability (i.e., modulation instability) $E_{ths} = \sqrt{|\Omega|/2}$, neglecting damping terms in (1) [4].

Numerical results

The system of equations (1) was solved by means of explicit second order Fourier pseudospectral method [9]. We applied periodic boundary conditions, with low-level random fluctuations. Great care was taken to simultaneously achieved good spatial, temporal, and spectral resolution. This typically meant using 2048-4096 spatial Fourier modes and time step $\sim 10^{-4}$. All spectral quantities were calculated after all initial transients had died out and quasi-stationary turbulence level had been reached.

Our finding is that the saturated turbulent state does not have any memory of its initial state (Fig. 1).

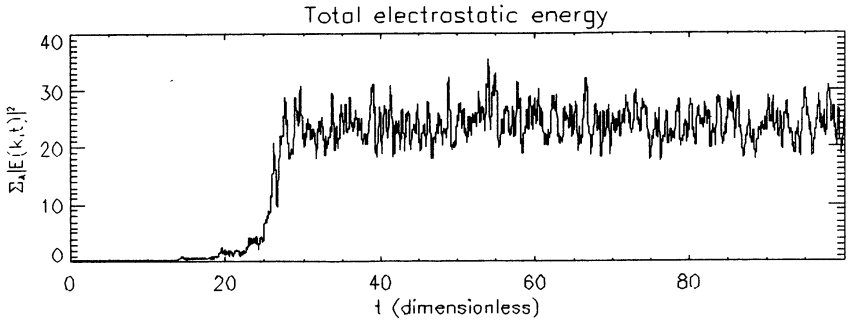

Fig. 1. Total energy of electrostatic excitations for Ω=-1, M/m=1600,T_e/T_i=3, developed from 10^{-4} initial fluctuation level.

We note that saturation turbulent state consists of nucleation-collapse-burnout cycles in the surroundings of propagating Langmuir waves and ion sound pulses (Fig. 2).

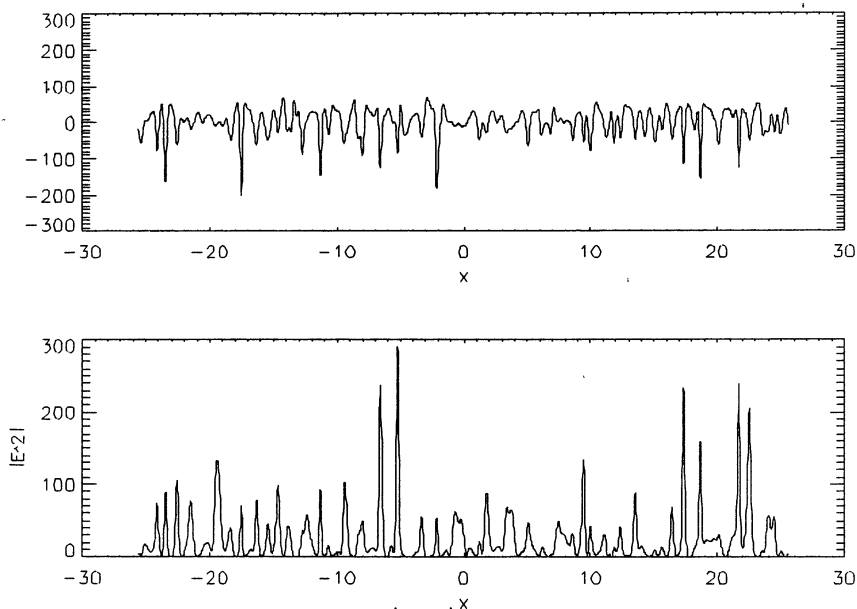

Fig. 2. Profiles of $n(x)$ and $|E(x)|^2$ at the end of computation of Fig. 1

Saturation wave number spectra of electrostatic and density excitations collapse type are shown on Fig. 3, 4. Note that broadening of

spectra is limited by damping depending on M/m, T_e/T_i and maximum position estimated by driving field E_0 [2, 3, 6].

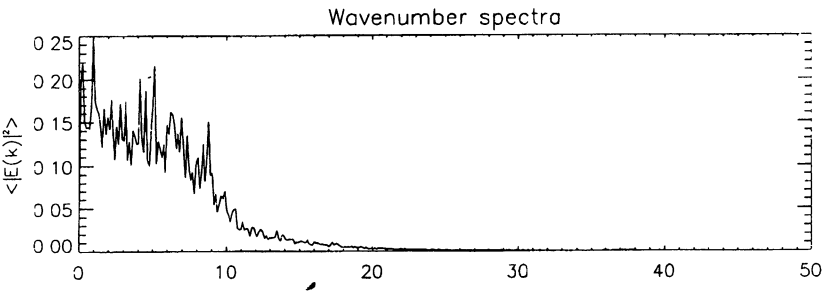

Fig. 3. Saturation wave number spectrum of electrostatic excitations $<|E(k)|^2>$, calculated for the parameters of Fig. 1

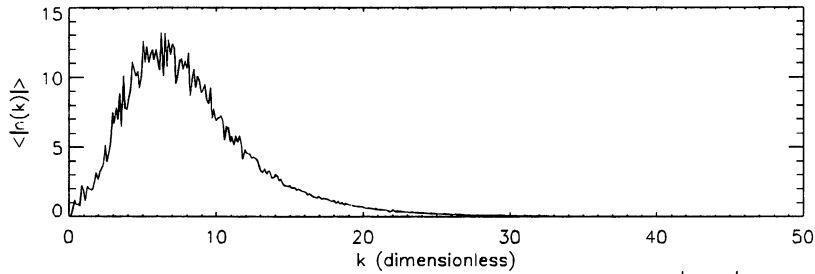

Fig 4 Saturation wave number spectrum of density excitations $<|n(k)|>$, corresponding to the electrostatic of Fig. 3

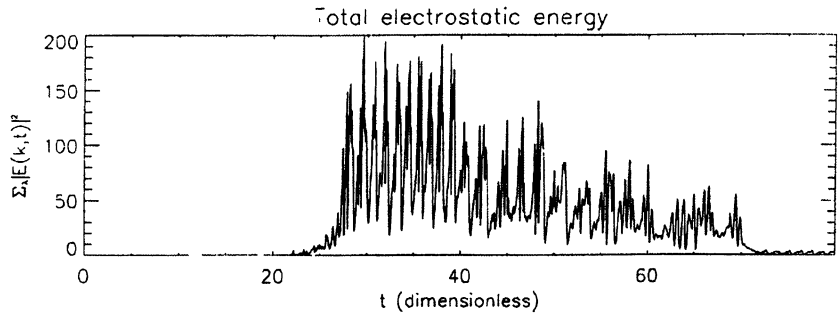

Fig. 5. Time evolution of total energy of electrostatic excitations for Ω=-18 (E_{th}=3) for step by step turning off the driving field, E_0=3.5>E_{th} (t< 40) and E_0<E_{th} (E_0=2.5, 40< t< 50; E_0=2.0, 50< t< 60; E_0=1.5, 60< t< 70; E_0=1.0, t >70)

We demonstrated that developed turbulence had memory about driving field evolution and can be supported by bellow threshold field (Fig. 5).

It was relevant for us to study the complex function:

$$\varepsilon_{eff}=\varepsilon_r+i\varepsilon_i=\Omega-\{nE\}(k=0,\omega=0)/E_0, \qquad (2)$$

where $\{nE\}$ –is Fourier transform the $nE(x,t)$ term in (1) to k, ω -space in dependence on E_0 (ε_{eff} is dielectric constant in the equation for E_0 in a self-consistent problem [4,6]). We obtain that space averaged $nE(x,t)=\{nE(k=0,t)\}$ strongly oscillates with amplitude depending on driving field (Fig. 6). It takes to be of great care to control the accuracy of calculations.

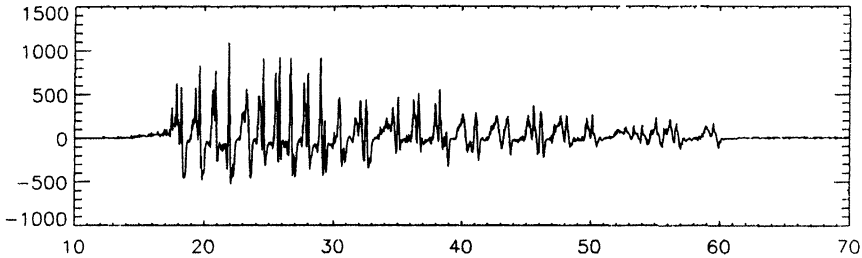

Fig. 6. Time evolution real part of $\{nE(k=0,t)\}$ for the same driving field and plasma parameters as Fig. 5

The results of calculations of $\varepsilon_{eff}(E_0)$ are shown on Fig. 7.

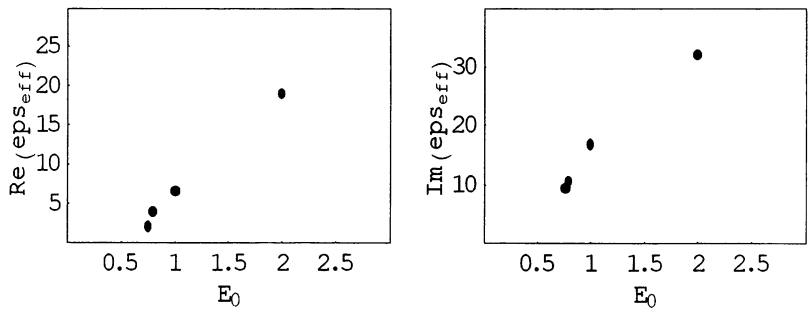

Fig. 7. Real and imaginary parts of effective dielectric constant (2) for plasma parameter of Fig. 1, depending on driving field E_0

If $E_0>E_{th}$ $\varepsilon_r>0$ and $\varepsilon_r/\varepsilon_i$ becomes smaller than E_0 increases.

Conclusion

Since real part of effective dielectric constant of overdense plasma becomes positive in strong electromagnetic field, imaginary one is of the same order and the ratio of them is decreasing with increasing of the driving field we can expect that incident electromagnetic wave can penetrate into the plasma deeper than the scale of linear opacity. In number of papers [1, 4, 5] the another type of Langmuir turbulence drive – "direct drive" was investigated. The states with small damping, i.e., with larger depth of penetration were obtained. Note that the self-consistent drive is not "direct" or "parametric" one and needs of further investigations.

Acknowledgements

The authors acknowledge the support of work by Norwegian Research Council through fellowship and grant for computing time. One of the authors (A. V. K.) acknowledges the support in part of Russian Foundation for Basic Research (Grants Nos. 98-02-17205, 99-02-16642) and thanks A. A. Balakin for the help in the manuscript preparation.

References

1. Litvak, A. G ,V. A. Mironov, G. M. Fraiman, JETP Lett., 1975, 22,174
2. Degtyarev L. M., Sagdeev R., Z., Solov'ev G., I., Shapiro V. D, V. I. Shevchenko, Plasma Phys., 1980, 6, 485
3. Shapiro V. D, V. I. Shevchenko, Handbook of Plasma Physics, Ed.. A. A. Galeev, R N. Sudan, Elsevier, 1984, vol.2, 119
4. Litvak A.G., Voprosy teorii plasmy (Problems of Plasma Theory), no.10, Moscow, Atomizdat,1980, sec.3.1
5. Litvak, A. G, V. A. Mironov, A. M. Feigin, Sov. Phys. JETP 1979, 50, 684
6. Moelhus E., A. Hanssen, D. F. DuBois, J. Geophys. Res., 1995, 100A, 17527
7. Zakharov V. E. Sov. Phys. JETP 1972, 35, 908
8. Hanssen A., E. Moelhus, D. F. DuBois, H. Rose, J. Geophys. Res., 1992, 97, 12073
9. Gotlib D., S. A. Orszag, Numerical Analysis of Spectral Modes: Theory and Applications, SIAM, Philadelphia, Pa., 1977

DYNAMICS OF THE PENETRATION OF STRONG ELECTROMAGNETIC WAVE INTO INHOMOGENEOUS PLASMA LAYER

*A.V. Kochetov, V.A. Mironov, G.I. Terina**

Institute of Applied Physics, RAS, Nizhny Novgorod, 603600, Russia
**Radiophysical Research Institute, Nizhny Novgorod, 603600, Russia*

The dynamics of the penetration of the intense electromagnetic wave into the layer with smoothly inhomogeneous plasma is investigated. The processes of the generation of the solitary structures by incident radiation and their relaxation are analysed. The thresholds for periodic and chaotic regimes are found. The nonlinear effects: shift of reflection region, "after-effect" and "super-reflection" are studied. The numerical results are compared with the observations of artificial ionospheric turbulence (AIT) by short probing radio pulses.

Introduction

The linear problem of incidence the plane electromagnetic wave onto the layer of isotropic smoothly inhomogeneous plasma with the monotonic increase of the density had been investigated in details [1]. The structure of the field in plasma is the standing wave which length and amplitude grow from vacuum to the plasma resonance point (point of reflection). For intense wave (non-linear problem) the stationary shift of the reflection region into the overdense plasma was found theoretically [2, 3]. Recently it has been demonstrated that dynamical regimes are the most typical for the penetration of the strong wave deep into homogeneous overdense plasma layer [4, 5]. In present paper the dynamics of the penetration of the incident wave deep into inhomogeneous plasma layer depending on characteristic scale of plasma inhomogeneity and the amplitude of the incident wave is studied. The main goal is to analyze of the peculiarities of the dynamic regimes by computer simulations, in particular, the stability of steady states and the ways of their setting on. The possible application of obtained results to qualitative interpretation of the signals scattered by AIT [6-9] is discussed.

Formulation of the problem. Basic equations

We assume that the half-space $x \geq -L$ is filled by the plasma with unperturbed density, $n_0(x)=(1+x/L)N_c$, where $N_c=m\omega^2/4\pi e^2$, ω - is wave

frequency, m, e - are electron mass and charge respectively. Plasma layer is radiated by normally incident electromagnetic wave. Density of plasma is modified in the field as $n(x)=n_0(x)\exp(-|u|^2)$, $u=E_0/E_p$ - is the complex amplitude of the wave, normalized to plasma field, $E_p^2=16\pi N_c T$, T, -is the temperature of electrons (we seek the solution of the electric field in the layer in the form $E(x,t)=E_0(x,t)\exp(-i\omega t)$).

For the description of the field evolution in plasma the modified nonlinear Shroedinger equation (NSE) is used

$$iu_t+u_{xx}+(1-n(x,|u|^2))u=0 \quad (1)$$

It is written in dimensionless variables with units $t=2/\omega$, $x=1/k_0=c/\omega$, c-is the light velocity.

Since the amplitude of the incident wave is given $u_0(t)$ and the depth of penetration is limited the corresponding boundary conditions have a form

$$u_x=-iu+2iu_0(t)\big|_{x=L} \quad (2)$$

$$u=0\big|_{x=\infty} \quad (3)$$

The typical laws of the turning on (at $t=0$) and turning off (at $t=t_1$) of the incident wave are

$$u_0(t)=u_0(1-\exp(-t^2/T_0^2)),\ T_0>>1, \quad (4)$$

$$u_0(t)=u_0\exp(-(t-t_1)^2/T_1^2),\ T_1>>1 \quad (5)$$

There is no initial field in the layer

$$u(x,t=0)=0. \quad (6)$$

Numerical simulations. Discussion of the results

The system of equations (1)-(6) has been solved numerically. For discrete approximation of NSE the Crank-Nicholson scheme is used. The field on the next moment is found by the method of tridiagonal inversion. Nonlinear term is taken into account by the predictor-corrector techniques. The program calculates $u(x,t)$, $n(x,t)$, the amplitude of the reflected wave $u_r(,t)=u(0,t)-u_0$. For analysis of regimes of the interaction the distribution of energy to spectral components have been performed

$$S(\omega)=\int_0^\infty u(x,t)\exp(i\omega t)dt\,.$$

It have been obtained that the steady states are stable when the $p=u_0(k_0L)^{1/2}\le 1.5$ (p is the unique parameter determining the problem of the interaction in the cubic nonlinearity approach [3]). If p is above threshold the periodical stage occurs. The periodical regimes specify the

oscillating fields in the layer and the amplitude of reflected wave as well (Fig. 1), k_0L=250, unless otherwise mentioned.

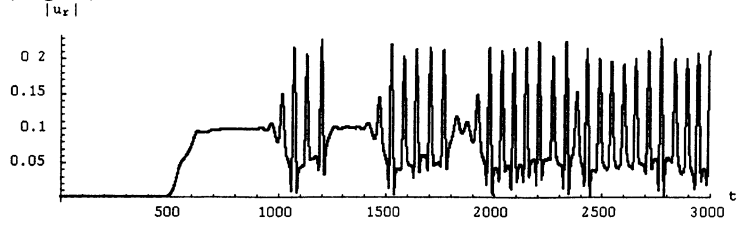

Fig. 1 (u_0=0.15)

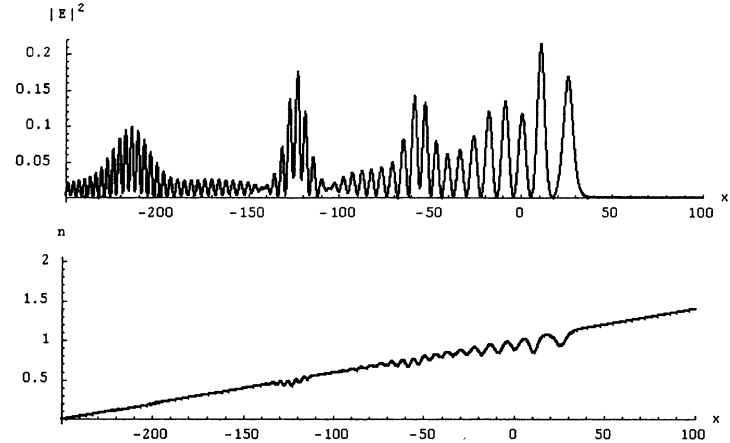

Fig. 2 (t=3400)

The spatial field distribution combines the number of envelope solitons of electromagnetic waves generating in the point of the reflection and moving out of the plasma to the boundary with vacuum (Fig. 2). We can separate out a few coherent components (harmonics) revealing the characteristic time scales (Fig. 3). The frequency of the soliton generation increases with the increase of u_0. The results allow interpreting peculiarities of the signals scattered by AIT [6, 8].

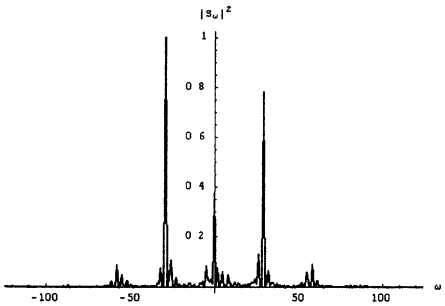

Fig. 3

For $p \geq 2.5$ oscillograms became extremely complicated (chaotic) (Fig. 4).

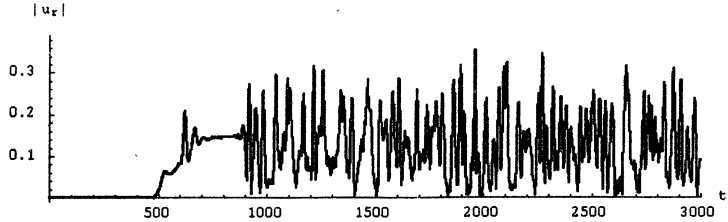

Fig. 4 (u_0=0.2)

So we investigate the smoothly inhomogeneous density profile we can conclude that the region for existence the periodical regimes isn't too large just as for homogeneous layer [5]. In spectra the incoherent components (broad continuum) appear (Fig. 5)). The incoherent component becomes comparable with the coherent one. The spatial wave structure contains a lot of quasi-solitons, which are situated close to each other and strongly affect one to another (Fig. 6).

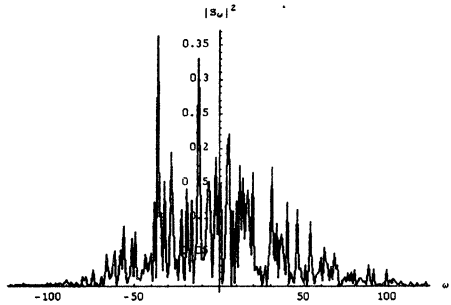

Fig. 5

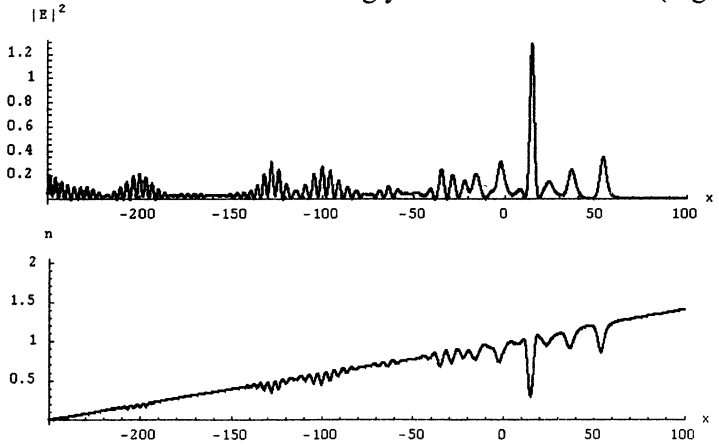

Fig. 6 (t=3000)

This regime obviously demonstrates the properties of strong wave turbulence [10]. Here the turbulence is driven by the incident wave.

Damping connects with the radiation loses from the turbulence regions due to reflected wave.

We must to pay attention to the existence of the large upshifted (HF) components in dynamical spectra, for example in Fig.5 the intensity of HF continuum is 44% of the reflected one. It can be explained as a consequence of the Doppler effect at the reflection of the incident wave from the quasi-solitons moving in the opposite direction.

For applications the question about the depth of penetration is important. We have demonstrated of the expansion of penetration in dynamics (periodical and chaotic) (Fig. 7, l_m – is the depth of penetration) in comparing to steady state [2, 3]. To our mind this effect is connected with the additional pressure of electromagnetic field to plasma in dynamics, especially in the conditions of typical for dynamics regimes of "super-reflection" [11], when the amplitude of reflected wave is large then the incident one.

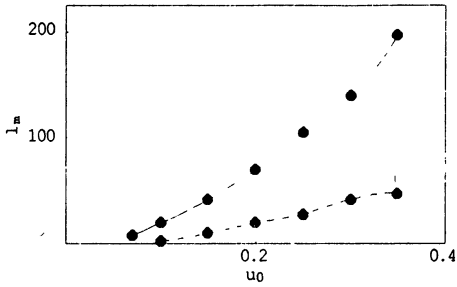

Fig.7 (k_0L=210–solid line, k_0L=70–dashed line)

The evolution of the fields in layer after the turning off the incident wave is studied also. According the inverse scattering problem [12] the solitons [13] are the asymptotic stage ($t\to\infty$) of the initial field distribution (Fig. 8).

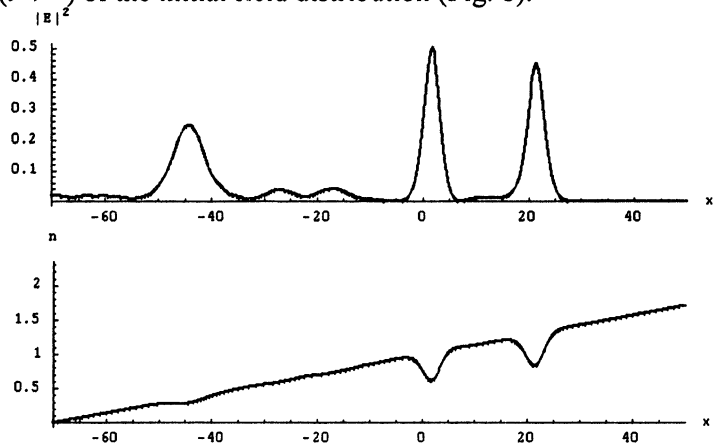

Fig. 8 (k_0L=70, u_0=0.2, t_1=500, t=575)

Some of the formed solitons can penetrate into the overdense plasma if they have the appropriate velocity. In the long run all solitons move to the boundary with vacuum and emit of the portion of electromagnetic energy with some time delay after turning off the transmitter. It causes the splashes of the receiving signals as under "super-reflection" effect (Fig. 9). The signals of this type were observed in probing of AIT by electromagnetic pulses. They were called the" after-effect signal" and are investigated now [7, 9].

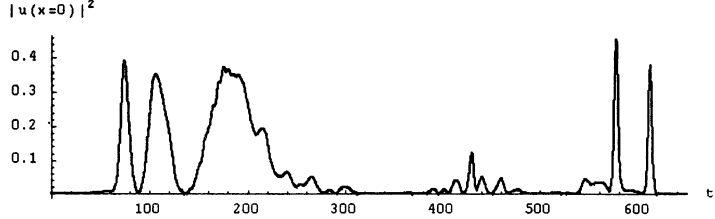

Fig. 9

The authors acknowledge the support of this work in part by Ministry of Higher Education of Russia (Grant No. 97-0-5.3-113) and Russian Foundation for Basic Research (Grants Nos. 98-02-17205, 99-02-16642) and A. A. Balakin for the help in the manuscript preparation.

References

1. Landau L.D., Lifshitch E.M., Electrodynamics of continuous media, Pergamon, Oxford, 1984
2. Gurevich A.V. and Shvartsburg A. V., Nonlinear theory of the propagation of radio-waves in ionosphere, Moscow, Nauka, 1973, 128
3. Fraiman G.M., Izv. VUZov, Radiophyzika, 1973, 16, 1146
4. Kochetov A.V., Sov.J. Plasma Phys., 1990, 551
5. Kochetov A.V., Pikovsky A.S., Proc.IV Intern. Workshop "Nonlinear World", USSR, Kiev, 1989, v 1, 352
6. Terina G.I, J. Atm. Terr. Phys, 1995, p. 273
7. Terina G.I., Izv. VUZov, Radiophyzika, 1996, 29, 203
8. Dmitriev C.A., Terina G.I, Tushentsova I.A., III Volga Intern. Summer Sch. On Space Plasma Ph., ISS97, N. Novgorod, Russia, Uppsala, Sweden, 1997, 44, Radiophyzika, in press
9. Terina G.I., Izv. VUZov, Radiophyzika, in press
10. Litvak A.G., Voprosy teorii plasmy (Problems of Plasma Theory), no.10, Moscow, Atomizdat,1980, sec.3.1
11. Andreev N.A., Baumgartel K., Gradov O.M., Sauer K., Sunder D., Plasma Phys., 1983, 9, 254
12. Novikov S.P., Manakov S.V., Pitaevsky L.P., Zakharov V.E.(eds), Theory of Solitons, Consultants Bureau, New York, 1984
13. Chen H., Liu C., Phys. Rev. Lett, 1976, 317, 693

DYNAMIC SELF-ACTION OF WAVE BEAMS IN THE MEDIUM WITH STRICTIONAL NONLINEARITY

N.A. Zharova, A.G. Litvak, V.A. Mironov

Institute of Applied Physics, RAS, N. Novgorod, Russia

The problem of self-focusing of wave beam is investigated analytically and numerically taking into account the inertia of the medium nonlinear response described by a sound-type equation. The peculiarities of the field self-action dynamics are analyzed in a paraxial optics approach. Self-similar structures and spatio-temporal instability of plain wave are examined. The stages of instability evolution, structures formation and stationary self-action are examined numerically.

A wide class of nonlinear wave processes connected with excitation of the sound motion in medium under the action of ponderomotive force (electro-strictional nonlinearity) is described by the following well-known equation set [1–3]

$$i\frac{\partial\psi}{\partial z}+\Delta_\perp\psi-n\psi=0, \tag{1}$$

$$\frac{\partial^2 n}{\partial t^2}-\Delta_\perp n=\Delta_\perp F\left(|\psi|^2\right), \tag{2}$$

where ψ is wave field envelope, and n is perturbation of the refraction index caused by the effect of the field. Scale invariance of these equations allows use them in the above form for different nonlinear media including plasma [4]. Here $\Delta_\perp = \partial^2/\partial x^2 + \partial^2/\partial y^2$ is transverse Laplasian, ψ is normalized to the characteristic nonlinear field, for which perturbation of the stationary refraction index is essential. New coordinates, $z = kz$, $\mathbf{r}_\perp = k\mathbf{r}_\perp$, and new time, $t = k_0 v_s t$, are also introduced, where k is wave number, and v_s is sound velocity (ion sound velocity for plasma). Introduction of arbitrary function $F(|\psi|^2)$ makes it possible to describe different situations from the simplest case of cubic nonlinearity, $F(|\psi|^2) = |\psi|^2$, and to nonlinearity saturation effects.

Let us consider spatio-temporal dynamics of the system basing on Eqs. (1)–(2) with the following boundary and initial conditions

$$\psi(x,y,z=0,t)=\psi_0(x,y,t),\quad n(t=0)=0. \tag{3}$$

The simplest case is $F(|\psi|^2)= |\psi|^2$, when for steady state $n = - |\psi|^2$ and the problem is reduced to the well-known nonlinear Shroedinger equation with cubic nonlinearity. Within the theory of stationary self-focusing it is known that if the power of the wave beam at the input of the nonlinear medium exceeds the critical value, $P=\int|\psi|^2\, dr^3 > P_{cr}$, then evolution of any form is inevitably terminated by formation of a singularity. If the power excess is significant then the wave beam becomes stratified in the transverse direction and forms filaments with the critical power value [1–3]. This work investigates nonstationary self-focusing of wave beams with electro-strictional nonlinearity analytically and numerically. Self-similar structures are found in a wide range of the supercritical power parameter. Peculiarities of wave field dynamics within the paraxial approximation with the sound-type relaxation of the nonlinear response are analyzed. Nonstationary self-action of wave beams is investigated numerically basing on the 2-D model system, which preserves the basic features of initial equations. This makes it possible to work out the transition processes in detail in the case of structural instability of wave fields.

1. In the nonstationary regime the whole class of solutions in the form of jets homogeneous in the z-direction and constricting with time (homogeneous waveguide channels) is common for the media with inertia of nonlinear response. The electromagnetic field is trapped and guided along these channels. Substituting

$$F = |\psi|^2, \qquad \psi = \frac{1}{a(t)}\Phi(\xi)\exp\left(iz/a^2\right), \qquad n = \frac{1}{a^2(t)}N(\xi), \qquad (4)$$

$$\xi = r/a, \qquad a = t_0 - pt$$

into the initial equations, one can easily obtain the following equations for self-similar functions:

$$\Delta_\xi\Phi - (1+N)\Phi = 0, \qquad (5)$$

$$p^2\xi^2 N_{\xi\xi} + 6p^2\xi N_\xi + 6p^2 N - \Delta_\xi N = \Delta_\xi\Phi^2, \qquad (6)$$

where Δ_ξ- is Laplasian in the cylindrical coordinate system. Numerical investigation of set (5), (6) shows that a space localized self-similar solution in a shape of self-contracting jet exists for the arbitrary value of parameter p that characterizes the compression rate. With $p \to 0$ the transition takes place to the well-known homogeneous waveguide in the me-

dia with cubic nonlinearity. Large values of p correspond to the strongly nonstationary case, when the time-derivative term in (1) plays the principal role. In the supersound regime the power guided by the dynamic jet $P=\int\Phi^2\, d\xi$ depends on the compression rate. This rate increases with the rise of parameter P as $p\sim\sqrt{P}$. It is important that the power in the dynamic jet may considerably exceed the critical value in the system with stationary nonlinearity ($p \cong 0$).

Note here the existence of a wider class of dynamical self-similar structures that corresponds to singularities of the running-focus type. The use of the generalized lens transformation

$$\psi = \frac{1}{a(z,t)}\Phi(\xi,z,t)\exp\left(i\frac{a_z}{4a}r^2\right), \quad n = \frac{1}{a^2}N(\xi,z,t), \quad \xi = \frac{a}{r}, \quad (7)$$

where a is yet an arbitrary function of z, t, leads to the following equation for the field:

$$ia^2\frac{\partial\Phi}{\partial z} + \Delta_\xi\Phi - \left(N + \frac{a^2 a_{zz}}{4}\xi^2\right)\Phi = 0. \quad (8)$$

Hence it follows that for the self-similar structure of the running-focus type ($a \sim z/\mathrm{v} - t + t_0$) the last (lens) term turns to zero ($a_{zz}=0$). The self-similarity is precise (perfect) and the basic eigenmode of Eq. (8) is strictly localized in this case. The basic eigenmode in this case is described by the equations set similar to (5), (6). These equations include only the squared focus velocity, v^2, so in contrast to other nonlinearity relaxation types (Kerr, diffusion) [4] one cannot define the direction of singularity motion from the local solution condition. Thus, the analysis of self-similar solutions shows a new, not existing in stationary case, opportunity of formation of the singularity with the trapped power considerably exceeding the critical value. However, the fact that appropriate self-similarities exist does not guarantee per se that the corresponding solutions are realized at any initial and boundary conditions. The wide class of self-similar solutions probably is an evidence of various types of self-focusing dynamics, particularly for the case of supercritical regime. Analysis of Eqs. (1), (2) in the paraxial optics approximation (aberrationless limit) makes it possible to find the expression for the compression rate,

$$p = \left(\frac{2(P-1)}{5} \right)^{1/2}, \qquad (9)$$

and to analyze the behavior of the wave beam with the power about (or larger then) the critical value. This behavior is characterized by periodic excitation of the maximum field regions near the boundary (z=0) and subsequent motion of them deep into nonlinear medium. The period of generation of striations is about $T = a_0/c_s$, and the velocity of their motion $V_M = c_s k_0 a_0$, where a_0 is characteristic scale of a beam.

2. The numerical simulation of nonstationary self-effect of wave beams that allows tracing of their long-time evolution and transition processes in detail was carried out basing on the model equation set, which describes the self-action processes of 2D wave beams in the medium with stronger nonlinearity:

$$i\frac{\partial \psi}{\partial z} + \frac{\partial^2 \psi}{\partial x^2} - n\psi = 0, \qquad \frac{\partial^2 n}{\partial t^2} + \Gamma \frac{\partial n}{\partial t} - \frac{\partial^2 n}{\partial x^2} = -\frac{\partial^2}{\partial x^2} \frac{|\psi|^4}{1+\alpha|\psi}, \qquad (10)$$

where Γ is the operator responsible for sound-type perturbation damping.

This equation set with $\alpha = 0$, $\Gamma = 0$ has the same scaling as the initial one (1), (2) and is completely analogous to it in terms of asymptotic behavior of field dynamics near the singularity of the same type. This fact allows us to explore the dynamic of spatio-temporal instability and also the formation of various singularities, and thus manage to simulate not only the auxiliary symmetric case [5, 6], but also the 3D one. Nonlinearity saturation ($\alpha \neq 0$) is used for the confinement of the field strength in the focus region.

Numerical solution of model equation set (10) was carried out under the periodic boundary conditions. In the case of localized field structures with the power about the critical value, the stationary state formation happens with the transient wave excitation as it was in the paraxial optics limit. The peculiarities of self-action of the wave beam with the power greatly exceeding the critical value are illustrated on the example of evolution of wave field with the following boundary conditions:

$$z=0, \qquad \psi = \Phi_0 + \Sigma\, q_r \cos nk_r x\,. \qquad (11)$$

Numerical simulation was accomplished on the space interval with transverse L_x =2 and longitudinal L_z =1.75 scales. Constant field Φ_0 =2

was modulated by sum of several space harmonics with the amplitudes q_r = 0.02 and $k_r = \pi$.

The results of the simulation are shown in Figure 1.

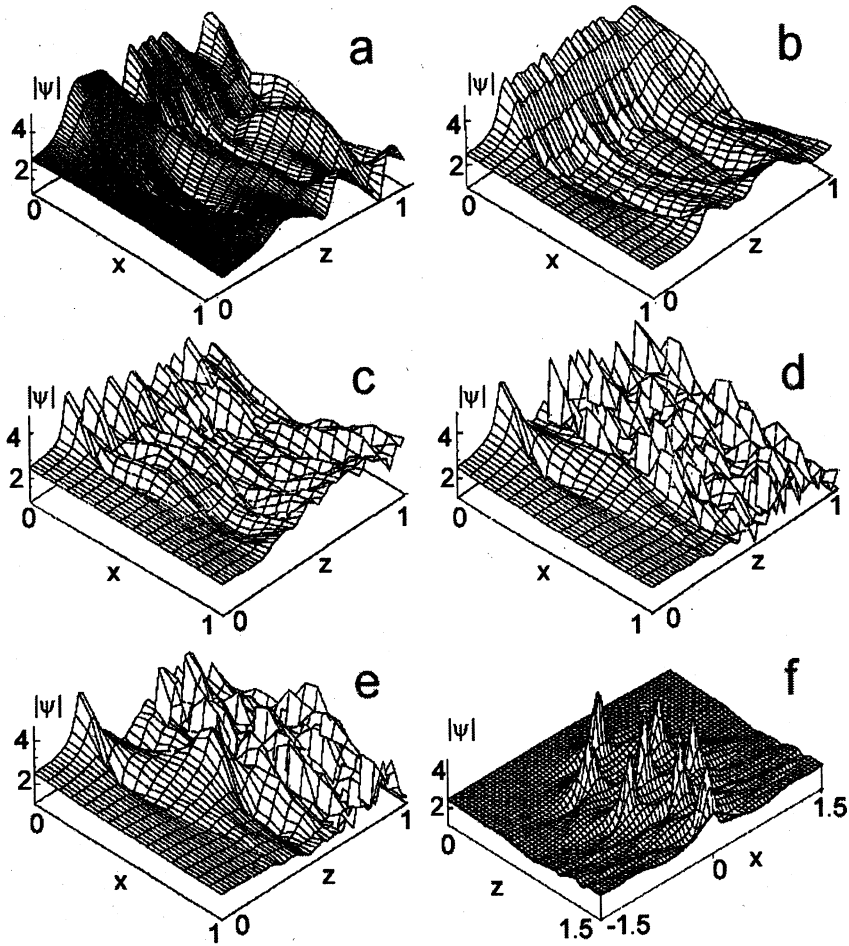

Fig. 1. Time evolution of the space structure of the field Ψ;
a corresponds t = 0.843;
b – t = 1.56;
c – t = 1.875;
d – t = 21.875;
e – t = 59.375
f – stationary picture.

First the plain wave instability develops. This stage gives place to formation of the compressing homogeneous waveguide channel. All the time the channel looks corrugated. Initially this corrugation is dynamic and is defined by sound relaxation of nonlinearity (Fig. 1a) but then is stipulated by the nonlinearity saturation effect (Figs. 1b, 1c). Notice that we failed to get a smooth homogeneous channel or the running focus regime by changing the initial perturbation spectrum (11) unlike to the case of Kerr or diffusive nonlinear response relaxation [4]. Final stage of formation of wave field stationary filamentation occurs by the same way, as for other types of nonlinearity relaxation: first structural instability develops that results in turbulization of the interaction region. It is important to mark that resulting, rather chaotic, spatial form of field (sometimes it has a shape of a homogeneous channel) gradually is forced out from the boundary deep into the nonlinear medium (Figs. 1d, 1e) and gives place to formation of entirely stationary picture, which is shown in Fig. 1f. This last one certainly coincides with stationary field forms for other types of nonlinearity relaxation. But unlike to the case of Kerr or diffusion [4] relaxation types in the considered case stationary state formation takes place without acoustic perturbations damping. As a result the characteristic time of stationary state formation is of the same order as for Kerr nonlinearity and half as much as for the diffusion case when sound perturbations are strongly damped. The coincidence of characteristic times for Kerr and sound-type relaxation mechanism seems to be casual.

Thus it can be noted that with the rise of power the structural instability of wave field becomes important. Appreciable role in the localized field dynamic belongs to forming of a homogeneous waveguide channel. It seems that this process is described by the structure of self-similar type (4). To prove this statement it is necessary to carry out the simulation with large values of the nonlinearity saturation level. It is important to note that the waveguide channel formation protracts the making of stationary state. In the process of decay of waveguide-type structures the excitation of long-live inhomogenuities and turbulization of the interaction region take place. Nonlinear diffraction of incident radiation on these inhomogenuities is accompanied by a slow ousting of the dynamical turbulence region towards large z. As a result, the multifilament structure of field becomes stationary ("laminar") on time scales significantly exceeding the nonlinear response relaxation time ($t \approx 60$). Such type of stationary picture forming scenario is rather typical in the case of

strong supercriticity. The same one was realized for Kerr and diffusion mechanisms of nonlinear response relaxation. In the case under consideration this process is even slower.

The authors are grateful to E.I. Rakova and A.A. Balakin for assistance in arrangement of paper. The work was supported by RFFI (grants No 98-02-17205 and No 99-02-16399).

References

1. Litvak A.G., in *Reviews in Plasma Physics*, edited by M.A.Leontovich (Consultant Burean, N.Y. 1980) **10**, 293.
2. Shen I.R., *The Principles of Nonlinear Optics*. (John Wiley & Sons, New York, 1984).
3. Vlasov S.N., Talanov V.I. *Self-focusing of Waves*. (IAP RAS. Nizhnii Novgorod. 1997).
4. Litvak A.G., Mironov V.A. and Sergeev A.M. Physica Scripta 1990, **T30**, 57
5. Andreev N.E., Gorbunov L.M., Tarakanov S.V. et al. Phys. Fluids, 1993, **B5**, 1986.
6. Andreev N.E., Gorbunov L.M., Zykov A.I. et al. Zh. Exp. Teor. Fiz. 1994, **106**, 1676.

HARMONIC GENERATION DUE TO ELECTRON-ION CORRELATED COLLISIONS IN SUPER STRONG LASER FIELDS IN PLASMAS

A. A. Balakin, G. M. Fraiman

Institute of Applied Physics, RAS, Nizhny Novgorod, 603600, Russia

The coherent and incoherent radiation of colliding electrons in super strong fields was analyzed. The strong enrichment of incoherent bremsstrahlung spectrum was predicted. The coherent part of bremsstrahlung was found out. The qualitative analytical model describing obtained results by means of electron bunching over collision phase was suggested. The application of obtained results was discussed.

Collisions of charged particles in plasmas become apparent in various processes. For example, it is plasma heating by electromagnetic waves, a gas discharge in electromagnetic wave and so on. The bremsstrahlung accompanying electron-ion collisions is a diagnostic tool for determination of plasma parameters. In the case of anisotropic electron distribution function the process of intensification of electromagnetic radiation called the Marcuse effect [1] is possible.

The revival of interest to investigation of coherent bremsstrahlung and harmonic generation in laser plasma was stimulated by the perspective ability of creating the attosecond pulses [2, 3]. The development of rather simple qualitative theory of harmonic generation of coherent bremsstrahlung was suggested in papers [4, 5]. It is based on using of Landau collisional integral and allows describing the peculiarities of harmonic generation in fully ionized plasma depending on the laser field polarization. That approach is allowed in rather weak fields. In the most interesting case of a strong field (electron thermal velocity smaller than oscillatory one) it is necessary to make more correct investigation.

Another approach developed in [7] consists in predicting and obtaining high harmonics due to unitary return of electron to atom simultaneously with gas ionization in strong fields. Besides it confirms that such effect is possible only in unionized gas.

Our numerical investigation of electron-ion collisions shows the important role of correlated effects for electron thermal velocity smaller than oscillatory one [6]. Under these conditions the oscillating electron multiple returns to the same ion that leads to essential modification of the character of interaction between electron and ion.

In this paper we present results of numerical simulation of bremsstrahlung in dipole approximation. By the analogy with the paper [6] we use a pair collision approximation, i.e. it is supposed that a beam of oscillating electrons in the strong EM field interacts with a single ion. The investigation of bremsstrahlung spectrum due to this process is the goal of this paper.

We consider the problem of collision of a single electron with the initial velocity v_- (Fig.1) in strong homogeneous electric field polarized along Oz axis with in the framework of classical equations of motion.

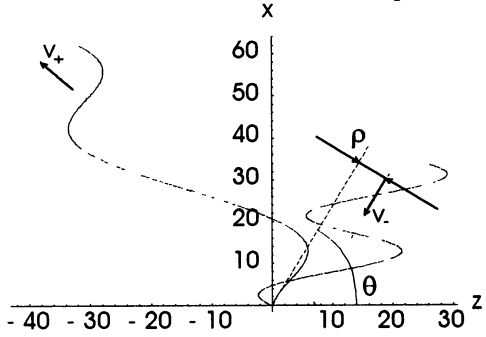

Fig. 1. A typical trajectory of electron (solid line), drift trajectory (dash line) and initial parameters of electron ($\boldsymbol{v}$ is drift velocity, ρ is impact parameter, θ is angle between drift velocity and external field $\boldsymbol{E}$).

This equation has characteristic scales

$$r_E = \sqrt{\frac{eZ}{E}}, \quad \omega_E = \sqrt[4]{\frac{eE^3}{m^2 Z}}, \quad v_E = \sqrt[4]{\frac{Ze^3 E}{m^2}} \tag{1}$$

where e is the absolute value of electron charge. In the dimensionless variables $\boldsymbol{R}_n=\boldsymbol{R}/r_E$, $t_n=\omega_E t$ the equation has the form

$$\ddot{\boldsymbol{R}} = -\frac{\boldsymbol{R}}{R^3} + \boldsymbol{n}\cos\Omega t, \tag{2}$$

where $\boldsymbol{n}$ is the unit vector along the external field ($\boldsymbol{E}=E\boldsymbol{n}$) and

$$\Omega = \omega\left(\frac{m^2 Z}{eE^3}\right)^{1/4} = \frac{\omega}{\omega_E}, \tag{3}$$

is the dimensionless frequency. The characteristic spatial scale of the problem $r_E = \sqrt{eZ/E}$ represents a distance from the ion where the Coulomb field is equal the amplitude of external field E; $\omega_E = \sqrt[4]{eE^3/m^2 Z}$ is a characteristic frequency for the motion on the Keplerian orbit with the radius r_E.

In the framework of classical electrodynamics the electron radiating in the non-relativistic case is considered in dipole approximation. Traditionally, the incoherent radiation cross-section is analyzed for electron-ion collisions

$$\chi_n(\omega) = \int\int I(\omega, \varrho) d\varrho d\varphi = \frac{2}{3c^2} \sum_n \int\int \left| \ddot{d}_n \right|^2 d\varrho d\varphi \cdot \delta(\omega - n\Omega), \quad (4)$$

where $d_{zn} = \int_{-\infty}^{\infty} d_z(\tau) e^{in\Omega\tau} d\tau$ is the n-th harmonic of the dipole moment of electrons. It is also interesting to analyze a coherent radiation cross-section because electron-ion collisions are correlated. After averaging over impact parameters and incoming phase the nonzero component of a dipole moment vector will be only a component d_z along the external field due to the symmetry of the system. The correlation between collision moments and the phase of external field provides the temporal dependence as the following: $t - \boldsymbol{r}_i \boldsymbol{k}_0 / \omega$, r_i is a co-ordinate of a i-th collision (or what is similar to the i-th ion), $\boldsymbol{k}_0$ is a propagation vector of external electromagnetic wave. The harmonic of external field Ω will be pointed up due to the periodicity of the problem with a period of external field (an incoming electron in a period pass the same trajectory). As a result of random ion positions the nonzero component is the component propagating along external field. The radiation cross-section will be:

$$\chi_{kog}(\omega) = \frac{2}{3c^2} \sum_n \left| \int\int d_{zn} d\varphi d\varrho \right|^2 \delta(\omega - n\Omega), \quad (5)$$

It is easy to see that expression (5) is the natural generalization of the incoherent cross-section (4) in the coherent case.

In the process of the numerical simulation we calculated the dipole momentum of electron beams with drift velocities from $0.01v_\sim$ ante $10v_\sim$ and impact parameters ante $2r_\sim$. The calculation was carried out for the frequency values Ω=0.1, 0.32, 1. Initially (at $t \to -\infty$) electrons were evenly distributed over field phase. Initial radius from Coulomb center was selected as $5 \cdot r_\sim$ ($5/\Omega^2$). A particle supposed to be left the interaction region if its drift center was $5 \cdot r_\sim$ far from the ion. Special attention was spared to use adequate number of particles within field period.

The main feature of radiation in super strong fields is a significant increase of radiation due to appearing of the representative electrons [6]. They appear as a result of attraction increasing caused by multiple correlated returns of these electrons to the single ion with sequent large angle collision (with large energy change). It is obvious that these electrons also radiate strongly. These effects are demonstrated in fig. 2.

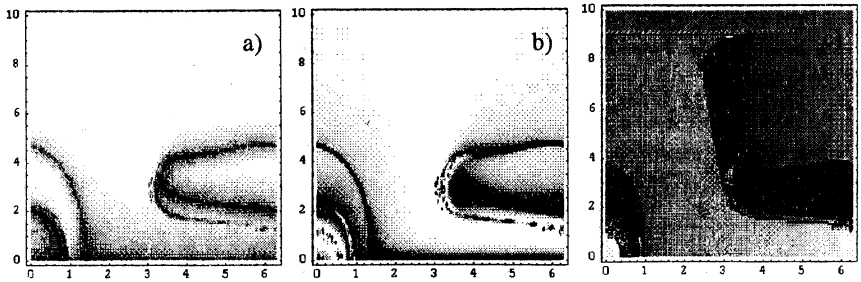

Fig.2. The minimal distance (a), energy change (b) and collisional phase (c) depending on impact parameter and incoming phase for ν=1, Ω=0.1

Let us remind that in the framework of classical model of bremsstrahlung the randomness assumption of collision moment is adopted and as a result the coherent component of radiation is absent. In the case of scattering over a HF electromagnetic field the situation changes cardinally. In the process of numerical simulation we found that in spite of different incoming phases all electrons had collided at strongly correlated phases (fig. 2c), closed to the phase of the maximal velocity. This correlation is prepared by adiabatic drift of particle in Coulomb field of the ion.

Increase of incoherent radiation cross-section is a consequence of the noted above. The step appearing in fig.3a is connected with electron colliding in quasi-static field in the process of multiple oscillations. The main characteristic of coherent radiation is the radiation cross-section (5), represented in fig. 3b. It is obvious, that the cross-section has a peak near frequency ω_E (ω_E=10 in this figure) and quickly decreases at higher frequencies. Presence of only odd harmonics is connected with spatial uniformity of plasma: summary radiation of two electrons moving symmetrically with respect to the ion is possible only at odd harmonics (in dipole approximation). This effect is demonstrated in fig. 3b.

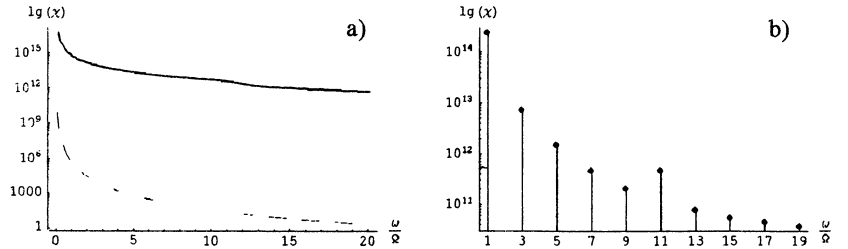

Fig.3 The incoherent (a) and coherent (b) radiation cross-section depending on frequency for ν= 1. Solid line– Ω=0.1, dash line – classical value.

Let us note that in rather strong fields the frequency ω_E may be much higher than the frequency of external field and the peak in the spectrum allows us to make effective high frequency harmonic generation. It becomes much more interesting if we take into account the possibility of coherent harmonics generation!

The discussed above results are formally correct only in rather low-density plasma $N << (\lambda\nu/c)^{-3}$ (where λ is radiation wavelength). But it is possible to expect that similar effects can take place in higher density plasma. Really it is solely necessary that only one particle will be in interaction volume determining an area of effective scattering $r_{\sim}\sigma_{eff}$. If we use our numerical results [6] we will receive the following condition:

$$r_e << r_d, \text{ for } \nu_T << \nu_{\sim}, \qquad (6)$$

where r_d is Debye radius.

In conclusion we should note that the essential modification of traditional models take place only in rather strong fields $r_{\sim} >> r_E$ ($\omega_E >> \omega$) or in dimensional variables:

$$\omega << \omega_E \sim Z^{1/4} \cdot 2 \cdot 10^{10} \left(P\left[\frac{Bm}{cm^2}\right]\right)^{3/8} \qquad (7)$$

As it was written before in such fields we should expect increase of bremsstrahlung (on some order higher in comparison with classical model) and appearing of the coherent part of radiation. Some other questions (such as: plasma as a nonequilibrium medium at high harmonics or influence of external wave polarization on radiation characteristics) is needed in further investigations.

The work was supported in part by the Russian Foundation for Basic Research (Grants Nos. 98-02-17205 and 99-02-16443).

References

1. Fedorov M.V., *Interaction of Intense Laser Light with Free Electrons*, Harwood Academic Publishers, Chur (1991) [Russian original, Nauka, Moscow (1991)].
2. Antoine P., L'Huillier A. and Lewenstein M., Phys. Rev. Lett. **77**, 1234 (1996).
3 Schafer K.J. and Kulander K.C., Phys. Rev. Lett. **78**, 638 (1997).
4 Sılın V.P., Quantum Electronics **29**, 11 (1999).
5. Sılin V.P., Zh. Eksp. Teor. Fiz. **114**, 864 (1998) [J. Exp. Theor. Phys. **87**, 486 (1998)].
6. Fraiman G.M., Mironov V.A. and Balakin A.A., Phys. Rev. Lett. **82**, 319 (1999); Fraiman G.M., Mironov V.A. and Balakin A.A., Zh. Eksp. Teor. Fiz. **115**, 463 (1999) [J. Exp. Theor. Phys. **88**, 254 (1999)].
7 Corcum P. B., Phys. Rev. Lett. **71**, 1994 (1993)

ELECTROMAGNETIC THEORY OF THE RADIATIVE PIERCE INSTABILITY

D.N. Klochkov, M.Yu. Pekar, A.A. Rukhadze

General Physics Institute, Russian Academy of Sciences, Moscow, Russia

Theoretical investigations of a nonresonance stimulated Pierce radiation by the relativistic electron beam (REB) in a waveguide are presented. By numerical modeling of the problem the efficiency of a beam energy transformation into the electromagnetic field energy as a function of beam current, its relativism and geometry are calculated.

The mostly wide-spread device is the Cherenkov microwave one using the slowing electrodinamical structures, such as: metallic waveguides with rippled walls or modulated guiding magnetic fields. Just due to this reason in the vacuum microwave sources the radiation breaks when the power exceed 100 MW. In the vacuum microwave sources the electric field reaches its maximal value near the walls of waveguides and initiates surface discharge if the radiation power is sufficiently high. As a result the high power vacuum sources are working during no more then $\approx$ 10ns. As the alternative the nonresonance microwaves sources based on the stimulated Pierce radiation of strightline REB in smooth waveguides are presented.

For smooth cylindrical waveguide with radius R and lenght L with ideal boundary conditions the growth rate $\delta\omega$ of instability is [1,2]

$$\delta\omega = (-1)^n \omega_b \frac{k_\perp^2 c^2 \gamma^{-1/2}}{(\omega^2 - a^2 u^2)^{3/2}} \frac{u}{L} \sin(\alpha \omega_b L) \sin\left(\frac{\omega L}{u}\right) \qquad (1)$$

where frequency ω is

$$\omega = \omega_{s,n} = c\sqrt{\left(\frac{\mu_{s,0}}{R}\right)^2 + \left(\frac{\pi n}{L}\right)^2}, \qquad (2)$$

and $a = \pi n/L$, $\alpha = \frac{\omega}{u}\gamma^{-5/2}(\omega^2 - a^2u^2)^{-1/2}$, $k_\perp = \mu_{s,0}/R$. From (1) we find the instability condition

$$(-1)^n \sin(\alpha\omega_b L)\sin\left(\frac{\omega L}{u}\right) > 0, \qquad (3)$$

The analysis of the nonlinear system of Maxwell-Vlasov equations is possible only by the numerical modeling of considered instability. The Maxwell equations were solved directly by finite-different elements [3] using unitless variables

$$\tau = \frac{u}{L}t, \quad p = \frac{p_z}{mc}, \quad \varepsilon = \frac{eL}{mc^2\gamma_0^3}E_z. \qquad (4)$$

Here $p_z = m\gamma v_z$, $\gamma_0 = (1 - u^2/c^2)^{-1/2}$ is unperturbated relativistic factor of beam electrons. The beam electrons were modeling by the method of particle in sells [3].

In all calculations an infinitelly thin annular beam with radius $r_b = 0{,}4R$ is considered, which was injected gently into the resonator. The Pierce parameter was choosen as a ratio the beam current to the Pierce current I_p, which for considered geometry is equal

$$I_p = \frac{mc^3}{e}\frac{u^3}{c^3}\frac{\gamma^3}{2\ln\left(\frac{R}{r_b}\right)}. \qquad (5)$$

For that the saturation of instability took place during 10–10000 of electron flight time through the resonator depending of the beam current and parameter $\xi = \frac{L}{R}$. In the most cases

we observed the exitation of the first fundamental radial mode with $s = 1$. In general one-mode exitation was dominative if $\xi \leq 12$. At the same time, when $\xi > 12$ (long systems) we observed simultaneously exitation of many modes. Really, if $\xi \gg 1$ then approximatelly

$$\xi = \frac{1}{2}\frac{c}{u}\frac{\pi}{\mu_{s,0}}\frac{n_2^2 - n_1^2}{\Delta\theta}, \tag{6}$$

where n_i is the number of a longitudinal mode. In accordence of (3) in this case simultaneously many longitudinal modes satisfy the condition $\Delta\theta < \pi$ and therefore all they can exited by beam. For example, when $\xi \geqslant 12$ the three-mode wave exitation is possible.

One can distinguish two different mechanizms of saturation of the instability. The first one is dominative in the relaively short systems ($\xi < 12$) when single-mode wave exitation takes place. In this case the process of confluence-decay

$$\omega_{1,n} + \omega_{1,n} \rightarrow \omega_{1,n-1} + \omega_{1,n+1}, \tag{7}$$

which leads in accordance of (3) the wave energy transformation back into the beam, is very important.

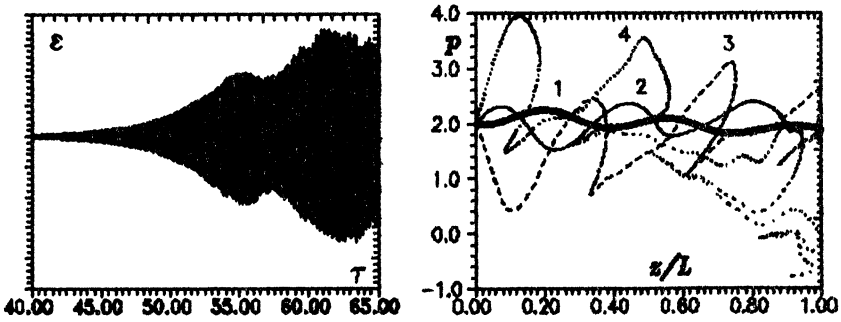

FIG 1. a — Wave amplitude dinamics in a short resonator for $\xi = 6$, $\gamma = 2$ and $\chi = 0{,}05$ (the corresponding beam current $I \approx 2{,}4$kA). b — phase plane of beam electrons in a resonator at the time moments (1) $\tau = 40$; (2) $\tau = 45$; (3) $\tau = 60$; (4) $\tau = 65$.

On the FIG 1a we see the saturation with the regular oscillations of exited wave amplitude with frequency $\delta\omega$. The phase picture of beam electrons is shown on the FIG 1b. Up to $\tau < 45$ the linear stage of the instability takes place with purely harmonic modulation of REB. Later the nonlinear distortions appear, which leads to the wave "overturn", corresponding to saturation of the instability. The beam modulation is very deep, but it stay "cold". At the same time, the shorteness of longitudinal wave numbers k_ν takes place.

Quite another picture of saturation arizes in long systems, when $\xi \geq 12$ and the instability has many-mode character. In this case, the saturation is stipulated by the stochastic motions of beam electrons in the field of many-mode electromagnetic waves (see FIG 2). As a result the phase distribution of waves becomes completely random in the phase interval $[0; 2\pi]$.

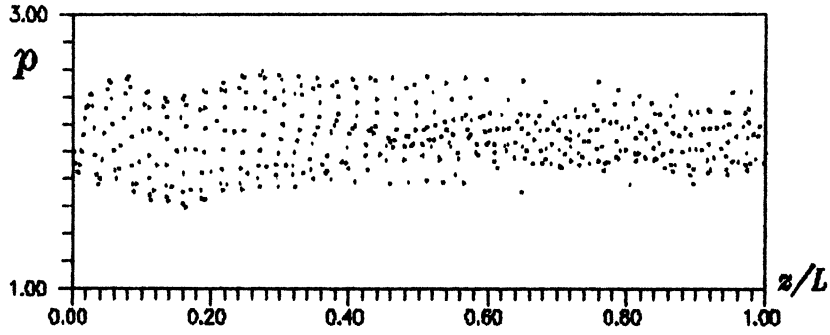

FIG 2. Phase plane of beam electrons in along resonator at the time moment of saturation for $\xi = 18$, $\gamma = 2$ and $\chi = 0{,}05$.

The results of modeling presented on FIG 2 corresponds to the saturation of the instability at $\tau = 40$. At this stage the effectiv temperature of beam electrons turned out very high, of the order of $0{,}1 \div 0{,}3$MeV and electric fields strength of the exited waves reach 100–300 kV/cm. Besides, the spectra of wave oscillations is wide, $\Delta\omega/\omega \sim 1$.

As beam current increases and Pierce parameter χ becomes of the order of unity the potencial Pierce instability developes [4].

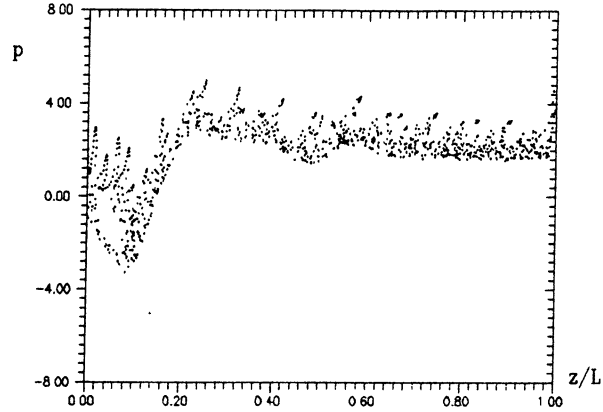

FIG 3. Phase plane of beam electrons at the time moment of saturation for $\xi = 25$, $\chi = 0{,}95$ and $\gamma = 2$.

Near the entrance of the resonator one can see the creation of virtual cathod from which a part of beam electrons reflected (see FIG 3). At the same time the existance of the radiative instability leads to the chaotisation of the beam electron motions. Thus both the aperiodical Pierce instability and the radiative one can be considered as two different regimes of the single instability.

We introduce the ratio of incident electromagnetic flux to the beam flux

$$\eta = \frac{\langle|\vec{S}|\rangle}{mc^2 nu\gamma}, \tag{8}$$

where $\langle|\vec{S}|\rangle$ – is the average (in time) Pointing flux of forward electromagnetic waves.

For the short systems, when $\xi < 1$, the growth rate of Pierce radiative instability is very small, $\approx \omega_b^2$. As a result the radiation efficiency occurs also too small. The maximum of $\eta(\xi)$ corresponds to the region $1 < \xi \leq 8$ (see FIG 4). On the

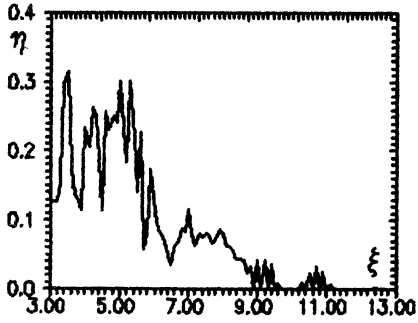

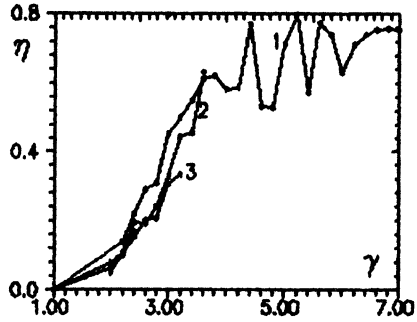

FIG 4. FIG 5 .

FIG 4. The dependence of the energy transformation coeffitient η on the geometry parameter ξ of resonator for $\gamma = 2$ and $\chi = 0{,}05$.
FIG 5. The dependence of the energy transformation coefficients on the relativism of electrons γ for $\chi = 0{,}05$: (1) $\xi = 4$; (2) $\xi = 5$; (3) $\xi = 6$.

FIG 5 the dependence of η from γ is presented, which similar for that of the Cherenkov instability. One can see that growth rate increases with γ and it becomes constant when $\gamma \geq 5$.

References

1. Klochkov D. N., Rukhadze A. A., "Plazma Physics Reports" **23** (1997), 598.
2. Klochkov D. N., Pekar M. Yu., Rukhadze A. A., Sov. Journ JETF **116** (1999) (to appear).
3. Berezin Yu. A., Vshivkov V. A., *Particle in Cells in the Dinamic of Rare Plasma*, Nauka, Novosibirsk, 1980.
4. Kuzelev M. V., Rukhadze A. A., *Plazma Free Electron Lazers*, Paris, Edit. Frontier, 1995.

NONLINEAR LOW-HYBRID OSCILLATIONS OF COLLISIONLESS PLASMA COLUMN IN HOMOGENEOUS MAGNETIC FIELD

D.S. Dorozhkina, V.E. Semenov

Institute of Applied Physics RAS, Nizhny Novgorod, Russia

Results of a general study of a set of kinetic equations describing the dynamics of a two-component quasi-neutral collisionless plasma column in homogeneous, nonstationary magnetic field are presented. The dynamics of the column is found to be completely determined by such parameters as initial values of total kinetic energy of plasma, total angular momentum of each plasma component, and total mass of plasma. In the case of stationary magnetic field the column cross-section is shown to oscillate harmonically at the low-hybrid frequency. The found peculiarities of the plasma dynamics are confirmed by exact self-similar solutions of the set of two Vlasov kinetic equations.

Plasma expansion into vacuum has received significant attention of physicists over the last decades. The particular interest to these phenomena can be justified by its potential application in space physics, investigation of dusty plasma, and study of collective ion acceleration. Theoretical solution of the problem is also important for study of laser flame in laboratory experiments. Following the pioneer work by A.Gurevich [1] most of the theoretical studies have been based on the model of semi-infinite collisionless plasma. The specific feature of the solution obtained in this model is the occurrence of ion distribution function excessively enriched with energetic particles (comparing with initial electron distribution). It is caused by non-limited energy resource in initial plasma. In real experiments, the described regime corresponds to the case of a presence of continuous sources of plasma and energy in definite region of space, so that the process of plasma expansion is considered to be quasi-stationary.

The analysis of the expansion of an initially confined plasma bunch requires another approach, because the process in this case is accompanied by considerable cooling of electrons. In a few words, the dynamics of an initially confined plasma bunch in vacuum in the absence of magnetic field is reduced to unlimited expansion of the bunch and its cooling with time. The full description of those processes using the kinetic model and quasi-neutral approach is presented in our last works [2, 3].

Recently, in laboratory experiments, caused by number of technical applications of laser-produced plasma, it has been observed that a magnetic field influences significantly transverse plasma expansion. In particular, the experimental studies [4] have shown the oscillatory behavior of plasma parameters in the presence of magnetic field. It is demonstrated below, that the method developed in [3] for analysis of plasma column expansion into vacuum is very fruitful for analytical investigation of the plasma dynamics in magnetic field too. Specifically, this method allows obtaining exact solutions of the problem within kinetic description.

Basic model

The exactly solvable physical model assumes that there is a column of collisionless plasma with two sorts of particles in given homogeneous nonstationary magnetic field, which is directed along the column (Fig. 1):

$$\mathbf{B} = B(t)\mathbf{e}_z .$$

Plasma column is axially symmetric and homogeneous along axis z. Respectively, vector-potential, $\mathbf{A}$, of the magnetic field, $\mathbf{B} = \left[\nabla_{\mathbf{r}} \times \mathbf{A}\right]$, and potential of charge-separation electric field, φ, can be presented in the form: $\mathbf{A}(\mathbf{r},t) = \frac{B}{2}\,\rho\,\mathbf{e}_\psi$, $\varphi = \varphi(\rho,t)$, $\rho \equiv \sqrt{x^2+y^2}$.

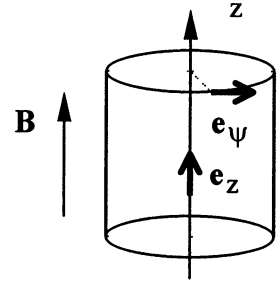

Fig. 1.

Particles of each sort are described by distribution functions, $f_\alpha(\mathbf{v},\mathbf{r},t)$, which satisfy the following Vlasov kinetic equations:

$$\frac{\partial f_\alpha}{\partial t} + (\mathbf{v},\nabla_{\mathbf{r}}) f_\alpha + \frac{Z_\alpha e}{m_\alpha}\left(\mathbf{E} + \frac{1}{c}\left[\mathbf{v}\times\mathbf{B}\right],\nabla_{\mathbf{v}}\right) f_\alpha = 0 ,$$
$$\mathbf{E} \equiv -\nabla_{\mathbf{r}}\varphi - \frac{1}{c}\frac{\partial \mathbf{A}}{\partial t} , \quad \nabla_{\mathbf{r}} \equiv \left(\frac{\partial}{\partial x},\frac{\partial}{\partial y}\right) , \quad \nabla_{\mathbf{v}} \equiv \left(\frac{\partial}{\partial v_x},\frac{\partial}{\partial v_y}\right) , \qquad (1)$$

where $Z_\alpha e$ and m_α are charge and mass of particles of sort α, respectively; c is light velocity.

An approximation of quasi-neutrality is used for analyzing of the dynamics of sufficiently dense plasma. It implies that

$$\sum_{\alpha} Z_{\alpha} n_{\alpha}(\mathbf{r},t) = 0, \qquad n_{\alpha}(\mathbf{r},t) \equiv \int f_{\alpha}(\mathbf{v},\mathbf{r},t)d\mathbf{v}. \qquad (2)$$

General analysis

A fruitful approach to the analysis of system of Eqs. (2)-(3) is based on the method of moments of distribution functions of plasma particles performed in paper [3]. The moments of second order of distribution functions f_{α}, describing the spatial structure of the plasma column, are defined as:

$$\langle r_j r_k \rangle_{\alpha} \equiv \frac{1}{N_{\alpha}} \iint r_j r_k f_{\alpha}(\mathbf{v},\mathbf{r},t)d\mathbf{v}d\mathbf{r}, \qquad (3)$$

where $N_{\alpha} \equiv \iint f_{\alpha}(\mathbf{v},\mathbf{r},t)d\mathbf{v}d\mathbf{r}$ is total number of particles of sort α. In analogy with Eq. (3) one can also define tensors $\langle r_j v_k \rangle_{\alpha}$, $\langle v_j v_k \rangle_{\alpha}$.

Note that in contrast to the well-known hydrodynamic description the full moments of distribution functions have been used for the analysis. It means the integration not only over velocity $\mathbf{v}$ but also over coordinates $\mathbf{r}$. The advantage of such approach is a finite consequence of equations for the moments. Specifically, for the two-component plasma column due to quasi-neutral approximation Eq. (2) the spatial moments $\langle \rho^2 \rangle \equiv \langle x^2 + y^2 \rangle_{\alpha}$, and mixed moments $\langle \rho v_{\rho} \rangle \equiv \langle x v_x + y v_y \rangle_{\alpha}$ are equal for different sorts of particles. At the same time the mixed moments describing the temporal evolution of z-components of total angular momentum of each plasma component, $\langle \rho v_{\psi} \rangle_{\alpha} \equiv \langle x v_y - y v_x \rangle_{\alpha}$, as well as velocity's moments, $\langle v^2 \rangle_{\alpha} \equiv \langle v_x^2 + v_y^2 \rangle_{\alpha}$, might not coincide for different sorts of particles. It appears, that the system of equation for these moments, which can be obtained from Eqs. (1), has the following integrals:

$$\left[\frac{2W}{M}+\sum_{\alpha}\frac{\omega_\alpha}{M}J_\alpha-\frac{\Omega^2}{4}l^2-\left(\frac{dl}{dt}\right)^2\right]l^2\equiv\sum_{\alpha}\mu_\alpha V_\alpha^2 l^2=\text{const},\quad(4)$$

$$J_\alpha\equiv\text{const},\ \mu_\alpha\equiv\frac{m_\alpha N_\alpha}{M},\ \omega_\alpha\equiv\frac{Z_\alpha e}{m_\alpha c}B,\ \Omega^2\equiv\sum_{\alpha}\mu_\alpha\omega_\alpha^2,\quad(5)$$

where $W\equiv\frac{1}{2}\sum_{\alpha}m_\alpha N_\alpha\left\langle v_x^2+v_y^2\right\rangle_\alpha$ is total plasma kinetic energy, $J_\alpha\equiv m_\alpha N_\alpha\left\{\left\langle\rho v_\psi\right\rangle_\alpha+\frac{\omega_\alpha}{2}\left\langle\rho^2\right\rangle\right\}$ is total generalized angular momentum of particles of sort α, $M\equiv\sum_{\alpha}m_\alpha N_\alpha$ is total mass of the plasma, $l\equiv\sqrt{\left\langle\rho^2\right\rangle}$ is characteristic plasma scale length, and moments V_α^2 can be treated as a spread of velocities of particles of sort α with respect to a definite hydrodynamic velocity:

$$V_\alpha^2\equiv\left\langle\left(\mathbf{v}-\mathbf{u}_\alpha\right)^2\right\rangle_\alpha,\quad\mathbf{u}_\alpha(\mathbf{r},t)\equiv\frac{\rho}{l}\frac{dl}{dt}\mathbf{e}_\rho-\frac{\omega_\alpha}{2}\rho\mathbf{e}_\psi.\quad(6)$$

Using the integrals (4)-(5) it is possible to reduce a description of evolution of the second order moments presented above to one differential equation for the plasma scale length:

$$l^3\frac{d^2}{dt^2}l+\frac{\Omega^2}{4}l^4=\sum_{\alpha}\mu_\alpha V_\alpha^2 l^2=\text{const}.\quad(7)$$

Therefore, the dynamics of plasma column is completely determined by initial values of such parameters as l, dl/dt, W, and J_α.

Specifically, in the simplest case of stationary magnetic field the total plasma kinetic energy is found to be constant and Eq. (7) has a stationary solution:

$$l_{st}^2=\frac{2}{M\Omega^2}\left[2W+\sum_{\alpha}\omega_\alpha J_\alpha\right]=\text{const},\qquad\frac{dl}{dt}=0.\quad(8)$$

If initially $l(t=0) \neq l_{st}$, and/or $dl/dt \neq 0$, the plasma cross section oscillates harmonically with time:

$$\frac{d^2}{dt^2} l^2 + \Omega^2 \left[l^2 - l_{st}^2 \right] = 0, \tag{9}$$

where frequency Ω appears to be equal to the low-hybrid frequency for sufficiently dense plasma.

Exact solution

Exact solutions of Eqs. (1)-(2) are closely connected with integrals (4), (5) and might be presented via arbitrary functions of two arguments:

$$f_\alpha = F_\alpha\left(G_\alpha, g_\alpha\right), \qquad \sum_\alpha Z_\alpha \iint F_\alpha d\mathbf{v} = 0, \tag{10}$$

$$G_\alpha \equiv \frac{\left(\mathbf{v}-\mathbf{u}-\mathbf{w}_\alpha\right)^2}{V_\alpha^2(t)} + \frac{\rho^2}{l^2(t)}, \quad g_\alpha \equiv \frac{\left[\mathbf{r}\times\left(\mathbf{v}-\mathbf{w}_\alpha\right)\right]_z}{V_\alpha(t) l(t)},$$

$$V_\alpha(t) l(t) = \text{const}, \quad \mathbf{u} \equiv \frac{\rho}{l}\frac{dl}{dt}\mathbf{e}_\rho, \quad \mathbf{w}_\alpha \equiv -\frac{\omega_\alpha}{2}\rho\mathbf{e}_\psi,$$

$$e\varphi(\rho,t) = -\left(\sum_\alpha \frac{1}{M_\alpha}\right)^{-1} \sum_\alpha \frac{1}{Z_\alpha N_\alpha}\left[\frac{V_\alpha^2(t)}{l^2(t)} + \frac{\omega_\alpha^2}{4}\right]\frac{\rho^2}{2}.$$

Here parameter of the solution, l, is nothing more than plasma scale length, which corresponds to the spatial moment of distribution functions: $l^2 \equiv \langle \rho^2 \rangle$. Respectively, it is governed by the Eq. (7). Parameters V_α are treated as spread of velocities of particles of sort α with respect to a definite hydrodynamic velocity: $V_\alpha^2 \equiv \left\langle \left(\mathbf{v}-\mathbf{u}-\mathbf{w}_\alpha\right)^2 \right\rangle_\alpha$. Note that the latter relationships coincide with the Eq. (6).

In general case the quasi-neutral approximations demands the functions F_α to satisfy the integral condition (10). Evidently, it can be fulfilled in the simplest case of similar distribution functions:

$$f_\alpha = \frac{N_\alpha}{l^2 U_\alpha^2} F\{\tilde{G}_\alpha\}, \quad \tilde{G}_\alpha \equiv \frac{\left(\mathbf{v}-\mathbf{u}-\upsilon_\alpha \mathbf{e}_\psi\right)^2}{U_\alpha^2} + \frac{\rho^2}{l^2},$$

$$\mathbf{u} \equiv \frac{\rho}{l}\frac{dl}{dt}\mathbf{e}_\rho, \quad \upsilon_\alpha \equiv \left(\frac{\kappa_\alpha U_\alpha}{l} - \frac{\omega_\alpha}{2}\right)\rho, \qquad U_\alpha(t) l(t) = \text{const},$$

$$l^2 \equiv \rho^2 \ , \ U_\alpha^2 \equiv \left(1+\kappa_\alpha^2\right)^{-1} V_\alpha^2, \ \kappa_\alpha = \text{const}, \ -\infty < \kappa_\alpha < \infty,$$

where $U_\alpha^2(t)$ describe a thermal spread of velocities of particle of sort α with respect to the hydrodynamic velocity, $\mathbf{u}_\alpha \equiv \mathbf{u} + \upsilon_\alpha \mathbf{e}_\psi$, and parameters κ_α define the total generalized angular momentum:

$$J_\alpha \equiv m_\alpha N_\alpha \kappa_\alpha U_\alpha l \,.$$

In conclusion, it has been given the complete description of the dynamics of the plasma column in the homogeneous magnetic field within kinetic model. In the case of stationary magnetic field the column cross-section is found to oscillate harmonically at the low-hybrid frequency. The method applied for the analysis, is very fruitful and can be used for the investigation of plasma dynamics in the number of other cases. For example, it allows obtaining temporal evolution of a two-component plasma bunch in nonstationary weakly inhomogeneous magnetic field of the mirror configuration.

References

1. A.V. Gurevich, and others, Sov. Phys. JETP, 1966, **22**, 449.
2. D.S. Dorozhkina, V.E. Semenov, Phys.Rev.Letters, 1998, **81**, 2691.
3. D.S. Dorozhkina, V.E. Semenov, JETP, 1999, **9** (to be published).
4. A. Neogi and R. K. Thareja, Physics of Plasmas, 1999, **6**(1), 365.

INVESTIGATION OF ECR HOT ELECTRON PLASMA IN A SIMPLE MAGNETIC MIRROR TRAP

V.V.Andreev, A.M.Umnov, V.B.Khromchenko, S.Y.Vazhnov, M.Y.Shlyakhov*

Peoples' Friendship University of Russia, Plasma physic, Moscow, Russia
*Institute for Opto-Physical Measurements, Moscow, Russia

Analysis of properties and characteristics electron cyclotron plasma in different cases of usual ECR discharge was carried out. Both experimental and numerical studies were performed to define optimal discharge conditions for x-ray generation.

The growing interest in microwave discharges with electron cyclotron resonance (ECR) is owed to such their properties as high plasma density for a low gas pressure (10^{-4} - 10^{-5} Torr) and to the possibility for control of the electron temperature in wide range from 1 to 10^5 eV for various scientific and technological purposes [1, 2].

ECR - discharge is defined as a kind of microwave-discharges taken place in inhomogeneous magnetic field (usually of mirror trap) where effective confinement of plasma's electrons in discharge volume is affected by magnetic field of mirror configuration under their heating by microwave field in ECR conditions - $\omega_{ce}=\omega$ ($\omega_{ce}= eB/m_0 c$ - cyclotron frequency for the rest mass, ω - angular frequency of HF field).

The present paper contains generalized results of studying parameters of ECR discharges obtained in mirror configuration in different discharge conditions by various diagnostics and numerical simulation experiments closed to natural ones. We studied evolution of plasma time formation of ECR-discharge, its temperature, density and life-time with respect to: a) gas pressure, b) ω_{ce}/ω value at the midplane of mirror configuration, c) different gradients of magnetic field at resonant zones. Experimental results for a) and b) were obtained on experimental device scheme of which is presented in Fig.1. Cylindrical TE_{111} resonator (h=7.8 cm, D=11 cm), placed in the static magnetic mirror field, formed by 2 coils, was excited by magnetron generator in pulse regime (pulse duration 1 ms, repetition rate f=300 Hz, carrying magnetron frequency — 2.4 GHz, 150 W, maximum electric field strength E≈500 V/cm). Magnetic field (mirror ratio – 1.4, distance between mirrors – 23 cm) can be smooth modified, thus in the center of resonator magnetic induction was varying from 0 to 1 kGs (resonant value — 846 Gs). In the consequence of big life-time of electrons in trap under ECR conditions the ionization process takes place at

value of gas pressure p lower then 10^{-5} Torr. The definition of plasma concentration, averaged by volume and its time - depending during decay process after microwave pulse, was made by resonator procedure [3]. It is useful to note that in the resonator with $h/D \approx 0.7$ there is a possibility to induce two modes of oscillations on two far-standing frequencies. One mode (TE_{111}) is useful for ionization and heating the plasma, another (TH_{010}) for diagnostic aim. The power of diagnostic generator was chosen in condition of small influence of microwave field on plasma dynamics. Using main and diagnostic generator in pulse regime allowed to measure the density in different moments and as a consequence have a possibility to define plasma density n in the beginning of plasma decay and characteristic time of plasma decay at different experimental regimes.

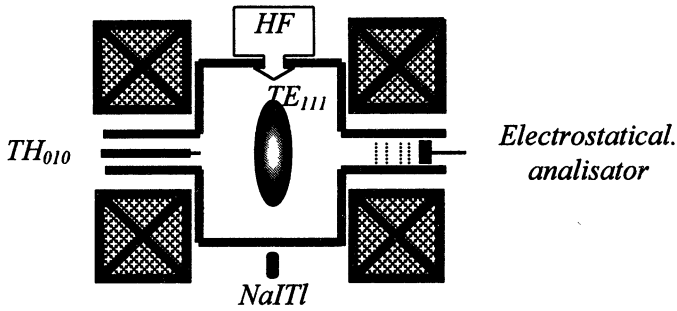

Fig.1. Scheme of experimental device

The results of experimental research on the space distribution of plasma density and plasma life - time obtained with different value of ω_{ce}/ω and pressure of residual gas p are shown in Figures 2-4. The range of ω_{ce}/ω in which we study ECR-discharge is 0.98 to 1.02 the plasma parameters of discharge corresponding to borders of interval are essentially different. This allows us to distinguish two main regimes of discharge. The first regime corresponds $\omega_{ce}/\omega < 1$, second corresponds $\omega_{ce}/\omega > 1$.

Axial and transverse probes allowed us to define the plasma volume in resonator and plasma build-up time in different discharge regime. Measurements of plasma noise made by thin (0,1 mm) Mo-probe that had possibility to move along the radius, are shown in Fig.2. This data permit to consider the transverse size of plasma discharge, which was unchangeable (r=2 см) for these regimes.

Defined plasma build-up time extremely depends on initial gas pressure and changes from 20 μs up to 100 μs for $\omega_{ce}/\omega = 1.02$ and $p = 5 \cdot 10^{-5} - 3 \cdot 10^{-6}$ Torr.

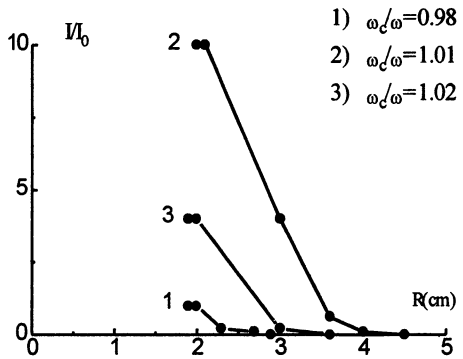

Fig.2 Plasma noise intensity (arb. un.) versus radius.

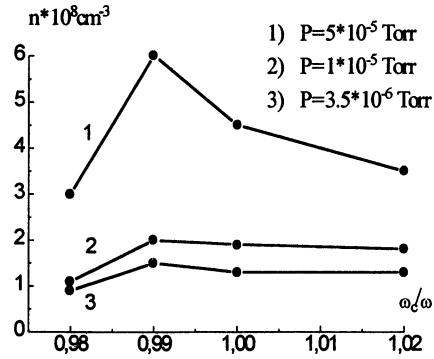

Fig.3 Plasma density versus ratio ω_c/ω

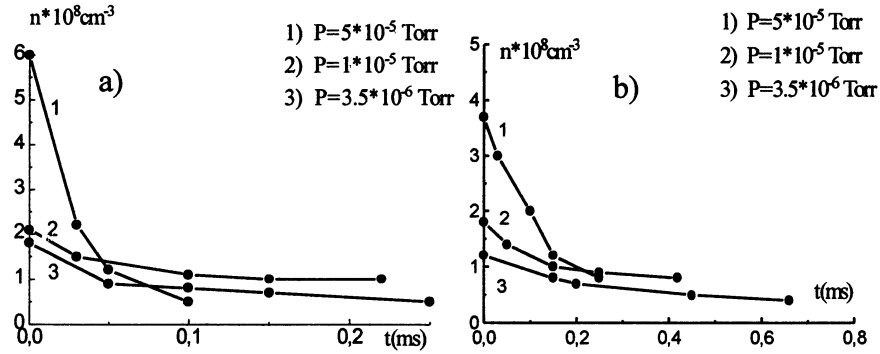

Fig.4 Plasma life-time versus ω_{ce}/ω: a) ω_{ce}/ω=0.99; b) ω_{ce}/ω=1.02

The experimental treatments show that plasma density achieves the maximum value when ω_{ce}/ω=0.99. The shift of ω_{ce}/ω to the values greater than 1 leads to the decrease of density and increase plasma life - time in the trap. It is connected with increasing electron temperature T_e.

The investigation of electrons energy spectrum made by multigrid analyser and by probes testified the existence in plasma two groups of electrons, which is usual for ECR-discharge [4, 5]. It was defined that increasing ω_{ce}/ω value leads to increase temperature T_e of cold component and to increase of maximal energy of hot component W_{eh}. Number of hot electrons is about 10-15% from total number of plasma electrons. In case ω_{ce}/ω=0.98 T_e=20 eV, W_{eh}=400 eV, and when ω_{ce}/ω=1.02 T_e=80 eV, $W_{eh}\approx$50 keV within above-mentioned interval of gas pressure.

The hot component temperature when $\omega_{ce}/\omega>1$ was evaluated after free-free X-ray spectrum from the gas which was detected by NaI(T1)-scintillator joined with height-pulse analyzer. In Fig.5 we plot typical histogram of X-ray spectrum in half-logarithmic scale. The hot component temperature defined by this method is 7.5 keV.

Plasma pin-hole photo in X-rays in longitudinal direction relative to magnetic field (Fig.6) testifies that hot component is located in ring-zone which radius considerably depends on ω_{ce}/ω (arrow indicates the zone in which bremsstruhlung radiation was registered).

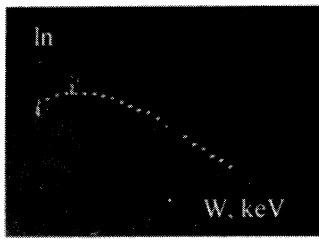

Fig.5 Histogram of X-Ray spectrum

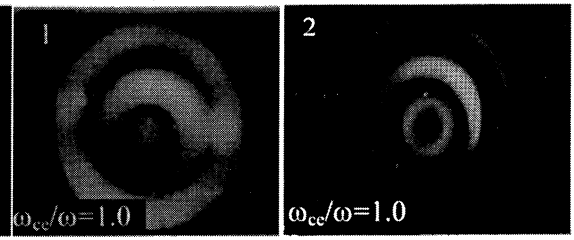

Fig.6 Plasma pin-hole photos

The results of measurement permit to conclude that plasma parameters are weakly sensitive to pressure when it is not high. If the pressure is lowered to $3.5\cdot10^{-6}$ Torr the luminosity of the discharge disappears, the discharge switches into reflecting mode (standing wave factor increases from 2 to 4). As seen from Fig.3 the plasma density in this case sharply decreases. Maximal achieved energy of electrons did not exceed 50 keV at ω_{ce}/ω=1.02 ànd 150 W input power. Obviously this fact bounded with the dependence of electron losses out the trap, when p is small and T_e is high, due to electron-atomic collisions frequency of which as the frequency of ionization is proportional to the pressure. Increasing pressure leads to considerable growth of plasma density and to reduction its life - time (Fig.4).

Simulation of ECR plasma was performed to analyze the dependence of configuration and inhomogeneity of magnetic field on the efficiency of generation of hot electrons in order to define optimal conditions for X-ray production. A model using particles has been applied [6].

Simulation was also aimed to define areas of hot electron locations in dependence on relative shift of the magnetic field. Figure 7 illustrates energy spectra of electrons in different cases of ω_{ce}/ω. Calculation was

performed in case of higher value of electric field strength (E=3 kV/cm) than it was in experiments. As seen from Fig. 7 the efficiency of hot electron generation depends on the ratio ω_{ce}/ω and plasma density. An optimal value of the ratio ω_{ce}/ω is equal to 1.1. Plasma density increase leads to higher maximal achieved electron energy (up to 180 keV), but typical bump at the energy spectrum tail is absent. This effect is possibly due to stochastic plasma heating.

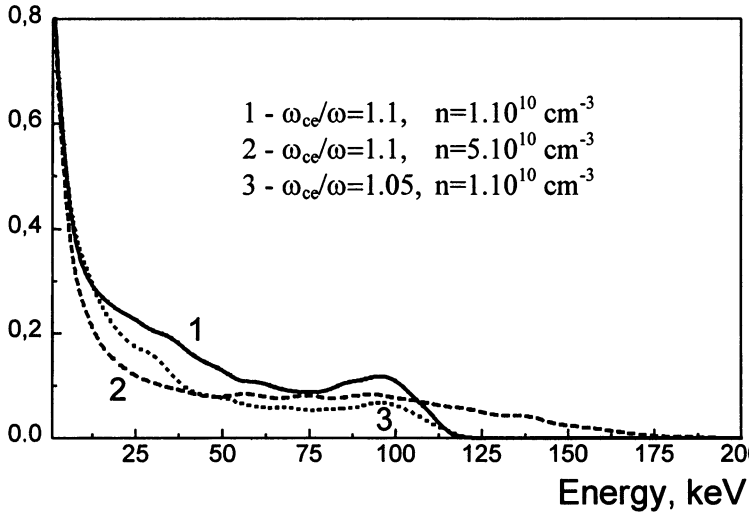

Fig. 7. Energy spectra of electrons.

Conclusion

Obtained results testify the presence in plasma of two sorts of electrons: cold and hot. The life-times τ_l of charged particles found with help the velocity of decreasing plasma concentration after stopping the SHF-pulse, show that rise of electron temperature, which is function of ω_{ce}/ω, leads, in other equal conditions, to the fast growing of τ_l. When $\omega_{ce}/\omega < 1$ the τ_l value is order of magnitude of electron - atomic collisions. When $\omega_{ce}/\omega > 1$, unless the linear dependence of $\tau_l(n_0)$ (n_0-neutral concentration), the life-time achieves high magnitude although it's considerably less than time of electron-atomic collision. Evidently, it is bound with the presence of diffusion in plasma discharge, during decay, which is determined by collective effects.

It is worth noting that the major part of hot electrons is located at the areas where magnetic field induction value is higher than that corresponding to non-relativistic ECR condition. This is possibly due to autoresonant acceleration of electrons in spatially growing magnetic field [7,8]. Such an effect was also observed in toroidal systems under ECR heating plasma experiments.

This work was undertaken for complex investigations of ECR - plasma parameters evolution in different discharge conditions to obtain optimal ones for intense x-ray generation in wide range of wavelength.

The research was supported by INTAS 97.0094.

References

1. K. S. Golovanivski, *Sov. J. Atomic Physics*, 1984, **5**, 303.
2. K. S. Golovanivski, *Sov. J. Technique of Experiment*, 1985, **5**, 7.
3. V. E. Golant, High frequency methods of plasma investigation, Moscow, Nauka, 1968.
4. N. C. Luhman and A.W. Trivelpiece, *Phys. Fluids*, 1978, **21**, 11, 2038.
5. I. H. Ikegami et. al. *Nuclear Fusion*, 1973, **13**, 351.
6. R. W. Hockney and J. W. Eastwood, Computer Simulation Using Particles (published by Alan Higler), 1988.
7. A. V. Zvonkov and A.V. Timofeev, *Sov. J. Plasma Physics*, 1986, **12**(4), 413.
8. V. V. Andreev and A. M. Umnov, *Plasma Sources. Science & Technology*, 1999, **8**, 479.

STOCHASTIC ELECTRON MOTION IN FIELD-REVERCED LOW-PRESSURE DISCHARGE

I.Yu. Kostyukov, J.M. Rax *

Institute of Applied Physics RAS, Nizhny Novgorod, Russia

*LPGP, Universite Paris XI, 91405 Orcay cedex, France

Capacitive or inductive stochastic heating relies on the repeated decoralated interaction of the electrons with a localized oscillating electromagnetic structures such as an electric sheath or an inductive skin depth. The periodic interaction with a third type of localized structure, the zero line of a magnetic field, provides an efficient and practical mean to sustain radio frequency (RF) low pressure discharges. First we identify the relevant variables and classify the electron trajectories in the magnetic field with null-line. Then we calculate the stochasticity threshold.

During the past decade high-density low-pressure plasma reactors have become a subject of increasing interest [1]. This growing interest was triggered mainly by the needs for better processing reactor particularly in the electronic industry. In a low-temperature plasma discharge as the neutral pressure decrease the mean free pass increase and both collisional heating and collisional confinement disappears. In order to overcome this difficulty and to sustain high density discharge at low pressure a collisionless heating mechanism is to be put at work [1].

The experiments with a magnetic neutral loop discharge was examined to minimize the loss of plasma to surrounding wall and produce more uniform plasma required for long wafers [2]. This discharge is characterized by the use of plasma produced in a magnetic neutral loop which consists of zero magnetic field points connected around a circle, where the plasma is generated by applying RF electric field along the loop. At the same time, the ``magnetic null point'' yields a strong nonlinearity to generate ``chaos'' of the particle motion and it has been recently pointed out on the basis of a numerical simulation [3]. This simulation shows the stochastical heating to sustain discharge. The purpose of the present study is to show analytically the existence of the chaos in such system and to calculate the stochasticity threshold.

Hamiltonian analysis

We consider the motion of an electron under the action of a nearly homogeneous RF electric field $E(t)$ linearly polarized along y axes and an inhomogeneous static magnetic field $\mathbf{B}(x)$

$$\mathbf{B}(x) = B_0(x/l)\mathbf{e}_z \qquad \mathbf{E}(t) = \mathbf{e}_y E_0 \cos\omega t\,, \tag{1}$$

where $B_0 = \omega mc/e$ is the intensity of the magnetic field at the point of the cyclotron resonance, where $\omega = \omega_{ce}(x), E_0$ and $\omega/(2\pi)$ are the amplitude and frequency of the RF electric field. Let l be the unit of length, ω^{-1} be the unit of time, m, the electron mass be the unit of mass and e, the electron charge, be the unit of charge. As the vector and scalar potentials do not depend on z we can restrict the analysis to the degree of freedom x and y. So the Hamiltonian can be written in the form:

$$H = \frac{P_x^2}{2} + \frac{\left(P_y + x^2/2\right)^2}{2} + E\cos t\ . \tag{2}$$

This Hamiltonian can be reduced to a one degree of freedom if we consider the integrability of the y dynamics. This leads to the constant of motion C and the Hamilton equation for P_y can be integrated to give

$$\frac{dy}{dt} - \frac{x^2}{2} + E\sin t = -C = const = \left.\frac{dy}{dt}\right|_{t=0} - \left.\frac{x^2}{2}\right|_{t=0}\ . \tag{3}$$

Then the Hamilton equation for P_x can be derived from an effective one degree of freedom Hamiltonian if we introduce $q = x$, $p = dq/dt$ and replace P_y by its expression as a function of t. The effective Hamiltonian of the final system takes the form

$$H = H_0(p,q,C) + V(p,q,t) + C^2/2\,, \tag{4}$$

$$H_0(p,q,C) = \frac{p^2}{2} - \frac{Cq^2}{2} + \frac{q^4}{8}\,,\quad V(p,q,t) = E\frac{q^2}{2}\cos t\,.$$

Orbit classification

Let us analyze the unperturbed motion ($V = 0$). The Hamiltonian of the unperturbed system, $H_0(p,q)$, describes the particle motion in bequadratic potential. There are three regimes of electron motion. The first two cases ($C > 0$) are those when the potential has two minimums, this case relevant to stochastic heating is illustrated on Fig. 1.

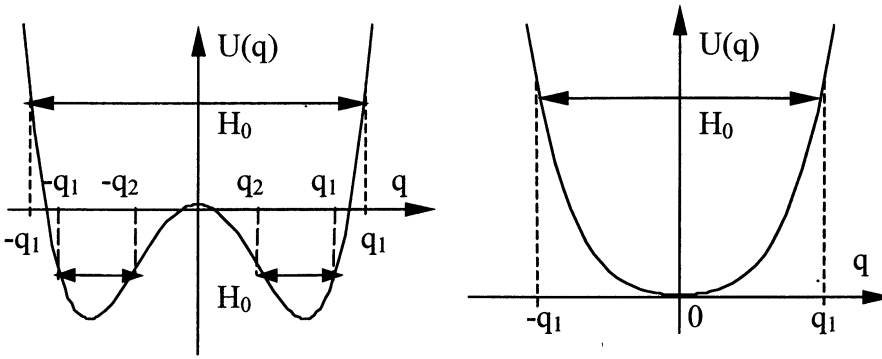

FIG. 1. Plot of quadratic double well potential $U(q)$ for $C > 0$.

Case A ($C > 0$, $-C^2/2 < H_0 < 0$)

The electron moves in the double-well potential and is trapped in one of the well. The solution of the equations of motion can be expressed in terms of elliptic function or in terms of Fourier series:

$$q(t) = q_1 dn\left(\frac{q_1 t}{2}, k\right) = \Omega(k)\left\{1 + 2\sum_{n=1}^{+\infty} \frac{\cos[n\Omega(k)t]}{\cosh[ng(k)]}\right\}, \qquad (5)$$

where $q_1 = \sqrt{2(C+v)}$ is the oscillation amplitude, *dn*, *cn* and *sn* are the Jacobi elliptic functions and the arguments k, Ω and g are given by relations: $k^2 = \dfrac{2v}{C+v}$, $\Omega(k) = \dfrac{\pi q_1}{2K(k)}$, $g(k) = \dfrac{\pi K\left(\sqrt{1-k^2}\right)}{K(k)}$,

where $K(k)$ is the complete elliptic integral of the first kind. Then action-angle variables can be introduced and expressed in terms of elliptic integral:

$$I(H_0,C) = \frac{2\sqrt{2v}}{3\pi}\left\{\frac{v-C}{v+C}\left[K(k)-E(k)\right]+E(k)\right\},\quad \theta(t)=\Omega(k)t\,, \quad (6)$$

where $E(k)$ is the complete elliptic integral of the second kind.

By the same way the solution of equation of motion can be found for the case B ($C>0,\quad H_0>0$) when the electron is free to move across the barrier and for the case C $-v<C<0,\quad H_0>0$ the potential $U(q)$ has only one minimum. The case C is not interesting from the point of view of stochastic heating because there is no separatrix so there is less opportunity to have stochastic motion.

Stochasticity threshold

Now let us consider the electron dynamics when the RF electric field is switch on. In order to identify the resonances induced by the RF field we express $H(p,q)$ in terms of the action-angle variables (I,θ). To do it the expression for q as a function of I and θ can be used. Thus we obtain for $H_0<0$

$$V = E\frac{q_1^2 E(k)}{2K(k)}\cos t + E\sum_n \frac{n\Omega^2(k)\cos(n\theta - t)}{\sinh\left[ng(k)\right]}\,. \quad (7)$$

By the same way the similar expression can be calculated in the case $H_0>0$.

The RF field induces an infinite number of primary resonances located near the action values $I=I_n$ that satisfy the equations

$$n\Omega(I_n)=1 \text{ if } H_0<0 \text{ and } (2n-1)\Omega(I_n)=1 \text{ if } H_0>0. \quad (8)$$

In the case $H_0<0$, the resonance condition (8) can be fulfilled only for $C>1/(2n)$. The threshold for the formation of the stochastic layer can be estimated by the Chirikov criterion for overlap the two resonance zones. To do it we make the two-resonance approximation [4] for the case $H_0<0$ and expand about the point I_1:

$$H(I,\theta) = H_0(I_1) + (I - I_1)\Omega(I_1) + (I - I_1)^2 \frac{1}{2}\frac{d^2 H_0}{dI^2}\bigg|_{I=I_1} \qquad (9)$$

$$+ V_1 \cos(\theta - t) + V_2 \cos(2\theta - t).$$

The amplitudes of the first two resonances are determined by Eq. (7). Performing a canonical transformation to coordinates (P, X) by use of generating function $S(I, X, t) = (I - I_1)(X + t)$ we obtain the relation between old and new coordinates $P = I - I_1$, $\theta = X + t$ and Hamiltonian takes the form

$$H(P, X) = H_0(I_1) - \frac{P^2}{2M} + V_1 \cos X + V_2 \cos(2X + t), \qquad (10)$$

where the effective mass of the associated non linear pendulum is defined by the curvature $M = \left| \left(\frac{d^2 H_0}{dI^2} \right)^{-1}_{I=I_1} \right|$. Then the threshold intensity of RF field can be found by applying Chirikov criterion [4]

$$\left[\sqrt{V_A(I_1)} + \sqrt{V_A(I_2)} \right] = 2^{-4} M. \qquad (11)$$

By the same way, the threshold intensity of RF field can be obtained for $H_0 > 0$.

For $C >> \sqrt{2H_0}$ we can use the following approximation for oscillation frequency

$$\Omega(H_0) = \frac{\pi\sqrt{C}}{2\ln\left(4C\sqrt{2/H_0}\right)} \begin{cases} 2, & for\ H_0 < 0, \\ 1, & for\ H_0 > 0. \end{cases} \qquad (12)$$

Using obtained relations we can derived the analytical expression for the threshold intensity of RF electric field for $H_0 > 0$ and $H_0 < 0$

$$E_{thr}(C) = \frac{8\pi C^{5/2}}{(\sqrt{2}+1)^2} \sinh\left(\frac{\pi}{2\sqrt{C}}\right) \exp\left(-2\pi\sqrt{C}\right). \qquad (13)$$

Fig.2 shows a good agreement between analytical formula (13) and numerical evaluation of the threshold value of RF field for $C > 0.5$. It is seen from Fig.2 that the stochasticity occurs near separatrix for $C >> 0.5$ that is quite natural [4].

The validity condition for the Chirikov criterion [4] is $\left\{\left(2\sqrt{MV_n(I)}\right)/I,\ \sqrt{V_n(I)/M}\right\} << 1$. A numerical evaluation shows that this condition is fulfilled for $C > C^* \approx 0.7$.

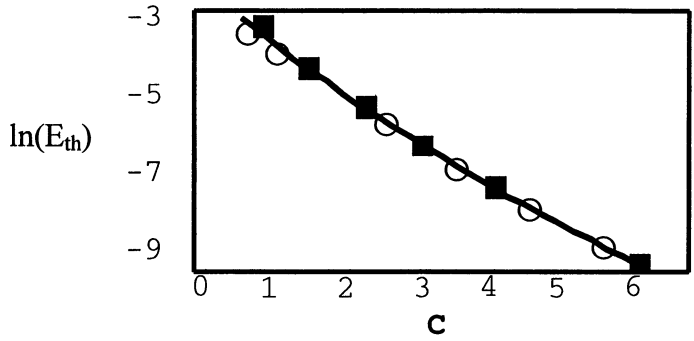

FIG.2. Logarithm of the threshold value of the normalised RF electric field $\ln E_{th}$ versus parameter C.

Conclusion

The collisionless heating in this type of the magnetized discharge have been observed at low-pressure [2]. Numerical simulation indicates [3] that there is the chaos in the dynamic system describing the discharge and the stochastic heating is more efficient mechanism at low gas pressure than the others. This conclusion agrees with our study, which show that the significant part of electrons moves chaotically under experimental condition $E \approx 1$.

Above stochasticity threshold the electron dynamics becomes stochastic and statistical approach can be used. The heating can be described by Focker-Planck equation and diffusion coefficient defining the heating can be found with help of the obtained results.

References

1. Lieberman M. A. and Lichtenberg A. J, *Principles of plasma Discharges and Materials Processing* (Wiley \& Sons, NY, 1994).
2. Uchida T., Jpn. J. Appl. Phys. 1994, **33**, L43; Sakoda T. *et al.*, Jpn. J. Appl. Phys. 1997, **36**, 6981.
3. Yoshida Z., Asakura H., Kakuno H., Morikawa J., Takemura K., Takizawa S., and Ushida T., Phys. Rev. Lett. 1998, **81**, 2458.
4. Reichl L. E. and Zheng W. M., Phys. Rev. A, **29**, 2186 (1984); *ibid* **30**, 1068 (1984).

A 3D SIMULATION OF PLASMAS PRODUCED AT ELECTRON CYCLOTRON RESONANCE AND SYNCHROTRON GYROMAGNETIC AUTORESONANCE

V.V. Andreev, A.M. Umnov, S.Yu. Vazhnov

Peoples' Friendship University of Russia, Moscow, Russia

A 3D simulation for plasmas heated by microwaves and confined in simple magnetic mirror trap in cases of electron cyclotron resonance (ECR) and synchrotron gyromagnetic autoresonance (SGA) was carried out. Simulation shows the possibility to obtain relativistic plasma with parameters (average electron energy, plasma density and dimension) which can be varied in wide intervals and to define optimal parameters of SGA. As it follows from simulation SGA regime also permits to produce a controlled bunch of relativistic electrons. The latter property of SGA can be used as a basis for designing a compact source of hard x-ray.

Introduction

In the early of 80^{th} it was proposed a method of relativistic plasma generation – synchrotron gyromagnetic autoresonance (electron cyclotron resonance in a magnetic field growing in time) [1]. Experiments performed on devices using this method – plasma synchrotrons GYRAC-0, GYRAC-D and GYRAC-X – demonstrated the phenomenon and showed the possibility of accumulation of relativistic plasma and generation relativistic electron bunches [2, 3]. These devices operate at the microwave frequency 2.4 GHz (150–300 W). Despite increasing interest to SGA it has not yet applied for practical purposes. The main reason is that the mechanism of the process in cases of greater values of initial plasma density, the velocity of magnetic field growth and input microwave power is still not clearly understood.

This work proposes a simulation model to study plasmas confined in a simple magnetic mirror trap in cases of ECR and SGA The model is based on particle – in – cell method [4] that is widely used to investigate dynamics of complex plasma objects. The aim of the simulation is to analyze the feasibility of practical implementation of SGA.

Simulation model

Simulation of SGA was carried out to investigate the main problem of SGA - the problem of trapping of electrons in a regime of autoresonant acceleration and to define the influence of SGA parameters and parame-

ters of initial plasma on trapping conditions. Considering the conditions of experiments [2] 3D-electrostatic model using particles has been applied. The numerical calculations provide information on 3D plasma evolution, trap losses of particles, energy spectra of electrons and ions, and plasma density that are beyond the reach of both analytical methods and 2D simulation. Simulation of SGA was aimed to analyze space particles distributions and electron energy spectra dependence on initial conditions (initial plasma density and volume occupied by plasma) and to determine trapping efficiency of electrons and losses particles from the trap.

To solve this problem a 3D electrostatic model with the use of seven-points CIC scheme [4] is explored. Plasma heating and confinement is simulated for 2.4 MHz plasma synchrotron (see Fig. 1).

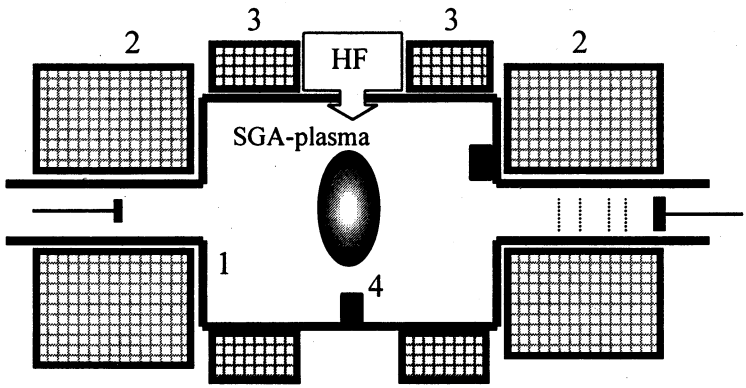

Fig. 1. Scheme of Gyrac type plasma synchrotron. 1 – TE_{111} vacuum cavity, 2 – static magnetic field coils, 3 –pulse magnetic field coils, 4 – target

Initially monoenergetic electrons (10–50 eV) and ions (1 eV) homogeneously distributed in space have random directions of velocities. We simulated hydrogen and argon plasmas of densities of $10^9 - 10^{11}$ cm^{-3} confined in a mirror trap (mirror ratio R = 1.2). Microwave electric field strength is varied in the range of 600 V/cm to 5 kV/cm. The velocity of magnetic field growth in time provided average electron energy increase 100 keV/μs. To satisfy requirements of a particle-in-cell method 10–20 particles in a cell are taken. Because of extreme complexity of the problem under investigation, schemes using Cartesian coordinates to solve equations for particles motion as well as Poisson equation have been used as the most cheapest and developed. Equation of motion for each charged particle after normalization to $m_o c\omega$ takes a form

$$\frac{\mathbf{u}^{n+1/2}-\mathbf{u}^{n-1/2}}{\Delta\tau}=\mathbf{g}^{n}+\frac{\mathbf{u}^{n+1/2}+\mathbf{u}^{n-1/2}}{2\gamma}\times\mathbf{b}^{n}, \qquad (1)$$

where $\mathbf{u}$ is an impulse of the electron in $m_o c$ units, $\mathbf{g}^n$ is the total dimensionless electric field strength at time moment n, $\mathbf{b}^n$ is the normalized magnetic field value, γ – relativistic factor, $\tau = \omega t$ is dimensionless time, $\Delta\tau$ is a time step. The equation (1) is solved by a second-order "leap-frog" Boris scheme [5]. For ions a nonrelativistic equation is used. This is justified, as the ions are not resonant particles.

The Poisson equation for periodic conditions (influence of the cavity walls is supposed to be neglected) is solved at each time step by using the Boisvert code. Spatial limitation of plasma is accounted for by assuming the particles reached the cavity walls to be lost.

Self-consistent electric field values are derived from the obtained potential distribution on the mesh with the use of finite difference derivatives. Electric field values at points of particle locations are obtained through inverse bilinear interpolation. Magnetic field formed by static magnetic coils and pulse magnetic coils is calculated at grid points.

The use of particle in cell method provides such an overwhelming spectrum of time depended plasma parameters and characteristics that one has to limit oneself just several of them. In the proposed model the following diagnostics have been applied:

1. Evolution of space distributions of electrons and ions.
2. Time dependence of losses for both sorts of particles: electrons and ions.
3. Time dependence of electron and ion energy spectra.
4. Space distributions of plasma potential and electric field.

Obtaining this data is enough to analyze collisionless processes taking place in the phenomena of interest.

Results and discussion

Fig. 2 presents typical space distributions of electrons and ions calculated for two SGA cases (E=3 kV/cm, f=2.4 GHz for both cases) of different initial plasma radii. It is seen from these figures that the SGA process gives a possibility of obtaining of different plasma objects. In case of comparatively small initial plasma dimension and plasma density one can obtain an accelerated bunch of electrons with narrow energy

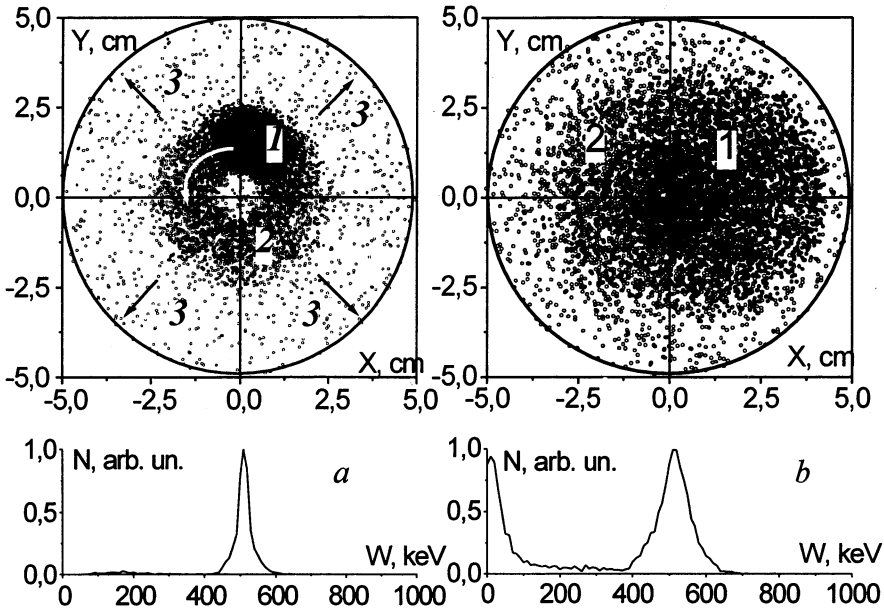

Fig. 2. Space distributions of electrons (black) and ions (gray) and electron energy spectra in cases r_0=0.8 cm (left) and r_0=2.4 cm (right). 1 – trapped electrons, 2 – ions captured by accelerated electrons, 3 – ions falling to the cavity's wall

spectrum (Fig. 2a). A portion of ions is trapped by the electric field of accelerated electrons. Non-trapped ions fall to the cavity wall. In case of greater plasma dimension and density relativistic plasma formation is generated (Fig. 2b). It is worth noting that there is no thermalization process in the case of SGA. Here the term "relativistic plasma" means that plasma has relativistic electron component with wide energy spectrum. It is seen from Fig. 2 the property of SGA to produce relativistic electron bunches as well as relativistic plasma.

Time dependence of losses from the trap is presented in Fig. 3 (N_c. is the number of particles confined in a magnetic trap, N is the total number of particles at the time moment τ=0). As seen from this figure initial stage of SGA is accompanied by losses of plasma particles of both sorts. End loss for electrons and transversal ones for ions take place. While trapped electrons gain energies the velocity of particle losses decreases tending to zero after the electrons reach considerable energies.

Fig. 4 presents time dependence of the maximal value of the electric field emerging in SGA-plasma. As shown from Fig. 4 acceleration of

electrons is accompanied by low frequency oscillations of two types. One of them is connected with electron energy oscillations, another (lower frequency) – with oscillations of plasma density. Despite self-consistent electric field strength reaches considerable values (up to 10 kV/cm) these oscillations do not lead to plasma decay. It is worth noting that the mean maximal self-consistent electric field strength of SGA-plasma tends to the value of microwave electric field.

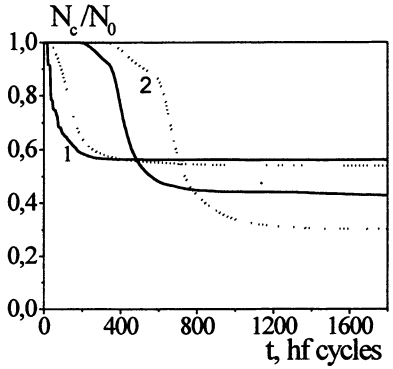

Fig. 3. Loss from the trap. $r_0 = 0.6$ cm, gas – hydrogen. 1 – $n_0 = 10^9$ cm^{-3}, 2 – $n_0 = 5 \cdot 10^9$ cm^{-3}, solid curves – electrons, dotted – ions

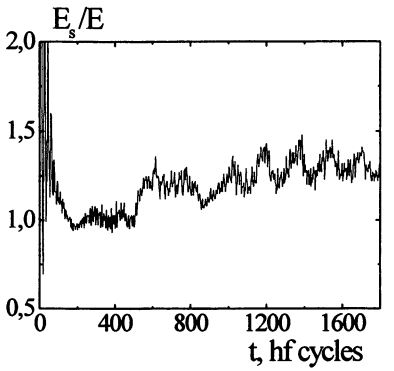

Fig. 4. Maximal value of self-consistent electric field E_s in SGA-plasma. $n_0 = 10^{10}$ cm^{-3}, $r_0 = 0.6$ cm, $E = 3$ kV/cm

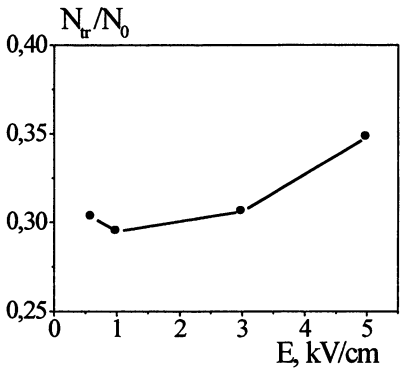

Fig. 5. Trapping efficiency versus electric field strength. $n_0 = 10^{10}$ cm^{-3}, $r_0 = 2.4$ cm, gas – argon

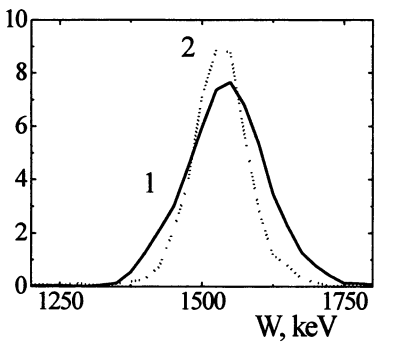

Fig. 6. Energy spectra of trapped electrons. $n_0 = 10^{10}$ cm^{-3}; 1 – $E = 5$ kV/cm, 2 – $E = 1$ kV/cm

Comparison study of trapping efficiencies N_{tr}/N_0 (N_{tr} – a number of trapped electrons, N_0 – a total number of initial plasma electrons) for different cases of electric field strength E shows that the trapping efficiency slightly rises with the growth of E (Fig. 5).

The width of the energy spectrum of trapped electrons mainly depends on the value of the microwave electric field strength (see Fig. 6) and the ratio $B(0)/B_0$, where $B(0)$ is a magnetic field magnitude in the center of vacuum cavity ($B_0 = m_e c\omega / e$), but unlike ECR the shift of initial magnetic field $B(0)/B_0>1$ in case of SGA does not lead to an increase of density of hot electron fraction.

Conclusion

The results of 3D simulation of SGA show the possibility of obtaining relativistic plasma as well as relativistic electron bunch. All things considered, one can estimate feasible parameters of the electron bunch produced by SGA in case of above mentioned plasma parameters: average energy of electrons 500 keV – 2.5 MeV, volume 0.5 – 2.0 cm^3, density $10^9 – 5 \cdot 10^{10}$ cm^{-3}. Dynamics of a bunch can be controlled by variation of magnetic field in time, for example, by short circuiting one of the magnetic coils to move the bunch to a heavy metal target. Typical x-ray burst in this case can range between 10 and 200 kilowatt during 1.0 – 5.0 ns.. The repetition rate can be as high as 50 Hz to 100 Hz. Such a source of intense hard x-ray can be used in atomic and nuclear physics, defectoscopy, material processing, medicine and biology.

The research was supported by INTAS 97.0094

References

1. Golovanivsky K.S., *Physica Scripta*, 1980, **22**, 126.
2. Andreev V.V. and Umnov A.M., *Physica Scripta*, 1991, **43**, 490.
3. Andreev V.V. and Umnov A.M, *Plasma Sources. Sci. & Technology*, 1999, **8**, 479.
4. Hockney R.W. and Eastwood J.W., *Computer Simulation Using Particles* (published by Alan Higler), 1988.
5. Birdsall C.K. and Langdon A.B., *Plasma Physics Via Computer Simulation* (A. Higler Series on Plasma Physics), 1995.

NONLINEAR SPATIAL-TEMPORAL DYNAMICS OF ULTRA-SHORT ELECTROMAGNETIC PULSE

A. A. Balakin, V. A. Mironov

Institute of Applied Physics, RAS, Nizhny Novgorod, 603600, Russia

The equation generalizing NLSE in the case of pulses with duration of few field periods is analyzed. Variation of primary parameters of the wave field (mass center, effective duration and width) is obtained by method of moments. The collapse appearance of spatial structure is shown and its forming peculiarities are investigated numerically.

Recent researches in laser technique, optoelectronics and semiconductor electronics lead to the creating of the systems generating electromagnetic pulses with duration of few field periods (see [1, 2] and citing there literature). The new theoretical problem of investigation of ultra-short pulse propagation peculiarities and interaction with matter arises.

One of the simplest generalizations of linear and nonlinear Shrodinger equation (NLSE) used for investigation of a spatial-temporal evolution of subcycle pulses is the following equation [3-6]

$$\frac{\partial^2 u}{\partial z \partial \tau} + \Delta_\perp u + |u|^2 u = 0 . \qquad (1)$$

It describes unreflected propagation of the wave field $u(z,\tau=z-v_{gr}t,\boldsymbol{r})$ along z axes with the group velocity v_{gr}. Dimensionless coordinates z, $\boldsymbol{r}$, and "time" τ are written in corresponding typical (spatial and temporal) scales. The field $u(\boldsymbol{r},z,\tau)$ is normalized to a typical nonlinear field.

It's not difficult to obtain an equation for the envelope $\psi(z,\tau,\boldsymbol{r})$ of the quasi-monochromatic pulse $u=\psi(z,\tau,\boldsymbol{r})\exp i\omega\tau$ from (1):

$$i\omega\frac{\partial\psi}{\partial z} + \frac{\partial^2\psi}{\partial z\partial\tau} + \Delta_\perp\psi + |\psi|^2\psi = 0 . \qquad (2)$$

The second term in this equation is smaller than the first one $\left(\frac{\partial^2\psi}{\partial z\partial\tau} << \omega\frac{\partial\psi}{\partial z}\right)$ and is usually omitted in approximation of a long (in the scale of the wavelength $2\pi/\omega$) quasi-monochromatic pulse. It's obvious that NLSE describes the evolution of such pulse. In the case of dispersion-free medium (for example, in rare plasma) just that NLSE is used usually for examination of a spatial-limited pulse self-action (see [6]). New effects connecting with additional term in (2) appears while decreasing of the pulse duration and increasing of propagation path. It is

possible to explain these effects in the following way. Let's transform the second term using the perturbation method. In accordance with NLSE $\psi_z = i\left(\Delta_\perp \psi + |\psi|^2 \psi\right)/k$, it allows to write the additional term in the form

$$\psi_{z\tau} = i\left(\Delta_\perp \psi_\tau + |\psi|^2 \psi_\tau\right)/k . \qquad (3)$$

The first term in (3) describes non-stationary diffraction of the wave field. It leads to forming of diffraction forerunner [3, 5] and horseshoe-like structure of the wave field [2, 5] in vacuum. Similar structure modification is connected with dependence of the group velocity on the field amplitude (second term in (3)). They are investigated in one-dimensional problem in application to optical fiber (see [8]).

In this paper we consider the peculiarities of dynamics of self-action for wave field with finite amplitude on the basis of equation (1) and equivalent equation (2). At first we obtain some analytical relationship allowing to analyze qualitatively the typical characteristics of the system evolution, then we present some results of numerical investigation of initial equation (1).

Note, that parameters are remaining constant during the propagation of an electromagnetic pulse

$$I = \int |u_\tau|^2 d\tau d\mathbf{r}_\perp , \; H = \int \left(\left|\nabla_\perp u\right|^2 - |u|^4/2\right) d\tau d\mathbf{r}_\perp . \qquad (4)$$

They generalize well-known NLSE expressions (I – "energy" or "number of quanta", H – hamiltonian). Further we obtain some expressions for the moments $I_{n,m} = \int \tau^n \boldsymbol{r}_\perp^m |u_\tau|^2 d\tau d\boldsymbol{r}_\perp$ (where m, n – integer numbers) with the help of continuity equation by analogy with NLSE [9]

$$\frac{\partial}{\partial z}|u_\tau|^2 = -div\left(u_\tau^* \nabla_\perp u + u_\tau \nabla_\perp u^*\right) + \frac{\partial}{\partial \tau}\left(\left|\nabla_\perp u\right|^2 - |u|^4/2\right). \qquad (5)$$

It's possible to show that the mass center (centroid) of the wave field $\tau = I_{1,0}$ moves with a constant velocity

$$\frac{\partial \bar{\tau}}{\partial z} = -H . \qquad (6)$$

Depending on the hamiltonian H sign the group velocity may be larger (H<0) or smaller (H>0) than the pulse velocity in the linear medium.

The behavior of the square of typical wave field length $\overline{(\tau - \bar{\tau})^2} = \int (\tau - \bar{\tau})^2 |u_\tau|^2 d\tau d\mathbf{r}_\perp$ shows another specific particularity of the considered problem. Equations (1) and (5) yield

$$\frac{d^2\overline{(\tau-\bar{\tau})^2}}{dz^2} = 2\int |\Delta_\perp q + p|^2 d\tau d\mathbf{r}_\perp , \qquad (7)$$

where $q_\tau = u$, $p_\tau = |u|^2 u$. From here it follows that the pulse is spreading in longitudinal direction during its propagation. This effect of pulse duration increasing is in proportion to the square of relative width of pulse spectrum $\Delta\omega^2/\omega^2$ ($\Delta\omega$ – spectrum width, ω – average frequency).

At last as in the case of NLSE, it is possible to obtain the expressions for effective width of the wave field $\overline{r_\perp^2} = \int r_\perp^2 |u_\tau|^2 d\tau d\mathbf{r}_\perp$

$$\frac{d^2\overline{r_\perp^2}}{dz^2} = 8H . \qquad (8)$$

Thus, the wave packet "collapses" (in the case of negative hamiltonian $H<0$) in the transverse direction at a certain finite z determined by the initial field distribution and the value of hamiltonian H. Unlike the similar process in NLSE the field peculiarity is formed in spite of longitudinal pulse spreading. I.e. the collapse takes place in spite of decreasing of running value of hamiltonian.

Let's discuss the result of numerical simulation of equation (1) in axial-symmetric case. An initial distribution of the wave field was represented in the form of envelope of Gaussian shape with carrier frequency ω:

$$u = u_0 \exp\left(-\left[\frac{\rho^2}{2a^2} + \frac{\tau^2}{2\tau_0^2}\right]\right)\exp i\omega\tau . \qquad (9)$$

Results of numerical simulation were controlled by integrals (4).

The wave field evolution in the case of positive value of hamiltonian runs as in the linear medium (in vacuum). The wave field spreads in the transversal direction. The duration increases. The centroid shifts to the trailing edge according to (6). The horseshoe-like structure is formed [2, 5] (fig. 1).

For the negative hamiltonian the collapse occurs at $z\approx 1$ for the parameters $a = 1$, $\tau_0 = 1$, $\omega = 10$, $u_0 = 1$. The computation method conserves the value of the hamiltonian H for the considered parameters when the field amplitude becomes 4 times larger. The route length of hamiltonian conservation is decreased with decreasing of the absolute

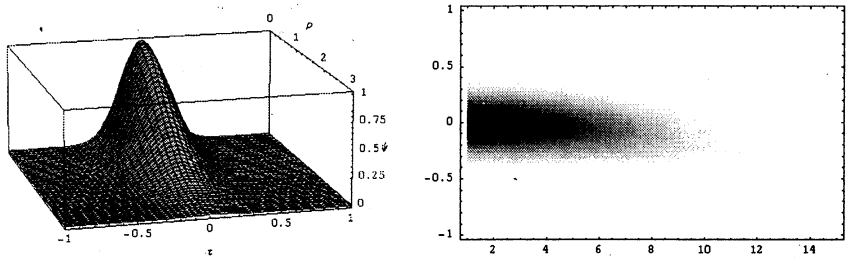

Fig. 1. Initial pulse distribution at z = 0 (left). Horseshoe-like structure at z = 5 (right).

value of hamiltonian $(|H| \to 0)$. The centroid shifting to the leading edge according to (6) is accompanied by its steeping and the trailing edge becomes modulated (fig. 2).

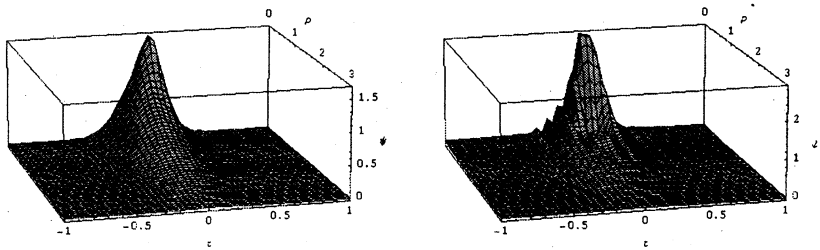

Fig. 2. Self-focusing of ultra-short pulse at z=0.3 (left), z=0.6 (right).

Two mechanisms were used for collapse stabilization: non-linearity saturation and inertia of nonlinear medium response. The parameters were chosen so that the maximum amplitude increasing was smaller then in 4 times. Both mechanisms lead to similar evolution of the wave field. The numerical results were represented on fig. 3. The inertia of nonlinear medium response was described by the equation

$$\tau_r \frac{\partial n}{\partial \tau} + n = |u|^2, \qquad (10)$$

where n – the perturbation of the nonlinear refractive index, τ_r – the relaxation time of the nonlinear response. Besides, nonlinear medium polarization in (1) $|u|^2 u$ was replaced by $n \cdot u$. The numerical results show that the development of crushing instability leads to the fragmentation of the wave field on the sequence of several pulses (3 pulses on fig.3). A ratio of amplitudes of such pulses is changed so that the order of them reverses in comparison with initial one (see fig.2 and fig.3). It is possible to see the side less intensive field maxima. Further,

the wave structure formed in nonlinear focal area spreads out in longitudinal direction.

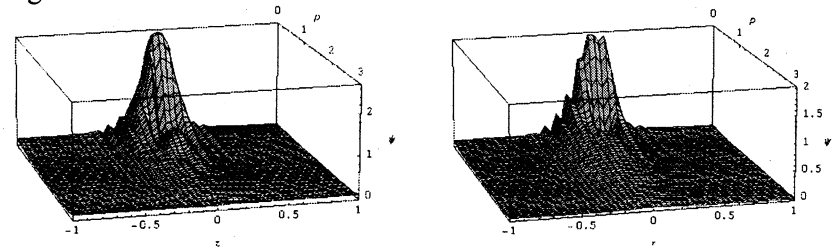

Fig. 3. Collapse stabilization at z=0.7: non-linearity saturation (left) and inertia of nonlinear medium response (right)

Thus, the peculiarities of the self-action of ultra-short electromagnetic pulse during its propagation become apparent in the uniform shifting of the centroid (6), making the leading edge steeper and the wave field collapsing in the case of negative hamiltonian ($H<0$). The effect of the pulse modification (7) leads to stabilization of the wave field beyond the nonlinear focus.

Authors are grateful to A. G. Litvak for useful discussion of the problem. The work was supported in part by the Russian Foundation for Basic Research (Grants Nos. 98-02-17205 and 99-02-16399).

References

1. Bakhrakh L.D. and Bliskovitskii A.A., Usp. Fis. Nauk **162**, 160 (1993).
2. IEEE J. of selected topics in Quan. Elect., section Terahertz Beams **2**, 679-747 (1996).
3. Belenov E.M. and Nazarkin A.V., Pis'ma Zh. Eksp. Teor. Fiz. **53**, 188 (1991).
4. Brabec T. and Krausz F., Phys. Rev. Lett. **78**, 3282 (1997).
5. Mironov V.A., Zh Eksp. Teor. Fiz. **116**, 32 (1999).
6. Sprangle P., Hafizi B. and Serafim P., Phys. Rev. E **59**, 3614 (1999).
7 Andreev N.E. and Gorbunov L.M., Pis'ma Zh. Eksp. Teor. Fiz. **56**, 144 (1992).
8. Zakharov V.E. and Kuznetsov E.A., Zh. Eksp. Teor. Fiz. **113**, 1892 (1998).
9. Vlasov S.N., Petrishchev V.A., Talanov B.I., Izv. Vuz. Radiofizika **14**, 1353 (1971) [Radiophys. Quantum Electron **14**, 1062 (1974)].

HIGH ENERGY ELECTRON EMISSION IN A HIGH POWER MICROWAVE-PLASMA NONLINEAR INTERACTION

H. Ito, T. Fuji, T. Handa, N. Yugami, and Y. Nishida*

Energy and Environmental Science, Graduate School of Engineering,
Utsunomiya University, 7-1-2 Yoto, Utsunomiya, Tochigi 321-8585, Japan
*Matsushita Electric Co., Utsunomiya, Tochigi 321-3231, Japan

Up to present, it is found that the hot electrons are generated near the critical layer by the resonance absorption phenomena. In the present experiments, we have tried to clarify the scaling law using high power microwave sources of 250 kW. When the incident microwave power up to 250 kW is irradiated on the inhomogeneous plasma, the high energy electrons of about 2 keV is detected. The scaling law of high energy electron emission has been investigated as a function of incident microwave power within 250 kW. The results show that the high energy electron emission have the dependence of $P^{0.5}$ (where P is the incident microwave power). The relationship is discussed with a model of wave breaking theory, showing the reasonable agreement the experimental results.

Introduction

It is well known that the high energy electron emission has been observed in both laser plasma and microwave plasma interaction experiments. With recent development of a new class of high intensity, short pulse laser systems, a number of experimental results on high energy electron emission have been reported. One of most interesting topics is high energy particle accelerators based on plasmas with ultrahigh acceleration gradients of plasma wave. The detailed investigation of the mechanism of high energy electron emission is very useful for the plasma-based accelerators.

When a microwave is obliquely incident on an inhomogeneous plasma, an electron plasma wave is excited by the resonance absorption phenomena due to nonlinear interaction at a critical layer and high energy electrons are ejected from the layer close to the critical layer. Up to present, the experimental investigations have been performed with about 10 kW power S band sources [1-3] in order to clarify the physical mechanism of high energy electron emission. It has been demonstrated experimentally that the electron energy has the dependence of $P^{0.5}$ and that the relationship is in fairly good agreement with the theory in case of low incident power [4].

To clarify the scaling law in higher power region, we have performed the experiments in the inhomogeneous plasma with p-polarized, high power microwave sources of up to 250 kW, which has never been tried so far, to our best knowledge.

Experimental Apparatus

The experimental arrangement used in the present studies is shown schematically in Fig.1. A cylindrical, unmagnetized argon plasma is produced in a stainless-steel chamber of 163.5 cm length by 32 cm diameter. The outside surface of the vacuum chamber is covered with a number of multidipole permanent magnets for a plasma confinement, the surface magnetic field strength of which are 4 kG. Although there are magnetic field on the inside wall of the vacuum chamber, a magnetic field free plasma is produced most of the part inside of the chamber by a pulsed discharge between four sets of LaB_6 cathode and the chamber wall (grounded). A typical discharge voltage and discharge duration are 180 V and 1.5 ms, respectively, with 10 Hz repetition. Typical plasma parameters are the maximum electron density $n_{max} \approx 2 \cdot 10^{12}$ cm^{-3} and electron temperature T_e=1~3 eV. An argon gas pressure is adjusted to P_{Ar}=3~5·10^{-3} Torr by a needle valve.

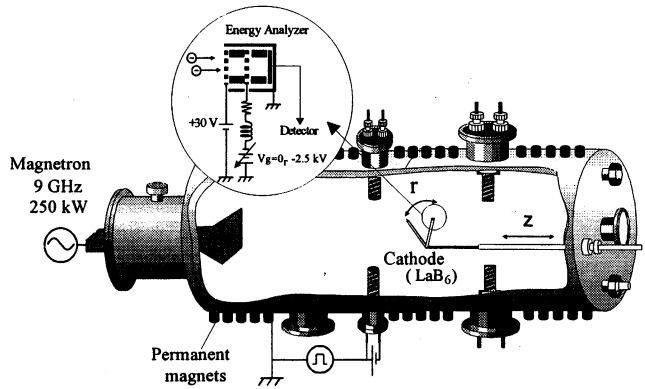

Fig. 1. Experimental apparatus used in the present studies. The inset shows the energy analyzer

The pulsed microwave has a frequency of f_0 =9 GHz (corresponding cut-off density $n_c \approx 1 \cdot 10^{12}$ cm^{-3}) and maximum power of 250 kW. The pulse duration is variable from 1 μs to 3 μs in full width at half maximum (FWHM) with a rise time 100 ns. Here, it is fixed on 1 μs in present experiment. The microwave is generated by a magnetron with a repetition

rate of 10 Hz and is irradiated into the plasma from the rectangular horn antenna (aperture area = 14.8×11.7 cm^2) with a metal lens which makes the ray trace of the incident microwave parallel along the propagation direction. Thus, the microwave is considered to be a plane wave, which has been confirmed in the air without plasma. The antenna is located at the lower end of the plasma density.

The plasma density and an rf electric field inside the plasma are measured by both a cylindrical probe with a tip of 1 mm length by 0.25 mm diameter and a plane probe with an area of 1×1 mm^2, movable along the axis and rotatable in the radial direction. We are not able to measure the exact hot electron energy by the probe applied to the high voltage because of the secondary electrons emitted from the probe surface. We employ the electrostatic energy analyzer with 25 mm length by 12 mm diameter which is shown in the inset of Fig. 1 for measuring the electron energy distribution function. The energy analyzer can determine the electron energy up to 3 keV.

Experimental Results

When the microwave pulse is injected into the plasma with critical density, it is observed that the high energy electrons are ejected from the layer close to the critical layer. Figure 2 shows a typical experimental result measured at z=134 cm and r=2 cm, where z and r are the axial and radial position, respectively. Top waveform in Fig. 2 is the incident microwave and bottom one is the signal of energy analyzer. Here, the incident power is 100 kW and the second grid of energy analyzer is biased V_g= =-500 V. The resonance absorption occurs at z=136 cm and this signal of energy analyzer vanishes beyond the critical density. Electrons with energy less than 500 eV are reflected and can't reach the collector, since the grid voltage is V_g=-500 V. Thus, we expect that the observed signal is due to high energy electrons having energy more than 500 eV generated by the resonance absorption.

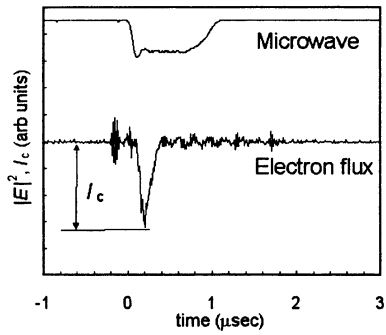

Fig. 2. Typical experimental result of energy analyzer

For the investigation of the maximum energy of hot electrons observed near the critical layer, the energy analysis is performed by changing the grid voltage. Figure 3(a) shows the dependence of the signal (I_c)

on the grid voltage at each incident power P=100, 150, 200, 250 kW, respectively. As seen in Fig. 3(a), the collector signal decreases and vanishes finally with deep enough bias voltages on the grid. Differentiating the data of Fig. 3(a), we obtain the energy distribution function and can estimate the electron energy. Examples of the energy distribution function are shown in Fig. 3(b). From these results, when the incident microwave power up to 250 kW is irradiated, the high energy electrons of about 1.8 keV are detected. It turns out from Fig. 3(b) that the increase of the incident power makes the maximum energy (ε) larger.

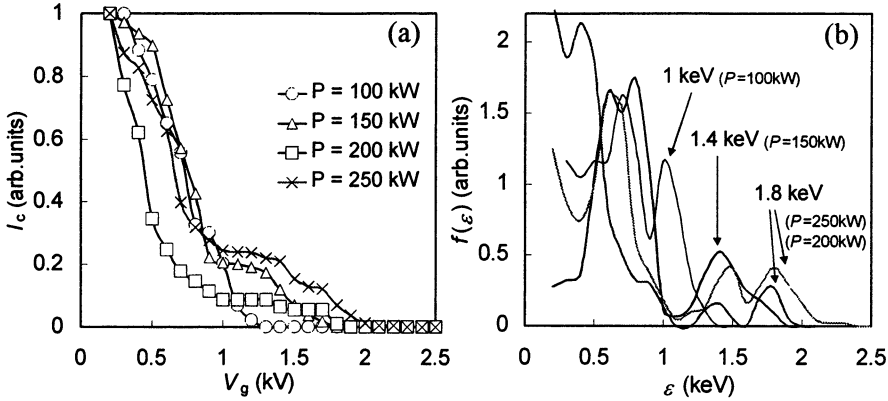

Fig. 3. (a) Collector signal as a function of grid voltage.
(b) Electron energy distribution function

The scaling law of high energy electron emission is obtained from the result of Fig. 3(b) by plotting the maximum electron energy as a function of the incident microwave power and is shown in Fig. 4. We measure the electron energy by employing the energy analyzer shown in the inset of Fig. 1 within the microwave power of 10 kW through 250 kW. On the other hand, when the incident power is smaller than 10 kW, we can use a plane probe to measure the electron energy. About 180 eV energy, which is independent of the incident power, is observed at the lower incident

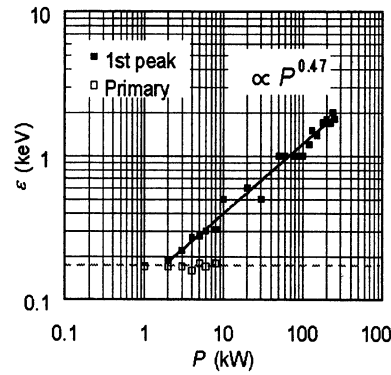

Fig. 4. The scaling law of high energy electron

power. Considering that the discharge voltage is 180 V, we can say that this energy is due to the primary electrons. The dependence of the electron energy on the incident microwave power turns out to be proportional to $P^{0.47}$ from Fig. 4. This relationship shows fairly good agreement with one of lower incident power. Thus, we consider that high energy electrons is generated by the wave breaking of theory localized electric field resulted from the resonance absorption.

Discussion

Let us employ the model of wave breaking theory for interpreting the scaling law of high energy electron production. The wave breaking occurs when the trapped electrons slip a phase from a plasma wave by about a half of wavelength, that is $\sim 1/k_p$. Thus, from the momentum equation of electron trapped into the plasma wave trough, the breaking electric field of plasma wave would be given by

$$E_p \approx m_e \omega_p^2 / e k_p , \tag{1}$$

where m_e and e are the electron rest mass and the electron charge, respectively. Thus, the electron energy ejected from the plasma wave field is given by

$$\varepsilon = \frac{1}{2} m_e v_e^2 \approx \frac{\lambda_p}{4\pi} e E_p . \tag{2}$$

The plasma wave is excited due to the resonance absorption by the incident microwave. Referring to Ref 5, you recognize that the amplitude of the plasma wave is proportional to the electric field of the incident microwave, that is

$$E_p = \delta E_d = \delta E \frac{\phi(\tau)}{\sqrt{2\pi k_0 L}} \frac{1}{s}, \tag{3}$$

where $\tau=(k_0L)^{1/3}\sin\theta$, $s=\nu_{eff}/\omega_0$, $\phi(\tau)$ is Ginzburg function, δ is the excitation efficiency, and ω_0, k_0, L, θ, and ν_{eff} are the electromagnetic (EM) wave frequency, EM wave wavenumber, the density gradient scale length, the incident angle and the effectively collision frequency, respectively. The field strength of the microwave power irradiated the plasma from the horn antenna has the dependence given by $P=\varepsilon_0 E^2 S_0/2$, where S_0 and ε_0 are the aperture area of the antenna and the dielectric constant, respectively. By substituting $E \propto P^{0.5}$ into Eq. (3), we obtain the relation $E_p \propto P^{0.5}$. Thus, you may see from Eq. (2) that there is the relationship between the electron energy and the incident microwave power, given by

$$\varepsilon = \frac{\lambda_p e}{4}\delta\sqrt{\frac{2}{\varepsilon_0 S_0}}A(\tau)P^{1/2} \propto P^{1/2}, A(\tau) \equiv \frac{\varphi(\tau)}{\sqrt{2\pi k_0 L}}\frac{1}{s}. \quad (4)$$

This result is fairly good agreement with the results observed in the present experiments and shows that the above mentioned mechanism is valid even under the strong nonlinear interaction.

Summary

We have discussed the mechanism of high energy electron production, in which the high energy particles are generated by the resonance absorption due to nonlinear interaction of a microwave with a plasma. When the microwave with a peak power of 250 kW is irradiated on the inhomogeneous plasma, the maximum energy electrons of 2 keV has been observed. The experimental results show that the scaling of high energy electrons up to 250 kW has the relation of $\varepsilon \propto P^{0.5}$, showing good coincidence with the case observed in lower incident power. The results derived from the model of wave breaking theory are fairly good agreement with those observed in the present experiments.

Acknowledge

This work is supported in part by the Grant-in-Aid for Scientific Research from the Ministry of Education, Science, Sports and Culture, Japan.

Reference

1. H.C.Kim, R.L.Stenzel and A.Y.Wong, Phys. Rev. Lett. **33**, 886 (1974).
2. K.Mizuno, J.S.DeGroot, and F.Kehl, Phys. Rev. Lett. **49**, 1004 (1982).
3. Y.Nishida, A.Lee, *et at.*, Plasma Phys. and Cont. Fusion **32**, 391 (1990).
4. Ann Y.Lee, Y.Nishida *et al.*, Phys Fluids 29, 3785 (1986).
5. V. L. Ginzburg, Translated by J. B. Sykes and R. J. Tayler, The Propagation of Electromagnetic Waves in Plasmas, 2nd ed. Pergamon Press, Oxford, 1970.

STOCHASTIC BROADENING OF HIGH ORDER ION CYCLOTRON RESONANCES DUE TO LOW HYBRID TURBULENCE

E.V. Suvorov, D.A. Ryndyk

Institute of Applied Physics, Nizhny Novgorod, Russia

Theory of stochastic broadening of ion cyclotron resonances has been applied to the dynamics of lower-hybrid wave instability excited by energetic ion beam in a magnetized plasma. The closed set of equations has been derived and the relaxation of ion beam has been investigated for the case of narrow $\mathbf{k}$-spectrum of excited waves.

Resonant cyclotron interactions between charged particles and electromagnetic waves play an important role in a magnetized plasma. This phenomenon is used for plasma heating and diagnostics and, at the same time, may be the cause of various instabilities resulting in the enhanced level of plasma turbulence. So modification of cyclotron resonances due to plasma turbulence may be of importance for the physics of resonant interaction. It is well known that stochastic motion (scattering of particles by random rf fields) leads to the additional broadening of resonances. The resonance broadening (RB) theory of plasma turbulence was initiated by the works of T. Dupree [1, 2, 3] and developed in a number of other papers [4, 5, 6]. Cyclotron resonance broadening was considered in [5] and [6]. We develop here the RB theory similar to that of Dum and Dupree [6] and apply this theory to the hydrodynamic instability of lower-hybrid waves due to the presence in the plasma of energetic transverse ion beam. The enhanced level of lower-hybrid turbulence was registered in Collective Thomson Scattering experiments at W7-AS stellarator [7] and was theoretically interpreted as the result of lower-hybrid instability under so-called double resonance condition $\omega_{LH} = n\omega_{cb}$ ($n \gg 1$) with the instability increment being proportional to the square root of the fast ion relative density $\gamma \propto \sqrt{n_b/n_0}$.

The main idea of RB theory of *weak* turbulence is to take into account particle diffusion on small enough time scale τ_d ($\tau_c \ll \tau_d \ll \tau_0$, where τ_c is the coherence time of random force acting on a particle and τ_0 is the characteristic time for a change of average (macroscopic) quantities, e.g. inverse increment γ^{-1}, time of quasilinear relaxation τ_{ql}, ion-ion collision time τ_{ii}, etc.) and to consider the turbulent elec-

tromagnetic field as a number of well defined modes with dispersion relation obtained from the solution of linearized kinetic equation *averaged over random particle orbits.* This leads to the "pseudolinear" dispersion relation which determines corrections for mode frequency and increment dependent on particle diffusion coefficient. The particle diffusion coefficient itself is dependent on the turbulence spectrum. Thus the dynamics of the turbulence can be described by set of equations for mode amplitudes

$$\frac{dE_k}{dt} = \gamma_k E_k, \tag{1}$$

where γ_k is nonlinear increment dependent on all $|E_k|^2$. The ordinary quasilinear diffusion equation for averaged distribution function and first-order nonlinear interactions between modes can also be included into this scheme with appropriate corrections.

The first key point of RB theory is the equation for effective transverse *one-particle* spatial diffusion coefficient $D(v_\perp)$, dependent on average cyclotron velocity $v_\perp$. Following [5, 6] to obtain $D(v_\perp)$ we use the equation of particle motion

$$\frac{d\mathbf{v}}{dt} + \frac{q}{mc}[\mathbf{B}_0 \times \mathbf{v}] = \frac{q}{m}\mathbf{E}(\mathbf{r}(t), t). \tag{2}$$

We confine ourself to the case of electrostatic turbulence $\mathbf{E} = -\nabla\varphi$, with $\mathbf{B}_0$ being dc magnetic field and $\mathbf{E}(\mathbf{r}(t), t) = \mathrm{Re}\sum_k \mathbf{E}_k e^{-i\omega t + i\mathbf{k}\mathbf{r}(t)}$ being turbulent electric field, we also assume that $\mathbf{k}, \mathbf{E}_k \perp \mathbf{B}_0$ and turbulence is isotropic in the plane perpendicular to $\mathbf{B}_0$ (that take place for LH cyclotron instability [7]). We solve eq. (2) in the approximation of *self consistent diffusion* (SCD). Taking $\mathbf{r}(t)$ in the right-hand part as a cyclotron trajectory with small random part $\mathbf{r}_1(t)$ and assuming that $\mathbf{r}_1(t)$ corresponds to Brownian motion with time-dependent Gaussian dispersion $< \mathbf{r}_1^2 >= 4Dt$, $< x_1^2 >=< y_1^2 >= 2Dt$, we formally integrate (2) and find the same averages for "left-hand" $\mathbf{r}_1$. Finally we obtain the self-consistency equation for $D(v_\perp)$:

$$D(v_\perp) = \frac{q^2}{m^2\omega_c^2} \sum_n \sum_k \frac{F_n(kv_\perp/\omega_c)|E_k|^2(k^2 D(v_\perp) + \gamma_k)}{(\omega_k - n\omega_c)^2 + (k^2 D(v_\perp) + \gamma_k)^2}, \tag{3}$$

where $F_n(x) = 1/4[J_{n-1}^2(x) + 2J_n^2(x) + J_{n+1}^2(x)]$.

The second key point of the theory is pseudolinear dispersion relation. We derive it from Vlasov kinetic equation, linearized for fast part of distribution function of some plasma specie (ion, electron, beam) $\tilde{f} = f - f_0$, where $f_0 =< f >$ is averaged distribution function,

$$\frac{\partial \tilde{f}}{\partial t} + \mathbf{v}\nabla\tilde{f} - \omega_c \frac{\partial \tilde{f}}{\partial \phi} + \frac{\mathbf{F}^*}{m}\frac{\partial \tilde{f}}{\partial \mathbf{v}} = -\frac{q}{m}\mathbf{E}\frac{\partial f_0}{\partial \mathbf{v}}, \tag{4}$$

where $\mathbf{F}^*$ is effective random force, originated from nonlinear term in kinetic equation. Due to SCD approximation this force leads to Brownian motion with $< \mathbf{r}_1^2 >= 4Dt$. Integrating (4) over random trajectory and averaging we obtain ($\epsilon_\perp = v_\perp^2/2$)

$$\tilde{f}(\mathbf{r},t) = \mathrm{Re}\sum_k \frac{q}{m}\varphi_k e^{-i\omega t + i\mathbf{kr}} \left\{ \frac{\partial f_0}{\partial \epsilon_\perp} - \left[(\omega - k_z v_z)\frac{\partial f_0}{\partial \epsilon_\perp} + k_z \frac{\partial f_0}{\partial v_z} \right] I \right\},$$

$$I = \sum_{n,m} \frac{J_n(k_\perp v_\perp/\omega_c) J_m(k_\perp v_\perp/\omega_c) e^{i\phi(n-m)}}{\omega - k_z v_z - n\omega_c + ik^2 D(v_\perp)}. \tag{5}$$

Then we can obtain charge density $\rho(\omega, \mathbf{k})$ as

$$\rho(\omega,\mathbf{k}) = q\int \tilde{f}(\omega,\mathbf{k})d\mathbf{v} = -\frac{1}{4\pi}\epsilon_l^*(\omega,\mathbf{k})k^2\psi_k(\omega,\mathbf{k}), \tag{6}$$

and, finally, pseudolinear dispersion relation as

$$\epsilon_l^*(\omega,\mathbf{k}) = 1 + \sum_\alpha \epsilon^{*(\alpha)} = 0, \tag{7}$$

with $\epsilon^{*(\alpha)} = -\frac{4\pi q_\alpha^2}{m_\alpha k^2}\int \left(\frac{\partial f_0^{(\alpha)}}{\partial \epsilon_\perp} - \right.$

$$\left. - \left[(\omega - k_z v_z)\frac{\partial f_0^{(\alpha)}}{\partial \epsilon_\perp} + k_z \frac{\partial f_0^{(\alpha)}}{\partial v_z} \right] I_0 \right) v_\perp dv_\perp dv_z,$$

$$I_0 = \sum_n \frac{J_n^2(k_\perp v_\perp/\omega_c)}{\omega - k_z v_z - n\omega_c + ik^2 D(v_\perp)}. \tag{8}$$

The equations (3) and (8) are equivalent to that of Dum and Dupree [6].

The last point of RB theory is quasilinear equation for averaged distribution function f_0. We derive this equation as usual by averaging the Vlasov kinetic equation with expression (5) for $\tilde{f}$. The result for some specie is

$$\frac{\partial f_0^{(\alpha)}}{\partial t} = -\frac{q_\alpha^2}{2m_\alpha^2} \sum_k |\varphi_k|^2 \mathbf{k} \frac{\partial}{\partial \mathbf{v}} \left(\left[(\omega_k - k_z v_z) \frac{\partial f_0^{(\alpha)}}{\partial \epsilon_\perp} + k_z \frac{\partial f_0^{(\alpha)}}{\partial v_z} \right] \mathrm{Im} I_0 \right). \tag{9}$$

Equations (1), (3), (7), (8) and (9) form the complete set of equations of modified quasilinear theory (ignoring nonlinear wave interactions).

Let us consider now the LH turbulence excited by transverse ion beam. For the sake of simplicity we assume that beam ions are of the same type as the bulk plasma ions. The parameters of plasma and ion beam are taken similar to that in experiment at W7-AS stellarator (see [7]): $T_e = 1 \div 10$ keV, $T_i = 100 \div 500$ eV, $n_e = n_i = 5 \cdot 10^{13} \mathrm{cm}^{-3}$, $B = 2.5 \div 4$ T, beam energy $\sim$10 keV. Then we have the following relation between ω_{lh} and other characteristic plasma frequencies

$$\omega_{ci} \ll \omega_{lh} \approx \omega_{pi} \ll \omega_{pe}, \omega_{ce},$$

and $(k_\perp r_{ce})^2 \ll 1$, $(k_\perp r_{ci})^2 \gg 1$, which allows to simplify essentially dispersion relation. Taking this into account we obtain the following pseudolinear dispersion relation for low hybrid waves in plasma with transverse ion beam

$$1 + \frac{\omega_{pe}^2}{\omega_{ce}^2} - \frac{\omega_{pi}^2}{\omega^2} - \frac{\omega_{pe}^2 \cos^2\theta}{\omega^2} + i \frac{\sqrt{\pi}\omega}{k^3 v_e d_e^2 \cos\theta} \exp\left(-\frac{\omega^2}{k^2 v_e^2 \cos^2\theta} \right) -$$

$$- \sum_n \frac{2\alpha n \sin^2\theta \omega_{pi}^2}{\xi_0 \omega_{ci}} \int_0^\infty \frac{f(x) J_n(\xi_0 x) J_n'(\xi_0 x)}{\omega - n\omega_{cb} + ik^2 D(x)} \frac{dx}{x} -$$

$$- \sum_n \frac{\omega_{pi}^2}{\omega_{ci}} \frac{n I_n(z_i) e^{-z_i}}{z_i(\omega - n\omega_{cb})} = 0, \tag{10}$$

where $\xi_0 = k v_0 / \omega_{ci}$, v_0 is characteristic velocity of ion beam, $x = v_\perp / v_0$, $f(x) = (v_0 v_\perp / n_b) f_0(v_\perp)$ is normalized distribution function of fast ions, $\int f(x) dx = 1$, $\alpha = n_b / n_0$, θ is the angle between $\mathbf{k}$ and $\mathbf{B}_0$. Here we neglect random diffusion of bulk ions and assume that the only fast ions are affected by turbulent diffusion.

The angular dependence of LH wave frequency neglecting ion beam contribution is defined by $\omega_{lh}^2(\theta) = \dfrac{\omega_{pi}^2 + \omega_{pe}^2 \cos^2\theta}{1 + \omega_{pe}^2/\omega_{ce}^2}$. We consider here the relaxation of initially monoenergetic beam with $f(x) = \delta(x-1)$. At the initial stage ($D(x) = 0$) correction δ to LH frequency ($\omega = \omega_{lh}(1+\delta)$) due to the ion beam may be presented (for $\omega_{lh}(\theta_i) = n\omega_{ci}$) as $\delta(k) = \sqrt{-H_n(k,\theta_i)/2}$, with

$$H_n = -\frac{2\alpha n \sin^2\theta \omega_{pi}}{\xi_0 \omega_{ci}} \int_0^\infty f(x) J_n(\xi_0 x) J_n'(\xi_0 x) \frac{dx}{x} - \frac{\omega_{pi}}{\omega_{ci}} \frac{n I_n(z_i) e^{-z_i}}{z_i}.$$

Thus the mode under consideration is unstable ($\gamma = \omega_{lh} \mathrm{Im}\delta > 0$) if $H_n > 0$. This is a rather strong instability of hydrodynamic type with increment proportional to the square root of small parameter $\sqrt{n_b/n_0}$.

Below we consider the case of narrow k-spectrum of excited waves, which can be realized for some special set of plasma and beam parameters (e.g. $T_e = 10$ keV, $T_i = 500$ eV, $n_e = n_i = 3 \cdot 10^{13}\mathrm{cm}^{-3}$, $B = 4$ T, $\alpha = 10^{-4}$), when the increment in the first zone over angles is much larger than in other zones and the spectrum of excited waves is narrow over k. In this case we can obtain complete set of equations for integral turbulence level $W = \frac{1}{8\pi} \int |E_k|^2 d^3k$ at $\omega_{lh}(\theta) = n\omega_{cb}$

$$\frac{dW}{dt} = \gamma W, \quad \gamma = -\frac{\alpha n \omega_{pi} \omega_{lh}}{\xi_0 \omega_{ci}} \int_0^\infty \frac{f(x) J_n(\xi_0 x) J_n'(\xi_0 x)}{\gamma + k^2 D(x)} \frac{dx}{x}, \tag{11}$$

$$D(x) = \frac{8\pi q^2}{m^2 \omega_c^2} \frac{F_n(\xi_0 x) W}{(k^2 D(x) + \gamma)}, \tag{12}$$

$$\frac{\partial f}{\partial t} = \frac{4\pi q^2 W}{m^2 v_0^3 k} \frac{\partial}{\partial x} \left\{ \frac{\omega_{lh} J_n^2(\xi_0 x)}{\gamma + k^2 D(x)} \frac{\partial f}{\partial x} \right\}. \tag{13}$$

Eqs. (11)-(12) allow simple analytical description under assumption that quasi-linear modification of beam distribution function, governed by Eq. (13), can be neglected:

$$\frac{dW}{dt} = \gamma_0 \frac{W}{\sqrt{(1 + W/W_c)}}, \tag{14}$$

here γ_0 is linear increment for $f(x) = \delta(x-1)$ and

$$W_c = \frac{\gamma_0^2 m^2 \omega_c^2}{8\pi k^2 q^2 F_n(\xi_0)} \tag{15}$$

is characteristic level of LH turbulence when resonance broadening becomes of importance. Above this value the increment is proportional to n_b/n_0 (instead of $\sqrt{n_b/n_0}$) and decreasing with time, so that exponential growth of W is changed by $W \propto t^2$. But resonance broadening itself cannot fully saturate the instability, - growth rate tends to zero remaining positive until quasi-linear modification of the beam distribution function becomes noticeable.

Rough estimate of quasi-linear time τ_{ql} may be obtained from Eq. (13) assuming $W = W_c$. Comparison of this time with the resonance broadening time $\tau_{rb} \sim \gamma_0^{-1} \ln(W_c/W_0)$, ($W_0$ is the initial level of unstable LH waves) results in the inequality:

$$\frac{\tau_{ql}}{\tau_{rb}} \sim \frac{\xi_0^2 F_n(\xi_0)}{n J_n^2(\xi_0)} \gg 1, \tag{16}$$

because the considered LH instability takes place only at $\xi_0 > n \gg 1$ and $F_n(\xi_0)/J_n^2(\xi_0) > 1$.

This work is supported by the Russian Fund for Fundamental Research, Grant No. 99-02-16230.

References

[1] T.H. Dupree, Phys. Fluids **9**, 1733 (1966)

[2] T.H. Dupree, Phys. Fluids **10**, 1049 (1967)

[3] T.H. Dupree, Phys. Fluids **11**, 2680 (1968)

[4] S.A. Orszag, R.H. Kraichnan, Phys. Fluids **10**, 1720 (1967)

[5] A.A. Galeev, Zh. Eksp.Teor. Fiz. **57**, 1361 (1969)

[6] C.T. Dum, T.H. Dupree, Phys. Fluids **13**, 2064 (1970)

[7] E.V. Suvorov et al., Nuclear Fusion **38**, 661 (1998)

TRAPPING OF LANGMUIR WAVES INSIDE AN EXTENDED INHOMOGENEITY OF A MAGNETIZED PLASMA

A. V. Kostrov, V. V. Vas'kov, A. A. Shaykin, G. A. Luchinin*

Institute of Applied Physics, Russian Academy of Sciences, N. Novgorod, Russia
*Institute of Terrestrial Magnetism, the Ionosphere, and Propagation of Radio Waves, Troitsk, Moscow Region, Russia

The trapping of Langmuir waves in a cylindrical plasma resonator with a negative density perturbation is observed experimentally.

It is well known that a small-scale structure consisting of thermal inhomogeneities in the form of cylindrical regions with a depressed electron density ($\delta N<0$) which and extended along the magnetic field H develops in ionospheric plasma in the field of a high-power radio wave. Such inhomogeneities form as a result of nonuniform heating of the plasma by the field of potential oscillations excited by the high-power radio wave near the upper-hybrid resonance $No\sim N=m(\omega^2—\omega_{He}^2)4\pi e^2$ as a result of polarization of the perturbations δN. Here N_0 is the electron density in the undisturbed plasma, N_R is the resonance value of the electron density, ω is the frequency of the radio wave, and $\omega_{He}=eH/mc$ is the electron gyrofrequency. The mechanism leading to the intensification of the local heating of inhomogeneities as a result of the excitation and trapping of short- wavelength plasma oscillations — upper-hybrid plasma waves which easily give up their energy to the electrons — in their interior volume was investigated theoretically in Refs. 1-3. This process appears under conditions such that the electron density $N=N_0+\delta N(r)$ inside an inhomogeneity at some point $r=r_R$ crosses the upper-hybrid resonance level $N=N_R$ (here r is the radial coordinate measured from the axis of the prolate inhomogeneity). When a plasma wave with frequency $\omega>2\omega_{He}$ is propagating nearly orthogonally to the magnetic field **H,** then short-wavelength plasma waves propagate inside the inhomogeneity ($r<r_R$, where the density $N<N_R$), with a transverse wave number $k_{p\perp}$ that depends on the electron temperature T_e, as

$$\kappa_{p\perp} = \sqrt{m(\omega^2 - 4\omega_{He}^2)(N_R - N)/3T_eN}$$

In the region outside the inhomogeneity ($r>r_R$, where $N>N_R$), plasma waves with high longitudinal wave numbers $k_{//}=k\cdot H/H>\omega/c$ can propagate in addition to the longer-wavelength waves of the cold Z mode, which is directly excited by a high-power radio wave. Near the upper

hybrid resonance $N=N_R$ the cold and plasma oscillations with small $k_{//}$ interact with and transform into one another. The mechanism leading to trapping of plasma waves inside an inhomogeneity δN depends on the value of the unperturbed electron density N_0 in the background plasma. For $N_0>N_{pr}\equiv m\omega^2/4\pi e^2$ modes with quite large wave numbers $k_{//}\geq\omega/c$ become trapped inside the plasma waveguide. These waves are reflected near the plasma resonance level $N=N_{PR}$. Wave trapping in a plasma with density $N_0<N_{PR}$ is due to the violation of the geometrical-optics approximation for cold oscillations. It occurs for inhomogene-ities with a sufficiently small radius $r_0<k_{z\perp}^{-1}$, where

$$k_{z\perp}=(\omega_{He}/c)(1+k_{//}^2c^2/\omega^2)^{1/2}\cdot(N_R/(N_0-N_R)^{1/2}\geq\omega/c$$

is the transverse wave number of the cold Z mode in the undisturbed plasma. In this case it can be assumed that a plasma wave is reflected from the upper-hybrid resonance level $N=N_R$ (this is the situation realized in ionospheric experiments). We note also that for $\omega<2\omega_{He}$ a prolate inhomogeneity δN with a depressed density does not confine plasma waves, i.e., trapping does not occur (for $\omega<2\omega_{He}$ the plasma waves, like the as cold oscillations, propagate only in the region $N>N_R$).

These experimental work was performed in two stages:

1. Study of excitation and propagation of plasma oscillations in the upper-hybrid frequency range in homogeneous plasma.
2. Study of excitation and trapping of short-wave plasma oscillations in the upper-hybrid range in a cylindrical inhomogeneity with lower electron density.

Experimental setup

The experiments were performed on the 'Ionosphere' setup, which is made as a vacuum chamber 150 cm long and 80 cm in diameter. The pumping system makes it possible to maintain the pressure of residual gases in the chamber at the level of $P_0=10^{-5}$ Torr. As the operating gas, argon or helium is used, at the pressures of $P_0=2\cdot10^{-3}$ Torr and $P_0=10^{-2}$ Torr, respectively. The magnetic field is produced by three coils with their diameter $D_L=0.8$ m and length $l_L=0.35$ m each. The length of the homogeneous part of the magnetic field is about 1.2 m. Characteristic times of variation of the external magnetic field exceed significantly the times of plasma formation and decay. This makes it possible to assume that the field is stationary. The plasma is produced by an induction microwave discharge. The frequency of the RF generator was 5 MHz, its

power was 60 kW. Duration of the microwave pulse was 2 ms. The studies were performed in the regime of decaying plasma. At the moment of switching the generator off the plasma density reaches the value of $N_e \sim 10^{13}$ cm^{-3}, and temperature of electrons is $T_e \sim 8$ eV. The temperature of ions and neutrals is ~0.4 eV. In about 1.5 ms the temperature of ions and electrons gets equal to 0.5 eV. The rate of plasma decay is determined by ambipolar diffusion along the magnetic field. Distribution of the density in the transverse cross-section of the chamber (Fig. 1) is weakly dependent on the operating gas (argon or helium) and does not change its shape qualitatively as the plasma is decaying.

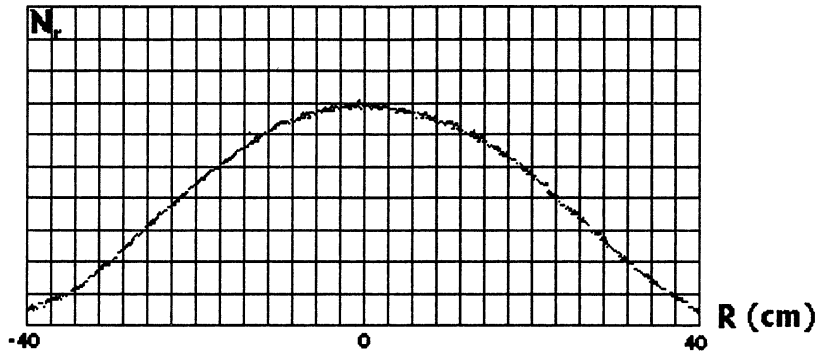

Fig. 1. Distribution of density in the transverse cross-section of the chamber

The experiments were performed at the center of the plasma column. Characteristic dimensions of the region under consideration were small as compared with the dimensions of the flat interval of the transverse distribution. That made it possible to assume that plasma density was homogeneous.

Homogeneous plasma

The regime of decaying plasma make it possible to study the spatial structure of electric fields radiated by the antenna at different values of plasma density. The emitting electrically-insulated antenna ~7 mm long was situated at the center of the homogeneous plasma part. The receiving antenna 1 cm long was set at the distance of about 8 cm from the emitting one. The design of the receiving antenna allowed her moving in the azimuthal plane relative to the emitting one. The radiating antenna was conitnuously fed with a high-frequency signal with its frequency f=1900 MHz. The value of the magnetic field was 400 and 320 Oe, which corresponded to different ratios of frequencies f and f_{He} ($f<2f_{He}$ and $f>2f_{He}$). It is known that when $f>2f_{He}$, in

plasma there is the possibility of excitation of plasma upper-hybrid waves, for which spatial dispersion determined by thermal effects if significant. Figures 2a and 2b show time dependencies of plasma density and the refraction ratio for the ordinary and extraordinary wave.

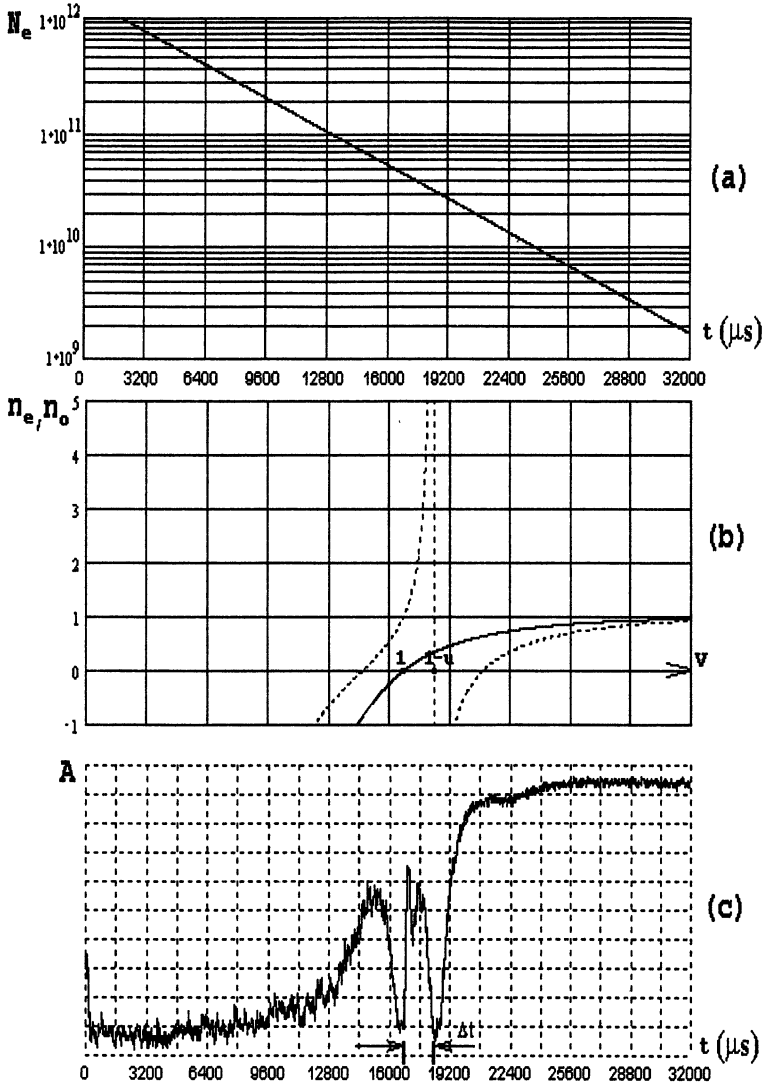

Fig. 2. Time dependence of plasma density (a) and refraction factor for the ordinary and extraordinary wave (b) ($v=\omega^2_{pe}/\omega^2$, $u=\omega^2_{He}/\omega^2$); (c) is characteristic oscillogram of the signal from the receiving antenna

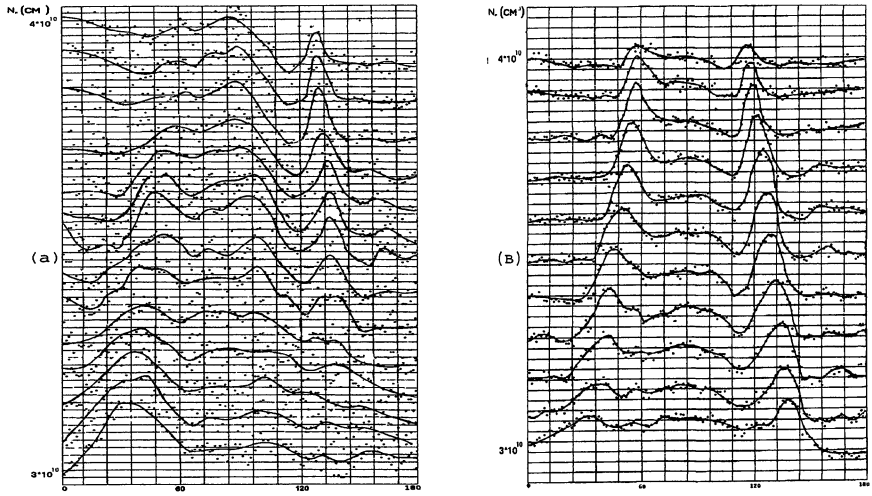

Fig. 3. Radiation pattern of the source: а – $f > 2f_{He}$, в – $f < 2f_{He}$

The refraction ratios correspond to the real lifetime of plasma and direction of propagation at angle $\theta=49^{\circ}$ to the external magnetic field. The characteristic oscillogram of the signal from the receiving antenna is shown in Fig. 2c. Time interval Δt shown in the Figure corresponds to density interval $N_R < N < N_{pr}$, i.e. to the upper-hybrid frequency range. In this frequency range the radiation pattern of the source is determined by resonance cones, as shown in Fig. 3(a) and Fig. 3(в). In the case of $f>2f_{He}$ (Fig. 3) a thin structure of the electric field is observed in the range of angles between the main resonance directions. This is associated with the influence of temperature effects on the spectrum of radiated waves.

Inhomogeneous plasma

A channel with lower density was formed using a dielectric target (10 mm long, 10 mm in diameter, dielectric permittivity $\varepsilon=1$) set at the center of the plasma column.

Due to diffusion of plasma to the target and further recombination on the dielectric surface, density became poorer. Relative variation of electron density $N(r)/N_0$ in the channel stayed the same in a wide range of densities of the background plasma. The maximum depth of the channel at the center of inhomogeneity was $|\delta N(r=0)|/N_0=0.4$.

At the channel axis, at the distance of 1 cm from the target, there was set a radiating electric antenna ~7 mm long. A high-frequency signal

($f = \omega/2\pi = 1.9$ GHz) was fed continuously to the antenna. Using a small-size movable receiving antenna we measured the structure of radial component of the electric field E(r) in the plasma inhomogeneity at different distances Z from the radiating antenna. The magnetic field and frequency of the signal fed to the antenna were chosen such as to fulfil the condition of excitation and trapping of short-wave oscillations in the channel ($f > 2f_{He}$).

Evolution of distribution of the electric field, E, of trapped oscillations in the plasma inhomogeneity is shown in Fig. 4.

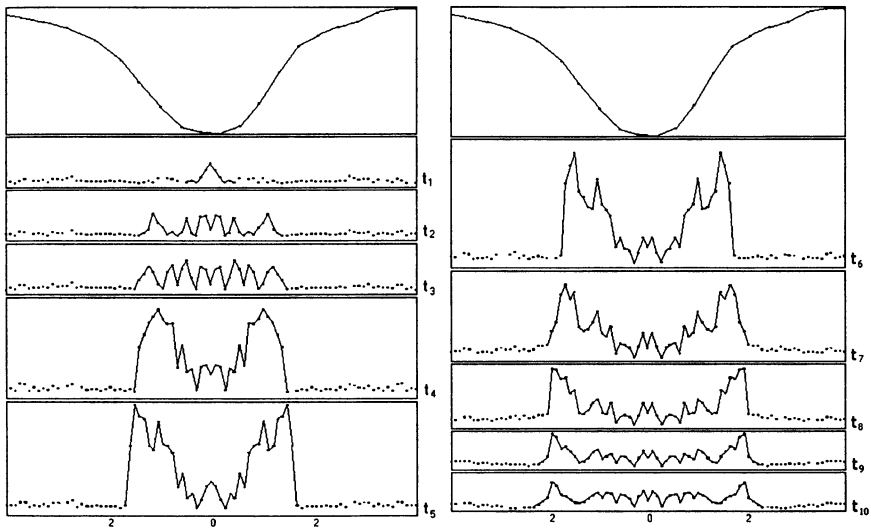

Fig. 4. Evolution of distribution of the electric field, E, of trapped oscillations in the plasma inhomogeneity (Z = 2 cm)

Formation of the field structure takes place at the moment, when density in the channel crosses the level of resonance that determines the position of the point of reflection of the plasma wave. In Fig. 4 it is easily seen how the structure of the electric field arises and develops as density $N_0(t)$ decreases in time beginning from the moment of appearance of the trapped mode, t_1, up to the moment of shifting of the resonance point beyond the inhomogeneity boundaries. At time moment t_2 the trapped mode is reflected near the base of the wave channel. It is seen that the structure of the electric field at that moment is shaped as a standing wave with an almost constant amplitude. With time, the wave reflection point moves along the inhomogeneity slope. This is accompanied by field

amplification at the boundary of the trapping region and field weakening at the center of the inhomogeneity (t_4-t_8). There are no pronounced oscillations E(r) characteristic for the standing wave observed. One can suppose that damping of spatial oscillations and a significant decrease of amplitude E near the inhomogeneity center is associated with the fact that at a distance from the reflection point the wavelength of plasma oscillations becomes shorter and, correspondingly, efficiency of their reception with a finite-length measuring antenna. It is necessary to note also that the amplitude of plasma waves decreases sharply beyond the boundary of the transparency region, in the vicinity of which amplification of the electric field takes place. As density N_0 decreases further, the amplitude of trapped waves also decreases and approaches the background value outside of the channel. In the experiments with the reverse ratio of frequencies f and f_{He} ($f<2f_{He}$), the amplitude of the electric field, E, in the channel was significantly lower and had no oscillations inherent for the standing wave.

Conclusion

In summary, our experiments have reveled trapping and amplification of plasma oscillations confined inside an elongated inhomogeneity with a depressed electron density ($\delta N<0$), oriented along the magnetic field H. The accumulation of energy of plasma oscillation in the resonator causes additional local heating of the inhomogeneities observed in "active" experiments on the effect of high-power radio radiation on the ionospheric plasma.

This work was supported by the Russian Fund for Fundamental reseach (Grant № 97-02-17809).

References

1. K.B. Dysthe, E. Mjolhus, H. Pecseli and K. Rypdal. Thermal Cavetons // Phisica Scripta. 2/2, 548-559 (1982).
2. V.V. Vaskov, A.V. Gurevich. Trapping and absorption of plasma waves in thermal small-scale inhomogeneities // Geomagnetizm i aeronomiya. 23, 4, 544-551, 1983 (in Russian).
3. V.V. Vaskov, A.V. Gurevich. Trapping and absorption of plasma waves in thermal small-scale cylindrical inhomogeneities // Geomagnetizm i aeronomiya. 23, 6, 901-908, 1983 (in Russian).

EXPERIMENTAL INVESTIGATION OF NONLINEAR PROCESSES BY LOWER-HYBRID TURBULENCE IN A MAGNETIC TRAP

A.V. Kostrov, A.V. Shashurin, A.V. Strikovsky

Institute of Applied Physics RAS, Nizhny Novgorod, Russia

Nonlinear interaction of intense lower-hybrid waves with plasma was investigated on the unique experimental set-up known as "KROT". The modulational instability evolving in plasma when the amplitude of the high-frequency pump exceeded the threshold value was observed. This instability caused appearance of filaments stretched along the magnetic field (so-called cavitons). The maximum value of density perturbation in such structures reached 20%. We observed a high-energy tail on the electron distribution function with characteristic temperature about 20-30 eV The collapse predicted in the collisionless case was not observed. It was demonstrated that thermal heating of plasma in cavitons resulted in stabilization of the collapse process, and this effect occurred on times essentially longer than the modulational instability time.

It is now a widespread point of view that lower-hybrid waves are essential for the processes of collisionless particle acceleration in space physics. The most important consequence of lower-hybrid turbulence is formation and collapse of cavitons leading to particle acceleration [1, 2].

Nonlinear interaction of intense lower-hybrid waves with plasma was investigated on the unique experimental set-up known as "KROT". This facility is a large-scale vacuum chamber (diameter 3 m, length 10 m). Plasma was created by a high-frequency discharge (f=5 MHz, τ_{pulse}=1.6 ms). Gas pressure in experimental conditions was about $5 \cdot 10^{-4}$ Torr. To produce a magnetic field of the trap configuration (trap ratio 2.3), a special solenoid 3.5 m long and 1.5 m in diameter was used. These experiments were performed in the afterglow plasma.

Lower-hybrid waves were excited with a pulse of the high-frequency pump (frequency 3 MHz, pulse duration 1 ms), which was applied to the magnetic loop (R=10 cm) placed at the center of the solenoid at 12 ms after switching off the generator creating plasma. Initial temperature of electrons and ions was about 1 eV, plasma density- $5 \cdot 10^{10}$ cm^{-3}. The condition $\omega_{pe}/\omega_{He} \gg 1$ was fulfilled in the experiment. In this case the frequency of lower-hybrid resonance does not depend on the temperature and is determined only by the value of magnetic field.

The main process determined the plasma decay was ambipolar diffusion along the magnetic field with characteristic time scale about 10 ms.

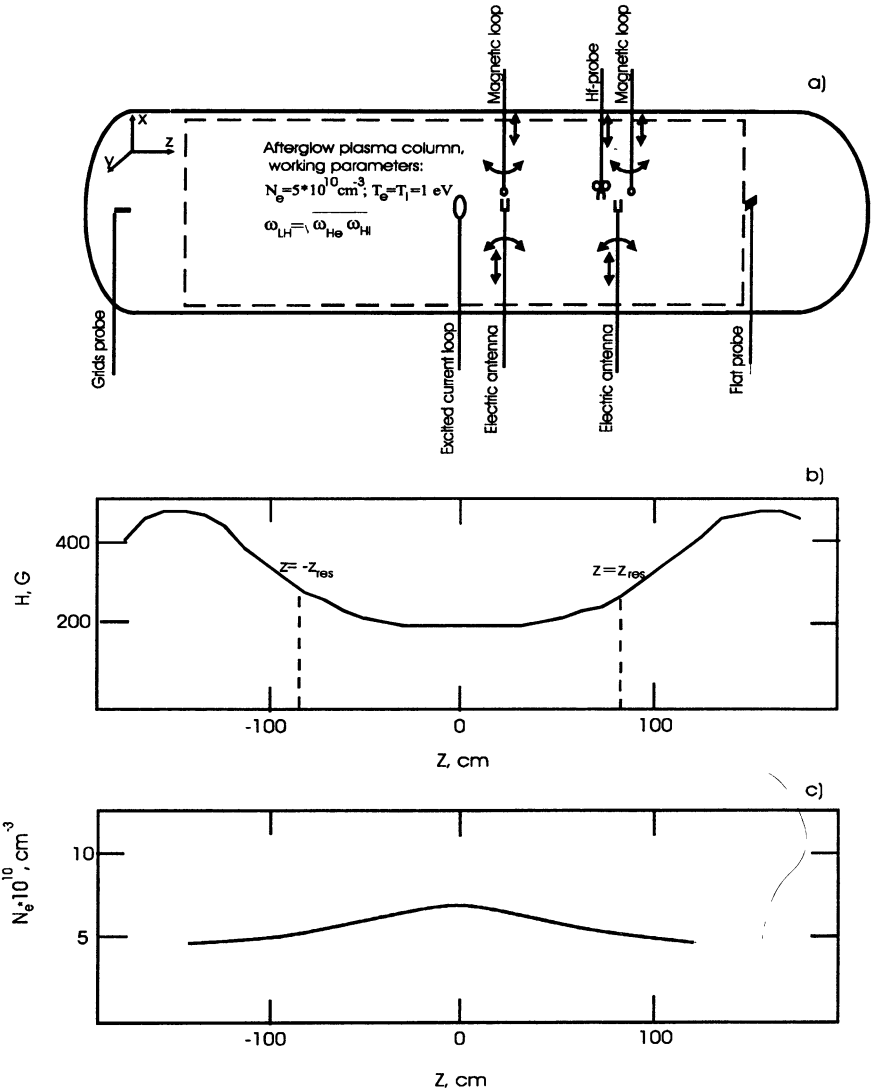

Fig. 1. The scheme of experimental setup and main diagnostics position (a); distribution of the magnetic field (b) and plasma density (c) along the axis of the trap at the moment of switching on the pump

The scheme of experimental setup and main diagnostics position (a), distribution of a magnetic field (b) and plasma density (c) along the axis

of the trap at the moment of switching on the pump are submitted in Figure 1.

To measure amplitudes of rf-fields in the plasma, the electrical and magnetic probes moving in the radial direction were used. The flows of accelerated electrons were analyzed by using a flat probe.

A special hf-probe for measurements of plasma density fluctuations was used [3]. The idea was based on a simple and convenient method of local measurements of plasma density, which consisted in measurements of resonant frequency of a small quarter-wave resonator placed in plasma. A probe is a resonant system whose resonant frequency depends on dielectric permittivity of environment space. The value of resonant frequency gives the possibility to determine plasma density. Sensitivity of this method to density fluctuations was of the order of 1%. The curve of plasma decay and characteristic oscillogrammes, obtained by using an hf-probe are shown in Fig. 2.

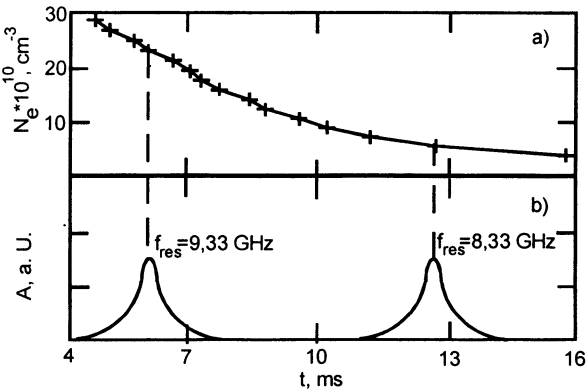

Fig. 2. The curve of plasma decay and characteristic oscillogrammes, received by using a hf-probe for two values of resonance frequency

Experimental results

The analysis of signals from various diagnostic tools testified that the influence of the pump on plasma on frequency near the lower-hybrid resonance has an essentially nonlinear character (Fig. 3). The threshold of nonlinear interaction of the pump with plasma corresponded to a voltage on inductor U_{pump}>100 V. The saturation of signal amplitudes from diagnostics at U_{pump}>400 V was registered.

The most interesting results were obtained with a hf-probe at a voltage on inductor U_{pump}>200 V. In this case, on a resonant curve of the probe characteristic oscillations of the signal were observed (Fig. 4). It

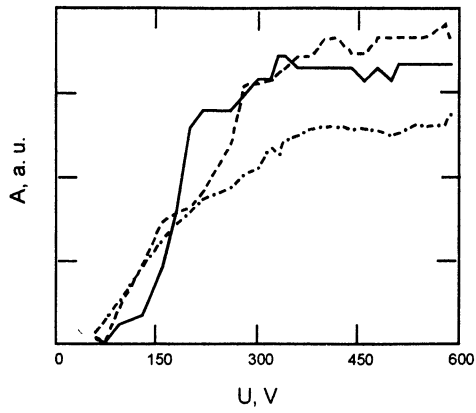

Fig. 3. Signals amplitudes from various diagnostics versus pump voltage

amplitude of lower-hybrid density oscillations (hf-probe)

current of accelerated electrons (flat probe)

rf-oscillations of magnetic field (magnetic loop)

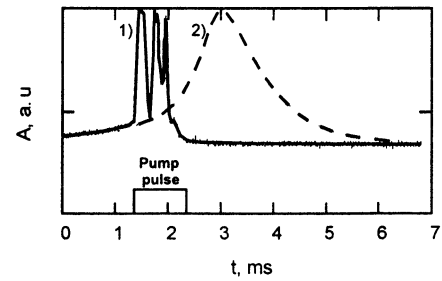

Fig. 4. Characteristic oscillogrammes received with a hf-probe at switched on the rf-pump (1) and without it (2)

proved the presence of low-frequency modulations of plasma density ($\frac{\delta n}{n} \geq 10\,\%$).

In Fig. 5 radial distributions of plasma density at the various moments of time are given (U_{pump}=200 V).

During the first 300 μs after switching on the pump we observed formation of small-scale plasma structures with characteristic depth of density modulation of the order 10-20 % and its size about several centimeters.

Later small-scale plasma density depressions blurred and merged, forming at times $t \geq 500$ μs a global failure of plasma density at the center of the chamber (R < 10 cm). At R>10 cm an increase of plasma density was observed, as compared with its unperturbed value (Fig. 5e, f).

In dynamics of system development two characteristic temporary scales are traced: 1 - first 300 μs of the pump pulse; 2 - times $t \geq 500$ μs.

Quasiperiodical modulation of plasma density (Fig. 5b, c) with the characteristic spatial period L≈3 cm arising already during the first

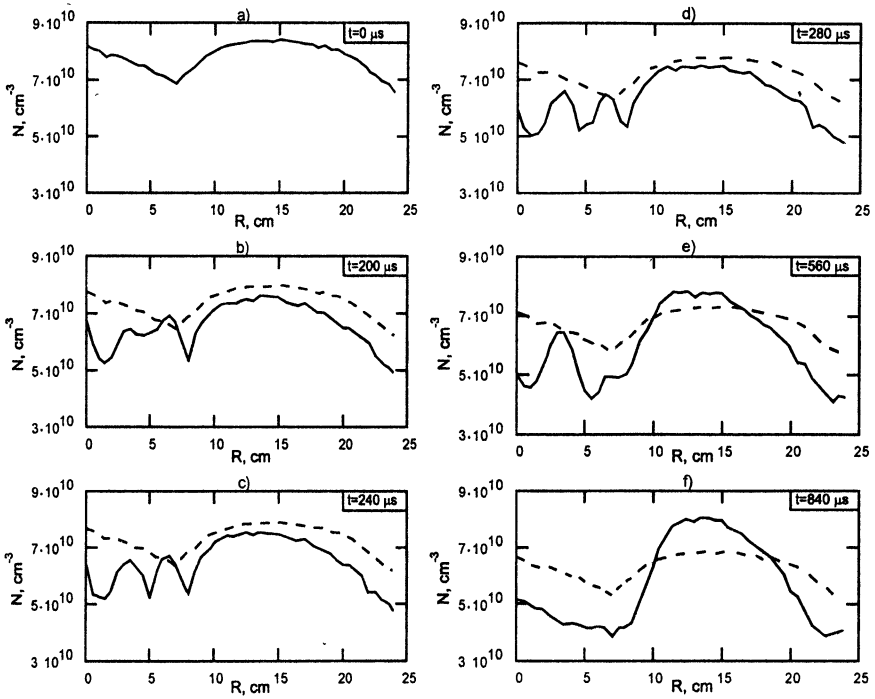

Fig. 5. Radial distributions of plasma density in the various moments of time
– – – without pump
——— with pump

300 μs after switching the pump on testifies to development a modulational instability in plasma. The fact of quasi-potential lower-hybrid waves excitation was registered by modulation (f_{mod} = 3 MHz) of high-frequency signal (f=8.3 GHz) from a hf-probe. Thus, the results of the experiment testified that influence of the pump caused development of a modulational instability. The characteristic spatial scale of instability corresponded to L≈3 cm. The condition of pressure balance installed along the magnetic field $\left(\frac{\delta n}{n} \approx \left(\frac{\omega_{pe}}{\omega_{LH}}\right)^2 \frac{|E_\parallel|^2}{16\pi(T_e+T_i)}\right)$ allows defining the value of longitudinal components of the electrical field $E_\parallel = 0.5 \frac{V}{cm}$ (at

$\frac{\delta n}{n} \approx 20\ \%$). However, further constriction (collapse) of cavitons did not occur and blurring of caverns happened.

During formation of cavitons ($\tau \approx 100\,\mu s$) its longitudinal scale becomes $L_{\|} = V_s t \approx 20$ cm, where V_s is speed of the ion-acoustic wave, t is characteristic time of cavern's formation. In this case, at nonadiabatical flight of such caviton ($L_{\|} \approx 20$ cm) the electron ($V_{Te} = 6 \cdot 10^7 \frac{\text{cm}}{\text{s}}$) can gain energy about 10 eV.

Measurements of the distribution function of accelerated electrons using a flat probe show appearance of electrons with characteristic energy 20-30 eV. This is in good correlation with the estimation mentioned above. Let us note that the increase of field amplitude inside the cavity correlates with the increase of accelerated electrons current along the magnetic field.

Thus, in first 300 μs after switching on the pump formation of cavitons as the result of modulational instability development was observed. However, the collapse predicted in the collisionless case was not observed. Obviously, in the conditions of a real experiment, the intense lower-hybrid field trapped in cavitons results, along with strictional effects, in heating of plasma electrons in the field of cavities. In this case, thermal nonlinearity results in stabilization of the collapse process and, further, in blurring of cavities (Fig. 5d, e, f) [4].

This work was supported by RFFI (grant № 98-02-17177, № 98-02-17028) and Russian Department of Sciences on "KROT" setup (registr. 01-18).

References

1. Shapiro V. D., Shevchenko V. I., Solov'ev G. I., Kalinin V. P., Bingham R., Sagdeev R. Z., Ashour-Abdalla M., Dawson J., Su J. J. Physics Fluids B., 1993, 5(9), 3148.
2. La Belle J., Kintner P. M., Yau A. W., Whalen B. A. J. Geophys. Res., 1986, 91(A6), 7113.
3. Stenzel R. L. Rev. Sci. Instrum., 1976. 47(5), 603.
4. Egorov S.V., Kostrov A.V., Tronin A.V. Pisma Zh. Eksp. Teor. Fiz., 1988, 47(2), 86.

GENERATION OF LANGMUIR TURBULENCE DUE TO THE OPTIC BREAKDOWN OF DENSE GASES

V.B. Gildenburg, N.V. Vvedenskii

Institute of Applied Physics RAS, N. Novgorod, Russia

Generation of Langmuir waves at the linear and nonlinear stages of ionization instability developing in the high intensity laser fields is studied. The main stages of the process are described. The parameters of the resulting quasiturbulent state are found.

Introduction

The performed before theoretical investigations of the conversion of the electromagnetic radiation to Langmuir oscillations and waves are connected with a rather great number of problems: the resonance absorption in the inhomogeneous plasma, dynamics of solitons and Langmuir collapse, excitation of Langmuir waves by the ponderomotive force. There being a variety of the used approaches, models and approximations; the common feature of all these studies is that they deal with the plasma as the before prepared medium (linear or nonlinear, homogeneous or inhomogeneous, but existing independently of external fields and being only slightly modified under their action). We should like to note that principally different in this term situation may occur where plasma cannot be considered as the medium prepared before, and the process of plasma waves generation cannot be separated form the process of generating the plasma itself. The study of such a situation is of interest in connection with the problems of getting and using the dense laser plasma, whose behavior and characteristic features during rather long time periods, as we shall see, may be defined by small-scale ionization instabilities, developing at the stage of its creation.

The given paper deals with the theoretical study of the effect of generation of plasma (Langmuir) waves and caused by them one-dimensional small-scale structures in the process of the tunnel ionization of the gas by laser pulses of high intensity. Ionization-field ("plasma-resonance") instability, leading to the formation of such structures at the laser breakdown of gas was studied before [1] without taking into account Langmuir waves. As we may see, being excited at the instant, when the plasma density passes its critical value, these waves influences greatly the characteristics of the linear and nonlinear stages of the given

instability, the dynamics of the breakdown process on the whole and the formation of the time and space field spectra.

Initial equations and approximations

As an example we consider the tunnel ionization of hydrogen atoms in the quasimonochromatic light field with linear polarization $\mathbf{E} = \mathrm{Re}(\mathbf{E}_0 \exp(-i\omega t))$. The average in light period rate of the plasma density increase is defined in this case by the equation [1]:

$$\frac{\partial N}{\partial t} = 6\Omega(N_g - N) f(|\mathbf{E}_0|), \quad f = \sqrt{\frac{2}{3}\frac{E_a}{|\mathbf{E}_0|}} \exp\left(-\frac{2}{3}\frac{E_a}{|\mathbf{E}_0|}\right). \qquad (1)$$

Here $E_a = m^2 e^5/\hbar^4 = 5.14\times10^9$ V/cm is the electric field at the first Bohr orbit, $\Omega = me^2/\hbar^3 = 4.16\times10^{16}$ s^{-1} is the atomic frequency unit, e и m are the charge and mass of electrons, $\hbar$ is the Planck constant, N_g is the concentration of gas neutral molecules before the process of ionization. It is assumed that the following conditions are fulfilled: $\omega << \Omega$, $|\mathbf{E}_0| << E_a$, $W_\sim = |\mathbf{E}_0|^2 e^2/(2m\omega^2) >> I$, ($W_\sim$ is the oscillatory electron energy, I – is the energy of ionization).

Limiting oneself to the analysis of one-dimensional potential perturbations in the frames of the qualitative (essentially, phenomenological) model, which permits to take into account merely the processes of excitation and damping of Langmuir waves in plasma with varying density, we write down the equation for the complex amplitude (slow time envelope) $\mathbf{E}_0 = \mathbf{x}_0 E_0(x,t)$ in the form (see. also [2]):

$$\varepsilon E_0 + \frac{2i}{\omega}\frac{\partial E_0}{\partial t} + \delta^2 \frac{\partial^2 E_0}{\partial x^2} + \hat{\gamma} E_0 = D_0(t). \qquad (2)$$

Here D_0 is the amplitude of the electric induction which in the frames of the considered one-dimensional model in the scales, small in comparison with the length of the electromagnetic wave, may be considered independent of the space coordinate; $\varepsilon = 1 - N/N_c$ is the plasma permittivity, $N_c = m\omega^2/4\pi e^2$ is the critical electron density, $\delta = \sqrt{3}V_T/\omega$ (V_T is the electron thermal velocity), $\hat{\gamma}$ is the operator which takes into account the energy dissipation caused by the electron collisions and Landau damping.

In the performed numerical calculations for $\hat{\gamma}$ we used the model equations of the form

$$\hat{\gamma} = i\left(\frac{\nu}{\omega} + b\delta^4 \frac{\partial^4}{\partial x^4}\right), \tag{3}$$

where ν is the frequency of the electron collisions, b is the constant of the order of the unit.

The range of the physical parameters we are interested in is as follows: the electromagnetic wave length $\lambda \sim 1-10\,\mu$, the laser intensity $W \sim 10^{14} - 10^{15}$ W/cm^2, the gas pressure $p \sim 0.3 - 30$ atm.

Linear stage of the ionization-field instability

Let the initial state of the homogeneous discharge is characterized by the slow time changes in the plasma density $N_0(t)$ ($\varepsilon_0(t) = 1 - N_0/N_c$) and the electric field amplitude $e_0(t)$. We investigate the stability of this state with respect to small space-periodic perturbations, neglecting at this stage the processes of dissipation , i.e. assuming $\hat{\gamma} = 0$. Writing down the field and the density in the form $N = N_0(t) + N_1(x,t)$, $E_0 = e_0(t) + E_1(x,t)$ and linearizing Eqs. (1), (2), we get the following equations for small perturbations E_1, N_1:

$$\varepsilon_0 E_1 - \frac{N_1}{N_c} e_0 + \frac{2i}{\omega}\frac{\partial E_1}{\partial t} + \delta^2 \frac{\partial^2 E_1}{\partial x^2} = 0, \tag{4}$$

$$\frac{1}{N_c}\frac{\partial N_1}{\partial t} - \alpha\,\mathrm{Re}(E_1) = 0, \tag{5}$$

where $\alpha(t) = 6\Omega\left((N_g - N_0)N_c^{-1}\right) df/d|E_0|$ at $|E_0| = e_0(t)$.

For the perturbations of the form $\exp\left(\int \gamma\, dt + ikx\right)$ (assuming that the characteristic time γ^{-1} is small in comparison with time of the change of the unperturbed homogeneous state) we find from the systems (4), (5) the cubic dispersion equation defining the increment of instability $\gamma(t)$ as the function of the arbitrary real wave number of perturbations k:

$$4\gamma^3/\omega^2 + \gamma\left(\varepsilon_0 - \delta^2 k^2\right)^2 - \alpha e_0\left(\varepsilon_0 - \delta^2 k^2\right) = 0. \tag{6}$$

The equation (6) has only one real root γ_1 and two complex conjugate roots $\gamma_{2,3}$ (with $\mathrm{Re}(\gamma_{2,3}) = -\gamma_1/2$), which may be written down in the form:

$$\gamma_1 = \omega \frac{\sqrt[3]{\varepsilon_0 - \delta^2 k^2}}{2}(A - B), \tag{7}$$

$$\gamma_{2,3} = -\frac{\gamma_1}{2} \pm i\omega \frac{\sqrt[3]{\varepsilon_0 - \delta^2 k^2}}{4}(A + B)\sqrt{3}, \tag{8}$$

where

$$A = \sqrt[3]{\sqrt{\frac{\left(\varepsilon_0 - \delta^2 k^2\right)^4}{3^3} + \left(\frac{\alpha e_0}{\omega}\right)^2} + \frac{\alpha e_0}{\omega}}, \tag{9}$$

$$B = \sqrt[3]{\sqrt{\frac{\left(\varepsilon_0 - \delta^2 k^2\right)^4}{3^3} + \left(\frac{\alpha e_0}{\omega}\right)^2} - \frac{\alpha e_0}{\omega}}. \tag{10}$$

It is seen from Eqs. (7)–(10) that the roots with the positive real part exist at any $\delta^2 k^2 \neq \varepsilon_0$. At $\delta^2 k^2 = \varepsilon_0$ all roots are identically equal to 0. At $\delta^2 k^2 < \varepsilon_0$ the instability is caused by the root γ_1, at $\delta^2 k^2 > \varepsilon_0$ it is due to the roots $\gamma_{2,3}$. At $\varepsilon_0 = 0$ ($N_0 = N_c$, $\omega = \omega_p$, $\delta^2 = 3r_D^2$, r_D is the Debye length) the dependence $\mathrm{Re}[\gamma_{2,3}(y)]$, where $y = (k\delta)^2$, is shown in Fig. 1.

It should be noted that the given results are valid only at not very great values of the wave number: $k > k_{\min} = k_0$. The value k_0 is defined either by the boundary of the region of applicability of the used potential description ($k_0 > (\omega/c)\sqrt{\varepsilon_0}$), or by the characteristic space scale L of the considered system ($k_0 \geq \pi/L$). We give the equations for the maximal increments $\gamma_{\max}$ and the corresponding values $k = k_m$ at different values of the parameters ε_0, αe_0, k_0:

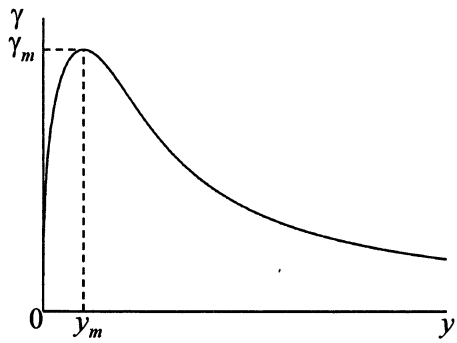

Fig. 1. The dependence of the instability increment γ on the parameter $y = 3k^2 r_D^2$ at $\varepsilon_0 = 0$; $y_m = \sqrt{\alpha e_0/\omega_p}$, $\gamma_m = \sqrt{\alpha e_0 \omega_p}/4$

at $\varepsilon_0 \geq \delta^2 k_0^2 + \sqrt{\alpha e_0/\omega}$:

$$\gamma_{\max} = \gamma_{1\max} = \frac{\sqrt{\alpha e_0 \omega}}{2},\ \delta k_m = \sqrt{\varepsilon_0 - \sqrt{\alpha e_0/\omega}};$$

at $\delta^2 k_0^2 + \frac{4-\sqrt{15}}{2}\sqrt{\alpha e_0/\omega} \leq \varepsilon_0 < \delta^2 k_0^2 + \sqrt{\alpha e_0/\omega}$:

$$\gamma_{\max} = \gamma_1(\varepsilon_0, \alpha e_0, k_0),\ k_m = k_0;$$

at $\delta^2 k_0^2 - \sqrt{\alpha e_0/\omega} \leq \varepsilon_0 < \delta^2 k_0^2 + \frac{4-\sqrt{15}}{2}\sqrt{\alpha e_0/\omega}$:

$$\gamma_{\max} = \mathrm{Re}(\gamma_{2,3})_{\max} = \frac{\sqrt{\alpha e_0 \omega}}{4},\ \delta k_m = \sqrt{\varepsilon_0 + \sqrt{\alpha e_0/\omega}};$$

at $\varepsilon_0 < \delta^2 k_0^2 - \sqrt{\alpha e_0/\omega}$:

$$\gamma_{\max} = \mathrm{Re}(\gamma_{2,3}(\varepsilon_0, \alpha e_0, k_0)),\ k_m = k_0.$$

Nonlinear stage of the ionization-field instability

The equations (1)–(3) were solved numerically in the range $0 \leq x \leq L$ for periodic boundary conditions and the following initial conditions:

$$N(x,0) = N_0 \exp\left(-\frac{x^2}{l^2}\right),\ E_0(x,0) = \frac{D_0(0)}{\varepsilon(x,0) + i\nu/\omega}. \qquad (11)$$

At the boundary of the considered range which was a half of the complete period of the system $2L$, the following conditions (assuming that $L >> l$)

$$\left.\frac{\partial E_0}{\partial x}\right|_{x=0} = \left.\frac{\partial^3 E_0}{\partial x^3}\right|_{x=0} = \left.\frac{\partial E_0}{\partial x}\right|_{x=L} = \left.\frac{\partial^3 E_0}{\partial x^3}\right|_{x=L} = 0 \qquad (12)$$

were set.

Based on the numerical solution of Eqs. (1)-(3), various scenarios and the main stages of the plasma and field evolution in the process of the breakdown at different methods of assigning the dependence $D_0(t)$ and different values of parameters were investigated. Here we give the results of the numerical calculation for the case $D_0(t) = D_0 = \text{const}$ at the values of the parameters $D_0 = 0.045E_a$, $N_0 = 0.2N_c$, $N_g = 1.5N_c$, $\Omega = 20\omega$, $L = 6l$, $\delta = 0.2l$, $b = 1$, $\nu = 0$. Spatio-temporal distributions of the plasma density and the electric field amplitude are given

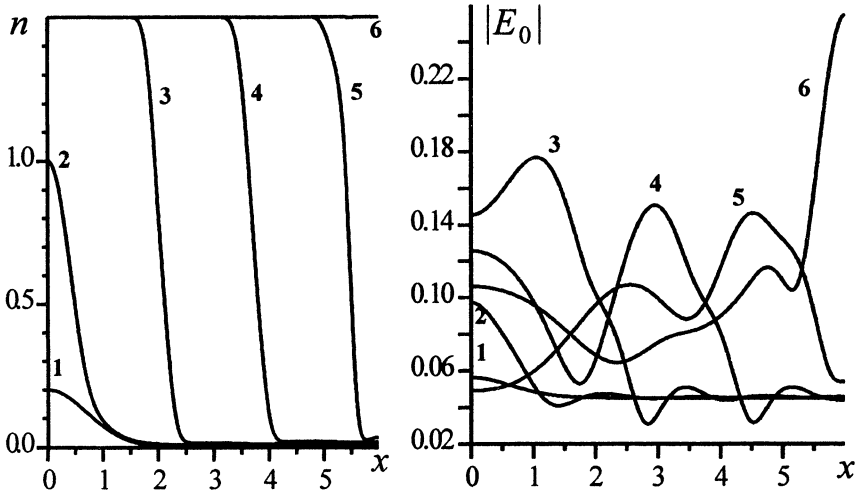

Fig. 2. The space distributions of the plasma density and the modulus of the electric field amplitude at different time instants at D_0=const=0.045 E_a; δ=0.2 l; ν=0. The curves 1-6 correspond to the instants t = 0; 27; 44.7; 60.7; 76.7; 84.7

in the dimensionless variables $x \to x/l$, $t \to \omega t$, $E_0 \to E_0/E_a$, $n = N/N_c$, in Fig. 2. We may distinguish the main stages of the plasma and field evolution in the process of the breakdown. At the first stage (the curves 1–2 Fig. 2) the maximum electron density grows with the increasing velocity till it reaches the critical value. The second stage of the process presents a fast ionization wave (the curves 3–6 Fig. 2) whose velocity is defined by a certain characteristic value of the Langmuir wave group velocity generated in the region of plasma resonance.

When the process of ionization is completed and the homogeneous stationary state is reached ($t > \tau$) with $\varepsilon = 1 - n_g$ the solution of Eq. (2) may be written down analytically: $E_0(x,t) = \sum_{k=0}^{\infty} e_k(t)\cos(\pi k x/L)$, where

$$e_0(t) = \frac{D_0}{\varepsilon} + \left[e_0(\tau) - \frac{D_0}{\varepsilon}\right]\exp\left[\frac{i\varepsilon\omega(t-\tau)}{2}\right],$$

$$e_k(t) = e_k(\tau)\exp\left\{-\frac{\omega(t-\tau)}{2}\left[b\left(\frac{k\delta\pi}{L}\right)^4 + i\left(\left[\frac{k\delta\pi}{L}\right]^2 - \varepsilon\right)\right]\right\},\ k \neq 0.$$

In Fig. 3 the time dependencies of the amplitudes $|e_k(t)|$ of the first six field harmonics are given. In Fig. 4 the time dependence of the module of the electric field amplitude at the point $x = 0$ is shown.

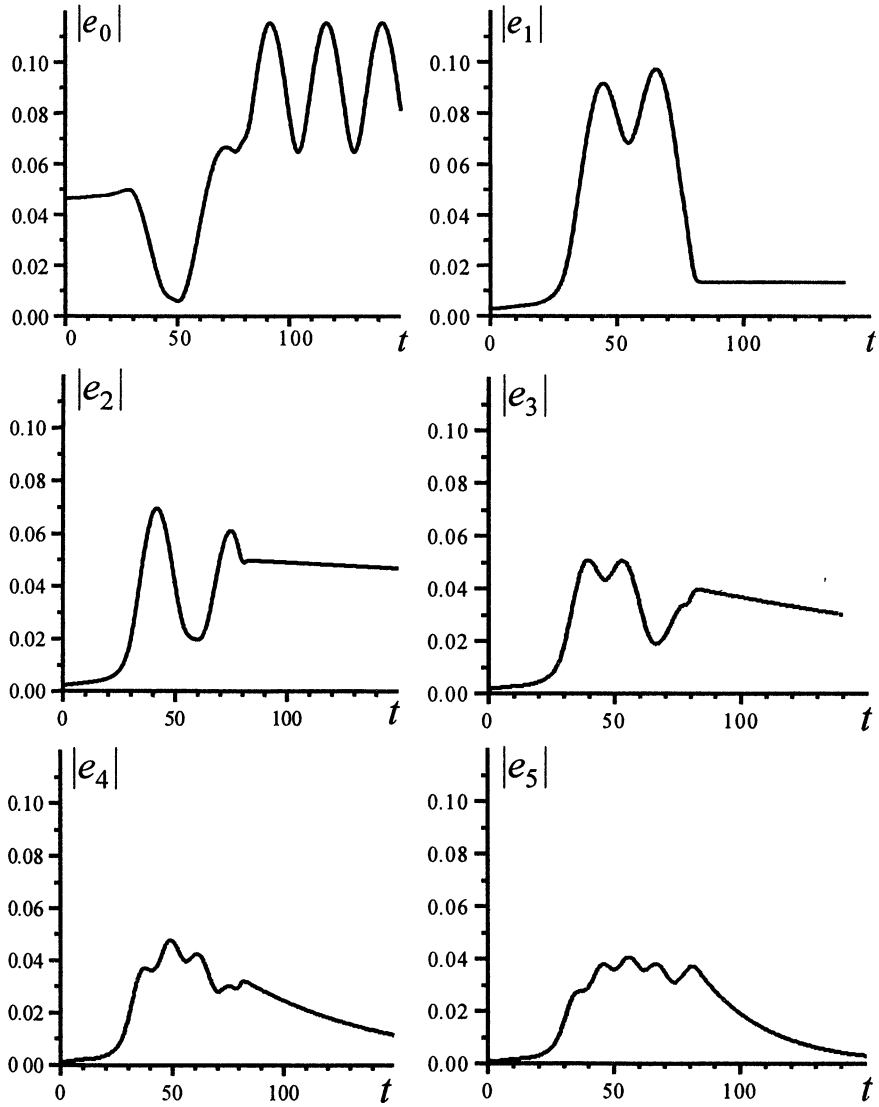

Fig. 3. The time dependence of the amplitudes of the first six harmonics of the electric field at the given amplitude of the induction D_0=0.045 E_a ; δ=0.2 l ; ν=0

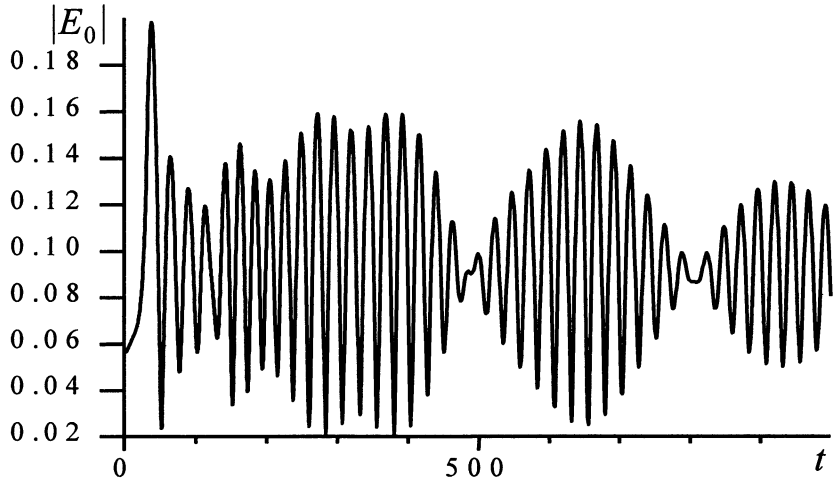

Fig. 4. Time dependence of the modulus of the electric field amplitude at the point $x = 0$; D_0=0.045 E_a ; δ=0.2 l ; ν=0

The analysis of the obtained results shows that the excitation of Langmuir waves in the process of the breakdown increases the velocity of the ionization wave in gas, and after the gas is completely ionized, the "quasiturbulent" state is reached with a great number of space field harmonics – Langmuir waves with various wave numbers, eigenfrequencies and damping constants.

The work was supported by the Basic Research Foundation, Grant № 99-02-16238.

References

1. Gildenburg V.B., Litvak A.G., Zharova N.A., Phys. Rev. Letters, 1997, **78**, 2968.
2. Bakunov M.I., Sorokin Yu.M. Izv. VUZov, Radiofizika, 1989, **32**, 122.

NONLINEAR STRUCTURES IN PLASMAS IN THE PRESENCE OF DUST PARTICLES

S.I. Popel[a], *V.N. Tsytovich*[b]

[a] Institute for Dynamics of Geospheres, Moscow, Russia
[b] General Physics Institute, Moscow, Russia

Abstract. The properties of nonlinear structures in dusty plasmas are studied. The dusty plasma is presented as an open, highly dissipative system where there is a tendency to self–organization. It is shown that (in contrast to the plasma systems in the absence of dust) the most important nonlinear structures in dusty plasmas are shock waves.

Self–organization is a characteristic feature inherent in a dusty plasma. It is related to the general property of plasma–dust systems, namely that they are *always* open systems. The plasma–dust systems cannot survive in the absence of either external sources of electrons and ions or plasma particle fluxes from the regions where there is no dust. The plasma particle fluxes recombine on the dust particles as well as the energy fluxes are absorbed by the dust particles. Thus external sources of energy which support its absorption in the plasma–dust systems are needed.

Since the plasma–dust system possesses the properties which are resulted from its nature as an ionized gas, the processes of self–organization inherent in the usual (without dust) plasma can take place in the dusty plasmas. In this case self–organization is related to the development of nonlinear plasma processes which can result in formation of nonlinear (coherent and dissipative) structures, such as solitons, collapsing cavities, shock waves, etc., the formation of self–organized structures being often due to the development of microscopic plasma instabilities. The most important nonlinear process resulting in self–organization

on microscopic level in the usual plasma is the modulational interaction [1, 2]. The nonlinear interactions in the dusty plasmas aquire new characteristic features in comparison with the case of the usual plasma. First, this is caused by the new time scales related to the presence of charged heavy dust particles in a plasma and results in new channels for nonlinear wave interaction. In particular, there is a possibility of modulational interactions associated with the new, inherent in the dusty plasmas, low–frequency modes (e.g., dust acoustic mode). Second, the new physics related to the *variable* charges of dust particles is manifested. This results, in particular, in an appearance of new types of nonlinear interactions (associated, e.g., with the nonlinearity caused by the variable charges). Furthermore, processes related to an anomalous dissipation originating from the charging processes become important. The strong dissipativity of the plasma–dust [3] system points to the exceptional role of the dissipative structures (like shock waves) in the dusty plasmas.

Already the first investigations of the modulational interaction in dusty plasmas (see, e.g., [4, 5]) showed that the modulational interaction can result in effective plasma heating. The modulational interaction of Langmuir waves caused by the dust particle charging process [5] can result in the energy transfer in one step to the dissipation region of Landau damping thus supressing the appearance of a strong nonlinearity which is a common phenomenon in the development of the modulational interactions of Langmuir waves in the absence of dust. This shows that the modulational interaction can serve as an efficient mechanism of plasma heating without creating large energy tails in the electron distribution. Furthermore, it is doubtful to expect the formation of quasi–stationary localized structures like solitons due to the development of the modulational interaction of Langmuir waves in dusty plasmas. Nevertheless, the dissipative structures (like shock waves) can be formed.

Shock waves often arise in nature because of a balance between wave breaking nonlinear and wave damping dissipative

forces. Collisional and collisionless shock waves can appear because of friction between the particles and wave–particle interaction, respectively. In dusty plasmas an appearance of anomalous dissipation which originates from the charging processes results in a possibility of existence of a new kind of shock waves related to this dissipation. They are collisionless in the sense that they do not involve electron–ion collisions. However, in contrast to the classical collisionless shock waves, the dissipation due to dust charging involves interaction of the electrons and ions with the dust grains in the form of microscopic grain currents.

The importance of shock waves in dusty plasmas is associated with different astrophysical applications [6]. For example, according to modern concepts [7], the formation of stars occurs mainly in interstellar dust–molecular clouds after compression shock waves propagate through them, creating the initial density condensations for further gravitational contraction. The presence of the dust in the interstellar clouds can influence significantly even the magnitude of the sound velocity, not to mention the shock wave propagation. The investigation of shock waves related to the dissipation originating from the dust particle charging processes can also be important [8] for the description of shocks in supernova explosions, particle acceleration in shocks, formation of dusty crystals, etc.

The case when the shock waves related to the dust particle charging process are rather intensive corresponds to the ion–acoustic wave propagation. The basic results which concern this new kind of ion–acoustic shocks are obtained in the papers [8, 9]. The exact solutions in the form of steady–state ion–acoustic shocks have been found for the case when the following assumptions are valid:

(1) the plasma constituents are electrons, ions, and dust particles;

(2) the dust–grain charge variation is solely due to the microscopic electron and ion grain currents originating from the potential difference between the plasma and the grain surface;

(3) the dust particles are massive ($m_i Z_d \ll m_d$, where $m_{i,d}$ are the ion and dust masses);

(4) in the absence of perturbations the quasineutrality condition $n_{i0} = n_{e0} + Z_d n_d$ (where n_α is the density of the particles of the kind α; $\alpha = e, i, d$ for electrons, ions and dust particles, respectively; the subscript 0 denotes unperturbed quantities) holds;

(5) the ions and electrons entering the dust grain recombine into neutral atoms, which then re–enter the plasma and re–ionize, thus preserving the number of ions and electrons.

Such exact solutions exist within the following range of Mach numbers $M(= V/c_s$, where V is the wave propagation speed, $c_s = (T_e/m_i)^{1/2}$, T_α is the temperature of the corresponding particles) [9]:

$$\left(1+\frac{1+P}{P}zG\right)\left(\frac{zG}{1+P}\right)^{-1} < M^2 < 1+P, \qquad (1)$$

where $P = n_d Z_d/n_e$, $z = Z_d e^2/aT_e$, $G = (1+z/\tau)/[1+(z+1)/\tau]$, $\tau = T_i/T_e$, a is the dust particle size, Z_d is the dust particle charge number, $-e$ is the electron charge. The jump of the potential φ in such waves can be very large ($\varphi \sim T_e/e$). The width of the wave front is of the order of c_s/ν_q, where $\nu_q = \omega_{pi} a(1+\tau+z)/\sqrt{2\pi}\lambda_{Di}$, ω_{pi} is the ion plasma frequency, λ_{Di} is the ion Debye length. The profile of the potential as well as the quantities characterizing ions and electrons (the speeds, the densities) in such shock waves contains an oscillating region in the vicinity of the front. This region is related to the charge polarization. Such oscillating region is absent in the profile of the dust particle charge.

It should be mentioned that under the assumption of a constant charge of dust particles the steady–state solutions in the form of ion–acoustic solitons have been obtained [10]. The consideration of our case shows that in real dusty plasmas (with variable charges of dust particles) the observation of shocks is much more probable than that of solitons.

In real situations of astrophysical or technological dusty plasmas its constituents are dust particles, electrons, ions, and

neutrals. Interaction of dust particles with ions and neutrals leads to the possibility of the so–called bombardment force [3] resulting in attraction between the dust particles which, in turn, means the new, more complicated physics of the shock waves. The way how one can develop the hydrodynamics for description of stationary shock waves in a dusty plasma containing electrons, ions, neutrals, and dust grains is presented in [8]. Here we mention only several relationships between the values before and behind the shock front in the wave and the width of the shock front for the case when

(1) the Mach number of the shock wave $M \gg 1$;

(2) the dust pressure is small as compared to the pressures of neutrals, electrons, and ions;

(3) the dust and the neutrals dominate in the mass density;

(4) the radiation is dominated in the energy transfer;

(5) the temperatures of the neutrals and the dust particles are equal to each other.

For the densities and temperatures of the neutrals before (characterizing by the subscript "0") and behind (characterizing by "1") the shock front we find:

$$n_1/n_0 \propto M^{8/3}, \quad T_1/T_0 \propto M^{-2/3}. \tag{2}$$

The front width is determined (see [8]) by the mean free path of electrons and ions in collisions with the dust:

$$\Delta\xi \sim \lambda_D^2 n_e / a n_d Z_d, \tag{3}$$

where $\lambda_D^{-2} = \lambda_{De}^{-2} + \lambda_{Di}^{-2}$, λ_{De} is the electron Debye length. The magnitude of $\Delta\xi$ is much less than the particle mean free path for binary (electron–ion, electron–electron, ion–ion) collisions. We emphasize that the process of the collisions of electrons and ions with the dust particles results in the charging of the latter. This confirms again that the origin of the shock waves considered is related to the dissipation due to the dust charging process.

Observation of shock waves related to the dust charging process is possible in active rocket experiments which involve the release of some gaseous substance in near–Earth space and have

the scheme analogous to the experiments which have been carried out by the Institute for Dynamics of Geospheres of the Russian Academy of Sciences at the altitudes of 150 km at night time [11]. The source for the charged particle release in the magnetosphere in these experiments is the generator of high–speed plasma jets. Macro (dust) particles in the experiment at the altitude of 600 km appear as a result of condensation. The optimum velocities to manifest the charging effect of the macro particles are $U \leq 10$ km/s [12].

Acknowledgements

This work is supported by INTAS (grant no. 97-2149) and INTAS–RFBR (grant no. IR–97–775).

References

[1] Vladimirov S.V., Tsytovich V.N., Popel S.I., and Khakimov F.Kh., *"Modulational Interactions in Plasmas"*, Kluwer Academic Publishers, Dordrecht–Boston–London (1995).
[2] Popel S.I., Physica Scripta, 1998, 57, 272.
[3] Tsytovich V.N., Physics–Uspekhi, 1997, 40, 53.
[4] Popel S.I. and Yu M.Y., Phys. Rev. E, 1994, 50, 3060.
[5] Benkadda S. and Tsytovich V.N., Phys. Plasmas, 1995, 2, 2970.
[6] Spitzer L.J., *Physical Processes in the Interstellar Medium*, (John Wiley, New York, 1978).
[7] Kaplan S.A. and Pikel'ner S.B., *Interstellar Medium* (Harvard Univ. Press, Cambridge. Mass., 1982).
[8] Popel S.I., Tsytovich V.N., and Yu M.Y., Astrophys. Space Sci., 1998, 256, 107.
[9] Popel S.I., Yu M.Y., and Tsytovich V.N., Phys. Plasmas, 1996, 3, 4313.
[10] Popel S.I. and Yu M.Y., Contrib. Plasma Phys., 1995, 35, 103.
[11] Adushkin V.V., Zetzer Yu.I., Kiselev Yu.N., et al., Doklady Akad. Nauk, 1993, 331, 486.
[12] Popel S.I. and Tsytovich V.N., "Shocks in Space Dusty Plasmas", Astrophys. Space Sci., 1999, in press.

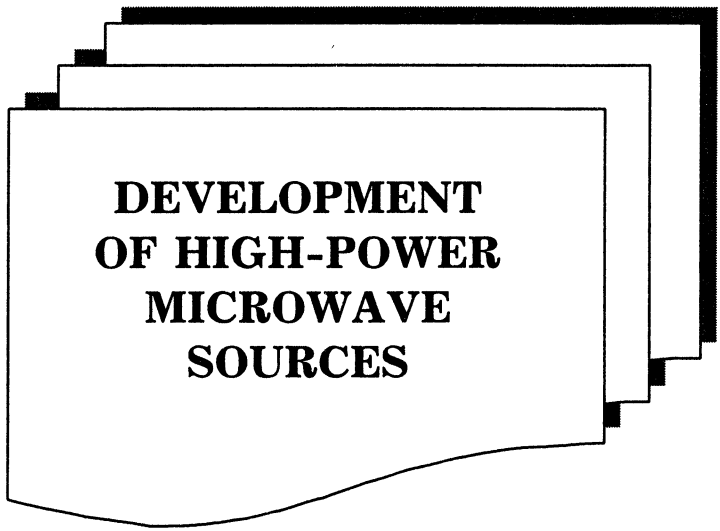
DEVELOPMENT
OF HIGH-POWER
MICROWAVE
SOURCES

1.6 MW FREQUENCY STEP-TUNABLE D-BAND GYROTRON

M.Thumm, E. Borie, O. Braz*, G. Dammertz, O. Dumbrajs, K. Koppenburg*, M. Kuntze, B. Piosczyk,*

Forschungszentrum Karlsruhe, Association EURATOM-FZK,
Institut für Hochleistungsimpuls- und Mikrowellentechnik,
D-76021 Karlsruhe, Postfach 3640, Germany
*also Universität Karlsruhe, Institut für Höchstfrequenztechnik und Elektronik,
D-76128 Karlsruhe, Germany

Abstract

Successful gyrotron experiments at FZK employing a conventional hollow cylindrical waveguide cavity, a quasi-optical mode converter with dimple-type launcher, a broadband silicon nitride Brewster window and a single-stage depressed collector (SDC) gave up to 1.6 MW output power at efficiencies between 48 and 60 % for all operating mode series in the frequency range from 114 to 166 GHz. Frequency tuning in 3.7 GHz steps has been achieved by slow variation (minutes) of the magnetic field strength in the cavity. A specific hybrid magnet system for fast frequency tuning (1 s) is being manufactured. These experiments confirm the preliminary results achieved with a prototype fused quartz glass Brewster window. Up to now, the pulse duration has been 1 to 5 ms. However the water-edge-cooled silicon nitride composite Brewster window with its thermal conductivity of k=60 W/mK, permittivity ε_r=7.85 ($\theta_{Brewster}$=70.35°), tanδ=3.5x10^{-4}, excellent mechanical properties and clear window aperture of 100 mm diameter will allow long-pulse operation (1 s) in the 1 MW power range. By increasing the beam current to 70 A (70 % of the limiting current!), a maximum power of 2.14 MW, the highest value ever generated by a weakly relativistic gyrotron, has been achieved at 140 GHz with an efficiency of 34 % (53 % with SDC).

1. Introduction

Gyrotron oscillators have a wide range of applications which includes radars, atmospheric sensing, advanced communication systems, technological processes, and extra-high-resolution spectroscopy, etc. [1] However, the main application of powerful gyrotrons is plasma start-up and electron cyclotron resonance plasma heating (ECRH) in tokamaks and stellarators as well as non-inductive current drive and stability control in tokamaks. [2] For example, for its ECRH system with power up to 100 MW the International Thermonuclear Experimental Reactor (ITER) will need about 50 to 100 continuous wave (CW) gyrotrons at a frequency of

170 GHz with 1 to 2 MW of output power per tube [3]. For the new German stellarator Wendelstein 7-X which is under construction at IPP Greifswald ten 140 GHz, 1 MW, CW gyrotrons will be needed to achieve a total output power of about 10 MW [4].

In this work we discuss how to tune the frequency of a high-power gyrotron. The importance of this problem increases when gyrotrons are used in large-size magnetic fusion reactors. The reason is that the magnetic field in large tokamaks and stellarators varies significantly over the distance from the plasma center to its surface. This means that the resonance condition between the plasma electrons and the millimeter (mm)-wave beam is fulfilled only in a relatively small layer of the plasma. To reach other plasma layers, e.g. for plasma stabilization [5], one must either use mechanically steerable mirrors to direct the mm-wave beam to the desired position and to employ the Doppler shift effect, or change the frequency of the source and, hence, the position of the resonance layer in the plasma. It is obvious that the second possibility is more attractive because it reduces the number of mechanically movable parts which must be cooled close to the plasma in a fusion reactor and thus increases the reliability of operation of the entire ECRH system. Additionally, several frequencies in the range of 90-140 GHz will be required for plasma start-up at different radial locations in the ITER torus [3].

2. Tunability of Gyrotrons

It is difficult to change the frequency of a gyrotron during operation because this is determined by the magnetic field and the operating mode in the cavity. Different methods of tuning a gyrotron have been discussed in detail in [6] where also references to earlier work can be found. It was pointed out that so-called mechanical, electrical, and magnetic frequency tuning should be distinguished. In the case of high-power long-pulse gyrotrons the most advanced method of step-wise changing of the frequency is with magnetic tuning.

The frequency of a gyrotron is always very close to the gyrofrequency of the electrons

$$f(\mathrm{GHz}) = 28 \cdot \frac{B(T)}{\gamma} \qquad (1)$$

or to its harmonics. Here B is the magnetic field and γ is the relativistic factor which is related in the following way to the electron beam energy eU:

$$\gamma = 1 + \frac{eU}{511\,keV}. \qquad (2)$$

From these expressions it is clear that the gyrofrequency can be changed by altering the accelerating voltage U or more effectively by changing the magnetic field B, because f is directly proportional to B, in contrast to the rather weak dependence of f on the accelerating voltage U. Here a mode whose resonance frequency is near the gyrofrequency or a harmonic will be excited. Operation jumps from one mode to another as the magnetic field is changed. As the main advantage of this method one should mention its simplicity: it is sufficient to change the current in the magnet solenoids. The main drawback, the slowness (minutes), is related to the fact that a large time constant is involved in changing the magnetic field. However, if one confines oneself to tunability in a narrow frequency range, e.g. for MHD-mode stabilization, one can keep the magnetic field in the main superconducting solenoid constant and only rapidly adjust the magnetic field of small auxiliary solenoids (0.1 - 1s).

Cavity Mode	Main Magnetic Field [T]	Acceleration Voltage [kV]	Frequency [GHz]	Relative Caustic Radius R_c / R_{cav}
$TE_{18,5}$	4.43	75.0	114.20	0.484
$TE_{19,5}$	4.59	80.6	117.80	0.495
$TE_{20,5}$	4.78	83.4	121.60	0.505
$TE_{21,5}$	4.91	83.4	125.30	0.515
$TE_{19,6}$	5.07	82.6	128.94	0.453
$TE_{20,6}$	5.25	84.0	132.62	0.463
$TE_{21,6}$	5.37	81.2	136.34	0.473
$TE_{22,6}$	5.49	81.2	140.10	0.482
$TE_{23,6}$	5.67	84.0	143.83	0.491
$TE_{24,6}$	5.83	84.8	147.50	0.499
$TE_{22,7}$	6.09	84.0	151.12	0.447
$TE_{25,6}$	5.97	83.4	151.23	0.508
$TE_{23,7}$	6.14	89.0	154.73	0.456
$TE_{26,6}$	6.15	85.4	154.94	0.456
$TE_{24,7}$	6.25	84.8	158.54	0.456
$TE_{25,7}$	6.37	80.6	162.30	0.473
$TE_{26,7}$	6.48	78.0	166.03	0.481

Table I: $TE_{22,6}$ gyrotron operating parameters required for frequency-step tuning at a beam current of approximately 47 A.

The different gyrotron working modes should have approximately the same caustic radius $R_c = (m/X'_{mp})\ R_{cav}$, where R_{cav} is the cavity radius, m the azimuthal mode index and X'_{mp} the p-th root of the derivative of the Bessel function J_m, so that the coupling of the electron beam to the mm-wave electric field is comparably good.
As an example, the operating parameters of the FZK gyrotron required for excitation of different cavity modes at high power levels, and the measured frequencies, are summarized in Table I [7,8]. The cavity has been optimized for operation at 140 GHz in the $TE_{22,6}$ mode.

3. General Considerations on Step-Tunability of Q.O. Converters

Due to the helical-cut-antenna of the internal quasi-optical (q.o.) mode converter [9], the different modes which have to be converted into a linearly polarized "Gaussian" beam profile must have the same sense of rotation. The q.o. launcher fixes its applicability to either right-hand (co-rotating with the electrons "-") or left-hand rotation (counter-rotating "+"). The length and the angle of divergence of the output beam of a smooth, conventional q.o. launcher are determined by the Brillouin angle and the ratio m/X'_{mp} of the gyrotron cavity mode [9]. The Brillouin angle is given by

$$\theta_{mp} = \sin^{-1}(X'_{mp}/kR_L) \tag{3}$$

and the transverse aperture angle by

$$2\phi_{mp} = 2\cos^{-1}(m/X'_{mp}), \tag{4}$$

where k is free-space wavenumber and R_L the launcher radius. The appropriate launcher cut length is

$$L_{mp} = 2\pi RL\cot\theta_{mp}\sin\phi_{mp}/\phi_{mp}. \tag{5}$$

The operating mode in a gyrotron cavity is very close to cutoff ($X'_{mp}/k\ R_{cav} \approx 1$). Therefore all operating modes have the same Brillouin angle, independent of the frequency. For our specific choice of mode series (Table I) e.g. the modes $TE_{-19,5}$ at 117.8 GHz, $TE_{-22,6}$ at 140.1 GHz and $TE_{-25,7}$ at 162.3 GHz have approximately the same transverse aperture angle 2ϕ (120.7°, 122.3°, 123.6°), launcher cut length L and caustic radius R_c (0.495 R_L, 0.482 R_L, 0.473 R_L). This means that in all three cases the phase corrected output beam pattern behind the quasi-parabolic mirror is very similar.

Advanced q.o. mode converters [9] employ an irregular cylindrical waveguide section (pre-bunching section) followed by a helical-cut launching aperture. In the pre-bunching section prior to the launch, a Gaussian profile of the field intensity on the waveguide wall can be achieved by specific periodic $\Delta m_1 = 1$ and $\Delta m_2 = 3$ wall deformations. As demonstrated in [10] such improved launchers work quite well for all the modes listed in Table I. The reflectors that follow behind the phase-correcting quasi-parabolic mirror have to be designed with Gaussian optics in confocal geometry in order to provide the required broadband characterics. In addition, one movable phase corrector must be included.

4. Development of Broadband Output Windows

4.1 Multi band-pass window

One possibility to remove the window reflections at least for a set of discrete frequencies is given by mounting a window plate of specially chosen thickness perpendicular to the output beam. To make sure that the part of the power reflected by the first material discontinuity (vacuum –to-material) interferes destructively with the parts reflected out of the window plate (multiple reflections) the plate's thickness has to be a multiple N of the half wavelength $\lambda_n/2$ in the material:

$$d_N = \frac{\lambda_n}{2} \cdot N \Rightarrow d_N = \frac{c_0}{2 \cdot f_0 \cdot \sqrt{\varepsilon_r'}} \cdot N, \tag{6}$$

$$f_n = f_0 + n \cdot \Delta f,\ \Delta f = \frac{f_0}{N},\ n = -0, \pm 1, \ldots \pm N. \tag{7}$$

Since the window in this case provides a resonant thickness for the mm-wave beam the amount of power oscillating between the two surfaces leads to an increase of the absorption coefficient, which results in the following expression for the absorbed power:

$$A_M \approx \frac{\pi \cdot f \cdot d \cdot \tan(\delta) \cdot (1 + \varepsilon_r')}{c_0}. \tag{8}$$

Here c_0 is the speed of light, d is the window thickness, $\tan(\delta)$ is the loss tangent and ε_r' is the permittivity of the window material. An example of

the reflection behavior of such a multi band-pass window is shown in Fig. 1. In addition to the design frequency of 140 GHz for this quartz glass window (ε_r' = 3.81) it was intended to provide additional reflection minima close to 118 GHz and 162 GHz. Since the window thickness of d =3.29 mm ($6 \cdot \lambda_n/2$) is not sufficient for a quartz glass plate to withstand twice the pressure difference, twice the thickness has been chosen providing the advantage of having additional reflection minima at 128 GHz and 151 GHz.

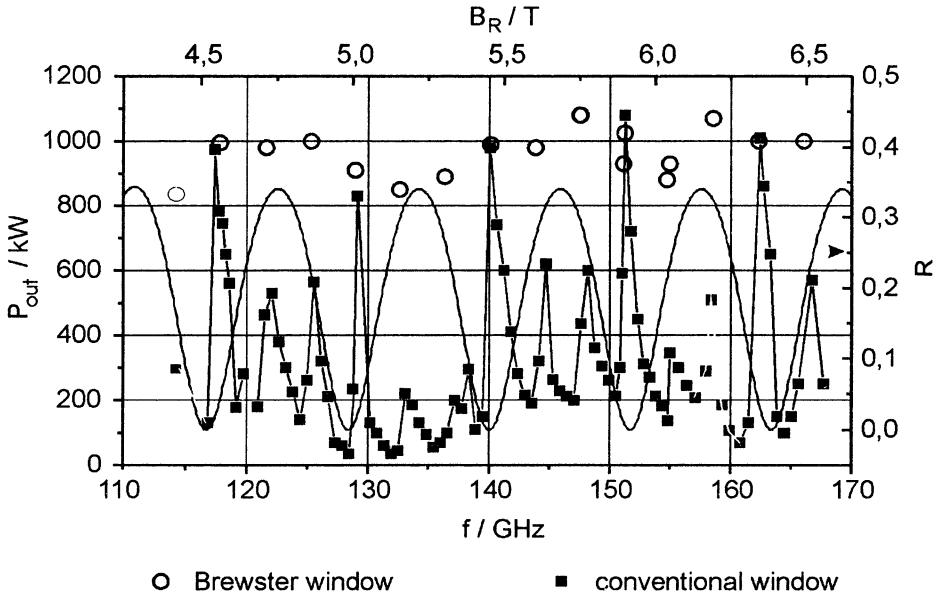

Fig. 1: Power reflectivity of two types of single-disk window versus frequency and calorimetrically measured gyrotron output power versus magnetic field [7,8].

4.2 Brewster window

A more elegant method to realize a gyrotron output window with very large bandwidth is given by using the Brewster angle. If the angle between the normal to the window plate and the propagation constant of the mm-wave beam is chosen according to the following equation it can be shown that the reflections vanish, independently of the frequency, for parallel polarization:

$$r_{\parallel} = 0 \Leftrightarrow \Theta_i = \Theta_B = \arctan\left(\sqrt{\frac{\varepsilon_{r2}'}{\varepsilon_{r1}'}}\right), \tag{9}$$

where ε_{r2}' represents the permittivity of the material and $\varepsilon_{r1}' = 1$ is that of air or vacuum.

Due to the parallel boundary conditions of the window plate there are further frequency dependent angles where the reflections vanish independently of the polarization. Similar to the case of a perpendicularly incident beam the reflections can vanish if the phase displacement of the first reflection and the ray scattered out of the material is a multiple of $(2n+1)\,\pi$. The relation derived from this is given by

$$\sin(\Theta_i) = \sqrt{\varepsilon_r' \cdot \left(1 - \left(N \frac{\left(\frac{\lambda_n}{2}\right)}{d}\right)^2\right)}; \text{int}\left(\frac{d}{\lambda_n/2}\right) > N > \text{int}\left(\left(\frac{d}{\lambda_n/2}\right)\sqrt{\frac{\varepsilon_r'-1}{\varepsilon_r'}}\right). \tag{10}$$

If it is intended to remove reflections of both the orthogonal and the parallel polarization for at least one frequency one has to choose the thickness of the Brewster window according to:

$$d_N = N \cdot \lambda_n \cdot \sqrt{\frac{\varepsilon_r'+1}{\varepsilon_r'}} \quad \Rightarrow \quad d_N = N \cdot \frac{c_0}{f} \cdot \frac{\sqrt{\varepsilon_r'+1}}{\varepsilon_r'}. \tag{11}$$

For a plate mounted at the Brewster angle each ray passes the window material only once, which results in the following absorbed power:

$$A_B \approx \frac{2 \cdot \pi \cdot f \cdot \sqrt{\varepsilon_r'} \cdot \tan(\delta)}{c_0} \cdot \frac{d}{\sin(\Theta_B)}. \tag{12}$$

Compared to the amount of power absorbed in the multi band-pass window it can be shown that the Brewster window with equal thickness provides a lower absorption, especially for higher permittivities ([7] and Table II).

Material	Quartz Glass	Diamond	Silicon-Nitride	Aluminium Oxid
ε_r'	3.81	5.66	7.85	9.6
Θ_B	62.87	67.2	70.35	72.11
A_M/A_B	1.1	1.3	1.5	1.6

Table II: Permittivity, the corresponding Brewster angle and the variation of absorbed power for different window materials and geometries.

4.3 The Silicon-Nitride Brewster Window

In order to achieve a simple window design for the first experiments, the quartz plate was glued to the metal housing without any additional cooling system. Due to the poor thermal conductivity of quartz glass, adequate cooling would not have been possible in any case. It is obvious that such a window assembly can only be used for short pulse tests at output power levels in the Megawatt range. In order to investigate an alternative window material, a Brewster window using a Silicon-Nitride plate (SN-287 composite of Kyocera) of thickness d = 3.16 mm hàs been developed. The 40 times higher thermal conductivity and much higher mechanical strength, compared to that of quartz glass, provides the opportunity to mount the metallized Silicon Nitride material with mm-wave resistant metal bonding to the window housing. Due to the thermal stress during the brazing process such a mounting technique is impossible for an elliptically shaped quartz glass plate.

To verify the isotropic behavior of the Silicon-Nitride material the angle dependent reflectivity was measured at several frequencies by a low power test setup. Fig. 2 shows the excellent agreement between the calculated (isotropic) reflectivity and the measurement at a frequency of 140 GHz. In agreement with theory, the window reflections vanish for parallel polarization at the Brewster angle of $\Theta_B = 70.35°$ and independent of the polarization at an angle of $\Theta_i = 45.68°$. The material parameters of the SN-287 material have been determined by fitting the calculated curve to the measured data. The values of $\varepsilon_r' = 7.85$ and $\tan(\delta) = 3.5 \cdot 10^{-4}$ were in excellent agreement with additionally performed Fabry-Perot resonator measurements. Thanks to the relatively small beam size in the resonator

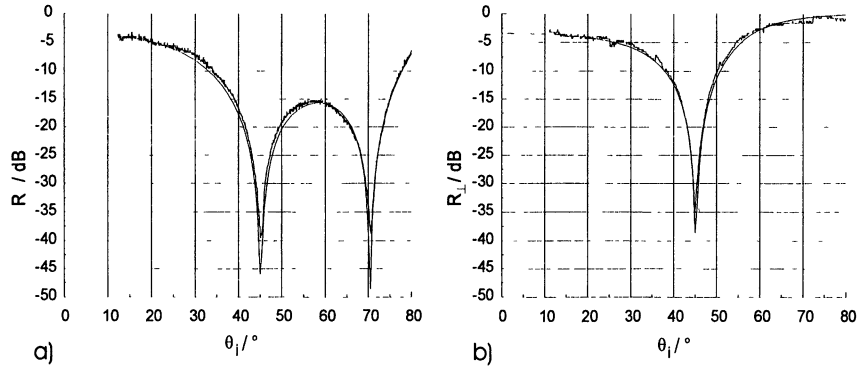

Fig. 2: Reflectivity of a single Silicon-Nitride disk in dependence of the angle of incidence measured and calculated at a frequency of 140 GHz:
a) parallel polarization (||) b) perpendicular polarization (⊥).

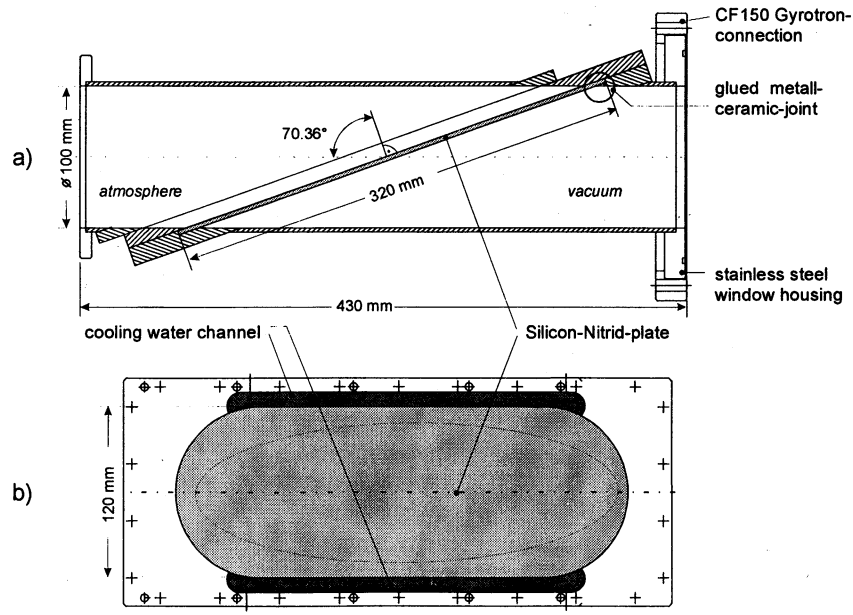

Fig. 3: Technical drawing of the Silicon-Nitride window housing:
a) Side view b) Top view.

it was possible to measure the dielectric parameters at several positions across the disk. From these measurements the uncertainties have been determined to be $\Delta\varepsilon_r' = 0.02$ for the permittivity and $\Delta\tan(\delta) = 0.6 \cdot 10^{-4}$ for the loss tangent.

To check the high power behavior of the Silicon-Nitride plate it was mounted in a new Brewster window housing as shown in Fig 3. In a first step the window plate is again glued to the housing. In contrast to the quartz glass Brewster window the new housing has been equipped with two water cooling channels. Additionally performed finite element calculations predict that a brazed window assembly will be able to withstand the transmission of a 1 MW power for at least 1 s, without any danger of thermal overload for the window plate.

5. Experimental Layout

Figure 4 shows a schematic outline of the gyrotron with Silicon-Nitride Brewster window installed in its magnet. The gyrotron consists of a diode-type magnetron injection gun with a LaB_6 emitter. The velocity ratio α (transverse velocity component divided by the axial one) can be modified in the range from 1.1 to 1.7 by changing the magnetic field gradient in the gun region. The beam tunnel is equipped with alternating staggered copper and highly RF-absorbing ceramic rings (aluminium nitride and 40% silicon carbide) in order to suppress parasitic oscillations in this region.

gun		cavity	
cathode voltage	80 kV	output power	1 MW
beam current	36 A	efficiency η	35%
emitter current density	3.6 A/cm^2	magnetic field (140 GHz)	5.6 T
emitter radius	45.2 mm	Ohmic loss density	3.5 kW/cm^2
cathode angle	21.48°	velocity ratio α	1.4
magnetic field	0.187 T	beam radius	7.93 mm
		beam thickness	0.53 mm
		compression ratio	36
		cavity radius	15.57 mm
		cavity length	15 mm
		input taper angle	3°
		output taper angle	2.5°
		diffraction Q-value	1000

Table III: Design parameters of the 140 GHz, $TE_{22,6}$ gyrotron.

The operating mode has been chosen to be the $TE_{22,6}$ mode at 140 GHz with a designed output power of 1 MW at a beam current of 36 A and a beam voltage of 80 kV (see Table III). The peak value of the Ohmic loss-density was calculated to be 3.5 kW/cm^2 for an output power of 1 MW and a surface temperature of 300°C. A factor of 1.3 is included to account for surface roughness, and RF losses of 15% between cavity power and output power were assumed in these calculations. The collector employs an insulation gap allowing a retarding voltage. This enables the study of efficiency enhancement by beam energy recovery in a single-stage depressed collector (SDC) [11].

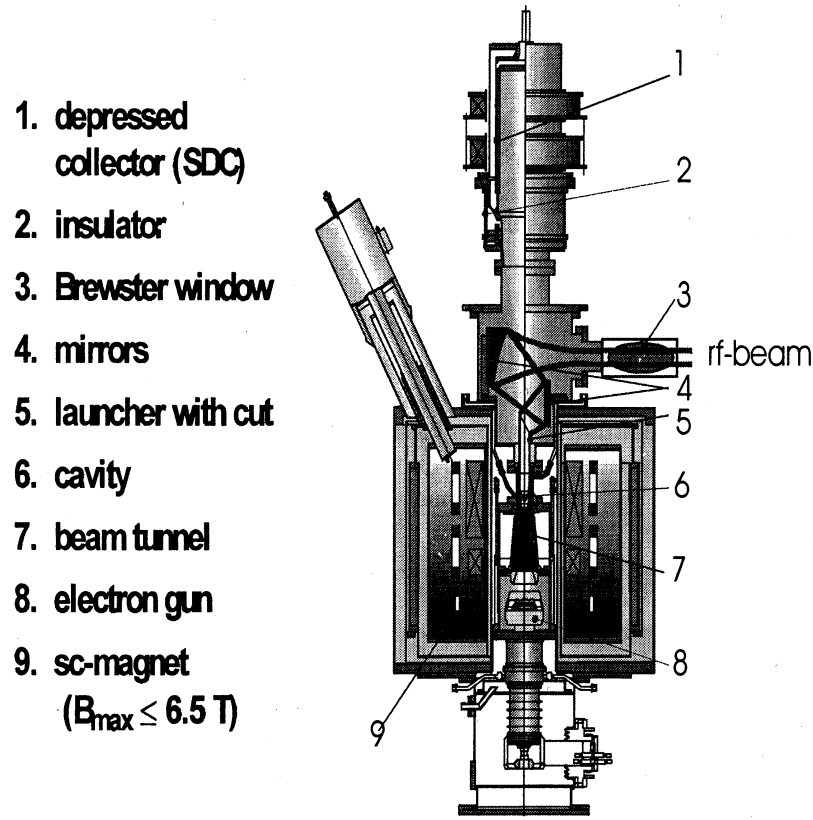

Fig. 4: Schematic layout of an advanced 1 MW gyrotron (FZK).

Because of the field distribution of the existing superconducting magnet at FZK it was not possible to use a fully optimized rippled-wall q.o. launcher (Denisov-type) [9] which would have been too long. In order to couple out as much as possible of the excited mm-wave power, a shortened launcher, without the intention to achieve a pure Gaussian beam profile, was used. However, a Gaussian distribution can be obtained by applying a phase correcting mirror outside the tube.

6. Experimental Results on Stepwise Frequency Tuning

First pilot experiments during which the $TE_{22,6}$ gyrotron was equipped with a prototype fused quartz glass ($\theta_{Brewster}$ =62.87°) Brewster angle window gave approximately 1 MW output power for all operating mode series in the D-band frequency range from 114 GHz to 166 GHz (frequency tuning in 3.7 GHz steps by variation of the magnetic field in the cavity) [7]. In Fig. 1 the results achieved with the Brewster window are compared to those measured by employing a conventional, plane single-disk window. This window (thickness d = 6.58 mm; 12 $\lambda_n/2$) has been optimized to have low reflections at least for a few number of frequencies (see power reflection coefficient R in Fig.1).

Due to mode competition problems, it was not possible to excite all the modes with the same magnetic compression. The magnetic compression was chosen so that single-mode operation was possible.

It is obvious that the window reflections have a significant influence on the mode spectrum of the measured output power. By using the Brewster output window nearly all modes are coupled out with the same intensity whereas the multi-band-pass window shows a strong frequency selective behavior. To be able to compare the gyrotron cavity internal field levels for corresponding modes in the two different designs, the values measured with the single disk window are corrected for the window reflections. ($P_{cor} = P_{out} / (1 - r^2)$). The calculated difference in output power given by this correction and those measured by using the Brewster window are shown in Fig. 5. The same results were obtained only for vanishing window reflections. On the other hand, modes located at high reflections are coupled out even less than expected by the correction. These results indicate that even when using a q.o. mode converter, window reflections cannot be neglected. Another interesting point was observed at a frequency of 152 GHz where the modes of the series n = 6 are competing with the mode series n = 7. By using the multi band-pass window it was not possible to excite the $TE_{22,7}$ mode. Only by using the

Brewster window has it been possible to identfy this mode properly. It seems that a reflectivity of 1.5 % is already sufficient to influence the cavity mode selection in this case.

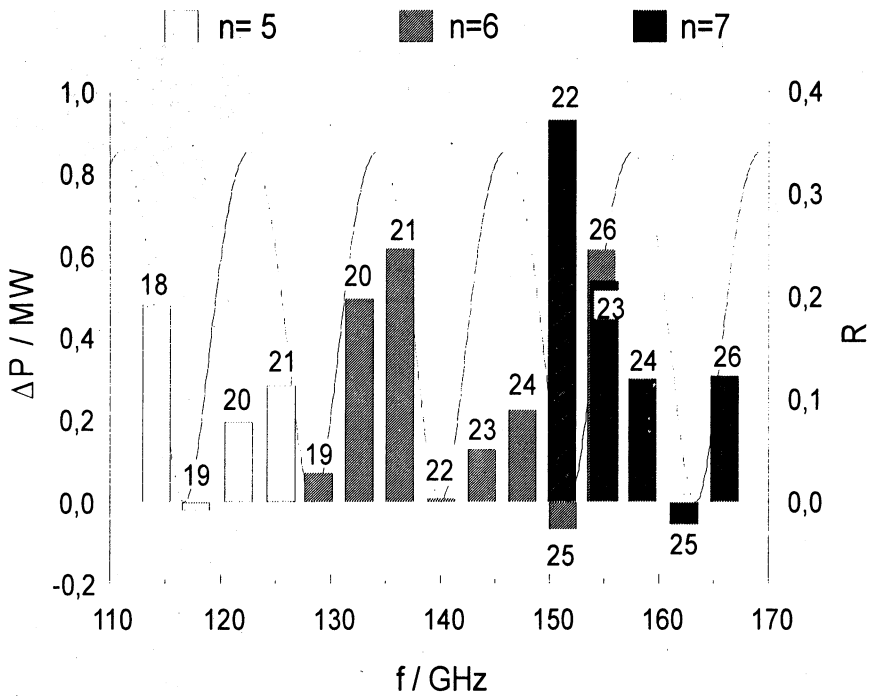

Fig. 5: Difference of the power levels generated in the cavity (measured with the Brewster window and calculated for the conventional window).

At those frequencies at which a transition between the different mode series occured, the output power is decreased by about 0.2 MW. Under these conditions, the mode competition problem seems to be more severe, as the two neighboring modes of the different series are very near in frequency. In addition to the output power, the field distribution of the output beams is also of interest. The field distributions for three different modes are shown in Fig. 6. The patterns look very similar for these modes, and this is also true for the others. This shows that a launcher designed for high-order modes operates very well in a wide range of frequencies and modes [10].

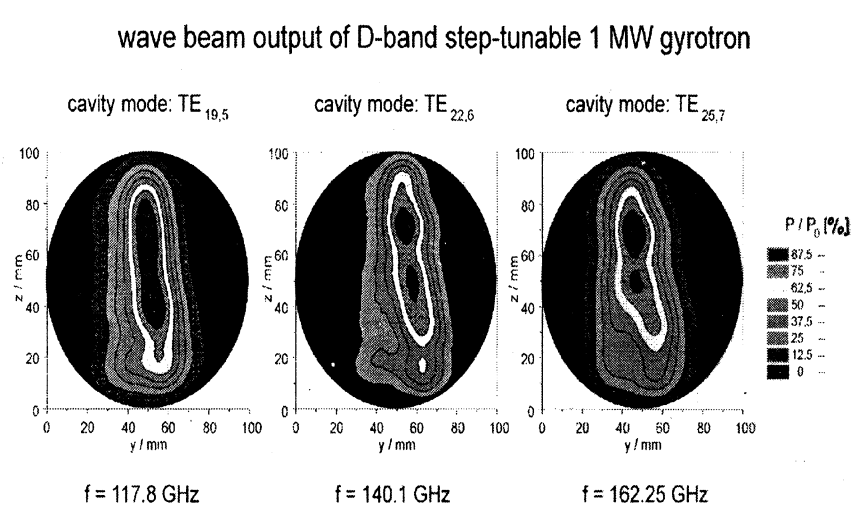

Fig. 6: Output field patterns for different modes at different frequencies.

After mounting the Silicon-Nitride Brewster angle window as the output window to the gyrotron the mm-wave output power spectrum formerly measured with the quartz glass Brewster window was reproduced almost identically [8].

Due to the significant influence of reflections on the gyrotron interaction the reflection behavior of the required power calorimeter also had to be taken into account. After rotating the ballistic calorimeter in use by less than 2° another significant increase in output power and efficiency was reached. The results obtained for the three most relevant modes are listed below [8]:

TABLE IV: Optimum Parameters of D-Band Gyrotron ($U_c \approx 87$ kV, $I_b \approx 51$A, $\tau = 5$ ms)

Cavity Mode	Frequency [GHz]	Output Power [MW]	Efficiency [%]	Efficiency (SDC) [%]
$TE_{19,5}$	117.9	1.55	31	48
$TE_{22,6}$	140.1	1.60	36	60
$TE_{25,7}$	162.3	1.48	35	57

7. World Record Power Experiments

By increasing the beam current at U_c=90 kV to 70 A, which is 70% of the limiting current, a maximum power of 2.14 MW (pulse length = 1 ms), the highest value ever generated by a weakly relativistic gyrotron, has been achieved at 140 GHz with an efficiency of 34 % (53% with SDC). In Fig. 7 the mm-wave output power as a function of the beam current is plotted [12]. This experimental result is in good agreement with numerical simulations. Figure 8 shows output power and efficiency for different beam currents as a function of the collector depression voltage which could be increased up to values around 33 kV. At higher depression voltages reflected electrons spoil the gyrotron interaction in the cavity resulting in a pronounced degradation of the output power and in an increased body current.

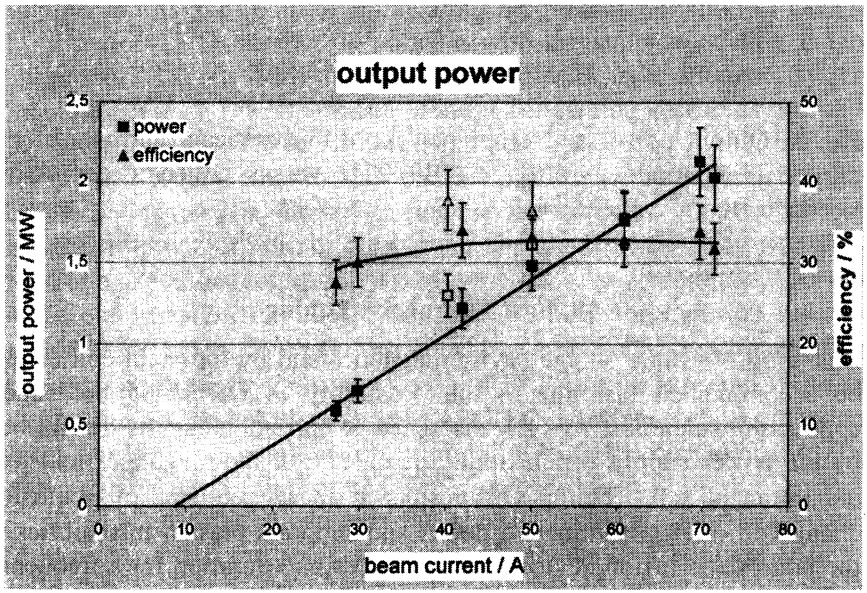

Fig. 7: Output power and efficiency of the $TE_{22,6}$-mode gyrotron at 140 GHz versus beam current (Uc≈90kV, B_o=5.55 T) [12].

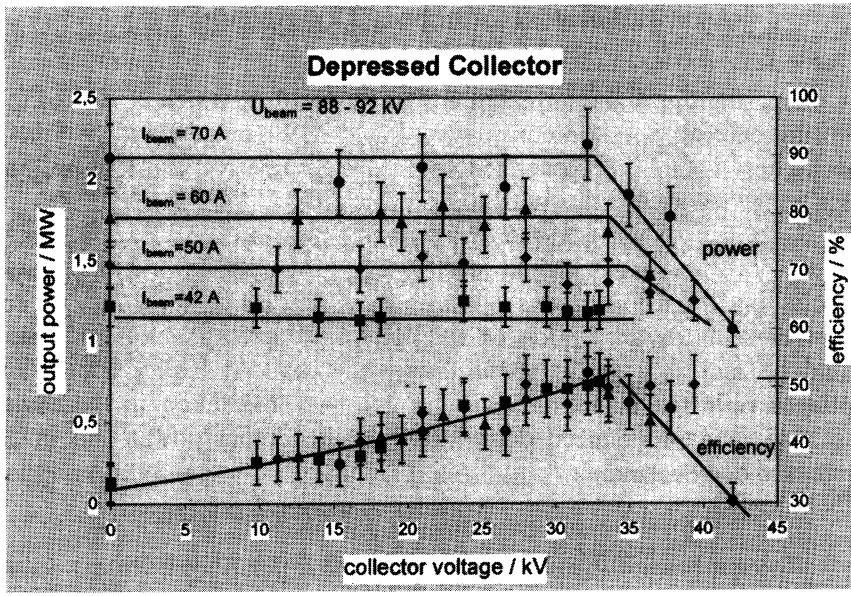

Fig. 8: Output power and efficiency for different beam currents of the $TE_{22,6}$-mode gyrotron at 140 GHz versus collector depression voltage.

8. Fast Frequency Tuning

Changing the value of the cavity magnetic field by the main coil cannot be accomplished fast due to the possibility of quenching the super-conducting solenoids. At FZK the speed of current change is determined by the power supply which limits the change of the magnetic field to a maximum of ~ 0.1 T/min. This results in an average step of frequency change of ~ 2.5 GHz/min. To detect and suppress plasma instabilities in the large-scale fusion devices the estimated time duration for a frequency variation is of the order of several GHz/s [5].

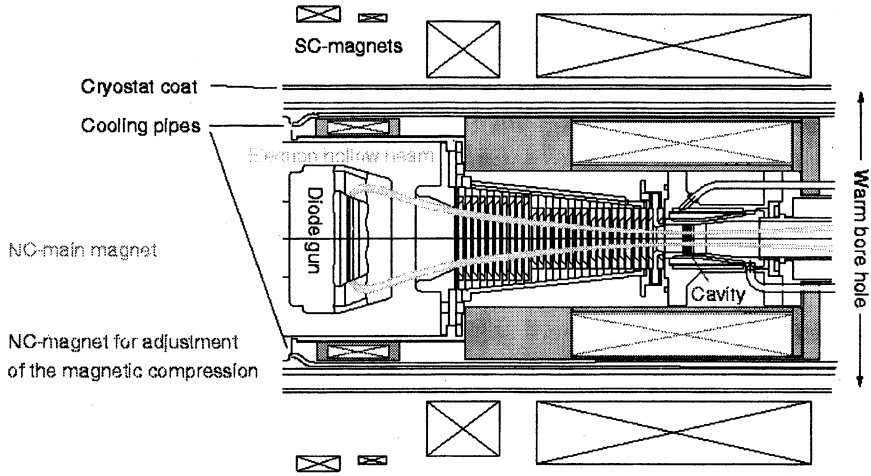

Fig. 9: Gyrotron hybrid magnet system consisting of 4 sc-coils in a cryostat and 2 nc-coils inside the warm bore hole.

In other words, for practical applications the frequency should be changed by a factor 25 faster than is possible with the superconducting magnet system at FZK. To fulfil these demands different hybrid magnet systems including one or several tunable normal conducting solenoids are under investigation [13]. The most promising one is shown in Fig. 9. Important for the fast-tuning experiment is the fact that the counterinduction voltage of the sc-magnets is limited at their power supplies. At FZK different experiments with a normal conducting test-magnet inside the warm bore hole of a superconducting solenoid system have shown that about 1 *s* after a *B*-field variation of 0.25 T the field stability for gyrotron operation would be sufficient. With the estimated $B_{max} = \pm 0.3$ T of the nc-solenoids a maximal possible frequency variation of ±7.5 GHz is expected. With this design the demanded value of several GHz/s is achievable. As is evident from Table I, this would result in jumping from the central mode $TE_{22,6}$ down to $TE_{21,6}$ and $TE_{20,6}$ or up to $TE_{23,6}$ and $TE_{24,6}$.

It is interesting to estimate the needed variation of the accelerating voltage to obtain the same frequency tunability at a constant magnetic field B = 5.55 T. It follows from Eq. (2) that U should be increased to about 115 kV to excite oscillations of the $TE_{20,6}$ mode or decreased to about 50 kV to excite oscillations of the $TE_{24,6}$ mode. It is quite obvious

that in the latter case due to the lower voltage the output power of the gyrotron will be significantly lower. However for a gyrotron with a modulation electrode it is possible to reduce this power degradation by means of changing the modulation voltage at a constant accelerating voltage [13]. For such experiments a triode-type electron gun and sophisticated power supply units are needed.

9. Conclusions

The experiments performed at FZK using a conventional cylindrical cavity gyrotron already have convincingly demonstrated that a slow frequency tuning over a wide frequency band is possible, even at 1-1.5 MW power level. Similar experiments are currently being performed on the 1.5-2 MW coaxial cavity gyrotron at FZK. The possibilities of fast and superfast frequency tuning will be investigated in the nearest future.

Acknowledgments

The authors gratefully acknowledge the contributions of H. Baumgärtner, H. Budig, P. Grundel, H. Kunkel, W. Leonhardt, J. Szczesny, and R. Vincon of the gyrotron team technical staff for the mechanical design, the precise machining and the careful assembly of the tube as well as for their assistance during the experiments. The authors also wish to express their deep gratitude to Mrs. Klenk and Mrs. Mosbacher for their careful typing of this manuscript.

References

[1] Gaponov-Grekhov, A.V., Granatstein, V.L., Application of high-power microwaves, Artech House, Boston, London (1994).
[2] Thumm, M., Fusion Engineering and Design, **30**, 139 (1995).
[3] Makowski, M., IEEE Trans. Plasma Science, **PS-24**, 1023 (1996).
[4] Erckmann, V., et al., IEEE Trans. Plasma Science, **PS-27**, 538 (1999).
[5] Zohm, H., et al., Nuclear Fusion, **39**, 577 (1999).
[6] Dumbrajs, O., RAU Scientific Reports. Computer Modeling of New Technologies **2**, 66 (1998).
[7] Braz, O., et al., Int. J. Infrared and Millimeter Waves, **18**, 1465 (1997).

[8] Dammertz, G., et al., IEEE Trans. Plasma Science, **PS-27**, 330 (1999).

[9] Möbius, A., Thumm, M.,Gyrotron output launchers and output tapers, in Gyrotron Oscillators, C. Edgcombe, ed., Taylor & Francis, London, Chapter **7**, 179 (1993).

[10] Thumm, M., Proc. 21st Int. Conf. Infrared and Millimeter Waves, Berlin, (1996), AT6.

[11] Piosczyk, B., et al., IEEE Trans. Plasma Science, **PS-24**, 579 (1996).

[12] Thumm, M., Proc. Radio Frequency Workshop (RF98), High Energy Density Microwaves,Pajaro Dunes, California, USA, AIP Conference Proceedings **474**, 146 (1998).

[13] Koppenburg, K., et al., Proc. 23rd Int. Conf. Infrared and Millimeter Waves, Colchester, UK, 124 (1998).

DEVELOPMENT OF 1-MW LONG-PULSE/ CW GYROTRONS IN 110–170 GHz FREQUENCY RANGE

V.E. Myasnikov, M.V. Agapova, V.O. Nichiporenko, L.G. Popov, S.V. Usachev, V.N. Iljin, V.A. Khmara, A.G. Litvak, G.G. Denisov, V.E. Zapevalov, V.A. Flyagin, A.Sh. Fix, V.V. Alikaev, V.I. Iljin

GYCOM Ltd., 46 Ulyanov St., Nizhny Novgorod, 603600, RUSSIA

The given paper represents the review of modern experimental results, design features and perspectives of GYCOM gyrotrons further development.

110 GHz and 140 GHz GYCOM gyrotrons are used as sources of electron cyclotron resonance heating (ECRH) of plasma on DIII-D tokamak (General Atomic, USA), TdeV tokamak (CCFM, Canada) W7-AX stellarator, ASDEX Upgrade tokamak (both IPP, Germany). 170 GHz gyrotron is developed for the ITER project.

110-GHz gyrotrons are characterized with the power levels of ~900 kW for 2-s pulse length and 500 kW for 5-s pulse length. In 140-GHz gyrotron power levels of ~900 kW for 1-s pulse length, ~650 kW in 2-s pulses and ~550 kW 3-s pulses are available. In the first 170 GHz gyrotron experimental sample the power of 1 MW at 32 % efficiency for 1-s pulse length and 500 kW in 5-s pulses was reached. Advanced 170 GHz gyrotron with depressed collector delivered 630 kW power at efficiency of 46 %.

At the same time, gyrotrons with 1 MW output power and 50 % efficiency in a CW regime should be developed according to request of ITER and programs of modernization for existing installations.

Design and main gyrotron parameters

The gyrotron design was developed in the end of 1993 initially for 140 GHz tube with output power 500–550 kW for 3-s pulse length.

More powerful gyrotrons at frequencies 110 – 170 GHz [1, 2, 3, 4] were created later basing on the same design.

The overall scheme of gyrotron is shown in Fig. 1. As it is shown on the scheme, a gyrotron consists from electron gun, cavity, mode converter, collector and vacuum window. Main features of these units within the existing gyrotron design and their necessary modifications for 1-MW CW gyrotron creation will be described below.

Cavity

The $TE_{19\,5}$, $TE_{22.6}$, $TE_{25.10}$ modes were chosen as operating ones for 110 GHz, 140 GHz and 170 GHz gyrotrons correspondingly. For a cavity maximal ohmic losses of about 1.8–2.2 kW/cm^2 at 1 MW power level a temperature on a wall internal surface does not exceed 250 °C.

This is provided by a cooling system design with the water flow of about 40 l/min at the pressure drop of about 4 bar. The measured frequency drift during 2-s pulse length due to cavity heating does not exceed 50 MHz.

Thus, basing on the calculation and test results, cavity present design can be used for CW regime.

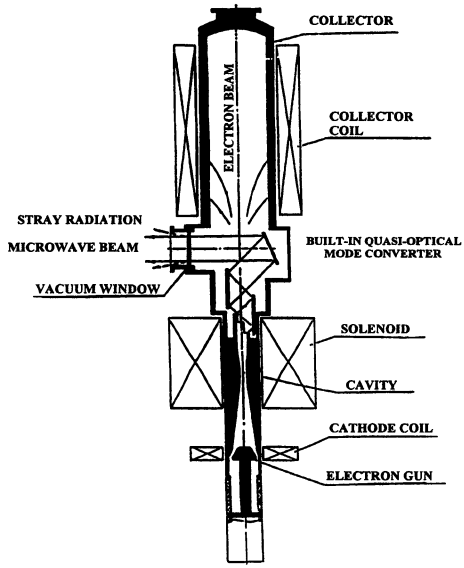

Fig. 1. Gyrotron overall scheme

Electron gun

The electron diode gun was used to form hollow electron beam with current of 25–40 A, pitch factor of about 1.3 and electron velocity spread not more than 40 % at a voltage of 70–80 kV.

The electron beam is produced by metal-porous cathode with operation temperature of 1050 °C. The width of emitter is 5 mm, average diameter is 83 mm and the current density is (3–5) A/cm^2 at operational regime.

Gun calculated parameters depend largely on space homogeneity and stability of cathode properties. Emission current inhomogeneity is checked during gyrotron assembling and conditioning. It should not exceed 20 %.

The work on improvement of emitter material properties is now conducting aiming in emission time stability and azimuthal homogeneity. It will allow to increase efficiency and to ensure a gyrotrons operation stability during pulse extension up to continuous regime.

Output window

The single-disk boron nitride (BN) output window with edge water-cooling was used. The thermal conductivity of boron nitride is insufficient to take away the heat deposited inside the disk at 1 MW power level. Window temperature in this case is determined by a power density and the material heat capacity. Allowable window temperature which was considered to be of about 1000 °C was the main restriction for the gyrotrons pulse extension. To reduce maximal window temperature one forms power quasi-uniform distribution over the disk

surface. The BN window diameter of 120–145 mm is optimal to pass maximal power at acceptable wave beam parameters.

New kind of window, based on recently developed CVD diamond disk, is capable to provide gyrotron CW operation due to material low losses and high heat conductivity. Taking into accounts the diamond disk price and beam forming resources one should consider the disk diameter of 60–70 mm as an optimal size. Diamond window is installed in advanced 170 GHz gyrotron, which is under testing now.

Mode converter

Quasi-optical (QO) mode converter is an important part of gyrotron internal electrodynamic system. It allows to separate a microwave radiation from a worked-out electron beam, to transform a cavity mode to linearly polarized narrow-directed wave beam and to minimize gyrotron reaction on rf-power reflection.

Wave beam formed by QO converter should have the highest content of main Gaussian mode, which is the most convenient for coupling with external waveguide. To create quasi-uniform power distribution over BN disk some fraction of higher order Gaussian mode had to be exited too. Built-in QO converter consisting of irradiator and three beam-forming mirrors created necessary power distribution over the window surface with Gaussian mode content of 0.85–0.9 % and diffraction losses of 8–10 %.

Due to its high capacity, CVD diamond disk can withstand power propagating in a pure main Gaussian mode. QO converter for 170 GHz gyrotron with diamond window has been modified. It consists of irradiator and four beam-forming mirrors creating Gaussian power distribution over the window surface. Diffraction losses inside gyrotron are about 6–8 %.

Collector

The collector has to withstand (1,5–2) MW spent electron beam, depending on the interaction efficiency. Therefore, the surface should be large enough and intensively cooled. There are two ways to spread electron beam over the collector surface. While using static magnetic field collector diameter should be chosen as large as about 600 mm. Collector of this size is not convenient for manufacturing and meets large problem under influence of even weak stray magnetic field. In described design 240-mm diameter collector is equipped with special coil for sweeping an electron beam along the axis. The collector length is about 800 mm. The characteristic growth and fall times for our collector

coil are 150–200 ms and 50–100 ms, accordingly. A maximum heat load averaged for period does not exceed, as a rule, 0,7 kW/cm^2 at electron beam power of (1,5–1,8) MW. Pulse temperature of inner surface reaches stationary value during ~1 s. It does not exceed 260–290 °C.

The priority aim for improvement of gyrotron base design is the use of depressed collector with reduced power deposition. The advanced 170 GHz gyrotron is equipped with depressed collector. This gyrotron installed in testing bed is shown in Fig. 2.

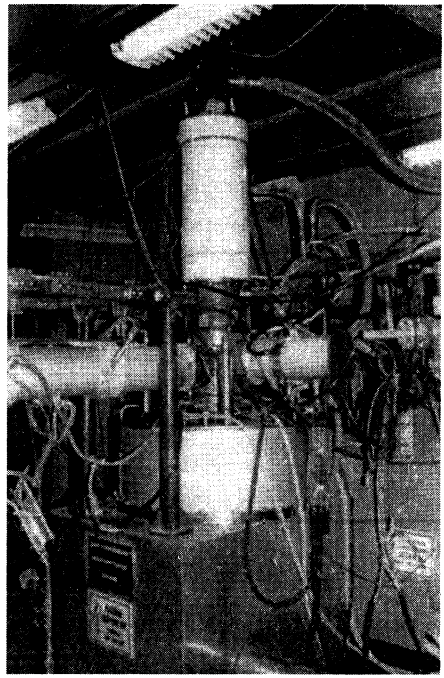

Fig. 2. The advanced 170 GHz gyrotron with depressed collector

Test results

Produced gyrotrons are operated with megawatt power level and 1–2 s pulse duration, which is limited by single-disk BN window capacity. To check capability of operation in longer pulse gyrotron with a dual rf-beam output was developed on basis of 140 GHz tube [5] and tested. To form two wave beams a new quasi-optical converter has been created. The corrugated mirror was used for splitting wave beam in to two parts and then two additional mirrors formed parallel rf-beams with equal polarization.

Gyrotrons test data characterizing the reached limit combinations of output power levels and pulse length are listed below.

170 GHz gyrotron with BN window and depressed collector delivered output power of 650–800 kW at efficiency up to 46 %. Pulse length was limited at the level of 1 s by BN window capacity. At present time the gyrotron is equipped with diamond window and the next stage of test is carrying out. The aim is to increase pulse length up to 10–20 s.

Frequency, GHz	Power, kW	Efficiency, %	Pulse length, s
110	930	38-42	2.0
	500		5.0
	330		10.0
140	960	38-42	1.2
	650		2.5
	550		3.0
	260		10.0
	100		80.0
design with dual-beam output	740	30	3.0
	600		5.5
	330		10.0
170			
design without depressed	1000	32	1.0
collector	500		5.0
	270		10.0
design with depress collector	630	46	1.0

Conclusion

On the basis of common design megawatt power level gyrotrons in a frequency range of 110–170 GHz with pulse length of 1–3 s are developed. They are used in research installations of controlled fusion.

The constant update of these installations and an increase of interest to ECRH, as an effective method of plasma diagnostics and monitoring, presents growing requests to used gyrotrons. Already in near future they should work at 1MW power level with pulse length of 10 s, and in the perspective (ITER program) – in continuous regime. Granting these requests the base gyrotron design is improved permanently.

References

1. Myasnikov V.E., et al. Megawatt power long-pulse 140 GHz gyrotron, 21st Int. Conf. on IR&MM Waves. 1996.
2. Myasnikov V.E., et al. Megawatt power level long-pulses 110 GHz and 140 GHz gyrotrons, Strong microwaves in plasma, Proceedings of the International workshop. 1997.
3. Myasnikov V.E., et al. Long-pulse operation of 110 GHz/ 1 MW gyrotron, 22nd Int. Conf. on IR&MM Waves. 1997.
4. Myasnikov V.E., et al. Long-pulse operation of 170 GHz/ 1 MW gyrotron for ITER, 23rd Int. Conf. on IR&MM Waves. 1998.
5. Myasnikov V.E., et al. Development of 140 GHz/ 1 MW gyrotron with a dual RF beam output, 23rd Int. Conf. on IR&MM Waves. 1998.

DEVELOPMENT OF ECRF COMPONENTS AND SYSTEM FOR ITER AND JT-60U TOKAMAK

T. Fujii, T. Imai

Naka Fusion Research Establishment
Japan Atomic Energy Research Institute, Naka, Japan

Recent progress of the JAERI ECRF development is described. The ITER prototype gyrotron with the CVD diamond window has achieved the results of 520kW/6s and 450kW/8s operations at 170GHz. The results have shown the diamond window has capability to deliver more than 1MW at 170GHz. The technology has applied to the 110GHz gyrotron for JT-60U. It has also been operated successfully delivering 1.0MW/0.6s and 0.3MW/5s. The CVD diamond window has enabled the simple Gaussian output from the gyrotron, which has brought the high transmission efficiency. The power of 0.7MW/0.6s and 0.25MW/5s was successfully injected to JT-60U plasmas in the initial operation and the remarkable on-axis heating (ΔT_{e0}~ 2.5keV) and the off-axis heating were observed as expected.

1. Introduction

An Electron Cyclotron Wave is a key tool for heating, current drive and plasma control of a tokamak fusion reactor. Many ECRH and ECCD experiments have started to be carried out, since the ECRF system has great advantages from a reactor point of view. In addition, ECCD seems to be a unique tool for the suppression of the neo-classical tearing mode, which is essential for high beta operation in a tokamak fusion reactor.

The most critical issue of the ECRF system in International Thermonuclear Experimental Reactor (ITER) is a gyrotron. The ITER requires ~50MW ECRF power injection to plasmas for heating and current drive. A major milestone of the ITER gyrotron development is 1MW, CW with 50% efficiency at 170GHz. The development has been done for about four years. There are several key points to develop the ITER gyrotron. The first is the development of high order volume mode cavity, which enables the 1MW power generation in CW at allowable RF dissipation on the cavity. This was done successfully and the output of 1MW was obtained using TE31,8 mode [1]. Energy recovery system to enhance efficiency of the gyrotron had already been demonstrated at 110GHz [2]. The final key element is an output window, which always limits the output power and pulse length of recent gyrotrons. Several candidates to overcome this have been tried. Chemical Vapor Deposition (CVD) diamond appears to be most promising for this purpose [3]. These technologies are also applied to the 110GHz gyrotron for JT-60U.

The second issue of the R&D is a 1MW transmissible torus window which is a tritium barrier as well. The CVD diamond window showed the 1MW capability as a gyrotron window, but it is necessary to demonstrate the high tolerance against the abnormal pressure in case of ICE (Ingress of coolant event) / LOVA (Loss of vacuum event). If the window is strong enough, it can be a passive barrier for the tritium confinement. The third issue is to develop high efficiency and high power transmission line. The diamond window does also contribute to this purpose.

The final issue is the real application of the ECRF power to the plasma. A 1MW 110GHz ECRF system was constructed to demonstrate the availability of these technologies on JT-60U. The initial results of the ECRF power injection to the JT-60U plasmas are described, too.

2. Gyrotron Developments

A high volume mode cavity gyrotron is necessary to output 1MW, CW at 170GHz for ITER. A short pulse without a mode converter was fabricated to study oscillation stability. The conventional cylindrical cavity and $TE_{31,8}$ mode were selected from the design consideration. The second ITER prototype gyrotron, which had $TE_{31,8}$ cavity, had been tested but the output was limited to 500kW/0.7s, because of the temperature increase of the sapphire or Si_3N_4 windows [4]. The development of a new window to solve this point was carried out with synthetic CVD diamond. The diamond has extremely high thermal conductivity (~2000W/mK) and low dielectric loss tangent ($1x10^{-4}$-$2x10^{-5}$) in a mm wave range, which are ideal performance for the gyrotron window.

Using the JAERI test stand, the 110kW/10s RF was transmitted through the diamond disk (~100mm in diameter, 2.2mm in thickness) whose configuration is the single disk type with peripheral water-cooling structure. The development of this novel window using the synthetic diamond was succeeded [3]. Based on this successful result, the world's first gyrotron, to which the CVD diamond window was installed, was rebuilt using the second prototype. By using the diamond for the window, RF transmission power capability of the window in CW operation increased from 0.2MW (conventional windows) to larger than 1MW.

The picture of the 170GHz gyrotron with the diamond window is shown in Fig.1 (left-hand side). The gyrotron was the same as the second prototype except the window and correspondingly the final mirror. Then, the design values are the same as the previous one [5]. The conceptual

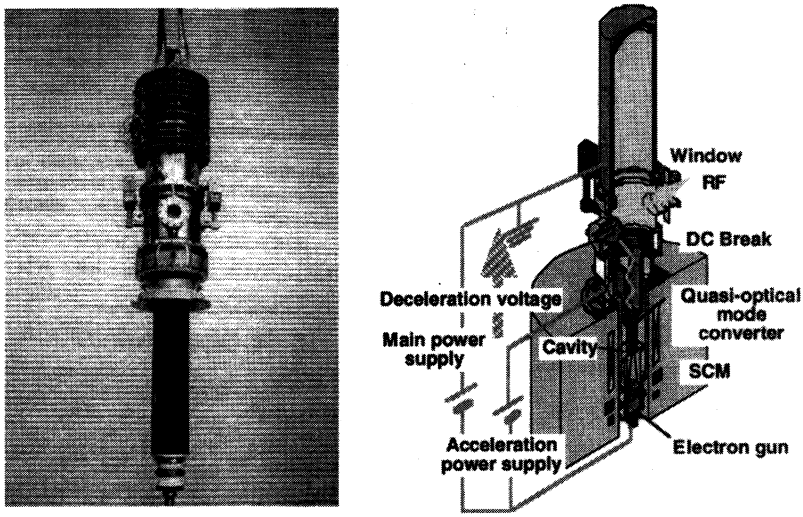

Fig.1 World's first diamond window gyrotron, which delivered the output of 450kW/8s at 170GHz and conceptual view of the gyrotron (right-hand side).

view of the gyrotron in collector potential depression (CPD) operation is also shown in Fig.1 (right-hand side). The lower part of the gyrotron is inserted into the super conductor magnet of 7T. The electron beam voltage V_b is supplied by the acceleration power supply. The power of the electron beam is supplied by main power supply V_c. The voltage difference appears between collector and body sections, which are insulated with ceramic. This difference enables the energy recovery from the spent electron beam and the gyrotron efficiency is improved by V_b/V_c.

The gyrotron experiment was carried out at the JAERI test stand, which has acceleration and main power supplies both with the 100kV capability [6]. The maximum current of the former is 0.3A and the latter is 50A. After the quick conditioning of the gyrotron, the pulse length gradually extended and reached to 6.2s with the output power of 0.52MW, where the beam voltage was 84kV and the beam current was 31A. The efficiency was 32% with a depressed collector. The efficiency is lower than the expected value. The degradation of the efficiency appears to come from the parasitic oscillation and/or unexpected modes generated around the cavity. The detailed studies are underway.

Temperature increase of the window at the power of 500kW is shown in Fig.2. The dielectric loss tangent of the diamond disk in this gyrotron

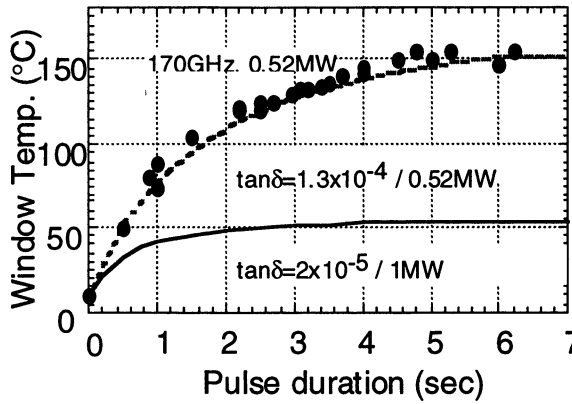

Fig.2 Temperature increase of the window center (closed circle) as a function of the pulse length. The dotted line is the simulation assumed heat transfer coefficient of 20kW/(m^{2}K). Thermal conductivity is 1800W/(mK) at 300K and linearly decrease with temperature to 1070W/(mK) at 500K. The solid line is also the simulation result (tanδ=2x10^{-5}, 1MW, Gaussian beam).

is relatively high as tanδ~1.3x10^{-4} and the temperature of the window center increased up to ~150°C. It, however, is almost thermally equilibrated after ~5s, which agrees well with the simulation (dotted line). If the high quality diamond disk whose tanδ is 2x10^{-5}, which was already developed, was used, the temperature increase at 1MW transmission with the Gaussian beam would be only 30°C. Number of operations (longer than 1s) is shown in Fig.3. The total shot number and the total output

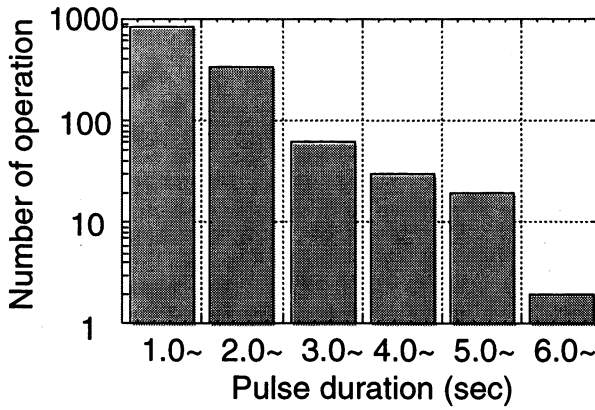

Fig.3 Number of operations at 0.52 MW.

energy were 1300 and 1.8GJ, respectively. After the experiment, the window assembly was removed from the gyrotron. Both surfaces of the diamond disk were inspected, and neither damage nor trouble was recognized. The operation of 0.45MW/8s was also performed, which was the world record of output energy at 170GHz. The results have shown the diamond window has capability to transmit more than 1MW at 170GHz.

The third prototype with the CVD diamond window was designed and has been fabricated. Its designed values are shown in the table I. The

Table I.170GHz Gyrotron Specifications

Frequency	**170 GHz**
Power	**1.1 MW at 80kV, 45A**
Pulse duration	**CW**
Mode	**TE31,8**
Q-value	**2000**
Output mode	**Gaussian beam**
Window	**Diamond**
Length	**3 m**
Weight	**800 kg**

Table II.110GHz Gyrotron Specifications

Frequency	**110 GHz**
Power	**1.2 MW at 95kV, 50A**
Pulse duration	**5 s**
Mode	**TE22,6**
Q-value	**1300**
Output mode	**Gaussian beam**
Window	**Diamond**
Length	**3 m**
Weight	**800 kg**

output mode is the simple Gaussian profile since it was designed to install the diamond window from the start. The Q-value is the same as previous one. The entrance diameter of the cavity (upstream side) was reduced to prevent the power flow to the electron gun region. The lower part of the mode converter was also modified to reduce the parasitic oscillations. A high quality diamond disk with $\tan\delta \sim 2\times10^{-5}$ was used and the expected temperature increase was 30°C, as shown in Fig.2.

As an application of the ITER ECRF technology development, the $TE_{22,6}$ cavity gyrotron has been developed for JT-60U aiming the experiments for ITER physics R&D. The design parameters of 110GHz gyrotron is listed in the table II. Main feature is 1MW/5-10s with the Gaussian output profile, whose picture is shown in Fig.4. The results of 1.1MW/0.1s with the efficiency of 39% have been obtained up to now with short conditioning at the test stand. The CVD diamond window has enabled the simple Gaussian output from this gyrotron, too.

3. Window Development

The diamond window has excellent performance as the mm wave

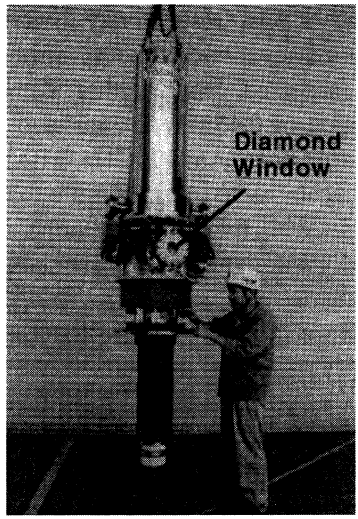

Fig. 4 The picture of the JT-60U gyrotron with diamond window.

window. It is natural to apply it to the torus window of the ECRF system. For safety requirement of FDR/ITER, the torus window must withstand pressure of 0.5MPa in case of the ICE/LOVA. The pressure test for a mock-up of the torus window assembly with a black diamond disk (aperture 71mm, thickness 0.8mm) was carried out to make the database of the diamond mechanical property for this purpose. The strain at the disk center gradually increased with pressure. The window disk failed at 0.47MPa in the plenum. The maximum stress at the aperture edge was estimated as 667MPa, which was consistent with its material strength [7]. It is expected that an actual torus diamond window could withstand 0.5MPa because of the margin in larger thickness and smaller diameter. Based on this data, the white diamond disk (optical grade) of the actual window size (aperture ~60mm) with the thickness of 2.25mm was tested up to 0.7MPa and the disk withstood at this pressure.

The torus diamond window was developed for JT-60U. The window was connected to two corrugated waveguides on both sides of the disk. The cooling channel was assembled to it and the window disk edge can be cooled by water. The thickness and the aperture of the window are 1.715mm and ϕ60.3mm, respectively. The window assembly is shown in Fig.5. The initial transmission test of HE11 mode at 110GHz was carried out. Transmission power of 0.6MW and the pulse duration of 0.3s were

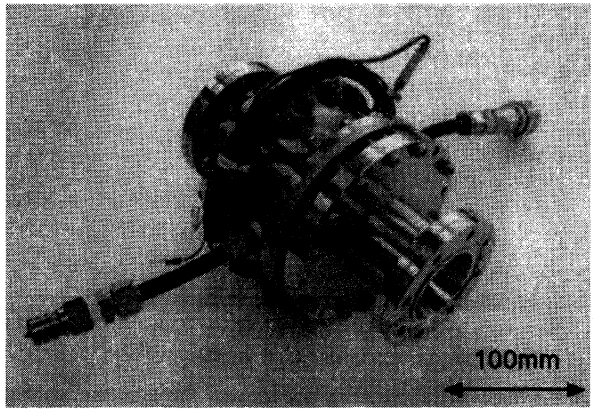

Fig. 5 Torus diamond window assembly.

demonstrated. The temperature increase at the window edge reached only 1.3K without water cooling, in good agreement with the simulation.

4. Transmission Line Development

The development of the high power and efficient transmission line for ITER/JT-60U ECRF system was carried out on the test transmission line. The diamond window also contributed to the improvement of the transmission performance, since it enabled the simple Gaussian output from the gyrotron and direct HE11 mode transmission through the torus window. For the first step, the frequency of 110GHz simulating the transmission line of the ECRF system for JT-60U was chosen. The inner diameter of 31.75mm transmission line was designed and constructed. The test line consisted of a mirror optics unit (MOU), corrugated waveguides, a waveguide switch, a pumping waveguide to evacuate the line, phase corrected miter bends, polarizers, directional coupler miter bends to monitor transmission power, and a dummy load as a termination. The total line length is about 40m. A Gaussian RF beam from the gyrotron coupled to the corrugated waveguide input via the MOU which had the capability to focus the beam and to control the beam axis. The waveguide transmission mode, HE11 mode was transmitted toward the dummy load with several reflections at the miter bends, the switch and the polarizers. High power and high efficient transmission was

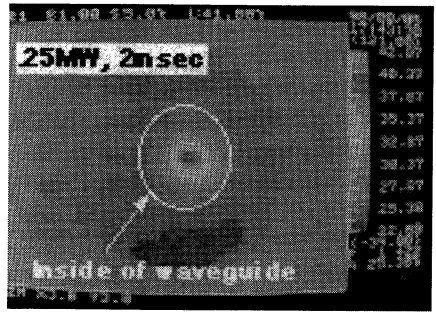

Fig. 6 Image of the transmitted power through the corrugated waveguide measured by the IR TV camera.

demonstrated with the test line. The transmission of 1MW/0.03s was performed and the transmitted power of 0.85MW was obtained at the end of the transmission line. The image of the transmitted power through the corrugated waveguide measured by the IR TV camera is shown in Fig.6. The peaked power density at the waveguide center was observed. It indicates that the transmission mode is mostly HE11 mode. The transmission efficiency of 89%, excluding the loss of 6% in the MOU, was obtained, which demonstrated the simple Gaussian output from the gyrotron quite well couples to the HE11 mode and then brings the high transmission efficiency. This result agrees with the estimated transmission efficiency of 90% from the loss estimation of each component. After the transmission test at the JAERI test stand, most of the components were used in the ECRF system for JT-60U [8].

5. Application to JT-60U Experiments

Based on the technology progress described in Sections 2-4, the ECRF system for JT-60U was constructed in March 1999 after one year from its start using the modified LHRF power supply for the CPD operation. The power of 0.7MW/0.6s and 0.25MW/5s was successfully injected to JT-60U plasmas in the initial operation, and the remarkable on-axis heating (ΔT_{e0}~2.5keV) and the off-axis heating, by controlling the RF beam angle with the steering mirror in the ECRF antenna, were observed as expected.

We intensively conducted the design study of the ECRF system and

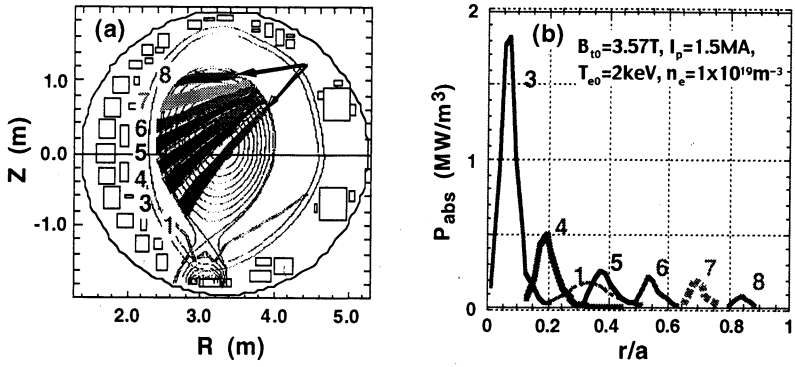

Fig. 7 Calculated deposition profiles for RF beam angles by the combined ray trace and Fokker-Planck code. (a) Plasma configuration and RF beam rays from the steering mirror. (b) Profiles of the absorbed power for the rays.

the numerical study on heating and current drive in JT60-U before starting of its construction [9-11]. Figure 7 shows the deposition profiles for RF beam angles calculated by the combined ray-trace and Fokker-Planck code [11], where the RF beam is poloidally changed by the steering mirror. The toroidal injection angle from the antenna is fixed at ~15° off-perpendicular direction of the optimum angle to obtain the most efficient current drive for the target plasma, B_{t0}=3.57T, I_p=1.5MA, T_{e0}=2keV, n_e=1x10^{19}m^{-3}. It is noted that a local control of heating and current drive is performed with injecting a fundamental O-mode from the low field side on JT-60U because the O-mode has no cut-off density and the X-mode has the cut-off density (~8x10^{18}m^{-3}). It, however, is predicted for relatively low densities (< ~5x10^{18}m^{-3}) that the O-mode is not much absorbed and rather the X-mode is well absorbed. Then we designed so as to provide a pair of polarizers for polarization control of the transmitted wave.

The specifications of the ECRF system for JT-60U are listed in Table III. In order to excite the fundamental O-mode by launching from the low field side (LFS) at the toroidal field of ~4T as mentioned above, the frequency of 110GHz was selected. The generated power is 1MW for 5s (objective 10s) by the developing 110GHz gyrotron with the diamond window in CPD as described in Section 2. Figure 8 shows an overview of the ECRF system for JT-60U. The output power of the gyrotron was guided into the MOU. Corrugated waveguides of the inner diameter of

Table III. Specifications of the ECRF system for JT-60U

Frequency	**110 GHz**
Generated Power	**1 MW**
Pulse Length (Objective)	**5 s (10 s)**
Number of RF Lines	**1**
Injection Mode	**O-mode from LFS**

31.75mm were aligned for a long transmission line in ~60m with five miter bends, two directional couplers, a waveguide switch, a pair of polarizers, a pumping waveguide and so on. The transmission line

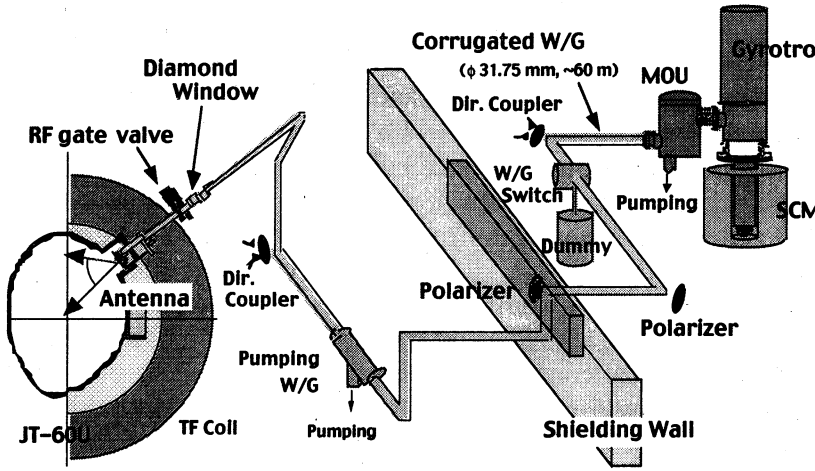

Fig. 8 Overview of the ECRF system for JT-60U.

was evacuated up to 10^{-4} Pa to suppress the RF breakdown in it. The torus diamond window was installed at the inlet of the antenna for a vacuum seal between the transmission line and the JT-60U vacuum vessel. The power transmission efficiency of the transmission line from the gyrotron to the antenna was estimated as 75% by calorimetric power measurement, including 6% power loss in the MOU as mentioned in Section 4.

An existing LHRF power supply was used as a main DC power supply of the gyrotron, and a solid state DC current switch and a beam

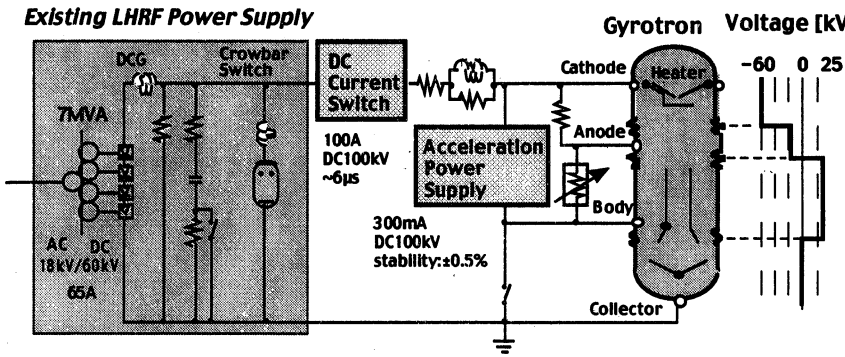

Fig. 9 Block diagram of the power supply system for the gyrotron CPD operation.

acceleration power supply were added to it in order to drive the gyrotron in the CPD operation, as shown in Fig.9. The DC current switch turns on/off the gyrotron oscillation within 10μs. The acceleration power supply gives the acceleration voltage up to 100kV, 300mA within a high stability of ±0.5% under the condition of the main DC voltage 60kV for the collector without regulation. The main DC voltage fluctuated about -15% in turn-on of the DC current switch. The gyrotron well oscillated in the CPD operation with the power supply system while the acceleration power supply was applied 10-20ms after the turn-on of the DC switch, where the DC voltage still fluctuated about -10%. It is noted that the power supply system well operates in the CPD operation even without regulation of the main DC supply, that is, with about 10% fluctuation.

The ECRF antenna was installed into the P17 port (upper, oblique port) together with other heating and current drive systems such as LHRF, ICRF and NBI systems on JT-60U, as shown in Figs.8 and 10. The ECRF antenna was composed by three lines, radiating the RF power quasi-optically, and each line consisted of two types of mirrors to focus and to control the RF beam in the poloidal direction and an corrugated waveguide (ϕ60.3mm, ~0.5m in length). Figure 11 shows the photograph of the front view of the antenna. Then, two more transmission lines can be connected to the antenna so that the antenna is designed to inject the power up to 3MW. The RF beam scan speed in the poloidal direction is about 50 degrees par 3s. Several thermocouples were provided to monitor the temperature increase for long pulse operation, especially on the mirror surface because it receives heat load from the plasma as well as

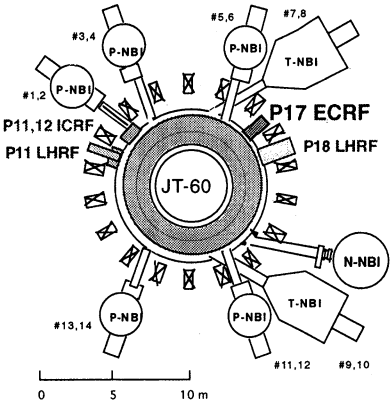

Fig. 10 Top view of the JT-60U and the ECRF antenna position.

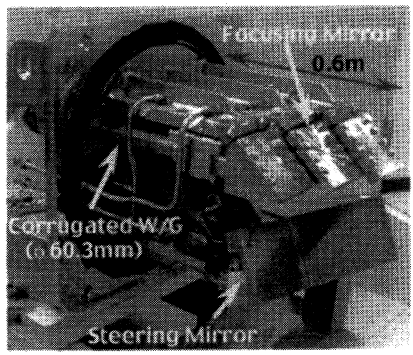

Fig. 11 Front view of the ECRF antenna.

the RF dissipation. The mirrors were made of stainless steel bonded diffusively with alumina dispersion strengthened copper, which is one of high heat resistive materials.

Up to now, the gyrotron has successfully generated the RF power 1MW for 0.5s and 0.3MW for 5s although the gyrotron is still under conditioning for high power, long pulse operation. In the initial operation for target plasmas of B_t=3.7T, I_p=1.5MA, n_e~0.6x10^{19}m^{-3}, the control of local electron heating was demonstrated by driving the steering mirror

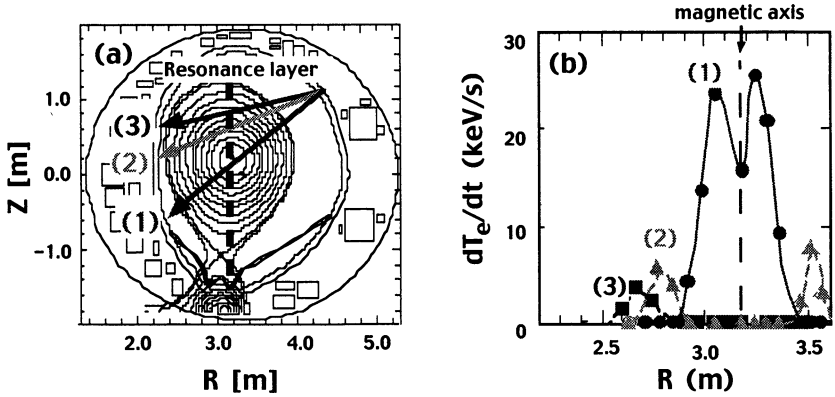

Fig.12 Control of the deposition profile by the steering mirror. (a) Plasma configuration and RF beam rays. (b) Profiles of the increase rate of the electron temperature measured by the ECE polychrometers.

poloidally. Figure 12 shows profiles of the increase rate of the electron temperature, dT_e/dt measured by the ECE polychrometers when the ray of the RF beam was changed from the plasma center to the plasma edge. The increase rate of T_e was evaluated by the average change in T_e at the first 10 ms of the RF injection. The width of the profile at half maximum is about 0.15m in all cases, which agrees roughly with the calculation results shown in Fig.7. Peaked electron heating was obtained, increasing the center electron temperature from 3keV to 5.5keV, when the RF beam was injected into the plasma center at the power of ~0.62MW for 0.3s. The driven current could not be estimated experimentally as it was quite smaller than the plasma current 1.5MA although the combined ray tracing and Fokker-Planck code showed that it was around 70kA for the plasma parameters of this injection. The detailed estimation of the driven current, however, will be done at next experimental campaign. The result of 5s ECRF injection at 0.25MW is shown in Fig.13. As the RF beam was radiated near the magnetic axis, the central electron temperature

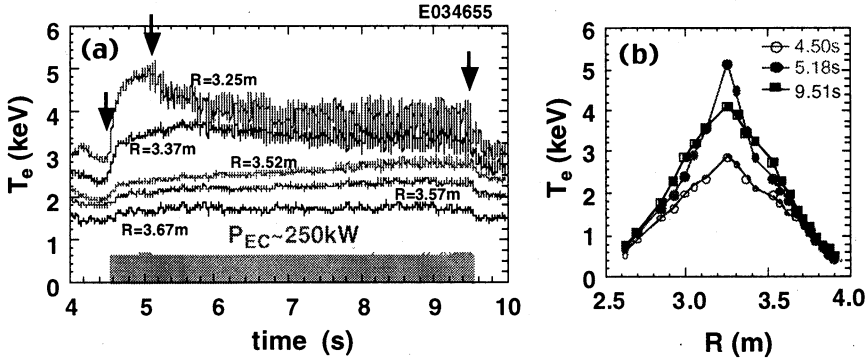

Fig.13 Changes in the electron temperature for the 5s ECRF injection measured by the ECE polychrometers. (a) Time evolution of the electron temperatures at the major radius R=3.25, 3.37, 3.52, 3.57, 3.67m. (b) Profiles of the electron temperature at t=4.50, 5.18, 9.51s.

increased from 2.9keV to 5.1keV, forming a sharp profile at n_e~$0.6x10^{19}m^{-3}$. The sawtooth oscillation took place at t=4.9s, 0.4s after the RF injection. The central electron temperature decreased from t=5.1s by the sawteeth, and the temperature profile was gradually broadening as shown in Fig.13. Based on these successful experiments, the upgrade of the ECRF system is planned from 1MW to 3MW of the generated power

by March, 2000 to intensively conduct ECRF experiments in JT-60U.

6. Conclusions

The ECRF development in JAERI was made great progress in recent years. The ITER prototype gyrotron with the CVD diamond window has achieved the results of 520kW/6s and 450kW/8s operations at 170GHz, which indicates the possibility of more than 1MW for ITER. The CVD diamond window withstanding up to the pressure 0.7MPa was developed to be used as a torus window. The CVD diamond window also has enabled the simple Gaussian output from the gyrotron, which has brought the high transmission efficiency. Indeed the transmission efficiency 75% was attained in the ECRF system for JT-60U. The ECRF system was successfully operated in March, 1999 after its construction of one year. In the initial operation, the remarkable on-axis heating (ΔT_{e0}~2.5keV) and the off-axis heating were observed in the power injection of 0.7MW/0.6s and 0.25MW/5s. Based on these successful operations and experiments, the upgrade of the ECRF system is planned from 1MW to 3MW of the generated power with three gyrotrons by March, 2000, constructing two more transmission lines.

Acknowledgements

The authors gratefully acknowledge Drs. K. Sakamoto, A. Kasugai, Y. Ikeda, S. Ide, and T. Hamamatsu for their valuable discussions and contributions. They would like to thank the members of RF Facility Division and RF Heating Laboratory who have contributed to these developments.

References

1. K. Sakamoto et al., J. Phys. Soc. Japan, 1996, **65**, 1888.
2. K. Sakamoto et al., Phys. Rev. Lett., 1994, **73**, 3532.
3. A. Kasugai et al, Rev. Sci. Inst., 1998, **69**, 2160.
4. K. Sakamoto et al., Rev. Sci. Inst., 1999, **70**, 208.
5. K. Sakamoto et al., Int. J. IR and Mmwaves,1997, vol18, No9, 1637.
6. M. Tsuneoka et al., Int. J. Electronics, 1999, **86**, 233.
7. K. Takahashi et al., Fusion Technology, 1998, Volume1, 415.
8. A. Kasugai et al., 13th Top. Conf. on Appl. RF Power to Plasmas, Annapolis, 1999.
9. Y. Ikeda et al., 17th IEEE/NPSS Symp. on Fusion Engineering, San Diego, 1997.
10. Y. Ikeda et al., 13th Top. Conf. on Appl. RF Power to Plasmas, Annapolis, 1999.
11. K. Hamamatsu, J. Plasma and Fusion Research, 1999, **75**, 143.

STATUS OF THE 1.5 MW, 165 GHz COAXIAL CAVITY GYROTRON

B.Piosczyk, O.Braz, G.Dammertz, M.Kuntze, G.Michel*, M.Thumm**

Forschungszentrum Karlsruhe, Association EURATOM-FZK, Institut für Hochleistungsimpuls- und Mikrowellentechnik (IHM),
D-76021 Karlsruhe, Germany; e-mail: bernhard.piosczyk@ihm.fzk.de
* also Universität Karlsruhe, Institut für Höchstfrequenztechnik und Elektronik,

Abstract

At 165 GHz an rf-power of 1.7 MW has been generated by the $TE_{31,17}$ coaxial cavity gyrotron with quasi-optical mode converter. For experiments on frequency step tuning the tube has been equipped with a Brewster window. In single mode operation 19 different modes have been excited with high power in a frequency range between 134 and 169.5 GHz. In all modes the rf-power was efficiently transmitted through the output window with only slightly varying rf-power distribution. For further investigations the main gyrotron components as electron gun, cavity and the mirrors of the quasi-optical mode converter have been redesigned, manufactured and assembled. RF-measurements started.

Introduction

A gyrotron with a coaxial cavity is under development at FZK Karlsruhe. The final goal of the development work is to prove the feasibility and to provide all necessary information for an industrial fabrication of a 2 MW, 170 GHz coaxial gyrotron being able to be operated at long pulses up to CW as required for ITER [1]. As a further goal the possibility of step frequency tuning by variation of the magnetic field is under investigation. Fast step frequency tuning with a frequency step of about 2 GHz over a range of up to about ± 7 GHz is of interest for suppressing MHD instabilities in fusion plasmas [2]. A slow variation of the microwave frequency from 90 up to 140 GHz is considered to be used for start-up procedure in ITER [1].

The investigations on the coaxial gyrotron at FZK have been performed up to now in several steps with encouraging results as has been reported in [3,4,5]. In those previous experiments an efficient rf-power generation has been demonstrated and the principal possibility of step-frequency tuning has been proved with a coaxial cavity gyrotron having an axial rf-output [3]. Recently the operation in the $TE_{-31\,17}$ design mode at 165 GHz has been investigated and step frequency tuning have been performed with the gyrotron equipped with a broad-band Brewster window. The results of these experiments are presented and discussed. An outlook for further steps of the investigations is given.

Set-up and performance of the experiments

The experimental set-up is as described in [5]. In order to be able to operate over a wide frequency range at negligible rf-reflections from the window plane, a

Brewster window out of SiN composite (Kyocera) with an effective diameter of 100 mm is employed which has already been used successfully in the conventional gyrotron [6]. The maximum magnetic field inside the cavity is limited by the capability of the utilized superconducting (sc) magnet to about 6.7 T. This restricts the operation on the high frequency side to values below 170 GHz. The frequency step tuning has been performed by a slow variation of the magnetic field of the sc-magnet. Both the magnetic field B_{cav} inside the cavity and in the cathode region B_{cath} have been adjusted independently allowing to vary the magnetic compression ratio $b = B_{cav}/B_{cath}$. The value b of the magnetic compression determines the electron beam radius R_b in the cavity approximately according to $R_b \cong R_c / b^{1/2}$ with R_c the radius of the emitter. The magnetron injection gun [7] is of diode type. Therefore the velocity ratio α is determined by the magnetic field B_{cav} inside the cavity and B_c around the gun as well as by the cathode voltage U_c and cannot be adjusted independently. The geometry of the cavity designed for operation at 165 GHz in the $TE_{-31,17}$-mode [3] is shown in Fig. 1. The high value of the quality factor Q = 3080 is due to the assumed parameters for operation (U_c = 74 kV, B_{cav} = 6.5 T) at that time [3]. The coaxial insert is down tapered with 1^0 and corrugated with a depth d = 0.45 mm corresponding to a coefficient of the impedance corrugation $w = (l/s)\tan(\chi d/R_0)$ = 10. The geometrical quantities l, s, d and R_0 are as defined in Fig. 1 and χ is the eigenvalue of the considered mode.

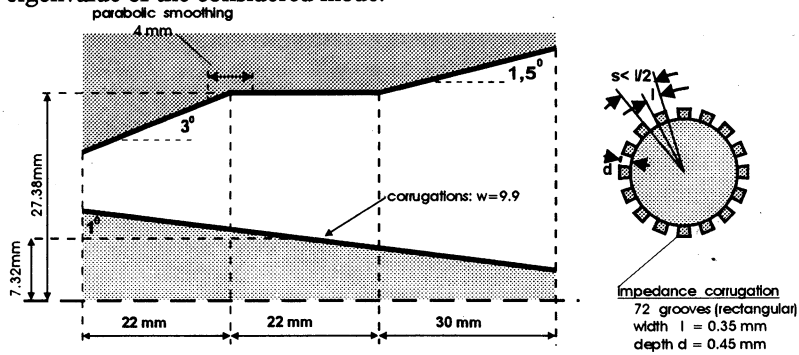

Fig. 1: Geometry of the $TE_{31,17}$ coaxial cavity with a radius R_0 = 27.38 mm.

The quasi-optical (q.o.) output system consists of a Vlasov launcher and two mirrors, one with a quasi-elliptic and the other with a non-quadratic phase correcting surface [8]. The rf-power is transmitted through a single output window. Its distribution has been measured with an infrared camera outside the window.

The measurements have been performed in general at pulses between 0.5 and 1 ms. In single pulses the pulse length has been extended up to several ms. The rf-frequency was measured with high accuracy with a time frequency analyzer. A filter bank enabled to observe if there was single or multi mode operation during a pulse. The rf-output power has been measured calorimetrically.

Operation in the 165 GHz, $TE_{31,17}$ - design mode

The $TE_{31,17}$ mode has been found to oscillate stably in single-mode operation over a wide range of operating parameters in good agreement with calculations. A maximum rf-output power of 1.7 MW at a beam current I_b = 69.7 A and a cathode voltage U_c = 93.2 kV has been achieved. A maximum output efficiency of 27.3 % has been measured at an output power of 1.3 MW with I_b=52.2 A at a magnetic field B_{cav} = 6.65 T. At an rf-power of 1.2 MW the output efficiency has been increased to 41 % in operation with a single-stage depressed collector. In Fig. 2 the experimentally achieved rf-power versus the beam current is shown. The operating parameters have been optimized for maximum rf-output power.

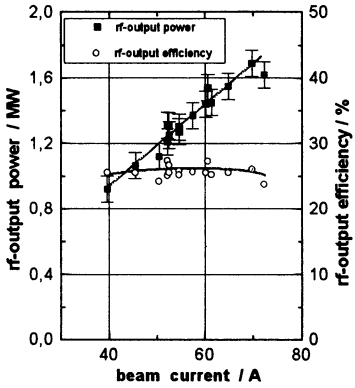

Fig.2: Rf-output power and efficiency vs. beam current

About 12 % of the generated rf-power are estimated to be lost inside the tube by Ohmic and diffraction losses and by absorption in the rf-output window. The measured values of the rf-power are in reasonable agreement with numerical calculations. Because of the high Q-value of the cavity overbunching occured at the operating parameters which prevented to achieve a higher efficiency.

Step frequency tuning

Measurements on step frequency tuning have been performed by slow variation of the magnetic field of the sc-magnet. Because of the limitation of the achievable value of the magnetic field to about 6.7 T, mainly modes with frequencies below the design mode could be excited. The $TE_{33,17}$-mode at 165 GHz is the excited mode with the highest frequency. Fig. 3 shows the rf-output power of 19 modes in the range between 134 and 169.5 GHz. The frequency spacing is $\leq$ 2.2 GHz. The beam current was kept approximately constant at $I_b \cong 50$ A. The cathode voltage U_c and the electron beam radius $R_b \propto 1/(b)^{1/2}$ have been adjusted independently in each mode. Due to the diode type gun no possibility of an independent

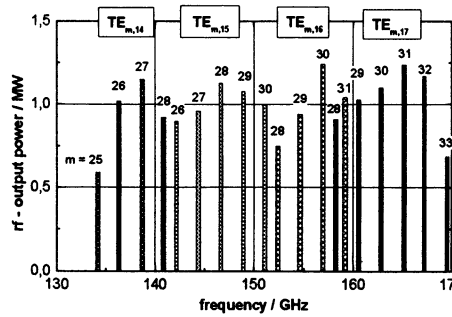

Fig.3: Excited rf-modes. $I_b \cong 50$ A, U_c, B_{cav} and R_b adjusted individually.

adjustment of the beam parameters, in particular of the velocity ratio α, exists. Therefore, in the experiments α varied between about 1.1 and 1.5 depending on the operating parameters. In the case of the $TE_{-33,17}$ mode the value of α was only about 0.9 because of the low maximum cathode voltage U_c = 75.6 kV as a consequence of the limitation of the maximum achievable value of B_{cav}. The excited modes belong to four $TE_{m,p}$-mode families with a different radial index p, namely $TE_{-m,14}$, $TE_{-m,15}$, $TE_{-m,16}$ and $TE_{-m,17}$. The modes have been identified by comparing the measured frequency with values calculated for the nominal cavity geometry (Fig. 1). For all observed modes an agreement within 200 MHz was found. Because of limited experimental time the operating parameters have not been optimized for maximum rf-output power in all modes. However, in the modes $TE_{-27,14}$, $TE_{-28,15}$, $TE_{-30,16}$, $TE_{-30,17}$, $TE_{-31,17}$ and $TE_{-32,17}$, for which a careful parameter optimization was done, an rf-output power between 1.1 and 1.3 MW with an efficiency of about 27 % has been achieved. This confirms the results of step frequency tuning performed with the conventional gyrotron [6]. The relatively low value of the rf-power in the $TE_{-33,17}$ mode at 169.5 GHz is due to the low operating cathode voltage.

Each mode excited by step frequency tuning in a gyrotron has in general a different caustic radius R_{caust}. The caustic radius corresponds approximately to the inner radius of the rf-field inside the cavity and is given for a $TE_{m,p}$ mode by: $R_{caust} = (m/\chi_{m,p}) \times R_0$. The indices m,p denote the azimuthal and radial numbers, respectively and $\chi_{m,p}$ is the eigenvalue of the $TE_{m,p}$ mode. R_0 means the radius of the cavity. Within a $TE_{m,p}$ mode family with constant p, R_{caust} is decreasing with the azimuthal index m. For a smaller caustic radius the rf-field is closer to the coaxial insert and viceversa. The geometry of the insert (radius and corrugation depth) has been optimized for the design mode with respect to mode competition and acceptable (< 0.1 kW/cm²) peak ohmic losses. For other modes with a different R_{caust} the situation of mode competition and the Ohmic losses change in general. In Fig. 4 the peak ohmic losses (for ideal copper at 293 K and normalized to 1 MW rf-power) at the insert are shown together with R_{caust} for modes of the $TE_{-m,17}$ family. Modes with a large R_{caust} as $TE_{-32,17}$ and $TE_{-33,17}$ have small peak ohmic losses (< 0.02 kW/cm²). In contrast the losses at the insert increase strongly in modes with small R_{caust}, e.g. in the $TE_{-28,17}$ mode with 0.3 kW/cm². From the technical point of view operation in modes with relatively large caustic radius is advantageous, since it keeps the loading at the insert within comfortable limits

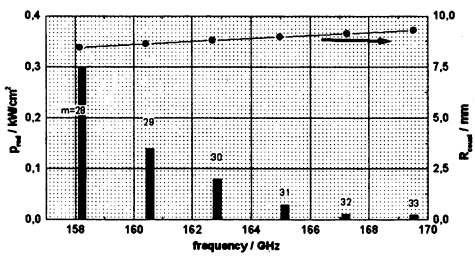

Fig.4: Losses at the insert normalized to an rf- power of 1 MW for $TE_{-m,17}$ – modes.

The situation of mode competition as it occurs for the different modes is demonstrated in Figs. 5a,b. In these figures the effective coupling between the electron beam and the rf-field, defined by the Q-value times the coupling coefficient, is shown for the modes $TE_{-31,17}$ and $TE_{-33,17}$ together with their neighbored modes. For calculation of the coupling between the electron beam and the rf-field the experimentally employed beam radius R_{bexp} has been taken. The coupling coefficient has been normalized to unity for the reference modes which are indicated in the graphs by (↓). All neighboring modes with a relative coupling < 0.7 have been neglected. In the case of the $TE_{-33,17}$ mode, which has a large caustic radius, the suppression of the nearest neighbors – $TE_{+30,18}$ and $TE_{+31,18}$ - is fairly weak compared with the situation in the $TE_{-31,17}$ design mode and its corresponding neighbors $TE_{+28,18}$ and $TE_{+29,18}$. In the experiment, however, stable single mode operation was still possible. From this it is expected that even operation in modes with larger caustic radius could be possible if at the optimum beam radius reasonable electron beam parameters could be adjusted by using a triode type electron gun. In further experiments the possibility of single mode operation limited by increased mode competition in modes with large R_{caust} will be investigated.

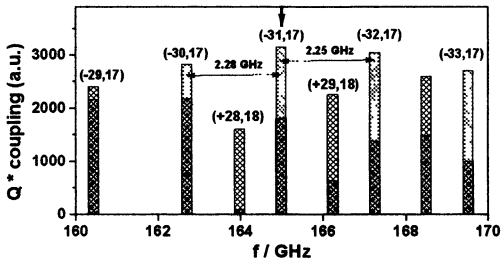

(a) : $TE_{-31,17}$ with R_{caust} = 8.97 mm

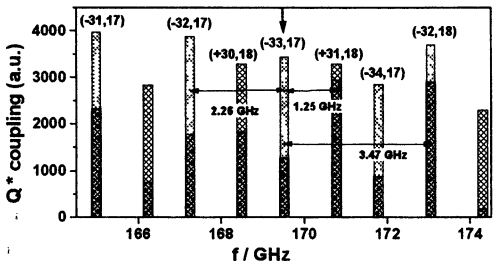

(b) : $TE_{-33,17}$ with R_{caust}=9.29 mm

Fig 5.: Coupling efficiency vs. frequency. Rotation (+,-) of dominating mode indicated.

Step frequency tuning over a large frequency range results in a big variation of the corrugation parameter w. For the performed frequency tuning w varies from 1.4 for the $TE_{25,14}$ at 134.1 GHz, (lowest measured mode) up to >10 for the $TE_{33,17}$ at 169.5 GHz. The value of the w - parameter influences the dependence of the eigenvalue $\chi_{m,p}$ along the z-axis inside the cavity which determines the Q-value of the operating mode and of its competitors [9]. For w-values below 1 the Q-value of a mode may increase very strongly and it has to be avoided as is discussed in [10]. Therefore the frequency step tuning over a wide range is limited approximately by the restriction $w \geq 1$. For the given cavity (Fig. 1) this results in a limitation on the low frequency side at around 122 GHz.

The power distribution of the rf-output beam has been observed by using an infrared camera. The measurements have been performed for all generated modes at the same plane at a radius 80 cm. In Fig.6 the rf-pattern of the mm-wave output beam is shown in a size of 5 x 5 cm^2. In all modes the generated rf-power is well transmitted through the window. The pattern of the rf-power is fairly the same and is in agreement with calculations [8]. The measurements prove that the employed q.o. output system with a non-quadratic phase correcting mirror has a fairly broad band frequency range.

Present activities

All redesigned components as electron gun, cavity with non-linear output taper and q.o.-output mirrors have been manufactured and assembled in the gyrotron tube. The electron gun is of conventional type with an adjustable and fully cooled coaxial insert. The cavity has been optimized for operation at 165 GHz with the expected parameters (B_{cav} = 6.65 T, U_c = 90 kV, α = 1.3, I_b = 50 A). The alignment of the insert has been performed and the reproducibility has been proved. The diffraction losses have been minimized in the mirror design. The rf-experiments are starting.

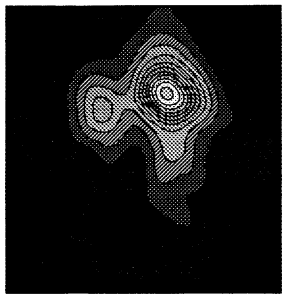

Fig.6: rf-power distribution

Summary and outlook

At 165 GHz a rf-ouput power of 1.7 MW has been achieved. In operation with a Brewster window 19 single modes with about 2.2 GHz frequency spacing have been generated in the range between 134 and 169.5 GHz with significant power. At present the coaxial gyrotron is equipped with redesigned components, electron gun, cavity and mirrors of the q.o. mode converter. The operation started with alignment of the coaxial insert and will be continued with rf-measurements.

References

[1] M. Makowski, IEEE Trans. Plasma Sci., **vol. 24,** pp. 1023-1032, 1996
[2] H. Zohm et al., Nuclear Fusion, **vol 39**, 1999.
[3] C.T. Iatrou et al., IEEE Trans. Plasma Sci., **vol. 25,** pp. 470-479, 1997
[4] B. Piosczyk et al., IEEE Trans. Plasma Sci., **vol.25,** pp. 460-469, 1997
[5] B. Piosczyk et al., IEEE Trans. Plasma Sci., **vol.27,** 1999
[6] G. Dammertz et al., IEEE Trans. Plasma Sci., **vol.27,** 1999
[7] V.K. Lygin et al., Int. J. Electronics, **vol. 79,2,** pp. 227-235, 1995
[8] G. Michel, et al., 24th Int. Conf. Infrared and Millimeter Waves, Sept. 6-10, 1999, Monterey, California, USA
[9] C.T. Iatrou, IEEE Trans. Plasma Sci., **vol.24,3**, pp. 596-605, 1996.
[10] C.T. Iatrou et al., IEEE Trans. Microwave Theory Tech., **44,1**, 1996.

OPTIMIZATION OF 80–170 GHz/1 MW GYROTRONS

V.E. Zapevalov, A.N. Kuftin, V.K. Lygin, M.A. Moiseev, N.A. Zavolsky

Institute of Applied Physics, Russian Academy of Sciences,
Nizhny Novgorod, Russia
GYCOM Ltd., Nizhny Novgorod, Russia

The report presents improved method and results of numerical simulation and experimental study of the possibility to optimize processes of mode interaction in the electron beam-cavity system for the 80–170 GHz/1 MW gyrotrons with different operating mode including the possibility for energy recovery (CPD-regime).

Introduction

Electron-cyclotron heating and current control in existing and planned plasma set-ups require gyrotrons with the level of CW power up to 1 MW and frequencies 80–170 GHz and efficiency not less than 40–50%. In the framework of such projects [1–3], from the preliminary analysis possible operating modes have been chosen and the general design concept of the gyrotrons has been developed (see table 1).

Table 1: Main parameters of 80–170 GHz/1 MW gyrotrons

Operating mode, TE	11.3	19.5	22.8	28.7	31.8	25.10
Operating frequency, GHz	83	110	140	170	170	170
Accelerating voltage, kV	70	80	80	80	80	80
Maximum beam current, A	45	45	45	45	45	45
Resonator radius, mm	12.35	16.65	17.94	15.86	17.9	17.77
Mean beam radius in resonator, mm	7.9	8.8	7.92	8.26	9.13	7.4
Resonator Q-factor/1000	0.76 (0.56)	1.1	1.2	1	1.1	1.1 (1.7)
Specific density of losses in cavity at 1MW output, kW/cm^2	2.4 (1.8)	2	1.8	2.5	2.1	1.9 (2.4)
Pitch-factor	1.5	1.4	1.3	1.25	1.25	1.25
Calculated maximum (electron) efficiency	0.5	0.46	0.43	0.4	0.4	0.4
Structure of output radiation	$TE_{11\,3}$	narrowly-directed wave beam				

The report presents improved method and results of numerical simulation and experimental study of the possibility to optimize processes of mode interaction in the electron beam-cavity system for the

80–170 GHz/1 MW gyrotrons with different operating mode including the possibility for energy recovery (CPD-regime) [4–7].

Numerical simulation

Stable single-mode generation in an oversized cavity at sufficiently high efficiency η and the megawatt level of output power P becomes an extremely complicated problem as the operating frequency grows [1–3, 8]. An essential circumstance here is, that this problem has to be solved within a number of limitations. The most difficult is the limitation on density of ohmic losses in cavity walls – energy removal is limited by possibilities of the cooling system, which are, as a rule, not higher than 2–3 kW/cm^2. For spatially developed modes conventionally used in gyrotrons at the cavity with the Gaussian field structure one can find the following estimate for efficiency depending on parameters

$$\eta \approx \eta_{\max}^{3/4} \cdot \frac{(1+g^2)^{1/4} \cdot \nu_s^{5/4} \cdot (\lambda^{5/2} P_{ohm})^{3/4}}{3 \cdot m^{1/4} \cdot U_0^{1/2} \cdot P^{1/2}} \qquad (1)$$

(where $\eta_{\max}$ is η at $I_0 = I_{0.\mathrm{opt}}$, λ is wavelength in millimeters, g –pitch factor, ν_s is the root of equation $J_m'(\nu_s) = 0$ corresponding to the considered mode $TE_{m.p}$ with azimuthal (m) and radial (p) indexes, and $J_m'(\nu)$ is argument derivative of Bessel function $J_m(\nu)$, P_{ohm}(kW/cm^2) is specific power of Ohmic losses in a cavity). It was taking into account Distinction of values of real Ohmic Q-factor and ideal one by 1.5–2 times was accepted. Results of numerical simulation for the detailed model of 170 GHz gyrotrons are shown in the fig. 1. Admissible values of m/p and R_0/R_r are limited by lower efficiency due to voltage depression and mode competition.

Effects of beam voltage depression and mode interaction as well as undesired mode conversion, methods of mode selection and energy recovery are taking into account and investigated also [8]. Fig. 2 shows the possibility of gyrotron efficiency improvements with single-stage depressed collector (CPD).

Experimental investigation of gyrotrons

Experimental investigation of short pulse prototypes of the 80–170 GHz gyrotrons were made on the automated set-up and dependencies of gyrotron parameters on the beam current, accelerating voltage and

magnetic field is analyzed. Magnetic system of the tube includes a main superconducting solenoid and a cathode coil for fine adjustment of electron beam parameters. All the gyrotrons uses the optimized magnetron injection guns, which forms a quasi-laminar helical beam [10].

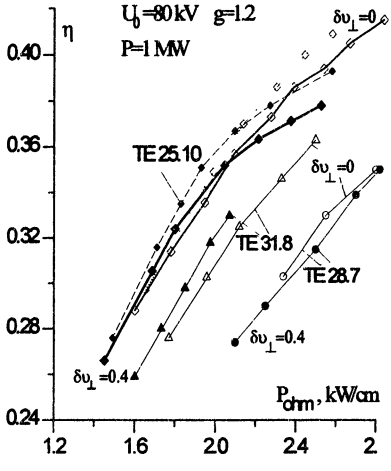

Fig. 1. Dependence of efficiency on specific power of Ohmic losses

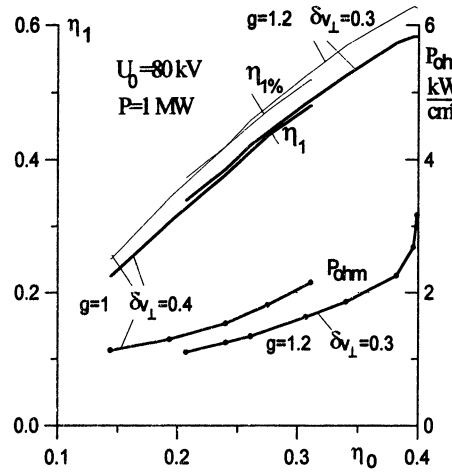

Fig. 2. Efficiency with CPD η_1, $\eta_{1\%}$ and P_{ohm} vs. cavity efficiency η_0

For 83 GHz experimental tube [1, 2] with the axial output which give us the possibility to check different solution for scientific and technical problem the $TE_{11,3}$ operating mode have been chosen. Fig. 3 shows output power and efficiency dependencies on the beam current for the $TE_{11,3}$ gyrotron. The output power level 1 MW was achieved at the $TE_{11,3}$ operating modes in design regime with efficiency 52%. The maximum output power near 1.5 MW with efficiency 36% was achieved at the operating mode [1, 2]. Fig. 4 shows the comparison of output power and efficiency dependencies on the beam current for two cavity versions of the $TE_{11,3}$ gyrotron [1, 2, 8] (see Table 1). The maximum efficiency 47% for the second cavity version (see Table 1) was achieved at the $TE_{11,3}$ operating mode with output power near 0.4–0.5 MW at the beam current near 12 A [8].

All the next experimental gyrotrons uses the optimized built-in quasioptical converter. The converter separates RF radiation from the worked-out electron beam, transforms a complicated cavity mode to an optimised wave beam and allows one to minimise harmful action of possible reflections of RF power back to the gyrotron.

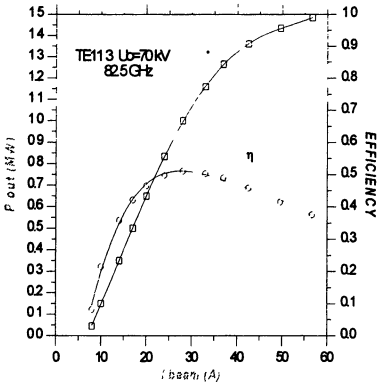

Fig. 3. Output power and efficiency vs. beam current for the $TE_{11,3}$ gyrotrons

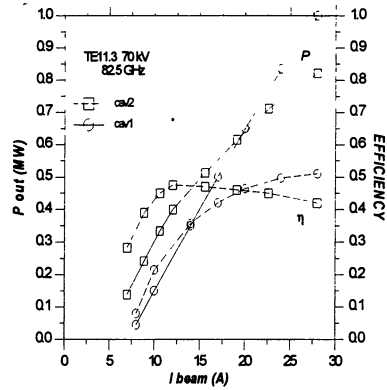

Fig. 4. Output power and efficiency vs. beam current for the $TE_{11,3}$ gyrotron

110 GHz high power experimental gyrotron using the $TE_{19.5}$ mode has been operated with a single-stage depressed collector (CPD) [7]. Measurements on a CPD with respect to the body current and the RF-output power in dependence of the retarding collector voltage are provided. Output power of 1 MW/0.05 ms is obtained at the beam parameters of 80 kV/30 A. The efficiency is 44% and the improved efficiency with single-stage depressed collector is 65%.

For the 140 GHz/1 MW experimental tube the $TE_{22.8}$ operating modes have been preferred. Fig. 5 shows output power and efficiency dependencies on the beam current of the $TE_{22.8}$ gyrotron. The output power level 1.0 MW was achieved at the $TE_{22.8}$ operating mode in design regime with efficiency 42%. The maximum output power near 1.7 MW with efficiency 42% was achieved at the beam parameter of 80 kV/50 A . The same $TE_{22.8}$ gyrotron has been used also with a single-stage depressed collector (CPD). Measurements of the RF-output power and efficiency in dependence on the retarding collector voltage were provided (fig. 6). Output power of 1.2 MW/0.1 ms was obtained at the beam parameters of 80 kV/35 A with efficiency 43%. The enhanced efficiency with single-stage depressed collector was near 70%.

Finally basing on the analysis of technical limitations the $TE_{28.7}$ and $TE_{25.10}$ operating modes have been chosen for 170 GHz experimental tube which give us the possibility to check different scientific and technical solution [11]. Fig. 7 shows output power and efficiency dependencies on the beam current for two cavity version of the $TE_{25.10}$ gyrotron (see Table 1). The output power level 1 MW was achieved at

the $TE_{28.7}$ and at two cavity version $TE_{25.10}$ operating modes in design regime with efficiency 32%, 34% and 38%, respectively. The maximum output power near 1.4 MW with efficiency 32% was achieved at the $TE_{25.10}$ operating mode. The same $TE_{25.10}$ gyrotron has been operated also with a single-stage depressed collector (CPD). Measurements of the RF-output power and efficiency in dependence on the retarding collector voltage were provided (fig. 8). Output power of 1 MW/0.1 ms was obtained at the beam parameters of 80 kV/(35–40) A. The improved efficiency with single-stage depressed collector was over 60%.

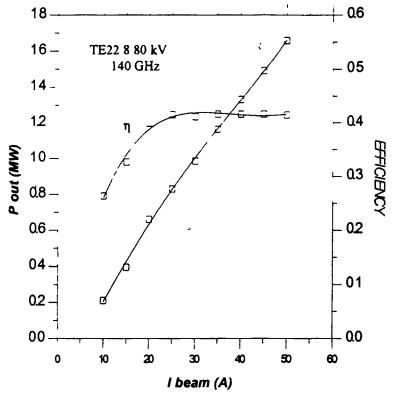

Fig. 5. Output power and efficiency vs. beam current for the $TE_{22,8}$ gyrotron

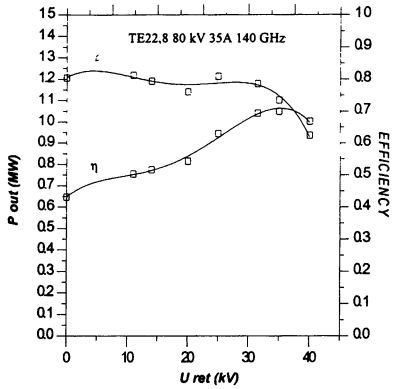

Fig. 6. Output power and efficiency vs. retarding voltage for the $TE_{22,8}$ gyrotron

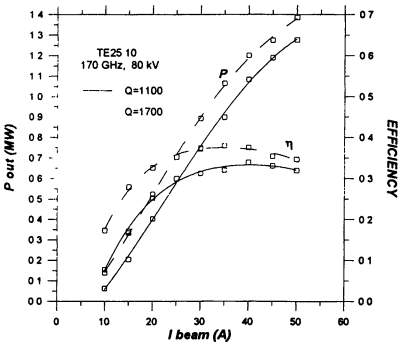

Fig. 7. Output power and efficiency vs. beam current for the $TE_{25,10}$ gyrotron

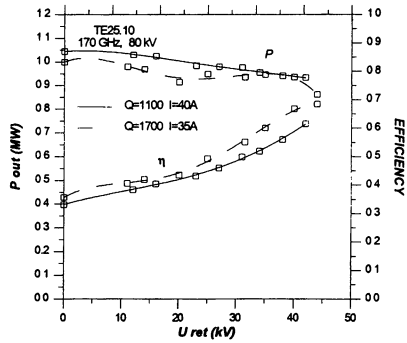

Fig. 8. Output power and efficiency vs. retarding voltage

Calculation and experimental data for short pulse gyrotron tubes are in a good correlation and were reproduced in the industrial long pulse tubes [12].

Conclusion

1. The possibility to make high efficient 80–170 GHz/1 MW gyrotrons for existing plasma set-ups and ITER is proved by calculations and experiments.

2. The data presented prove that in gyrotron for ITER it is possible to obtain single-frequency generation at the operating mode with output power 1 MW and efficiency 33–36% at pitch factor g = 1.2–1.4, velocity spread $\delta v_{\perp}$ = 0.2–0.4 and specific power of Ohmic losses in the cavity wall less than 2 kW/cm^2.

3. The use of a collector with single-stage recovery (CPD) makes efficiency by 1.6 times higher, up to 60–70%.

4. Calculation results and experimental data for the 80–170 GHz/1 MW gyrotrons are in good correlation.

References

1. Flyagin V.A., et al. Proc. of IAEA Technical Committee Meeting on ECE&ECRH at Hefei, China, 1989, 355.
2. Kuftin A.N., Zapevalov V.E. Proc. Of Int. Workshop Strong Microwaves in Plasmas, Suzdal, 1990, 726.
3. Denisov G.G., Flyagin V.A., Zapevalov V.E. Conf. Proc. 20 Int. Conf. on IR & MM waves. Orlando, USA. 197 (1995).
4. Sakamoto K., et al. Phys. Rev. Letters, 1994, V. 73, № 26. 3532.
5. Bratman V.L., Denisov G.G., Savilov A.V. Int. J. of IR and MM Waves, 1995, V.16, № 3. 459.
6. Goldenberg A.L., et al. Int. J. of IR and MM Waves, 1997, V. 18, № 1. 43.
7. Glyavin M.Yu., et al. Int. J. of IR and MM Waves, 1997, V. 18, № 11. 2129.
8. Zapevalov V.E. Proc. of III Int. Workshop Strong Microwaves in plasmas. Nizhny Novgorod, Russia, 1997. V. 2. 599.
9. Zapevalov V.E., et al. Izv. Vuzov, Radifizika, 1994. V. 37, № 3. 381.
10. Kuftin A.N., et al. Int. J. Electronics, 1992, **72**, 1145.
11. Zapevalov V.E., et al. Conf. Proc. 22 Int. Conf. on IR & MM waves. Wintergreen, USA. 1997. 108.
12. Mjasnikov V.E., et al. Proceedings International University Conference "Electronics and Radiophysics of Ultra-High Frequencies", 1999, St.Petersburg, Russia, St.Petersburg STU, 138.

70-140 GHZ 1 MW GYROTRONS ON THEIR WAY TO CW OPERATION

V.I.Kurbatov, S.A.Malygin, V.B.Orlov, E.A.Solujanova, E.M.Tai

Gycom Ltd, Nizhny Novgorod, Russia

Information about series produced and tested in GYCOM gyrotrons with collector power depression (CPD gyrotrons) at frequencies 70, 82.7, 84 and 140 GHz are presented. All output parameters are given as dependence on operating voltage and current and by the way of comparison between different tubes. The dynamic of movement to the 1 MW output power level in conditions of CW operation is considered. Special attention is given to the thermal loads in gyrotron units and the problem of there thermostabilization. Last cryomagnets characteristics are presented also.

INTRODUCTION

The developed CPD gyrotrons design (see Fig.1, 2) suppose the using of insulated anode-cavity block with positive potential to ground supplied by low power source, gyrotron body and collector are grounded. Cathode is supplied by high power source with negative potential to the ground. Such gyrotrons have relatively simple design. Most of them can be installed in the cryomagnet with warm bore diameter 140-160 mm. All tubes have about 35 kV anode from ground insulation and relatively free proportion between anode and cathode voltage value. It means that such type suppling scheme leads to the capability of output power modulation by anode low power supply.

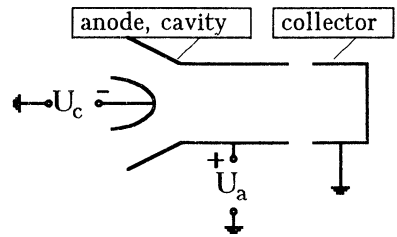

Fig.1. Supplying scheme of CPD gyrotron.

CPD GYROTRONS EXPERIMENTAL RESULTS

The series CPD gyrotrons was produced and tested at the period from 1996 to 1999. Below the experimental results with long pulse (up to 3 s)

gyrotrons will be presented. Besides, the perspectives of 1 MW power level at the CW operation regime achievement will be discussed. The main information about output power and efficiency dependencies on the beam current for presented gyrotrons is united in the Fig.3a,b. 140 GHz gyrotron was produced in 1996, 82.7 GHz - in 1997. 70 and 84 GHz are a new one, they was tested in 1999. 84 GHz tube is prototype of 1 MW CW gyrotron. The work under it improvement and investigation is continued. 70 and 82.7 GHz gyrotrons can be considered as about 650 kW power level, 140 GHz - as about 900 kW power level, where efficiency is 50 percent or even more.

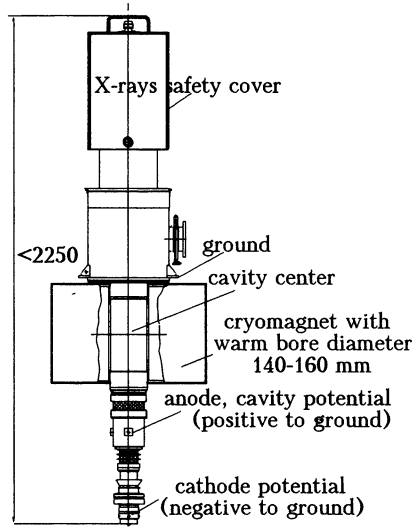

Fig.2. Set-up scheme of CPD gyrotron.

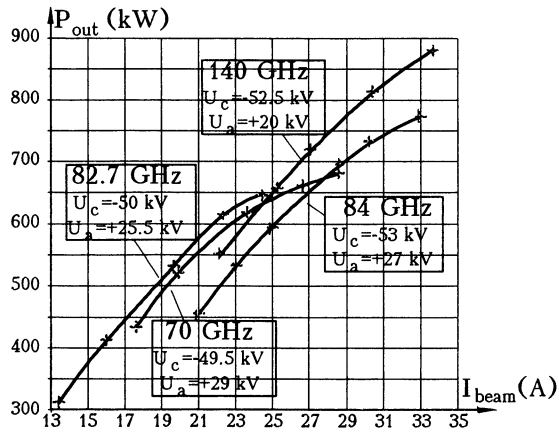

Fig.3a. Output power P_{out} dependencies on the beam current I_{beam}.

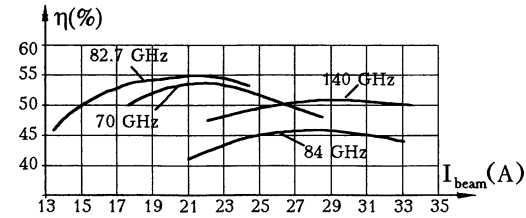

Fig.3b. Efficiency η dependencies on the beam current I_{beam}.

Experimental regimes with maximum power and efficiency separately are presented at the tables 1, 2. The 84 GHz gyrotron maximum power was obtained at the total beam voltage risen up to 87.5 kV, in this case gyrotron operates quite reliable. Maximum deepness of depression and accordingly - gain of efficiency in comparison with depression absence version took place in the 70 GHz tube. 55% efficiency in 82.7 GHz case was obtained also due to the high "natural" efficiency of it's prototype without depressed collector.

Table 1. Experimental regimes with maximum output power.

	70 GHz	82.7 GHz	84 GHz	140 GHz
Total beam voltage U_{beam}	78.5 kV	75.5 kV	87.5 kV	72.5 kV
Cathode voltage U_{cath}	-49.5 kV	-50 kV	-60 kV	-52.5 kV
Beam current I_{beam}	28.5 A	24.5 A	31 A	33.5 A
Output power P_{out}	680 kW	650 kW	875 kW	880 kW
Efficiency η	48 %	53 %	47 %	50 %
Pulse duration τ	3 s	3 s	2 s	1 s

Table 2. Experimental regimes with maximum efficiency.

	70 GHz	82.7 GHz	84 GHz	140 GHz
Total beam voltage U_{beam}	78.5 kV	75.5 kV	82 kV	72.5 kV
Cathode voltage U_{cath}	-49.5 kV	-50 kV	-53 kV	-52.5 kV
Beam current I_{beam}	22 A	21.5 A	28.5 A	29.5 A
Output power P_{out}	583 kW	591 kW	745 kW	790 kW
Efficiency η	53.5 %	55 %	49.3 %	51 %
Pulse duration τ	3 s	3 s	2 s	1 s

Gyrotrons have typical possibility of power modulation by anode voltage, which is illustrated by the graphs at Fig.4.

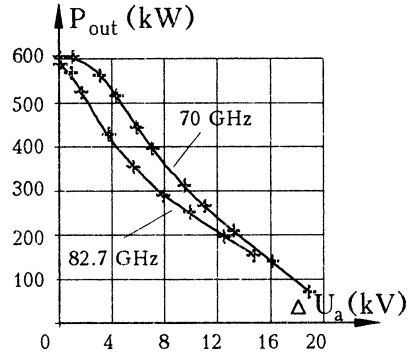

Fig.4. Output power P_{out} modulation by anode voltage U_a.
The output power diminution $\Delta P_{out} \approx$ 60-70% is achieved by ΔU_a=12 kV;
$\Delta P_{out} \approx 90\%$ - by ΔU_a=19-20 kV.

GYROTRON PARAMETERS WITH ELECTRON BEAM POWER DEPRESSION

Output power dependence on the depressed voltage is individual for each gyrotron (see Fig.5a, b) and the question about this characteristics behavior requires detail investigations, including the analysis of gyrotron cavity position relatively magnetic field center.

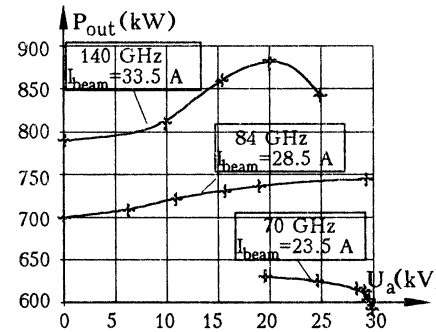

Fig.5a. Output power P_{out} dependencies on anode (cavity) voltage U_a under constant accelerating voltage U_{beam}.
$U_{beam} = |U_c| + |U_a|$
(U_c - cathode voltage)
70 GHz: U_b=78.5 kV
84 GHz: U_b=82 kV
140 GHz: U_b=72.5 kV

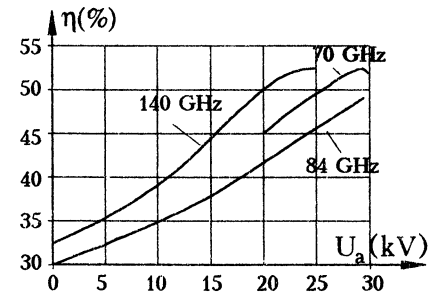

Fig.5b. Efficiency η dependency on anode (cavity) voltage U_a.

The achievement of 1 MW power level with high pulse duration became possible due to the thermal load of collector reduction by means of spent electron beam energy recuperation. Ratio of undepressed beam power on the collector to the depressed power is expressed by the relation:

$$\frac{P_0}{P_{CPD}} = a\frac{(1-\eta_0)}{(1-\eta_0 \times a)}\ ,\ a = \frac{U_{beam}}{U_c},$$

where η_0- efficiency without CPD, P_0 and P_{CPD} - absorbed on collector power (P_0 - without CPD). When "natural" efficiency is equal 0.3 and ratio of total accelerating voltage to voltage of powerful supply is equal 1.5 the saving of the power density is 1.9. Really it can be more.

Efficiency gain with depression is expressed by formula:

$$\eta_{CPD} = \eta_0 \times \frac{U_{beam}}{U_c}.$$

Maximum efficiency is more than 50% (Fig.6) and achieved at parameter "a" equal 1.5-1.6. Than the fall of the output power and the body current change are observed. Normal body current for the last CPD gyrotrons is about 20 mA.

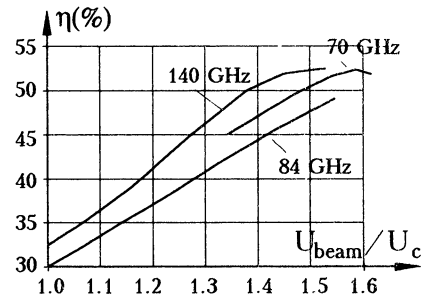

Fig.6. Efficiency η dependency on relation U_{beam}/U_c.

Resulting electron beam power densities on the depressed collectors in regimes with maximum output power are shown in the table 3. In 70, 82.7 and 84 GHz gyrotrons the residual power can be taken out in CW operation regime by non intensive cooling water flow. Maximum thermal loads of cavities are shown in the table 4. 84 GHz gyrotron has relatively high ohmic quality factor and low ohmic losses even at the 1 MW level.

Main parameters of electron guns are shown in the table 5. All of them have high temperature cathodes. 82.7 GHz gyrotron has relatively wide emitter, therefore it's operating current density appeared to be less

than in another gyrotrons. In this case the increase of current density up to usual about 3 A/cm^2 doesn't give the rise of output power. Intensity of electric field on emitter in 84 GHz gyrotron was chosen as 4.5 kV/mm, with purpose to try the increase of total accelerating voltage up to about 90 kV and to realize the regime with CW operation at the 1 MW level in future.

Table 3 Electron beam power density on the CPD gyrotron collector (in regimes with maximum power):

70 GHz	82.7 GHz	84 GHz	140 GHz*
0.6 kW/cm^2 (P=680 kW)	0.8 kW/cm^2 (P=650 kW)	0.6 kW/cm^2 (P=875 kW)	1.6 kW/cm^2 (P=880 kW)

* - with additional collector coils

Table 4. Maximum thermal loads of cavities (in regimes with maximum power):

	70 GHz	82.7 GHz	84 GHz	140 GHz
Operating mode	$TE_{9\,3}$	$TE_{10\,4}$	$TE_{12\,5}$	$TE_{22\,6}$
Max. power density on the wall, kW/cm^2	1.1	1.2	1.0	2.5

Table 5. Electron guns of gyrotrons:

	70 GHz	82.7 GHz	84 GHz	140 GHz
Intensity of electric field on emitter (cold), kV/mm	5.3	5.1	4.5	5.5
Current density in regime with max. η, A/cm^2	3.0	2.1	2.5	2.7
Current density in regime with max. power, A/cm^2	3.9	2.4	2.8	3.1

Output power and efficiency dependencies on the accelerating voltage under constant anode voltage and beam current in 84 GHz gyrotron are shown at the Fig.7. The output power increases with the beam voltage and efficiency doesn't fall even by the decrease of the depression coefficient and keeps up near 47 %. Hence, accelerating voltage of this gyrotron can be rise up to 88 kV as least, in this condition optimum cathode voltage must be about 55 kV when efficiency exceeds 50 %. The gyrotron output power can be really equal 1 MW and for achievement of CW 1 MW operation only the problem of thermal stabilization of all gyrotron units must be decided.

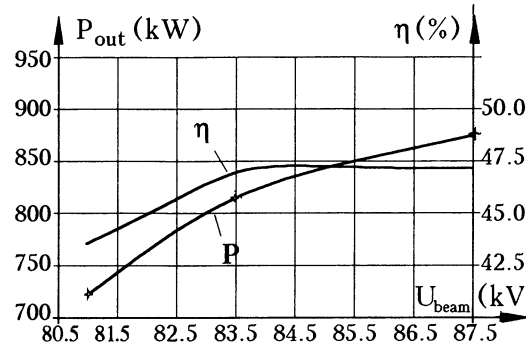

Fig.7. Output power P_{out} and efficiency η dependencies on accelerating voltage U_{beam} under constant anode voltage in 84 GHz gyrotron.
U_a=+27.5 kV, I_{beam}=31 A.
U_{beam}=87.5 kV:
U_{beam}/U_c=1.46, η=47 % ;
if U_{beam}/U_c=1.6, η=51.5 %.

CPD GYROTRONS COOLING

The tables 6, 7 illustrate the possibilities of used cooling systems for cavity and collector. They oriented on non intensive water flow with inlet pressure less than 6 atm. 70, 82.7 and 140 GHz gyrotrons are pulsed in principle as are cooled by copper wall thermal capacity. 84 GHz gyrotron has CW cavity and collector channel cooling with time of temperature stabilization about 1.5 second. Maximum possible pulse duration at regimes with maximum power with existing boron nitride output windows are shown in the table 8.

Table 6. Gyrotrons cavity water cooling.

	70 GHz	82.7 GHz	84 GHz	140 GHz
Type	by copper wall thermal capacity with additional channel using	by copper wall thermal capacity	by channel using	by copper wall thermal capacity
Water rate	~0.15 l/s	~0.15 l/s	~0.2 l/s	~0.15 l/s
Inlet press.	~3 atm	~3 atm	~3 atm	~3 atm

Table 7. Gyrotrons collector water cooling.

	70 GHz	82.7 GHz	84 GHz	140 GHz
Type	by copper wall thermal capacity	by copper wall thermal capacity	by channel using	by copper wall thermal capacity
Water rate	~6 l/s	~6 l/s	~6 l/s	~6 l/s
Inlet press.	~6 atm	~6 atm	~6 atm	~6 atm

Table 8. Maximum possible pulse duration with BN output window ∅100 mm (in regimes with maximum power).

70 GHz	82.7 GHz	84 GHz	140 GHz
4 s<τ<5 s	3 s<τ<4 s	2 s<τ<3 s	~1.5 s

Confirmation of the cavity thermostabilization can be obtained by the frequency dependency on pulse duration (see Fig.8a, b, c). Full frequency deviation 130 MGz is not so low as it is desirable. It can be reduced by some additional measures. But the main conclusion is, that 84 GHz gyrotron really is the prototype of the 1 MW CW gyrotron in all elements with exception of the output window.

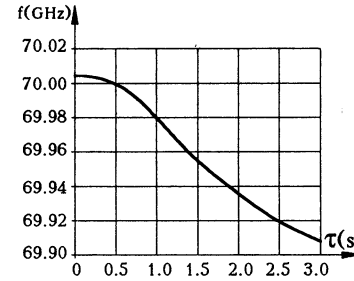

Fig.8a. Frequency f dependency on pulse duration τ in 70 GHz gyrotron at P_{out}≅600 kW. Frequency deviation $\Delta f \approx$ 90 MHz at pulse duration 3 s.

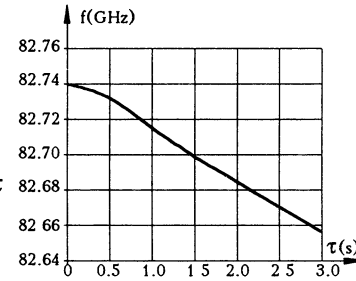

Fig.8b. Frequency f dependency on pulse duration τ in 82.7 GHz gyrotron at P_{out}≅600 kW. Frequency deviation $\Delta f \approx$ 85 MHz at pulse duration 3 s.

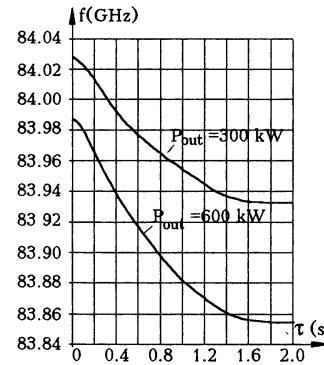

Fig.8c. Frequency f dependency on pulse duration τ in 84 GHz gyrotron.
Frequency stabilization is reached since ~1.5 s from the pulse start.
$\Delta f \approx$ 95 MHz at P_{out} =300 kW,
$\Delta f \approx$ 130 MHz at P_{out} =600 kW.

LAST CPD GYROTRONS RESULTS

Continuation of the 84 GHz gyrotron investigation in August 1999 allowed to reach new results on increased operating voltage. Correspondent output power and efficiency dependencies on beam current are shown at the Fig.9. Maximum pulse duration is 3 s and full frequency deviation at this longevity is equal 150 MGz (at the 800 kW output power).

First experiments with pulse prototype of new 140 GHz CW gyrotron in September 1999 gave more than 900 kW output power at duration up to 0.3 s in the regime of U_c=-60 kV, U_a=+30 kV, I_{beam}=32 A. The prototype was created to test new electron gun with 90 kV total beam voltage and new cavity mode $TE_{22,10}$.

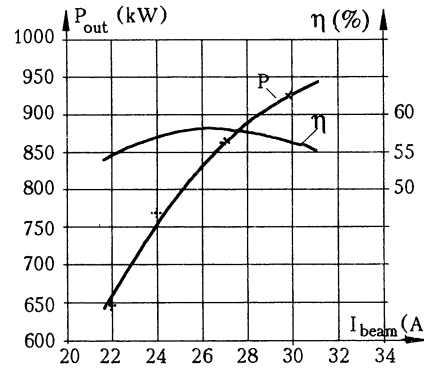

Fig.9. Output power P_{out} and efficiency η dependencies on beam current I_{beam} in 84 GHz gyrotron. U_{beam}=85 kV, U_c=55 kV.

CRYOMAGNETS FOR GYROTRON APPLICATION DEVELOPMENT

Cryomagnets development can be demonstrated by the table 9. All cryomagnets have similar design. Helium capacity and it consumption allow the continues operation during 90 hours without the helium filling in condition of 12 hours work with current daily.

Table 9. Cryomagnets development.

• maximum magnetic field:	for 28÷110 GHz gyrotrons ..	4.5 T
	for 110÷170 GHz gyrotrons ..	7.0 T
• magnet constant:	for 28÷110 GHz gyrotrons ...	0.07 T/A
	for 110÷170 GHz gyrotrons ..	0.1 T/A

• warm bore	160 mm
• maximal external diameter	700 mm*
• height of cylindrical part	400 mm
* can be increased up to 1000 mm	
• LHe capacity	41 l
• LHe consumption (off/on current)	0.15/0.3 l/h
• LHe minimum operation volume	15 %
• LN_2 capacity	26 l
• LN_2 consumption	0.7 l/h

SUMMARY

Thus summary is the next:

•Produced CPD gyrotrons allow to reach the power level 0.5-1 MW at pulse duration up to 3 s.

•CPD gyrotrons require the powerful cathode supply with maximum voltage 60 kV and current 25-35 A in dependence on desirable power, the anode supply with 30-35 kV and useful at body current about 20 mA with some reserve. It must be marked, that gyrotrons conditioning can be fulfilled in the depressed regime at once, therefore voltage of powerful supply must not provide the total accelerating voltage. Cooling systems require the water flow with 6 atm inlet pressure and 6 l/s flow rate for collector and 3 atm, 3 l/s for another elements.

•After replacement of output window to the CW-type (with correspondent modification of build-in converter) 84 GHz gyrotron becomes capable for CW operation. Gyrotrons from another frequency ranges (in particular 140 GHz) are prepared to be 1 MW CW too.

•Developed gyrotron systems include also two type of cryomagnets.

MODULATIONS AND STABILIZATIONS OF SUBMILLIMETER WAVE GYROTRONS

T. Idehara, S. Mitsudo, M. Ui and T. Hatakenaka
Research Center for Development of Far-Infrared Region, Fukui University
Fukui 910-8507, Japan

I. Ogawa
Cryogenic Laboratory, Faculty of Engineering, Fukui University

M. Pereyaslavets
Department of Applied Physics, Faculty of Engineering, Fukui University,
Fukui 910-8507, Japan

High frequency, medium power gyrotrons (Gyrotron FU series) have been developed in Fukui University as radiation sources covering a broad band from millimeter to submillimeter wave region. They have achieved many new advances in gyrotron operations and have been already applied to high frequency ESR spectrosopy and to submillimeter wave scattering in plasma. Many parameters of the gyrotron series could be useful for its applications in several new areas. Especially, amplitude and frequency modulations of the outputs, as well as stabilization of amplitude and frequency, are important in various applications. The development and some applications of Gyrotron FU series are summarized in this paper.

1. Introduction

The development of gyrotrons is proceeding in two directions. One is the development of high power, millimeter wave gyrotrons as the power sources for electron cyclotron heating of plasmas, electron cyclotron current drive of tokamaks[1-4] and for ceramic sintering.[5,6] The second direction is the development of high frequency, medium power gyrotrons[7,8] as millimeter to submillimeter wave sources for plasma scattering measurements,[9,10] ESR experiments[12] and so on.

Gyrotrons developed in Fukui University belong to the second group. High frequency, medium power gyrotrons covering a broad frequency band from millimeter to submillimeter wavelength region have been developed. 'Gyrotron FU series' consisting of 8 gyrotrons has many

achievements including frequency tunability from 38 GHz to 889 GHz, high harmonic operations up to the fourth harmonics, study of mode competition and mode cooperation, high purity mode operation, frequency and amplitude modulations, frequency step switching, cw operation for a long time for stabilization of the output and so on.
This paper summarizes achievements of 'Gyrotron FU series' and describes modulations and stabilizations of the outputs having in mind extending gyrotron applications in various new fields. As the instances, the applications to high frequency electron spin resonance (ESR) and to submillimeter wave scattering in plasma are also briefly descibed.

2.Main results of Gyrotron FU series

Gyrotrons included in Gyrotron FU series are frequency step-tunable sources covering a wide wavelength range from millimeter to submillimeter wave region. The output powers are not so high, that is, from several hundreds watt to several tens kilowatt for fundamental operation and from several tens watt to several kilowatt for second harmonic operation. The main results are summarized as following.

(a) Frequency tunability in broad band from 38 GHz to 889 GHz[12-16]

All frequencies achieved up to now by 5 gyrotrons included in

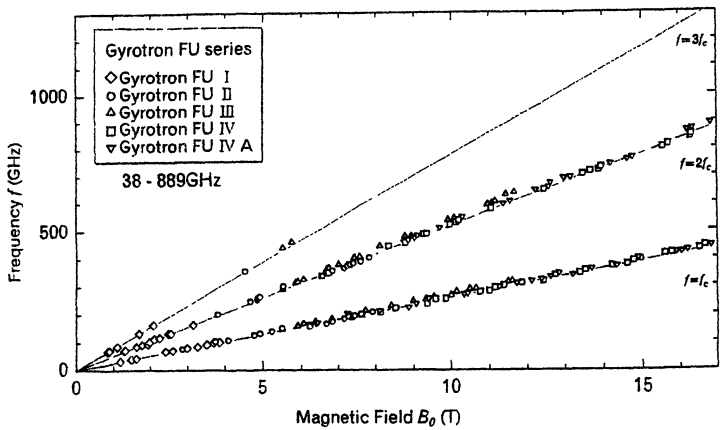

Fig.1 All frequencies achieved up to now by Gyrotron FU series as functions of field intensity B_0. Solid curves show the fundamental, the second harmonic and the third harmonic resonances.

Gyrotron FU series are summarized as functions of field intensity B_0 in Fig. 1. Solid lines represent the fundamental (N=1), the second and the third harmonic (N=2, 3) resonances. Frequency step-tunability from 38 to 889 GHz is achieved for the fundamental, second and third harmonic operation. Gyrotron FU IVA has achieved the highest frequency of 889 GHz for single mode operation on the $TE_{8,6,1}$ cavity mode at the second harmonic (N=2). The corresponding wavelength is 337 μm.

(b) Higher harmonic (N≧4) operation[17-19]

Higher harmonic (N≧4) operation enables us to decrease magnetic field intensity and to develop a high frequency gyrotron. Therefore, higher harmonics are necessary for development of high frequency, medium power gyrotrons as submillimeter wave sources. Gyrotron FU I, II and III have achieved third (N=3) and fourth (N=4) harmonic operation.

We used a Michelson interferometer combined with a signal analyzer for Fast Fourier Transform (FFT) to obtain the frequency spectrum of the gyrotron output. Fig.2 presents the frequency spectrum obtained by FFT of the interferometer pattern for Gyrotron FU II. It is obvious that an intense third harmonic operation occurs together with more intense fundamental and second harmonic and weak fourth harmonic

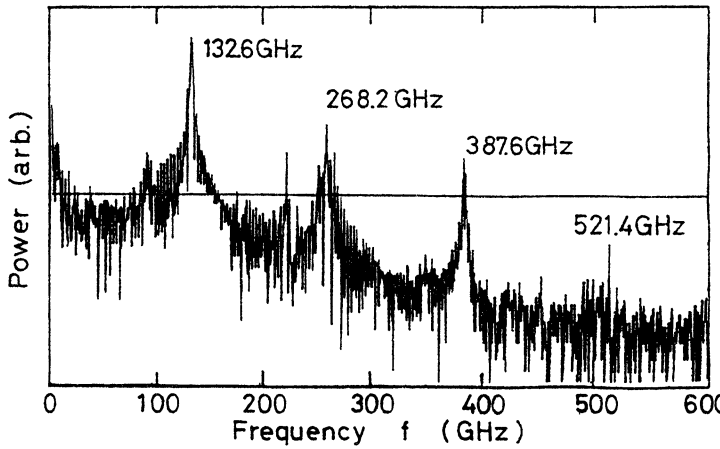

Fig.2 A typical result of frequency measurement using a Michelson interferometer. Frequency spectrum obtained by FFT of the interference pattern.

operations. Higher harmonic operation enables us to operate Gyrotron FU II at high frequency modes up to about 600 GHz.

(c) Mode competition[20] *and mode cooperation*[21]

Sometimes, mode competition between the fundamental (N=1) and the second harmonic (N=2) occurs in our high frequency gyrotrons. In such a case, the higher frequency mode (N=2) is suppressed by excitation of the lower frequency mode (N=1) of higher output power. This phenomenon is not convenient for high frequency, harmonic gyrotrons and should be avoided.

Using Gyrotron FU III, mode competition between the fundamental, the second and the third harmonics was studied in detail. A set of Fabry-Perot interferometer patterns is shown in Fig. 3, for different field intensities B_0. The third harmonic peaks are indicated in the figure by open circles, the fundamental by triangles and the second harmonic by crosses. On the peaks labeled with triangles, the second and the third harmonics are overlapping on the fundamental. The operating conditions were following: the accelerating voltage V_b= 40 kV and the beam current I_b= 1.1 A. It was found that the second harmonics is

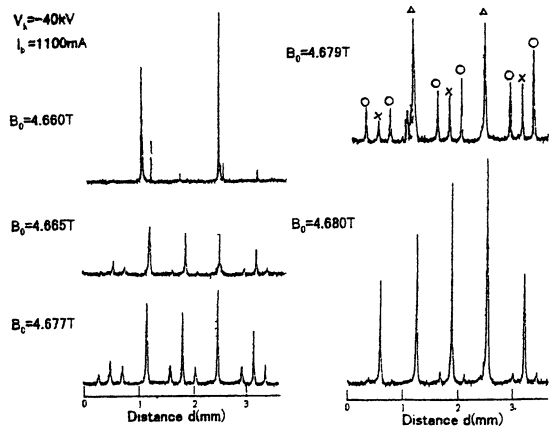

Fig.3 Interference patterns of Fabry-Perot interferometer with the field intensity B_0 in the cavity region as a parameter. Triangles △ labeled on the highest peaks correspond to the overlap of the fundamental operation at f=118 GHz ($TE_{5,1,1}$ cavity mode), the second harmonic at f=236 GHz ($TE_{10,1,1}$) and the third harmonic at f=354 GHz ($TE_{15,1,1}$). Crosses × the second harmonic only and circles ○ the third harmonic only.

suppressed completely, when the fundamental operation becomes intense. (mode competition).

In some other circumstances, one mode helps the other mode to become enhanced. One could define this as 'mode cooperation'. A phenomenon observed in Gyrotron FU II suggests phase bunching due to the second harmonic operation acts as a prebunching to initiate the fundamental operation. This mechanism results in a reduced starting current for fundamental operation and perhaps offers a more efficient way of achieving useful output powers from a gyrotron operating at lower voltages and currents.

(d) High purity mode operations[12]

Gyrotron FU IVA is designed for high purity mode operations. Carefully designed cavity with a nonlinear up-taper at the output and smoothly connecting parts at the beginnings of the cutoff down-taper and the nonlinear up-taper, is installed. Such structure of the cavity will minimize mode conversions from the main cavity mode to competing modes. The cavity was designed by D.Wagner, M.Thumm et al.

Each mode in a cylindrical waveguide has its own propagation angle. (Different modes have different angles.) We have set a step-cut waveguide on the top of the gyrotron tube and measured the angle dependency of emitted power using a Vlasov type antenna. This measurement determines the power distribution for each mode.

Observed mode purity for TE_{03} mode is 82 percent. This is comparable with the calculation result of 89.6 percent. Similar results have been obtained for other cavity modes.

3.Modulations and stabilizations of the outputs

Modulations and stabilizations in amplitude and frequency of submillimeter wave gyrotrons are useful for their applications as radiation sources in various new areas.

(a) Amplitude modulation[22,23]

Gyrotrons FU III and IV have achieved amplitude modulation of their outputs. A modulation of the anode voltage V_a will modulate the velocity distribution function of beam electrons, which, in its turn, will modulate the gyrotron output. Fig. 4 shows a typical result of amplitude modulation in the submillimeter wave gyrotron (Gyrotron

FU III) with the ratio $\Delta V_a/V_{a0}$ as a parameter. This ratio represents the modulation level of the anode voltage V_a. The gyrotron, in this instance, is operating on the second harmonics of the cyclotron frequency. The cavity mode is $TE_{1,6,1}$, the frequency is 444 GHz, and the output power is about 300 W. The modulating frequency is 5 kHz and modulation mode is sinusoidal wave. The upper traces show the high voltage pulse applied to the anode. The small sinusoidal wave modulation signal is visible on the traces. The lower traces show the output power of the gyrotron. The modulation rate $\Delta P_{out}/P_{out}$ of gyrotron output increases with the modulation rate $\Delta V_a/V_a$ of the anode voltage. The 100 percent modulation of the output ($\Delta P_{out}/P_{out}$=1.0) is attained, when $\Delta V_a/V_a$ is only several percent ($\Delta V_a/V_a$~0.055). The modulation rate $\Delta P_{out}/P_{out}$ of output

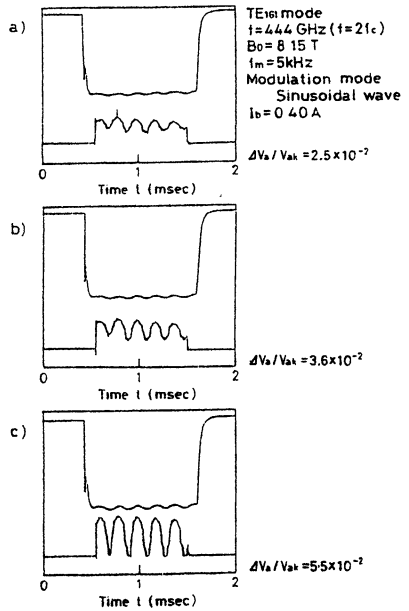

Fig. 4 Amplitude modulation result for Gyrotron FU III. Upper traces are high voltage pulses applied to the anode and lower traces output powers of the gyrotron. Operation conditions are shown beside the figure. Unmodulated beam voltage V_b=40 kV.

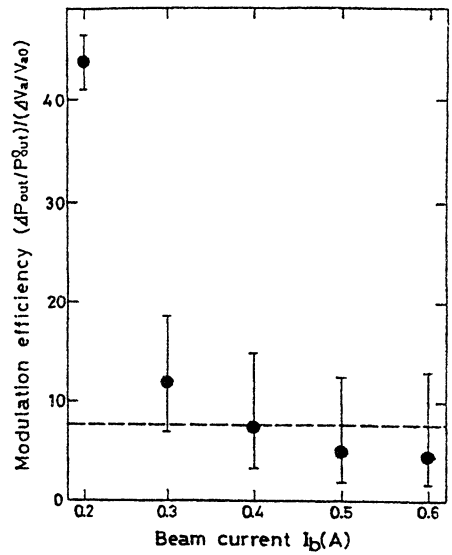

Fig. 5 Amplitude modulation efficiency of $(\Delta P_{out}/P_{out})/\Delta V_a/V_{a0})$ as a function of beam current I_b.

power is almost linearly proportional to $\Delta V_a/V_{a0}$. This means the sinusoidal modulation of output power is possible by the sinusoidal modulation of anode voltage. Sinusoidal modulation of P_{out} at the modulation frequency up to 600 kHz has been achieved with the low $\Delta V_a/V_{a0}$ value of $1.1 \cdot 10^{-3}$.

In Fig.5, the amplitude modulation efficiency $(\Delta P_{out}/P_{out})/(\Delta V_a/V_{a0})$ is plotted as a function of the beam current I_b. The theoretical prediction for the efficiency is derived from the energy transfer function between electrons and electromagnetic wave, as follows,

$$(\Delta P_{out}/P_{out})/(\Delta V_a/V_{a0}) = (1 + P_{ohm}/P_{out})(3\alpha^2 + 4),$$

where P_{ohm} is the ohmic power loss in a cavity and α the pitch angle of beam electrons. The broken line in Fig.5 shows the efficiency when P_{ohm}/P_{out} is neglected. In the figure, experimentally obtained efficiency becomes close to the theoretical prediction (the broken line), when I_b is so high that P_{out} is high enough.

(b) Frequency step switching due to switching of operating cavity modes[24]

One kind of possible frequency modulation is obtained by step switching from one cavity mode to another, by switching the energy of the beam electrons. It is useful for many applications of gyrotrons, for example, plasma heating at several frequencies (a simultaneous heating at the electron cyclotron fundamental and the second harmonic resonances), heat pulse propagation experiments at two different frequencies, and so on. The principle of frequency step switching of the gyrotron output is as follows. Usually, gyrotrons operate at a frequency near the electron cyclotron frequency f_c or its harmonics nf_c. The electron cyclotron frequency is $f_c=eB_0/(2\pi\gamma m_0)$, where e is the electric charge unit and m_0 the rest mass of the electron, B_0 the static magnetic field and $\gamma=(1-v^2/c^2)^{-1/2}$ the relativistic factor.

When the energy of an electron is changed, γ, which is related to the beam voltage V by $(\gamma-1)m_0c^2=eV$ changes and, as a consequence, the electron cyclotron frequency f_c changes. If the cathode voltage is switched from V_1 to V_2, the electron cyclotron frequency changes from f_{c1} to f_{c2} and the frequency step is $\Delta f_c=f_{c2}-f_{c1}=f_{c0}eV_1(1-V_2/V_1)/(m_0c^2)$, where f_{c0} is the geometric mean of f_{c1} and f_{c2}. If there are two cavity modes whose operating conditions are very close, it becomes easy to switch

from one to the other. In such a way, rapid frequency step switching of a gyrotron can be realized. This principle was proposed by Dumbrajs et al.[25]

In the experiment, typical conditions are V_1=30 kV, V_2/V_1=0.75, so, $\Delta f_c/f_c$=1.47 · 10^{-2} If at least two cavity modes lie in the range Δf_c of electron cyclotron frequency, frequency step switching can occur, when operation changes from one mode to the other. This is frequency step switching between two fundamental modes. Similar frequency step switching is possible between a fundamental and a second harmonics, when the frequency of the latter is nearly equal to twice the frequency of the former.

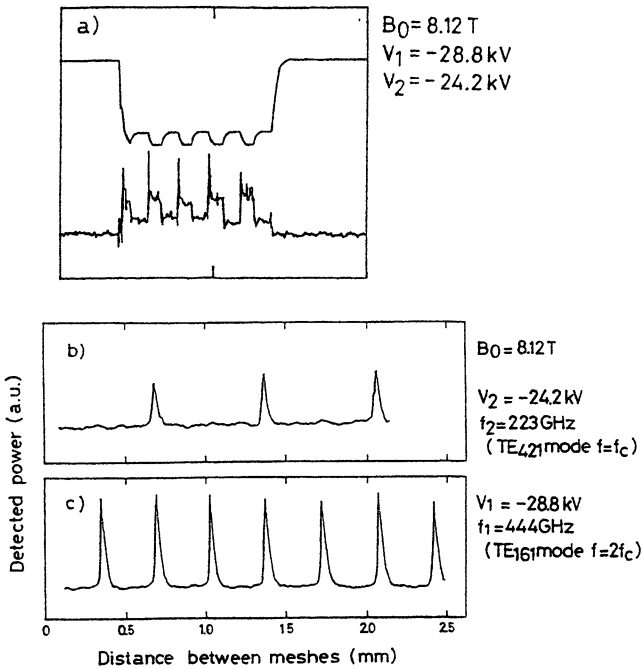

Fig. 6 (a) Upper trace; High voltage pulse applied to the cathode of the electron gun, which is modulated by a 5 kHz square wave. The magnetic field is B_0=8.12 T, V_1=28.8 kV and V_2=24.2 kV. Lower trace; Output power measured by a pyroelectric detector. It was sampled at each phase and fed on a Fabry-Perot Interferometer for frequency measurement. (b) A Fabry-Perot Interferometer at the phase of V_2. Measured frequency f_2 is 223 GHz. (c) A Fabry-Perot Interferometer at the phase of V_1. Measured frequency f_1 is 444 GHz

Fig. 6 shows a typical result for frequency step switching between a fundamental and a second harmonics. In Fig. 6(a), the upper trace shows the high-voltage, 1 ms pulse applied to the cathode of the electron gun. The anode voltage is obtained using a resistive voltage divider. The modulation superimposed on the high-voltage pulse was a 5 kHz square wave. In this case, V_1=28.8 kV, and V_2/V_1=8.40 · 10^{-1}, so $\Delta f_c/f_c$=9.94 · 10^{-3}. The lower trace shows the gyrotron output pulse. Modulation of the energy of electron results in the modulation of gyrotron output. The drastic variation of output power observed in the figure occurs, because a beam efficiency changes when cavity mode is switched. In our case, both powers are several hundred watts. It is possible to get nearly equal powers for both modes by controlling injection point of electron beam in the cavity.

Frequency switching is confirmed by sampling the output, first, when the voltage is V_1 (Fig.6(b)) and again when it is V_2 (Fig. 6(c)) and measuring the frequencies by a Fabry-Perot interferometer. The measured frequencies are f_1=444 GHz and f_2=223 GHz. In this case, a drastic frequency step switching is achieved.

(c) Frequency modulation[26]

Following the same principle as for the frequency step-switching,

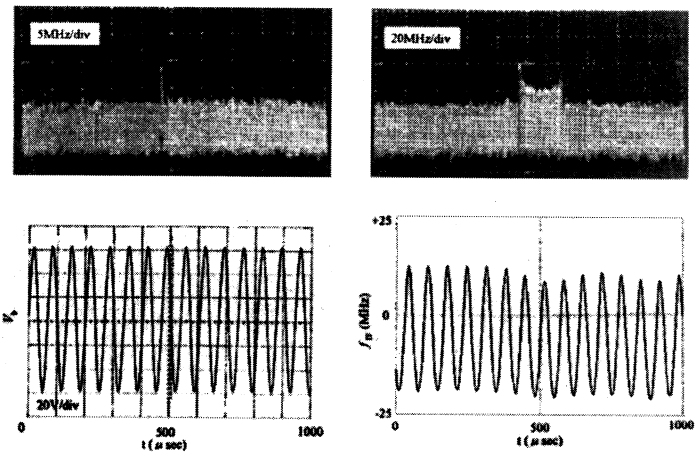

Fig. 7 Experimental results for frequency spectra without and with frequency modulation, for variation of body potential V_b and for observed frequency f_{IF}. f_m=15 kHz, ΔV_b=120 V and Δf=31.1 MHz.

modulation of the cathode voltage enables a fast frequency modulation of the gyrotron output. Gyrotron FU IV has achieved the frequency modulation within the limit of resonance frequency width of a cavity mode. The energy of beam electrons is modulated by variation in the body potential. The body includes the cavity and is separated electrically from the beam collector by a ceramic insulator.

The output power is transmitted by circular waveguides and emitted to a horn antenna. The frequencies measured by a heterodyne detection system consisting of a sweep oscillator, a frequency counter, a harmonic mixer and a modulation domain analyzer. The detected signal is mixed with a high harmonic of the local oscillator. The time and frequency resolutions of the detection system are 10 μsec and 10 kHz, respectively. A typical result of the frequency modulation experiment is demonstrated in Fig. 7. A spectrum analyzer trace on the left-hand side presents the frequency spectrum of the output signal without frequency modulation and a trace on the right-hand side with frequency modulation. The frequency width δf of the gyrotron output itself is about 100 kHz. A well-known pattern of a frequency spectrum under modulation is obvious in the right-hand side trace. The frequency width δf of the spectrum is in good agreement with the amplitude Δf of the

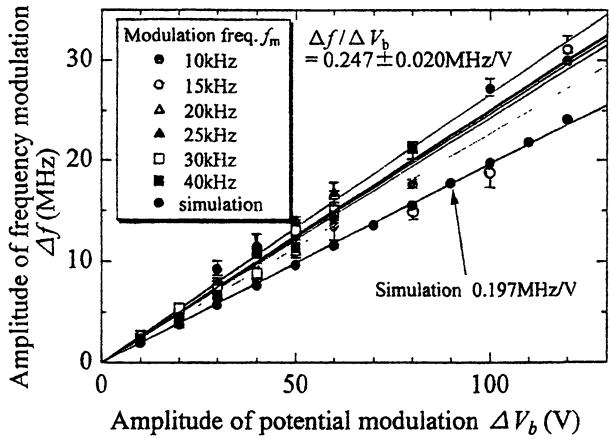

Fig. 8 Experimental and simulation results for frequency modulation amplitude Δf versus the amplitude of body potential modulation ΔV_b for f_m=10, 15, 20, 25, 30 and 40 kHz, $\Delta f/\Delta V_b$=0.247 MHz/V. Output power P=20 W.

frequency modulation determined from the f_{IF} trace in the figure. The corresponding V_b modulation with the amplitude of 120 V is also plotted in the figure.The frequency modulation amplitude Δf versus the body potential modulation amplitude ΔV_b is plotted in Fig. 8 for several values of the modulation frequency f_m. There is an almost linear dependence between Δf and ΔV_b for all values of f_m. The efficiency of frequency modulation is $\Delta f/\Delta V_b$=0.247 MHz/V. The simulation results are also indicated in the figure. The estimated efficiency is distributed close to the experimentally obtained values.

The submillimeter wave gyrotron is used as a radiation source for plasma scattering measurement and ESR experiment in our laboratory. The advantages of frequency step switching and frequency modulation, as well as amplitude modulation, will be useful in these applications.

(d) Complete cw operation with high stability of amplitude and frequency[27]

The variations of temperature of the water in the water load was measured for several cavity modes by a thermocoupler as a function of time. The slope of each observed line is proportional to the corresponding output power. The results of power estimations are following: 4.5 Wfor TE_{021} mode at the frequency of 207.5 GHz, 20.1 W for TE_{321} mode at 238.3 GHz and 17.1 W for TE_{031} mode at 301.9 GHz. The longest period of the operation was five hours, which means 'complete cw'.

Table 1.The results of measurements of output power P_{out}, together with field intensity in the cavity region B_0, acceleration voltage of electron beam V_b, beam current I_b, cavity mode TE_{mn}, frequency f measured by a Fabry-Perot interferometer and/or a heterodyne detection system, input power P_{in}, and operation efficiency η.

B_0 (T)	V_b (kV)	I_b (mA)	TE_{mn}	f (GHz)	P_{in} (W)	P_{out} (W)	η (%)
7.09	12	64	2 2	199.3	768		
7.53	12	32	0 2	207.5	384	4.5	1.2
7.95	14	32	6 1	221	448	2.0	0.45
8.52	14	68	3 2	238.3	952	20.1	2.1
9 06	14	75	1 3	252	1050	9.8	0.93
9.14	14	67	7 1	253.6	938	3.2	0.34
10.53	15	80	2 3	295	1200	11.6	0.97
10.88	14	80	0 3	301.9	1120	17.1	1.53

Similar measurements have been made for many other cavity modes. Table 1 summarizes the results, together with the field intensity in the cavity region B_0, the accelerating voltage of electron beam V_b, the beam current I_b, a cavity mode TE_{mnl}, the frequency f measured by the Fabry-Perot interferometer and/or the modulation domain analyzer, the input power P_{in}, and the operation efficiency η.

The electron beam current I_b is several tens of milliamperes. It was limited by the water cooling capacity. It is close to the starting currents of corresponding cavity modes. Therefore, operation is not so stable, but the powers obtained are moderately high and the efficiency η exceeds 1 percent for a few modes.

One of the advantages of complete cw operation is stabilization of the frequency and the amplitude of the gyrotron output. We employ a current-stabilized high voltage power supply in our experiment to ensure stable operation. A variation in the output frequency was measured by a time-resolved frequency measurement system.

Fig. 9 shows a typical result of frequency measurement together with the

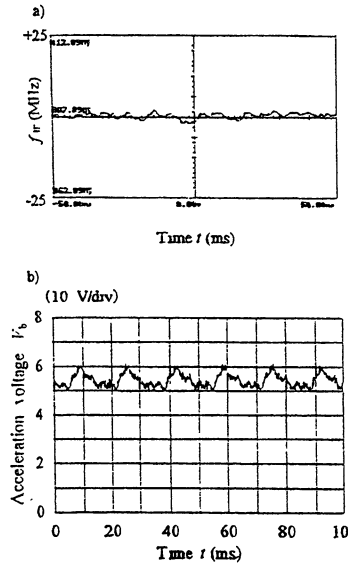

Fig. 9 (a) A result of frequency measurement. A full scale in the vertical axis is 50 MHz. (b) A simultaneous observation result of acceleration voltage V_b. 10 volt/div in the vertical axis.

accelerating voltage V_b. The operation conditions are following: the field intensity in the cavity region B_0=10.88 T, the accelerating voltage of electron beam V_b=14 kV, the beam current I_b=80 mA, the cavity mode TE_{031}, the frequency f=301.9 GHz, the input power P_{in}=1.12 kW, the output power P_{out}=17.1 W and the operation efficiency η=1.53 percent. The measured frequency variation δf during 100 msec is δf - =4.1MHz. The variation ratio $\delta f/f = 1.3 \cdot 10^{-5}$. The frequency variation is increased probably due to a variation in the accelerating voltage V_b. The variation amplitude of V_b in the figure is about 10 volt. It causes a small variation in the electron mass, and from it we can estimate the variation in the electron cyclotron frequency δf_c as 5.6 MHz. Its variation ratio $\delta f_c/f_c = 1.9 \cdot 10^{-5}$. The experimentally obtained values of $\delta f/f$ are in good agreement with the estimated value of $\delta f_c/f_c$.

Similar measurements have been carried out for several other modes. The results are summarized in Table 2. In the table, the frequency variation δf during 100 msec is listed for several cavity modes, together with the cavity mode TE_{mnl}, the frequency of the local oscillator f_L, the harmonic number of the mixer n, the frequency f_{IF} detected by the modulation domain analyzer, and the determined operation frequency f, as well as the calculated resonant frequency of the cavity. For all cases, δf is several MHz and $\delta f/f$ is of the order of 10^{-5}.

The stability of the operation frequency may be improved by further stabilization of the output voltage of a high voltage power supply.

Table 2 The frequency variation δf during 100 msec is listed for several cavity modes, together with cavity mode TE_{mnl}, frequency of local oscillator f_L, harmonic number of the mixer n, frequency f_{IF} detected by the modulation domain analyzer, determined operation frequency f, and calculated resonant frequency f_{cal} of the cavity.

Mode	Local Oscillator f_L (GHz)	Harmonic Number n	Modulation Domain Analyzer f_{IF} (MHz)	f meas. (GHz)	δf (MHz)	f cal. (GHz)
TE_{22}	16.572	12	429	199.293	3.4	198.395
TE_{02}	12.227	17	342	207.517	4.4	207.526
TE_{32}	13.246	18	168	238.260	2.6	237.027
TE_{71}	10.548	24	483	253.630	5.2	253.634

4. Application of Gyrotron FU series

(a) Application to plasma scattering measurement

Gyrotron FU II is employed as a radiation source for plasma scattering measurements on the Compact Helical System (CHS) of the National Institute for Fusion Science (NIFS). A gyrotron is a well suited source for plasma scattering measurement, because of its high power possibilities in submillimeter wave range. Gyrotron FU II delivers long pulses (pulse width is changed up to 0.6 s) of moderately high power (~110 W) at submillimeter wavelengths (f~354 GHz, λ=0.847 mm).[9] Its application enables us to improve the S/N ratio of a measurement and to observe low level density fluctuations.

Fig. 10 shows the installation of a scattering measurement system on CHS. The gyrotron output is converted to a linearly polarized, quasi Gaussian beam and transmitted by a quasi-optical mirror system, before it is injected into plasma. The wave scattered from plasma is received by horn antennas installed in the plasma vessel. It is converted into low frequency signal by a homodyne detection system.

The scattering measurements with scattering angles of 4.4 degree and 8.8 degree are carried out in NBI heated plasma and in ICRF heated plasmas. A typical result of scattering measurement with the angle of 8.8

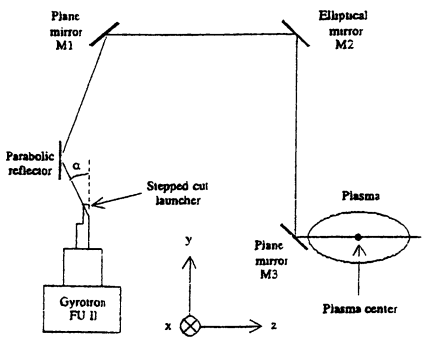

Fig. 10 Schematic drawing of installation of scattering measurement system using Gyrotron FU II on CHS.

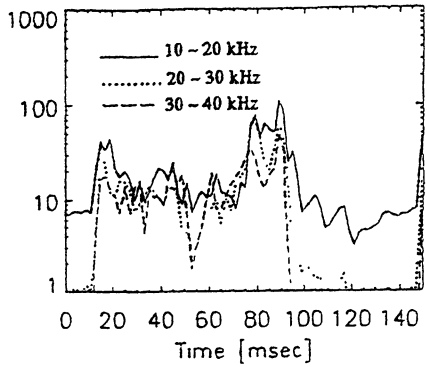

Fig. 11 Time evolution of scattered wave power for respective frequency interval.

degree for NBI heated plasma suggests an excitation of drift wave. The plasma is produced by a microwave pulse for electron cyclotron heating (ECH) and heated by a neutral beam injection (NBI) pulse. Frequency spectra of scattered signals were measured. Each spectrum covers the frequency band from 0 to 1 MHz and has been obtained in 20 msec. Some broadening of the spectrum occurs during NBI heating. After the NBI pulse, the broadening cannot be observed. It is detected up to about 600 kHz and is possibly due to scattering by drift waves excited spontaneously in the NBI heating phase.

Fig. 11 shows a scattering measurement result for ICRF heated plasma. The plasma is fired at the time of 10 msec by an ECH pulse and an ICRF heating pulse is applied in the time interval from 40 to 90 msec. Each curve shows time evolution of scattered wave power for respective frequency interval. The scattering angle of 8.8 degree corresponds to wavenumber of 11.4 cm^{-1}. The increase in scattered wave power is observed during the ICRF heating. Reflection measurement using a reflectmeter was carried out at the same time. The results are in reasonable agreement with the scattering measurement and support the availability of both measurements.

Observed scattered signals suggest that some instability connected with the drift wave occurs during NBI or ICRF heating. This phenomenon will be dangerous for a good plasma confinement. We will continue the measurement under various plasma parameters, to study the effect of this instability on plasma confinement.

(b) Application to ESR experiment[11,28]

Gyrotrons FU I, FU E, FU IV and FU IVA are employed as radiation sources for ESR spectroscopy. The gyrotrons as millimeter to submillimeter wave sources have important advantages, compared to other conventional sources, for example, frequency tunability in broad band and moderately high output power. Because of such advantages, our gyrotrons are useful for ESR spectroscopy in the millimeter to submillimeter wavelength range to study nonlinear phenomena of ESR. Fig. 12 is a block diagram of an ESR spectrometer using Gyrotron FU I as a radiation source and a pulse magnet whose maximum intensity can be increased up to 30T. The output power of the gyrotron is transmitted

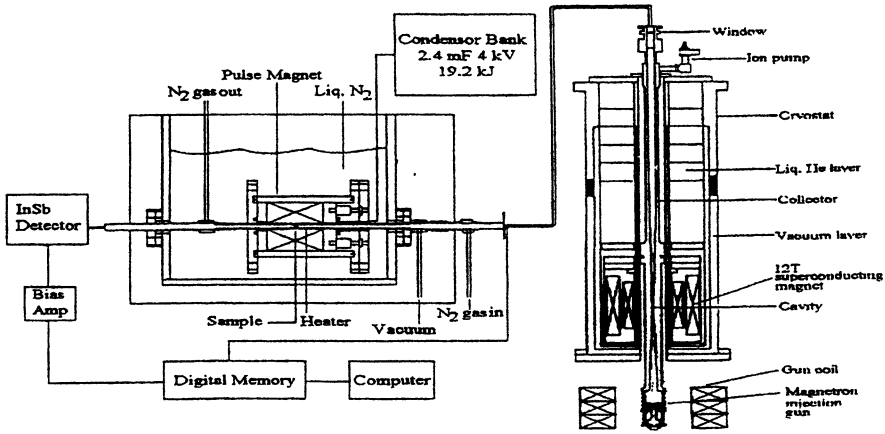

Fig. 12 A block diagram of ESR spectrometer using Gyrotron FU IV as a radiation source.

by an oversized circular waveguide and fed on the sample. The transmitted power is detected by a crystal detector or an InSb hot electron detector.

An ESR of Cr^{3+} in dark ruby is measured using Gyrotron FU IV as a radiation power source. Fig. 13 shows a typical ruby ESR spectrum obtained by sweeping the magnetic field. Absorption signals are observed at three different magnetic fields corresponding to fine

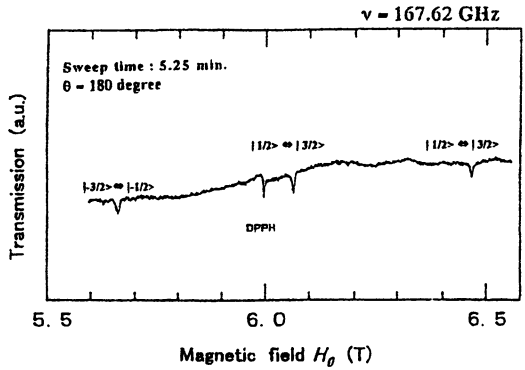

Fig. 13 ESR spectrum of $Cr^{3+}(^4A)$ in ruby as a function of magnetic field H_0 at ν=167.62 GHz. ESR signal around 6.0 T is DPPH's one as a correct marker of the field.

structure transitions of the spin state interval ^4A ground state of the Cr^{3+}. Fine structure spectral lines for three transitions are observed on the spectrum. The two ESR signals around 3.2 T are for a DPPH ESR signal (on the low magnetic field side) and for ruby (for the transition between $|+1/2>$ and $|-1/2>$), respectively. The resonant magnetic fields depend on the orientation of the c-axis.

The field intensities H_0 corresponding to the resonant absorptions are plotted in Fig. 14, as functions of the angle θ between the directions of the magnetic field and the c-axis of ruby. Solid curves are calculation results, where g-factors and the fine structure constant D are determined for the best fit with the experimental results, as follows,

$g_{\parallel}=1.9803$, $g_{\perp}=1.9813$ and $D=-5.742$ GHz.

Figs. 15 shows the frequency dependence of the fine structure constants. Solid curve is a calculation result using formulae including ν^2 terms. It seems that the experimental results are in good agreement with the calculation results. ESR studies at higher frequency help to understand the variation in the D value.

We will extend the ESR experiment in a near future to a broad frequency band in submillimeter wave region.

5. Summary

Gyrotron FU series in Fukui University consists of 8 gyrotrons. Each of them is designed to get many single mode operations on fundamentals, second and even third harmonics of electron cyclotron resonance. Such a design results in high frequency, medium power gyrotrons covering broad frequency band from millimeter to submillimeter wave region. The results achieved by our gyrotrons are summarized as follows,

(1) These gyrotrons have achieved frequency tunability from 38 GHz to 889 GHz.

(2) The output powers are moderately high, that is, from several hundreds watt to several tens kilowatt for fundamental operation and from several tens watt to several kilowatt for second harmonic operation.

(3) Higher harmonic operation is demonstrated up to the fourth harmonics. This is necessary for development of high frequency gyrotrons covering the whole submillimeter wavelength range.

(4) Mode competition and mode cooperation between the fundamental

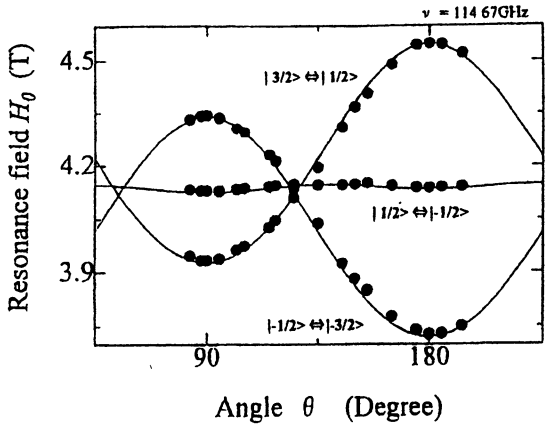

Fig. 14 The angular dependence of the three ESR transition lines of $Cr^{3+}(^4A)$ in ruby. Solid lines are calculation results by third order perturbation on the Price Hamiltonian.

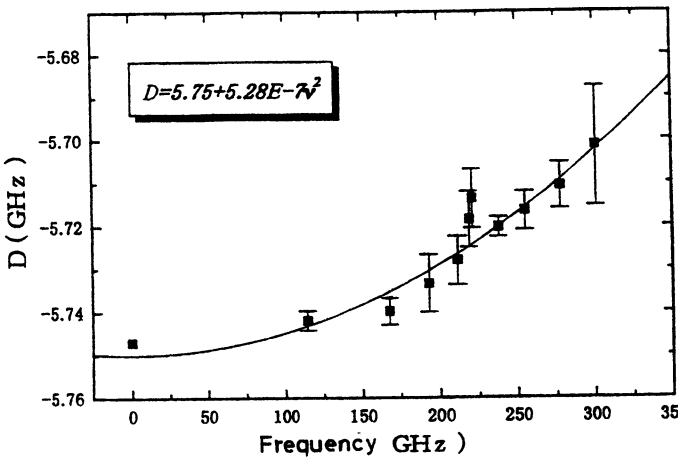

Fig. 15 The fine structure constant D of $Cr^{3+}(^4A)$ in ruby versus the resonance frequency. Solid lines are calculation results, supposing that the frequency dependence of D is proportional to ν^2.

and second harmonics are studied in detail. A mode competition is not convenient for our high frequency, harmonic gyrotron. Therefore, 9it should be avoided.

(5) Amplitude modulation, frequency step switching and frequency modulation of gyrotron output were achieved for its application in

various new areas.

(6) Complete cw operation has been performed with high stability of amplitude and frequency of the gyrotron output.

Gyrotron FU II has been already employed for plasma scattering measurements on CHS in NIFS, and Gyrotron FU I, FU E and FU IVA for ESR experiments to study the resonance line widths of DPPH and frequency dependenciy of a fine structure constant D of ruby.

At the present, the newest gyrotron Gyrotron FU V has just been constructed and begun to operate. The gyrotron consists of a helium-free 8T superconducting magnet and a demountable tube. It should achieve time-unlimited, high quality mode operation for applications in far infrared spectroscopy.

Acknowledgments

The authors wish to thank Dr. G.F.Brand from the University of Sydney, Professor M.Thumm from Forschungszentrum Karlsruhe and Drs. W.Kasparek and D.Wagner from Universität Stuttgart for their invaluable discussions. The work was partially supported by a Grant-in-Aid from the Ministry of Education, Science and Culture (Monbusho) of Japan, International Joint Research Project from the Japan Society for the Promotion of Science and the German-Japan Scientific Research Program from DFG in Germany.

References

1) B. Piosczyk et al., *Digest of 22nd Int. Conf. on Infrared and Millimeter Waves*, Wintergreen, Virginia, USA, July 1997, edited by H.E.Freund, pp. 114-115.

2) K.Sakamoto et al., ibid., pp. 106-107.

3) V.E.Myasnikov et al., ibid., pp. 102-103.

4) K.Felch, P.Borchard, C.Cahalan, T.S.Chu, H.Jory, C.M.Loring and C.P.Moeller, *Digest of 21st Int. Conf. on Infrared and Millimeter Waves*, Berlin, Germany, edited by M. von Ortenberg and H.U.Mueller (Humboldt University zu Berlin) AM16.

5) Antakov, I.G.Gachev, V.I.Kurbatov, E.BV.Sokolov, E.A.Solujanova and E.V.Zasypkin, ibid. AM3.

6) H.Asano, T.Kikunaga, K.Memmi, F.Sato and T.Tsukamoto, ibid., AM5.

7) T.Idehara, T.Tatsukawa, I.Ogawa, Y.Shimizu, N.Nishida and K.Yoshida, *Proc. of 3rd Int. Conf. on Strong Microwave in Plasmas,* vol. 2, pp.634-659 (1997).

8) K.D.Hong, G.F.Brand and T.Idehara, J. Appl. Phys., **74**, 5250 (1993).

9) I.Ogawa, K.Yoshisue, H.Ibe, T.Idehara, K.Kawahata, Rev. Sci. Instrum., **65**,

1788 (1994).
10) P.W.Fekete, G.F.Brand and T.Idehara, Plasma Phys. and Controlled Fusion, **36**, 1407 (1994).
11) T.Tatsukawa, T.Maeda, H.Sasai, T.Idehara, M.Mekata, T.Saito and T.Kanemaki, Int. J. Infrared and Millimeter Waves, **16**, 293 (1995).
12) T.Idehara, N.Nishida, K.Yoshida, I.Ogawa, T.Tatsukawa, D.Wagner, G.Gantenbein, W.Kasparek and M.Thumm, Int. J. Infrared and Millimeter Waves, **19**, 919 (1998).
13) T.Idehara, Y.Shimizu, K.Ichikawa, S.Makino, K.Shibutani, T.Tatsukawa, I.Ogawa, Y.Okazaki and T.Okamoto, Phys. Plasmas, **2**, 3246 (1995).
14) Y.Shimizu, S.Makino, K.Ichikawa, T.Kanemaki, I.Ogawa, T.Tatsukawa, T.Idehara, Phys. Plasmas, **2**, 2110 (1995).
15) T.Idehara, T.Tatsukawa, I.Ogawa, H.Tanabe, T.Mori, S.Wada, G.F.Brand, M.H.Brennan, Phys. Fluids B, **4**, 267 (1992).
16) T.Idehara, T.Tatsukawa, I.Ogawa, T.Mori, H.Tanabe, S.Wada, G.F.Brand and M.H.Brennan, Appl. Phys. Lett. **58**, 1594 (1991).
17) T.Idehara, T.Tatsukawa, I.Ogawa, S.Wada, K.Yoshisue and F.Inoue, Phys. Fluids B, **4**, 769 (1992).
18) T.Idehara, T.Tatsukawa, I.Ogawa, Y.Yamagishi and T.Kanemaki, Appl. Phys. Lett., **62**, 832 (1993).
19) T.Idehara, I.Ogawa, Y.Shimizu and T.Tatsukawa, Int. J. Infrared and Millimeter Waves, **19**, 803 (1998).
20) T.Idehara, T.Tatsukawa, H.Tanabe, S.Matsumoto, K.Kunieda, K.Hemmi and T.Kanemaki, Phys. Fluids B, **3**, 1766 (1991).
21) T.Idehara and Y.Shimizu, Phys. Plasma **1**, 3145 (1994).
22) T.Idehara, Y.Shimizu, S.Makino, K.Ichikawa, T.Tatsukawa, I.Ogawa and G.F.Brand, Phys. Plasma **1**, 461 (1994).
23) T.Idehara, Y.Shimizu, S.Makino, K.Ichikawa, T.Tatsukawa, I.Ogawa and G.F.Brand, Int. J. Infrared and Millimeter Waves, **18**, 391 (1997).
24) T.Idehara, Y.Shimizu, S.Makino, K.Ichikawa, T.Tatsukawa, I.Ogawa and G.F.Brand, Phys. Plasma **1**, 1774 (1994).
25) O.Dumbrajs and J.Heikkinen, Proc. of 11th Topical Meeting on the Technology of Fusion Energy, New Orleans, U.S.A., June 19-23, 1995.
26) T.Idehara, M.Pereyaslavets, N.Nishida, K.Yoshida and I.Ogawa, Phys. Rev. Lett. **81**, 1973 (1998).
27) T.Idehara, K.Yoshida, N.Nishida, I.Ogawa, M.Pereyaslavets and T.Tatsukawa, Int. J. Infrared and Millimeter Waves, **19**, 793 (1998).
28) T.Tatsukawa, T.Shirai, T.Imaizumi, T.Idehara, I.Ogawa and T.Kanemaki, Int. J. Infrared and Millimeter Waves, **19**, 859 (1998).

5.8–62 GHz CW GYROTRONS WITH WARM AND PERMANENT MAGNETS FOR TECHNOLOGICAL APPLICATION

A.N. Kuftin, V.A. Flyagin, V.K. Lygin, A.G. Luchinin, O.V. Malygin, V.E. Zapevalov, N.A. Zavolsky

Institute of Applied Physics, Russian Academy of Sciences, Nizhny Novgorod, Russia
GYCOM Ltd., Nizhny Novgorod, Russia

The fulfillment of the new project of creation of the industrial prototype of a technological gyrotron on worm and permanent magnets are discussed. The permanent magnetic system was designed, constructed and successfully tested for a gyrotron. A 30 GHz/10 kW CW gyrotron (n = 2) is under development with the TE_{12} operating mode. An output power of 12 kW was obtained (efficiency 24%).

Introduction

One of the important problems of modern high-power electronics is development of efficient sources of microwave radiation for technological purposes. Specifically, the practical interest is application of microwave radiation to processing of dielectric materials with relatively low losses (baking and production of ceramic materials, formation of ceramic items, production of composite materials, outbaking of semiconductors, etc.). The above tasks require microwave generators operating in the continuous regime with output power up to 30 kW in the range of 15 through 50 GHz. The most promising type of the generator with the said parameters is the gyrotron. Recently at IAP a laboratory prototype of the technological gyrotron complex has been developed and manufactured. This complex is based on a gyrotron (P = 10 kW, f = 30 GHz) with a traditional magnetic system. It made it possible to realize microwave processing of materials and at the first stage demonstrated all advantages of such processing associated with volume absorption of microwave power (considerable reduction of energy consumption and time of processing, selective heating of materials, etc.) [1–2].

Design of gyrotrons and magnetic systems

Using the same general design it is possible to create gyrotrons for permitted industrial frequencies with the same or increased power. Table 1 demonstrates examples of possible set of main parameters of CW gyrotrons and its magnetic systems.

Table 1. Main parameters of CW gyrotrons and magnetic system

Operating frequency, GHz	24.125	5.8	61.125
Operating mode	TE_{62}	TE_{11}	TE_{12}
Operating harmonic number	2	2	2
Accelerating voltage, kV	50	30	30
Anode voltage, kV	30	20	15-20
Maximum beam current, A	10	6-10	2
Resonator radius, mm	23.35	15.0	4.16
Mean beam radius in resonator, mm	10	7.3	1.4
Resonator Q-factor	2600	1600	2300
Pitch-factor	1.4	1.5	1.33
Calculated maximum (electron) efficiency	0.4/0.32	0.4/0.3	0.3/0.2
Output power, kW	100	≥50	8-10
Structure of output radiation	operating mode		
Water consumption (technical/ distillate), m^3/h	25/3	25/3	4-5/0.5
Length of tube, mm	1200	1500	1000
Magnetic field, T	0.5	0.11	1.12
Diameter of magnet bore, mm	105	80-105	20-30
Magnet power consumption, kW	15	1-1.5	≤35
Cooling liquid	Transformer oil		

For more extensive, and more so, for industrial application of gyrotrons it is necessary to solve a number of scientific and technical problems aimed at making operation of the complex easier, its efficiency higher, and the complex itself, more reliable. From this point of view, the use of magnetic systems on permanent magnets seems rather advantageous. The project is aimed at development of a prototype of a serial technological gyrotron on permanent magnets for an industrial microwave high-efficiency technological complex.

At present a number of new, relatively inexpensive and promising materials for permanent magnets have been created, which have significant coercivity and high specific power. The best of them are, evidently, compounds of samarium and cobalt (Sa-Co). However, from the cost-saving point of view more promising are rare-earth alloys of the Nd-Fe-B type. New magnetic materials and new methods for synthesis of magnetic systems make it possible to obtain magnetic fields up to 1 T with sufficiently high temporal and temperature stability in required volumes. This allows creation of gyrotrons operating at the main

gyrofrequency harmonic at frequencies 15–30 GHz including 24.125 GHz, which is adopted in many countries as the industrial frequency, and at the second gyrofrequency harmonic up to 60 GHz.

IAP RAS has a great scientific and engineering experience for creation of technological gyrotrons on permanent magnets [3–5]. New principles for developing magnetic systems of powerful gyrotrons on permanent magnets with imminent reversal of the magnetic field have been proposed for the first time. This method is based on extension of the "tails" of axial distribution of the magnetic field in the region of the electron gun and the collector by using the extended area of the magnet with radial magnetization. Criteria for axial distribution of the magnetic field, which provides efficient operation of the electron gun and collector system of the gyrotron in the presence of deep reversal of the magnetic field. Basic principles for development of gyrotrons on permanent magnets have been developed. Calculations for gyrotrons on permanent magnets have been performed and they were modeled in full-scale experiments, which revealed the most promising lines of activity when solving this problem.

In the course of project implementation we studied the magnetic system of an experimental prototype of a serial industrial technological gyrotron on permanent magnets. This system provided the required dependence of the magnetic field on the coordinate along the system axis at preset internal dimensions and was modeled and optimized in terms of its weight, dimensions and cost. The weight of the magnetic system is 88 kg (Nd-Fe-B), the field is B_0 = 0.4510 T, the length of the homogeneous section at the level $\leq 0.5\%$ at the resonator region with bore diameter 65 mm is L_0 = 120 mm. The design parameters of the gyrotron are given in Table 2.

Table 2. Main parameters of the gyrotron on permanent magnets

Oscillation frequency, GHz	24.125
Accelerating voltage, kV	20-35
Maximum beam current, A	3.0-3.5
Output power, kW	25-30
Efficiency, at least, %	30
Structure of output radiation	TE_{12} mode

Electron optical and electrodynamical calculations of the technological gyrotron were performed. Requirements to basic elements of the electron-optical system of the gyrotron on permanent magnets were elaborated basing on trajectory analyses and optimization of

electron guns in various regimes of operation. Preliminary studies demonstrated the possibility to create different types of gyrotron electron guns (including new, non-traditional electron-optical systems with a number of advantages) by choosing alternative distributions of the magnetic field, electrode topography and electric regimes.

Experimental prototype of gyrotron on permanent magnet

In the course of project implementation we calculated, designed and manufactured an experimental prototype of small-scale technological gyrotron on permanent magnet (λ = 10 mm (n = 2), TE_{12}, P = 10 kW, weight of the magnet system is ϕ8 kg, field B_0 = 0.54 T, the length of the homogeneous section at the level ≤ 0.5% at the resonator region with bore diameter 40 mm is L_0 = 100 mm). This generator is the basic version for development of the prototype of an industrial technological gyrotron on permanent magnets (see Table 2).

Experiments with the prototype of a small-scale technological gyrotron in various regimes, necessary modification of the design of the gun and magnetic system basing on analysis of experimental and calculation data were the main research line during this period.

At the first stage of our studies, in order to form the electron beam, we optimized numerically and manufactured an adiabatic magnetron-injection gun of the triode type operating in the following regime: accelerating voltage 25 kV, anode voltage 20 kV, operating current ≤ 2.5 A, pitch-factor g = 1.5. The average radius of the beam in the resonator is 2.86 mm, radius of the cathode is 8.5 mm. Density of the cathode emission current is $j \leq 2.5$ A/cm^2 at the width of the emitter l = 2 mm.

The gyrotron collector system provides landing of the electron beam on the profiled cylindrical collector with its radius R = 18 mm with specific power density Psp ≤ 1.2 kW/cm^2. The gyrotron is designed as a metal-ceramic sealed unit, which can be dismantled for required modification of the gun, resonator and other elements of the gyrotron basing on the analysis of experimental and calculated data. To maintain required vacuum, an external electric-discharge pump is used. The power output is made of quartz shaped as a disk with preset thickness. The magnetron injection gun allows formation of the required electron beam and achievement of operation lifetime in the heating regime over 1000 hours, when high-temperature emitting materials are used, which are stable to sharp variations in regimes of operation and to breakdowns. The

magnetic system that provides gyrotron operation includes three additional axially symmetric corrections coils with independent current regulation and mounted directly on the gyrotron. The resonator coil is used for fine adjustment of the magnetic field for ±0.02 T (power consumption $P < 15$ W). The cathode and collector coil provide the field up to 0.03 T ($P < 50$ W). The use of these coils makes it possible to fix the point of electron beam's landing on the collector rigidly and choose optimal regimes of operation of the magnetron-injection gun when controlling the output power of the gyrotron.

The experimental study of the technological gyrotron in the complex was aimed at the following:

1. Studying the time and temperature stability of the magnetic system on permanent magnets and their influence on gyrotron operation.
2. Determining dependencies of gyrotron power and efficiency on current and voltage of the electron beam. Finding optimal operation regimes and determining optimal ways to control the gyrotron output power.
3. Testing operability of the power supply system.

Time and temperature stability of the magnetic system on permanent magnets was studied by the method of repeated forced long-term variation of the magnet temperature from 10°C to 28°C and measurement of topography of the magnetic field in the operation volume. According to the experimental data, the temperature coefficient of the magnet does not exceed 0.08 %/°C, which corresponds to real characteristics of high-quality rare-earth magnetic materials. Relative distribution of the magnetic field stayed constant. Absolute variation of the value of the magnetic field at variation of the magnet temperature is easily compensated by three additional axially symmetric correction coils mounted directly on the gyrotron (see above). No time instability of the magnetic system was observed during the whole term of operation of the system (about 2 years).

In experiments with the gyrotron stable generation was obtained at the frequency 28.5 GHz (TE_{12}) with output power 12 kW, efficiency 24% ($U_b = 25$ kV, $I = 2$ A). Resonance frequency of the experimental gyrotron cavity was adjusted to achieve value of magnetic field. Optimal regimes for operation and control over the output power of the gyrotron were found, which is necessary for further practical works with microwave processing of dielectric materials with various heating scenarios.

At the next stage of the research aiming at improving quality of the electron beam and suppress its instability in regimes with high power it is planned to further optimize the electron-optical system, specifically, to use new, non-traditional electron-optical system, which have a number of advantages. This stage will include experiments with high-temperature LaB_6 emitters manufactured in accord with various techniques and low-temperature emitters (of metal alloys or metal-porous ones) that provide longer lifetime of the cathode and gyrotron as a whole. At the next stage it is also planned to correct longitudinal distribution of the high frequency and magnetostatic fields in the resonator. All this makes it possible to increase efficiency and maximum output power of the gyrotron.

Conclusion

The chosen design version used for 30 GHz/10 kW/CW gyrotron (n = 2, warm oil cooled magnet) may be used as the promising basis for further development of technological 5.8 GHz/100 kW, 24.125 GHz/100 kW and 61.125 GHz/10 kW CW gyrotrons.

Permanent magnetic system (weight 68 kg) with the axial magnetic field 0.54 T was designed, manufactured and successfully tested. In experiments with the gyrotron stable generation was obtained at the frequency 28.5 GHz (TE_{12}) with output power 12 kW, efficiency 24%.

New permanent magnetic system (weight 88 kg) with the axial magnetic field 0.45 T was designed for industrial 24.125 GHz/30 kW/CW gyrotron.

Experimental parameters of the magnetic system and gyrotron correspond to the calculated models, and the chosen version can be used for further development of technological gyrotrons on warm and permanent magnets in the wide frequency range for broad industrial application.

References

1. Bykov Yu., et al. Ceramic Transaction, Microwaves: Theory and Applications in Materials Processing III, Westerville, Ohio, 1995, V. 59, 133.
2 Flyagin V.A., et al. Proc. of the 7th ITG Conf. on Vacuum Electronics and Displays, Garmisch-Partenkirchen, ITG-Fachbericht, 1995, V. 132, 187.
3. Kuftin A.N., et al. Izvestiya Vysshikh Uchebnykh Zavedenii, Radiofizika, 1992, 35(6-7), 614.
4. Kuftin A.N., et al. Int. J. of Infrared and Millimeter Waves, 1993, V. 14, № 4, 783.
5. Flyagin V.A., et al. Proc. 10th Joint Russian-German Meeting on ECRH&Gyrotrons, IAP, N.Novgorod, 1998, 297.

IMPACT OF REFLECTIONS ON GYROTRON OPERATION

O. Dumbrajs, M. Glyavin, M. Moiseev*, V. Zapevalov*, N. Zavolsky**

Helsinki University of Technology, Espoo, Finland
*Institute of Applied Physics Russian Academy of Sciences, Nizhny Novgorod, Russia

Influence of some types of reflections on oscillatory processes in gyrotrons has been studied. Processes in a gyrotron and in gyrotron complexes with a common load have been simulated numerically. Conditions for a stable single-mode gyrotron operation are discussed.

Introduction

Powerful gyrotrons are widely used in fusion plasma experiments under ECR conditions. It is unavoidable that a part of the microwave power is reflected from the electrodynamic system of a gyrotron, transmitting line components, dielectric windows, and from chamber walls. The reflected signal turns back into the operating volume of a gyrotron – the cavity – and changes the interaction conditions of the electron beam and the RF field [1, 2]. In this paper impact of reflections on gyrotron operation is investigated.

The importance of reflections will increase in gyrotron complexes in large fusion installations where waves from many individual gyrotrons have to be transmitted to the plasma through only a few transmission lines. Here some unexpected interference effects caused by possible reflections from some elements of the transmission line and from plasma itself may occur.

Basic equations

To investigate the mode competition we used the well-known system of equations (see, for example [3, 4]) consisting of the electron motion equation and the equation of mode excitation for the complex amplitude $C = F\exp(-i\varphi)$, which in the presence of reflections has the following form:

$$\frac{dC_S}{d\tau} = C_S\left(\Phi_S - \frac{1}{2Q}\right) + C_S(t-T)\cdot\left(\frac{R}{Q}\right)\exp\left(i\int h(z)dz\right).$$

Here $\tau=\omega_0 t$ is the dimensionless time and Φ is the factor of mode excitation by the electron beam. The perturbation introduced by the reflected signal to the cavity is described by the delay time T, the reflection coefficient R, and the phase shift due to passage to the reflection point and back. In the general case R is a complex quantity (see [2] for details).

Results and discussion

In order to simulate the reflections numerically, we approximated the longitudinal structure of the RF field by a Gaussian, assumed optimal operating parameters, and considered several reflection coefficients. We found good agreement between the results obtained in the cold cavity approximation and in the self-consistent approach in which a non-fixed structure of the RF field in the cavity was used.

Estimates show that $T \approx 0.5$ in the case of reflections from a standard vacuum window of a gyrotron, or from some irregularities of the inner electrodynamic system, and $T \approx 5$ in the case of reflections from distant components of the transmission line, or from a vacuum window of the torus. In the case of absence of a reflected signal the character of stabilization of oscillations is similar to the trajectory in the phase space resembling the equilibrium state of a "stable node" type. For the typical ratio $I/I_{st} \approx 2$ in powerful gyrotrons and for $R < 0.25$ the character of oscillations is similar to a "stable focus", and the stabilization time increases with increase of the amplitude of the reflected signal and of the delay time. For $0.25 < R < 0.35$ we observe self-modulating oscillations where modulation depth increases with increasing reflection coefficient. For $R > 0.35$ we observe stochastic oscillations (Fig. 1).

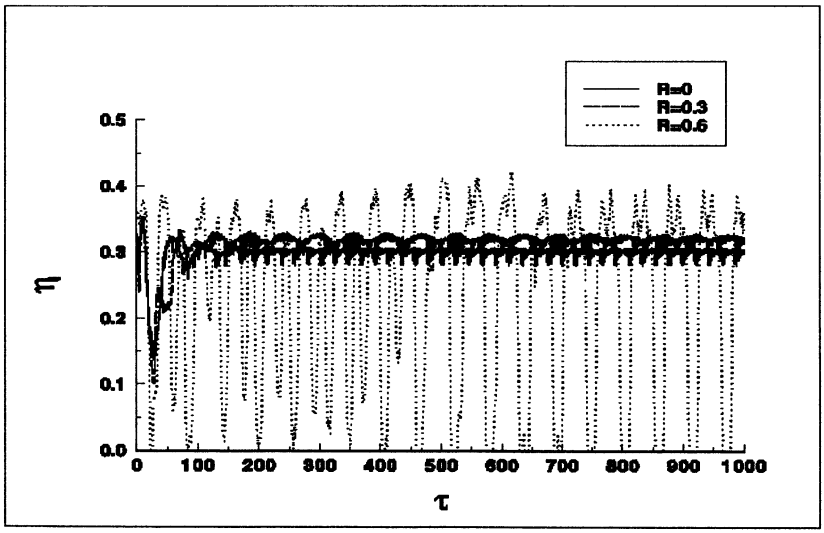

Fig. 1. Gyrotron oscillation regime for different reflection coefficients and $I/I_{st} = 2.5$

Here oscillations with a constant amplitude are almost monochromatic, but in the self-modulating and stochastic regimes the frequency spectrum becomes much broader which is related to the increase of the integral power at frequencies different from the carrier frequency (see details in [2, 5]). Similar behavior was observed experimentally in gyrotrons for technological applications [6].

In Fig. 2 we show the results of multimode simulations in the presence of reflections. For moderate reflection, R=0.3, of the satellite modes and no reflection of the central mode we observe a narrowing of operation domains of the satellites and extension of the operation domain of the central mode. Here the maximum efficiency of the left-hand satellite is noticeably lower than in the case without reflections. If the satellite modes are not reflected but the reflection coefficient of the central mode is R=0.3, the operation domain of the central mode noticeably shrinks at the expense of broadening of the operation domain of the right-hand satellite. However, the efficiency of the central mode remains high. The situation drastically changes in the case of large reflections (R=0.6). If only the satellites are reflected, then at high voltages we observe a low efficiency multimode operation. Here the central mode is practically completely suppressed. On the other hand, if the satellites are not reflected, but the central mode is reflected, then the right hand satellite is completely suppressed, and the gyrotron operates in the central mode in a very broad range of high voltages.

The results of the mode competition calculations obtained in the self-consistent approach are shown in Fig. 3. Calculations with R=0.6 predict multimoding with rather low efficiency, while cold cavity results foresee oscillations only of the central mode with a very high efficiency.

In modern nuclear fusion installations many gyrotrons (up to 50 in the case of ITER) will operate with common load. In this case operating regimes will significantly depend on the coupling between individual gyrotrons which will result either in a mode synchronization or competition. As an illustration in Fig. 4 we present the results of calculations for two gyrotrons operating with a common load. If gyrotrons are not effectively coupled we observe a single frequency and the same output power for each of the two gyrotrons (dashed lines). In the case of an effective coupling the operation becomes stochastic (solid line).

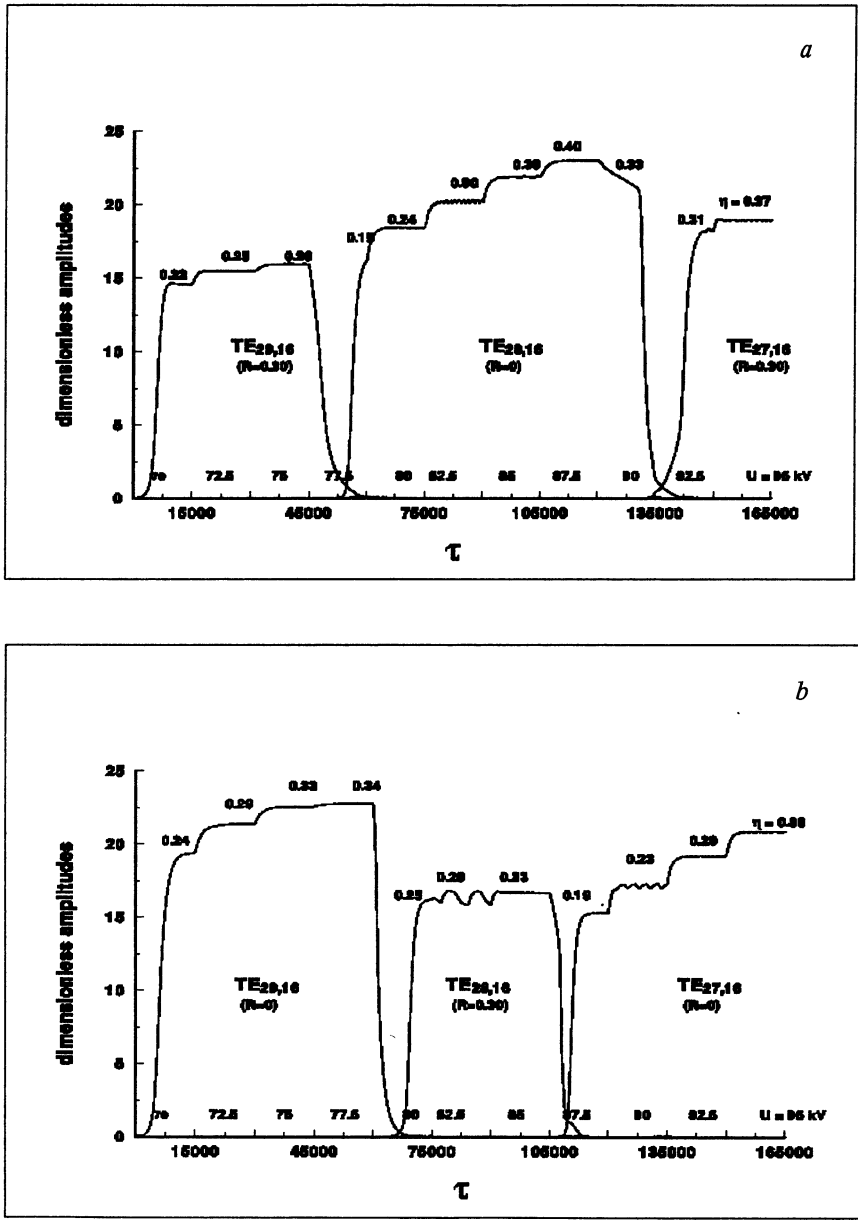

Fig. 2. Operating regimes vs. accelerating voltage for a multimode gyrotron

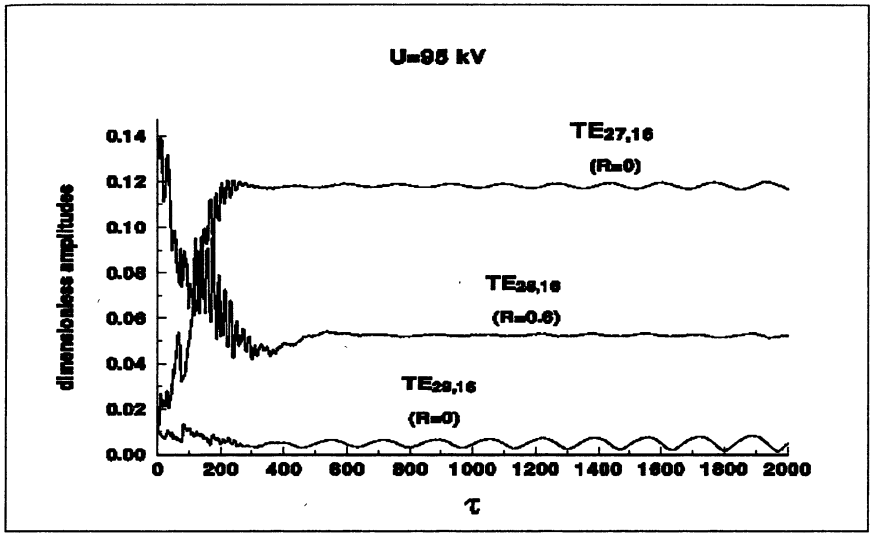

Fig. 3. Operating regime of a multimode gyrotron with high reflection coefficient calculated in the self-consistent approach

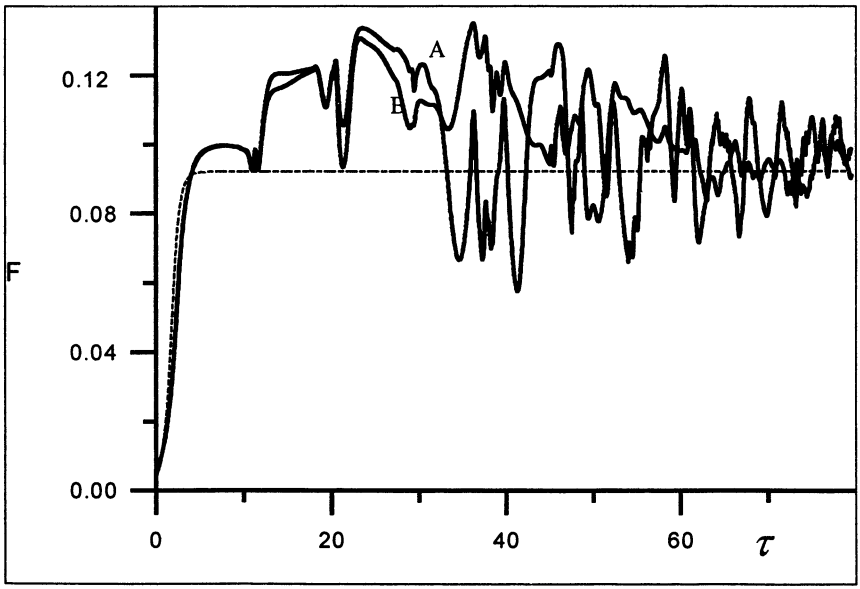

Fig. 4. Amplitude evolution of two gyrotrons (A and B) with a common load and equal beam currents $I_A = I_B$. Dashed line corresponds to R=0 and solid line to $R \neq 0$

Conclusions

The obtained results demonstrate a significant influence of reflections on the operation stability and on the composition of the gyrotron output radiation. With increasing level of the reflected signal oscillations change from the constant amplitude regime to the self-modulating, and finally to the stochastic regime. It is important to emphasize that these transitions occur at significantly smaller ratios I/I_{st} (by an order of magnitude) than in the case without reflections. This means that transitions occur already at currents comparable to operating currents. Already a 10 % reflection at optimal operating current of a gyrotron may result in stochastic oscillations with a broad frequency spectrum of the output radiation. In the case of several gyrotrons working with a common load reflections may significantly change the operation regime of the entire complex. This may have important consequences for the ECRH in large fusion installations.

The authors are deeply grateful to N. S. Ginzburg and M. I. Petelin for their continuous interest in this work and for valuable discussions.

The work was particle supported by RFFI, grant 97-02-17061.

References

1. Antonsen T., Sai S., Nusinovich G. Phys. Fluids, 1992, 4, 12, 4131.
2. Glyavin M., Zapevalov V. Int. J. IRMM Waves, 1998, 11, 1499.
3. Dumbrajs O. Gyrotron Oscillators, C.J.Edgcombe, Ed. London: Taylor&Francis, 1993, ch. 4.
4. Moiseev M., Nusinovich G. Radiophys. Quantum Electron., 1974, 17, 11, 1305.
5. Ginzburg N., et al. Letters to ZhTPh, 24, 11, 1998, 53.
6. M.Glyavin et al. Izv. VUZov, Radiofizika (in print).

NOVEL TYPES OF CYCLOTRON RESONANCE DEVICES

V.L. Bratman, G.G. Denisov, Yu.K. Kalynov,
S.V. Samsonov, A.V. Savilov,
A.W. Cross, W. He*, A.D.R. Phelps*, K. Ronald*,*
C.G. Whyte, A.R. Young**

Institute of Applied Physics, Russian Academy of Sciences,
Nizhny Novgorod, Russia

*Department of Physics and Applied Physics, University of Strathclyde,
Glasgow, Scotland, U.K.

New results for gyrodevices with thin helical beams of electrons encircling the axis of an axi-symmetrical microwave system are presented. The possibility of efficient single-frequency co-generation of an autoresonant mode at fundamental and a gyrotron mode at the second cyclotron harmonic is proved both theoretically and experimentally. Selective operation at 3rd and 4th harmonics with wavelengths of 2.3 and 2.6 mm giving an output power of 70 kW was demonstrated in a Large-Orbit Gyrotron with a thermionic electron gun (10 μs pulse duration). A saturated output power of 1.1 MW and an efficiency of 29% with a gain of 37 dB and an instantaneous bandwidth of 21% was demonstrated for a novel X-band gyro-TWT.

Introduction

This paper presents results of studies for three promising types of Cyclotron Resonance Masers (CRMs) with mildly-relativistic electron beams. Unlike conventional gyrodevices, thin beams of electrons encircling the axis of the microwave systems are used. This allows an improvement in transverse mode selectivity.

In Section 1, a novel oscillator, combining features of High Harmonic Gyrotrons (HHGs) and Cyclotron Autoresonance Masers (CARMs), is described. In this oscillator, resonance conditions are simultaneously fulfilled for an autoresonant mode at the fundamental and for a gyrotron mode at the second cyclotron harmonic. Due to effective coupling of the modes on a phase-synchronized electron beam, a high-efficiency regime of co-generation of the modes is realized. In such a system it is sufficient to provide feedback for the gyrotron mode only. Once excited, the gyrotron mode scatters into the autoresonant mode which is then amplified by the electron beam. Theoretical simulations are confirmed by experimental study of an oscillator in the Ka-band.

In Section 2, results of experiments for a HHG in the so-called Large-

Orbit Gyrotron (LOG) configuration are presented. Unlike our previous LOG experiments, which had explosive-electron-emission cathodes, a quasi-Pierce thermionic electron gun with magnetic confinement of a very thin electron beam is used. Selective generation at 3rd and 4th cyclotron harmonics with high power at short millimeter wavelengths was demonstrated.

Section 3 is dedicated to experimental results from gyro-TWTs with a novel operating waveguide. The first bandwidth measurements of this gyro-amplifier are presented. The coupling between the second-harmonic negative-energy (fast) cyclotron mode of a large-orbit-gyrating electron beam and the radiation field was achieved in the region of near-infinite phase velocity over a broad bandwidth by using a cylindrical waveguide with a helical corrugation on its internal surface.

1. CARM-Gyrotron

There are two main approaches to frequency enhancement in relativistic Cyclotron Resonance Masers (CRMs). The first is to achieve a large Doppler up-conversion of the electron cyclotron frequency in the Cyclotron Autoresonance Maser (CARM) [1-4], which is based on excitation of a traveling RF wave propagating along the guiding magnetic field with a phase velocity close to the speed of light. The second is the operation at high cyclotron harmonics in the relativistic gyrotron (a type of CRM based on excitation of a near-cutoff wave). According to the theory [2-3], the important advantage of the CARM would be a high electronic efficiency. However, most CARM experiments (with exception of the work described in [5]) demonstrate a relatively low efficiency. This is primarily caused by a strong sensitivity of the CARM to spread in electron velocity, in conjunction with the difficulty of producing high quality gyrating beams of relativistic electrons. As for the high-harmonic relativistic gyrotron, its efficiency decreases with the increase of the harmonic number. However, its advantage is stable and selective excitation of a near-cutoff mode in a simple cavity.

In this section, we propose a device which could combine the advantages of the CARM and the relativistic gyrotron. Its principle is based on the fact that a beam of phase-synchronized cyclotron oscillators can provide an effective interaction between two modes excited at the same frequency. Namely, we consider the $TE_{1,1}$ and $TE_{2,1}$ modes of a cylindrical cavity, which are excited by an axis-encircling electron beam at the

fundamental ("CARM" interaction) and second ("gyrotron" interaction) cyclotron harmonics respectively (Fig.1). In such an oscillator, both modes are excited simultaneously in a single cavity, being a piece of cylindrical waveguide with cut-off narrowings at the beam injection and output ends (Fig.2). Such a simple cavity is closed for the near-cut-off "gyrotron" mode. Correspondingly, the quality of this mode is very high and defined basically by Ohmic losses in the cavity walls. At the same time, the slight output narrowing scarcely reflects the traveling "CARM" mode. Therefore, this cavity provides an effective and selective feedback for the "gyrotron" mode only. The operating "CARM" mode is excited due to the electron bunching caused by the "gyrotron" mode and provides a high electronic efficiency. The output radiation is formed by the "CARM" mode only; the power of the "gyrotron" mode is dissipated in the cavity walls.

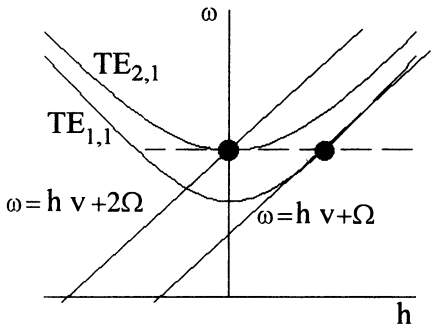

Figure 1. Dispersion diagram for the fundamental CARM and second-harmonic gyrotron resonances at the same frequency.

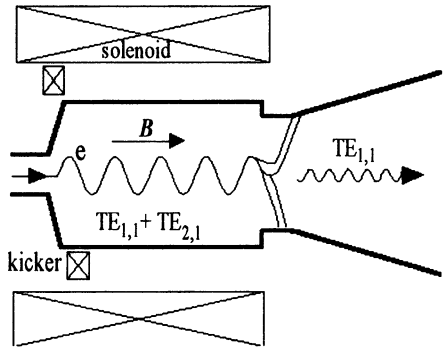

Figure 2. Schematic of CRM-oscillator based on simultaneous excitation of "gyrotron" and "CARM" modes

One should note some advantages of this scheme of feedback for the traveling wave, which propagates almost parallel to the cavity axis. Along with simplicity of the microwave system, it solves the problem of mode control, which is very important for CARMs. The stable generation of the "gyrotron" mode can fix the frequency of the operating "CARM" mode.

In principle, the proposed scheme of this CRM-oscillator is analogous to the sectioned, multi-wave CRM based on Doppler multiplication of the frequency [6]. In this device, a near-cut-off mode with some frequency, ω_1, is excited in the first section and then, in the second section, it is scattered into a traveling wave with a frequency $\omega_2=n\omega_1$. However, even for an ideal

electron beam the predicted efficiency of this device does not exceed 10%, while the length required for the interaction region is rather long. Another analogy is related to a novel type of gyro-TWT [7,8] (see also Sect. 3). It is also based on coupling of near-cut-off and traveling modes; however, the coupling is provided not by an electron beam but by a helical corrugation of the waveguide walls.

In the CRM-oscillator shown in Fig. 2, a thin rectilinear electron beam enters the operating cavity. Inside the cavity, a magnetostatic kicker imparts transverse (rotary) momentum to the electrons. Having been kicked, the electrons are assumed to be in cyclotron resonance simultaneously with the traveling $TE_{1,1}$ mode at the fundamental cyclotron harmonic, n=1, and with the near-cut-off $TE_{2,1}$ mode at the 2nd harmonic, n=2, (Fig. 1):

$$\omega \approx h v_z + \Omega \approx n\Omega \quad . \tag{1}$$

Here ω is the frequency, h is the longitudinal (axial) wavenumber of the $TE_{1,1}$ mode, v_z is the longitudinal electron velocity, $\Omega = eB/mc\gamma$ is the cyclotron frequency, and γ is the electron Lorentz factor. Let us introduce phases of an electron with respect to both waves,

$$\theta_1 = \omega t - hz - \psi \quad , \quad \theta_2 = \omega t - n\psi \, . \tag{2}$$

Here z is the longitudinal coordinate and ψ is the gyrophase of the particle. At z=0 the initial phases are defined as follows

$$\theta_1(z=0) = \omega t_0 - \psi_0 \quad , \quad \theta_2(z=0) = \omega t_0 - n\psi_0 , \tag{3}$$

where the entering times, t_0, and the initial electron gyrophases, ψ_0, are distributed within the intervals $0 \le \omega t_0 < 2\pi$ and $0 \le \psi_0 \le \Delta\psi_0$. For a helical electron beam formed by a kicker, $\Delta\psi_0 << \pi$. In this case, every particle has the same initial phase with respect to both modes. Therefore, the modes are coupled by the electron beam.

In order to describe the interaction of electrons with the two modes, we shall use a modification of the well-known averaged (over the fast cyclotron rotation) equations [3]. Let us represent the electron Lorentz factor as follows

$$\gamma = \gamma_0 \left(1 + w_1 + w_2\right) . \tag{4}$$

Here w_1 and w_2 describe the energy exchange between the electron and the two modes ("CARM" and "gyrotron" modes respectively) and satisfy the following equations:

$$\frac{\mathrm{d}\,w_1}{\mathrm{d}\,\zeta} = -\chi_1 \,\mathrm{Im}\left(a_1 \mathrm{e}^{\mathrm{i}\theta 1}\right) \;,\; \frac{\mathrm{d}\,w_2}{\mathrm{d}\,\zeta} = -\chi_2 \,\mathrm{Im}\left(a_2 \mathrm{e}^{\mathrm{i}\theta 2}\right) \quad . \tag{5}$$

Here $\zeta = \omega z / c$, $a_{1,2}$ are the normalized amplitudes of the "CARM" and "gyrotron" modes, $\chi_1 = p_\perp / 2p_z$ and $\chi_2 = p_\perp^2 / 2p_z$ are the coupling coefficients, and $p_{\perp,z} = \gamma v_{\perp,z} / \gamma_0 c$ are the normalized components of the electron momentum. We also take into account that the change in longitudinal momentum of a particle is caused by its interaction with the "CARM" mode only and is approximately described by the well-known integral [3]

$$p_z - \beta_{z_0} = w_1 / \beta_{\mathrm{ph}} \quad . \tag{6}$$

Here β_{ph} and β_{z_0} are the phase velocity of the "CARM" mode and the initial longitudinal electron velocity normalized by the speed of light. This allows the equations for the electron phases with respect to the modes to be written in the following form:

$$\frac{\mathrm{d}\,\theta_1}{\mathrm{d}\,\zeta} = \frac{-\delta_1 - \left(1 - \beta_{\mathrm{ph}}^{-2}\right) w_1 - w_2}{p_z} - F \;,\; \frac{\mathrm{d}\,\theta_2}{\mathrm{d}\,\zeta} = \frac{-\delta_2 - w_1 - w_2}{p_z} - 2F \quad . \tag{7}$$

Here $\delta_1 = 1 - \beta_{z_0} / \beta_{\mathrm{ph}} - \Omega_0 / \omega$ and $\delta_2 = 1 - 2\Omega_0 / \omega$ are the mismatches of the cyclotron resonance for each mode, Ω_0 is the initial electron cyclotron frequency, and F describes the so-called "forced" electron bunching.

We assume that the "gyrotron" mode has a fixed longitudinal structure coinciding with the first "cold" longitudinal mode of the cavity,

$$a_2(\tau, \zeta) = \hat{a}_2(\tau) \sin(\pi\zeta / \hat{L}) \,. \tag{8}$$

Here $\hat{L}$ is the normalized cavity length, $\tau = \omega t$ is the normalized time. A slow temporal evolution of the "gyrotron" mode amplitude during its interaction with the electron beam is described by the equation:

$$\frac{\mathrm{d}\,\hat{a}_2}{\mathrm{d}\,\tau} + \frac{\hat{a}_2}{2Q_2} = \mathrm{i}\frac{G_2}{\hat{L}} \int_0^{\hat{L}} \sin(\pi\zeta / \hat{L}) \left\langle \chi_2 \mathrm{e}^{-\mathrm{i}\theta 2} \right\rangle \mathrm{d}\zeta \quad . \tag{9}$$

Here Q_2 is the quality of this mode, and $\langle \ldots \rangle$ indicates averaging over the initial parameters t_0 and ψ_0 of all electrons. For the "CARM" mode, the cavity is assumed to provide no feedback. In this situation, the excitation of this mode is described by the spatial equation for a waveguide mode with zero amplitude at the beam injection aperture.

$$\frac{d a_1}{d \zeta} = iG_1 \left\langle \chi_1 e^{-i\theta_1} \right\rangle \ , \ a_1(\zeta = 0) = 0 \ . \qquad (10)$$

In Eqs.(9) and (10),

$$G_1 = \frac{2I\beta_{ph}\left(1-\beta_{ph}^{-2}\right)}{I_A N_1 \gamma_0}$$

and

$$G_2 = \frac{8I}{I_A N_2 \gamma_0}$$

are the factors of excitation. Here I is the electron current, $I_A = mc^3 / e$, and $N_{1,2}$ are the wave norms. Thus, the quasi-stationary equations Eqs.(5)-(10) describe simultaneous excitation of the "gyrotron" and "CARM" modes at a frequency which is fixed by the "gyrotron" mode. The efficiency of the interaction between the electron beam and each mode is described by the averaged (over all electrons) fractions of the initial kinetic electron energy passed to that mode,

$$\eta_{1,2}(\tau) = -\left\langle w_{1,2}(\tau) \right\rangle / (1 - \gamma_0^{-1}) \ .$$

We have simulated a CRM configuration similar to the experiment described in [5], where a high-efficiency CARM was realized for the first time, (500kV / 50 A electron beam, operating frequency of 38.7 GHz, with a cavity diameter and length of 0.77 cm and 8 cm respectively), but with a slightly modified cavity of a gyrotron type (Fig. 2). Calculations show that over a wide parameter space (operating electron-beam current, electron pitch factor, quality of the cavity) it is possible to obtain regimes with a very effective excitation of the "CARM" mode (Fig. 3 a). In these regimes, a very small part of the electron energy (less than 1%) is lost due to excitation of the "gyrotron" mode (Fig. 3 a). Given a sufficiently high quality cavity and transverse component of the initial electron velocity, $\beta_{\perp 0} = 0.60 - 0.65$, the electronic efficiency, corresponding to the excitation of the operating "CARM" mode, can be as high as $40 - 60\%$. This is at least twice the theoretical limits for the simplest CARM-oscillator schemes [3].

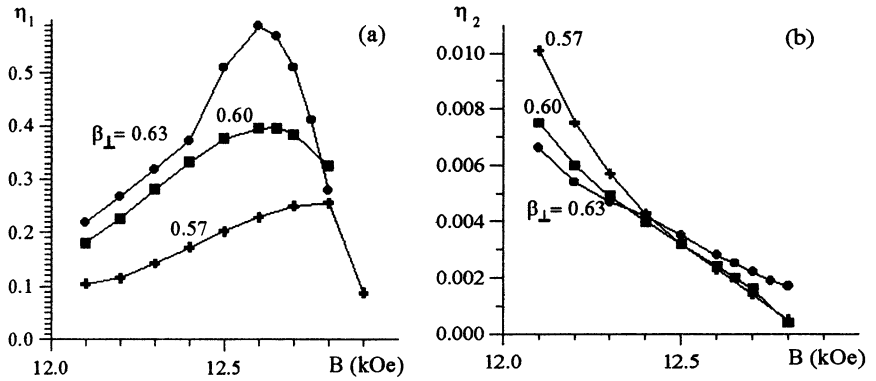

Figure 3. Efficiency of the energy exchange with the operating "CARM" mode, η_1, (a) and the fraction of the electron energy passed to the "gyrotron" mode, η_2, (b) versus the magnetic field, B, at various initial oscillatory electron velocities, $\beta_{\perp 0}$.

In fact, the oscillator operates as an amplifier of the "CARM" mode. It amplifies perturbations in the electron beam, which are induced by the "gyrotron" mode. This can be understood from Fig. 4, which illustrates the energy exchange between the modes at the stable stage of the optimal regime (the regime giving highest "CARM" efficiency, η_1). In the first half of the interaction region the beam passes the energy mainly to the "gyrotron" mode. In the second half, the "CARM" mode takes almost the entire energy of the "gyrotron" mode. Thus, the suppression of the "gyrotron" mode increases the efficiency, η_1, due to the decrease of the energy losses, η_2, which are expended in the excitation of this mode.

In order to clearly confirm this mechanism of the interaction between a second-harmonic gyrotron mode and a CARM mode, an experiment similar to that described in [5] was performed. A thin helical axis-encircling electron beam was produced using an almost identical electron-optical system and was injected into the 60 mm long section of circular waveguide 7.7 mm in diameter having a 37.8 GHz cut-off frequency for the $TE_{2,1}$ mode. Unlike the experiment [5], the cavity was terminated at its output not by a Bragg reflector but by a section of smooth circular waveguide with a smaller diameter, 7.1 mm giving a 41 GHz cut-off frequency for the $TE_{2,1}$ mode (Fig. 2). Thus, the "cold" microwave feedback for the $TE_{1,1}$ mode was eliminated while a high-Q cavity for a second-harmonic gyrotron was provided.

The experiment produced microwave radiation at a frequency of 40±1 GHz having a mode pattern corresponding to a $TE_{1,1}$ mode. The maximum output power was measured for an axial magnetic field of 11.0 - 11.3 kG and an electron pitch factor of about 1. The electron beam voltage, current and output microwave power were 460 kV, 60 A and 6 MW respectively (Fig. 5), which corresponded to a 22% electronic efficiency (presumably the slightly lower efficiency, compared to the experiment [5], can be explained by the lower electron current).

An experiment with the same cavity but terminated by the Bragg reflector was repeated. The reflector had grooves with minimum and maximum diameter of 7.1 mm and 8.5 mm respectively, and effectively reflected the $TE_{1,1}$ mode within a frequency band of 35-36 GHz. In this case, two regimes of oscillations were clearly observed: CARM-gyrotron and "pure" CARM operation. At lower magnetic fields (10.3-10.5 kG) the "pure" CARM operation at 35.5 GHz with an output power of nearly 4 MW was detected. At a higher magnetic field the CARM-gyrotron regime with parameters close to those described above dominated. When the Bragg reflector had been replaced by a section of a smooth waveguide with the same diameter as the cavity, the output microwave signal had about 5 times less power, shorter pulse duration and was unstable from shot to shot.

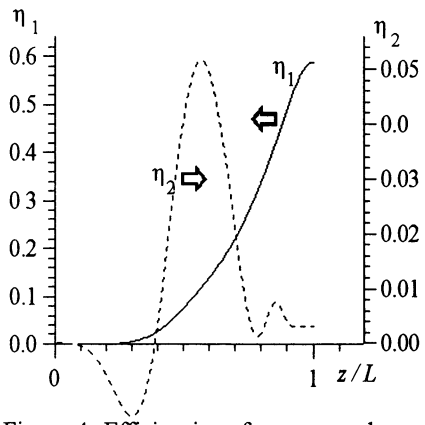

Figure 4. Efficiencies of energy exchange between electron beam and the "CARM" and "gyrotron" modes, η_1 and η_2, versus the longitudinal coordinate.

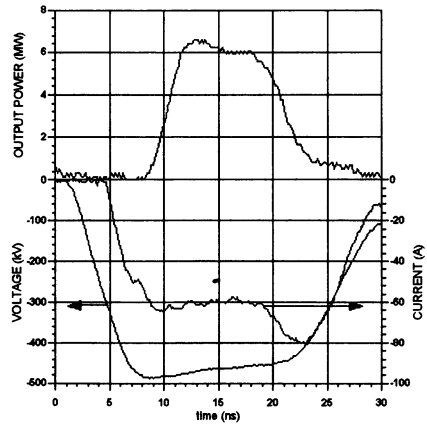

Figure 5. Oscilloscope traces of voltage, current and output microwave power for a CRM based on simultaneous excitation of near-cut-off and traveling modes.

2. Large-Orbit Gyrotron

It is well known that the excitation of high cyclotron harmonics is significantly stronger at relatively high electron energy. In order to provide single-mode operation at higher harmonics, along with the electron energy increase, the gyrotron mode selectivity must also be enhanced. One approach is the use of a Large-Orbit Gyrotron configuration [9-12] where a thin electron beam encircling the axis of an axi-symmetric electrodynamic system is utilized. Such a beam excites only co-rotating modes with azimuthal indices equal to the resonant harmonic number. Selective excitation of the first five cyclotron harmonics ($TE_{1,1}$-$TE_{5,1}$ operating modes) was demonstrated in prototype experiments with a short-pulse LOG [12]. These experiments used a beam source similar to the experiments described in Sect.1. A 300keV/30A/20ns pencil electron beam containing the most rectilinear central particles was selected by a narrow anode aperture from the total current of 3-5 kA of a field-emission diode. Microwave power of about 1.5 MW was generated at the fundamental and the second harmonic (wavelengths of 13.9 and 8.4 mm, respectively) with 600, 200, 120 kW at the 3rd-5th harmonics (wavelengths of 6.1, 4.8 and 4.0 mm, respectively). The operating magnetic field at the fifth harmonic was 8.0 kG.

The results obtained for the short-pulse LOG have been used to design a long-pulse LOG with a thermionic electron gun. The LOG is designed to operate at the 3rd-5th cyclotron harmonics at wavelengths of 2.6, 2.3 and 2.0 mm respectively. The corresponding operating modes are $TE_{3,2}$, $TE_{4,2}$, and $TE_{5,2}$; the radial index is increased from 1 to 2 in order to increase the diameter of the cavity and diminish ohmic losses. Based upon the parameters of an existing high-voltage long-pulse power supply and preliminary calculations, the following requirements for the electron beam were determined: energy of 250 keV, current of 10-15 A and beam diameter of 0.6 mm. The electrons should gyrate around the axis with a minimum displacement of their guiding centers and with a pitch factor g=1.2-1.5 in a resonant magnetic field of 1.6-1.7 T.

To produce such a beam, a two-stage electron-optical system has been designed [12]. First a thin electron beam is formed, and then the electrons acquire the necessary transverse velocity passing through a kicker. Compared to the short-pulse prototype, the use of a thermionic emitter (requiring the utilisation of the entire cathode current) combined with the decrease of the beam diameter, (because of the halfing of the operating

wavelength) complicates the formation of the rectilinear beam. For the conventional current density from thermionic cathodes, 5 A/cm^2, the beam cross-section must be compressed more than 1000 times. To achieve such a compression without creating large transverse velocities before the kicker, a system providing electron trajectories parallel to the guiding magnetic field lines is designed and constructed.

If such a compression is to be achieved, the magnetic field at the cathode should be very low ~1.5 mT, corresponding to a Larmor period of 8 m. The space required for adiabatic compression is therefore too great. To overcome this the electron-optical system is designed so that in the vicinity of the cathode the electron trajectories are governed by the electrostatics of the "Pierce-like" electrodes and the space charge fields. A system of magnet coils are configured to match the axial magnetic field profile to the particle trajectories. When the electrons achieve a sufficiently strong magnetic field, a conventional adiabatic compression decreases the beam diameter to the required level (Fig. 6). The kicker is located in the region of adiabatic compression, where the field is relatively weak (about 0.5 T). After the kicker, the electron transverse velocity is further increased in the tapered guiding magnetic field (Fig. 7). The kicker is optimized to impart upon the beam the required pitch factor with minimum displacement of the electron guiding centers from the axis and minimum sensitivity to position spread. For the operating parameters, simulations predict a transverse velocity spread $\left(\delta v_\perp / v_\perp\right)_{rms}$ =7%, which is small enough for effective operation at both 4th and 5th harmonics. The kicker can function over a very wide range (about 50%) of axial magnetic field strength.

A traditional axi-symmetrical gyrotron cavity consisting of a cut-off narrowing at the beam injection end, a cylindrical part (6.7 mm diameter and 22 mm length), and an output taper, is used. After leaving the cavity, the radiation propagates along a waveguide with a diameter of 20 mm and is launched from a horn antenna with a length of 150 mm and an aperture diameter of 50 mm (Fig. 8).

The generation of the $TE_{5,2}$ mode has not been observed in the experiment because of its suppression by a long-wavelength (5 mm) mode. Presumably, this is the $TE_{3,1}$ mode at the 2nd cyclotron harmonic; its spurious excitation is possible if the electron-beam displacement from the axis is about 0.6 mm (Fig. 9). However, stable selective excitation of the

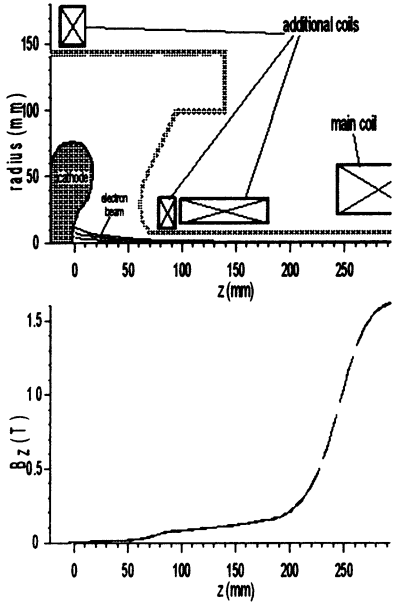

Figure 6. Schematic of the electron-optical system.

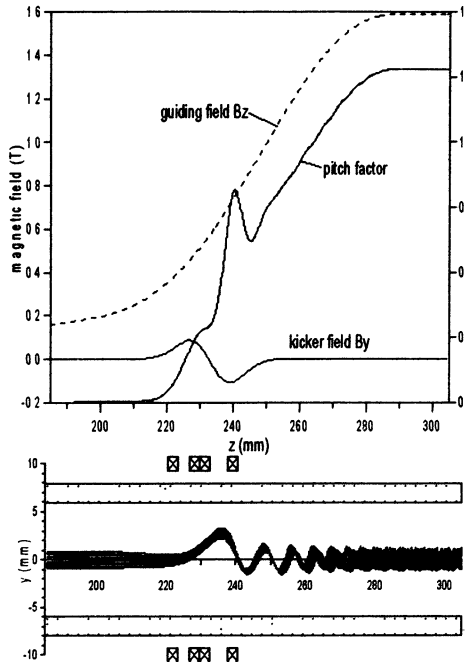

Figure 7. Axial magnetic field profiles and the pitch factor evolution of an initially axial electron. Also illustrated are the trajectories in the kicker region

other operating modes, $TE_{4,2}$ and $TE_{3,2}$, was clearly observed at magnetic fields 1.67-1.75 T and 1.92-1.99 T, respectively. The selective excitation of the proper modes was confirmed by measurement of the wavelength of the output radiation, as well as its transverse structure. For instance, Figs. 10 and 11 illustrate the measured structure of the $TE_{4,2}$-mode. Spurious generation and electron-beam instability limit the operating current, $I \leq 10$ A, and the pitch factor of electrons. A maximum efficiency, 4.0% for the $TE_{4,2}$ mode (Fig. 12) and 4.8% for the $TE_{3,2}$ mode, was achieved at a current of 4-6 A (Fig. 13). A maximum power of 70-80 kW was measured at an efficiency of 3.5% for both modes.

The same electron-optical system has allowed a test of the possibility of stable selective generation of the $TE_{4,2}$ operating mode at the 4th cyclotron harmonic for lower electron energies down to 130 keV. Simulations predict selective generation for a yet further decrease of the electron energy down to a typical gyrotron value of 80 keV.

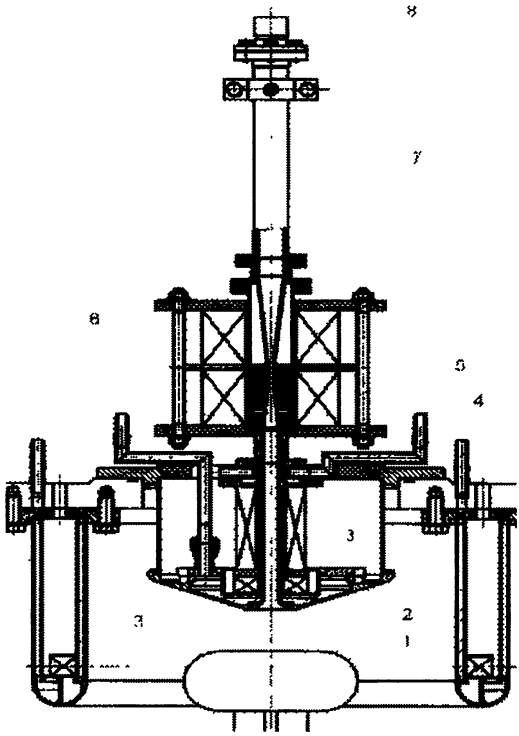

Figure 8. Experimental scheme of LOG: cathode (1), anode (2), supplementary coils (3), kicher (4), main coil (5), cavity (6), collector (7), and output window (8).

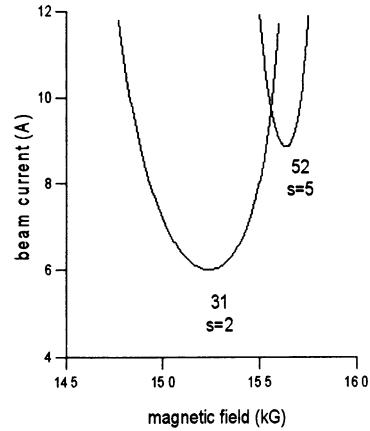

Figure 9. Calculated ranges of excitation for spurious 2nd-harmonic $TE_{3,1}$-mode and operating 5th-harmonic $TE_{5,2}$ - mode in the case of 0.6 mm electron-beam displacement.

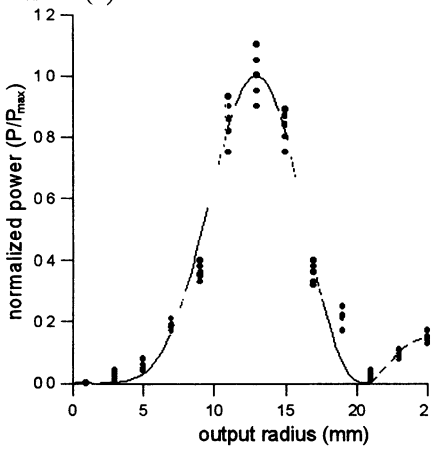

Figure 10. Measured radial component of the electric field of the $TE_{4,2}$-mode.

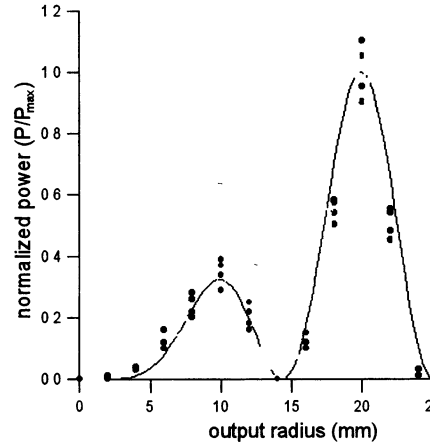

Figure 11. Measured azimuthal component of the electric field of the $TE_{4,2}$-mode.

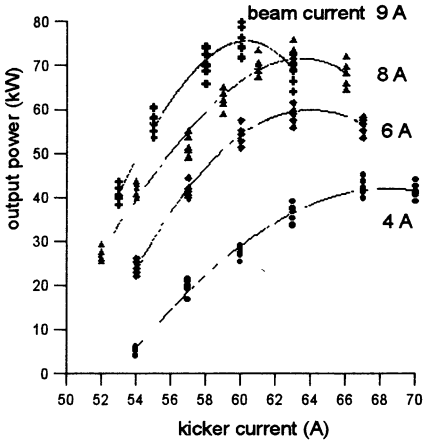

Figure 12. LOG operation at 4th harmonic. Output power versus the kicher current and the electron-beam current.

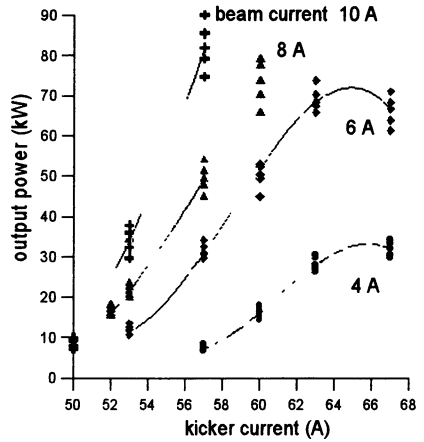

Figure 13. LOG operation at 3rd harmonic. Output power versus the kicher current and the electron-beam current.

3. Gyro-TWT with a helically corrugated waveguide

The CRM instability between a gyrating electron beam (in a guide magnetic field) and a mode of a cylindrical waveguide has long been investigated due to its potential for efficient, broadband amplification of radiation [13,14]. The relative dispersion relations of the beam and the radiation have conspired to seriously limit this potential. In the regime of low axial wavenumbers the bandwidth is limited by the curvature of the hyperbolic wave dispersion (as compared to the linear beam dispersion) and the fact that in this regime the wave group velocity is close to zero means that the interaction is prone to undesirable oscillations. On the other hand if one operates with high axial wavenumbers, where the group velocity becomes close to "c", then Doppler broadening of the resonance spoils the efficiency of the interaction and limits the bandwidth [15]. Nonetheless, broadband amplifiers have a rather large range of applications, and the ability to increase the radiation power capability above that possible in conventional slow-wave amplifiers is desirable. Gyroklystrons have thus far been developed to offer the high power and frequency capabilities of the CRM instability to amplifier applications, but these experiments use resonant cavities as their interaction spaces, inherently limiting the relative bandwidth ~1% [16,17]. A number of variations to increase the bandwidth of Gyro-TWT's have been investigated [18-21]. However, the experiments have consistently met

serious difficulties due to the sensitivity of the interaction to the beam quality and to spurious oscillations.

A new idea has recently been reported [7,8] which has re-opened the potential for a broadband gyro-TWT where a helical corrugation on the wall of the interaction waveguide couples together a near to cut-off mode and a far from cut-off mode to produce a wave dispersion with a finite and nearly constant group velocity in the region of near infinite phase velocity. This dispersion may be readily matched to an electron beam's linear dispersion characteristic over a rather broad bandwidth. Because the group velocity is large over the resonance, the problem of oscillations is considerably reduced whilst the small axial wavenumbers limit the impact of electron velocity spread. An experiment based on this approach has recently been reported [8] at two rather close frequencies, but the potential of the system for high gain and efficiency with good stability against oscillations was demonstrated. This Section presents the first measurements of the bandwidth capabilities of such an amplifier.

The surface of a helically grooved waveguide can be represented in cylindrical coordinates r, φ, z as follows:

$$r(\varphi,z) = r_0 + l\cos\left(\overline{m}\varphi + \overline{h}z\right), \qquad (11)$$

where r_0 is the waveguide mean radius, l, $\overline{m}$ and $\overline{h} = 2\pi/d$ are the amplitude, azimuthal and axial numbers of the corrugation respectively, and d is the corrugation period. The desired change of the dispersion will be achieved if the corrugation couples two partial rotating waves of a waveguide with a radius of r_0; one partial wave is near-cut-off, mode (A), and has a small axial wavenumber, $h_A << k$, where $k=\omega/c$, while the other partial wave, a traveling wave (B), has a large axial wavenumber, $h_B \sim k$. For such conditions to be realized, the axial wavenumbers and azimuthal indices of the waves and the corrugation should satisfy the Bragg conditions,

$$h_B \approx \overline{h}, \quad m_A + m_B = \overline{m} \ . \qquad (12)$$

The resonant coupling of the waves corresponds to the intersection of their dispersion curves or, more exactly, the intersection occurs between mode A and the first spatial harmonic of wave B with cutoff frequencies ω_0 and ω_{0B} respectively (Fig.14).

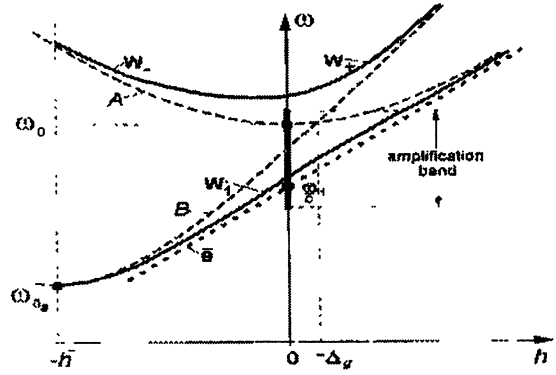

Figure 14. Dispersion diagram for a helical waveguide: *A, B* - the partial near-cut-off and traveling waves of a smooth waveguide, respectively, which are coupled due to the helical corrugation of the inner surface, W_1 and $W_\pm$ - the operating and "spurious" eigenwaves of the helically corrugated waveguide, $\bar{e}$ - unperturbed electron cyclotron wave.

If the corrugation amplitude l is small compared with the wavelength, the field structure and dispersion characteristics of the helically corrugated waveguide can be calculated by means of the method of perturbation [22].

The eigenwaves $W_\pm$ and W_1 (Fig.14), which arise as a result of coupling the partial waves *A* and *B,* can then be found. When parameters of the corrugation are properly chosen, the wave W_1 has the desirable dispersion. The relative frequency gap between W_1 and the "spurious" waves $W_\pm$ at "zero" axial wavenumber is of the order of the coupling coefficient of the waves σ, which is proportional to the relative amplitude of the corrugation l/r_0 and depends also on the azimuthal and radial indices of the partial waves. For a relatively small corrugation depth, when $\sigma \le 0.1$, the method of perturbation provides good agreement with "cold" experiments [8]. It is clear from the dispersion curves of the helically corrugated waveguide (Fig.14) that mode $W_\pm$, having a region with a small group velocity, can be easily excited like an operating mode of a conventional gyrotron-oscillator. But for attractive amplification regimes, when the corrugation is sufficiently deep, a large separation of curves W_1 and $W_\pm$ occurs. The mode $W_\pm$ can still be excited but at magnetic fields significantly higher than the operating values.

An improved version of the University of Strathclyde direct action accelerator is used. A 120 ns accelerating voltage pulse of amplitude 185 kV is applied across a Pierce-like diode [23] drawing a rectilinear electron beam with a current of 20 A and a diameter of 8mm from the velvet emitting surface (Fig.15). The electron beam traverses a microwave coupler where the input radiation is introduced through the side of the cylindrical drift region from a rectangular WG16 waveguide (8.2-12.5 GHz). The input radiation is passed through a "quarter wave plate" consisting of an elliptically deformed waveguide region converting it to circular polarization. Transverse velocity is imparted to the electron beam in a "kicker" consisting of 4 pairs of small (short) rectangular multi-turn coils arranged in a Helmholtz like configuration. The arrangement of these coils is such that the electron beam perceives a single full turn rotating transverse magnetic field component as it drifts through the kicker. In the present experiment, with an axial guide magnetic field (provided by a water cooled DC solenoid) of 0.21 T, a pulsed current of 112 A applied to the kicker produced a beam with a pitch factor of 1.2 and a transverse velocity spread $\left(\delta v_{\perp} / v_{\perp}\right)_{rms}$<15%. The resulting electron beam describes a helical, axis encircling, trajectory with the electron gyro-radius being greater than the transverse size of the electron beam itself.

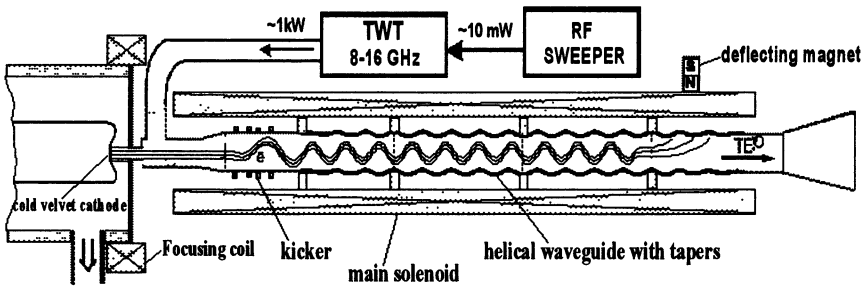

Figure 15. Schematic diagram of the gyro-TWT with a helically corrugated waveguide.

In the present experiment the operating mode is synthesised by coupling the $TE_{2,1}$ mode (azimuthal index, m_A =2) and the counter-rotating $TE_{1,1}$ mode (m_B =1) as the near and far from cut-off modes respectively on a three fold helical corrugation in the wall of a cylindrical copper waveguide having a mean diameter 28.2 mm. The corrugated waveguide was 60cm in length with a corrugation amplitude of 2.2mm and period of 47.5mm plus entrance tapers of 12cm length at each end where the

corrugation tapered linearly to meet the smooth 28.2mm bore of the input and output waveguides. The operating band is below the cut-off frequency of the $TE_{2,1}$ mode of the smooth input/output waveguides. Therefore at the input to the corrugated waveguide, radiation in the $TE_{1,1}$ mode, counter-rotating with respect to the helix, converts totally to the operating mode of the amplifier. The output radiation at the other end undergoes the opposite transition so that the output radiation from the amplifier is in the fundamental mode of the cylindrical waveguide, counter-rotating with respect to the electron beam. The theoretically predicted dispersion plot for this waveguide is illustrated in Fig.16.

Distributed losses were introduced over a 5 cm length in the centre of the interaction waveguide to counter the possibility of oscillations. Cold test experiments measured 6 dB losses between 8 and 10.5 GHz. A permanent magnet could be used to vary the length of the interaction space by deflecting the electron beam to impact on the waveguide wall, which facilitated study of the gain process as a function of interaction length.

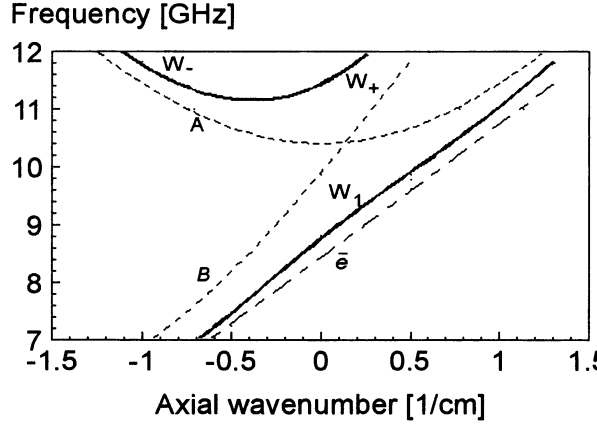

Figure 16. Dispersion diagram for the helically corrugated waveguide: dotted and solid lines correspond to partial and eigen modes respectively.

The input signal for the experiment was provided by a conventional broadband helix TWT with a peak output power of 400 W driven by a solid state oscillator producing up to 20 mW. A calibrated variable attenuator was used to control the input power. The radiation power launched into the operating wave was calibrated as a function of frequency.

The input power provided to the amplifier was sufficient to saturate

the CRM interaction as illustrated in Fig. 17 a where the output power is plotted against the input power for a frequency of 9.2 GHz (using the calibrated attenuator in the input waveguide to control the launched radiation power). Fig. 17 b illustrates the effect of changing the interaction length on the gain, using an input power of 200 W clearly showing saturation in the region close to the end of the helical waveguide. In this plot, the length origin is taken to be the start of the input taper to the helix, and the location of the microwave absorbing section was 42 cm.

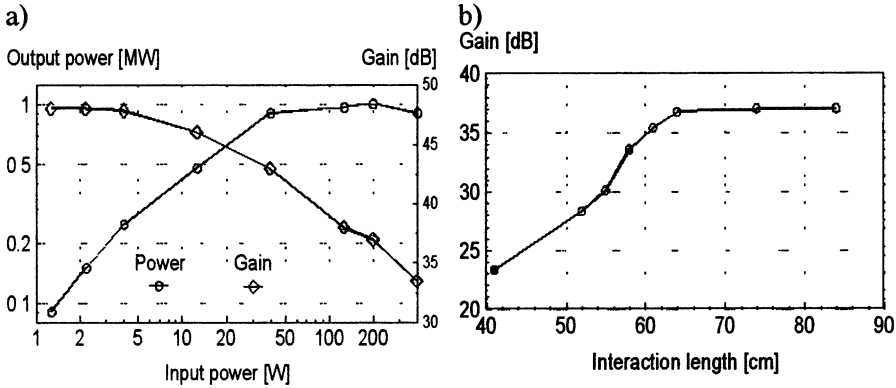

Figure 17. Measured output power and gain versus input power (a) and as a function of interaction length (b) at a drive frequency of 9.2 GHz.

A bandpass filter was used to verify that the amplified output radiation followed the input frequency. The experiment proved to be zero drive stable. By combining a carefully calibrated attenuator and rectifying detector, the gain of the amplifier was measured as a function of the input frequency, both in the saturated and linear regimes. The results of these measurements are presented in Fig.18. A saturated gain of 37 dB was obtained with a relative bandwidth (3 dB points) of 21% centred on 9.4 GHz. Using an input power of less than 10 W a linear gain of up to 47 dB was measured. Taking the saturated gain plot and combining it with the calibrated input power launched into the operating mode, the efficiency was calculated as a function of frequency and is illustrated in Fig.19. The microwave output signal had a peak of 1.1 MW at a frequency of 9.4 GHz corresponding to an efficiency of 29%. This performance compares well with the predictions of non-linear theory (Fig.19). The simulations were performed for the experimental parameters taking a mean electron

pitch-factor of 1.2 and a transverse velocity spread of $(\delta v_\perp / v_\perp)_{rms} = 10\%$.

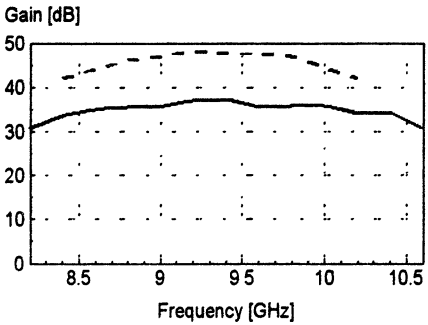

Figure 18. Measured saturated gain (solid line) and linear gain (dotted line) as a function of frequency.

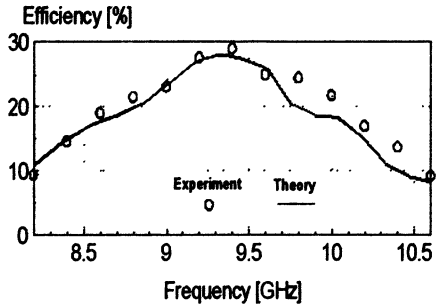

Figure 19. Comparison of measured and predicted saturated efficiency as a function of frequency.

This experiment confirms that with the addition of a small amplitude helical corrugation to the wall of a cylindrical waveguide, broadband amplification of guided radiation by the CRM instability can be achieved with high efficiency and good stability against oscillations. The high efficiency of this second harmonic gyro-amplifier compares well with the performance of second harmonic gyrotron oscillators.

The realization of a broadband gyro-amplifier with efficiency close to that of a comparable gyrotron oscillator has some important implications for a range of potential applications in radar and broadcast telecommunications where requirements exist for broadband amplifiers having a higher power/frequency capability than the current generation based on slow-wave instabilities. If this novel approach proves to scale in a manner comparable with the gyrotron oscillators, then the potential for high power >100 kW, high frequency >100 GHz broadband amplifiers could create new applications.

Further experiments are planned at both the IAP Nizhny Novgorod, Russia and at the University of Strathclyde, Glasgow, Scotland, UK. These experiments will explore the potential of this new concept with lower energy <100 kV electron beams and will look at increased beam pulse durations (using a thermionic cathode electron gun) which will be attractive for a number of applications.

At the Institute of Applied Physics, another gyro-TWT experiment has

recently been completed at Ka-band frequencies. In the regime of single-frequency amplification at 36.5 GHz, the gyro-TWT operating at the second harmonic with a 290 keV, 36 A electron beam moving in a uniform magnetic field of 0.95 T has generated the high output power of 2.8 MW corresponding to a gain of 33 dB and an efficiency of 27%.

This work was supported by the United Kingdom DERA, Gycom Ltd. (Nizhny Novgorod, Russia), and the Russian Foundation for Basic Research under Grants 98-02-17068, 98-02-17208, and 99-02-16361.

References

1. Petelin M.I., Radiophys. Quantum Electron. **17** (1974) 686.
2 Bratman V.L., Ginzburg N.S., and Petelin M.I., Opt. Commun. **30** (1979) 409.
3. Bratman V.L., Ginzburg N.S., Nusinovich G.S. et al, Int. J. Electron. **51** (1981) 541
4 Sprangle P., Tang C M., Serafim P., Nucl. Instr. Meth. Phys. Res. **A250** (1986) 361.
5 Bratman V.L., Denisov G.G., Kolchugin B.D. et al, Phys. Rev. Lett. **75** (1995) 3102.
6. Aleksandrov A.F. et al., Radiotekhnika i Elektronika **29** (1984) 1788.
7. Cooke S.J. and Denisov G.G., IEEE Trans. Plasma Sci. **26** (1998) 519.
8. Denisov G.G., Bratman V.L., Phelps A.D.R., and Samsonov S.V., IEEE Trans. Plasma Sci. **26** (1998) 508; Denisov G.G., Bratman V.L., Cross A.W. et al, Phys. Rev. Lett. **81 (**1998) 5680,
9. Jory H.R., Research and Development Technical Report ECOM-01873-F, Varian Associates, Palo Alto, California, 1968.
10. McDermott D.B., Luhmann N.C., Jr., Kupiszewski A., and Jory H.R., Phys Fluids **26** (1983) 1936.
11. Lawson W., Destler W.W., Striffler C.D., IEEE Trans. Plasma Sci. **13** (1985), 444.
12. Bratman V.L., Kalynov Yu.K., Ofitserov M.M. et al, IEEE Trans. on Plasma Sci. **27** (1999) 456.
13. Gaponov A.V., Izv. Vuzov. Radiofizika **2** (1959) 443.
14 Sprangle P. and Drobot A.T., IEEE Trans. MTT **MTT-25** (1977) 528.
15. Latham P E. and Nusinovich G.S., Phys. Plasmas **2** (1995) 3494.
16. Calame J.P., Garven M., Choi J.J. et al, Phys. Plasmas **6** (1999) 285.
17. Chu K.R., Drobot A.T., Granatstein V.L. and Seftor J.L., IEEE Trans. Electron Devices **MTT-27** (1979) 178.
18. Ferguson P.E., Valier G , Symons R.S., IEEE Trans. MTT **MTT-29** (1981) 794.
19. Ganguly A.K. and Ahn S., Int. J. Electron **53** (1982) 641.
20. Park G.S., Choi J.J., Park S Y. et al, Phys. Rev. Lett. **74** (1995) 2399.
21. Chu K.R., Chen H.Y., Hung C.L. et al, Phys. Rev. Lett. **81** (1998) 4760.
22. Katselenenbaum Z., "Theory of non-regular waveguides with slowly changing parameters", Moscow: Academy of Sciences of USSR, 1961.
23 Cooke S.J., Cross A.W., He W., Phelps A.D.R., Phys. Rev. Lett. **77** (1996) 4836.

EXPERIMENTAL DEMONSTRATION OF A HIGH-AVERAGE POWER W-BAND GYROKLYSTRON AMPLIFIER

M. Blank, K. Felch, B.G. James, P. Borchard, P. Cahalan, T.S. Chu, H. Jory

Microwave Power Products Division
Communications and Power Industries
Palo Alto, CA

T.A. Hargreaves, R.B. True, A.J. Theiss, G.R. Good

Electron Devices Division
Litton Systems, Inc.
San Carlos, CA

B.G. Danly, B. Levush, J.P. Calame, K. Nguyen[a], D. Pershing[b], J. Petillo[c]

Vacuum Electronics Branch
Naval Research Laboratory
Washington, D.C. 20375

W.G. Lawson and T.M. Antonsen, Jr.

University of Maryland
College Park, MD

The experimental demonstration of a high average power W-band (75–110 GHz) gyroklystron amplifier is reported. The gyroklystron has produced 118 kW peak output power and 29.5% electronic efficiency in the TE_{011} mode using a 66.7 kV, 6 A electron beam at 0.2% rf duty factor. At this operating point, the instantaneous full-width-half-maximum (FWHM) bandwidth is 600 MHz. At 11% rf duty factor, the gyroklystron has produced up to 10.1 kW average power at 33% electronic efficiency with a 66 kV, 4.15A electron beam. This represents world record performance for an amplifier at this frequency. At the 10.1 kW average power operating point, the FWHM bandwidth is 420 MHz. At higher magnetic fields and lower beam voltages, larger bandwidths can be achieved at the expense of peak and average output power.

The continuing need for high power sources of microwave and millimeter wave radiation for such varied applications as high resolution radars [1], linear accelerators [2], and magnetic resonance imaging [3] has led to extensive research on gyroklystron amplifiers [4–17]. The gyrotron amplifier has a considerable advantage over the conventional millimeter wave sources, such as klystrons or traveling-wave-tube (TWT)

amplifiers, in its increased power handing capability. The gyrotron interaction is based on the cyclotron maser instability, in which a cyclotron beam mode imparts energy to a fast-wave electromagnetic mode with a phase velocity faster than the speed of light. In these devices, the beam can interact with higher order electromagnetic modes. As a result, the transverse circuit dimensions of a gyrotron amplifier are typically comparable to or larger than a free-space wavelength. The gyroklystron is a special case of gyrotron amplifiers in which the beam interacts with standing wave cavity modes. This is contrasted with slow-wave devices, where the phase velocity of the wave is less than the speed of light and transverse circuit dimensions are typically 10% of a free-space wavelength. Because of this small circuit size, thermal loading due to both beam interception and rf heating severely limits the peak and average power that can be achieved at millimeter wave frequencies. For example, the W-band coupled cavity traveling wave tube amplifier, the slow-wave device with the highest average power capability at millimeter wave frequencies, is limited to approximately 5 kW peak and 500 W average output power. Without the heating and breakdown problems associated with small interaction circuits, gyrotron amplifiers are capable of producing significantly higher peak and average powers than their slow-wave counterparts.

Since gyrotron amplifiers can achieve higher output powers than conventional slow-wave devices at high frequencies, they are now being considered for a wide variety of existing and future millimeter wave radar systems where increased power results in increased radar performance [1]. For example, the use of gyrotron amplifiers for cloud physics radars would result in the ability to study clouds at greater ranges than is possible with the extended interaction klystrons currently used. Also, gyrotron amplifiers are of considerable interest for ground based space debris detection and asteroid tracking. Other radar applications that could benefit from the increased power of the gyrotron amplifier include space object identification and planetary mapping studies by means of inverse synthetic aperture radar.

As evidenced by numerous experiments, gyroklystron amplifiers can reliably and efficiently generate high peak power and moderate bandwidth electromagnetic radiation at millimeter wave frequencies. For example, a two-cavity Ka-band (26–40 GHz) gyroklystron, developed for radar applications, produced 750 kW at 35 GHz in the TE_{021} mode at 24% efficiency and 0.1% bandwidth [12]. Two and three-cavity Ka-band gyroklystrons operating in the TE_{011} modes produced 210 kW at 0.36%

bandwidth [13] and 225 kW at 0.82% bandwidth [14], respectively. In W-band, a pulsed four-cavity gyroklystron amplifier achieved 65 kW peak output power at 26% efficiency with 300 MHz bandwidth [10]. A continuous wave version of the device demonstrated 2.5 kW average output power, a result that represented the highest average power from an amplifier in this band prior to the work described below. Another W-band gyroklystron amplifiers produced peak output powers up to 80 kW and bandwidths up to 640 MHz [15–17]. In this paper, the generation of very high average power from this type of amplifier is reported.

Below, the design and experimental demonstration of a W-band gyroklystron amplifier is described. The circuit consists of a drive cavity, two idler cavities, and an output cavity. The circuit was designed using a time-dependent version of a non-linear code [18]. In this formalism, the cold cavity electric fields are determined by a scattering matrix method [19]. A linear theory analysis [20] was used to determine the stability of each cavity and drift section for the nominal operating parameters. A more detailed description of the theoretical tools and design methodology can be found in Ref. 21.

To determine the optimal circuit parameters, an extensive study was made of the tradeoffs in gain, power, and bandwidth that come through varying cavity and beam parameters. A complete description of this design study can be found in Ref. 22. For the optimized circuit parameters detailed in Table 1, the predicted efficiency and peak output power versus frequency for a 65 kV, 6 A electron beam is shown in Fig. 1. As shown in the figure, efficiencies up to 25% and bandwidths greater than 700 MHz are expected for beam velocity ratios, $\alpha=v_\perp/v_z$, between 1.5 and 1.7 and an rms perpendicular velocity spread of 2.2%. The output power and efficiency are sensitive to relatively small changes in the beam velocity ratio.

Table 1. Design and measured values of cavity parameters for four-cavity gyroklystron amplifier circuit

	Design			Cold Test	
	L (cm)	f_0 (GHz)	Q_L	$f_{0\,vac}$ (GHz)	Q_L
cavity 1	0.36	93.41	126	93.67	130
cavity 2	0.48	94.21	175	94.24	175
cavity 3	0.48	93.28	175	92.82	175
cavity 4	0.87	93.89	162	93.67	160

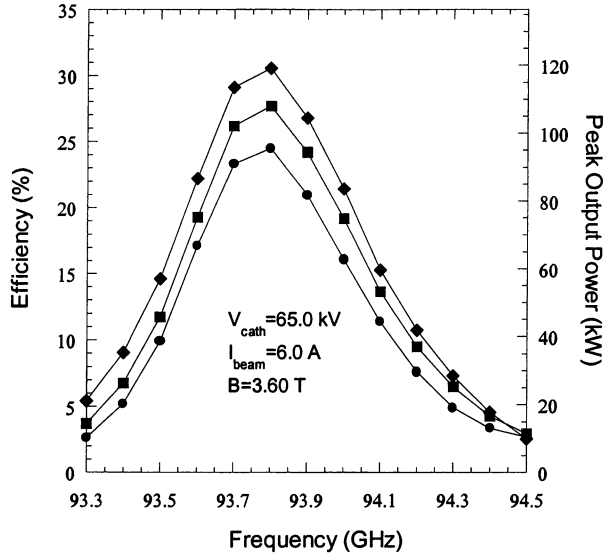

Figure 1. Theoretical prediction for peak output power and efficiency versus drive frequency for the four cavity gyroklystron amplifier detailed in Table 1 for beam velocity ratios α=1.5 (filled circles), α=1.6 (filled squares), and α=1.7 (filled diamonds)

In the experiment, the beam is formed by a 65 kV, 6 A magnetron injection gun which was designed to have very good beam quality, with perpendicular rms velocity spreads near 2% [23]. The beam α is controlled by the voltage on the modulating anode, which is nominally 17 kV above cathode potential, and by the superconducting coil that controls the magnetic field over the cathode. The interaction circuit is positioned in the flat field region of the 4T superconducting magnet. The power generated in the idler cavities, which is approximately 400 W average at the nominal operating point, is diffractively coupled out of the cavities and dissipated in external loads. Following the output cavity is a non-linear up taper to the collector, which also serves as the output waveguide. The shape of the taper was specially designed to minimize mode conversion while tapering up to a large radius in a short length. The power is coupled out of the device through a CVD (chemical vapor deposition) diamond window. Cold tests showed that for frequencies in the range of 93 GHz to 95 GHz, between 0.25% and 1% of the power incident on the window is reflected. A water load is positioned on the atmospheric side of the vacuum window, and the temperature rise of the water for a given volumetric flow rate is used to measure the average rf power.

The input drive power is coupled into the interaction circuit through a coaxial input coupler described in Ref. 21. A single rectangular waveguide excites the TE_{411} mode of the outer coaxial cavity. Power is then coupled from the TE_{411} mode in the outer cavity to the TE_{011} mode in the inner cavity through four slots positioned symmetrically around the azimuth of the cavity. The input coupler was designed using HFSS, a finite-element electromagnetics code. Two different drivers were used in the experimental demonstration. For low-duty testing (< 0.2% rf duty factor) the drive power was supplied by an extended interaction oscillator (EIO), which is mechanically tunable from approximately 92.5 GHz to 95.5 GHz. The EIO produces up to 2 kW peak output power at pulse lengths up to 2 μsec. For high-duty testing, a coupled-cavity TWT amplifier was used. This amplifier produces up to 100 W peak output power over the 93 GHz to 95 GHz frequency range at duty factors up to 100% (cw). The drive power is measured with a calibrated directional coupler at the gyroklystron input flange and the frequency of the input and output rf signals are measured with a spectrum analyzer. Losses in the drive line between the source and gyrotron input flange were found to be approximately 3 dB.

Parametric studies of circuit operation with beam current and magnetic field variations were made at low rf and beam duty to determine the best operating point for subsequent high duty operation. As shown in Fig. 2, the gyroklystron produced up to 118 kW peak output power and 29.5% electronic efficiency in the TE_{011} mode using a 66.7 kV, 6 A electron beam at 0.2% rf duty factor. At this operating point, the instantaneous FWHM bandwidth was 600 MHz and the gain was 24.7 dB. At higher magnetic fields the bandwidth increases and the peak output power and gain decrease. This trend is predicted by the theoretical model, which shows that at lower fields, the input cavity operates in the negative beam loading regime, which increases the Q of this cavity and leads to lower bandwidth and higher gain and output power. As the magnetic field is increased, the cavity moves into the positive beam loading regime, where the negative beam Q decreases the overall Q of the cavity, resulting in wider bandwidth and lower gain and output power.

Also evident in Fig. 2 is the ripple in the peak output power across the frequency band. This effect is due to reflections from the CVD diamond window, which create standing waves between the window and output cavity and modulate the output power of the device. This effect was modeled with the MAGY code, a fully self-consistent non-linear formalism [24]. The code showed that the spacing and amplitude of the

output power across the band is consistent with reflections from the output window. The code also showed that the amplitude of the ripple is reduced at higher magnetic fields, as was observed experimentally. More detailed theoretical analyses of the measured data will be presented in forthcoming papers.

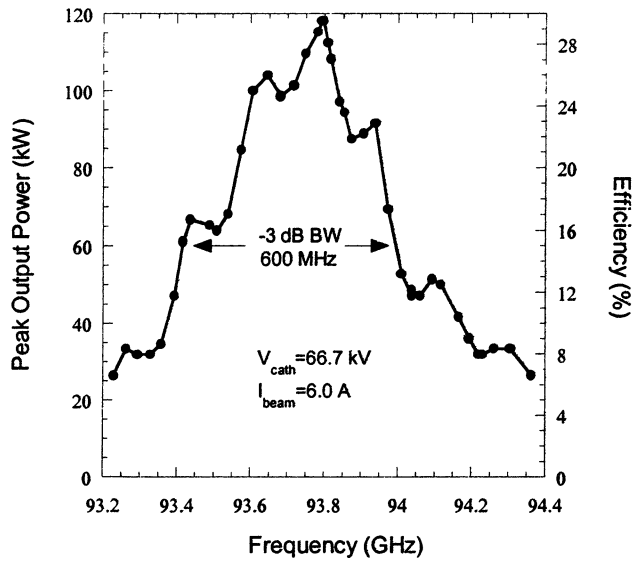

Figure 2. Measured peak output power and efficiency versus frequency a 66.7 kV, 6 A electron beam

Upon completion of the low duty demonstrations, the EIO was replaced with the 100 W coupled cavity TWT driver amplifier for high duty tests. Because of input power limitations, a high-gain operating point was chosen for the high duty tests. Figure 3 shows the measured peak and average output power versus drive frequency for a 66 kV, 4.15 A electron beam. The rf pulse width was 100 μsec and the pulse repetition frequency was 1.1 kHz, corresponding to 11% rf duty factor. The gyroklystron produced 10.1 kW average output power, corresponding to 90 kW peak output power and 32.9% efficiency. The measured FWHM bandwidth was 420 MHz. Figure 4 shows the average output power and gain versus drive power. As shown in the figure, the maximum output power of 10.1 kW average and 92 kW peak is achieved for 53 W peak driver power, corresponding to 32 dB gain.

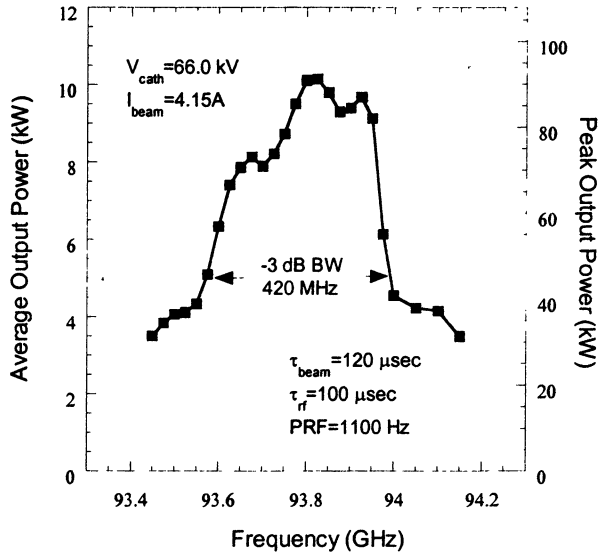

Figure 3. Measured average and peak output power for a 66 kV, 4.15 A electron beam and 11% duty factor

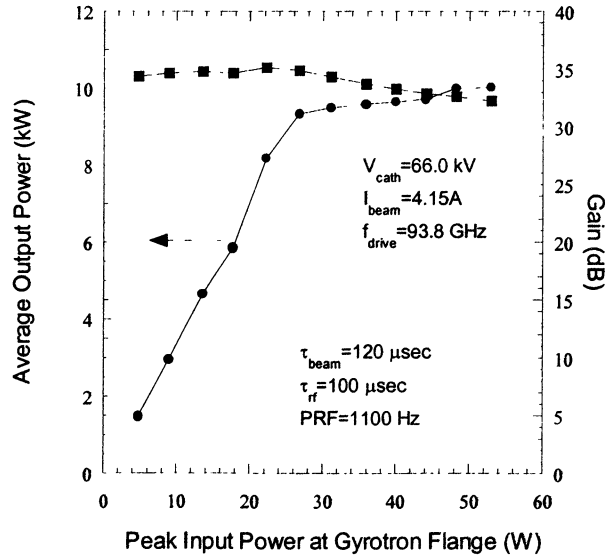

Figure 4. Measured average output power and gain for a 66 kV, 4.15 A electron beam and 11% rf duty factor. The drive frequency was held fixed at 93.8 GHz

Figure 5 shows the peak output power versus drive frequency for rf pulse widths of 10 μsec, 40 μsec, and 70 μsec. For each curve, the beam current and beam voltage pulse widths were held fixed at 90 μsec and the pulse repetition frequency was 1 kHz. As seen in the figure, for rf duty factors ranging from 1% (10 μsec pulse width) to 7% (70 μsec pulse width), the differences in peak output power over the operating bandwidth were negligible. The measured results show that for duty factors in this range (1–7%), there were no significant changes in the circuit or circuit performance resulting from thermal effects.

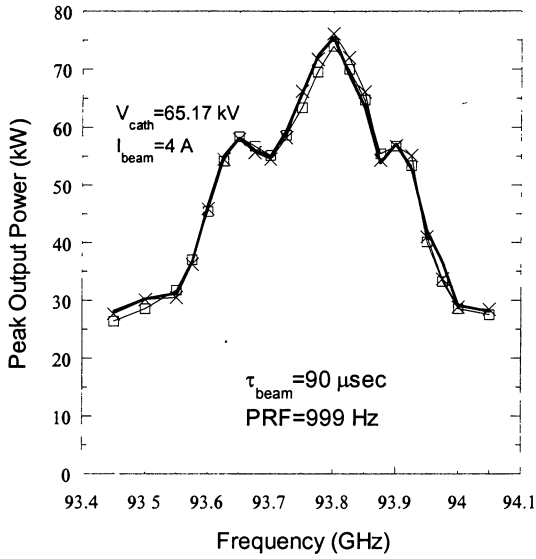

Figure 5. Peak output power for rf beam pulse widths of 10 μsec (open circle), 40 μsec (open square), and 70 μsec (x). For each curve, the beam pulse width, pulse repetition frequency, beam current, beam voltage, and all other parameters were held fixed

Parametric studies were also performed at high duty. By increasing the magnetic field, bandwidths up to 600 MHz could be obtained with reduced peak and average output powers, typically near 50 kW and 5 kW, respectively. The theoretically predicted trend of reduction in the amplitude of the bandwidth ripple at higher magnetic fields was also observed at high duty. In addition, calorimetric measurements were made for the window, the interaction circuit, and other cooled components of the device and were found to be close to the theoretically predicted values of losses.

In summary, a four-cavity TE_{011} mode high average power gyroklystron amplifier was designed, built successfully and tested. At low duty, the amplifier produced up to 118 kW peak output power at 600 MHz bandwidth. At high duty, 10.1 kW average output power and 420 MHz bandwidth were achieved at 11% rf duty. This results represents world record setting performance for an amplifier at this frequency.

Future work will also be centered on improving the certain aspects of the device performance. Because of the limited availability and relatively high cost of high-power, high-duty drivers at millimeter wave frequencies, future work will be focused on improving the gain of the device. A subsequent amplifier currently in construction will be comprised of 5 cavities to improve the gain of the device by more than 10 dB. Future work will also consider bandwidth improvement by replacing the output cavity with a traveling wave output section, a configuration commonly referred to as a gyrotwystron amplifier. A low-duty prototype of a W-band gyrotwystron has demonstrated 50 kW peak output power and 900 MHz FWHM bandwidth [25]. For bandwidths greater than 2 GHz, gyro-traveling-wave tube amplifiers are under investigation.

The authors would like to acknowledge the contributions of N. Dionne, for his help in the collector analysis, S. Cooke, for his analysis of the rf circuit, and J. Feinstein, for his useful discussions. The authors also thank R. Heidinger, R. Spörl and M. Thumm for window loss measurements. This work was supported by the Office of Naval Research. Computational work was supported by the MSRC centers and NAVO and ARL.

References

[a]KN Research, Silver Spring, MD 20906
[b]Mission Research Corp., Newington, VA 22122
[c]Science Applications International Corp., Burlington, MA 01803

1. W.M. Manheimer, G. Mesyats, M.I. Petelin, *Applications of High-Power Microwaves*, A.V. Gaponov-Grekhov and V.L. Granatstein, eds., (Artech House:Boston) p. 169-207, 1994.
2. V.L. Granatstein, W. Lawson, IEEE Trans. Plasma Sci., **24**, 648 (1996).
3. L.R. Becerra, G.J. Gerfen, R.J. Temkin, D.J. Single, R.G. Griffin, Phys. Rev. Lett. **71**, 3561 (1993).
4. W.M Bollen, A.H. McCurdy, B. Arfin, R.K. Parker, A.K. Ganguly, IEEE Trans. Plasma Sci. **13**, 417 (1985).
5. E.V. Zasypkin, M.A. Moiseev, E.V. Sokolov, V.K. Yulpatov, Int. J. Electron. **78**, 423 (1995).

6. W.G. Lawson, J.P. Calame, B. Hogan, P.E. Latham, M.E. Read, V.L. Granatstein, M. Reiser, C.D. Striffler, Phys. Rev. Lett. **67**, 520 (1991).
7. H.W. Matthews, W. Lawson, J.P. Calame, M.K.E. Flaherty, B. Hogan, J. Cheng, P.E. Latham, IEEE Trans. Plasma Sci. **22**, 825 (1994).
8. H.R. Jory, F. Freidlander, S.J. Hegji, J.R. Shively, R.S. Symons, IEDM Digest, 234 (1977).
9. E.V. Zasypkin, M.A. Moiseev, I.G. Gachev, I. I. Antakov, IEEE Trans. Plasma Sci. **24**, 666 (1996).
10. I.I. Antakov, E.V. Zasypkin, E.V. Sokolov, Conf. Digest of the Eighteenth Intl. Conf. On Infrared and MillimeterWaves, Proc. SPIE **2104**, 166 (1993).
11. R.P. Fischer, A.W. Fliflet, W.M. Manheimer, B. Levush, T.M. Antonsen, Jr., V.L. Granatstein, Phys. Rev. Lett. **72**, 2395 (1994).
12. I.I. Antakov, A.V. Gaponov, E.V. Zasypkin, E.V. Sokolov, V.K. Yulpatov, L.A. Aksenova, A.P. Keyer, V.S. Musatov, V.E. Myasnikov, L.G. Popov, B.A. Levitan, A.A. Tolkachev, Proc. Of the Int. Workshop on Strong Microwaves in Plasmas, ed. A.G. Litvak, Nizhny Novgorod 1993, Nizhny Novgorod Press: Nighzny Novgorod, 587.
13. J.J. Choi, A.H. McCurdy, F.N. Wood, R.H. Kyser, J.P. Calame, K.T. Nguyen, B.G. Danly, T.M. Antonsen, Jr., B. Levush, R.K. Parker, IEEE Trans. Plasma Sci, **26**, 416 (1998).
14. J.P. Calame, M. Garven, J.J. Choi, K. Nguyen, F. Wood, M. Blank, B.G. Danly, B. Levush, Physics of Plasmas, **6**, 285 (1999).
15. M. Blank, B.G Danly, B. Levush, P.E. Latham, D.E. Pershing, Phys. Rev. Lett., **79**, 4485 (1997).
16. M. Blank, B.G. Danly, B. Levush, D.E. Pershing, IEEE Trans. Plasma Sci., **26**, 409 (1998).
17. M. Blank, B.G. Danly, B. Levush, submitted to IEEE Trans. Plasma Sci., August 1999.
18. P.E. Latham, W. Lawson, V. Irwin, IEEE Trans. Plasma Sci **22,** 804 (1994).
19. J.M. Neilson, P.E. Latham, M. Caplan, W. Lawson, IEEE Trans. Microwave Theory Tech. **37**, 1165 (1989).
20. P.E. Latham, S.M. Miller, C.D. Striffler, Phys. Rev. A **45**, 1197 (1992).
21. B. Levush, M. Blank, J. Calame, B. Danly, K. Nguyen, D. Pershing, S. Cooke, P. Latham, J. Petillo, T. Antonsen, Jr., Physics of Plasmas, **6**, 2233 (1999).
22. M. Blank, B. G. Danly, B. Levush, IEEE Trans. Plasma Sci., **26**, 426 (1998).
23. K.T. Nguyen, B. G. Danly, B. Levush, M. Blank, R. True, G.R. Good, T.A. Hargreaves, K. Felch, P. Borchard, IEEE Trans. Plasma Sci., **26**, 799 (1998).
24. M. Button, T. Antonsen, Jr., B. Levush, K. Nguyen, A.N. Vlasov, IEEE Trans. Plasma Sci., **26**, 882 (1998).
25. M. Blank, B.G. Danly, B. Levush IEEE Trans. Plasma Sci, **27**, 405 (1999).

200 KW PULSED W-BAND GYROKLYSTRON AMPLIFIER

I. G. Gachev, I. I. Antakov, M. A. Moiseev, E .V. Sokolov, N. A .Zavolsky and E. V. Zasypkin

Institute of Applied Physics, Russian Academy of Science,
46 Uljanov Str. 603600 Nizhny Novgorod, Russia

The results of theoretical and experimental investigations of 2- and 3-cavity versions of high power pulsed W-band gyroklystron amplifier, operating in TE_{021} cavity mode, are presented. Due to solving of a problem of spurious oscillations in the input oversized waveguide the peak output power of 205 kW with an efficiency about 30% have been attained in 2-cavity gyroklystron. Half-maximum bandwidth and gain are 140 MHz and 20.5 dB respectively. 3-cavity gyroklystron has demonstrated 26 dB gain and 450 GHz bandwidth. It also has produced 195 kW peak output power.

Introduction

In last decade, a great progress in the development of high power pulsed W-band gyro-amplifies has been attained. At Institute of Applied Physics (IAP), a pulsed gyroklystron amplifier produced 65 kW peak output power in the TE_{011} cavity mode with a 26% efficiency and 300 MHz bandwidth [1]. A 94-GHz , 10 kW average power gyroklystron has been developed by a collaboration of NRL, CPI, Litton Ind. and University of Maryland [2]. This average power was obtained with 11% duty factor and 92 kW peak power in the TE_{011} cavity mode. The instantaneous bandwidth was 420 MHz, and the efficiency was 33,5%.

Recent IAP and GYCOM W-band activity was centered in the development of a gyroklystron amplifier capable to produce 200-300 kW peak output power with a set of other parameters suitable for radar applications. Last year, a 140 kW peak power with 18% efficiency and 18-dB gain has been attained at 93,5 GHz in a two-cavity gyroklystron operating in the TE_{021} mode [3]. Here the results of two-and three-cavity gyroklystron amplifier examination obtained this year are presented.

Design

In designing a gyroklystron, three problems coupled together should be solved. First, to prevent spurious mode self-excitation in the drift space between gun and first cavity, the magnetic field in this region should drop sharply enough therefore a cryomagnet with a 43-mm bore was chosen to produce a dc magnetic field in the circuit. Secondly, inner

mirror transformer should convert not less than 60% of the TE_{01} mode in the input wave to the desired TE_{02} mode. Thirdly, the gun should produce high quality electron beam with a voltage of 60 kV and a current up to 18 A propagating far enough from as transformer mirror as drift tube wall. In reality, the optimal design is the tradeoff between these requirements.

In a simplest gyroklystron amplifier, the RF circuit comprises two oversized cylindrical cavities operating in the TE_{021} mode at the fundamental cyclotron frequency. The length and quality factor of the input cavity is 1,8λ and 150, respectively. The output cavity length is about 2.1λ and its Q-factor is 600. The calculated eighen-frequencies are a) 92.7 GHz for the first cavity, and b) 92.97 GHz for the output one. In a three-cavity tube, the intermediate cavity has the following parameters: length is 1,4λ, Q-factor is 150, eighen-frequency is 93 GHz. To attain the required Q-factor, the cavity was loaded with ring of lossy ceramic placed at its output end.

The drive power is coupled into the circuit through an input circular waveguide inside cathode, then input TE_{01} mode is transformed to the TE_{02} mode by an inner mirror transformer, and then TE_{02} wave excites the operating TE_{021} mode in the first cavity.

Two-cavity results

To enhance power output and improve efficiency in comparison with the previous data, an axial magnetic field distribution in the circuit and RF circuit profile of two-cavity gyroklystron were optimized. An optimal magnetic field axial profile is characterised by a several percent magnetic field strength reduction in the cavities in regard to that in the drift tube. As a result, a peak saturated output power of 207 kW with an efficiency of 30% was produced for a 60-kV, 11.5-A electron beam (Fig.1). A 20-dB gain was measured at the power level of 150 kW (Fig.2). These output parameters were achieved at a central frequency of 93.5 GHz with 140 MHz bandwidth (Fig.3). The output power was found to be limited by spurious oscillations excited at 89,36 GHz and 86,2 GHz

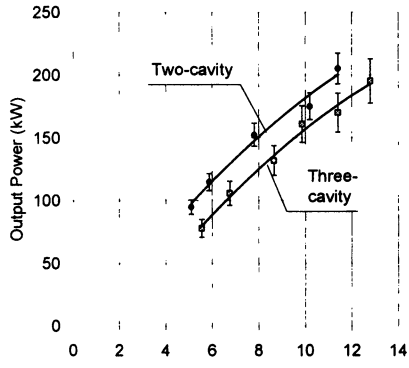

Fig. 1 Output power of a 2- and 3-cavity gyroklystron vs beam current.

closed to the cold frequencies of the TE_{221} and TE_{511} mode for both cavities. Second problem was the tube adjustment in regarding to the dc magnetic field due to the small distance between electron beam and drift tube wall (about 0,35 mm only). At a beam voltage higher than 60 kV

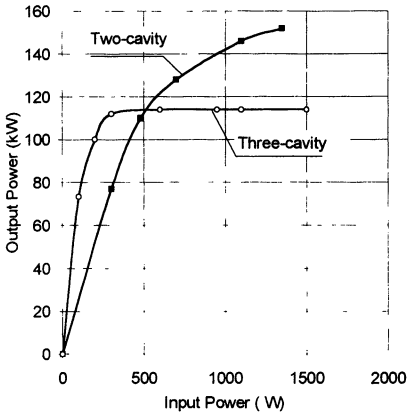

Fig. 2 Output power as a function of a drive power, U=60 kV, I=7.1A

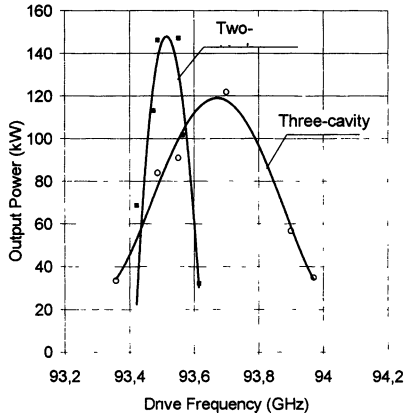

Fig. 3 Output power as a function of a drive frequency, U=60 kV, I=7.7A

and a current larger than 12 A, a vacuum deterioration has usually taken place due to the beam intersection with the drift tube.

First problem was studied as theoretically as experimentally. A special code based at the scattering matrix method was developed to simulate frequency and starting current of the spurious oscillations. As it follows from the simulation results, the instability is caused by the beam-RF field interaction lengthening due to the coupling of the TE_{221} mode in the first cavity with the TE_{232} mode in the conical waveguide positioned between the input cavity and mode converter. These modes are coupled due to:

a) transformation of the TE_{221} mode in the cavity to the TE_{232} mode in the conical uptaper (of about 5-10% power)

b) transformation of the travelling TE_{22} wave to the TE_{23} and vise versa at the boundary between gun and converter mirror with the following their reflection from the gun. For the experimental configuration, the reflection coefficient for the TE_{22} and TE_{51} modes is depicted in Fig.4

Both these coupling mechanisms were taken into account in the developed code. Simulation showed the start-oscillation current of the

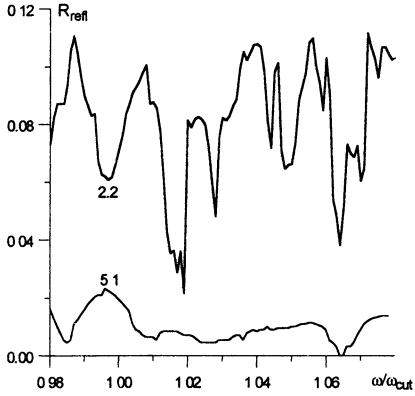

Fig. 4 Reflection coefficient of the gun for modes TE_{22} and TE_{51} excited in the first cavity versus ratio ω/ωcut. (ω_{cut} is a cutoff frequency of the input cavity).

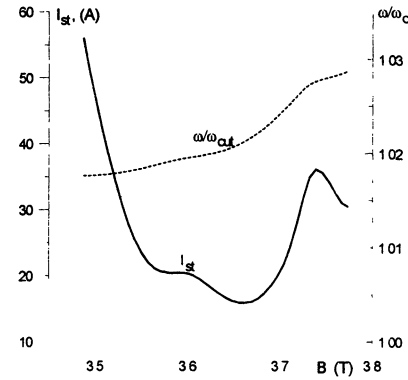

Fig. 5 Starting current of TE_{22} mode (solid line) and ratio ω/ω_{cut} (dashed line) versus magnetic field in the circuit.

spurious mode of about 20 A if the electron beam pitch-factor $\alpha = 1.6$ and velocity spread $\delta v_{\perp} = 0.2$ (Fig.5). It is interesting to note the TE_{221} mode start-oscillation current in the single input cavity at the same beam parameters is being evaluated as 26 A.

To exclude vacuum deterioration and RF breakdown arisen due to the beam intersection with the drift tube wall, we developed two-cavity gyroklystron with the reduced cathode diameter. It allowed to enlarge beam voltage up to 65 kV and current up to 17 A. This tube is under investigation.

Three-cavity results

The motivation of the three-cavity gyroklystron development was to demonstrate higher gain and probably larger bandwidth than those obtained for two-cavity amplifier. Therefore, the intermediate cavity was positioned at the equal distances from both other cavities, and its eighen-frequency was closed to the output one. As expected, the bunching improvement provided by the penultimate cavity results in the drive power decrease necessary to saturate the output power down to 0.3 kW. In this tube, a peak output power of 195 kW was attained for a 60 kV, 12.8 A electron beam with 25,5% efficiency. A 26-dB saturated gain with

at 114 kW power output has been measured (Fig.2). From Fig.3, one can observe the FWHM bandwidth of about 460 MHz at the central frequency of 93,7 GHz. Some efficiency reduction in comparison with the two-cavity counterpart may be explained by the non-optimal mismatch of the penultimate and output cavity cold frequencies which was chosen to be zero. However, to attain optimal efficiency the second cavity cold frequency should be of about 0,5-0,7% low than that for the output one [4]. Practically, the results obtained are the first successive experience to develop three-cavity gyroklystron with the oversized cavities operating at the high-order radial mode.

Conclusions

In summary, two-and three-cavity, TE_{021}-mode, high-power gyroklystrons were designed, built and tested. Two-cavity gyroklystron produced 207 kW peak power with 30% efficiency, 20-dB gain and 140 MHz bandwidth. In a three-cavity amplifier, the output power of 195 kW at 25,5%, 26-dB gain, 460 MHz bandwidth has been demonstrated. The peak power attained represents world record for an amplifier in W-band. Future work will be focused on improving of the three-cavity tube performance.

References

1. I. I. Antakov, E. V. Zasypkin, E. V. Sokolov, Conf. Digest of the 18th Int. Conf. on Infrared and MM Waves, Proc SPIE. 2104, 166 (1993)
2. B. G. Danly et al., Conf. Digest of the 24th Int. Conf. on Infrared and MM Waves, Monterey, CA, USA, p. M-3 (1999)
3. E. V. Zasypkin, I. G. Gachev, I. I. Antakov, M. A. Moiseev, V. K. Lygin and E. V. Sokolov, Proc. of the 23rd Int. Conf. on Infrared and MM Waves, Colchester, U.K., 1998.
4. E. V. Zasypkin, M .A. Moiseev, E. V. Sokolov, V. K. Yulpatov, Int.J.Electron., 1994

PHYSICS AND TECHNOLOGY ISSUES OF THE GYROTRON TRAVELING WAVE AMPLIFIER

K.R. Chu[1], T.H. Chang[1], H.Y. Chen[1], C.L. Hung[1], L.R. Barnett[1], S.H. Chen[2], and T.T. Yang[3]

1. Department of Physics, National Tsing Hua University, Hsinchu, Taiwan
2. National Center for High-Performance Computing, Hsinchu, Taiwan
3. Synchrotron Radiation Research Center, Hsinchu, Taiwan

Stability issues comprise the key factors limiting the performance of the gyrotron traveling wave amplifier (gyro-TWT), a promising source of high power millimeter waves based on the relativistic electron cyclotron maser instability. We present a brief review of recent progress made on the stability studies of the gyro-TWT. Physical origins of spurious oscillations in the gyro-TWT are analyzed and characterized. Fundamental understanding of these processes leads to a device concept which provides zero-drive stability at ultra high gain. The scheme was verified in a proof-of-principle experiment, the results of which significantly advanced the state-of-the-art of millimeter wave amplifiers in gain, power, bandwidth, and efficiency.

I. Introduction

The millimeter wave region of the electromagnetic spectrum is a relatively unexploited band between the microwave and optical frequencies. A myriad of applications[1] of millimeter waves, such as high resolution radars, long range and high directivity communications, atmospheric mapping, space object detection and identification, and advanced particle accelerators are being conceived which require powerful sources well beyond currently available technology. The electron cyclotron maser mechanism discovered in the 1950's[2-4] has since evolved from a basic relativistic physics effect into a new class of millimeter wave devices referred to as the gyrotron. Consider an electron beam in which electrons move in helical orbits in an external magnetic field. Because of the relativistic mass dependence of the cyclotron frequency, the electrons in the RF field will bunch in their gyrotional phase space and thereby amplify the RF field which causes the bunching to occur. The gyrotron traveling wave amplifier (gyro-TWT) is an amplifier version of the gyrotron which features a fast-wave structure for high-power and broad-band interaction. Traveling wave amplification

Table 1. Achieved performance of gyro-TWT's based on a weakly relativistic electron beam

year	institution (references)	cyclotron harmonic	voltage (kV)	center frequency (GHz)	3dB bandwidth (%)	peak power (kW)	saturated gain (dB)	efficiency (%)
1979	NRL (7)	1	70	35	1.5	16.6	20	7.8
1981	Varian (8)	1	60	5	6	120	18	26
1982	Varian (9)	1	50	95	2	28	33	8
1993	NRL (10)	1	33	35	20	8	25	16
1994	UC Davis (11)	2	80	16	2.1	207	16	13
1998	NTHU (12, 13)	1	100	35	8.6	93	70	26.5

based on the electron cyclotron maser interaction was first demonstrated in a device called the Trochotron [5] in which the electrons move along the waveguide through the $E \times B$ or $E \times \nabla B$ drift motion. Current gyro-TWTs[6], on the other hand, employ a helical electron beam generated by, for example, a magnetron injection gun. Table 1 summarizes the achieved gyro-TWT performances [7-13] over a twenty-year period of research and development. The current paper, mostly based on Refs. 12 and 13, reviews the key physics issues of the gyro-TWT as well as the experimental demonstration of the gyro-TWT as a millimeter wave amplifier of unprecedented capabilities in power, gain, bandwidth, and efficiency.

In contrast to conventional linear beam microwave devices such as the traveling wave tube (TWT), the electron beam employed in the gyrotron possesses a transverse motion at the electron cyclotron frequency. It is this property that allows the beam to selectively interact with a high order waveguide mode at a high cyclotron harmonic by properly matching the resonance conditions. However, the additional degree of freedom provided by the multitude of cyclotron harmonics can also generate numerous spurious oscillations. Interactions with backward waves are sources of absolute instabilities[14-19], whereas the forward wave interactions are normally, but not always, convective instabilities[19]. The gyro-TWT is a complicated case because it exploits a convective instability near the cutoff frequency which turns into an absolute instability at sufficiently high beam current when the unstable spectrum extends into the backward wave region. These various absolute

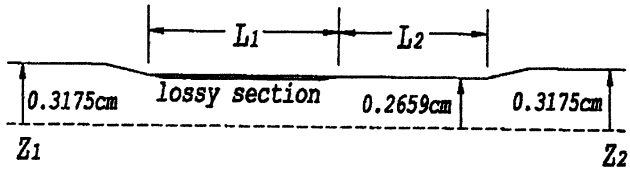

Fig. 1. Schematic of a Ka-band, TE_{11} mode, fundamental harmonic gyro-TWT. Section L_1 and L_2 form the interaction region. The ends are tapered for broadband coupling.

instabilities can easily be the dominant sources of oscillations in the gyro-TWT.

Feedback due to reflections at structural nonunifomities presents a different source of oscillation in the high gain regime (referred to as the reflective oscillation). Reflective oscillations are common in traveling wave structures. The feedback loop can be effectively eliminated by a sever as has been a standard practice in TWTs. However, the absolute instability, a much more serious problem to the gyro-TWT than to the conventional TWT, is basically different from the reflective oscillation in that the backward wave associated with the absolute instability is internally generated by the ac electron beam current. Hence, the two stages, though separated by the sever, are coupled by the beam. With the beam providing an internal path, the sever does not really quite separate the interaction structure into two isolated sections to produce a substantial stabilizing effect. Recently, an interaction structure with distributed wall losses was shown to be effective in suppressing both types of oscillations[20]. The losses are distributed over much of the linear interaction region (Fig. 1). Like the sever, the lossy section cuts off the path of the reflective feedback loop. In contrast to the sever, however, it is an integral part of the linear amplification stage. To the predominantly backward power flow of the absolute instability, the lossy section also functions as an effective energy sink.

II. A Scheme for Ultra High Gain

The distributed-loss structure can also yield ultra high stable gain[12, 13]. The scheme is based on the different responses to wall losses between the cold tube and hot tube modes. The cold tube mode has all of its energy in the electromagnetic fields. In a hot tube, however, energy of the beam generated mode resides not only in the electromagnetic fields

but also in the kinetic energy of the oscillatory motion of the electrons, the latter being an integral part of the hot tube mode. The lossy wall absorbs the electromagnetic energy, but not the oscillatory energy of the electrons. Thus, wall losses of the amplifier circuit attenuate the reflected wave (basically a cold tube mode) significantly more than they reduce the gain of the amplifying wave (a hot tube mode). It can be shown analytically[21] that the reduction in hot tube gain due to wall losses is only one third of the cold tube attenuation over the same distance.

Such unequal effects can be exploited to simultaneously achieve both high gain and reflective stability. In Fig. 1, the lossy and conducting-wall sections comprise the linear and nonlinear stages of the amplification, respectively. The linear section is made sufficiently long to provide the desired gain, while the nonlinear section length is constrained to a minimum to enhance the threshold of absolute instabilities.

III. Classification and Characterization of Oscillations

We first discuss three types of oscillations studied in Refs. 12 and 13 by employing the trajectory tracing technique[22-25] to follow the beam and wave dynamics throughout the lossy section. Imposition of physical boundary conditions at both ends allows the evaluation of a self-consistent rf field profile, $f(z)$, to account for wave reflections at all interfaces and nonuniformities. Such details in the modeling allow oscillations of various origins to be studied on the basis of the overall rather than sectionalized interaction structure.

Reflective oscillations of a global nature start when the total gain exceeds the reflection at the input/output ends plus the attenuation in the lossy section (all in dB). Figure 2a shows the field profile of a typical global reflective oscillation. Calculations indicate that the oscillation can be stabilized by lowering the operating current (I_b) and magnetic field (B_o), or by increasing the wall resistivity. Beam current is usually fixed by the power requirement and the magnetic field must be fine tuned for maximum efficiency; hence, wall resistivity provides the most effective means for stabilization. Wall resistivity reduces the gain, but this can be easily compensated by a lengthened lossy section.

The conducting-wall section (of length L_2 in Fig. 1) by itself is subject to localized oscillations due to reflections at the lossy-wall junction on the left and the output structure on the right. Figure 2b illustrates the field profile of such an oscillation in the lowest order

(TE_{111}) axial mode. Since the oscillation is localized to the conducting-wall section, the oscillation power is found to be nearly independent of the length (L_1) and wall resistivity (ρ) of the lossy section. These two features are in contrast to the high sensitivity of the global reflective oscillation to L_1 and ρ.

The gyro-TWT shown in Fig. 1 is most susceptible to the TE_{21} mode absolute instability at the second cyclotron harmonic (14). Figure 2c illustrates the field profile of such an oscillation. Figure 3 displays the

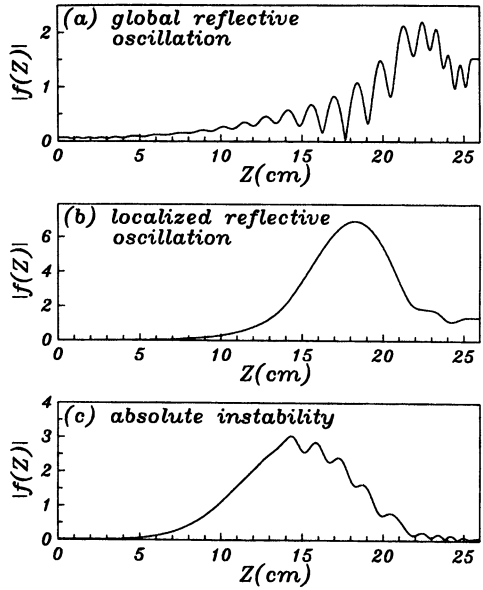

Fig. 2. Calculated profiles of the RF field amplitude $|f(z)|$ in the structure of Fig. 1 for A. the global reflective oscillation, B. the localized reflective oscillation, and C. the absolute instability.

start-oscillation current (I_{st}) versus the electron pitch angle $\alpha(= v_\perp / v_z)$ for different values of ρ. I_{st} decreases with increasing α as expected. Again, the wall resistivity is shown to be highly effective in stabilizing the absolute instability. Increasing the wall resistivity will allow stable operation at higher I_b and α values, hence achieve higher power and efficiency.

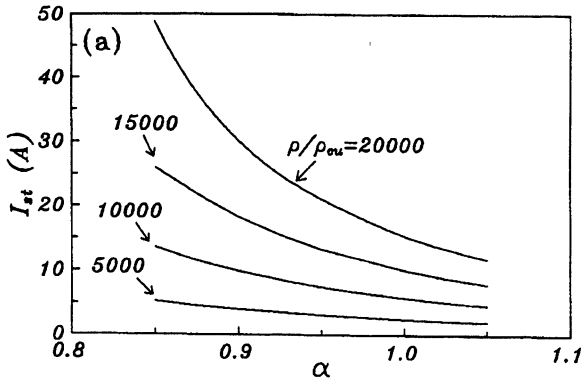

Fig. 3. Calculated start-oscillation current of the second harmonic absolute instability (TE_{21} mode, $f_{osc} \cong 56$ GHz) versus the electron pitch angle α for different values of wall resistivity ρ (normalized to that of copper).V_b =100 kV, L_1=10 cm, L_2=9.7 cm, B_o=12.5 kG, and r_c=0.09 cm, where r_c is the radial position of the electron guiding centers. A cold beam is assumed.

Of the three types of oscillations, only the localized reflective oscillation cannot be effectively suppressed by distributed wall losses. It has indeed been observed in the experiment described below, but at a magnetic field value above the optimum range for the amplifier operation.

IV. Experiments

An experimental gyro-TWT[12, 13] (photo shown in Fig. 4) was assembled to verify the ultra high gain scheme just described.

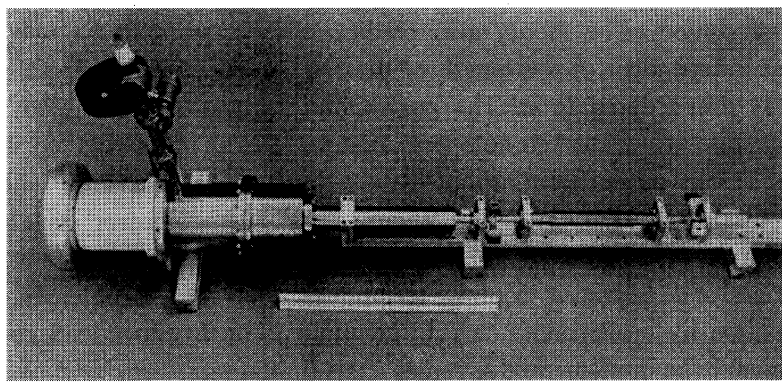

Fig. 4. Photo of the Ka-band gyro-TWT detached from the superconducting magnet

A mechanically tunable magnetron injection electron gun[26] was attached to the interaction structure of Fig. 1. Lengths of the graphite-coated lossy section (L_1=20 cm with~100 dB loss) and the conducting-wall section (L_2=4 cm) were chosen to achieve high gain as well as stability. Input/output waves were coupled at z_1 and z_2 through the side walls with newly designed oscillation-free couplers which also function as converters between circularly and linearly polarized waves. The magnetic field was provided by a superconducting magnet system. Output power at low duty was measured with a calibrated crystal detector (with estimated accuracy of ±5%) and verified with a calorimeter (agreement was within ~5%). At the operating beam current of 3.5 A, the gyro-TWT was found to be zero-drive stable from all three types of instabilities in the optimum range of the operating magnetic field ($12.65kG<B_0<12.75kG$). As the magnetic field was increased, a localized reflective oscillation was observed and identified to be the TE_{111} mode of the conducting-wall section.

Figure 5 plots the saturated output power and gain (dots) as functions of the frequency. The peak power of 93 kW corresponds to a saturated gain of 70 dB and efficiency of 26.5%. The ultra high gain, 30 dB beyond that previously achieved (Table 1), permits the use of solid state sources as drives. The full-width half-maximum bandwidth is 3 GHz, approximately 8.6% of the center frequency. Measured data are closely matched by theoretical predictions (solid line) using the simulated beam parameters (23) α=1, $\Delta v_z / v_z$ = 5% and r_c=0.09 cm, where $\Delta v_z / v_z$ is the electron velocity spread and r_c is the radial position of the electron guiding centers. The theory also predicts that the saturated power is almost independent of the length of the lossy section while the gain is linearly proportional to it. The peak Ohmic power dissipated on the waveguide is calculated to be approximately 10 kW. With profiled wall losses, it can be evenly distributed over the lossy surface area with a peak dissipation rate of ~300 W/cm^2. The average-power handling capability will be limited by the availability of proper heat-resistant lossy materials and advanced cooling techniques. However, supplementary attenuation by broadband side-wall coupling to an external load could conceivably be implemented to remove this limitation.

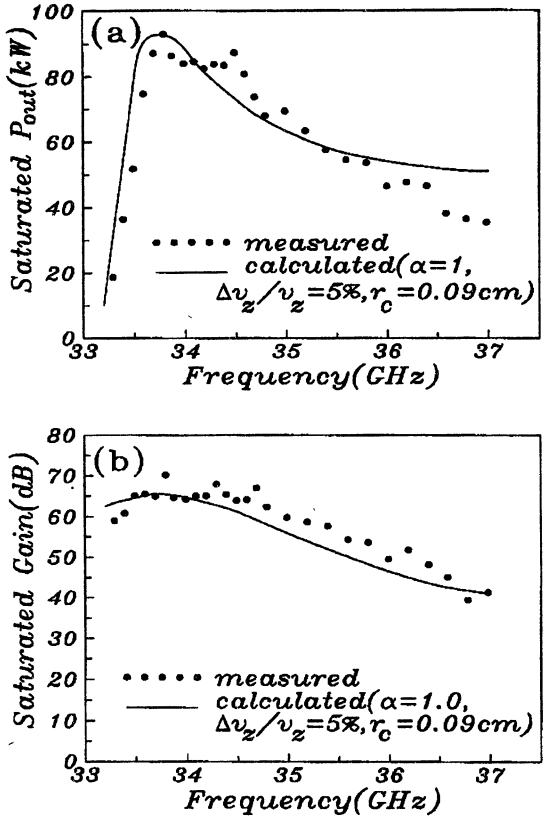

Fig. 5. Saturated output power (*a*) and gain (*b*) versus the frequency. Measured and calculated data are shown by dots and lines, respectively. V_b =100 kV, I_b=3.5 A, and B_o=12.7 kG.

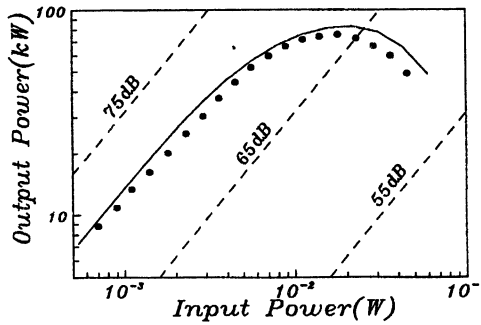

Fig. 6. Measured (dots) and calculated (lines) output power versus the drive power. V_b =100 kV, I_b=3.5 A, B_o=12.7 kG, and f=34.2 GHz.

Figure 6 shows the measured output power versus the input power (dots). Linear and saturated behaviors are consistent with the calculated data (solid line). Again, α=1, $\Delta v_z / v_z = 5\%$, and r_c=0.09 cm were assumed in the calculations. In all the measurements for Figs. 5 and 6, we have not detected any spurious oscillation. Table 2 compares the key parameters of the current gyro-TWT with those of the state-of-the-art TWT.

Table 2. Comparison of the experimental gyro-TWT with the state-of-the-art TWT (Varian/CPI model VTA 5701)

type	band	voltage (kV)	current (Amp)	magnet	peak power (kW)	efficiency (%)	gain (dB)	bandwidth (%)
gyro-TWT	Ka	100	3.5	cryogenic	93	26.5	70	8.6
TWT	Ka	45	7	solenoid	50	16	40	6

V. Summary

These studies indicate that a basic understanding of the intricate interplay between the absolute/convective instabilities, circuit losses, and reflective feedback is of fundamental importance to the scientific demonstration of the potential capability of the gyro-TWT. Significantly higher power can be obtained by employing the harmonic cyclotron maser interaction[11, 27, 28], a novel helically corrugated waveguide[28], as well as these new physical insights, thereby ushering in a new generation of coherent millimeter wave amplifiers.

Acknowledgements

This work was supported by the National Science Council.

The authors are grateful for many stimulating discussions with Prof. Neville C. Luhmann, Jr.

References

1. A.V. Gaponov-Grekhov, V.L. Granatstein, Eds. *Application of High Power Microwaves* (Artech House, Boston, MA, 1994).
2. R.Q. Twiss, *Australian J. Phys.* **11**, 564 (1958).
3. J. Schneider, *Phys. Rev. Lett.* **2**, 504 (1959).
4. A.V. Gaponov, *Izv, VUZ, Radiofizika* **2**, 450 (1959), ibid., p.836.

5. A.V. Gaponov, M.I. Petelin, and V.K. Yulpatov, *Radiophys, Quantum Electron.* **10**, no. 9/10, 794 (1967).
6. V.L. Granatstein, P. Sprangle, A.T. Drobot, K.R. Chu, and L. Seftor, U.S. patent no. 4224576 (1980).
7. L.R. Barnett et al., in *Technical Digest of the International Electron Devices Meeting* (IEEE, New York, 1979), pp.164-167.
8. R.S. Symons, H.R. Jory, S.J. Hegji, and P.E. Ferguson, *IEEE Trans. Microwave Theory Tech.* **29**, 181 (1981).
9. V.L. Granatstein, B. Levush, B.G. Danly, and R.K. Parker, *IEEE Trans. Plasma Sci.* **25**, 1322 (1997).
10. G.S. Park et al., *Phys. Rev. Lett.* **77**, 2399 (1995).
11. Q.S. Wang, D.B. McDermott, and N.C. Luhmann, Jr., *Phys. Rev. Lett.* **75**, 4322 (1995).
12. K.R. Chu, H.Y. Chen, C.L. Hung, T.H. Chang, L.R. Barnett, S.H. Chen, and T.T. Yang, Phys. Rev. Lett. 81, 4760 (1998).
13. K.R. Chu, H.Y. Chen, C.L. Hung, T.H. Chang, L.R. Barnett, S.H. Chen, T.T. Yang, and D. Dialetis, IEEE Trans. Plasma Sci., **27**, 391 (1999).
14. Y.Y. Lau, K.R. Chu, L.R. Barnett, and V.L. Granatstein., *Int. J. Infrared Millimeter Waves* **2**, 373 (1981).
15. J.A. Davies, *Phys. Fluids B* **1**, 663 (1989).
16. A.T. Lin, and C.C. Lin, *Phys. Fluides B* **1**, 2286 (1989).
17. L.R. Barnett et al., *Phys. Rev. Lett.* **63**, 1062 (1989).
18. K.R. Chu et al., *Phys. Fluids B,* **3**, 2403 (1991)
19. K.R. Chu, and A.T. Lin, *IEEE Trans. Plasma Science* **16**, 90 (1988).
20. K.R. Chu et al., *Phys. Rev. Lett.* **74**, 1103 (1995).
21. Y.Y. Lau, K.R. Chu, and L.R. Barnett, *Int. J. Infrared and Millimeter Waves* **2**, 395 (1981).
22. P. Sprangle, and W.M. Manheimer, *Phys. Fluids* **18**, 224 (1975).
23. A.K. Ganguly, and S. Ahn, *Int. J. Electron.* **53**,641 (1982).
24. Fliflet, A. W., *Int. J. Electron.* **61**, 1049 (1986).
25. C.S. Kou et al., *IEEE Trans. Plasma Science* **20**, 155 (1992)
26. Ch Wang et al., *Rev. Sci. Instru.* **68**, 3031 (1997).
27. A.T. Lin et al., *Int. J. Electron.* **72**, 873 (1992).
28. V.L. Bratman, A.W. Cross, G.G. Denisov, W. He, N.G. Kolganov, V.N. Manuilov, M.M. Ofitserov, A.D.R. Phelps, K. Ronald, S.V. Samsonov, A.B. Volkov, C.G. Whyte, A.R. Young, paper S15, this Workshop.

20 GHz HIGH-POWER GYROHARMONIC CO-GENERATION

J. L. Hirshfield,[1,2] M. A. LaPointe,[1,2] C. Wang,[2] and A. K. Ganguly[1]

[1]Omega-P, Inc., Suite 100, 345 Whitney Ave., New Haven, CT 06511 USA
[2]Department of Physics, Yale University, PO Box 208120, New Haven, CT 06520 USA

Seventh-harmonic gyroharmonic co-generation [Wang, Hirshfield and Ganguly, *Phys. Rev. Lett.* 77, 3819 (1996)] has been suggested as a mechanism that could be the basis for a multi-MW cm- or mm-wavelength rf source for use in research on high-gradient accelerators. This mechanism is based on the coincidental fact that, for cylindrical waveguides, a 7^{th}-harmonic TE_{72} wave has nearly the same group velocity as a fundamental-frequency TE_{11} wave. An apparatus to demonstrate 7^{th}-harmonic co-generation has been built and tested, in which a 250 kV, 23 A laminar beam has over 10 MW of 2.856 rf power added to it in the TE_{11} mode of a cylindrical waveguide terminated in a matched load, whence the spectrum of generated harmonic power is analyzed. Conditions are found in which 7^{th}-harmonic 20 GHz output is dominant within the harmonic spectrum.

Introduction

This paper describes work motivated by desire for new types of high-power cm-wavelength rf sources for application in advanced accelerator research. A need is perceived for high peak power pulsed rf amplifiers, with parameters that include peak power levels >50 MW at 10 GHz, appropriately reduced when scaled to higher frequencies, and efficiencies >45% [1]. Gyroharmonic co-generation, a process that was recently proposed as a possible basis for such a source [2, 3], is based on the coincidental fact that, for a uniform cylindrical waveguide, a wave at frequency 7ω in the TE_{72} mode has nearly the same group velocity as a wave at frequency ω in the TE_{11} mode. This natural degeneracy is peculiar to cylindrical waveguides and cavities, and allows strong synchronous coupling between these two modes when a non-linear medium is present in the waveguide; in the present instance the non-linear medium is an electron beam. Thus, for example, when the beam is strongly pumped by injecting rf power at 2.855 GHz, efficient harmonic

conversion can occur preferentially at the 7th harmonic in the same rf structure, and a significant portion of the injected rf power can emerge at 20.0 GHz. Since rf pumping (acceleration) of the beam and harmonic generation (deceleration) coexist during the interaction, it has been dubbed "co-generation" to distinguish it from other gyroharmonic interactions [4].

An experiment to demonstrate co-generation has been assembled and run that utilizes facilities available at the Yale University Beam Physics Laboratory. These facilities, described in detail below, include a 300 kV, 30 A electron gun, a 24 MW S-band klystron, and a versatile 15-cm bore 1.5-m long solenoid system. The objective of the experiments was to demonstrate that gyroharmonic co-generation can allow a significant fraction of injected S-band rf drive power to be converted to output at 20 GHz, the 7th harmonic; and that 7th harmonic output can dominate other harmonics. A two-cavity device based on this mechanism is to be designed and built which is expected to have high efficiency for conversion of 2.857 GHz power to 20 GHz power. Scaling this device to use as a driver existing 65 MW S-band or 75 MW X-band klystrons or magnicons extrapolates to several 10's of MW output at either 20 GHz or 80 GHz. No rf amplifier at this power level has yet been built at either of these multiples ($7\times$ and $28\times$) of the SLC S-band frequency.

Experimental arrangement

As stated, experiments were conducted using a test stand consisting of an electron gun and an rf input coupler. The gun is a convergent-flow triode configuration, capable of providing a laminar pencil beam at up to 300 kV, with current independently adjustable between about 10 and 31 A. The test stand serves as the injector and rf input coupler for a (up to) 1.2 MeV CARA S-band 35 MW accelerator [4] to produce an electron beam with properties that are suitable for high-power gyroharmonic radiation studies. The input coupler is designed to launch a TE-11 mode wave that rotates in the same sense as electrons in the applied guide magnetic field. The test stand has a demountable flange after the input coupler that allows a variety of rf circuits to be installed as needed. The 3.30-cm radius waveguide used in preliminary tests to be described here has relatively low TE_{11} and TE_{72} group velocities $n = v_{gr}/c = 0.3605$ and 0.3521 at 2.856 and 19.992 GHz, respectively.

According to theory, this near equality should promote strong coupling on the beam between the fundamental and the 7th harmonic. Analysis shows, for these parameters, that a 1.2 MeV beam executes axis-encircling orbits at a radius of about 60% that of the waveguide radius, and is thus is able to interact strongly with the synchronous rotating TE_{72} whispering-gallery fields.

A further novel feature of the test stand makes it well suited for optimizing 7th harmonic generation; this is the variable perveance of its two-anode electron gun. The gun is a 30-100 kV, 1.0 μP Pierce-type diode, with a 50–200 kV post-acceleration second anode. As a result, beams with energies between 100 and 300 kV can be obtained, with currents ranging from about 10 A to 31 A, pulse width of 2.5 μs and repetition rate of 1–10 Hz. The variable-current feature can be important for the co-generator, since beam acceleration imparted by the TE_{11} mode fields is limited by the available 24 MW rf drive power; higher beam current implies lower net acceleration: a 30 A beam can have up to 667 kV added, while a 20 A beam can have up to 1.0 MeV added. Flexibility in varying the injected beam current, for fixed injected beam voltage, can be a decided advantage in optimizing parameters for the co-generator. Few high-voltage beam injectors enjoy this flexibility.

Fig. 1 depicts the interaction waveguide that was connected to the input coupler for the experiments to be described in this paper. The gun and coupler are on the left, and a conical matched load with a hole to permit passage of the beam to a collector is on the right. Experiments were

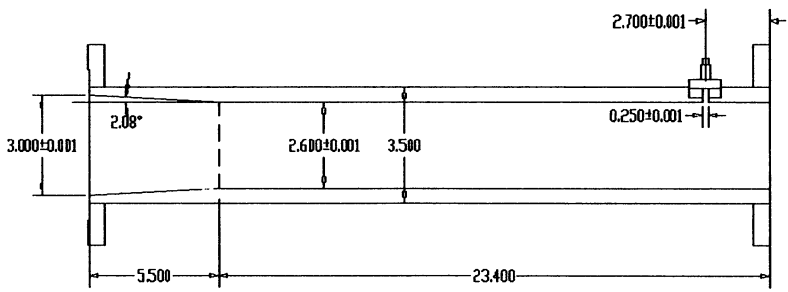

Fig. 1. Drawing of the interaction waveguide.
Dimensions are in inches

conducted by adjusting the rf input drive level, the electron gun voltage and current, and the magnetic field profile so as to optimize 20 GHz

output, as measured at the sampling probe shown in Fig. 1; and to minimize output at other harmonics. Radiation spectra were recorded by slowly scanning a narrow-band spectrum analyzer (Tektronix 492P) operating in the "max-hold" mode, and by accumulating data pulse-by-pulse with run times of an hour or more. The temporal envelopes from the sample probe of S-band rf drive power with and without the beam, and of rf power detected after insertion of a high-pass filter with a cutoff frequency of 18 GHz, are shown in Fig. 2. As can be seen, a large fraction

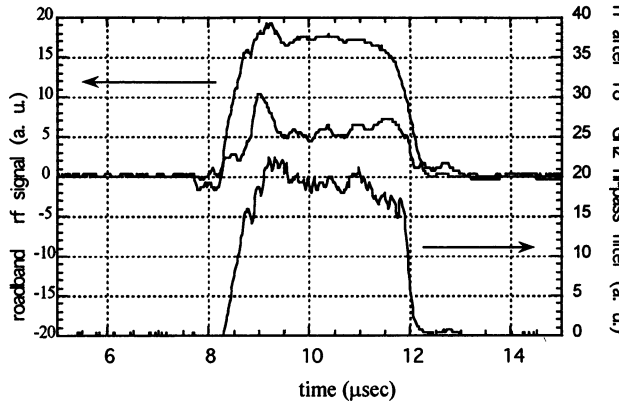

Fig. 2. Envelopes of S-band rf drive power with and without the beam (top two traces), and of rf power above 18 GHz (bottom trace)

of the S-band drive power has been absorbed by the beam; theory indicates that some should have be regenerated. But a strong signal above the 6th harmonic (17.1 GHz) with a pulse-width comparable to that of the drive signal is clearly in evidence.

Fig. 3 shows with the solid curve an example of an optimum magnetic field profile B_o that maximizes 7th harmonic generation, as computed from a particle simulation code for the co-generator geometry shown in Fig. 1, assuming a 250 kV, 18 A injected Brillouin beam, and an input 2.856 GHz rf power level of 11 MW. Fig. 3 also shows with the dashed curve a measurement of actual magnetic field that was imposed when the data shown in Figs. 2 and 4–7 were taken. When 11 MW of S-band power was imposed upon the beam, the axial magnetic field profile was adjusted to gradually bring the beam into resonance. As rf drive power was observed to become absorbed by the beam, rf output was observed at frequencies ranging up to 21 GHz, the upper limit for the Tekt-

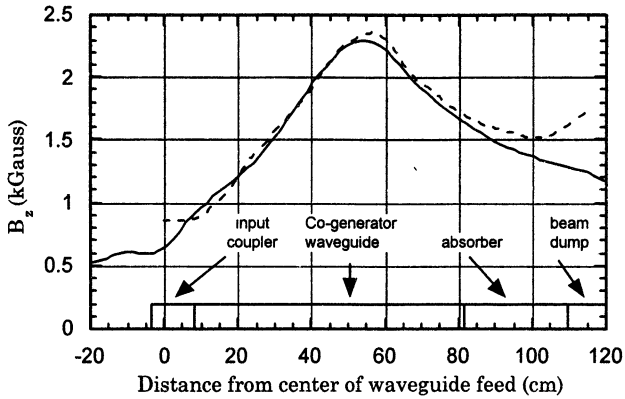

Fig. 3. Theoretical (solid) and experimental (dashed) axial magnetic fields for the case of a 250 kV, 18 A injected Brillouin beam with 11 MW of 2.855 GHz rf power.

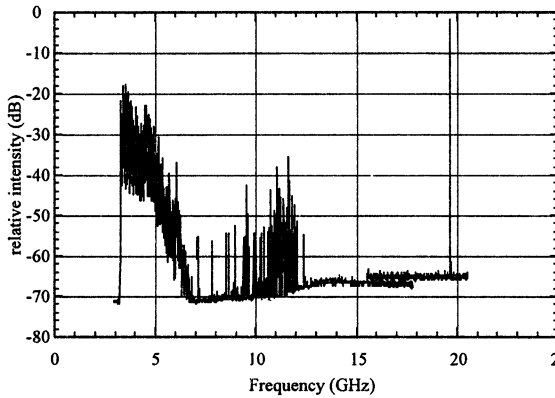

Fig. 4. Wide band sweep of radiation spectrum at the sampling pickoff in the co-generator. Note the solitary feature near 20 GHz.

ronix 492P spectrum analyzer. As the magnetic field profile approached the theoretical field profile, seventh harmonic radiation near 20 GHz was seen to increase and other frequencies begin decreasing in amplitude. Figs. 4 and 5 show an example of the observed rf spectra, on a wide-band sweep and on a narrow-band sweep near 20 GHz under conditions that optimized 7th harmonic output.

The spectra displayed in Figs. 4 and 5 provide strong evidence for the predicted co-generation mechanism. A clearly dominant coherent 7^{th} harmonic signal is seen near 20 GHz. While a weaker broad spectrum of radiation is seen near 11 GHz and below 6 GHz, the only discrete gyro-harmonic seen is the 2^{nd} (at 5.7 GHz); and that is much weaker than the 7^{th} in Fig. 4. A narrow-band sweep of the prominent feature of Fig. 4 is shown in Fig. 5. It is seen that a narrow feature is present at 19.67 GHz and a broader component (weaker by 7 dB and more) extends up to about 19.70 GHz. The main feature is seen to have a FWHM of about 960 kHz, roughly double the Fourier transform limit for a 2 μs pulse. For the rf circuit structure planned to be built in the future (see below), low frequency radiation as shown in Fig. 4 should not be generated, since the output waveguide will be cutoff in the design mode below about 15 GHz; furthermore, the 20 GHz output may be sharpened by self-injection, as also described below. Experiments conducted under slightly higher power rf drive and beam conditions than those for Figs. 4 and 5 gave rise to additional notable features in the rf spectra that deserve attention. One example from such a spectrum is shown in Fig. 6.

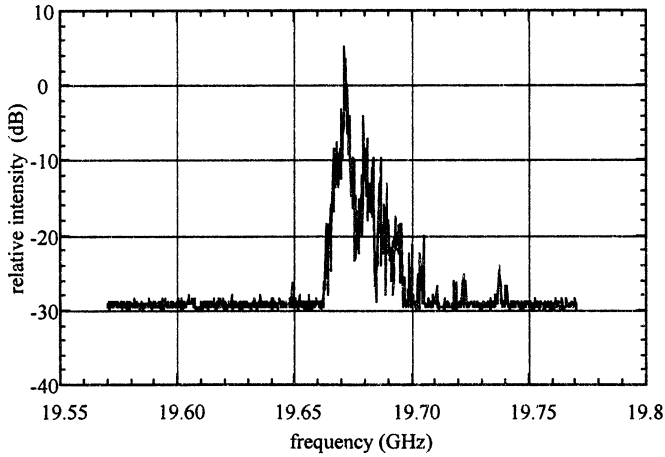

Fig. 5. Narrow band sweep of radiation spectrum from Fig. 4. FWHM of main peak located at 19.67 GHz is 960 kHz

In an attempt to understand the discrete lines seen in Fig. 6, the squares of their frequencies were plotted *versus* the squares of integers; results of this exercise are shown in Fig. 7 under conditions where the best

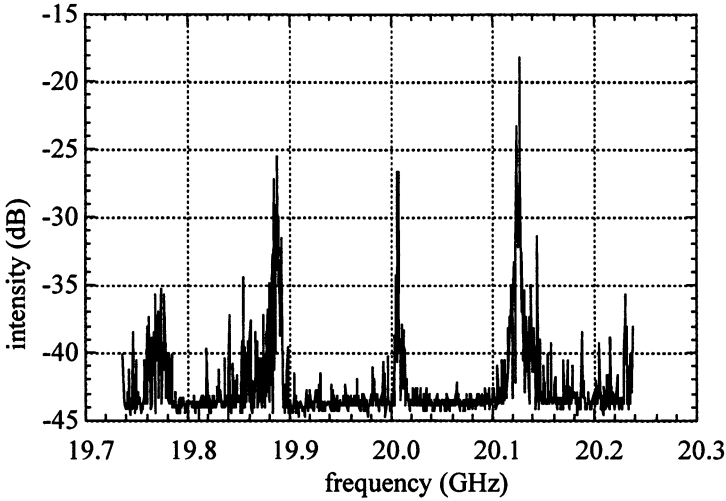

Fig. 6. Spectra observed near 20 GHz with higher drive power than in Fig. 5

straight-line fit was obtained. This comparison is motivated by the suspicion that reflections within the structure might allow excitation of axial standing-wave modes. If so, then these modes would satisfy an eigenfrequency relation $f_n^2 = f_c^2 + (nc/2L)^2$, where f_c is the cutoff frequency and L is an effective cavity length as defined by points of reflection. For the best-fit case shown in Fig. 7, mode numbers 26–29, a cutoff frequency of 18.248 GHz (R = 3.38 cm) in the TE_{72} mode, and an effective length of 51.25 cm are inferred. The design cutoff frequency is 18.711 GHz (R = 3.30 cm) and the length (taper-to-sample point) is 52.6 cm. These fairly close agreements suggest that 7th-harmonic gain is evidently high enough to excite several unintended cavity modes.

Given the strong 7th-harmonic radiation generated by the beam as shown in Figs. 4–7, it is natural to consider a resonant cavity configuration that can eliminate spurious modes and perhaps allow high-efficiency, high-power 20 GHz output. One such structure under consideration employs a combination TE_{111}/TE_{727} cavity, followed by a TE_{71} mode output waveguide. This structure is sketched in Fig. 8. A second such structure might employ a TE_{71m} mode output cavity in place of the output waveguide. Analysis to predict operation for the first configuration is described in the next section of this paper.

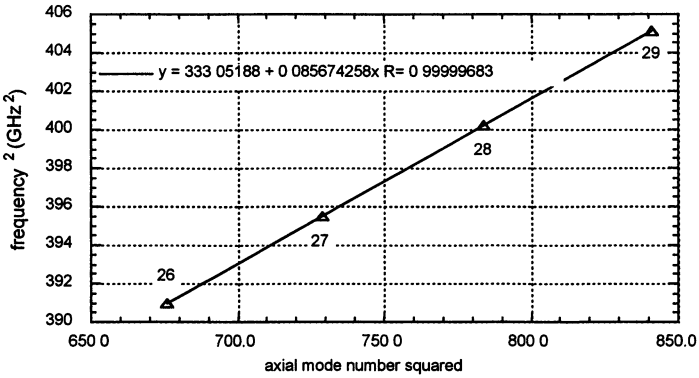

Fig. 7. Best straight-line fit for the squares of frequencies from Fig. 6 plotted *versus* the squares of integers

Analysis of a modified structure for co-generation

A preliminary analysis of the modified co-generator structure shown in Fig. 8 has been carried out based on a simplified model that idealizes

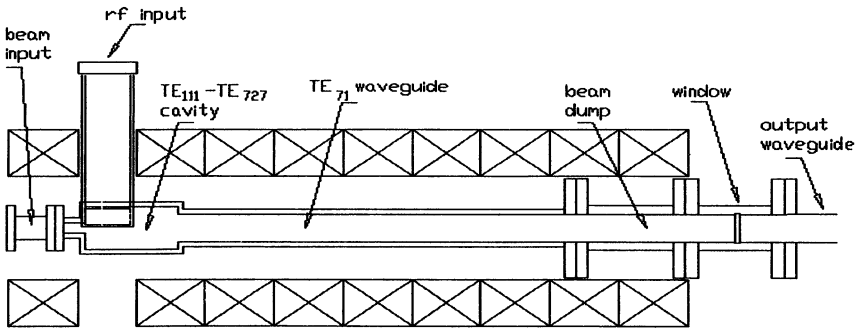

Fig. 8. Sketch of the co-generator configuration to be built for future tests

field distributions in the structure and that neglects spurious modes. The new co-generator concept combines two desired features that were shown to be advantageous in early analysis of co-generation [2]: (*i*) to prevent

the TE_{11} fields from regenerating themselves once the beam has been accelerated, and once the 7th harmonic fields begin to grow; and (*ii*) to inject a small amount of 7th harmonic power at the input of the device, so as to enhance growth of 7th harmonic fields through mode-locking, and to suppress growth of competing harmonics. The means planned to attempt to achieve these features requires careful rf circuit and wave-beam interaction studies which are as yet incomplete. However, an approximate model has been used to expand the range of parameters over which the interaction has been explored. Use of a cavity as the output structure is a natural extension of the concept, but discussion of this is beyond the scope of this paper.

A modified rf circuit configuration as shown in Fig. 8 is intended to suppress the fundamental rf pump mode beyond its first minimum, and provides for injection of an initial level of 20 GHz power. The 2.856 GHz rf drive structure is a TE_{111} cavity, tuned to also resonate at 20 GHz in the TE_{727} mode; this is possible because of the near-degeneracy discussed above. This arrangement prevents 2.856 GHz rf drive power from entering the TE_{71} output waveguide (or a TE_{71m} output cavity), and prevents other radiation below about 15 GHz to arise, since the output structure will be cutoff. Bragg reflectors (not shown in Fig. 8) are to be designed and introduced to reflect 20 GHz radiation at the WR-284 waveguide input couplers. The TE_{727} mode cavity can be conveniently diffraction-coupled to the TE_{71} mode output structure, since the output pipe radius equals the radius of the first null in E_θ for the TE_{727} mode, and since both modes thus have identical field patterns within that radius. RF injection (i.e., coupling a small amount of 20 GHz drive power into the input of the output section) is achieved with this configuration as well, since co-generation in the input drive cavity can generate some 20 GHz power which couples directly into the output section. Results of three simulation studies to describe the performance of this configuration are shown in Figs. 9–11. For these simulations, the electron beam energy spread, pitch angle spread and radius are taken to be those for a Brillouin beam for the given current and magnetic field values. Fig. 9 shows the results when parameters are adjusted for injection from the drive cavity of 0.53 MW of 20 GHz power, and for a linearly-decreasing magnetic field profile in the output section.

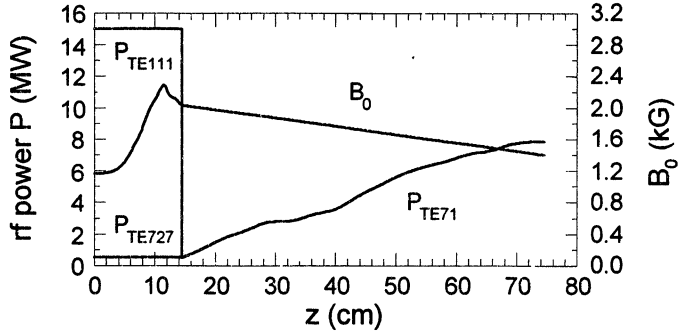

Fig. 9. Results of simulation study for 20 GHz generation in the planned co-generator configuration. Injected Brillouin beam is 300 kV, 32 A and input 2.856 GHz power is 15 MW. Drive cavity has ohmic and loaded Q's of 5000 and 180 at 2.856 GHz, and 50,000 and 3000 at 20 GHz. Magnetic field profile is linearly decreasing over the output section. At end of the drive cavity, beam energy is 752 kV and mean pitch angle ratio is 1.50. 20 GHz output is 7.9 MW

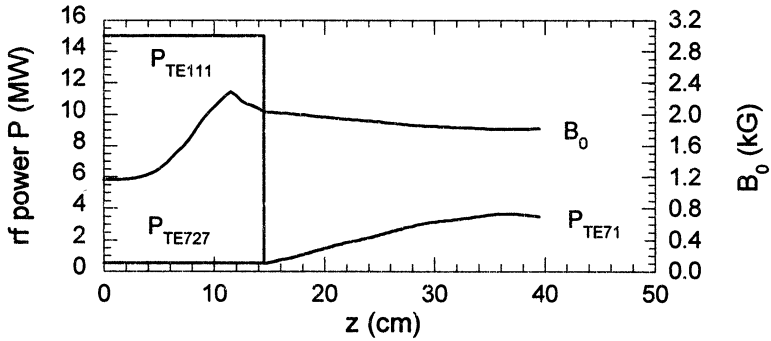

Fig. 10. Same as Fig. 9, except for a resonant magnetic field profile in the output section. 20 GHz output is 3.7 MW

Fig. 10 is for injection of 0.53 MW of 20 GHz power, as in Fig. 9, but with a resonant magnetic field profile in the output section. Otherwise, the parameters are the same as in Fig. 9. Fig. 11 is for no injection of 20 GHz power, and for the resonant magnetic field profile in the output section, and other parameters as in Figs. 9 and 10. The 20 GHz output

power levels for these three cases are 7.9 MW, 3.7 MW, and 2.7 MW, including wall losses. These simulations illustrate the strong influence of injection and magnetic profile tailoring for achievement of efficient 7th-harmonic co-generation. The 7th harmonic rf conversion efficiency in Fig. 9 is 53 %.

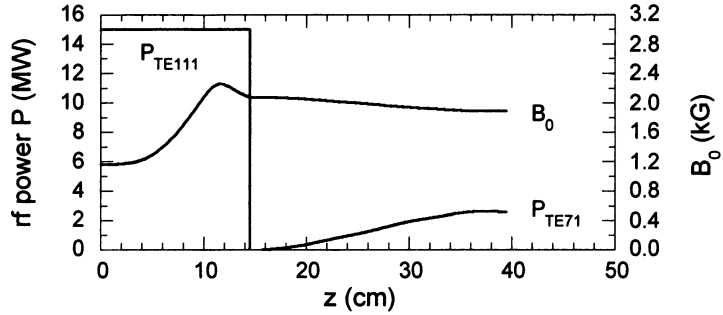

Fig. 11. Same as Fig. 10, except for no injected 20 GHz power into output section. 20 GHz output is 2.7 MW

Discussion

Experimental evidence shows strong radiation near the 7th-harmonic from a relativistic gyrating electron beam when conditions for co-generation are satisfied. In particular, a 250 kV, 23 A beam has had up to 11 MW of 2.856 GHz power incident upon it under conditions of cyclotron autoresonance, increasing its energy to over 700 kV. In this circumstance the beam is capable of exciting the TE_{72} mode which is inherently synchronous in phase- and group velocity with the TE_{11} mode. Excitations are seen at frequencies other than 20 GHz, including a set of four discrete lines near 20 GHz. These can be explained as the excitation of high-axial-order cavity modes arising from reflections at the ends of the rf structure. A modified rf structure planned for future experiments promises to support excitation at a single frequency near 20 GHz. This structure embodies a TE_{111}/TE_{727} drive cavity to both energize the beam and to provide a modest amount of 20 GHz power to be injected in the TE_{71} mode output waveguide (or cavity). Calculations predict 7th-harmonic conversion efficiencies of greater than 50% for this structure.

Acknowledgments

The authors are grateful for fruitful discussions that occurred with O. A. Nezhevenko and V. P. Yakovlev. This research was sponsored by the US Department of Energy.

References

1. Wilson P. B. *SLAC-Pub-7449,* April 1997; R. B. Palmer, *Pulsed RF Sources for Linear Colliders, AIP Conf. Proc.* **337**, NY, Am. Inst. Phys. (1994), pp.1-15.
2. Changbiao Wang, Hirshfield J. L., and Ganguly A. K. *Phys. Rev. Lett.* **77**, 3819 (1996).
3. Hirshfield J. L., Changbiao Wang, and Ganguly A. K. *IEEE Trans. Plasma Sci.* **26**, 567 (1998).
4. Hirshfield J. L., Changbiao Wang, and Ganguly A. K. *IEEE Trans. Plasma Sci.* **24**, 758 (1996).

7 GHz 55 MW PULSED MAGNICON

E.V. Kozyrev, O.A. Nezhevenko, A.A. Nikiforov, G.N. Ostreiko, B.Z. Persov, G.V. Serdobintsev, S.V. Shchelkunoff, V.V. Tarnetsky, V.P. Yakovlev*, I.A. Zapryagaev*

Budker Institute of Nuclear Physics, Novosibirsk, Russia 630090
*Omega-P, Inc., 345 Whitney Av., New Haven CT, US 06511

The report presents experimental results obtained on the 7 GHz pulsed magnicon amplifier and outlines the features of operation. The magnicon was developed at Budker INP as a prototype RF source for linear colliders. To achieve a power and efficiency of more than 50 MW and 50 % the tube was built as a frequency-doubling amplifier. At present the magnicon efficiency is 56 % at 55 MW of an output power for a 1.1 microseconds pulse width and gain of 72 dB.

Introduction

The work on creation of high-power microwave amplifiers with circular deflection of an electron beam has been carried out at INP since 1967. In 1970 the first device of that type called gyrocon [1,2] was created. Further development of this class of microwave amplifiers has been made possible with invention and development of a magnicon [2]. The first magnicon – a prototype of CW or long pulse microwave amplifier was built and tested in the 1980's [3].

In the beginning of 1990's the work was started on the development of the advanced magnicon version Fig.1. That magnicon was developed as a prototype of a microwave power source for linear colliders [4]. It includes: electron gun, RF-system, magnetic system, and collector. The tube operates at 7 GHz in frequency-doubling mode, so the RF system consists of the set of deflecting cavities (the first is externally driven) for a beam modulation at 3.5 GHz and output cavity for conversion of beam energy into the microwave power at the second harmonic (7 GHz).

The creation of codes for simulation of electron optics, electromagnetic systems, and dynamics of an electron beam of finite size in realistic fields in both steady state and time dependent regimes was carried out simultaneously with the experimental study [5]. An electron source with unique parameters [6] has been manufactured and successfully tested. In the process of experimental investigation various versions of the design of the tube and its individual components [4] have

been studied in order to overcome instabilities and to optimize power and efficiency.

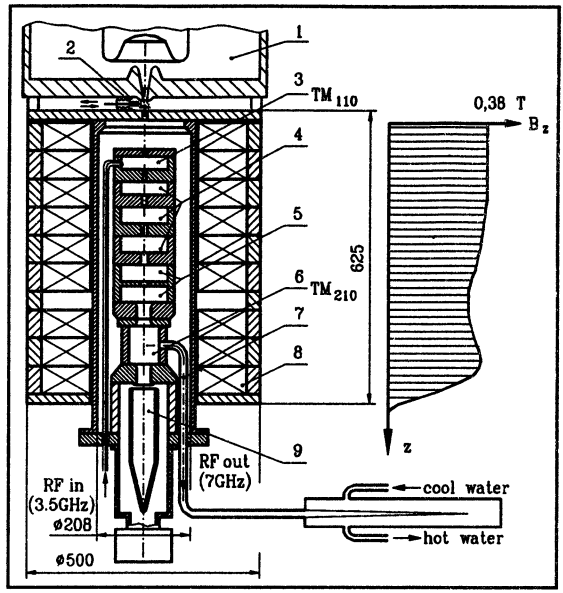

Figure 1: Schematic layout of the magnicon: 1 – electron source; 2 – vacuum valve; 3 – drive cavity; 4 – gain cavities; 5 – penultimate cavity; 6 – output cavity; 7 – waveguide (×2); 8 – solenoid; 9 – collector.

Experimental Studies

The latest major improvements include modifications in the electron gun and output cavity. The gun geometry was modified and the matching of the electron beam with the magnetic system was also improved. This improvement was made in order to work with magnetic field of 0.38 T. As a result the beam transverse size in the magnetic system is in the range of 1.9÷2.5 mm [7] and an area compression ratio exceeds 2000:1.

It has been also found that the magnicon efficiency significantly drops due to the longitudinal inhomogeneity and azimuthal asymmetry of RF fields in the output cavity, which are caused by the coupling holes with waveguide power outputs. These problems were overcame by introducing 6 compensating protrusions and 2 side grooves (Fig.2) [8].

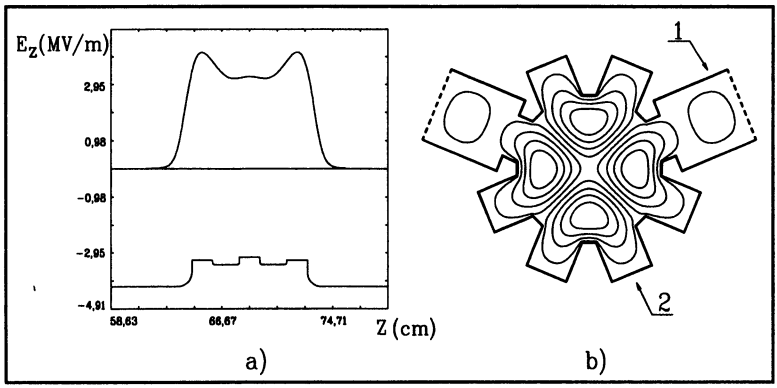

Figure 2: The output caviy with power extraction in the mid plane:
a) longitudinal distribution of the RF electric field at 1 cm from the axis;
b) field map, waveguides (1) and compensating protrusions (2).

The latest improvements allowed us to achieve the results (see Table 1) which are very close to the design parameters and simulation results.

Table 1: Measured parameters.

Operating frequency	7.005 GHz
Drive frequency	3.5025 GHz
Output power	55 MW
Gain	72 dB
Pulse duration	1.1 μs
Efficiency	56 %
Beam voltage	427 kV
Beam current	230 A

Figure 3 presents a general view of the experimental 7 GHz magnicon assembly.

Oscillograms of the pulses, experimental and calculated curves are shown in Fig. 4-5. Parameters obtained at the device optimal operating regime are marked by "•" symbol. The output power calibration was carried out by calorimetric measurements.

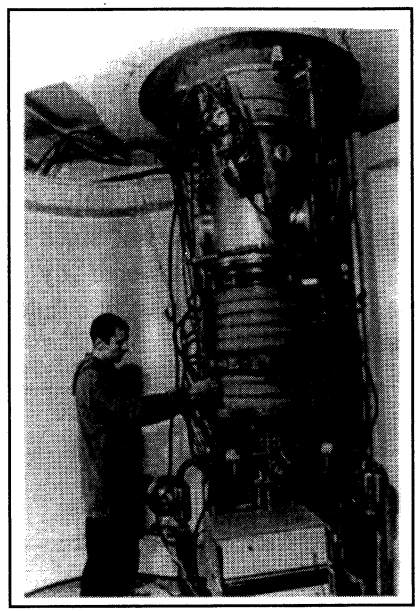

Figure 3: 7 GHz pulsed magnicon.

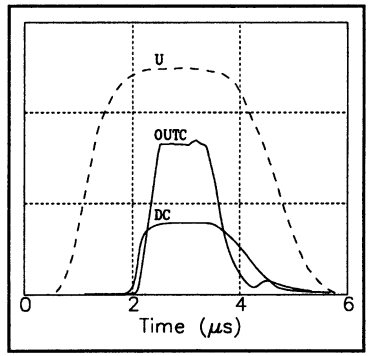

Figure 4: Oscillograms: U - beam voltage; DC - drive cavity signal; OUTC - output cavity signal.

The output cavity with a loaded Q-factor Q_l =230, which is higher than the optimal value Q_l =180, was used in experiments (seen from the calculated curve in Fig.5a), that decreases efficiency by 2 %. The increased Q-factor has been chosen in order to move out from the region of possible instability causing a sharp efficiency drop.

Figure 5b illustrates the magnicon efficiency response of drive frequency.

Simulation results show that increasing in efficiency can be achieved by decreasing DC magnetic field (Fig.5c). In this case the gain drops but still remains high enough. In the given series of experiments we was not able to decrease DC magnetic field significantly, for a beam quality is impaired because of mismatching. However, since the magnetic system solenoid consists of two sections powered by individual sources, dependence between an efficiency and magnetic field value in the output cavity area has been studied (Fig.5d).

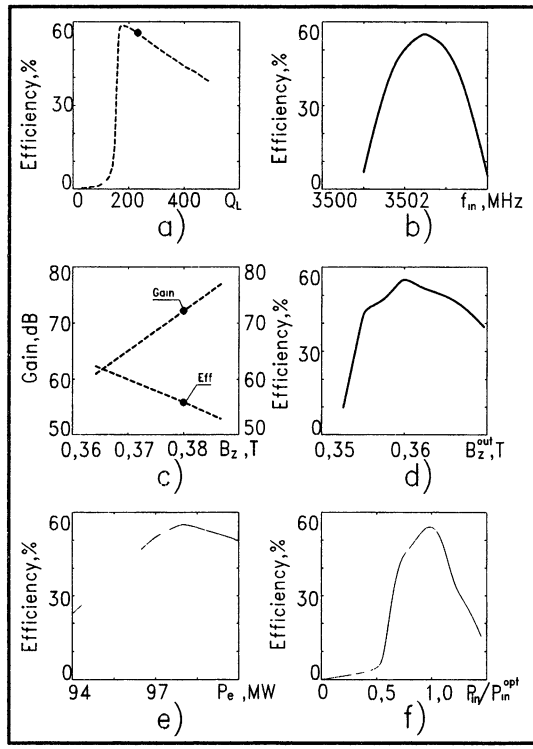

Figure 5: Experimental and calculated curves:
a) loading dependence; b) input frequency dependence; c) DC magnetic field dependence of gain and efficiency; d) output cavity DC magnetic field dependence of efficiency; e) efficiency vs. beam power; f) efficiency vs. drive power. Continuous lines correspond to experimental data, dashed – to simulation results.

One of possible reasons of the RF output pulse length reduction is related to an excitation of the 0-mode of oscillations in a double-cell penultimate cavity. The penultimate cavity consists of two cells coupled through the central hole with the coupling coefficient of 0.7 % (see Fig.1). The operating mode of this cavity is π-mode. However, simulation results show, that self-excitation of the 0-mode may limit a pulse length of the output signal. This effect was detected in the course of 11.424 GHz magnicon development [9].

Figure 6 shows a typical outlook of instability growth in the penultimate cavity at 0-mode exciting, obtained by simulation. This problem can be solved replacing this double-cell penultimate cavity by two uncoupled penultimate cavities [9].

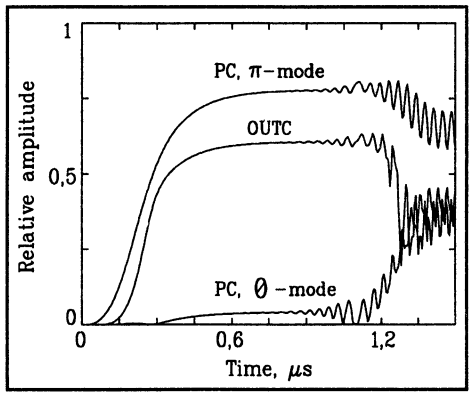

Figure 6: Transient process in the magnicon when both 0- and π- modes are excited in the penultimate cavity; PC corresponds to penultimate cavity, OUTC – to output cavity;

Summary

In the latest set of experiments on 7 GHz magnicon almost all design parameters have been achieved: the output power of 55 MW, efficiency of 56 %, and gain of 72 dB. Experimental data are in an excellent agreement with simulation results obtained by the special magnicon computer codes. Achieved results allow us to consider a magnicon as an alternative power source for linear colliders applications.

Acknowledgements

Work is supported by Russian Fund of Basic Research.

References

1. G.I.Budker et al., Particle Accelerators vol. 10, 1979, pp. 41–59.
2. O.A.Nezhevenko, in IEEE Trans. of Plasma Science, vol. 22, No. 5, 1994, pp. 756–772.
3. M.M.Karliner et al., NIM, vol. A 269, No. 3, 1988, pp. 459–473.
4. E.V.Kozyrev et al., Particle Accelerators vol. 55, 1996, pp. 55–64.
5. V.Yakovlev et al., in Proc. of Part. Acc. Conf., Dallas, 1995, vol.3, pp.15–69.
6. Y.V.Baryshev et al., NIM, vol. A 340, 1994, pp.241–258.
7. E.V.Kozyrev et al., in Proc. of Part. Acc. Conf., Vancouver, 1997, vol.3. pp. 3114–3116.
8. O.A.Nezhevenko et al., in AIP Conf. Proc. 398, 1997, pp. 912–919.
9. O.A.Nezhevenko, V.P.Yakovlev (to be published).

EFFICIENT 24 – 30 GHz CW GYROTRONS FOR TECHNOLOGICAL APPLICATIONS

Yu. Bykov, M. Glyavin, A. Goldenberg, A. Luchinin, V. Lygin, N. Zavol'skii

Institute of Applied Physics, Russian Academy of Sciences, and GYCOM Ltd., Nizhny Novgorod, Russia

At present, gyrotron systems are finding increasing use in research into processing of materials with the millimeter-wave energy. The enhancement of operating efficiency of gyrotron system is a necessary condition for their introduction into industrial applications. Recent progress in improvement of the 24–30 GHz CW gyrotrons is described in the paper. The efficiency of 50 % at a 10–30 kW CW power level was obtained in gyrotrons operated on fundamental and second harmonic of the electron cyclotron resonance.

Introduction

Currently, gyrotron systems specifically designed for millimeter-wave (mm-wave) processing of materials are coming into increasing use for research and development of innovative technological processes. Since 1993, when the Institute of Applied Physics introduced the first 10 kW CW 30 GHz gyrotron system for processing of materials [1], they have been acquired by many leading scientific centers in the USA, Germany, and China. Recently, several systems based on the 10 kW 28 GHz gyrotrons were produced in Japan for internal use.

The features inherent in the mm-wave processing systems that differ them advantageously from the commonly used 2.45 GHz systems are well known (see, e.g., [2]). A marked increase in the efficiency of heating of low loss materials and the possibility to heat uniformly large size specimens are of greater practical importance among others factors. Mm-wave sintering of advanced ceramic materials is probably most interesting among various areas of current investigations. As a result of fast volumetric heating of ceramic materials, sintering time is reduced by a factor of 5–7 as compared with the time which is typical for conventional sintering. Specific energy consumption in sintering of such ceramics as Al_2O_3, Si_3N_4 is decreased almost ten times, even when 2.45 GHz radiation is used for heating [3]. It is beyond question that an enhancement of operation efficiency of all key components of gyrotrons systems and especially of the gyrotron itself is of paramount importance for the introduction of technologies based on the mm-wave heating into a broad practical use.

The prototype 10 kW 30 GHz gyrotron system for processing of materials, described in detail elsewhere [1], exploits a tube operating on the second harmonic of the electron cyclotron resonance. The use of the 2nd harmonic gyrotron in the system of moderate power intended for laboratory research appears to be quite justified. The 2nd harmonic operation is associated with less stringent requirements for highly stabilized DC power supply, smaller throughput of the cooling water for its magnet, and may be accompanied by enhancement of the total efficiency of system, provided that the efficiency of gyrotron itself is high enough. The tube designed for the first gyrotron system operated in the H_{02} mode and had an efficiency of about 25 % at the output power level about 10 kW.

In a later time, CW gyrotrons of the same output power, operating also on the H_{02} mode, were produced by CPI (U.S.A) and Mitsubishi Electr. (Japan). The latter tube operated with a permanent magnet system fabricated of a Sm-Co alloy material.

Experiments

Results of computer simulation of the electromagnetic wave interaction with the electron beam on the second harmonic of cyclotron frequency suggest a higher efficiency than the one obtained in the prototype gyrotron. It is well known that the 2nd harmonic gyrotron has capacity to be ranked in the maximal theoretical value of efficiency only slightly below the fundamental frequency tube [4].

Recently, efforts have been made to modify the essential components of the gyrotron by an all-inclusive computer simulation. The mathematical codes that were developed previously at IAP for electron trajectory analysis and for analysis of interaction of the helical electron beam with the electromagnetic field in a resonator were applied to comprehensive numerical optimization of the gyrotron elements. As a result of the optimal choice of structural parameters of components, the output mm-wave power of the gyrotron and its efficiency became about 2 times larger than before. High values of efficiency were obtained in tests in a wide range of both the beam current (up to 2.5 A) and voltage (15–25) kV. Upon slight modification the gyrotron is capable of operating, practically with the same output power and efficiency, at the H_{12} mode at a frequency of about 24 GHz. This fact serves as an additional proof of a successful selection of gyrotron parameters.

Frequency (GHz)	Power (kW)	Efficiency (%)
30	9	40
30	30	30
24	12	50
24	20	38
24	31	35

All modifications were introduced keeping the overall dimension of gyrotron fixed in order to allow replacement of dated gyrotrons with new ones in the systems which are now in operation. The data obtained in the gyrotron tests can be considered as the upper limit achievable when all power supplies are simultaneously adjusted. However, the gyrotron as a source of microwave power in processing systems is ordinarily exploited in a different manner. The processing is performed under continuous variation of microwave power aimed at maintaining a required temperature-time schedule for processed sample. As a rule, in microwave processing the necessary variation of the gyrotron output power is achieved by control of high voltage on the gyrotron cathode with all other power supply parameters fixed. Naturally, the efficiency in this mode of operation is somewhat less than in the "maximum maximorum" regime. The modified gyrotron serves as a base component of the up-graded 15 kW 30 GHz gyrotron system [5].

The 24 GHz gyrotron of higher output power was designed as a base model for a system intended for industrial application. The frequency of 24.125 GHz is allocated by the International Telecommunication Union for industrial use. The tube operates on the fundamental frequency of the electron cyclotron resonance. The portion of DC power necessary for feeding the magnet system becomes less with increase in the designed microwave power of gyrotron. At the same time, a gyrotron operating on the fundamental frequency is more robust and less sensitive to alterations of external parameters, such as parameters of power supplies and matching with the load. In addition, the tube has an injection gun of a diode type, which make easier control over the gyrotron operation. The condition to be user-friendly is an indispensable factor for a device to be exploited in an industrial process.

The gyrotron operates in the H_{32} mode. The dependence of output power and efficiency upon the beam voltage is shown in Fig. 1. The solenoid has inner diameter larger than the minimal one required for a device of the given output power. This provision was made to allow

future use of a depressed collector. Recovery of the electron beam energy can permit to increase the efficiency of the gyrotron up to 60–65 %. Thereby, a gyrotron becomes highly competitive in efficiency with high-power 2.45 GHz magnetrons, while exceeding them considerably in the output microwave power.

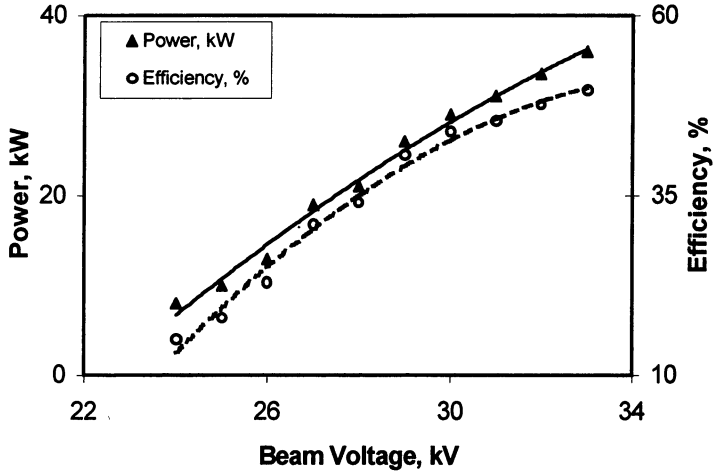

Fig. 1. Output power and efficiency of the 24 GHz 30 kW gyrotron versus beam voltage at a beam current of 2.2 A

The gyrotron processing systems can be advanced to higher mm-wave power levels with no significant changes in the general design which has been proven in the practical use of the 10 kW 30 GHz system.

References

1. Bykov Yu., Eremeev A., Kaurov V. et al., in Ceramics Trans., 1995, 59, 133.
2. Bykov Yu.,and Semenov V., in Applications of High Power Microwaves, ed. by A.V.Gaponov-Grekhov, V.L.Granatstein, Artech House, Boston, London, 1994, 319.
3. Patterson M., Apte P., Kimber R., et al., Mat. Res. Soc. Symp. Proc., 1992, 269, 291.
4. Nusinovich G., and Erm R., Electronnaya Tekhnika, ser.1, Electronika SVCh, 1972, 8, 55.
5. Bykov Yu., Denisov G., Eremeev A., et al., in Proceedings of 29th European Microwave Conference, MIOP 99, October, 1999 (*in print*).

ESR SPECTROMETER USING SUBMILLIMETER WAVE GYROTRONS AND PULSED HIGH MAGNETIC FIELDS

S. Mitsudo, Aripin, T. Matsuda, K. Kitai , T. Kanemaki and T. Idehara

Research Center for Development of Far Infrared Region, Fukui University

Bunkyo 3-9-1, Fukui 910-8507, Japan

I. Ogawa

Cryogenic Laboratory, Faculty of Engineering, Fukui University

Bunkyo 3-9-1, Fukui 910-8507, Japan

ESR spectrometer with a submillimeter wave gyrotron as a radiation source and a pulse magnet for high field up to 30 T has been constructed and applied to some cases of EPR measurements. The frequency of gyrotron is increased up to 301 GHz in complete cw mode, with the power kept at several tens to several hundred watts. Now, the frequency dependency of the fine structure constant D, in turn, the dependency on the field intensity, was measured and compared with the theoretical prediction derived from the spin Hamiltonian including nonlinear terms.

Introduction

Electron spin resonance (ESR) spectroscopy in millimeter and submillimeter wave regions using high magnetic fields is one of the most powerful tools for study of the magnetic properties of materials. However, there are many technical problems that we have to overcome, including the following. 1) The power of radiation sources and the sensitivity of available detectors is too low in these frequency regions. 2) High magnetic field is necessary with intensity up to several tens Tesla.

A submillimeter wave gyrotron is used in our ESR spectrometer as a high power radiation source, and an InSb hot electron detector as a high sensitive measurement device. A pulse magnet is useful for generating such a high magnetic field. This high power technique enables us to measure an ESR spectrum during one pulse of magnetic field, instead of the integration technique using a lock-in amplifier.

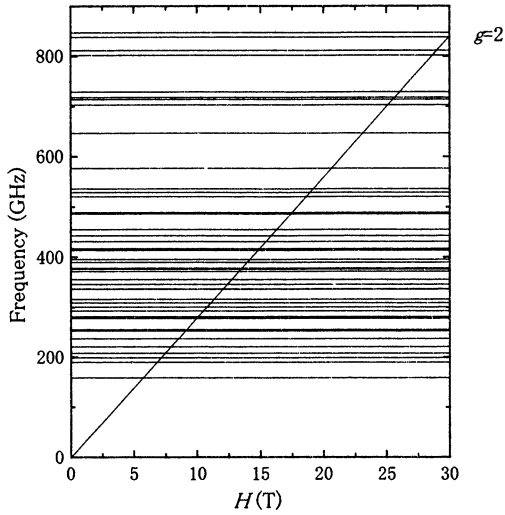

Fig.1 Available frequencies of Gyrotron FU IV and the magnetic field in our ESR spectrometer. The thick solid line shows g=2 resonance line.

Medium power, high harmonic gyrotrons in Fukui University (GYROTRON FU Series) have achieved frequency tunability in wide range from 38 GHz to 889 GHz along with high powers in the range from several tens watt to several tens kilowatt[1-3]. Therefore, the spectrometer has advantages of high power and wide frequency range. The superconducting magnet employed our old ESR spectrometer achieves the maximum magnetic field of 8.5 T[4,5]. This is not enough for ESR experiment in full frequency range of our gyrotrons. Subsequently, we have developed a pulse magnet with the maximum field intensity of 30 T for a new submillimeter wave ESR spectrometer.

Gyrotron FU series

Gyrotron FU series are frequency step-tunable sources covering a wide frequency range from millimeter to submillimeter wave region. The output powers are not so high, comparing with the output power of other high power millimeter wave gyrotrons, that is, from several hundreds watt to several tens kilowatt in fundamental operations and from several tens watt to several kilowatt in second harmonic operations. However, these powers are much higher than other radiation sources in this

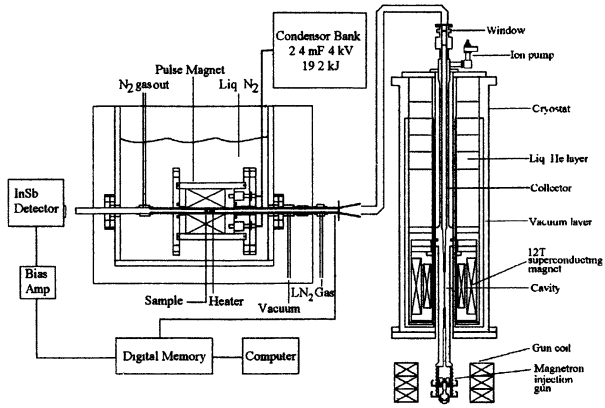

Fig.2 The schematic diagram of ESR spectrometer using Gyrotron FU IV as a radiation source and a pulse magnet with the maximum field intensity of 30 T.

frequency region. Fig.1 indicates all frequencies achieved by Gyrotron FU IV in fundamental and second harmonic operations, and the ESR condition for the case of g=2. The cross sections in this figure correspond to available conditions of ESR. In this case, ESR spectrometer is frequency tunable from 160 to 850 GHz. If we use other gyrotron included in Gyrotron FU series, the available frequency range would possibly be extended to below 160 GHz.

ESR System

Fig.2 shows the schematic diagram of our ESR spectrometer. The electromagnetic power from the Gyrotron FU IV is transmitted by an oversize circular waveguide system with three quasi-optical bends, and fed on a sample located at the center of the pulse magnet. The power transmitted through the sample is measured by an InSb hot electron detector.

The magnet is fabricated by winding the formbar-coated copper wire on a stainless steel cylinder reel up to eight layers. Each layer is insulated from the next layer and has 25 turns. The inner diameter and the thickness of the stainless steel reel are 12 mm and 0.5 mm, respectively. The cross section of wire is 3 x 2 mm^2. The magnet is reinforced by a composite of water and alumina powder impregnated between the coil and stainless steel guide. This structure prevents the coil from expanding under Maxwell stress of high magnetic field [6]. The magnet coil is

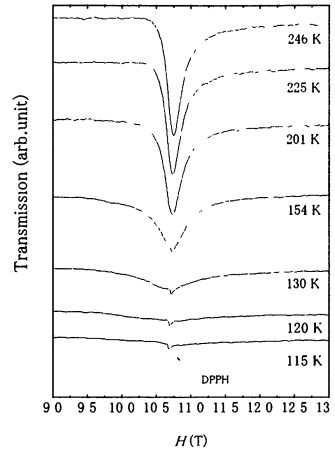

Fig.3 Transmission curve of MnO observed at the frequency of 301 GHz using Gyrotron FU IV.

immersed in liquid nitrogen. The pulsed magnetic field is produced by discharging a capacitor bank of 19.2 kJ into the magnet coil. When the capacitor bank is charged up to 3 kV, the field intensity is increased up to the maximum of 24 T and decreased. The field intensity pattern is similar to a half sinusoidal one with the width of 2.5 ms.

The signals from the pickup coil for magnetic field and from the InSb detector are measured as functions of time and recorded in a personal computer. Thereafter, the computer arranges automatically both signals for constructing an ESR spectrum as a function of magnetic field intensity.

The waveguide in the magnet region has a complicated three layer structure. The electromagnetic wave is transmitted through the inner pipe surrounded by the second layer in which dry nitrogen or helium gas flows for controlling the temperature of the sample set in the inner pipe. The outer layer is a vacuum layer for the thermal insulation. The temperature of the sample can be varied from liquid nitrogen temperature to room temperature by the flow of dry nitrogen gas and down to 30 K by cooled helium gas. Passing a current through the heater surrounding the sample can further increase the temperature. The temperature is measured by the FeAu 0.007 at. % - Ag thermocouple.

Results and discussion

The spectrometer using the Gyrotron FU IV and the pulse magnet has

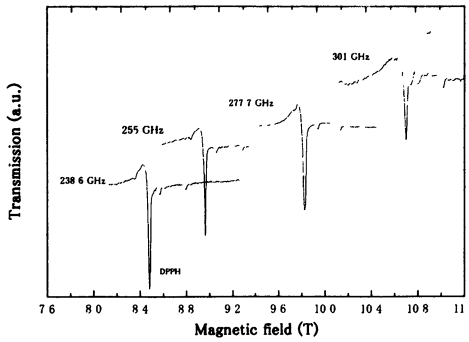

Fig.4 The observed EPR spectra at deferent frequencies.

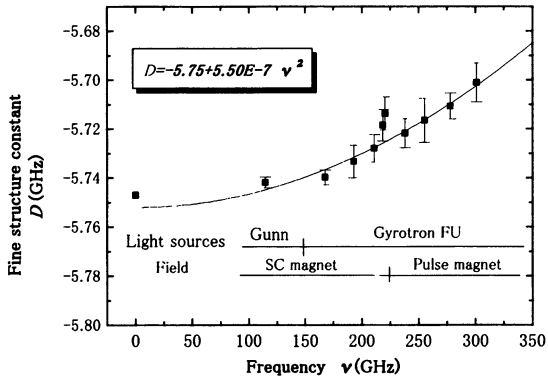

Fig.5 The frequency vs. the fine structure constant D plot. Zero field value was determined by Kikuch et al. [7].

been applied to some cases of ESR measurement.

In the first case, the gyrotron is operated in completely cw mode [2]. The cw mode operation is useful for the gyrotron application. The electron paramagnetic resonance (EPR) of MnO powder sample was measured by the spectrometer. As it is well known, MnO is an antiferromagnetic material. It has a Neel temperature T_N=116 K. Fig. 3 shows the temperature dependence of the EPR absorption curves of MnO observed at the frequency of 301 GHz. This is the first ESR observation at submillimeter wave region using a gyrotron as a radiation source.

Above 225 K, the absorption curve has essentially the same shape. As the temperature is decreased below 200 K, the absorption curve

becomes broader and the resonance position shifts slightly to the lower field side. At 115 K, the EPR absorption signal can not be observed, because of the antiferromagnetic ordering at T_N=116 K. This behavior of EPR spectrum for MnO is in good agreement with other studies [8].

In the second case of application of submillimeter wave gyrotrons (Gyrotron FU series) to EPR measurement, the frequency tunability in wide range is quite effective. In this case also, the gyrotron is operated in cw mode. We perform the EPR measurement of the Cr^{3+} ions in the ruby over the frequency ranges from millimeter to submillimeter wave region. Fig. 4 shows the observed EPR spectra. Each EPR spectrum has the four absorption lines at different fields. The strongest absorption line is caused by DPPH, which is the well-known standard ESR sample and has the *g*-value of 2.0036. Other three weak absorption lines come from the fine structure of the ruby. The fine structure constant *D* was determined from the observed field intensities at the absorption lines and plotted in Fig. 5 as a function of frequency. As the frequency is increased, the fine structure constant *D* increases. It suggests that *D* has the dependency of the magnetic field, because the resonant field intensity is proportional to the frequency ν. In Fig. 5, the solid curve shows the best fit curve obtained by a formula including the nonlinear term of the spin Hamiltonian. The experimental values are in good agreement with the theoretical curve. The frequency dependency of *D* is determined experimentally as $D = -5.75 + 5.50 \times 10^{-7} \nu^2$ GHz, where ν is in GHz.

References

1. T. Idehara, N. Nishida, K. Yoshida, I. Ogawa, T. Tatsukawa, D.Wagner, G.Gantenbein, W Kasparek and M. Thumm, Int. J. Infrared and Millimeter Waves, **19**, 919(1998).
2. T. Idehara, K. Yoshida, N. Nishida, I. Ogawa, M. L. Pereyaslavets and T. Tatsukawa, Int. J. Infrared and Millimeter Waves, **19**, 793(1998).
3. T. Idehara, I. Ogawa, Y. Shimizu and T. Tatsukawa, Int. J. Infrared and Millimeter Waves, **19**, 803(1998).
4. T. Tatsukawa, T. Maeda, H. Shirai, T.Idehara, M. Mekata, T.Saito and T.Kanemaki, Int. J. Infrared and Millimeter Waves, **16**, 293(1995).
5. T.Tatsukawa, H. Shirai, T. Imaizumi, T.Idehara, I. Ogawa, and T. Kanemaki, Int. J. Infrared and Millimeter Waves, **19**, 859(1998).
6. M. Motokawa, H. Nojiri and Y. Tokunaga, Physica B **155**, 96 (1989).
7. C. Kikuchi, J. Lambe, G. Makuhov and R. W. Terhune, J. Appl. Phys, **30**, 10619(1959).
8. H. Mori, Prog. Theor. Phys. **30**, 238(1963).

HIGH-POWER EXPERIMENTS WITH THE FOM FREE-ELECTRON MASER

A.G.A. Verhoeven, W.A. Bongers, V.L. Bratman, M. Caplan#, G.G. Denisov*, C.A.J. van der Geer, P. Manintveld, A.J. Poelman, A.V. Savilov*, P.H.M. Smeets, W.H. Urbanus*

FOM-Instituut voor Plasmafysica 'Rijnhuizen',
Association EURATOM-FOM, ; www.rijnh.nl; verhoeve@rijnh.nl;
*Institute of Applied Physics, Nizhny Novgorod, Russia
#Lawrence Livermore National Laboratories, Livermore, CA, USA

The free-electron maser (FEM) at Rijnhuizen is the pilot experiment for a high-power mm-wave source for applications on future fusion research devices like ITER, the International Tokamak Experimental Reactor. A unique feature of the Dutch FEM is the possibility to tune the frequency over the entire range from 130 to 260 GHz at an output power exceeding one MW. In the first phase of the project, the so-called inverse set-up is used, where the electron gun is mounted inside the high-voltage terminal. A peak power of 730 kW was measured at 200 GHz and 350 kW at 167 GHz. Now, the inverse experiments were finalized and the complete system is re-installed in the normal set-up, including the multi-stage depressed collector. First experiments in this set-up are scheduled to start in 2000. As a follow-up of this project we recently started the design work for a FEM with an extended pulse-length from 0.1 to 1 s. Detailed thermal behavior of the critical components is studied. The device will eventually be connected to the TEXTOR tokamak in Jülich, Germany.

Introduction

A free electron maser (FEM) has been built as a pilot mm-wave source for applications on future fusion research devices such as ITER, the International Tokamak Experimental Reactor [1]. A unique feature of the Dutch FEM is the possibility to tune the frequency over the entire range from 130 to 260 GHz at an output power exceeding 1 MW.

The system consists of a 12 A thermionic electron gun and a 2 MeV electrostatic accelerator. The undulator and mm-wave systems are located inside a terminal at 2 MV level. The terminal is placed inside a steel vessel, 11 m long and a 2.6-m diameter, filled with SF_6 at 7 bar, see Figure 1. After interaction with the mm waves in the undulator, the energy of the spent electron beam is recovered by means of a decelerator and a multi-stage depressed collector. Simulations show that this approach is expected to lead to an overall system efficiency of 50% [2].

For long-pulse generation, a low loss current, lower than 20 mA, is essential. Therefore, the electron beam line is entirely straight from the gun

to the collector. The mm waves are directed sideways from the electron beam by means of a stepped waveguide. This is a symmetrical step in the transverse dimension of a low-loss HE_{11} waveguide. Furthermore, an adjustable reflector enables adjustment of the feedback power over the entire range from 0 - 100%.

In the first phase of the project, a so-called inverse set-up is used, see Figure 2. Now, the electron gun is mounted inside the high-voltage terminal at -2 MV. The undulator and waveguide system are outside the pressure vessel at ground potential for easy adjustments and fine-tuning of the entire system. In this phase, the decelerator and depressed collector are not installed yet, therefore the FEM pulses are limited to 10 - 20 μs.

Basic layout

The basic layout of the FEM is largely determined by the requirement for high overall efficiency. This together with fast tunability and CW operation determines the choice for a dc, rather than an RF acceleration and deceleration system. The choice for a maximum electron energy of 2 MeV and a beam current of 12 A has been made on the basis of simulations of the interaction between the electron beam and the mm waves.

The required high system efficiency demands an efficient recovery of the spent electron beam leaving the undulator. For this purpose, a decelerator and a multi-stage depressed collector are incorporated. The undulator and the mm-wave system are located at high-voltage level. This enables to locate the high-voltage power supplies for the cathode of the electron gun at earth potential.

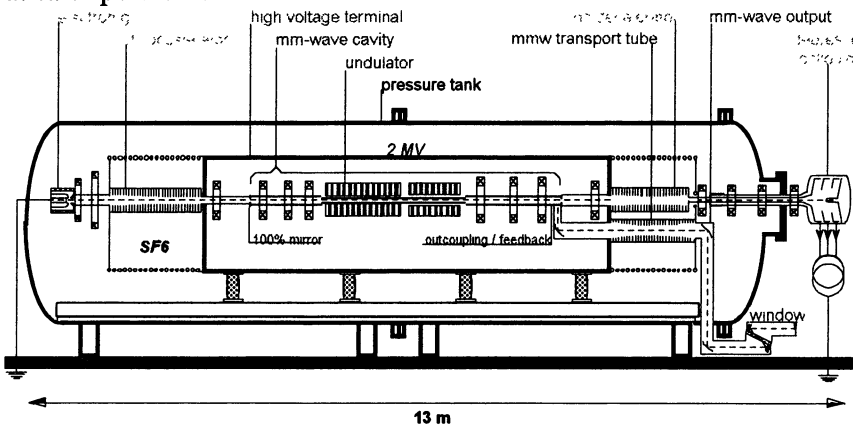

Figure 1
The general layout of the FEM in the normal set-up.

Furthermore, the power supplies that are connected to the depressed collector, with a total current of 12 A, can now be located outside the pressure tank at earth potential. Components that need little or no power are inside the high-voltage terminal. Furthermore, the 2 MV high-voltage power supply only has to supply the loss current of 20 mA maximum.

Simulation of the interaction

The interaction between the electron beam and the mm waves inside the FEM has been simulated using several codes. At the start of the project, mostly the CRMFEL (Cyclotron Resonance Maser Free Electron Laser) code was used. Later the General Particle Tracking (GPT) code was introduced [3]. CRMFEL is a fully three-dimensional (3-D), non-linear, particle-EM wave interaction code. Until recently, these simulations were done with a single-frequency, stationary version of this amplifier code [4]. Simulations for three different energies indicated that for a 12 A beam the net mm-wave power generated is above 1 MW for all frequencies between 130 GHz (at 1.35 MeV) and 260 GHz (at 2 MeV).

The undulator consists of two sections with different magnetic fields. In the first undulator section the net mm-wave power (i.e., the total power minus the injected feedback power of around 400 kW) grows to 700 kW at 200 GHz and saturates at the end of the first undulator section. In the second undulator section the electron energy, which is now lower due to the interaction with the mm waves, matches the lower undulator strength. The mm-wave power grows to 1.3 MW, saturating at the end of the second undulator section.

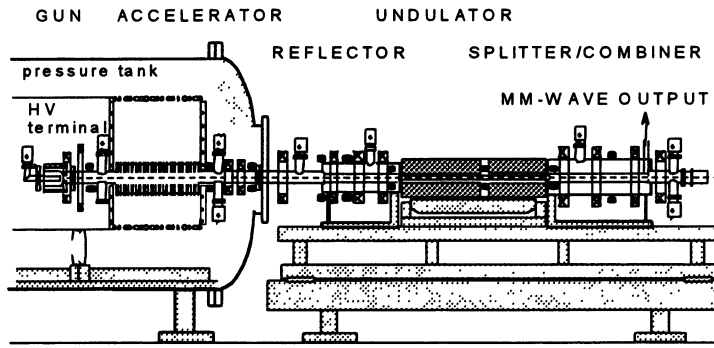

Figure 2
The layout of the FEM in the inverse set-up is shown. The electron gun is mounted in the high-voltage terminal, which is at -2 MV. The undulator, mm-wave system and most of the electron beam line are outside the tank at earth potential for easy accessibility.

Simulations with a modified non-stationary (space charge and high gain included) code developed jointly by the University of Maryland and LLNL indicate that a parameter regime can be found with a pure single-frequency operation, without any sidebands. A result of a simulation with this code is given in Figure 3. Parameters are very similar to those used during the first experiments, including the time behaviour of the accelerator voltage. The reflection coefficient of the mm waves, the size of the electron beam and especially the distance between the two undulator sections have a strong effect on the FEM behaviour [5,6,7].

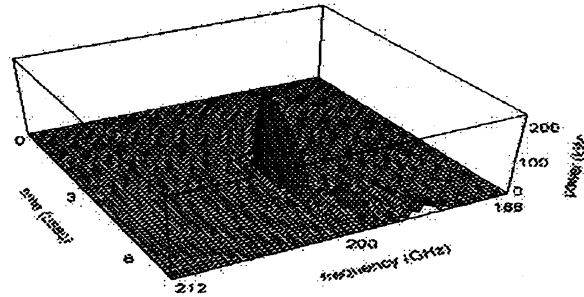

Figure 3
Frequency spectrum as calculated by Malt 1D code [5]. Beam current is 6 A. Voltage droop is 6 kV/μs. Accelerator voltage starts at 1.75 MV. Measured data for mm-wave reflection and transmission coefficients are taken into account. The radius of the beam is 1.4 mm. At these parameters, it can be noted that a pure frequency develops and decays followed by a much broader frequency spectrum.

Millimeter-wave system

The FEM is configured as a mm-wave oscillator, consisting of a waveguide amplifier section (inside the undulator) and a feedback and outcoupling system. Since the electron beam line is completely straight, the mm waves have to be coupled out sideways. Further, the fraction of the electron current intercepted in the mm-wave system should be as small as possible, which means that there should be enough transversal space for the electron beam. After considering all requirements, a rectangular corrugated waveguide was chosen, carrying the very low-loss hybrid mode HE_{11}, with the E-field parallel to the broad side of the waveguide [8].

Outcoupling and reflection systems are realised through stepped waveguides, as follows. Both before and after the undulator the transverse cross section of the waveguide changes stepwise from 15x20 mm^2 to 60x20 mm^2 (for a frequency of 260 GHz), where the 60-mm direction is parallel to the undulator magnetic field. This ensures that the primary HE_{11} mode is fully separated into two off-axis beams. These beams have

identical profiles and plane wave fronts. Full separation of the beams takes place after a distance $L=a^2/2\lambda$ from the step, where a is the height of the waveguide [9]. At the location of full separation two mirrors are placed, which reflect the two mm-wave beams, while the electron beam passes on-axis through the opening between the mirrors, see Figure 4. On the left side simulation results show the field intensities of an HE_{11} beam, propagating in a stepped waveguide. Here it splits into two identical beams. The two beams merge into one HE_{11} beam after reflection on the two mirrors. In this way the 100% reflector is formed. The power in the aperture is lower than -30 dB compared to the peak value.

Outcoupling and feedback of the mm waves is realised by a similar stepped waveguide behind the undulator. By giving one of the two mirrors a small displacement in z-direction, the reflected beams have a phase difference and one on-axis and two off-axis backward-propagating beams are formed. By variation of the phase difference, i.e., by translating one of the mirrors, the reflected on-axis power can be varied from 0 to 100% of the generated mm-wave power. The on-axis beam propagates back all the way through the primary waveguide. In this way, part of the mm-wave power is fed back.

On the right side of Figure 4 simulation results are given for the out-coupling system. The two off-axis beams are coupled out by way of 90° mitre bends. In a similar way, the two output beams are merged into one beam in a combiner system that is mounted in parallel to the described beam-splitter system, see Figure 5.

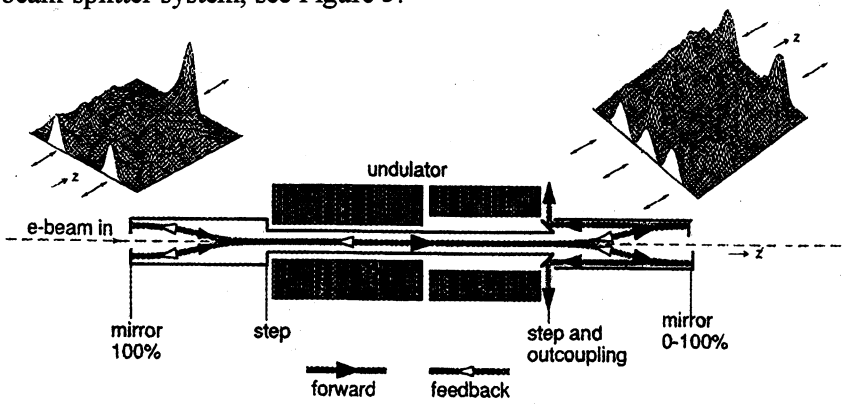

Figure 4
A principle sketch of the mm-wave system gives on the left side of the undulator the 100% reflector and on the right side the splitter system. The splitter separates the feedback power (going through the primary waveguide back to the 100% reflector) from the output power.

For a given amplitude feedback, the phase of the feedback power is fixed. Therefore, on the output side (in the combiner part) the phase difference of the two output beams is adjusted by shifting the double mitre bend over a small distance.

Without changing any of the dimensions, a fast tunability around the chosen central frequency can be achieved by varying only the electron energy. The full-width half-maximum frequency range is about 4%. However, to adjust the frequency over the entire frequency range of 130-260 GHz, it is necessary to also make a variation of a, the height of the stepped waveguide. Therefore, the sidewalls of the splitter can be adjusted to optimise the height from a = 60 mm for frequencies around 260 GHz to a = 85 mm for 130 GHz. The frequency dependency of the mm-wave feedback coefficient plays an important role in the width of the output frequency spectrum. This enables a very small bandwidth at a fixed acceleration voltage [10, 11].

By using a quasi-optical confocal mirror-system the single mm-wave beam is transferred from the 2 MV location through an insulator tube to ground potential. The insulator tube is very similar to the accelerator and decelerator tubes. Since the frequency of the FEM has to be varied over a very wide range, it is necessary that the vacuum barrier window is broadband as well. We have chosen a window at the Brewster angle, since this is the only possibility with a bandwidth of one octave.

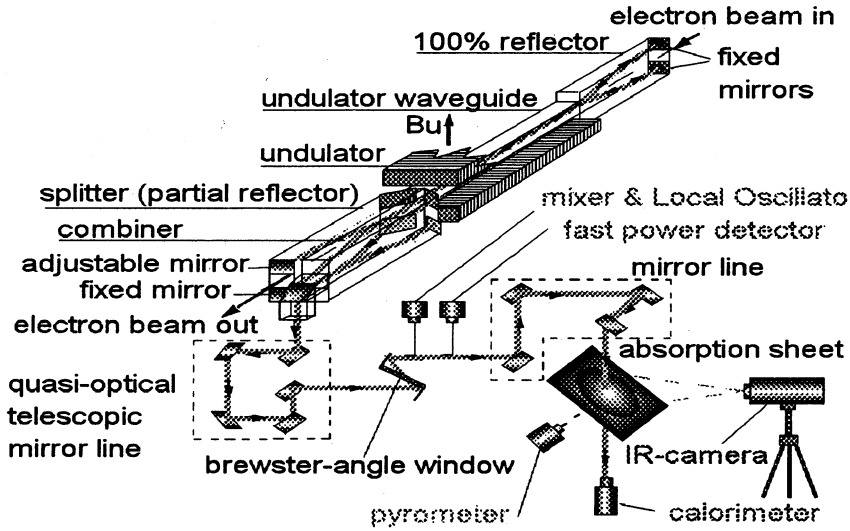

Figure 5

The mm-wave system, showing the 100% reflector, the undulator, the splitter/combiner, the outcoupling waveguide and the confocal mirror system to the window. Furthermore, the high-power measurement system is shown.

For the first stage of the FEM project a single-disc, edge-cooled boron-nitride Brewster-angle window with a diameter of 140 mm can withstand pulses of 0.3 to 1 s depending on the frequency.

First experimental results

The first experiments were performed in the inverse set-up. The electron gun is mounted inside the high-voltage terminal and the undulator and waveguide systems are outside the pressure vessel.

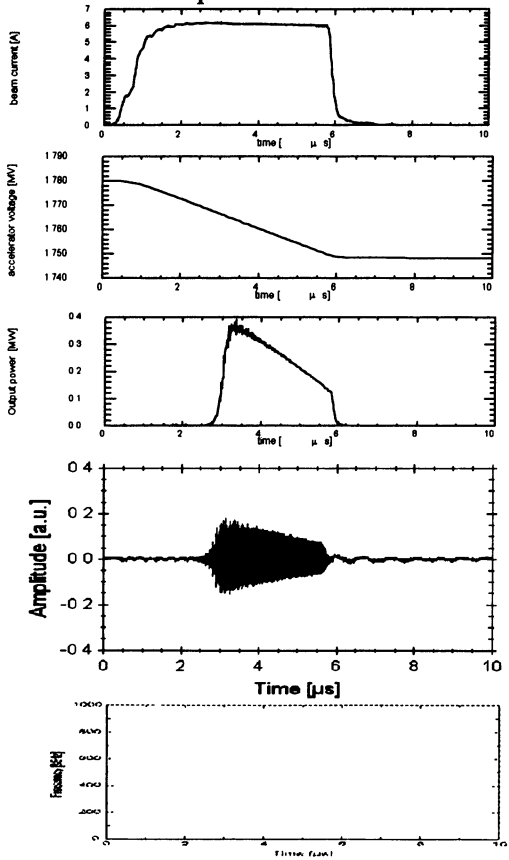

Figure 6

The results of one of the first high-power experiments are given. Plotted are the beam current vs. time, the accelerator voltage and the mm-wave power as measured by a fast broadband detector. Then, the mm-wave power as measured by a narrow-band hetero dyne system, with a local oscillator frequency of 200.5 GHz. At the bottom the FFT frequency spectrum is given. The frequency difference between the local oscillator and the measured signal is given. With these parameters, the spectrum is very pure and the output power grows to 375 kW. Feedback coefficient: 0.35.

In this set-up, with mm-wave system at earth potential for easy adjustments and fine-tuning of the entire system the decelerator and depressed collector are not installed yet, which means that the FEM pulse duration is limited. In October 1997, the FEM generated mm-wave power for the first time. Using an electron beam current of 6 A and an accelerator voltage of 1.76 MV, the mm-wave pulse starts after 3 μs and lasts 3 μs, and reaches a peak power level of 375 kW, see Figure 6 [12]. Output power and start-up time correspond well with simulation results. The power signal has a strong peak and drops sharply. A more-or-less flat output power signal is seen if it just happens that an increasing power level at a lower frequency is combined with the usual decaying signal. See Figure 8.

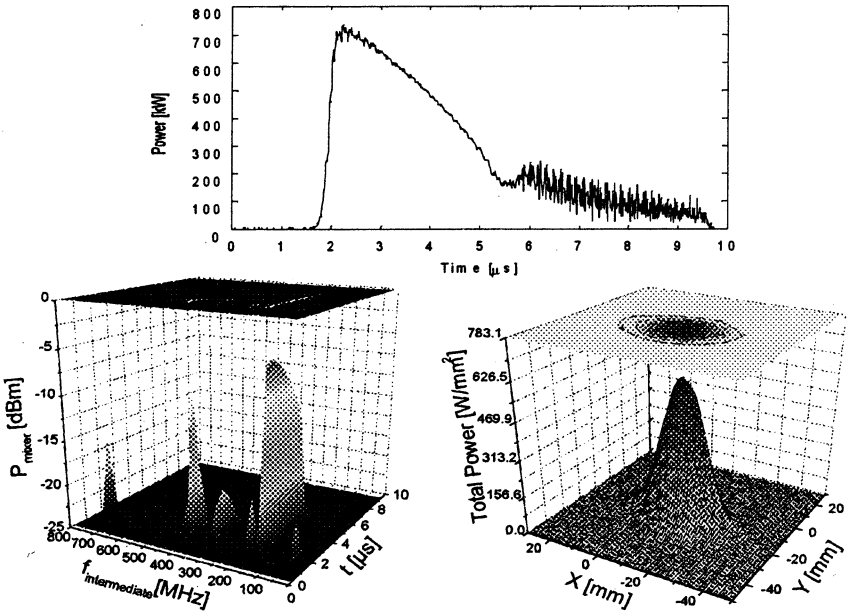

Figure 7
Highest power achieved so far, reaching just over 700 kW. In the frequency spectrum (at logarithmic scale, in the lower left plot) a decaying signal can be seen at a frequency about 200 MHz from the local oscillator frequency. After a few 5 μs the frequency jumps to a lower frequency, outside the frequency band of ± 1 GHz from the local oscillator frequency of 205.4 GHz. Accelerator voltage at start: 1.77 MV. Feedback coefficient: 0.6. Beam current 7.2 A. A measurement of the output mm-wave beam is given in the right-lower plot using an absorbing film under an angle of 45°. Measurements are performed by means of an infrared camera. A nearly Gaussian profile can be seen in both directions.

A parameter scan has been performed for feedback coefficient, undulator drift gap and accelerator voltage. In the case of very similar parameters, the output power can be completely different by just changing the start value of the accelerator voltage slightly. See Figure 9. The different behaviour of the output power for just marginally changing initial beam energies can be explained as follows, see Figure 10 [11]. The amplification band shifts rapidly across the cavity frequency curve. Depending on their relative positions the amplifying effect can lead to a non-linear suppression of all but one mode (leading to a single mode, single frequency) or to an amplification of several frequencies, leading to a wide spectrum. Simulation results for the single-frequency case are given in Figure 11 for high initial energy and a high amplification. We see very much correspondence with measured results, see e.g. Figure 9 top.

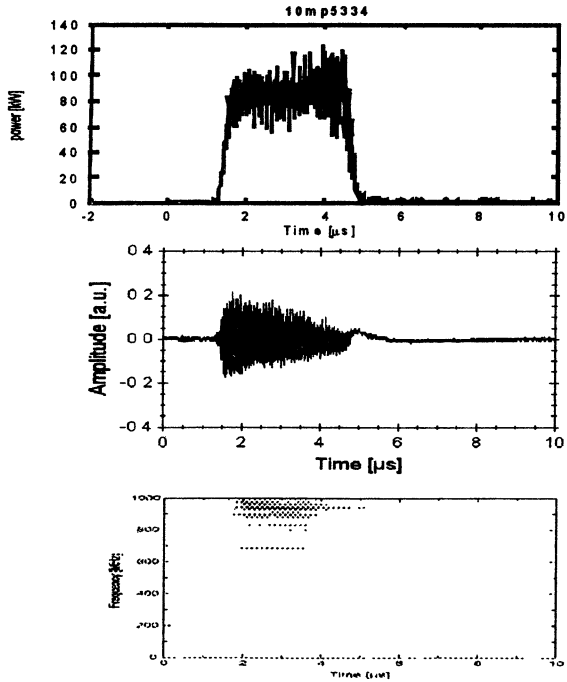

Figure 8
A more-or-less flat output power signal can be seen if an increasing power level at a lower frequency is summed to the usual decaying signal. In this case, the decaying power is composed of a number of frequencies 0.7 - 1 GHz apart from the local oscillator frequency of 205.4 GHz. Acceleration voltage at start: 1.76 MV. Feedback coefficient: 0.7. Beam current 6 A

Wide-band tunability of the FEM was demonstrated by operation in another frequency range. Now the cavity was tuned at a frequency around

170 GHz in stead of 200 GHz and a new series of experiments were performed. In Figure 12, the accelerator voltage is adjusted to around 1.6 MeV, corresponding to a frequency around 170 GHz. Around this frequency cavity losses are much higher because of some imperfections of the undulator waveguide, Therefore, the output power is substantially lower. Now power levels up to 350 kW were measured [14]. In the present set-up (without electron beam recovery) the accelerating voltage drops rapidly during the pulse (1 kV per A of beam current per μs, so 6 A means: 6 kV/μs).

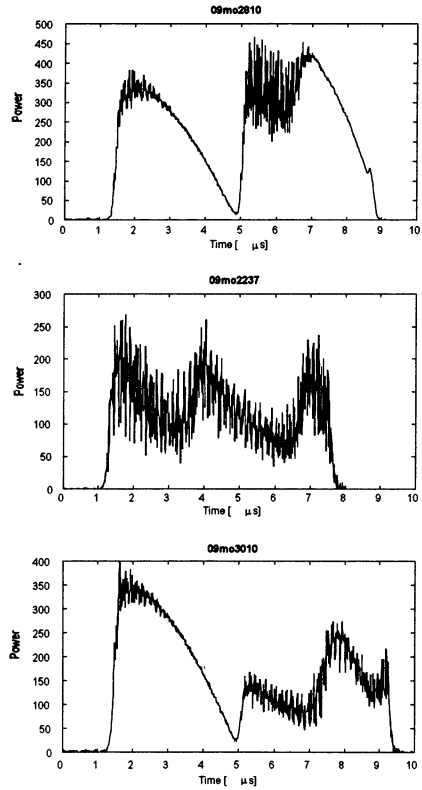

Figure 9
At very similar parameters (feedback coefficient: 0.7, beam current 6 A), the temperal behaviour of the output power can be completely different by just changing the start value of the acceleration voltage.
Top: acceleration voltage at start: 1.754 MV.
Middle: acceleration voltage at start: 1.755 MV.
Bottom: acceleration voltage at start: 1.769 MV.

Due to a bandwidth of the mm-wave cavity of just 4%, the pulse length is limited to a few μs, since the gain curve thus rapidly shifts across the cavity bandwidth. Consequently, the output power drops sharply and the pulse length is limited. The highest power achieved so far is just over 700 kW. See Figure 7 [13].

Follow-up project: 1 MW, 1 s

Now a follow-up project is being undertaken to increase the pulse length from 0.1 to 1 s. Although the basic principles are now demonstrated and we are confident that we made the right choices, still a number of issues have to be looked at. Most of the issues have to do with the much higher heating of the components, because of the longer pulse length.

The most critical components are the mirrors in the mm-wave cavity, with a heat load up to 27 W/mm^2. Furthermore, temperature rise of the window is too high for the present BN disk at the higher frequencies, and therefore another material, e.g. diamond, is required.

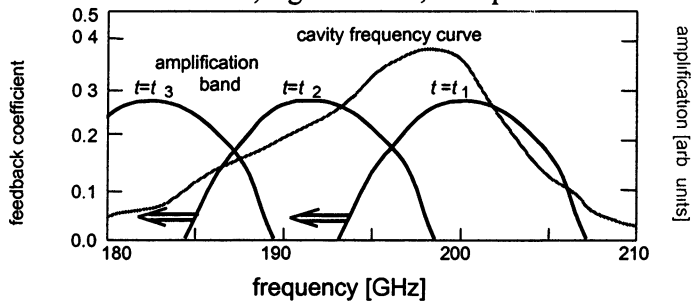

Figure 10

Frequency behavior of the cavity, when set at a central frequency of 200 GHz. As an example amplification curves are given schematically for three different positions of the amplification band (three different initial electron beam energies).

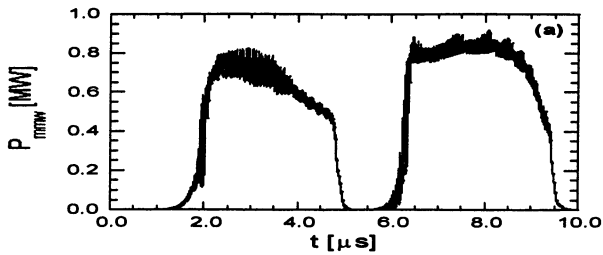

Figure 11

Simulation results on the mm-wave output power, for the situation of a relatively high initial electron beam energy.

Further, the vacuum quality is of great concern and therefore we will replace the existing accelerator tubes, now with glued aluminum-glass connections to brazed metal-ceramic types. This would enable to have a bake-out of the entire electron beam line (see Figure 13) and mm-wave system to temperatures as high as 300 to 500 °C.

Energy recovery

To increase the overall efficiency to over 50 % and to diminish the heat load on the collector, an electron beam recovery system is currently being installed. This system consists of an electrostatic decelerator to decelerate the beam from 2 MeV to an average of 200 keV (for 260 GHz), and a depressed collector, see figure 14.

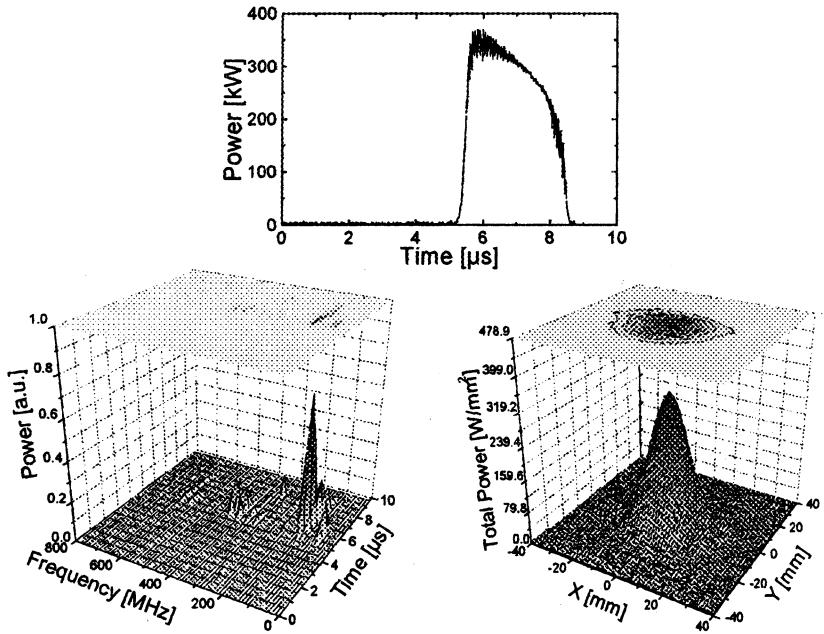

Figure 12
Highest power achieved at 170 GHz setting: 350 kW, measured by the fast detector. The middle figure shows the FFT IF spectrum of the same shot around LO frequencies of 169.5 GHz. The corresponding beam energy and current are 1.61 MeV and 7.1 A, respectively. The lower figure gives the power profile of the mm-wave beam, measured with the IR-camera. In the right-lower plot. The output mm-wave beam is given in the right-lower plot A nearly Gaussian profile can be seen in both directions.

The multi-stage collector is designed so that electrons fall on the backside of one of the three electrodes, thus ensuring that secondary electrons will immediately be accelerated back towards the electrodes, see figure 3. However, scattered primary electrons can cause back streaming, hereby reducing the efficiency and possibly damaging the machine.

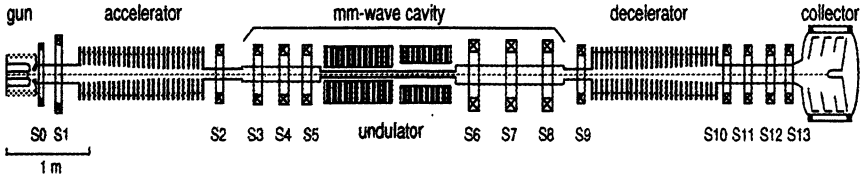

Figure 13 FEM beam line.

An off-axis bending scheme, using a rotating perpendicular magnetic field lowers the back streaming and hereby increases the pulse length of the machine. This deflection system reduces the return current from 100 mA to 10 mA. The General Particle Tracer (GPT) code has been used to design the guiding and deflection system [3,15]. The deflection system causes an angle dependency for the current distribution on the collector electrodes, shown as example in figure 15.

Without the bending system there is a nearly uniform distribution over the surface of the electrode. With the deflection system the beam is bent into the collector and the electrons hit the plate at a larger radius. This information is important for the design of the cooling system, especially with the further increase of the pulse-length to 1 s. The local intensity peak is very high with the bending system on.

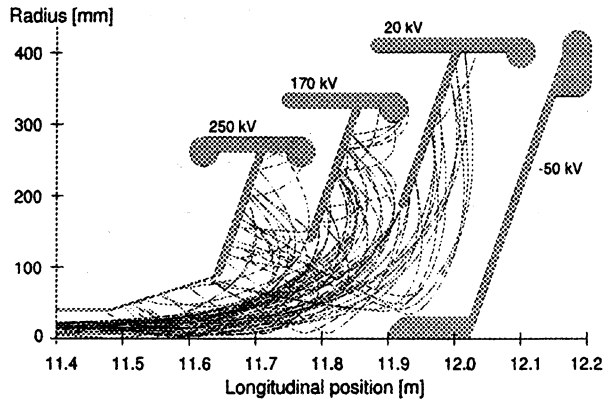

Figure 14
FEM depressed collector with sample trajectories. Both primary and scattered particles are shown.

However, because the peak will be smoothed over all azimuthal angles, by the rotation of the bending system, the maximum value is: 7 W/mm^2. This is comparable to the uniform angle dependency. Furthermore, the total power dissipation, summed over all collector plates, decreases.

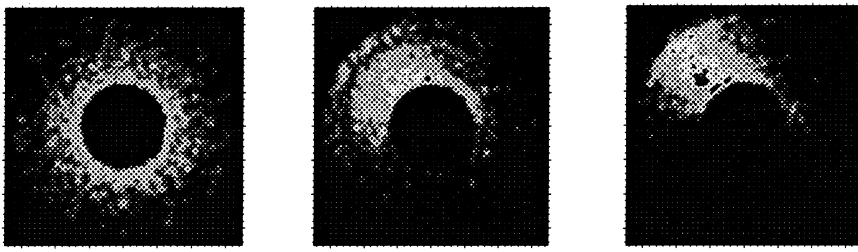

Figure 15.
Simulation results for the current dissipation on the second collector plate. The plots represent 0, 1, and 2 mT in the deflection system.

Cooling of the cavity mirrors

The mirror with the highest heat load in the mm-wave cavity is considered in more detail with a finite-element method, see Figure 16. The mirror of OFHC copper is 10 mm thick and 40 mm wide. A heat dissipation of 2 kW is assumed, with a cosine shape and a maximum power density of 27 W/mm^2. The cooling channels are rectangular 1*1.5 mm^2. In figure 5, upper plot, the temperature rise after a 1 s. pulse is given, the maximum temperature is 229 °C.

In the central plot the displacement magnitude is given, having a maximum of 0.02 mm. In the lower plot the Von Mises stress is calculated, leading to a value as high as 460 N/mm^2. The calculations show that the Von Mises stress is much higher in this configuration than the allowable stress, resulting in non-elastic deformation.

For this reason we are now designing a cooling system such that the cooling flow is much more concentrated on the most heated center of the mirror. We did experiments with the encouraging result that boiling of the cooling water could give a valuable improvement of the cooling capacity in a practical configuration.

Conclusions

In the first phase of the project, experiments were done in the inverse set-up. First generation of mm-waves was achieved in October 1997. Highest peak power measured so far is 700 kW at 200 GHz. A series of experiments around 170 GHz showed high output powers again.

Output power, start-up time and frequency correspond well with simulation results. It was demonstrated that single-frequency operation can be reached for every frequency by adjusting the cavity in such a way that the peak of the feedback curve coincides with the peak of the amplification band.

After the series of experiments in the inverse set-up, the equipment is now being reinstalled in the final set-up. From that moment on (now scheduled for early 2000), the pulse length can be extended up to 100 ms. At the same time, a follow-up project is being undertaken to increase the pulse length from 0.1 to 1 s. Because of the longer pulse length, the heat load plays a much more important role. The most critical components have been identified and heat-load finite-element simulations show that the 1 MW power level can be handled for 1 s.

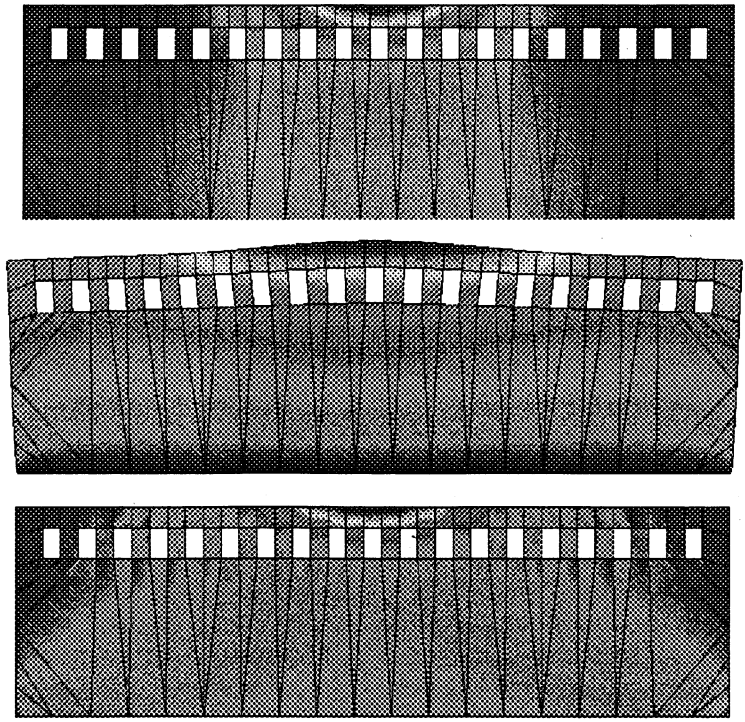

Figure 16:
Finite-element calculations for the cavity mirror;
Upper: temperature rise (scale from 32 to 229 °C)
Central: displacement magnitude (scale from 0 to 0.02 mm)
Bottom: Von Mises stress (scale from 12 to 460 N/mm^2)

Acknowledgements

The authors are grateful to the many people who had very valuable contributions to this report:
P. Eecen, W. Kooijman, G. Land, A. Putter, F. Wijnoltz, and many others, *Rijnhuizen*
A.A. Varfolomeev, S.N. Ivanchenkov, A.S. Khlebnikov and A.V. Smirnov, S.V. Tolmachev,
A.V. Tulupov, *Russian Research Centre, Kurchatov Institute Moscow*
M. Thumm, *Forschungszentrum Karlsruhe,*
W. Kasparek, D. Wagner, *Intitut für Plasmaforschung, Stuttgart*
M. Cattelino and G. Miram, *CPI/Varian, Palo Alto, USA*
P.C.T. van der Laan, P. van Deursen, J. Wetzer and P. Wouters, *Univ. of Techn. Eindhoven*

This work was performed as part of the research programme of the association agreement of EURATOM and FOM with financial support from NWO and EURATOM.

References

[1] M.A. Makowski, F. Elio and D. Loesser, "Design and technical aspects of ITER ECRF systems", Proc. 10th Workshop on ECE and ECRH, EC10, Edited by A.J.H. Donne and A.G.A. Verhoeven (World Scientific, Singapore, 1998), pp. 549-559.

[2] W.H. Urbanus, W.A. Bongers, G. van Dijk, P.J. Eecen, B.S.Q. Elzendoorn, C.A.J. van der Geer, R. de Kruif, P. Manintveld, J. Pluygers, A.J. Poelman, P.R. Prins, F.C. Schüller, P.H.M. Smeets, A.B. Sterk, M. Valentini, A.G.A. Verhoeven and M.J. van der Wiel. "Electron beam line and mm-wave experiments of the Fusion-FEM", Proc. 10th Workshop on ECE and ECRH, EC10, Edited by A.J.H. Donne and A.G.A. Verhoeven (World Scientific, Singapore, 1998), pp. 497-506.

[3] S.B. van der Geer *et al.*, Proc. 1999 Particle Accel. Conf., New York (1999)
GPT User Manual, Pulsar Physics; http://www.pulsar.nl/gpt

[4] M. Caplan, R. Best, A.G.A. Verhoeven, M.J. van der Wiel W.H. Urbanus, V.L. Bratman, G.G. Denisov, "Predicted performance of a DC beam driven FEM oscillator designed for fusion applications at 200-250 GHz", Nucl. Instr. and Meth. A331, 243 (1993).

[5] M. Caplan, T.M. Antonsen, B. Levush, A.V. Tulupov, W.H. Urbanus. "Predicted operating conditions for maintaining mode purity in the 1 MW 200 GHz FOM Free Electron Maser", Nucl. Instr. and Meth. A358, 174 (1995).

[6] A.V. Tulupov, M.J. van der Wiel, W.H. Urbanus, M. Caplan. "Simulations of the performance of the FEM oscillator for Fusion at 130-250 GHz", Nucl. Instr. and Meth. A341, 305 (1994).

[7] M. Caplan, W.A. Bongers, A.G.A. Verhoeven, C.A.J. van der Geer, M. Valentini, W.H. Urbanus. "Prediction of the FOM-FEM experimental results using multi-mode time-dependent simulations", Nucl. Instr. and Meth. A407, pp. 45-49 (1998).

[8] G.G. Denisov, and M. Yu. Shmelyov, "Quasi-optical confocal schemes for high-power microwave components", Proc. 21st International Conference on Infrared and Millimeter Waves, Berlin, BF3, Conference Proceedings, M. von Ortenberg, H.U. Müller Eds. (1996), ISBN 3-00-000800-4

[9] L.A. Rivlin and A.T. Semenov, "Transmission of images through optical waveguides", Laser Focus, Vol. 17, no. 2, p. 82 (1981).

[10] W.A. Bongers, G. van Dijk, B.S.Q. Elzendoorn, C.A.J. van der Geer, R. de Kruif, P. Manintveld, J. Pluygers, A.J. Poelman, P.R. Prins, F.C. Schüller, P.H.M. Smeets, A.B. Sterk, M. Valentini, A.G.A. Verhoeven, M.J. van der Wiel and W.H. Urbanus, Proc. 10th Workshop on ECE and ECRH, EC10, "Microwave measurements and engineering at the Fusion-FEM", Edited by A.J.H. Donne and A.G.A. Verhoeven (World Scientific, Singapore, 1998), pp. 507-514.

[11] V.L. Bratman, G.G. Denisov, A.V. Savilov, M. Yu. Shmelyov, A.G.A. Verhoeven, W.H. Urbanus. "Simulation of the build-up of transverse and longitudinal structures of the microwave field in the Fusion-FEM", Nucl. Instr. and Meth. A407, pp. 40-44 (1998).

[12] A.G.A. Verhoeven, W.A. Bongers, V.L. Bratman, M. Caplan, G.G. Denisov, G. van Dijk, C.A.J. van der Geer, P. Manintveld, A.J. Poelman, J. Pluygers, M.Yu. Shmelyov, P.H.M. Smeets, A.B. Sterk, W.H. Urbanus, "First high power experiments with the Dutch free electron maser", Physics of Plasmas. Vol. 5, no. 5 (May 1998). pp. 2029-2036.

[13] A.G.A. Verhoeven, W.A. Bongers, V.L. Bratman, M. Caplan, G.G. Denisov, C.A.J. van der Geer, P. Manintveld, A.J. Poelman, J. Plomp, A.V. Savilov, P.H.M. Smeets, A.B. Sterk, W.H. Urbanus, "First mm-wave generation in the FOM Free Electron Maser", IEEE Trans. on Plasma Science, Vol. 27, No. 4, August 1999, .

[14] W.H. Urbanus, W.A. Bongers, C.A.J. van der Geer, P. Manintveld, J. Plomp, J. Pluygers, A.J. Poelman, P.H.M. Smeets, A.G.A. Verhoeven, V.L. Bratman, G.G.Denisov,, A.V. Savilov,, M. Yu. Shmelyov, M. Caplan, A.A. Varfolomeev, S.V. Tolmachev and S.N. Ivanchenkov. "high-power electrostatic free-electron maser as a future source for fusion plasma heating: Experiments in the short-pulse regime" Phys Review E, volume 59, Number 5, (1999) pp 6058-6063

[15] C.A.J. van der Geer, M. Caplan, N. Dione, S.B. van der Geer, M.J. de Loos, A.G.A. Verhoeven, M. Valentini, M.J. van der Wiel, W.H. Urbanus. Nucl. Instr. and Meth. A 407 (1998) 70-75.

EXAMPLES OF SHORT-PULSE PHENOMENA IN MICROWAVE FREE ELECTRON LASERS

*T.C. Marshall and T-B. Zhang**

Department of Applied Physics, Columbia University, New York City 10027, N.Y.
*Omega-P, Inc., New Haven 06520 CT

Under certain conditions, a free electron laser will produce a single pulse of coherent radiation having high intensity and a width containing about 10 rf cycles. The conditions favoring this output are obtained in an amplifier configuration, using an optimized tapered undulator. This pulse is nearly smooth and contains no sidebands. In this paper, we review a sample calculation appropriate to a 1.5 mm wavelength FEL, which shows that a 50 ps pulse of radiation will propagate in a nearly self-similar way down the amplifier as it grows in power; intensity level ~ GW/cm^2 is found. Numerical studies are done with a 1D "Compton" code, taking an initial power level of 9 kW/cm^2; a Gaussian pulse is input into the rear part of an electron pulse and slips forward. Because of the slippage of the radiation pulse through the electron pulse, the peak microwave intensity can exceed the kinetic power of the beam. We also study superradiant pulses that may be obtained from a microwave inverse FEL accelerator device, when the electron bunches are very short, and the wiggler has very little or no taper.

I. Introduction

This paper uses a numerical model of a traveling wave, high gain, "Compton" FEL to explore the physics of a microwave amplifier which can produce an intense "clean" spike of output power that has a spectrum largely free of sidebands. An external low power source with a Gaussian-shaped input pulse provides input to a high efficiency FEL travelling-wave amplifier having an appropriately tapered undulator. Our findings are that one might expect to produce a millimeter wavelength pulse having peak power ~ GW/cm^2 with FWHM ~ 50 ps, using a 0.75 MeV, 100 A electron beam as a (typical) source. This powerful pulse is about ten wavelengths in length. We also use this same formalism to study particular "superradiant" pulse phenomena that might occur in a recent IFEL ("Inverse" FEL accelerator) experiment that uses very short electron pulses and 10.5 cm wavelength radiation.

It has been found that the FEL oscillator can provide an output of very narrow, chaotic, high power "spike" pulses of radiation, featuring a

wide, irregular spectrum [1-3]. Further, FEL oscillators show, in experiment [4] as well as in numerical theory which carries the analysis into the nonlinear regime [5], output power characterized by low efficiency together with a narrow spectrum, or in a mode having higher efficiency and a broad spectrum. The latter has to do with the sideband instability [6] which has been observed in experiment [7, 8] and which is also obtained in connection with superradiant spiking studies [9-13] since both effects [14] arise from slippage of the electromagnetic pulse through the electrons. However, the sideband instability can be stabilized with an appropriately chosen undulator taper [15-17]; this possibility can only be exploited through the use of the FEL amplifier, a matter which has received far less experimental study than the oscillator, and which offers interesting possibilities. In this study we present the results of a numerical study of short millimeter wavelength pulse of radiation which is propagating through a much longer pulse of electrons that is traversing an undulator [18], together with results pertaining to the case of a long pulse of microwave radiation passing through a shorter pulse of electrons.

II. Theoretical Formulation

At FEL resonance, as the light wave moves down one undulator period, it slips ahead of the electrons by one optical wavelength λ_s. We study first the case where the electron beam pulse is much longer than the overall slippage distance $L_s = N_w \lambda_s$ in N_w undulator periods, so that essentially no radiation appears ahead of or behind the electron pulse (thus we do not effect of the consider the "superradiant" pulse [9-13] here; but see section IV). We use a set of 1D equations to gain insight into the physics of this Compton FEL (it is assumed that in an actual device, a waveguide would be used to confine the waves, but this 2D configuration does not alter the physics of this 1D study in an important way):

$$\partial\gamma_j (x,y) / \partial x = - [2\rho\gamma_r^2 A_s \sin \Psi_j] / [\gamma_j \beta_{j||}], \quad (1)$$

$$\partial\Theta_j (x,y) / \partial x = (2\rho)^{-1} [1 - (k_s /k_w)(1 - \beta_j)/\beta_{j||}], \quad (2)$$

$$\partial A(x,y)/ \partial y = i \gamma_r \langle e^{-i\Theta} / \gamma \rangle. \quad (3)$$

The above equations are derived directly from the original 1D time-dependent FEL equations [6] by transforming the variables z and t into new independent variables x and y [9], i.e. $x = (ct - z)/ l_c$, $y = (z - - v_{||} t)/ l_c \beta_{||}$; here, $l_c = \lambda_s /4\pi\rho$ is the cooperation length which is the slippage in a characteristic gain length [10] , $\rho = (1/\gamma)(a_w \omega_p/4ck_w)^{2/3}$ is the Pierce parameter; $\beta_{j||} = [1 - (\mu - 2a_w a_s \cos \psi_j)/ \gamma_j^2]^{1/2}$ is the axial velocity of the jth electron, $\mu^2 = 1 + a_w^2 + a_s^2$, a_w and a_s are the normalized vector potentials of the undulator ($eB_\perp/k_w mc^2$) and radiation field ($eE_s/k_s mc^2$); γ_j is the relativistic factor of the jth electron, $\Psi_j = \Theta_j + + \phi$ is the relative phase of the jth electron with respect to the radiation pulse, $A(x,y) = A_s e^{i\phi}$ is the complex amplitude of the radiation pulse with amplitude $A_s = (\omega_s/\omega_p)a_s/(\rho\gamma_r)^{1/2}$, and ϕ is the phase shift of the radiation pulse. The angular brackets in the right-hand side of equation (3) indicate an ensemble average over all electrons. For the other quantities: γ_r is the resonant energy of electrons in units of mc^2, $k_w = 2\pi/l_w$ is the wave number of the undulator, l_w is the undulator period; $k_s = 2\pi/\lambda_s = \omega_s/c$ is the wave number of the radiation, λ_s is the radiation wavelength, l_w and λ_s satisfy the resonance condition $\lambda_s = l_w(1+ a_w^2)/ 2\gamma_r^2$, and $\omega_p = (4\pi e^2 n_e /m)^{1/2}$ is the plasma frequency of the beam electrons having density n_e electrons/cm^3. The characteristic electric field e-folding length, L_g, in the high-gain exponential regime is $l_w/4\pi\rho$. The original FEL wave equations have been obtained assuming the field amplitude is a slowly varying function of time; this approximation has been verified in the application for the short pulse propagation discussed here. The operation of the FEL described here is on the borderline between the Compton and Raman regimes, and if an actual device is to be constructed, the beam space charge effects should be included to insure accuracy; however, for this illustrative example, we have not incorporated this complication, nor that of an overmoded waveguide to contain the waves. From the 1D formulation we shall obtain the output wave intensity, namely the power normalized to the cross section of the electron beam, as well as the distribution of electron energies.

The numerical simulation involves a computational model using equations (1) to (3). The FEL works as a traveling wave amplifier. The spatial distribution of simulation electrons has a rectangular profile, the electrons are taken to be monoenergetic, and at the undulator entrance, they are uniformly distributed inside the beam length L_b with one

thousand simulation electrons per radiation wavelength. For each wavelength-size "strip" of electrons, the relative phase location of the electrons with respect to the radiation field is uniformly distributed from $-\pi$ to π. The input radiation pulse is "seeded" inside the electron beam, with its initial amplitude $a_{s0} = 10^{-4}$ (9 kW/cm^2 at 1.5 mm wavelength). The pulse profile and width can be varied so that we can study the evolution of various pulses. For the output format of the computational results, the electron beam pulse and the radiation spike are plotted as the function of independent variables x and y respectively, which implies two moving "windows" with the former at the speed of light c and the latter at the speed of electrons $v_{\|}$, both scaled in the units of the radiation wavelength λ_s from their leading edges. Since all these quantities are recorded at various undulator positions, these results will describe the time evolution of the pulses. In several test runs, we have carried out simulations for different FEL parameters, including different lengths of beam pulses and radiation pulses. Our results for "superradiant" pulse evolution are in a very good agreement with that of previous authors [9] and provide a calibration of our code.

III. Numerical Study of a 1.5 mm Wavelength Short-Pulse FEL Amplifier

Our main interest is to investigate an initial short radiation pulse propagating through a sufficiently long electron pulse. The initial radiation pulse has a Gaussian profile, and is injected into the trailing part of the electron beam pulse; the peak of the initial pulse is located at $y = 170\ \lambda_s$. The radiation pulse starts from that position at the undulator entrance, and then moves toward the front of the electron pulse as it moves along the undulator. The Fourier-transformed spectrum is also Gaussian and has a central frequency $\omega_s = 1.26 \times 10^{12}$ s^{-1}. Other simulation parameters of the FEL amplifier are listed in Table I, where a representative electron beam pulse length of 30 cm (~ 1ns) is taken; this beam pulse is 200 wavelengths long, and so the optical pulse moves only halfway through as it traverses 100 undulator periods.

Fig. 1 shows the pulse evolution in a constant period undulator ($l_w = 1.5$ cm) at four undulator positions $N_w = 0$, 25, 50, and 100. In these figures, the electron envelope is at rest and the optical spike propagates from the right to left as N_w increases. The radiation spike retains the initial profile until approximately 50 undulator periods where

the growth becomes saturated. Saturation occurs when the loss of beam energy causes the interaction to drop out of resonance. Examining the spectrum of the pulse at N_W = 100 (see right side of Fig. 3), we find the spectrum has developed prominent sidebands; these become comparable to the carrier power by 150 periods.

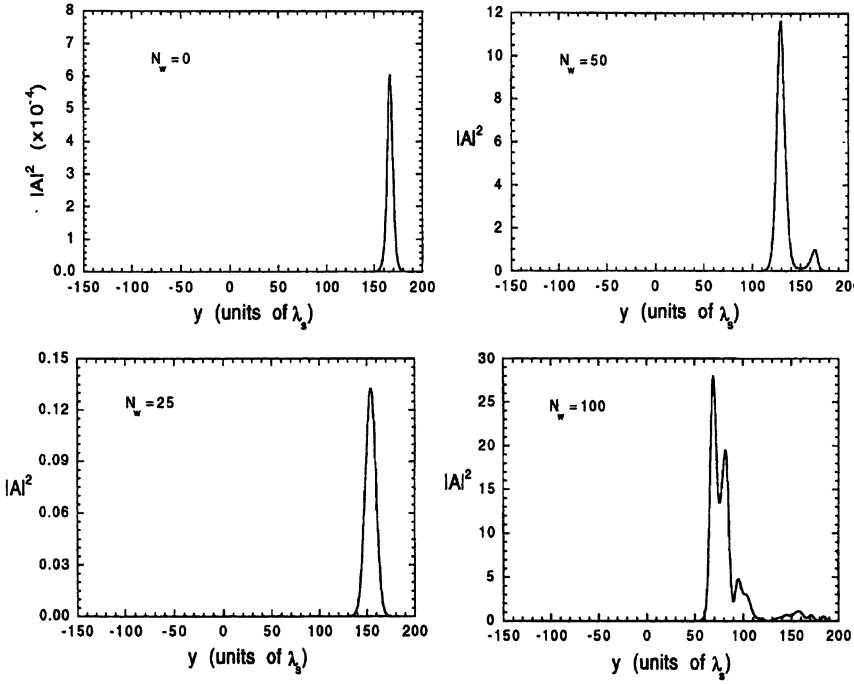

Fig. 1. Constant undulator period simulation. The radiation pulse slips forward into the electron beam from left to right at N_W = 0, 25, 50, 100; abscissa in units of λ_S

If the undulator is tapered, we expect the growth of the sideband can be suppressed [17], and in Fig. 2 we show the results. The undulator period is linearly tapered from 1.5 cm to 1.05 cm in 150 periods. All other conditions are the same as in Fig. 1 and are obtained from Table I. In this numerical experiment, we did not optimize the undulator taper to pursue the highest efficiency enhancement: instead, the appropriate taper was chosen for the purposes of obtaining the "cleanest" spike (however, this optimized taper is not very different from the taper which extracts maximum energy from the beam). Unlike the untapered case, the radiation pulse at high amplitude does not radically change its shape, but displays a narrow, regular profile throughout the slippage region.

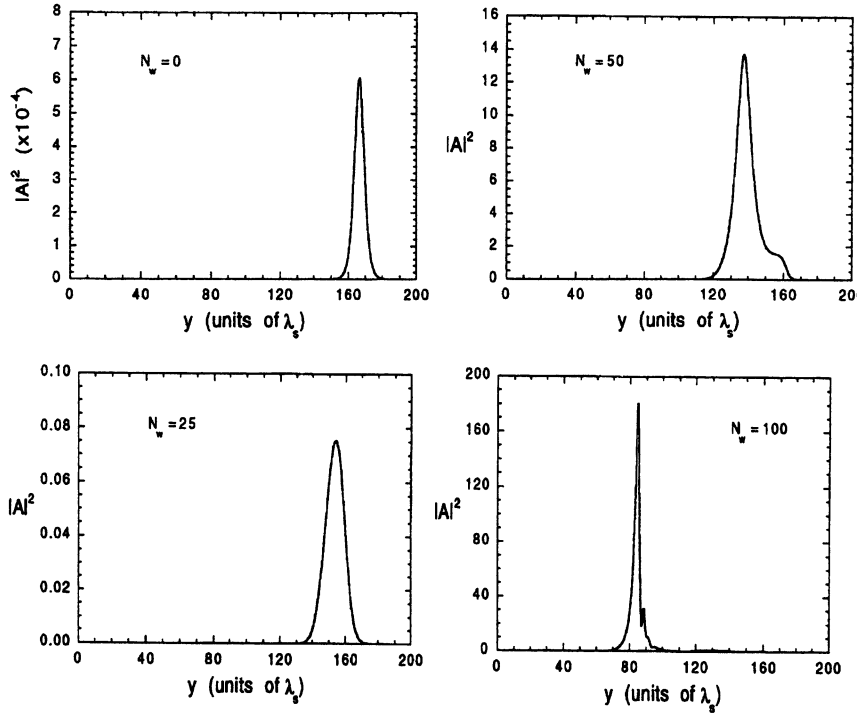

Fig. 2. Same as Figure 1, except the undulator period is linearly tapered from 1.5 cm to 1.05 cm in 0 to 100 periods. The ordinate axis is in units of A_s^2

The width of the initial Gaussian pulse is FWHM ~ 10 λ_S in intensity; it grows in amplitude and broadens during the first 25 periods; it continues to grow while keeping a nearly regular profile as it narrows in width between 50 and 100 periods. We have tried various widths of the initial Gaussian pulse, as well as a different initial amplitude profile varying as ~ 1/ cosh(αy) (a solitary wave solution [19]), and we find the variation of initial choices converges to a similar output pulse profile and width, although the number of undulator periods needed to form the self-similar pulse profile may vary. This suggests that a short optical pulse may eventually evolve to a self-similar spike in the slippage region of the tapered undulator. The characteristic width of the spike is similar to the prediction of the Ginzburg-Landau solitary wave theory [19]. In the constant period undulator, the self-similar feature is lost when the FEL system goes out of resonance. Returning to Fig. 3 (left side), we find not only a cleaner spectrum, but evidence of sideband suppression as well.

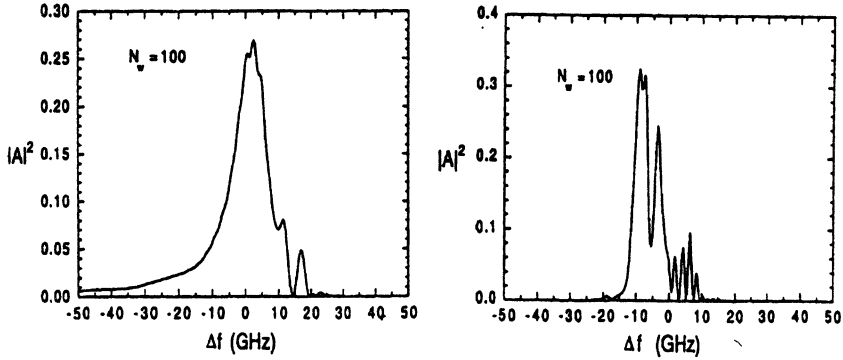

Fig. 3. Spectrum of the pulse at 100 periods, tapered undulator (left) and untapered undulator (right)

If a longer pulse is input to the FEL, we find that narrowing will commence when appreciable energy begins to be extracted from the electron beam. Starting with a Gaussian pulse having 50 wavelengths FWHM, taking the same parameters as given in Table I, we find narrowing to about 10 wavelengths FWHM occurs after the pulse has moved beyond 50 undulator periods (Fig. 4). A clear narrowing of a wide input pulse would be a good experimental test of the theory, providing hardware capable of providing an input pulse of perhaps 50 wavelengths FWHM can be obtained (this is more likely to be available at centimeter wavelengths).

Table I

Simulation parameters: A short millimeter-wavelength radiation pulse propagating in a much longer electron beam pulse.

Beam parameters		Radiation Pulse	
Electron beam energy	$\gamma = 2.5$	Wavelength	$\lambda_S = 1.5$ mm
Electron beam current	~ 100 A	Length (FWHM)	$\sim 10\,\lambda_S$
Beam Intensity	0.63 GW/cm^2	Initial ampl.	$a_S = 10^{-4}$
Electron beam radius	0.2 cm	Max. Intensity	3 GW/cm^2
Beam Pulse Length	$200\,\lambda_s$		
Undulator Parameters		Other Parameters	
Undulator Period	$l_w = 1.5$ cm$\rightarrow$1.05 cm	Pierce parameter	$\rho = 0.023$
Undulator Taper	2×10^{-3} cm^{-1}	Cooperation length	$l_c = 6$ mm
Undulator Parameter	$a_w = 0.2$ (constant)	Gain length	$l_w / 4\pi\rho = 5.2$ cm
Undulator Length	$N_w = 100$		

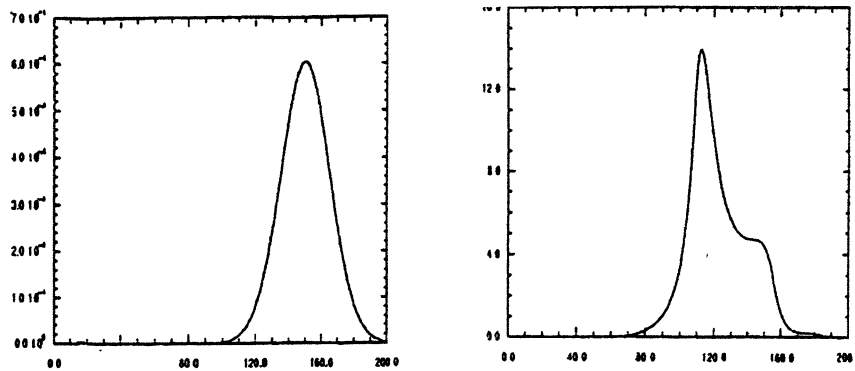

Fig. 4. Pulse-narrowing as pulse moves from N_w =0 to 50 (left to right)

In Fig. 5 we compare the cases of an untapered undulator (dotted line), a taper as given in Table I (solid line), and a steeper taper (dot-dash line) which is about 20% larger than that given in the Table. Examining the electron energy profile, we find considerable efficiency enhancement in the tapered undulators; however, the optimum taper yields not only higher peak power, but also a better pulse shape. The maximum value of the field amplitude a_s = 0.06 (~ 3 GW/cm^2) corresponds to an intensity higher than the beam kinetic energy intensity; this enhancement in power is caused by the slippage of the radiation pulse over the "new" electrons as it moves down the undulator. The ragged profile of the electron energy in the constant undulator is found to smoothen in the tapered undulator. The strong intensity of the spike forms a very deep potential well which may trap most of electrons, regardless of energy spread.

The choice of the 1.5 mm wavelength was arbitrary although this is representative of FEL performance with the chosen beam parameters. (The same qualitative features were obtained in another tapered undulator FEL simulation for much higher beam energy and wavelength of 8 μm.) The pulses narrow to ~ 10 wavelengths FWHM, and so a 1.5 mm FEL source produces a pulse width of roughly 50 ps. Because of the large intensity achieved, one would not expect optical guiding to be effective beyond the region of exponential growth [20], so an overmoded waveguide should be used to guide the radiation along the electron beam. Several runs of the code were made including the Raman correction: from these, we conclude that the Raman term causes lower

output power (and gain), but generally has only a slightly negative effect on the pulse shape and spectrum.

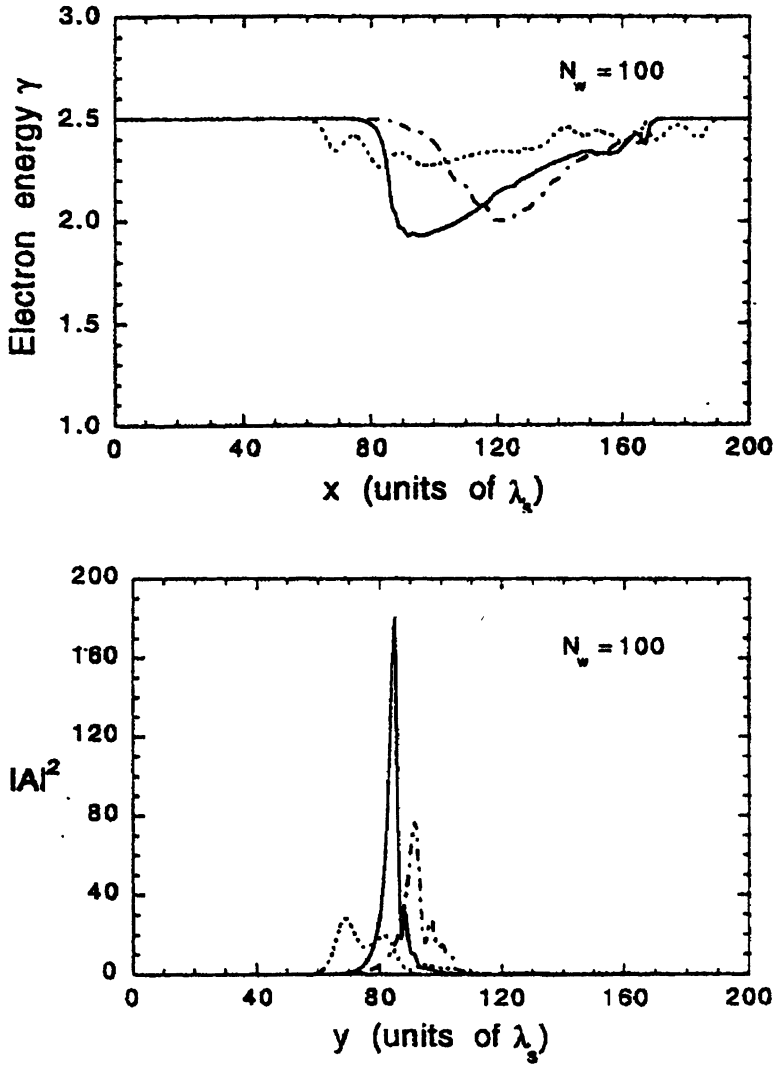

Fig. 5. Electron energy profile (above) and pulse profile (below) for untapered undulator (dotted line); tapered undulator according to Table I column 1 (solid line); and a taper 20% larger yet (dot-dash line)

The overall power gain of the spike pulse is ~ 50 dB. This raises the question of input noise, particularly the electron random noise, and how it affects the amplified pulse. We have introduced particle noise [21] into the code and find that this can cause, under certain conditions, a "spiky" noise signal that both leads and trails the main pulse. Small energy present in the wings of the Gaussian pulse can be amplified under noisy conditions to high amplitude, and if there is sufficient gain, the noisy energy that precedes the main pulse will broaden the energy distribution of the electrons that this pulse will slip into, resulting in degraded amplifier performance. However, starting from our choice of initial power, we find that particle noise has no effect on the output (however, the effect becomes more important at shorter wavelengths). The type of noise we have introduced into the simulation is Gaussian, and an actual electron beam may have particle noise in excess of this.

From this we have found that injection of a single short radiation pulse into a long electron beam pulse at the input of a tapered undulator traveling wave FEL amplifier should result in the development of an intense spike which is comparatively "clean" in both time and frequency domains, and which propagates in a self-similar way along the undulator. Because of the slippage, the peak pulse intensity is enhanced and is of the same order as the electron beam intensity. Since the pulse spectrum is regular and nearly Gaussian, the output pulse from the FEL is useful for technical applications and indeed might be compressed and intensified even further using standard optical or quasi-optical techniques. To place this work in context, we observe that FEL development has proceeded mostly using the convenient hardware of a laser oscillator. However, FEL amplifiers have greater flexibility and can provide better quality output, and therefore deserve more theoretical and experimental attention than they have received up to now.

IV. "Super-radiant" Pulses

"Superradiant" emission can be obtained from a group of electrons which occupies a region of space much smaller than one wavelength; then the electric field vectors add constructively and the radiated power scales as N_e^2, which is its characteristic signature (N_e is the total number of electrons in the bunch). For the FEL, one might expect this would be simply an enhancement of the spontaneous radiation ("coherent

spontaneous emission") from the electron bunch as it moves along the undulator, by a factor of N_e; however there is the progressive slippage of the radiation pulse ahead of the electrons which can complicate the problem. Furthermore, depending on the overall gain of the system, superradiance can occur in the linear regime of growth, or possibly proceed into the regime of strong bunching and saturation.

As an example, we point to an experiment located at Yale University that is configured as an "IFEL": that is, the apparatus will accelerate a 6 MeV pulse of electrons, ~ 10 ps in length, a few MeV using high power microwaves obtained from a 2.85 GHz pulsed klystron source [22]. The equipment includes an 11cm period helical undulator that has a slightly "reverse" -taper, and the pulse of spiraling electrons (obtained from an rf gun) is contained in a waveguide having 3.14 cm radius. If this apparatus were to be operated as a FEL with small input power at the resonant 10.5 cm wavelength, superradiance could occur since the electron bunch length is only 3 mm. Unlike the example in section III, where a short pulse of radiation slips through a much longer electron pulse, in this case a longer pulse of low-level radiation emerges from a much shorter pulse of electrons. The phase of the radiation with respect to the bunch determines whether electron deceleration (wave growth) or electron acceleration (wave energy decrease) is to occur. The cooperation lengths and gain lengths are each ~ 100 cm ~ $N_w l_w$, since $l_w \sim \lambda_s$ here.

In the IFEL example there would be several short electron bunches (provided by the rf gun macropulse) inside the undulator at any given time, since the bunch spacing is approximately one undulator period. Then any given bunch will find itself in the weak field caused by emission from the prior bunches, given the slippage is one wavelength per undulator period traversed. However, both the experimental and numerical studies can be simplified by injecting only a single bunch. As the gain of the system is quite low and the signal levels are small, one can linearize eqs (1-3) and perform a Laplace transform analysis to obtain the solution [23] if necessary; the output radiation is much below the FEL saturation level. The pulse peak power amplitude scales as $N_e^2 a_w^2$ and if the signal begins from noise, yields a pulse power ~ 10 – 100 W.

More relevant to section III is the example of a system which will enter the nonlinear regime of saturation due to a combination of high

gain, long undulator, and/or large input signal (using the parameters of Table I). In Fig. 6 is shown the result where a pulse of radiation, initially overlapping with the electron bunch, grows to saturated level as it slips ahead of the electron bunch. A distinct intense leading pulse of radiation, incorporating a substantial fraction of the electron bunch energy and having FWHM approximately 10 λ_s appears ahead of the bunch; at this point, the intensity of this superradiant pulse ($y < 0$) exceeds the FEL saturation level ($0 < y < 50$). This is the "long pulse" ($l_b > l_c$) case [24] in which the slippage length is comparable with or larger than the bunch length; the intensity of the pulse builds up without saturating because it is fed continuously by radiation emitted from electrons entering the slippage region from the region of steady state. Following the pulse further may show emission of a series of pulses. The superradiant pulse can extract energy very efficiently from the electrons even in the "short pulse" limit [24], although the pulse power would itself not be remarkable in the IFEL apparatus example above because of the large slippage distance and low electron bunch energy.

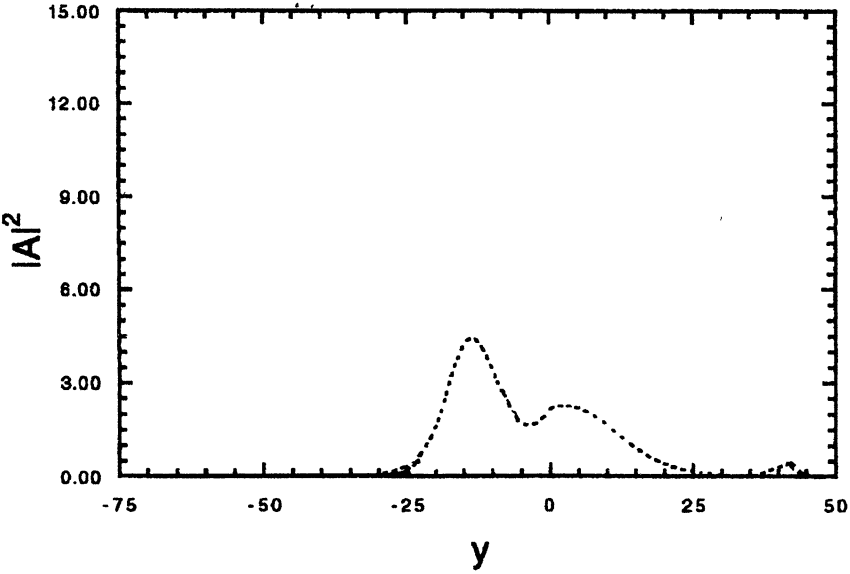

Fig. 6. Conditions given in Table I, (untapered undulator case): a low-level square pulse of radiation (at $N_W = 0$) initially coincident with a square pulse of electrons slips forward (to the left) as it is amplified and becomes saturated (at $N_W \sim 50$, shown). The leading edge of the electron bunch is at y=0 (y is the ordinate in units of wavelength). As plotted, this is qualitatively "pulse power versus time"

References

1. 1.Warren R.W., Goldstein J.C., Newnam B.E., Nucl. Instrum. Methods. 1986 **A250**, 19
2. Richman B.A., Madey J.M.J., Szarmes E., Phys. Rev. Lett. 1989 **63**, 1682
3. Dodd J.W., and Marshall T.C., IEEE Trans. Plasma Sci., 1990 **PS-18**, 447
4. Iracane D., Fontenay V., Guimbal P., Joly S., Striby S., and Touati D., Phys. Rev. Lett. 1994 **72**, 3985
5. Iracane D. and Ferrier J.L., Phys. Rev. Lett. 1991 **66**, 33
6. Kroll N.M., Morton P.L., and Rosenbluth M.N., IEEE J. Quantum Electron. 1981 **QE-17**, 1436
7. Warren R.W., Newnam B.E., and Goldstein J.C., IEEE J. Quantum Electron. 1985 **QE-21**, 882
8. Yee F-G., Masud J., Marshall T.C., and Schlesinger S.P., Nucl. Instrum. Methods 1987 **A259**, 104
9. Bonifacio R., McNeil B.W.J., and Pierini P., Phys. Rev. 1989 **A40**, 4467
10. Bonifacio R., Piovella N., and McNeil B.W.J., Phys. Rev. 1991 **A44**, 3441
11. Sharp W.M, Fawley W.M., Yu S.S., Sessler A.M., Bonifacio R., and DeSalvo Souza L., Nucl. Instrum. Methods 1989 **A285**, 217
12. Moore G.T. and Piovella. N, IEEE J. Quantum Electron. 1991 **QE-27**, 2522
13. Hahn S.J., and Lee J.K., Phys. Rev. 1993 **E48**, 2162
14. Caloi R.M., Phys. Rev. 1992 **A46**, 7934
15. Yee F-G., Marshall T.C., and Schlesinger S.P., IEEE Trans. Plasma Sci., 1988 **PS-16**, 162
16. Hafizi B., Ting A., Sprangle P., and Tang C.M., Phys Rev. 1988 **A38**, 197
17. Pila R.P., and Bhattacharjee A., Phys. Plasmas 1994 **1**, 390
18. Zhang T-B., and Marshall T.C., Phys. Rev. Lett. 1995 **74**, 916
19. Cai S.Y., and Bhattacharjee A., Phys. Rev. 1991 **A43**, 6934
20. Scharlemann E.T., p. 291 in Laser Handbook Vol. 6, "Free Electron Lasers", Colson W., Pellegrini C., Renieri A., editors, N. Holland (1990)
21. Penman C., and McNeil B.W.J., Opt. Commun. 1992 **90**, 82
22. Yoder R.B. et al, in "Advanced Accelerator Concepts", AIP Conference Proceedings No. 472, p. 635, Wes Lawson, editor (1999)
23. Cai S.Y., Cao J., and Bhattacharjee A., Phys. Rev. 1990 **A42**, 4120
24. Bonifacio R. et al, Nucl. Instrum. Meth. in Phys. Res. 1990 **A296**, 358; and 1994 **A341**, 285

SUPERRADIANCE AS METHOD OF GENERATION OF ULTRASHORT MICROWAVE PULSES

N.S.Ginzburg, I.V.Zotova, Yu.V.Novozhilova, A.S.Sergeev, A.D.R.Phelps, A.W.Cross*, S.M.Wiggins*, K.Ronald*, V.G.Shpak**, M.I.Yalandin**, S.A.Shunailov**, M.R.Ulmaskulov**, V.P.Tarakanov****

Institute of Applied Physics, RAS, Nizhny Novgorod, Russia
*University of Strathclyde, Glasgow G4 0NG, UK
**Institute of Electrophysics, RAS, Ekaterinburg, Russia
***High Energy Research Centre, RAS, Moscow, Russia

Experimental results of the observation of superradiation from intense, subnanosecond electron bunches moving through a periodic waveguide and interacting with a backward propagating TM_{01} wave are presented. The ultra-short microwave pulses in Ka, W, and G band were generated with repetition frequencies of up to 25 Hz. Observation of RF breakdown of ambient air, as well as direct measurements by hot-carrier germanium detectors, leads to an estimate of the peak power as high as 60-140 MW for the 300-400 ps pulses at 38 GHz. The initial observation of 75 GHz 10-15 MW radiation pulses with duration less than 150 ps, and of 150 GHz microwave spikes with a risetime of 75 ps are also reported. Comparison with simulations is discussed as well.

Introduction

Coherent emission from short electron bunches with lengths much smaller than the wavelength is well known and was first observed in the Smith-Purcell experiment. Another type of conventional coherent emission, which is used extensively in microwave electronics, arises from continuous or quasi-continuous electron beams with length much greater than the wavelength. In this case coherent emission is related with stimulated processes resulting in selfbunching of the electrons. For the intermediate case, i.e. for electron bunches with a size of several wavelengths, it was traditionally assumed that radiation can be related only with density fluctuations inside the electron bunch (incoherent component) or with coherent emission from the sharp edges of the bunch. Only recently it was recognised that much more intense coherent emission can occur from the entire volume of such bunches due to selfbunching and slippage of the wave over the electron pulse. Based on a similar mechanisms investigated early in quantum electronics for ensembles of inverted atoms [1-3] coherent emission of such bunches can be regarded as super-

radiance. According to theoretical considerations of superradiance from non-equilibrium ensembles of classical electrons undertaken in recent years [4-11], this phenomenon involves features present in stimulated processes (selfbunching and coherence) as well as spontaneous processes (absence of threshold) and can be utilised to generate intense ultrashort electromagnetic pulses. Superradiance can be related with different mechanisms of stimulated emission: bremsstrahlung, cyclotron, Cherenkov, etc. All these mechanisms of SR have been observed recently experimentally [11-16]. For microwaves maximal peak power was obtained for the Cherenkov mechanism of SR when electron bunches moving though the periodical corrugated waveguide interacted with a backward propagating wave (for the long pulse regime this type of interaction is traditionally used in BWO).

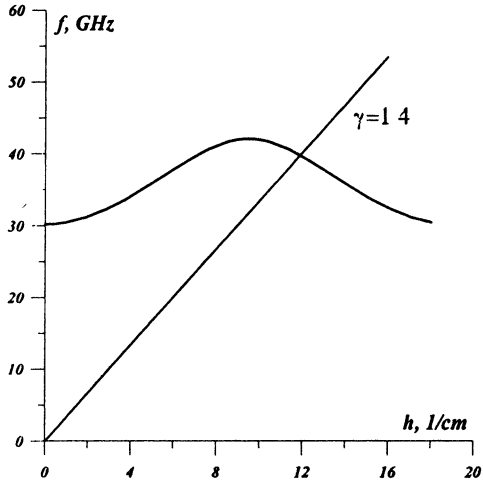

Fig.1 Dispersion diagram for Cherenkov synchronism with backward wave in a periodically corrugated waveguide (period of corrugation - 3.5 mm, corrugation depth - 0.75 mm, mean radius - 3.75 mm)

The basic theoretical description of SR related with different mechanisms of stimulated emission was given in [11] as well as results of the first experimental observation. In this paper we present results of advanced studies of Cherenkov type emission in corrugated waveguides and their comparisons with results of numerical simulations based on the PIC code KARAT [16]. New series of experiments are reported directed mainly at increasing the peak power of the SR pulses as well as on increasing the carrier frequency of these pulses. As a result powerful SR pulses have been observed throughout the band of 38-150 GHz.

Basic description of Cherenkov SR in corrugated waveguide

Cherenkov SR in the slow-wave structure in the form of periodically corrugated metallic waveguides was observed under synchronism with a slow spatial harmonic of the backward wave (Fig.1):

$$\omega = (-h + h_c)V_0, \tag{1}$$

where ω and h are the wave frequency and longitudinal wave number respectively, $h_c = 2\pi/\lambda_c$, and λ_c is the corrugated period.

In this case the longitudinal electric field of the synchronous wave can be presented in the form

$$E_z = \mathrm{Re}\left[E_z^s(\mathbf{r}_\perp)A(z,t)\exp(i\omega(t - z/V_0))\right],$$

where $E_z^s(\mathbf{r}_\perp)$ describes the transverse distribution and $A(z,t)$ describes a temporal evolution of the longitudinal distribution. The interaction of the electron with the radiation can be described by the following equations

$$\left(\frac{\partial}{\partial\zeta} - \frac{\partial}{\partial\tau}\right)a = Gf(\zeta)J,$$

$$J = \frac{1}{\pi}\int_0^{2\pi}\exp(-i\theta)d\theta_0, \tag{2}$$

$$\frac{\partial^2\theta}{\partial\zeta^2} = \mathrm{Re}[a\exp(i\theta)] \tag{3}$$

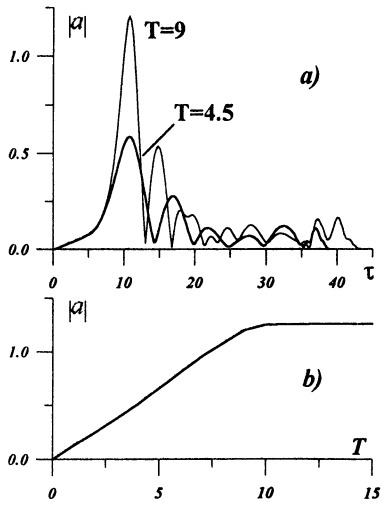

Fig.2 SR pulse profile for different values of electron pulse duration (a). Peak amplitude vs pulse duration (b). L=34, G=0.15

Here we are using dimensionless variables:

$$\zeta = z\frac{\omega}{2c}\gamma_0^{-2}\beta_0^{-1},$$

$$\tau = \frac{\omega}{2\gamma_0^2}\frac{(t - z/V_0)}{(1 + V_0/V_{gr})},$$

$$a = \frac{4e\gamma_0 AE_z^s(R_0)}{mV_0\omega},$$

$$G = \frac{4\gamma_0^3 eI_0|Z|}{mc^2\beta_0^2},$$

I_0 is the electron current, R_0 is the radius of electron injection, Z is the coupling impedance of the TM_{01} mode, $\theta = \omega t - h_s z$ is the electron phase with respect to the synchronous wave, $h_s = h_c - h$, V_0 is the electron drift velocity, V_{gr} is the electromagnetic wave group velocity. The function $f(\tau)$ describes the unperturbed electron density $f(\tau) = 1$, $\tau \in [0, T]$, where T is the dimensionless duration of the electron bunch. In the case when emission start up related with electron density fluctuations, is described by parameter $q<<1$ the boundary conditions can be presented in the form

$$\theta|_{\zeta=0} = \theta_0 + q\cos\theta_0, \left.\frac{\partial\theta}{\partial\zeta}\right|_{\zeta=0} = 0, \ \theta_0 \in [0, 2\pi], \ a|_{\zeta=L} = 0,$$

where L is the length of the interaction region.

In Fig.2a the SR pulse profile is shown for different values of electron pulse duration for the parameter G=0.15. As it is seen from Fig.2b that peak amplitude growth proportional to the electron pulse duration until this duration rather short T<10. It corresponds to a squared dependence of the peak radiation power with respect to the total number of electrons. It means that the all electrons of bunch radiate coherently. Confirmation of this fact can be also found from the dependence of peak power on parameter G, i.e. total pulse current (Fig.3). As it follows from Fig.2b saturation of the growth of peak amplitude occurs when electron pulse duration exceeds certain value T>10 because electron pulse becomes too long to provide coherent radiation from all over pulse length. It should be also noted that effective SR pulse duration decreases with increasing its amplitude (see, Fig 2a, 3a).

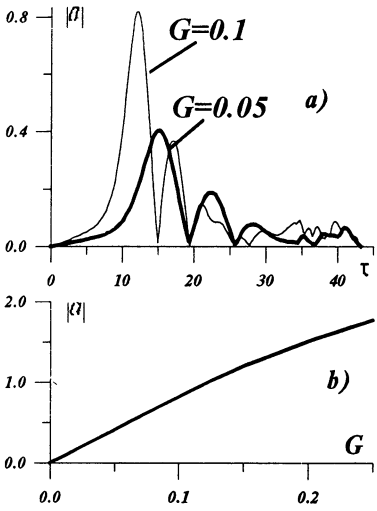

Fig.3 SR pulse profile for different values of electron current (a). Peak amplitude vs total electron current (b). L=34, T=9

In physical variables for electron pulse duration 500 ps, current 1.5 kA, electron energy 200 keV, impedance Z=1 and V_{gr} estimated from Fig.1 as 0.3 c we obtain SR duration about 250 ps and peak power 200 MW (for accurate power estimation instead pendulum Eqs. (3) we have used full relativistic electron motion equations).

Experimental set-up

A compact pulsed accelerator based on the RADAN 303 modulator equipped with a subnanosecond pulse sharpener was used to inject typi-

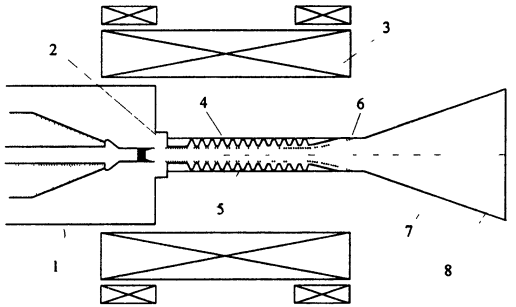

Fig.4 Experimental configuration of the interaction region (1-cathod, 2-anode, 3 superconducting soleno id, 4-druft chamber, 5-slow-wave structure, 6 – electron trajectory, 7-horn, 8-microwave window).

cally 0.5-1.2 ns, 1-2 kA, 200-250 keV electron bunches [17,18] into the interaction region. These electron bunches were generated from a magnetically insulated coaxial diode, which utilised a cold, explosive emission cathode (Fig.4). A cathode unit provided the possibility of the smooth, precise adjustment of the accelerating gap to vary the electron current. The fast rising e-beam current and accelerating voltage pulses were measured using a Faraday cage strip line current probe and an inline capacitive voltage probe respectively, with both signals recorded using a 7 GHz Tektronix 7250 transient digitising oscilloscope. High current electron pulses were transported through the interaction space in the form of corrugated waveguide of 3-10 cm, total length in a longitudinal guiding magnetic field of up to 8.5 T created by a superconducting magnet. The period of corrugation of the Ka band slow wave structure was approximately 3.5 mm, the corrugation depth was 0.75 mm and had a mean radius of 3.75 mm. The mean electron bunch diameter varied between 5.5 mm (Ka band) and 2.5 mm (W band). For measurement of the Ka (26.5 to 40 GHz) and W (75 to 110GHz) band radiation a hot-carrier germanium detector which had a transient response as fast as 150ps was used. At Ka band the power-to-voltage dependence of the detector was calibrated from 100 ns magnetron pulses.

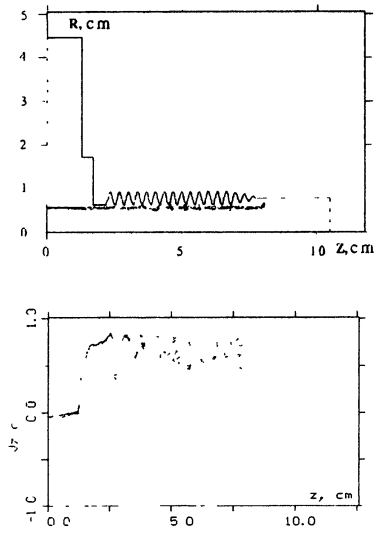

Fig.5 Geometry of interaction region and positions of electrons at time t=1 ns (a). Phase plane ar the same moment.(b)

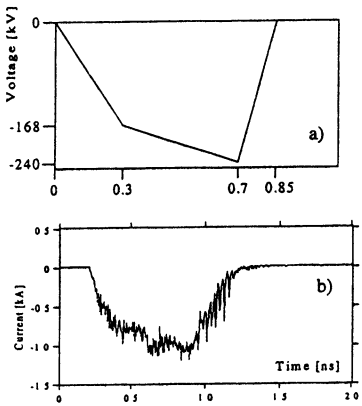

Fig.6 Voltage pulse (a) and self-consistent electron current pulse (b).

Simulation of the radiation from subnanosecond electron bunches passing through periodic waveguide structures under experimental conditions was carried out using the particle-in-cell (PIC) code KARAT. In Fig 5(a) is shown the system geometry (all sizes are in centimetres) and electron bunch 1 ns after a 240 kV driving voltage pulse was imposed on the coaxial line. In the presented simulations the strength of the guide magnetic field was 5 T. The self-consistent current pulse through the cross-section at z=2.5 cm is plotted in Fig.6. The pulse duration of about 0.8 ns and peak current ~1.3 kA was close to the experimental measurements of the current pulse. In Fig.5(a) we see modulation of the bunch density. The phase plane (p_z, z) (Fig.5(b)) shows strong modulation of the longitudinal momentum developing by this time. The dependence of RF output power on time is presented in Fig.7. The microwave pulse duration is about 300 ps. The peak power reached 75 MW (after averaging over the high frequency it should be half of the peak magnitude presented in Fig.4) and the electron efficiency was about 7%. The spectrum of radiation (see Fig.8(a)) with a central frequency about 38GHz agrees with the experimental data and the frequency which can be found from the resonance conditions. The distribution over radius

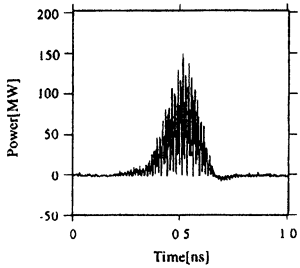

Fig.7 Pointing vector integrated over transverse cross section as a function of time at z=9 cm.

of the radial component of the electric field at the output cross-section z=9 cm is presented in Fig.8(b) and corresponds to the excitation of the TM_{01} mode.

The dependence of peak power on the voltage pulse duration is shown in Fig.9. Because the electron peak current was practically constant and the electron pulse duration corresponded to the voltage pulse duration, actually this diagram represents the dependence of peak power on the total charge in the bunch. Obviously this dependence is rather close to a square law when the pulse duration is close to the correlation time

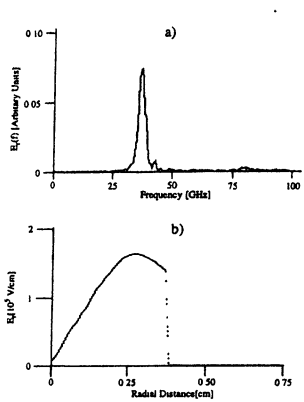

Fig.8 (a) Frequency spectrum of output signal. (b) The distribution over the radius of the radial component of the electric field at output cross-section

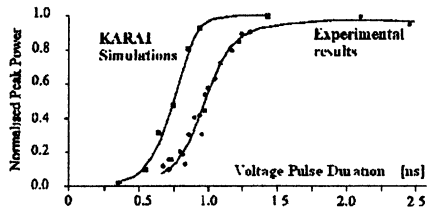

Fig.9 Dependence of peak power on accelerating pulse duration

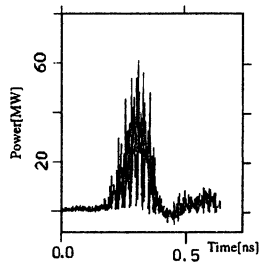

Fig.10 Simulation of 4 mm SR pulses

$$T_c = L\left(\frac{1}{V_0} + \frac{1}{V_{gr}}\right) \sim 0.8 \text{ ns},$$

Note that for small pulse duration the given interaction length of 6 cm is not sufficient for formation of SR spikes. For long electron pulses saturation of the growth of the peak power is obviously related with the fact that the pulse becomes too long to provide coherent radiation emission

from the entire pulse length. Actually, subsequent microwave spikes are emitted when the pulse duration is increased. Alongside the investigation of the generation of sub-nanosecond microwave pulses at Ka-band, a similar experiments were performed for a W-band and G bands backward-wave microwave structures (all geometrical sizes of slow-wave structures were reduced proportionally to the radiation wavelength). The PIC-code simulations have shown a peak power of up to 30 MW can be attained for the pulsewidth of 100-150 ps at the frequency of 75 GHz (Fig.10).

Experimental results

Ka-Band Experiments.

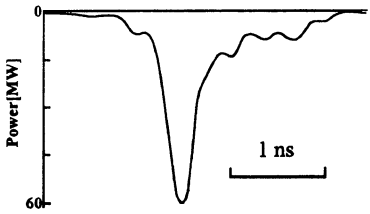

Fig.11 Ka-band superradiative microwave pulse recorded by the germanium detector

A typical oscilloscope trace of the Ka band microwave signal from an electron pulse passing through a periodic waveguide of total length 6 cm is presented in Fig.11. The observed microwave spikes have duration of about 300 ps and a rise time of 200 ps. It is important to note that for optimal conditions the pulse waveform, as well as the peak power, did not change when the interaction length was increased up to 10 cm. This fact agreed with the result of the simulations, which also indicated that a 6 cm interaction length is sufficient for the formation of a superradiance spike.

The dependence of the peak power on the strength of the guide magnetic field is shown in Fig.12. In this diagram it is clearly seen that there is a region of cyclotron absorption near the resonance magnetic field value of 3.25 T and then two operating regimes with low 1.5-3 T and high >4 T magnetic fields. The initial experiments on the observation of SR in corrugated waveguide were carried out only in the region of low magnetic fields [14]. Implementing the strong guide magnetic field resulted in a drastic 4-5 times increase of peak power. The increase in power can be easily explained by the improvement in the quality of the electron beam, the decreasing gap between the beam and the slow-wave structure as well as the decrease to 0.4mm of the transverse width of the hollow electron bunch. Note that all the experimental data for the Ka band pulses discussed below were obtained for a magnetic field of 5 T.

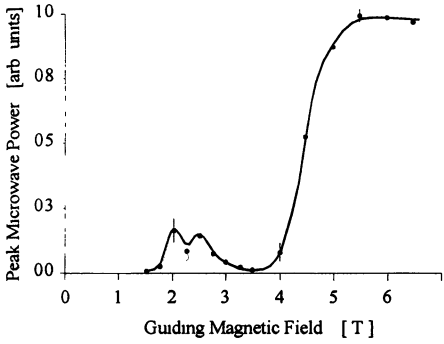

Fig.12 Peak microwave power as a function of the guide magnetic field

Frequency measurements at Ka band have been made using a set of cut-off waveguides filters showed that the main peak had a central oscillating frequency of approximately 38 GHz. The relative radiation spectrum bandwidth found from these measurements was about 5 %. The radiation had a polarisation corresponding to the TM_{01} mode. The measured radiation pattern also corresponded with good accuracy to the excitation of the TM_{01} mode (Fig.13). Thus, operating mode, microwave pulse width, spectrum, as well as the absolute power found from experiments are in a good agreement with the results of simulations. This measurement allowed the absolute peak power to be estimated by integrating the signal from the detector over its radial position. The peak power estimated by this method was about 60 MW. A rather high level of radiation power was indicated by the observation of RF breakdown of ambient air for subnanosecond pulses in the focus of a parabolic reflector as well as inside the receiving concentrating conical horn with minimal output diameter 12 mm (Fig.14(a)). It is reasonable to try to determine the real peak microwave power based on the previous experimental obser-vation of breakdown initiated by both 2-4 nanosecond, high-power Ka band microwave sources [19,20] as well as subnanosecond, high voltage modulator produced unipolar (without microwave carrier) voltage pulse [21]. A summary of these experimental data is presented in Fig.15. It follows

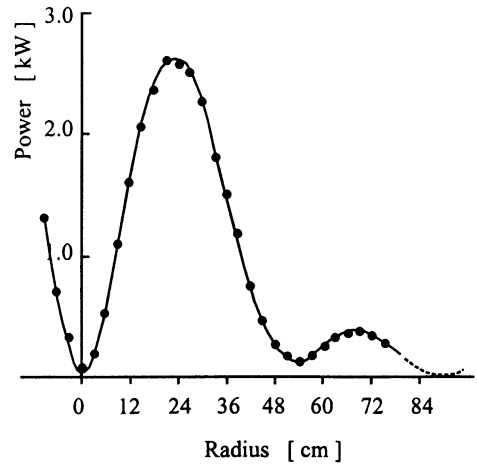

Fig.13 Radiation pattern measured by the germanium detector

from this diagram that for microwave pulse duration of 300 ps, the air breakdown strength is about 130 kV/cm. The utmost, limiting plasma spot observed during the breakdown processes in the field of the standing wave was located in the horn cross-section having the diameter of 13.5 mm (point 2, Fig.15). The separate plasma spot was excited in the horn

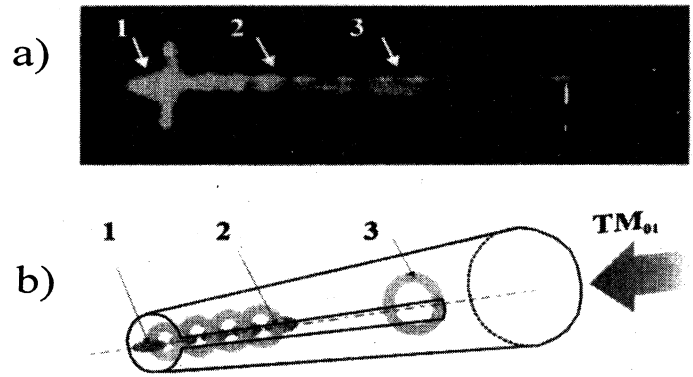

Fig.14 Breakdown of ambient air caused by subnanosecond microwave pulse nside the conical horn. (a) Photography. (b) Geometry of the horn and scheme of the breakdown

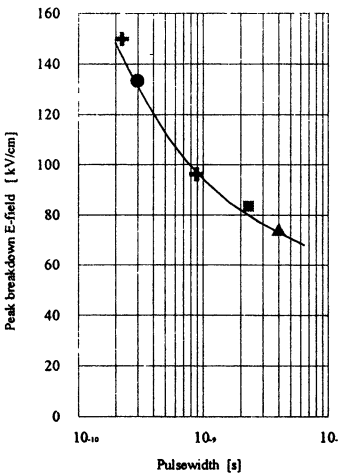

Fig.15 Summary of previous peak breakdown E-field measurements for several microwave and unipolyar pulses with different durations. Point 1 and 2 correspond to breakdown induced by microwave pulses, and point 3 and 5 to breakdown induced by unipolar pulses. Point 4 corresponds to the 300-ps duration of the output pulse from the SR experiment, and indicate a field strong of 130 kV/cm.

region of 15-16 mm diameter. (point 3, Fig.15). Based on the above data, and applying the standard method of calculation for the fields inside a circular waveguide it is easy to see that a radial electric field of 130 kV/cm at a cross-section with diameter of 15 mm corresponds to an input power of ~ 60 MW. So the estimation of the peak output power

from observations of breakdown are in good agreement with the results of measurements of the power by the germanium detector.

The simple calculations show that the energy of the electromagnetic pulse with peak power of 60 MW and half-amplitude pulsewidth duration of 300 ps is about $2x10^{-2}$ J which corresponds to a 5% efficiency of energy transformation from the $4x10^{-1}$ J electron bunch into the microwave pulse. For some applications it is also an important factor that the microwave power rise time was very high, being up to 300 MW/ns.

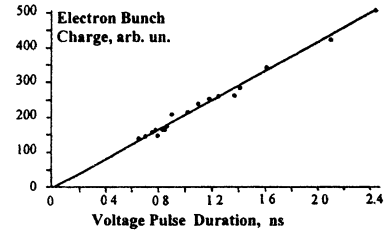

Fig.16 Dependence of the electron bunch total charge on the accelerating voltage pule duration

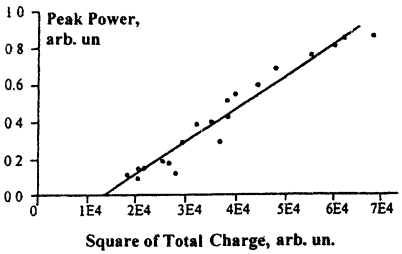

Fig.17 Dependence of the peak microwave power on the square of the electron bunch total charge

It is pertinent to note that the generated Ka-band microwave pulses possess high stability and reproducibility. Coupled with the capability of operation of the RADAN 303 modulator in the repetition rate mode and the availability of permanent magnetic fields for the electron bunch transportation, the ability to generate reproducible microwave pulses with a repetition frequency of 25 Hz was demonstrated.

Application the technology of the energy compression for a high voltage subnanosecond pulses generated by the modulator provided up to 25% increasing of the pulse amplitude. By attaining in the experiments the electron energies of 300 keV we found essential rise of the power of Ka band supperradiation. Estimations shown that the power level of 140 MW was achieved for the 300-400 ps microwave spikes.

The dependence of peak power on electron pulse duration is presented in Fig.9. To obtain this dependence the accelerating pulse duration was varied while keeping the accelerating voltage amplitude constant. Obviously this dependence is rather close to square law in the region of pulse duration 0.5-1.2 ns. This means that the electrons radiate coherently from the entire volume of the electron pulse. Note that for small pulse durations of less than 0.5 ns the given interaction length of 6 cm is not sufficient for formation of SR spikes. With increasing electron pulse dura-

tion above 1.2 ns, saturation of the growth of the peak power is obviously related with the fact that it is impossible to provide coherent emission from the pulse with duration substantially exceeding the co-operation time and actually subsequent microwave spikes are emitted. Note that the experimental dependence is rather close to the results of the simulations (see Fig.9).

By integrating the electron current pulse over time the total charge of the electron bunch has been found (Fig.16). Based on the results presented in Fig.9 and 16 the dependence of peak power on the square of the total charge is drawn in Fig.17. This dependence is very close to linear. Some shift of the fitted linear function from the origin can be explained by the fact that at the leading and trailing edges of the accelerating pulse there are low energy electrons. These electrons can not participate in the resonance interaction of the electromagnetic pulse. With decreasing accelerating pulse duration the relative number of such electrons increases. That is why the radiation power tends to zero faster than the total charge.

W-Band Experiments

Alongside the investigation of the generation of sub-nanosecond microwave pulses at Ka-band, a similar series of experiments were performed for a W-band backward-wave microwave structure (all geometrical sizes of this structure were half the size of those of the Ka band structure). The PIC-code simulations have shown a peak power of up to 30 MW can be attained for the half-amplitude pulsewidth of 100-150 ps at the frequency of 75 GHz. (Fig.10). The risetime of the front of the pulse did not exceed 100 ps. In the experiments such pulses were clearly observed (Fig.18) with the use of the detector which was re-calibrated using 3-ns W-band pulses produced by relativistic BWO oscillators [20] and a specially-developed calorimetr. The integral mode pattern scan has shown the total peak power of the W band pulses was between 10-15 MW when the accelerating voltage at the cathode was as high as 250 kV, e-beam current was of up to 800 A, and the axial B-field was 3.5T. The W-band spikes possessed an extremely sharp leading edge < 120ps i.e. rising two-times faster than the Ka band pulses. Such a

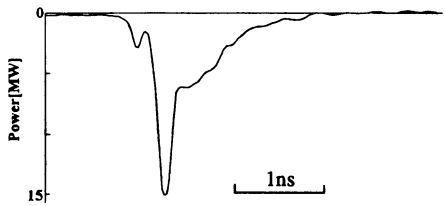

Fig.18 Oscilloscope trace of W-band superradiative microwave pulse.

fast front corresponded to the limits of the transient response of the oscilloscope's cable delay line provided for the measurements (120 ps). Due to these bandwidth limitations of the measuring system we believe that the peak power was somewhat underestimated. This is also a contributing factor in explaining the discrepancy in the peak power obtained in the simulations (~30MW) as compared to the value measured experimentally. The air breakdown from W band pulses has been experimentally observed when the output cross-section of the conical horn was reduced down to 8 mm. However cross-checking the peak power using the air breakdown measurements appears to be less accurate for the W-band pulses as compared to Ka-band pulses, because of the instrumental uncertainty in the measurements of the shorter microwave pulse duration as well as the more restricted availability of data on the breakdown strength of air for ~100ps duration pulses. It is reasonable to conclude therefore that the estimate of the experimentally measured peak power in W-band of 10-15 MW represents a lower limit on the actual emitted peak power.

G-Band experiments

For generation of G band subnanosecond microwave spikes the energy of the electron beam was reduced down to 180-200 keV. This was required to prevent strong collimation of the current pulse at the inlet of the slow-wave structure, which had a drift channel of 1.5 mm diameter. Reducing the accelerating voltage leads to a decrease of the transverse velocities of the electrons emitted from the cathode. It is also important to note that in the G band experiment a pulsed axial magnetic field of 2.5T was applied.

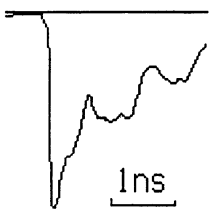

Fig.19 Oscilloscope trace of G-band superradiative microwave pulse.

Fig.19 shows the 150 GHz microwave pulse obtained for the conditions when only electrons emitted at the peak of the accelerating pulse were in synchronism with the TM_{01} wave. The measured pulse rise time did not exceed 75 ps which was the limit of the transient characteristic of the 5-GHz oscilloscope, type C7-19.

This corresponds well with the PIC-simulations (Fig.20), which predict that the half- amplitude pulsewidth of the G band spike is as short as 70 ps. Calibration of the oscilloscope, cable delay line and other components with a 100ps probing voltage pulse has shown that the amplitude of the pulse from the microwave detector was attenuated at least 2-2.5 times.

In addition it was impossible to re-calibrate the detector sensitivity at G band as was done for the W band. Nevertheless we estimate the value of the peak power to be in the range of 5-10 MW, two times less than predicted by the PIC-simulations.

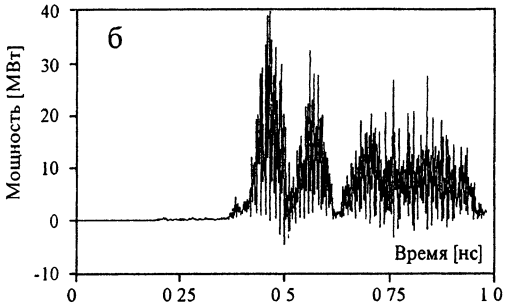

Fig.20 Simulations of 2 mm SR pulses.

Conclusion

In conclusion we believe that these experiments carried out together with the simulations of the electron bunch/electromagnetic wave interaction give us reason to affirm that the observed emission can be interpreted as superradiative. The microwave pulses generated by such a mechanism have an unique short duration of 300 ps with a 140 MW peak power level measured in Ka band. In addition we have reported preliminary observations of ~150 ps pulse durations with at least 10MW peak power level in W-band. The achieved repetition frequency of 25 Hz also supports the conclusion that a novel source of powerful subnanosecond pulses has been developed. In this context an important factor is that the whole device is in the form of a table-top system

Even at the present stage when these novel sources are still very rapidly developing to the 140 MW level and beyond, it is promising to consider the application of subnanosecond multi-megawatt Ka, W and G band pulses in areas such as novel diagnostics and the study of non-linear phenomena in plasmas and solids. Another area is related with using such pulses in radiotechnical applications. It would be interesting also to test the influence of such pulses on biological matter.

Acknowledgements

This work was supported by the Russian Foundation for Basic Research (grant 98-02-17308) and DERA and EPSRC (UK). The authors are grateful to N.F. Kovalev and S.E Filchenkov for helpful discussions and assistance in calculations of characteristics of slow-wave structures.

References

[1] Dicke R.H. Phys.Rev. 1954, **99**, 131.
[2] MacGillivray J.C. and Feld M.S., Phys. Rev., A 1976, **14**, 1169.
[3] Scribanowitz N. et al., Phys. Rev. Lett., 1973, **30**, 309.
[4] Bonifacio R., Maroli C., and Piovella N., Opt. Comm. 1988, **68**, 369.
[5] Bonifacio R., Piovella N., and McNeil B.W.J., Phys. Rev. A 1991, **44**, 3441.
[6] Ginzburg N.S., Sov. Tech. Phys. Lett. 1988, **14**, 197.
[7] Robb G.R.M., Ginzburg N.S., Phelps A.D.R. and Sergeev A.S., Phys. Rev. Lett. 1996, **77**, 1492.
[8] Ginzburg N.S., Zotova I.V., and Sergeev A.S. Pis'ma v ZhETF, 1994, **60**(7) 501
[9] Ginzburg N.S., NovozhilovaV, and Sergeev A.S., Sov.Tech.Phys.Lett. 1996, **22**, 359.
[10] Piovella V, Chaix P., Shvets G., and Jaroszynski D.A., Phys. Rev. E 1995, **52**, 5470.
[11] Phelps A.D.R., Cross A.W., Cooke S.J., Ginzburg N.S., Zotova I.V., Sergeev A.S., Konoplev I.V., Peskov N.Yu., Shpak V.G., Yalandin M.I., Shunailov S.A., and Ulmaskulov M.R., Strong Microwaves in Plasmas, Proceedings of the Int. Workshop, N.Novgorod, Russia, 1997, V,2, pp.791-810
[12] Ginzburg N.S., Zotova I.V., Sergeev A.S., Konoplev I.V., Phelps A.D.R., Cross A.W., Cooke S.J., Aitken P., Shpak V.G., Yalandin M.I., Shunailov S.A., and Ulmaskulov M.R., Phys.Rev.Lett. 1997, **78**, 2365
[13] Jaroszynski D.A.et al, Phys. Rev. Lett. 1997, **78**, 1699.
[14] Ginzburg N.S., Zotova I.V., Sergeev A.S., Novozhilova Yu.V., Peskov N.Yu., Konoplev I.V., Phelps A.D.R., Cross A.W., Cooke S.J., Shpak V.G., Yalandin M.I., Shunailov S.A., and Ulmaskulov M.R. Nucl.Instr. and Meth. in Phys.Res.A, 1997, **393**, 352
[15] Shpak V.G., Yalandin M.I., Shunailov S.A., Ginzburg N.S., Zotova I.V., Sergeev A.S., Phelps A.D.R., Cross A.W., and Wiggins S.M., Doklady Akademii Nauk, 1999, **365**(1), 50.
[16] Ginzburg N.S., Zotova I.V., Sergeev A.S., Novozhilova Yu.V., Peskov N.Yu., Konoplev I.V., Phelps A.D.R., Cross A.W., Cooke S.J., Shpak V.G., Yalandin M.I., Shunailov S.A., and Ulmaskulov M.R. Phys.Rev.E 1999, **60**(3), 3297
[17] M.I.Yalandin, G.T.Smirnov, V.G.Shpak, and S.A.Shunailov Proceedings of the 9th IEEE Int. Pulsed Power Conf., Albuquerque, NM (Publisher, City, 1993), pp.835-838
[18] M.I.Yalandin, V.G.Shpak, S.A.Shunailov, and M.R.Ulmaskoulov, Pis'ma v ZhTF., 1999, **25** (10), 19.
[19] M.I.Yalandin, G.T.Smirnov, V.G.Shpak, and S.A.Shunailov, in Proc. 9th IEEE Int. Pulsed Power Conf., Albuquerque, NM, 1993, pp.388-391.
[20] M.I.Yalandin, G.A.Mesyats, V.G.Shpak , G.T.Smirnov, , and S.A.Shunailov Proc. SPIE 1993, **1872**, 333
[21] M.I.Yalandin, V.G.Shpak, S.A.Shunailov, and M.R.Ul'maskulov, Proc. SPIE 1995, **2557**, 289

GENERATION OF HUNDRED JOULES PULSES OF 4-MM RADIATION BY PLANAR FEM WITH TWO-DIMENSIONAL DISTRIBUTED FEEDBACK

N.V.Agarin, A.V. Arzhannikov, V.B.Bobylev, N.S.Ginzburg V.G. Ivanenko, P.V.Kalinin, S.A.Kuznetsov, N.Yu.Peskov*, A.S.Sergeev*, S.L.Sinitsky, V.D.Stepanov,*

Budker Institute of Nuclear Physics, Novosibirsk, Russia
*Institute of Applied Physics, Nizhny Novgorod, Russia

The W band FEM of planar geometry driven by sheet electron beam was realized on the base of the pulse accelerator ELMI (0.8 MeV / 3 kA / 5 μs). To provide a spatial coherence of the radiation from the electron beam of cross-section 0.4 x 12 cm Bragg resonators of planar geometry providing traditional 1-D and novel 2-D distributed feedback mechanism were used. The total energy in microwave microsecond pulse amounted to 100 J. Prospects of further increasing of pulse energy and purification of radiation spectrum are discussed.

Introduction

One of the most promising ways to achieve extremely high power in free electron masers (FEM) is to extend one of its transverse dimension by using planar geometry of interaction space [1 - 4]. Following this idea on the base pulse accelerators U-2 and U-3 (ELMI) we are developing a planar FEMs operating in W band driven by a large size sheet electron beams. The main problem for a such FEM is providing coherence of radiation from different parts of the electron beam. To solve this problem a two-dimensional distributed feedback has been proposed [1 - 3], which may be realised in a 2-D Bragg resonator. Two-mirror scheme of FEM with such a resonator is presented in Fig. 1. On the doubly periodical corrugation mutual coupling and scattering of four electromagnetic energy fluxes propagating in forward, backward and transverse directions relative to the direction of electron beam motion take place. According to theoretical analyses the transverse electromagnetic energy fluxes should synchronise radiation from different parts of the sheet electron beam.

In the first series of the experiments we studied a planar FEM with traditional 1-D Bragg resonator [4, 5]. These experiments were carried out at the U-2 accelerator and, then, in 1998-1999 at the specialized ELMI-device that was constructed on base of the U-3 accelerator [6]. At the last experimental session a 2-D Bragg gratings were installed at the ELMI-device in order to provide a 2-D distributed feedback and, thus, the

effective mode selection at 4-mm wavelength. This paper describes the recent stage of the experiments where the first operation of FEM with 2-D feedback was observed.

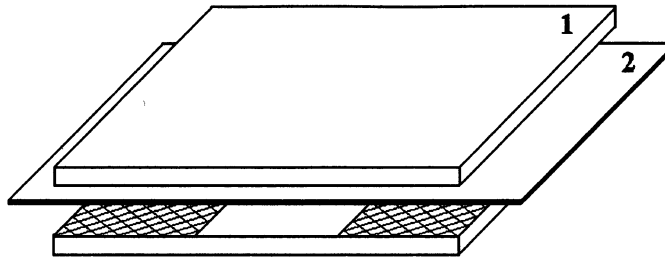

Fig. 1. Schematic of FEM-oscillator with a two-mirror 2-D Bragg resonator (1) and sheet electron beam (2).

Experimental setup

Description of the ELMI-device

In 1998 the experiments on microwave generation were transferred from the U-2 to the U-3 accelerator. For this purpose some part of experimental equipment used in experiments at the U-2 device was moved to the U-3 accelerator with adding a set of new elements and units. The new setup created in such way was called ELMI-device [6]. The ELMI-device (Fig. 2) consists of five basic units: a magnetically-insulated ribbon diode, a former of the sheet beam, a slit vacuum channel with undulator and resonator, a pulse magnetic system for the electron beam dumping, and a diagnostic system to measure the generated radiation directly in a special vacuum chamber.

A high voltage pulse of 1 MV is applied to a strongly elongated cathode made of fibrous graphite. Anode was made in the form of a graphite plate with a slit. The electron beam passes through the anode slit and then it comes with sizes 1 × 20 cm to a sheet beam former. The former and the undulator are located inside a slit vacuum channel with the inner cross-section 4 × 25 cm, which has external coils producing a uniform longitudinal magnetic field up to 14 kG.

Operating transverse velocity of the beam electrons is pumped in a smoothly up-tapered wiggler section. To form the electron beam with the quality acceptable for the FEM operation the regime with a strong guide magnetic field (exceeding cyclotron resonance value) was chosen.

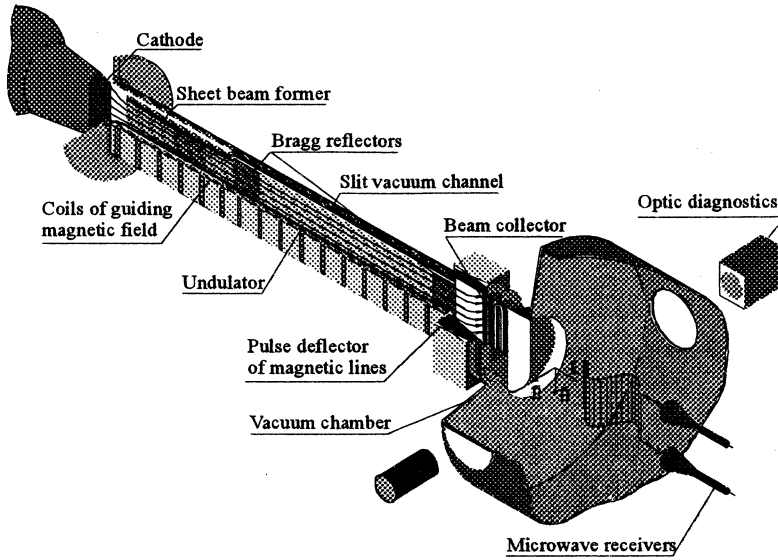

Fig. 2. Schematic of the ELMI device

Decrease in initial angular spread of the beam electrons was achieved decreasing non-homogeneity of electric and magnetic fields in the regions of the beam acceleration and transportation. Accordingly to computer simulations all these methods allow to form driving sheet beam with a small (less than 10%) value of parasitic cyclotron oscillations of the electrons.

The sheet beam former includes two graphite plates approaching to each other at the angle 1^0 to the central plane. These plates smoothly cut off from the beam some outer part of its cross-section so that the beam electrons have a small angular spread.

After passing through the former the electron beam with a cross-section 0.4×12 cm comes into a planar copper resonator. The resonator consists of two Bragg reflectors separated by a regular rectangular waveguide of the 64 cm length. Two Bragg gratings located symmetrically from the central plane formed each the reflector. The transverse cross-section of the reflectors and the regular waveguide was $0.9 \div 20$ cm. The cooper plates of the Bragg resonator are embraced outside by the windings of the plane active magnetic undulator. The windings are located symmetrically on both sides of the central plane of the beam channel. Each plane winding was 96 cm long and 20 cm wide and contains a set of 48 multi-turn coils located one by one. The number of

turns in the coil for a homogeneous part of the undulator was 15. All the coils inside a separate plate are connected consecutively but the connection polarity alternates. The cross-section profile of a separate coil was chosen so that to provide a harmonic dependence of the transverse magnetic field on the axis of the undulator. To provide adiabatical entrance for pumping the electron oscillations the number of turns in the first 6 coils was smoothly up-tapered from 4 up to 15. To suppress the free cyclotron oscillations in the beam current in a few entrance coils was also decreased in 30% by shunting the resistors.

Distribution of the wiggler field was measured in the experiment and obtained in numerical calculations as well. The spatial period was 4 cm, the length of the field up-tapered section was 12 cm. The maximal value of the perpendicular component of the field on the axis was 2 kG when the transverse magnetic field nonhomogeneity within a resonator cross-section was less than 7% and the portion of higher harmonics on the axis was less than 1%.

In order to decline the beam electrons to the beam collector (Fig. 2) a pulse deflector of magnetic lines was used. It produces the component of the magnetic field perpendicular to the guiding field for the short time (the pulse duration is 25 μs). This system of deflector-collector should satisfy a requirement to dump the beam on a large area of the collector in order to eliminate a creation of a dense plasma near it. The plasma can absorb and reflect back the output radiation.

To avoid the breakdown phenomena, which can occur on the output window, in our experiments all measurements of the power were carried out directly in vacuum. For such measurements a special vacuum chamber, where the RF-detectors could be placed, was added to the exit of the vacuum channel (Fig. 2).

Bragg resonators

Spectral properties of the Bragg reflectors were measured in "cold" microwave tests at frequency range 55 ÷ 80 GHz. The reflectivity was measured in two different schemes. In the first scheme the radiation from the sweep-generator comes to a parabolic mirror forming a flat wave profile. This wave propagates through the Bragg reflector and, then, through a converting planar horn to the RF-detector registering the passed power. Calibration of the passed RF-power was achieved using a directional coupler with the detector.

The other scheme is intended for direct measuring of the RF-power reflected from the Bragg mirrors. The radiation from the sweeper-

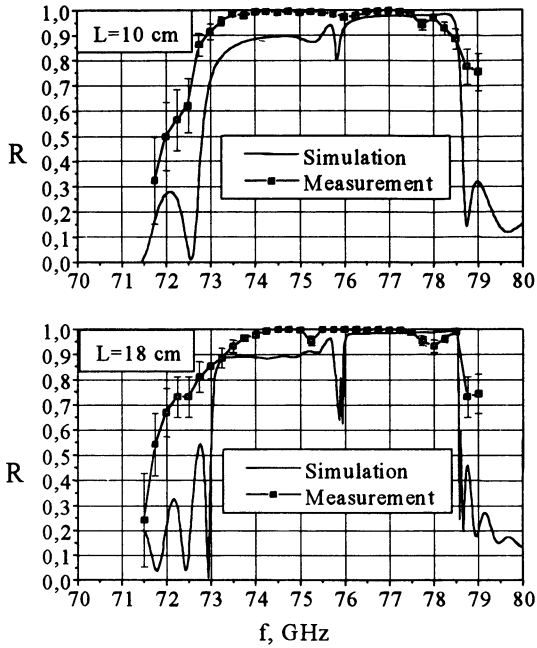

Fig. 3. Reflectivity of the 1-D Bragg reflectors.

generator is transported to the mirror through the planar horn. Two directional couplers with RF-detectors are used for measuring of the incident and reflected power.

Bragg gratings realizing a traditional 1-D distributed feedback which was used in the resonator for the first series of experiments were corrugated in one (perpendicular to the channel axis) direction with a period of 2 mm and a depth of 0.3 mm as a rectangular groove profile. The lengths of the up-stream and down-stream reflectors were 18 cm and 10 cm correspondingly. Comparison of results of "cold" tests and computer simulations for manufactured reflectors is shown in Fig. 3. Note that transformation of the waveguide modes of different types takes place on the Bragg structures. Following to the calculations the operating forward wave of $H_{1,0}$ type undergoes transformation into the backward wave of the same ($H_{1,0}$) type in the vicinity of 75 GHz and into the backward wave of $E_{1,2}$ type in the vicinity of 78 GHz. Moreover, the wave coupling coefficient on the grating determining the frequency width of zones of effective Bragg reflections was rather high that result in a partial overlapping of the different reflection zones. Thus, for correct calculation of the reflection coefficient both these backward waves should be taken into consideration in theoretical model. Presence of transformation of the modes of different types on the corrugation result in additional increase in reflectivity and widening of the frequency range of the Bragg reflection zone.

Results of the computer simulations which taken into account the different modes transferring on the grating and "cold" measurements for

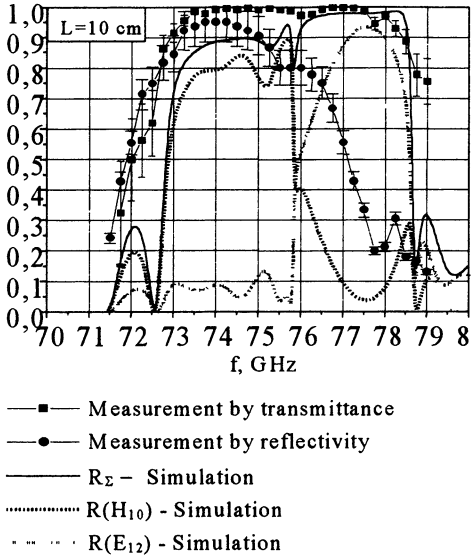

Fig 4. Comparison of measuring by different schemes.

reflectivity (R) of the reflectors with different lengths are compared in Fig. 3. The measurements were carried out using the first scheme.

The use of the second measuring scheme gave different width of the reflection zone (Fig. 4). The difference is explained by peculiarity of the methods and the presence the directional coupler for the reflected power registration in the second scheme. This directional coupler is designed for the H_{10} mode and therefore part of the power of the $H_{1,0}$ wave, which is transformed into the wave $E_{1,2}$, was not registered. Thus, Fig. 4 illustrates the difference between the results of measuring by the different methods and the mode content in the different Bragg reflection zones.

It should be pointed that in the experiments we used a two-mirror resonator consisting of the 1-D reflectors. This resonator possesses a set of eigenmodes with the frequencies positioned inside narrow frequency band (inside the effective Bragg reflection zone) and approximately the same Q-factors. Nevertheless, computer simulations [8, 9] demonstrated the possibility a single-mode operation for a FEM with such a resonator. This regime is established at nonlinear stage via competition of the different modes.

In the recent series of experiments, in which we studied a two-dimensional feedback, the gratings for the reflectors was made having the corrugation in two directions at the angle 45^0 to the beam axis each with the period 2.82 mm and depth 0.2mm (so called 2-D gratings). At the first stage of the experiment a quite easily manufactured two-dimensional gratings were used. The grooves of these gratings were like two sets of perpendicular strips (Fig. 5,b). A Fourier expansion for this surface is shown in Fig. 5 also. In contrast with the harmonic grooves ("an ideal 2-D structure", Fig. 5,a) the spectrum of the translational vectors for the

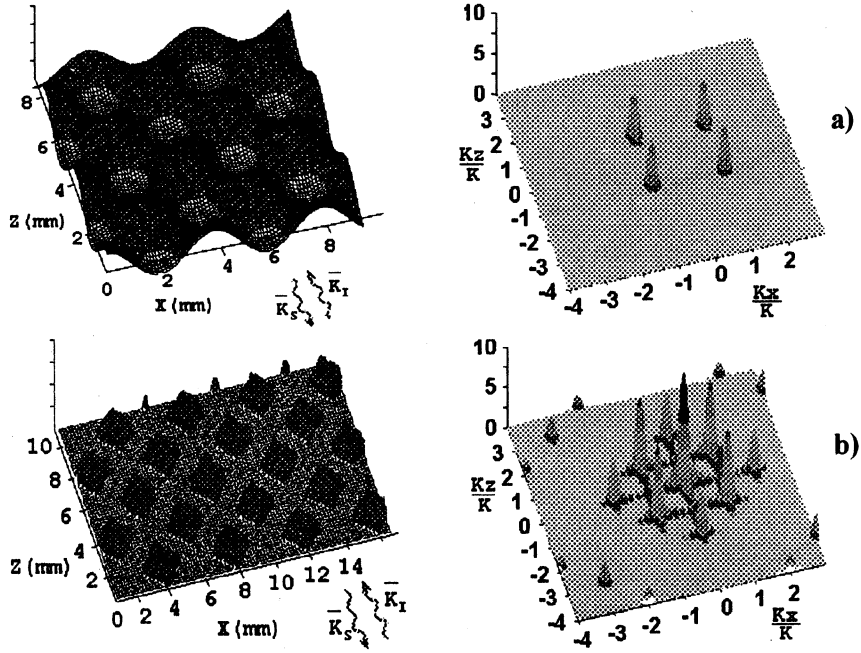

Fig. 5. Spectral properties of two-dimensional Bragg grating with harmonic (a) and rectangular (b) grooves.

grating used in the experiments possesses some additional harmonics. These harmonics provide direct 1-D reflection simultaneous with 2-D reflections. These harmonics also result in appearance of additional zones of 1-D Bragg scattering (see, in detail [10]).

Measured spectral dependence of the reflectivity for the 2-D reflectors used in the experiments at ELMI-device are represented in Fig. 6. The reflection scheme (i.e. the second scheme) of the "cold" tests was used. The computer simulations were made with a specially developed 3-D code solving Maxwell equations [7]. Following to the simulations the reflection zone near 75 GHz is originated from the 2-D scattering with participation of four partial waves of the same ($H_{1,0}$) transverse index. At the same time, the zone near the frequency of 78 GHz is appeared due to 1-D scattering of the operating $H_{1,0}$ mode into backward $E_{1,2}$ mode (compare with Figs. 3 and 4). Note that as a result of the used method of "cold" tests, Fig.5 presents the frequency dependence of "pure" reflection of the mode $H_{1,0}$ into itself (i.e. without admixture of $E_{1,2}$ mode in the reflected signal). The measured dependence is similar to one found by

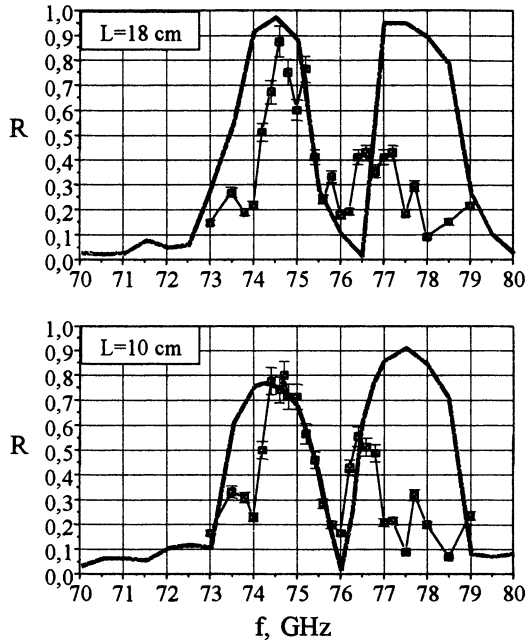

Fig. 6. Selective properties of 2-D Bragg reflectors: computer simulation (thick line) and experimental measurements (square points with thin line).

coupling waves method [10]. It should be noted that the 3-D computer simulations were made with rather large step on the frequency and, thus, can not display the fine frequency behaviour of the reflection coefficient.

At the next stage of the experiment to suppress "parasitic" 1-D feedback circles which takes place on the used profile of corrugation at the frequency range near 78 GHz we are going to change the corrugation profile. It is possible to avoid the "parasitic" feedback effects by using the gratings with the corrugations like "a chessboard" or like "round holes". The spectral properties of these gratings were discussed at AFEL'99 Conference [7].

Diagnostics of E-beam and mm-wave radiation

Energy of the beam electrons was obtained by measuring of the accelerator diode voltage. Beam current at the entrance of the resonator and on the collector after passing of the beam through the FEM was measured by Rogowsky coils.

To measure the absolute value of microwave radiation power in the experiments we used two identical semiconductor detectors on "hot carriers". A voltage on the detectors arises as a result of the resistance increase under the influence of a powerful microwave radiation. The detector sensitivity was calibrated by using of a technology magnetrons at two wavelength bands: 8 mm and 4 mm. Comparison of the calibration curves showed that the detectors had sensitivity at least 3 times larger for 8mm-radiation than for 4mm-radiation. To estimate the power in definite

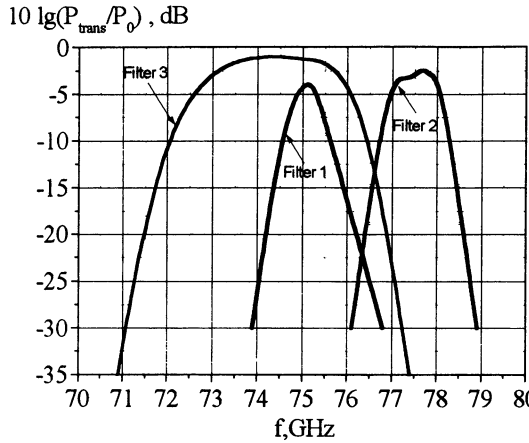

Fig. 7. Filters transmission in logarithmic scale versus frequency.

frequency ranges we used replaceable pieces of cut-off waveguides mounted before the detector sections.

For spectral analysis of the maser radiation narrow-band resonance filters inside the chosen spectral intervals (Fig. 7) was used. The radiation power passing through such filters was measured by semiconductor microwave diodes. In the experiment a set of receivers wit h the filters was located inside the diagnostic vacuum chamber at the distance of about 1 m from the maser output. Microwave radiation was collected by each receiver, attenuated by an absorber, and then passed through the waveguide with the resonance filter. The spectral intervals of the filters transmission are shown in Fig. 7. To obtain the average spectral density of the microwave radiation in the chosen frequency bands the signals of the diodes are divided by the bandwidth of the filters.

In addition to the microwave diagnostics the specialized systems on the base of a digital camera were used for measuring in optical and X-ray bands. The system in optical band was intended to register the plasma appearance near the exit of the beam from the resonator. The X-ray system was intended to check the touching of the resonator's walls by the e-beam.

Results of the experiments and discussions

In the described series of the experiments with a 2-D distributed feedback we varied strength of both the longitudinal and transverse components of the undulator magnetic field. The signal from the radiation power detector together with signal from the 4-mm diode equipped by narrow band filter are presented in the Fig. 8. The experiments have shown that the efficiency of the beam–wave interaction strongly depends on the strength of the transverse component of the wiggler field. The

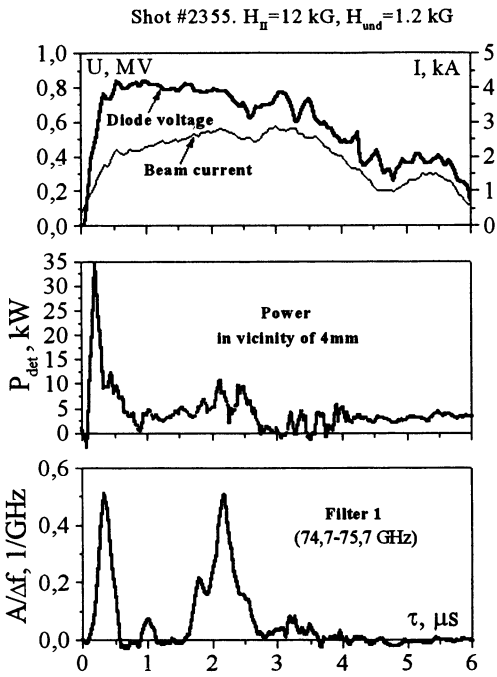

Fig. 8. Generated power of 4-mm radiation

results of measurements by the radiation power detectors in two wide bands near 4 mm and 8 mm wavelengths are presented in Fig. 9. The power of the 4 mm radiation measured by the hot carriers detectors at the guide magnetic field of 12 kG as a function of the transverse wiggler field has a very distinctive maximum. This maximum located near 1 kG. The effective generation has been observed in the range of the wiggler fields amplitudes close to the value predicted by theory. It should be pointed that the maximum power on the theoretical curve was chosen as equal to the experimental one. The power of 8mm-radiation was low and does not exceed 20% of total power.

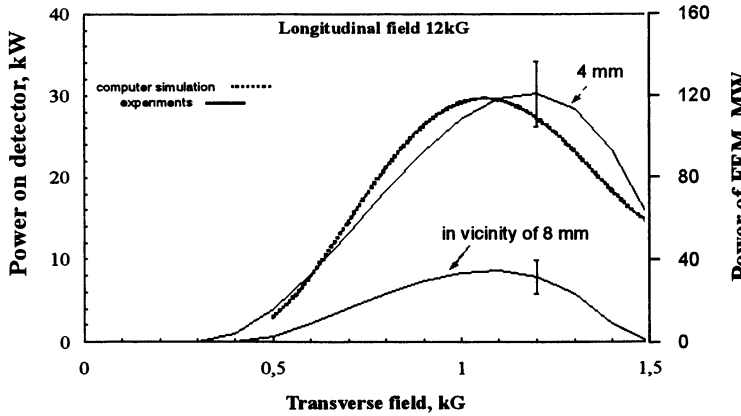

Fig. 9. Power of radiation as a function of transverse wiggler field

Other important experimental fact is that the power of the radiation at zero amplitude of the wiggler field is negligibly small. It demonstrates the absence of the microwave generation caused by initial cyclotron oscillations of the beam electrons. We have to say that agreement between experimental and theoretical data at the value of 10 kG of the guide field was somewhat worse that can be explained by influence of the cyclotron oscillations on the process of the microwave generation for the magnetic fields close to the resonance value.

Using the calibrated detectors we measured maximal 4mm-radiation power on the level of 30 kW inside the waveguide at the detector. It allows us to estimate the FEM power as 100 MW that was about 5% of the beam power. Total energy content in the radiation was estimated about of 100 J for these conditions.

Spectral content of the radiation in the vicinity of the operating frequency 75 GHz was analyzed by means of the narrow-band filters. The signals from the diodes placed after the filters were divided by the width of the filter's bands. The signals modified in such way are presented in the Fig. 10 for 10 kG of longitudinal field.

From the relation of the average spectral density of radiation in three frequency bands one can make the following conclusion. The highest

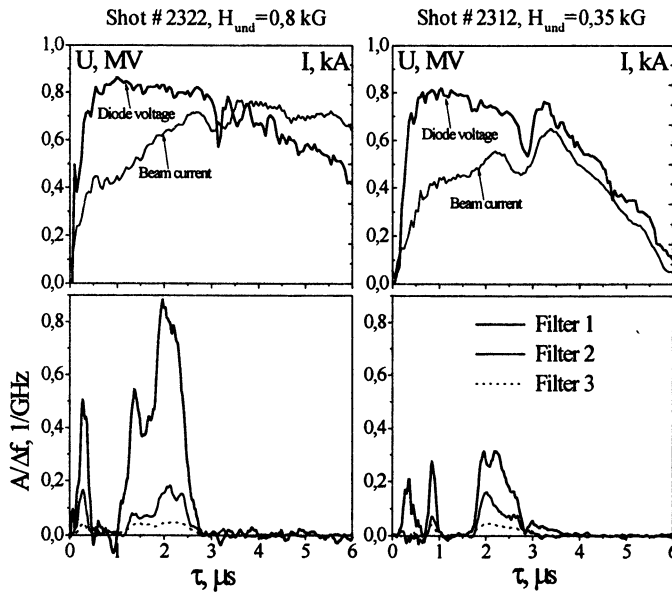

Fig. 10. Spectral properties of generated 4-mm radiation

spectral density of generated radiation is located in the range 74 ÷ 76 GHz that corresponds to the frequency zone for the 2-D Bragg scattering in the resonator. About 20% of that quantity is registered in the range 76 ÷ 80 GHz that is occurred due to the spurious 1-D feedback circuit $H_{1,0} \leftrightarrow E_{1,2}$. The spectral density of the radiation with frequency lower than 74 GHz, according to the measurements, was very small.

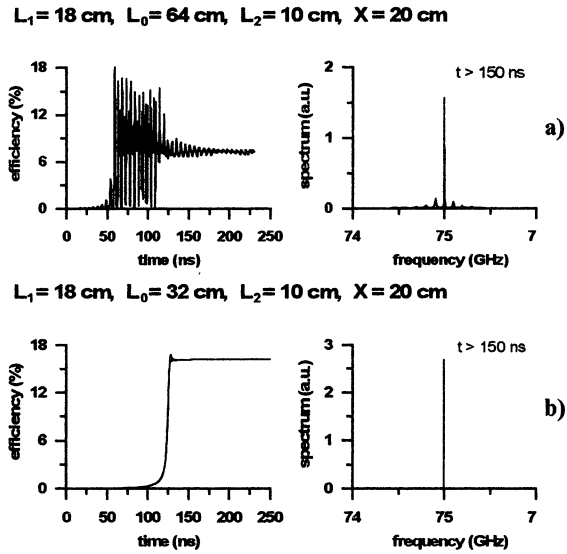

Fig.11. Efficiency and frequency spectrum of FEM with different length of resonator regular section.

Computer simulation of 4mm-wave-length generation by the FEM under the parameters close to the experiment gave the electron efficiency on the level about of 7% that is rather close to experimentally obtained value (see Fig. 11,a). The simulations were based on a time domain analysis taking into consideration the coupling of 4 partial waves inside the Bragg resonator [8, 9]. Fig. 11 presents results of the simulations for resonators with different lengths of regular section. For resonator with long regular section L_0 = 64 cm and high Q-factor (Fig. 11,a) the time dependence of the output RF signal demonstrates a large oscillations of efficiency at the first stage caused by excitation of different longitudinal modes disposed at the zone of effective Bragg reflections. However later at the second stage the longitudinal modes at the frequency of precise Bragg resonance, which possesses the highest Q-factor grows and suppresses other modes due to a nonlinear mode competition mechanism. It should be noted that the stationary regime of oscillations is established at this highest-Q mode for any mismatches of undulator synchronism (that in experiment is achieved by changes in the guide and wiggler fields) inside the zone of self-excitation. Thus, frequency stability of oscillation is significantly improved as it compared with traditional 1-D Bragg resonators. Moreover a

decrease in the resonator Q-factor by decrease in the length of regular section up to 32 cm leads to the establishment of the fundamental highest-Q mode, practically without other "parasitic" modes even during the transient stage (Fig. 11,b). Optimisation of parameters of the resonator shows that maximum efficiency about 18% may be achieved in this regime. Basing on these results the new series of experiments with optimized resonator configuration is under progress currently.

Acknowledgements

We are grateful to Prof. V.S.Koidan for his support of the work and Drs A.V.Burdakov, V.S.Burmasov, V.S.Nikolaev and A.F. Rovenskikh for help in experiments.

This work is partially supported by ISTC (grant #531), Russian Foundation for Basic Research (grant # 97-02-7379), and Russian Scientific Program "Physics of Microwaves" (project # 1.3).

References

1. Arzhannikov A.V., Ginzburg N.S., Nikolaev V.S., Peskov N.Yu., Sergeev A.S., Sinitsky S.L., Zotkin R.P., Yushkov M.V., 14th Int. Conf. on Free-Electron Lasers, 1992, Kobe, Japan, p.214.
2. Ginzburg N.S., Peskov N.Yu., Sergeev A.S., Sov. Techn. Phys. Lett., 1992, vol.18, no.9, p.23 (in Russian).
3. Ginzburg N.S., Peskov N.Yu., Sergeev A.S., Phelps A.D.R., Konoplev I.V., Robb G.R.M., Cross A.W., Arzhannikov A.V., Sinitsky S.L., Phys. Rev. E, 1999, vol.60, no.1, p.935.
4. Arzhannikov A.V., Bobylev V.B., Sinitsky S.L., Tarasov A.V., Ginzburg N.S., Peskov N.Yu., Nucl. Instr. and Meth. in Phys. Research A, 1995, vol.A358, p.112.
5. Agafonov M.A., Arzhannikov A.V., Ivanenko V.G., Ginzburg N.S., Kalinin P.V., Kuznetsov S.A., Peskov N.Yu., Sinitsky S.L., IEEE Trans. on Plasma Science, 1998, vol.26, no.3, p.531.
6. Arzhannikov A.V., Bobylev V.B., Ivanenko V.G., Shcheglov M.A., Sinitsky S.L., Stepanov V.D., Ginzburg N.S., Peskov N.Yu., 12th Int. Conf. on High-Power Particle Beams, 1998, Haifa, Israel, p.262.
7. An Yen Huan, Arzhannikov A.V., Diankova E.V., Ginzburg N.S., Kalinin P.V., Peskov N.Yu., Petrov P.V., Sinitsky S.L., Stepanov V.D., 4th Asian Symp. on Free-Electron Lasers, 1999, Taejon, Korea, p.12.
8. Ginzburg N.S , Peskov N.Yu., Sergeev A.S., Arzhannikov A.V., Sinitsky S.L., Sov. Techn. Phys. Lett., 1999, vol. 25, no.5, p.28 (in Russian).
9. Ginzburg N.S., Peskov N.Yu., Sergeev A.S., Robb G.R.M., Phelps A.D.R., IEEE Trans. on Plasma Science, 1996, vol.24, no.3, p.770.
10. Peskov N.Yu., Arzhannikov A.V., Ginzburg N.S., Denisov G.G., Kalinin P.V., Petrov P.V., Sergeev A.S., Sinitsky S.L. "Electrodynamic properties of spatially extended 2-D Bragg resonators of planar geometry" (this book).

DEVELOPMENT OF HIGH-EFFICIENCY FEL-OSCILLATOR FOR FEEDING HIGH-GRADIENT ACCELERATING STRUCTURES*

N.S.Ginzburg, A.K.Kaminsky, N.Yu.Peskov*, S.N.Sedykh, A.P.Sergeev, A.S.Sergeev**

Joint Institute for Nuclear Research, Dubna, Russia
*Institute of Applied Physics RAS, Nizhny Novgorod, Russia

An FEL-oscillator with a new type of Bragg resonator was realized on the base of linac LIU-3000 (JINR, Dubna) (1 MeV, 200 A, 200 ns). This resonator consists of two corrugated waveguide sections having a step of phase π between the corrugations at the point of connection. The selective properties of a resonator of this type are significantly improved in comparison with a traditional two-mirror Bragg resonator. Under the optimal parameters of the resonator at the frequency of 30.7 GHz the output power was about 50 MW corresponding to a record for millimeter wavelength FEL efficiency of 35%. Radiation spectrum corresponds to excitation of the fundamental mode with the frequency coincided with that found in "cold" microwave testing. The radiation spectrum width and the frequency stability in a single-mode regime allow considering the FEL-oscillator as a possible RF-source for high-gradient accelerating structures

Introduction

High efficiency millimeter-wave FEL-oscillators was developed in collaboration between JINR and IAP on the base of an induction linac LIU-3000 (0.8 MeV / 200 A / 200 ns) [1 - 3]. The attractive field of applications of these oscillators is driving high-gradient accelerating structures. The main features of the oscillators are the use of reversed guide field regime and the Bragg resonators as a selective feedback system. At previous stage of experiments the FEL with a two-mirror Bragg resonator was realized with the efficiency of 26% and the output power of 35 MW [1, 2]. The radiation frequency of 31 GHz and spectrum width in a single-mode regime $\Delta\lambda/\lambda \leq 0.25\%$ was very close to the values required in the CLIC project [4].

However, several important problems must be solved to design a FEL-oscillator suitable for applications in the accelerating techniques. A traditional two-mirror resonator has a set of longitudinal eigenmodes with integer number of half-waves between the mirrors and frequencies inside

* This work is supported by grants 97-02-16643 and 97-02-17379 of Russian Foundation for Basic Research.

the zone of effective reflection of the Bragg mirrors. The frequency difference between the neighboring modes is about 0.5%, so fixing one of them is rather difficult taking into account inevitable jitter of the beam energy and the pulsed wiggler and guide fields strength. Another problem in experimental realization of feeding the accelerating structure is the precise frequency matching between the FEL-oscillator and the structure. Typical Q-factor of the structure is about 300, so the value of 0.3% is an upper limit for admissible frequency mismatch. Central frequency of a Bragg resonator is determined by corrugation period (about one-half of wavelength), hence the required precision of the corrugation period can be estimated as 0.1% of 5 mm, i.e. 5 μm. This size tolerance is rather hard to realize.

Requirements on the mode selection and smooth frequency tuning can be satisfied using different type of Bragg resonator described in [5]. Such a resonator consists of two corrugated sections of lengths L_1 and L_2 having a step of phase of between the corrugations in the point of their connection. This resonator possesses only one mode inside the effective Bragg reflection zone (fundamental "central mode") at the frequency of precise Bragg resonance with the Q-factor greatly exceeding the Q-factors of other modes. The other modes are positioned symmetrically just outside the Bragg reflection zone ("side modes").

In this paper results of simulation and experimental studies of FEL with novel configuration of Bragg resonator are presented (see, also [3]). Possibility of precise mechanical frequency tuning in the resonator of this type is discussed as well.

Radiation frequency stabilization

Dynamics of oscillation build-up in FEL with a Bragg resonator with step of phase of corrugation was studied numerically. Time domain analysis taking into consideration partial wave coupling on Bragg structures was used [6]. It allows us to investigate both the transient process and the stationary regime.

When the Q-factor of fundamental mode is high enough for the central mode but low for the side modes (insufficient for self-excitation) a single-mode oscillations are realized both in the transient regime and in the stationary regime at all the possible values of the undulator synchronism mismatch (Fig. 1,a). If the Q-factor is large enough for self-excitation of both the central mode and the side modes beating of several modes occur in the transient stage. However in the stationary regime a

nonlinear mode competition results in the single-mode operation (Fig. 1,b). For too large Q-factor it is possible to operate at the central mode as well as at one of the side modes depending on the synchronism condition. Figure 1,c corresponds to the steady-state regime with excitation of one of the side modes. Note that increase in the Q-factor over the optimal value leads to decrease in the oscillator efficiency.

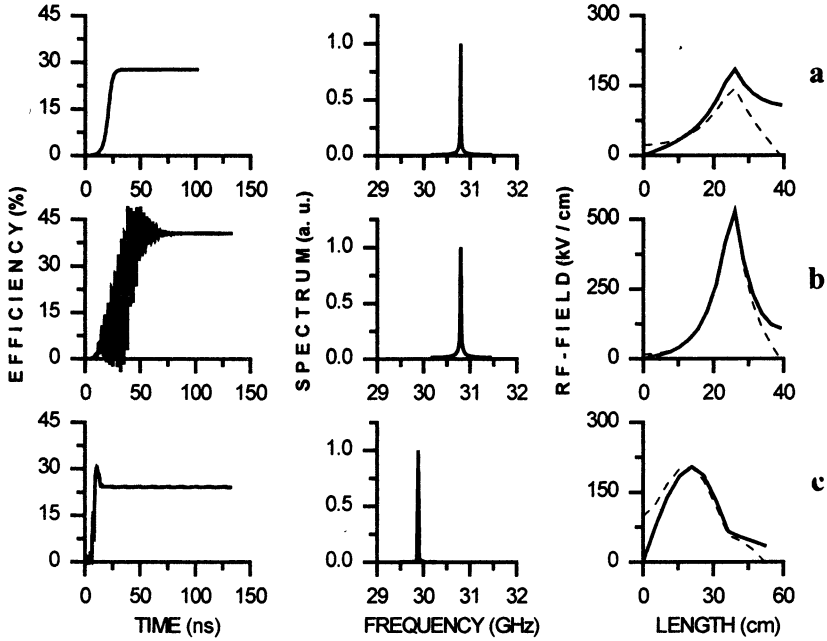

Figure 1. Computer simulation of excitation of FEL-oscillator with Bragg resonator having a step of phase of corrugation for different resonator configurations: $L_2 = 13$ cm and **a)** $L_1 = 26$ cm, $a_1 = 0.4$ mm; **b)** $L_1 = 26$ cm, $a_1 = 0.6$ mm; **c)** $L_1 = 39$ cm, $a_1 = 0.6$ mm. Left column: time dependence of efficiency. Middle column: spectrum of radiation in the stationary regime. Right column: longitudinal structure of partial waves in the stationary regime (solid lines - forward wave and dashed lines - backward wave).

Experimental results

Experimental investigations of FEL-oscillator with Bragg resonator having a step of phase of corrugation were carried out at the linac LIU-3000 [3]. Bragg structures forming the resonator were machined with the outer diameter of 22 mm, the corrugation depth (a_1) varies from 0.4 to 0.6 mm and the corrugation period (d) of 5.4 cm. The phase shift between the corrugations of the different structures in the point of their connec-

tion was equal to π. In the experiments we changed the reflector lengths and the values of the wiggler and guide magnetic fields. The maximal value of the output power (about 45 ÷ 50 MW) was registered on the fundamental mode at the frequency of 30.7 GHz when the Bragg structures of the lengths of 26 cm and 13 cm were used. The electron beam current was 170 A and, correspondingly, the FEL efficiency was 35%. This efficiency outstrips the efficiency of previous Bragg FEL-oscillator experiments [7 - 9].

Generation on the side modes with frequencies of 31.8 GHz and 28.4 GHz was registered in the resonator with the Bragg structures of length of 39 cm and 13 cm. The output RF-power in this case was about 30 ÷ 35 MW.

At the same time, we investigated experimentally the FEL-oscillator with "single section Bragg resonator" also described in [5]. This resonator consists of continuous Bragg structure of length of 52 cm. Separate excitation of both side modes existing in a such resonator has been observed. For tuning to the different modes we varied values of the wiggler and guide fields. Without detail optimization the efficiency amounted 12%.

Possibility of precise frequency tuning

Precise frequency tuning in FEL with a two-mirror Bragg resonator may be achieved by change in distance between the mirrors. Let us consider Bragg resonator with the length of regular section varying from zero to the period of corrugation. Obviously, because each the mirror has many periods of the corrugation, the change in length of the regular waveguide is equivalent to the change in phase of corrugation in the point of connection of two Bragg structures. At the phase shifts equal to zero or 2π, the resonator spectrum must be the same and coincides with the spectrum of a "single section Bragg resonator" [5]. There are two resonance frequencies outside the effective reflection zone and symmetrical to the precise Bragg frequency (Fig. 2,a). The frequency interval between the two side modes is defined by the corrugation depth and close to the width of Bragg reflection zone.

When the phase shift increases, the spectrum becomes asymmetrical, and the upper side eigenfrequency moves inside the reflection zone (Fig. 2,b). At the π step of phase we have another type of resonator described in [5], where the eigenfrequency coincides with the exact Bragg frequency (Fig. 2,c). Then with the increase in the value of step of phase

the eigenfrequency moves to the lower border of the reflection zone (Fig. 2,d). The total tuning range is restricted by the reflection zone bandwidth and for the typical Bragg structures used in our experiments this value is about 1 GHz that equals to 2 ÷ 3% of the operation frequency.

The estimated tuning accuracy is high enough: at the corrugation period of about 0.5 cm it will be: $\Delta f/\Delta l \approx 1\,\text{GHz}/0.5\,\text{cm} \approx 0.2\,\text{GHz/mm}$. It means that at the operating frequency of 30 GHz the required frequency tolerance of 0.3% ($\delta f \approx 0.1\,\text{GHz}$) may be realized when the gap between the mirrors will be varied with the accuracy of 0.5 mm.

Note that mostly the frequency linearly depends on the phase shift. The Q-factor of the eigenmode in general also changes with the shift of phase, but its variation can be minimized by the proper choice of the

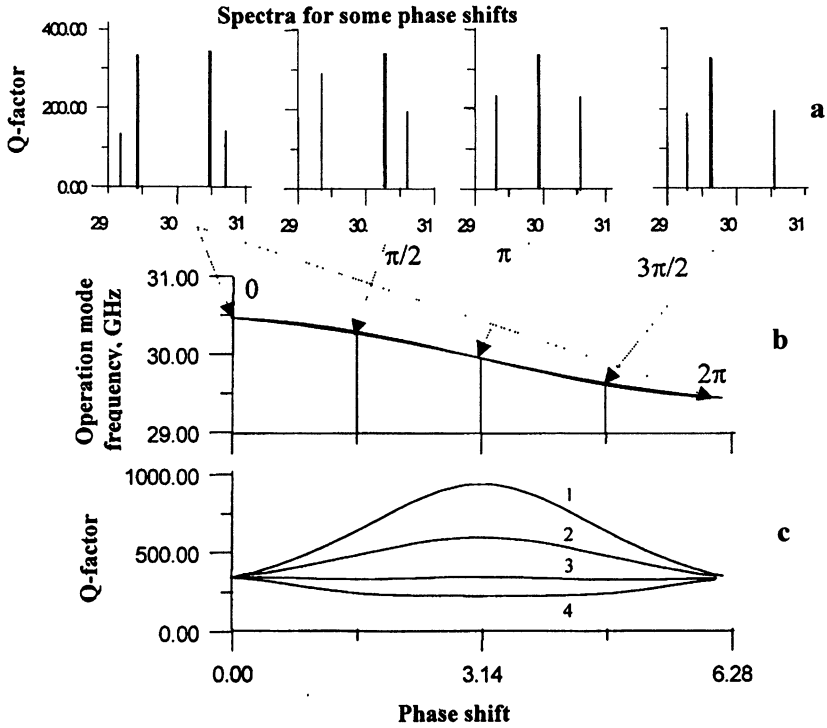

Figure 2. Mode spectra for different phase shifts for $L_1 = 28$ cm and $L_2 = 12$ cm (a). Operation frequency (b) and Q-factor (c) versus value of shift of corrugation phase for different resonator configurations: 1) $L_1 = 20$ cm, $L_2 = 20$ cm; 2) $L_1 = 25$ cm, $L_2 = 15$ cm; 3) $L_1 = 28$ cm, $L_2 = 12$ cm; 4) $L_1 = 30$ cm, $L_2 = 10$ cm ($d = 0.56$ cm).

lengths ratio for the Bragg structures. Figure 2,a corresponds to the optimal lengths providing approximately constant Q-factor. In such a resonator the starting conditions for the operating mode, output power and spectrum width of the output radiation will stay constant with the change in phase shift between the corrugated structures. Hence it is possible to provide exact frequency matching with an accelerating structure.

Conclusion

The use of Bragg resonator with tuneable phase shift between the Bragg structures makes it possible to tune output radiation frequency of the FEL-oscillator with accuracy better than 0.3% while the radiation spectrum width does not exceeding 0.3%. The high Q-factor of the fundamental mode in a Bragg resonator with step of phase of corrugation allows decrease in the interaction length resulting in a low sensitivity to the initial spread in electron beam parameters and efficiency enhancement. Experimental study of FEL with such a resonator demonstrated possibility to achieve the efficiency of 35%. This type of FEL-oscillator can be considered as a suitable RF-source for testing the high-gradient accelerating structure at the frequency of 30 GHz and the output power of 50 MW [10].

References

1. Kaminsky A.K., Kaminsky A.A., Sarantsev V.P., Sedykh S.N. et al, Nucl. Instr. and Meth. in Phys. Research A, 1996, vol.A375, p.215.
2. Ginzburg N.S., Kaminsky A.K., Kaminsky A.A., Peskov N.Yu. et al, IEEE Trans. on Plasma Science, 1998, vol.26, no.3, p.536.
3. Peskov N.Yu., Ginzburg N.S., Kaminsky A.K., Kaminsky A.A. et al, Sov. Techn. Phys. Lett., 1999, vol.25, no.11, p.19 (in Russian).
4. CERN/PS/98-009 (LP), Jean-Pierre Delahaye for the CLIC Study Team: 6th European Particle Accelerator Conf. (EPAC 98), Stockholm, Sweden, 1998.
5. Bratman V.L., Denisov G.G., Ginzburg N.S., Petelin M.I., IEEE J. of Quant. Electr., 1993, vol.QE-19, p.282.
6. Ginzburg N.S., Peskov N.Yu., Sergeev A.S., Robb G.R.M., Phelps A.D.R., IEEE Trans. on Plasma Science, 1996, vol.24, no.3, p.770.
7. Chu T.S., Hartemann F., Danly B.G., Temkin R.J., Phys. Rev. Lett., 1994, vol.72, p.2391.
8. Wang M., Wang Z., Chen J., Lu Z., Zhang L., Nucl. Instr. and Meth. in Phys. Research A, 1991, vol.A304, p.116.
9. Zambon P., Witteman W.J., Van der Slot P.J.M., Nucl. Instr. and Meth. in Phys. Research A, 1994, vol.A341, p.88.
10. Elzhov A.V., Ginzburg N.S., Ivanov I.N. et al, XVII Int. Conf. on High Energy Accelerators, Dubna, Russia, 1998, p.C20.

THEORETICAL AND EXPERIMENTAL STUDIES OF BUNCH DYNAMICS IN MM-WAVE FEL-OSCILLATORS ♣

S.V.Filin, N.S.Ginzburg, A.K.Kaminsky, E.M.Laziev, N.Yu.Peskov*, A.I.Puzynin, S.N.Sedykh, A.P.Sergeev, A.S.Sergeev**

Joint Institute for Nuclear Research, Dubna, Russia
*Institute of Applied Physics RAS, Nizhny Novgorod, Russia

Bunch dynamics was studied both theoretically and experimentally in a JINR-IAP FEL-oscillator with Bragg resonator. Computer simulation of bunch dynamics in different resonator configurations was done. Preliminary observation of beam bunching inside the FEL was carried out. A silica aerogel target with the refraction index of 1.1 allowed to obtain the Cherenkov radiation from bunches inside the undulator. A streak-camera IMACON-500 was used for registration of the radiation with the time resolution of 20 - 50 ps/mm.

Introduction

Detailed information about electron bunch dynamics in the interaction region is very important for development of high-efficiency FEL-oscillators and amplifiers. Numerical simulation is the most traditional method for such investigation. However direct experimental registration of bunched beam can deliver very helpful data. It should be noted that there is one more important reason to study bunch dynamics in FEL. It is using a FEL (first of all, a FEL-amplifier) as a buncher of intense electron beams with energies $1 \div 10$ MeV to drive linear collider [1, 2]. One of the possible scheme of drive beam injector for CLIC project (a CERN prototype of a two-beam accelerator with operating frequency of 30 GHz) includes the FEL-amplifier as a buncher of the beam with current of 1 kA and electron energy of $3 \div 10$ MeV. Experimental investigation of such scheme is undertaken in CESTA laboratory (France) [3].

At JINR in collaboration with IAP RAS a possibility to use both mm-wave FEL-amplifier and oscillator configurations as a drive beam buncher for CLIC test facility have been studied. Advantages of the amplifier buncher are the possible linear regime and simple variation of the bunching length. The oscillator configuration with Bragg resonator allows (see, [4]) to provide bunches with the frequency precisely corresponding to the CLIC Transfer Structure requirements.

♣ This work is supported by grants 97-02-16643 and 97-02-17379 of Russian Foundation for Basic Research.

Our group has recently started experiments on registration of beam bunching inside and outside the FEL. The diagnostic complex including the quartz or aerogel Cherenkov radiator, optical system, streak-camera IMACON-500, video camera and TV-signal digitizer has been created. A key element of the installation is the complex of time-resolved registration of the beam. The most suitable is the direct observation of the optical radiation from thin target installed in the beam channel. For the frequency of 30 GHz the time interval between centers of bunches is 33 ps, so the bunch radiation should be registered by the streak-camera with time resolution about 1 ps.

In this paper the results of the first experimental observation of beam bunching alongside with simulation of bunch dynamics in different schemes of FEL-oscillator are presented.

Numerical simulation of bunch dynamics in the oscillators with different types of the Bragg resonators

Using the approach described in [5] we simulated bunch dynamics inside and outside of the interaction region for the FEL-oscillators with different types of Bragg resonators. Figure 1 corresponds to a traditional two-mirror configuration with a regular waveguide section between the mirrors (described in [6]). Figure 2 corresponds to a novel scheme of the resonator with π-step of corrugation phase [4].

The new resonator configuration possesses relatively shorter interaction length and relatively higher maximal field amplitude inside. This leads to a high efficiency operation of this scheme what, however, accompanied by rather large dynamical energy spread at the resonator exit. At the same time, in this configuration the synchronous with the electrons forward wave undergoes a large decrease in amplitude inside the downstream Bragg structure. As a result, the electron bunch can not be trapped by the wave outside the interaction region. It is proved by the fact that amplitude of the forward wave as well as the FEL efficiency outside the resonator are approximately constant, while in traditional two-mirror oscillator longitudinal variation of these parameters is about 50%. (compare Fig. 1 and 2) Maximum bunching parameter in both variants is approximately the same, but it rapidly decreases in new configuration due to kinematic bunch expansion outside of resonator. In traditional oscillator the bunch remains trapped by the wave.

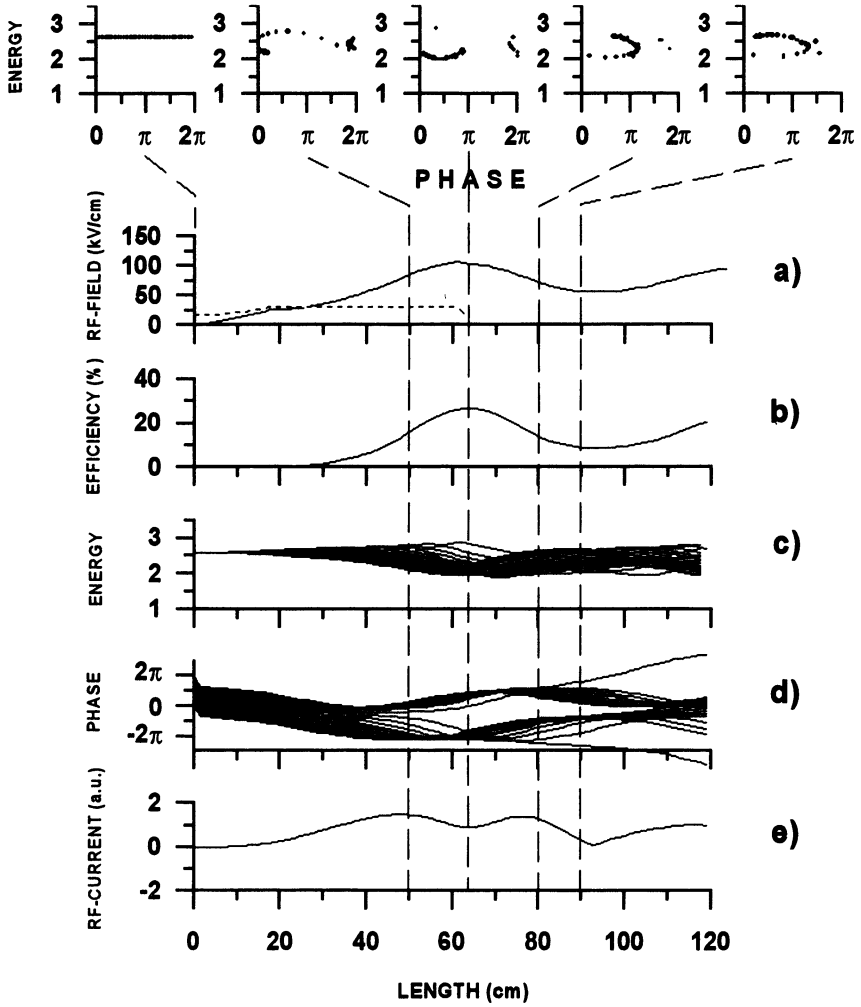

Figure 1. Simulation of bunch dynamics in FEL-oscillator with two-mirror Bragg resonator (up-stream mirror of 18 cm, down-stream mirror of 4 cm, regular section of 42 cm) in the stationary regime of generation. Dependencies on the axial coordinate:

a) amplitudes of forward (solid line) and backward (dashed line) waves;
b) electron efficiency;
c) energies of particles having different initial phases;
d) electron phases in the respect with synchronous wave;
e) module of first harmonics of the RF-current.

The phase-plane portraits of the beam in different cross-sections over the interaction length are shown on the top.

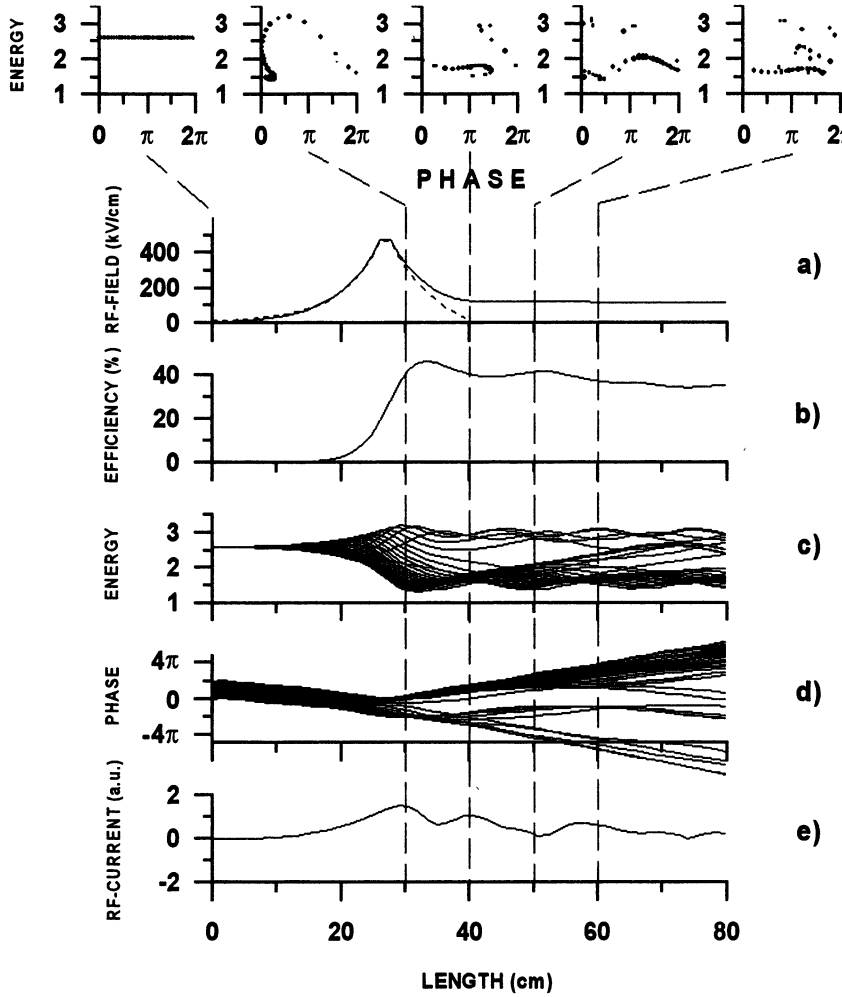

Figure 2. The same as Fig. 1 for FEL-oscillator with step of phase of corrugation (up-stream Bragg structure of 26 cm, down-stream structure of 13 cm)

Experimental observation of beam bunching

Experiments on the beam bunch observation inside the FEL-oscillators and amplifier were started recently. The scheme of the experiment (Fig. 3) was similar to one used in CESTA [3].

We have installed a Cherenkov radiator in the undulator between the mirrors of the oscillator or after the output mirror. A streak-camera IMACON-500 registered the optical radiation of the bunched beam with time resolution 20 - 50 ps/mm. The image of the output screen of the streak-camera was observed by a TV-camera and then digitized.

Material of Cherenkov radiator is silicon aerogel with extremely high refraction index of 1.1. It has two important features:

1) Beam energy of 0.8 MeV is slightly above the threshold of Cherenkov radiation in it, so most of the light is directed along the tube.

2) Because speed of the light in the radiator almost equals to the speed of the beam, thickness of the radiator does not decrease the temporal resolution of the method.

The typical streak-camera images shown in Fig. 4 present a temporal structure of the bunched beam into and just after the interaction region of the FEL-oscillator with Bragg resonators.

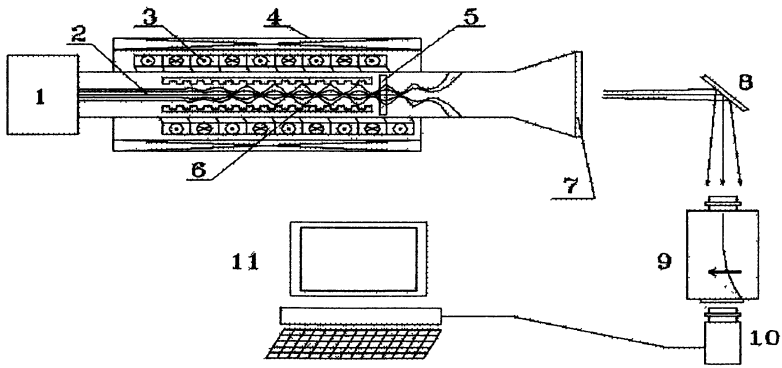

Figure 3. Experimental setup for bunching observation: *1* - electron beam injector (induction linac), *2* - electron beam, *3* - helical undulator, *4* - solenoid, *5* - Cherenkov radiator, *6* - microwave resonator, *7* - output window, *8* - mirror, *9* - streak-camera IMACON 500, *10* - TV camera, *11* - computer.

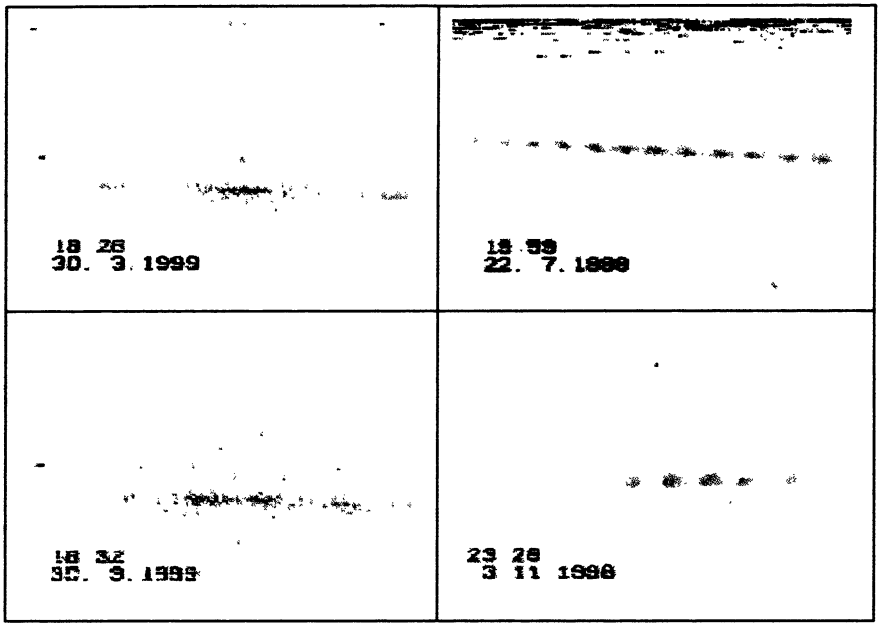

Figure 4. Typical streak-camera images of the beam bunched in the FEL-oscillator. Time resolution is 20 ps/mm (left column) and 50 ps/mm (right column). Visible area is 20 mm.

Conclusion

Numerical simulation shows rather remarkable difference in bunch dynamics in the FEL-oscillators with two types of Bragg resonators.

Preliminary experiments on the beam bunch observation inside the FEL-oscillator were carried out using the registration of the bunch Cherenkov radiation by a streak-camera. This experimental technique can be used both for FEL improvement and for investigation of drive beam buncher for colliders.

References

1. W.Schnell, CERN-LEP-RF/86-27, 1986; CERN-LEP-RF/88-59, 1988.
2. H.D.Shay, R.A.Jong, R.D.Ryne e.a., Nucl. Instr. and Meth. in Phys. Research A, 1991, vol.A304, p.262.
3. J.Gardelle, J.Labrouche, J.L.Rullier, Phys. Rev. Lett., 1996, vol.76, no.24, p.4532.
4. N.S.Ginzburg, A.K.Kaminsky, N.Yu.Peskov, S.N.Sedykh e.a. Development of high-efficiency FEL-oscillator for feeding high-gradient accelerating structures" (this book).
5. N.S.Ginzburg, N.Yu.Peskov, A.S.Sergeev, G.R.M.Robb, A.D.R.Phelps, IEEE Trans. on Plasma Science, 1996, vol.24, no.3, p.770.
6. N.S.Ginzburg, A.K.Kaminsky, A.A.Kaminsky, N.Yu.Peskov et al, IEEE Trans. on Plasma Science, 1998, vol.26, no.3, p.536.

ABOUT THE EXPLOSIVE PARAMETRIC INSTABILITY OF MODES WITH POSITIVE ENERGY IN THE PROCESS OF ELECTROMAGNETIC FIELD AND ELECTRON ENSEMBLES INTERACTION

M.A.Eroukhimova, M.D.Tokman

Institute of Applied Physics Russian Academy of Science, Nizhny Novgorod, Russia

The processes of parametric interaction of two high-frequency (HF) waves with the modulated at low-frequency (LF) electron beams under condition of the cyclotron resonance are investigated. Such a parametric coupling represents the new mechanism of stimulated cyclotron emission by electron aggregates—generation of two HF modes with positive energy by electron ensembles which are stable with respect to monochromatic radiation. Two different regimes of such generation are proposed.

1.It is traditionally assumed that if two HF modes with positive energy are coupled parametrically in the modulated medium only transfer of energy from one mode to another is possible. The situation changes if we deal with modes with different signs of energy. But here we are interested in other regimes, when the modulated medium is capable of amplifying two HF modes with positive energy. In [1] the authors paid attention to the possibility of such amplification in the medium with modulation of the conductivity but not the real-valued permittivity. Later in [2] Gaponov-Grechov and Tokman pointed that just the same amplification process from the macroscopic point of view is realized in the well-known quantum scheme of amplification without inversion, —so-called Λ-scheme[3]. In [2] they proposed the classical analog of Λ-scheme— "inversionless" maser on the cyclotron resonance.

In the present paper we investigate the scheme of the cyclotron parametric instability, proposed in [2]. Apart from it we consider another scheme of cyclotron generation where parametric instability becomes possible in the modulated reactive electron medium.

2. Let us examine the scheme of the parametric cyclotron generation, proposed in [2]. Consider two linearly polarized waves

$$\mathbf{E} = \mathbf{y}_0 \sum_{j=1}^{2} E_j \exp(ik_j x - i\omega_j t), \qquad (1)$$

propagating perpendicular to the constant magnetic field $\mathbf{B} = \mathbf{z}_0 B$, which

are resonant to the same relativistic electrons with γ-factor γ_0 at the N_1 and N_2 harmonics of the cyclotron frequency: $\omega_j = N_j \omega_B / \gamma_0$. This field interacts with ensemble of electrons with energy dispersed near the resonant value $mc^2\gamma_0$. The parametric interaction of two waves is provided by the modulation of electron ensemble in time, coordinate X and in angle of the cyclotron rotation θ, at $\Omega = \omega_1 - \omega_2 = L\omega_B/\gamma_0$, $\kappa = k_1 - k_2$ and $L = N_1 - N_2$, correspondingly. So at the initial moment we put the distribution function of electrons to be modulated in X and θ, so that at subsequent times the unperturbed distribution function can be presented as

$$f(w) = f_0(w) + f_M(w)\cos(\varphi_0 + L\theta + \kappa X - (L\omega_B/\gamma)t), \qquad (2)$$

where $w = \gamma - \gamma_0$. The distribution function averaged over t, X or θ is assumed to be "inversionless" so that $\partial f_0/\partial w|_{w=0} < 0$. Under this condition the electron system is not capable of amplifying each of HF waves separately, but it can impart energy to the bichromatic field.

The analysis is based on the system of the kinetic equation for the distribution function and the wave excitation equations [2]:

$$\begin{cases} (\partial/\partial t + \omega_H \partial/\partial\theta) f = -\sum_{j=1}^{2} F_j \, \partial f/\partial w \\ \dot{\alpha}_j = -(2\pi e/mc) I_j \end{cases} \qquad (3)$$

Here $\alpha_j = eE_j/mc$, $F_j = \mathrm{Re} g_j \alpha_j \exp(iN_j\theta + ik_jX - i\omega_j t)$, g_j —are the coupling constants depending on N_j, k_j and resonant values of the electron momentum. The problem is solved in the frame of the initial statement and in the linear approximation to the field amplitude. At sufficiently large times, when the asymptotic "Landau response" is formed, but at times restricted so that the "ballistic" mixing of the modulation phase can be neglected we evaluate the resonant harmonics of the current I_j, which are the sources in the wave excitation equations:

$$\begin{aligned} I_1 &\sim -\alpha_1 \int dw \, \hat{\xi}(\Delta_1) df_0/dw - \alpha_2 \exp(i\varphi_0) 1/2 \int dw \, \hat{\xi}(\Delta_2) df_M/dw, \\ I_2 &\sim -\alpha_2 \int dw \, \hat{\xi}(\Delta_2) df_0/dw - \alpha_1 \exp(-i\varphi_0) 1/2 \int dw \, \hat{\xi}(\Delta_1) df_M/dw. \end{aligned} \qquad (4)$$

Here $\Delta_j = \omega_j - N_j\omega_H(w) = \omega_j w/\gamma_0$ —the cyclotron synchronism de-

tunings, $\hat{\xi}(\Delta) = \pi\delta(\Delta) + iP/\Delta$ —the operator corresponding to the Landau's "bypass rule". Finally we obtain the wave excitation equations which take the following form:

$$\begin{cases} \dot{\alpha}_1 + (\gamma + i\delta)\alpha_1 = -e^{i\varphi_0}(\Gamma + iD)\alpha_2 \\ \dot{\alpha}_2 + (\gamma + i\delta)\alpha_2 = -e^{-i\varphi_0}(\Gamma + iD)\alpha_1 \end{cases} \tag{5}$$

and get the following condition of instability

$$|\Gamma| > \gamma, \tag{6}$$

which reduces to the inequality:

$$1/2\left|df_M/dw\right|_{w=0} > -df_0/dw\big|_{w=0}. \tag{7}$$

The mechanism of amplification in this scheme is the following. The condition (7) requires the sufficiently strong periodic in time and coordinates "inversion" of the distribution function with respect to both HF waves. Such periodic inversion corresponds to the strong modulation of the real part of the medium conductivity $\mathrm{Re}\sigma$. The unstable solution of eqs.(5) corresponds to the optimal synchronization between beats of the HF field and the LF modulation of $\mathrm{Re}\sigma$.

Going out the frame of the linear theory and examining the problem in the quasi-linear statement we managed to obtain the energy relations and to show that in the "inversionless" generation the HF field receives energy from the "slow" distribution function f_0 as it does in the ordinary maser instability. We showed that in this process the function f_0 relaxes not to the standard "plateau" but to the state with negative derivative with respect to w.

It is worth to note that the character of the parametric coupling of two HF waves changes in an interesting way at the large times, when the ballistic phase shift $(\omega_1 - \omega_2 - L\omega_B/\gamma)t$ becomes significant. We obtained the asymptotic equations:

$$\begin{cases} \dot{\alpha}_1 + (\gamma_1 + i\delta_1)\alpha_1 = 0 \\ \dot{\alpha}_2 + (\gamma_2 + i\delta_2)\alpha_2 = -e^{-i\varphi_0}(\gamma_{21} + i\delta_{21})\alpha_1 \end{cases} \tag{8}$$

which are distinguished by the nonreciprocal mode coupling, when the first mode is independent from the second one but it influences the energy exchange process between the second mode and the medium.

Thus the scheme just considered demonstrated that in the process of the parametric interaction of two HF fields in the "inversionless" medium with modulation of the real part of conductivity the simultaneous increase

of two HF modes with positive energy is possible. But it's been still believed that in the modulated reactive medium such amplification is impossible. Next we examine another scheme of the parametric generation which illustrates that it is not so.

3. Let us examine the instability of the modulated electron beam with respect to the bichromatic field propagating at an angle to the magnetic field. Consider components of the bichromatic field with similar transverse structure

$$\mathbf{E} = \mathbf{y}_0 \sum_{j=1}^{2} E_j \exp(ik_\perp x + ik_{\|j} z - i\omega_j t), \qquad (9)$$

resonant to the same particles with γ-factor γ_0 and longitudinal velocity $\beta_\|^0$ at the first harmonic of the cyclotron frequency: $\omega_j = \omega_B/\gamma_0 + ck_{\|j}\beta_\|^0$. In our model ω_j and $\mathbf{k_j}$ are connected by the "quasivacuum" dispersion relation. Consider interaction of this field with an ensemble of electrons with momentum components close to the resonant values $p_\|^0, p_\perp^0$. The parametric coupling of two waves is provided by the modulation of the electron ensemble in z and t at $\kappa = k_{\|1} - k_{\|2}$ and $\Omega = \omega_1 - \omega_2 = c\kappa\beta_\|^0$, correspondingly. So the unperturbed distribution function of electrons can be presented in the following way:

$$f = f_0(p_\|, p_\perp) + f_M(p_\|, p_\perp)\cos(\varphi_0 + \kappa z - \Omega t). \qquad (10)$$

In contrast to the previous scheme here at least two different regimes of the parametric generation are realized. The first one has been already discussed. It is the instability on the modulation of the Reσ. The second regime is

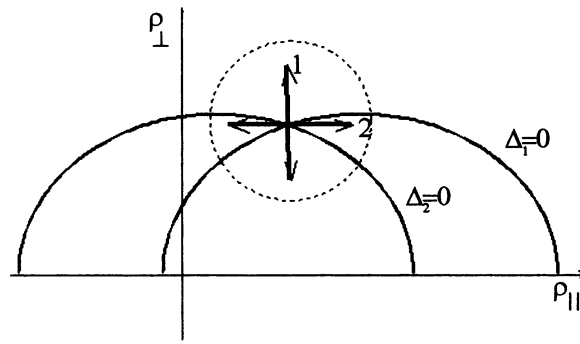

Fig.1

novel. It is the instability of the modulated reactive electron medium. Here it is the specific resonant conditions for two waves that are of principal value. The resonant curves in the momentum space of the waves propagating at an angle to the magnetic field unlike the perpendicular propagation always intersects at one point. As far as $k_{\perp 1} = k_{\perp 2}$, these curves have inclination of different signs at the cross point (fig.1). The electron ensemble in the momentum space is localized in the vicinity of the cross point, where the specific behavior of synchronism detunings $\Delta_j = \omega_j - \omega_B/\gamma - ck_{\|j}\beta_{\|}$ with two waves must be pointed out. Exactly, two different directions in the momentum space can be selected (see fig.1). In the first direction, close to the vertical one, Δ_1 and Δ_2 are changing in a similar way, but in the second direction, close to the horizontal one, the detuning with one wave is increasing but the detuning with another wave is decreasing simultaneously. What response to each HF field is formed in the electron medium is defined by the character of the dependence of the particle number in ensemble on the synchronism detuning with this field. According to the pointed out behavior of Δ_1 and Δ_2 we can find two different types of the modulated component of the

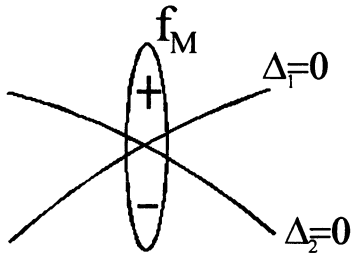

Fig.2a

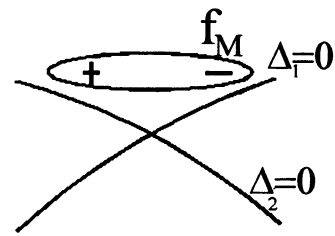

Fig.2b

distribution function $f_M(\rho_{\|}, \rho_{\perp})$ when the parametric coupling of HF waves becomes sufficiently different. The first type of the modulation, depicted in fig.2a, is that the dependence of the particle number on Δ_1 and Δ_2 in the modulated component of the beam is the same. In this case

we obtain the wave excitation equations similar to (5) and amplification condition analogous to (7). As in the previous scheme we get the parametric instability on the modulation of $\mathrm{Re}\sigma$.

The second type of the modulation (see fig.2b) is that the dependence of the particle number on Δ_1 and Δ_2 in the modulated component is opposite. There is an excess of particles in the vicinity of the resonance with one wave and the deficiency of particles near the resonance with another wave. In contrast to the previous situation now the responses to HF waves are modulated with phase shift at π. As a consequence the signs of the coupling coefficients in the wave excitation equations will be different. So instead of inequality (6) we get the amplification condition $|D| > \gamma$, which can be fulfilled in the absence of the resonant particles, when $\gamma = 0$. So we get the parametric cyclotron generation of HF bichromatic field due to the LF modulation of the distribution function of nonresonant particles. In other words we obtain the amplification of two HF modes with positive energy in the modulated reactive medium.

4. We suppose that the presented results are of undoubted interest for developing the theory of the radiative processes. They broaden our ideas about both the classes of aggregates of charged particles that are able to generate stimulated radiation and about possible parametric processes. As for the practical value of these results we have to admit that the contemporary level of these processes comprehension is not high enough. Nevertheless we can assume that the cyclotron parametric instability on the resonant particles can be used as a method for converting microwave radiation to a higher frequency. In addition, the "invertionless" nature of this instability let as hope that such a method is not very sensitive to the quality of the electron beam.

This work was supported by the RFBR; Grant No 99-02-16230.

References

1. S.V.Kiyashko, M.I.Rabinovich, and V.P.Reutov, JETP Lett. **16**, 271 (1972)
2. A.V.Gaponov-Grechov, M.D.Tokman, JETP **85** (4), 640 (1997)
3. O.Kocharovskaya, Phys. Rep. **219**, 175 (1992)

ELECTRODYNAMIC PROPERTIES OF SPATIALLY EXTENDED 2-D BRAGG RESONATORS OF PLANAR GEOMETRY

N.Yu.Peskov, A.V.Arzhannikov, N.S.Ginzburg, G.G.Denisov, P.V.Kalinin*, P.V.Petrov**, A.S.Sergeev, S.L.Sinitsky**

Institute of Applied Physics RAS, N.Novgorod, Russia
*Institute of Nuclear Physics SB RAS, Novosibirsk, Russia
**All-Russian Institute of Technical Physics, Snezhinsk, Russia

Theoretical and experimental studies of electrodynamic properties of two-dimensional Bragg resonators of planar geometry realizing a two-dimensional distributed feedback are carried out. High selectivity of the resonators over both longitudinal and transverse mode indexes are proved. It is shown that the eigenmodes spectrum is defined by a profile of corrugation surface.

Introduction

2-D microwave Bragg resonators based on a two-dimensional distributed feedback was proposed recently [1-3] for FELs to provide spatial coherence of radiation from a large-size sheet electron beam. First operation of FEL exploring the new feedback mechanism was demonstrated in joint experiments of INP RAS (Novosibirsk) and IAP RAS (N.Novgorod) on the base of the specialized accelerator ELMI [4]. Present paper describes microwave properties of planar 2-D Bragg resonators and their optimization to be used for FEL.

Eigenmodes of a 2-D planar Bragg resonator

A 2-D Bragg resonator consists of two metal plates (Fig. 1,a), which are doubly corrugated in directions having an angle to each other. Operation of a 2-D Bragg resonator is based on scattering of four partial waves on this corrugation:

$$\vec{E} = \mathrm{Re}\left[\left(\mathcal{A}_+\vec{E}_{a+}e^{-ih_{a+}z} + \mathcal{A}_-\vec{E}_{a-}e^{ih_{a-}z} + \mathcal{B}_+\vec{E}_{b+}e^{-ih_{b+}x} + \mathcal{B}_-\vec{E}_{b-}e^{ih_{b-}x}\right)e^{i\omega t}\right].$$

Let us assume that the $\mathcal{A}_+$ wave propagates along the electron beam and provides an interaction with the electrons. Thus, two other partial waves ($\mathcal{B}_\pm$) propagate in transverse directions and should provide synchronisation of radiation from different parts of a wide sheet electron beam. The backward in the respect with the electron beam wave $\mathcal{A}_-$ forms the feedback circuit.

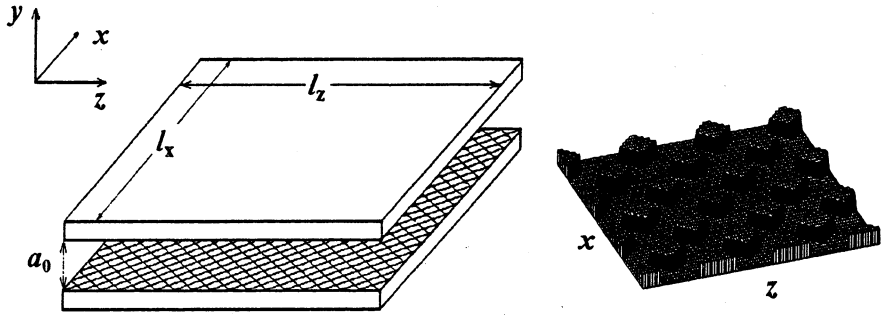

a) b)

Fig. 1. Schematic of a planar 2-D Bragg resonator (a) and a 2-D Bragg grating with rectangular threads (b).

For a technological simplicity Bragg structure may be machined as rectangular grooves in two perpendicular directions (Fig.1b) and may be presented as a multiplication of two periodical functions:

$$a(x,z) = a_1 f(x+z) f(x-z) \,, \tag{1}$$

where $f(\xi) = 0$ when $0 < \xi < d/2$ and $f(\xi) = 1$ when $d/2 < \xi < d$, d is the corrugation period ($f(\xi+d) = f(\xi)$). For a small depth a_1 this corrugation may be approximated by the following Fourier expansion:

$$a(x,z) = \frac{a_1}{\pi}\left(\cos(\bar{h}x - \bar{h}z) + \cos(\bar{h}x + \bar{h}z) + \frac{2}{\pi}\cos(2\bar{h}x) + \frac{2}{\pi}\cos(2\bar{h}z)\right) , \tag{2}$$

where $\bar{h} = \sqrt{2}\pi/d$. As a result, this corrugation provides two feedback circuits. The first two terms in (2) provide are responsible for a so-called 2-D coupling for partial waves (i.e. $\mathcal{A}_- \leftrightarrow \mathcal{B}_\pm \leftrightarrow \mathcal{A}_-$). This feedback circuit is completed by four partial waves, which should have the same wavenumbers $h_{a\pm} = h_{b\pm} = h$, and takes place when the following Bragg resonance condition is satisfied:

$$h \approx \bar{h} \,. \tag{3}$$

Simultaneously, the two last terms in (2) provide a traditional 1-D Bragg coupling (i.e. $\mathcal{A}_+ \leftrightarrow \mathcal{A}_-$ and $\mathcal{B}_- \leftrightarrow \mathcal{B}_-$) [5] when two counter propagating partial waves meet the resonance condition:

$$h_{a+} + h_{a-} \approx 2\bar{h} \,, \quad h_{b+} + h_{b-} \approx 2\bar{h} \,. \tag{4}$$

These waves may have different transverse structures and wavenumbers.

It should be noted, that in previous theoretical papers [1-3] it was considered an "ideal" model of a 2-D Bragg resonator and the corrugation surface was taken in the form of only the first two terms from the Fourier expansion (2), i.e.:

$$a(x,z) = a_1\left(\cos(\bar{h}x - \bar{h}z) + \cos(\bar{h}x + \bar{h}z)\right) . \quad (5)$$

In this assumption spectrum of the eigenmodes was found and a high selective properties of the resonator was proved. At the same time, in the first experiments at the ELMI accelerator [4] the Bragg structure made in the form (2) was used. The additional resonances appeared on this structure lead to significant changes in the eigenmodes spectrum and require the special consideration.

Figure 2 presents eigenmodes spectra of both "ideal" resonator (5) and resonator with corrugation given by (2). It is evident from Fig.2 that both resonators possess a high selectivity over both longitudinal (n) and transverse (m) mode indexes. At the same time, direct scattering of forward and backward partial waves (i.e. $\mathcal{A}_+ \leftrightarrow \mathcal{A}_-$ and $\mathcal{B}_+ \leftrightarrow \mathcal{B}_-$) destroys symmetry of the eigenmodes spectrum in comparison with the case of "ideal" resonator. Simultaneously, the spectrum is shifted into a low frequency region. The highest Q-factor in this case is realized for eigenmodes with indexes $n = m = 1$, i.e. having one field variations along both coordinates (compare with the case of "ideal" resonator, where the mode $n = 0$, $m = 1$ at the frequency of the precise Bragg resonance possesses the highest Q-factor [3]). Note, that under the same geometrical parameters the fundamental mode Q-factor is higher for the resonator with corrugation (2) than for "ideal" case (Fig. 2).

To simulate "cold" testing of the resonators we considered its excitation by the microwave beam coming in through one of the resonator sides. The theoretical analysis was carried out for the resonators of differ

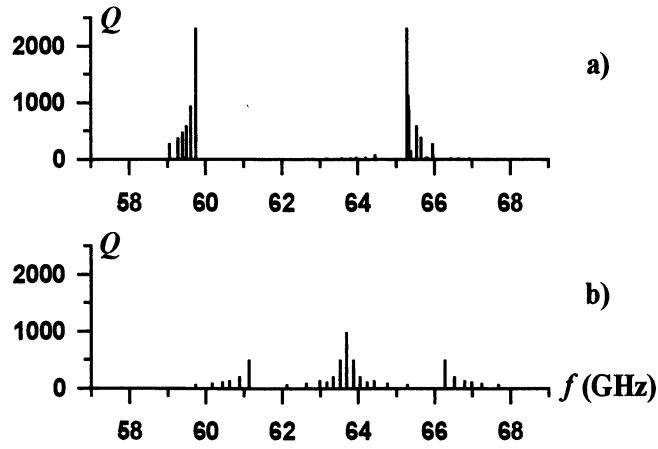

Fig. 2. Spectrum of 2-D Bragg resonator corrugated as (2) (a) and as (5) (b).

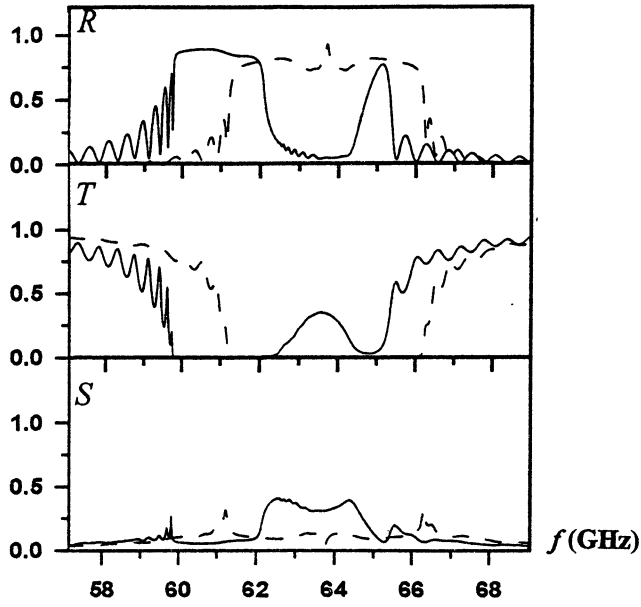

Fig. 3. Dependencies of the integral coefficients of reflection (R), transmission (T) and scattering in transverse direction (S) on frequency (computer simulations). Solid lines - for Bragg resonator (2), dashed lines - for "ideal resonator" (5).

ent geometries as well as for the different phase profile of the incident wave-beams. Figure 3 gives the frequency dependencies of the integral coefficients of reflection (R), transmission (T) and scattering in transverse direction (S) for the case of the input wave with the plane phase. Parameters for the simulations corresponded to the parameters of "cold" experiments carried out (see below). One can see from the comparison of Figs. 2 and 3 that for the high-Q resonator the minimum in reflection coefficient as well as maximum in transmission and transverse-scattering coefficients correspond to the frequency of the resonator eigenmodes. It should be noted however, that for the given case of the input wave of constant phase profile (i.e. having symmetrical distribution at the resonator edge) eigenmodes with the frequencies positioned near the high-frequency boundary of the zone of effective Bragg scattering and having anti-symmetrical structures are not exited (compare Fig. 2 and 3). As a result, in this frequency region the transmission coefficient is about zero and reflection coefficient is more than 80%. Far from Bragg resonance the transmission coefficient close to 100%, reflection and scattering in transverse direction tend to zero.

Results of "cold" tests

Experimental study of the electrodynamics properties was carried out. 2-D Bragg resonator was constructed in the form of two metal plates of the size 25 × 25 cm having the gap of 0.5 cm between them. These plates were doubly-corrugated at the inner surface with the period 0.32 cm and depth 0.04 cm, the angle between the rectangular threads of the corrugations was 90°.

The microwave parameters of the resonator were measured using a scalar network analyser in the frequency range 55 ÷ 80 GHz. For the resonator excitation the wave beam with a plane phase profile was formed at the resonator input. To produce such a beam the additional quasi-optical transmission line was constructed. It was made from two parallel metal plates and the parabolic mirror placed between these plates. The wave beam in the form of the $H_{1,0}$ mode of a rectangular waveguide of 0.7 × 0.5 cm size positioned at the focus of the parabolic mirror irradiates the mirror. As a result, the wave beam of the 40 cm width having plane phase profile and structure of TEM-mode of a plane waveguide was formed at the output of the mirror. The same transmission lines were used

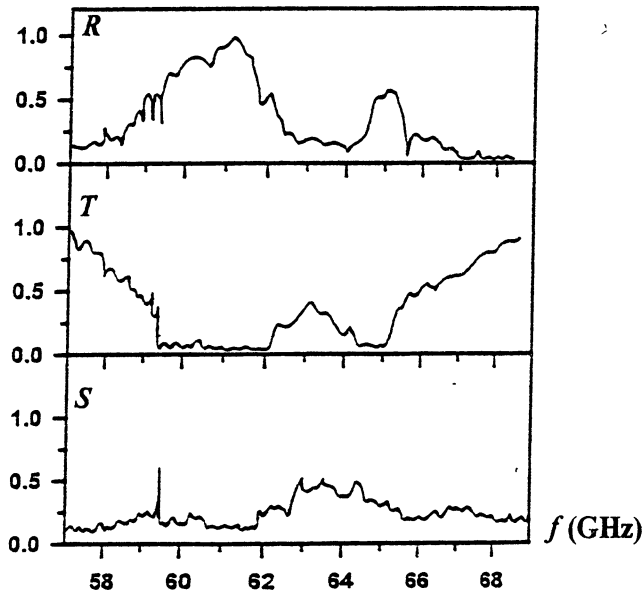

Fig. 4 Results of "cold" measurements of the coefficients *R*, *T* and *S*.

to receive the wave beams passed through the resonator as well as scattered in the transverse directions.

In accordance with the calculations two zones of effective Bragg scattering were observed in the frequency regions near 60 GHz and 75 GHz. The zone near 60 GHz corresponds to the mutual scattering of four partial waves of TEM-types. The results of measuring of the coefficients R, T and S are presented at Fig. 4 that demonstrates a good agreement with the simulations (compare with Fig. 3). In particular, the non-symmetry of the coefficients and mode positions was registered. The Q-factor of the mode with the indexes (1,1) at the frequency of 59.5 GHz was measured as 1500. It should be noted, however, that the wave coupling coefficient, which determinates the width of Bragg effective scattering zone, slightly exceeds the value found in the calculations under the assumption of small depth sinusoidal corrugation. Evidently, the real profile of the corrugation should be taken into account. The observed in the experiments some small shift of the Bragg zone may be explained by accuracy of manufacturing the Bragg structure.

Conclusion

Operability of 2-D Bragg resonators was demonstrated in "cold" experiments. Measured zone of effective scattering on 2-D Bragg structure, frequencies and Q-factors of eigenmodes were in a good agreement with calculations. Method for "cold" microwave testing of oversized planar waveguide systems was developed. In particular, it was used to study characteristics of planar 1-D and 2-D Bragg resonators used in "hot" experiments [4].

References

1. Ginzburg N.S., Peskov N.Yu., Sergeev A.S., Sov. Techn. Phys. Lett., 1992, vol.18, no.9, p.23 (in Russian).
2. Arzhannikov A.V., Ginzburg N.S., Nikolaev V.S., Peskov N.Yu., Sergeev A.S., Sinitsky S.L., Zotkin R.P., Yushkov M.V., 14th Int. Conf. on Free-Electron Lasers, 1992, Kobe, Japan, p.214.
3. Ginzburg N.S., Peskov N.Yu., Sergeev A.S., Radiotehnika i Electronika, 1995, vol.40, no.3, p.401 (in Russian).
4. Agarin N.V., Arzhannikov A.V., Bobylev V.B., Ginzburg N.S., Ivanenko V.G., Kalinin P.V., Kuznetsov S.A., Peskov N.Yu., Sergeev A.S., Sinitsky S.L., Stepanov V.D. "Generation of hundred joules pulses of 4-mm radiation by planar FEM with two-dimensional distributed feedback" (this book).
5. Bratman V.L., Denisov G.G., Ginzburg N.S., Petelin M.I., IEEE J. of Quant. Electr., 1993, vol.QE-19, p.282.

STUDY OF SPONTANEOUS MICROWAVE PULSE SHORTENING IN THE RELATIVISTIC BWO

S. D. Korovin, G. A. Mesyats, I. V. Pegel, S. D. Polevin, and V. P. Tarakanov***

Institute of High Current Electronics SD RAS, Tomsk, Russia
*Institute of Electrophysics UD RAS, Ekaterinburg, Russia
**Institute of High Temperatures RAS, Moscow, Russia

It is experimentally demonstrated that pulse shortening in a gigawatt BWO is accompanied by formation of explosive-emission plasma at the surface of a corrugated slow wave structure. Termination of microwave emission is explained in terms of the increase of the BWO starting current due to the absorption of the operating electromagnetic wave by electrons emitted from the plasma, while the intensity of absorption radically increases owing to the presence of positive ions emitted from the plasma. Improving SWS surface conditions in an X-band BWO allowed generation of 3-GW, 26-ns microwave pulses thereby demonstrating pulse lengthening with a factor of four.

Introduction

In the relativistic microwave generators driven by high-current relativistic electron beams, the width of microwave pulses is usually limited to $10^{-8} \div 10^{-7}$ s, while the electric field strength at the surface of the electrodynamic structure ranges $10^5 \div 10^6$ V/cm [1 - 4]. The circle of possible reasons for this phenomenon is rather wide [4 - 9]. For Cherenkov devices with a guide magnetic field, at a pulse width ~10 ns, when the motion of cathode and collector plasmas is insignificant, the main part in the pulse shortening is probably played by the dense plasma forming on the slow wave structure (SWS) in the intense RF field. Possible sources of this plasma are explosive-emission centers and the desrobed gas ionized by secondary and scattered electrons.

Experimental Study of Pulse Shortening

Experiments described below employed the high-current electron accelerator SINUS-6 with a 18-ns beam pulse length. A uniform relativistic BWO with the operating wave TM_{01} and wavelength $\lambda \approx 3.3$ cm was used. The length of the SWS consisting of separate stainless steel rings was $L=9d$ with the mean radius $R \approx \lambda/2$ and period $d \approx \lambda/2$. The tube was evacuated to 10^{-4} Pa using an oil diffusion pump.

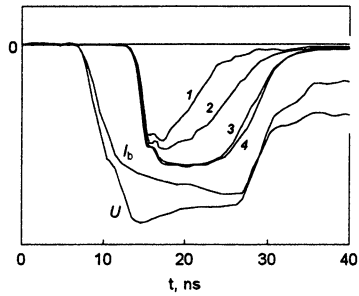

Fig. 1. Waveforms of e-beam current, diode voltage, and microwave detector signals. Number of the ripple containing graphite (counted from BWO cutoff-neck): *1* – 4th, *2* – 8th, *3* – 1st, *4* – no graphite.

In the optimum regime (cathode voltage U=600 kV, beam current I=4.7 kA, magnetic field strength 26 kOe) the microwave pulse power was ~500 MW. At this power level, no pulse shortening is observed under ordinary conditions (Fig. 1, see also Ref. [3]). To prove the effect of explosive emission, one of the SWS rings was replaced with a ring of the same geometry but having a graphite insert (Fig. 2). Introduction of graphite did not change the electrodynamic properties of the waveguide but promoted the development of explosive emission [10]. The waveforms of cathode voltage and electron beam current did not change.

Introduction of graphite caused a noticeable pulse shortening. The most pronounced shortening occurred when the insert was placed in the middle of the SWS. A partial restoration of the pulse width observed once a number of pulses was generated without opening the system was probably associated with the degradation of explosive emission from graphite due to RF-field training. The more pronounced shortening of first pulses corresponded to the larger number of restoring pulses (about 20-30). In those cases where the microwave pulse terminated, intense electron flow between SWS ripples was observed. The prints (Fig. 2) evidenced high current density (~ 1 kA/cm^2) peculiar to explosive electron emission.

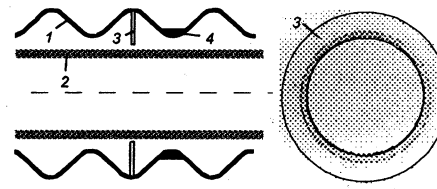

Fig. 2. Print of electron current flowing between SWS ripples. *1* – SWS, *2* – REB, *3* – plastic target, *4* – graphite insert.

Theory

In theory, we assumed that the BWO pulse shortening is due to the absorption of the operating wave by the electrons emitted from explosive-emission plasma at the SWS surface. The generation process can

terminate if the BWO critical current (coincident with the starting one) becomes higher than the actual current of the driving electron beam.

The dependence of BWO starting current on the wave decrement was obtained from steady-state hydrodynamic consideration. For a classical uniform BWO without space charge, assuming distributed wave absorption resulting in its decay $E \sim \exp(-h''z)$, we have $I_{st} = I_A \frac{(\gamma_0^2 - 1)^{3/2}}{4\pi^3 cZ} \left(\frac{\lambda}{L}\xi_L\right)^3$ where $I_A \approx 17.06$ kA is the Alfven's current, $Z = 2|\hat{E}(r_b)|^2 / k^2 N$ is the coupling impedance, and the dimensionless starting length $\xi_L = kLC$ (as well as the starting dimensionless synchronism mismatch $\Delta' = \delta/kC$) depends on the dimensionless decrement $\Delta'' = h''/kC$ (Fig. 3). In the absence of absorption ($\Delta''=0$) have the known values $\Delta'_{st}=1.52$, $\xi_{L,st}=1.97$. Note that in the expression for the Pierce parameter $C = \left(I_b cZ / 2I_A (\gamma_0^2 - 1)^{3/2}\right)^{1/3}$ we must set $I_b=I_{st}$. The above value of starting current agrees well with the quantity obtained from 1D time-dependent BWO model [11]. For example, for a BWO with λ=3 cm, L=12 cm, Z=1 Ohm, ε_0=500 keV, reduplication of starting current occurs at $h''=0.12$ cm^{-1}.

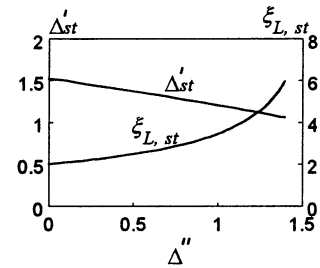

Fig. 3. BWO starting eigenvalues

For a classic BWO with a localized wave absorber, the maximum (factor of 8) increase of starting current corresponds to middle positioning of the absorber in the SWS. For a BWO with the above listed parameters, reduplication of starting current occurs at 76-% wave power absorption that corresponds to the efficient value of $h''=0.06$ cm^{-1}. Placement of absorber at any edge of the device does not effect the internal generation process.

The source of wave absorption in a BWO could be the electrons emitted from explosive-emission plasma. At the same time, nonlinearity of energy absorption by electrons with a space charge limited current makes it incapable of terminating the generation. In fact, to increase the BWO starting current we should have a non-vanishing ratio between the wave power losses and the wave power flow in the limit of small field amplitude (the BWO efficiency tends to zero in the proximity of starting regime). The non-relativistic space charge limited current density for

electrons is $j_{em} \propto E^{3/2}$ and the energy gained by electrons in the wave is $\varepsilon \propto E^2$ where E is the wave electric field strength. Thus, $P_{loss} \propto E^{7/2}$. Since the wave power $P_w \propto E^2$, we have $P_{loss}/P_w \propto E^{3/2} \to 0$ at $P_w \to 0$. Thus, the non-relativistic space charge limited electron load can not effect the BWO starting current. Besides, a high-current driving electron beam is present in the system whose electrostatic potential with respect to the waveguide wall is $\sim 10^5$ V. If the microwave power drops below certain level, the RF field drawing the electrons from the SWS surface is totally compensated by the beam static field that prevents electron emission.

Nevertheless, the wave absorption can explain the termination of generation. Consider the fact that positively charged ions are extracted from the plasma in the appropriate phases of RF oscillation. The cyclotron radius for ions far exceeds that one for electrons and can be comparable with the transverse size of SWS. Therefore, early in the process, ions move towards SWS axis tending to compensate the space charge of the driving REB. For single-charged ions, the ion density to compensate a 5-kA REB is $\sim 10^{11}$ cm^{-3}. The time of compensation ranges few nanoseconds for light ions, for example, protons or carbon ions.

Due to space charge compensation, the electric field drawing the electrons from the SWS surface reaches the amplitude of the wave field E_0. This speeds up the excitation of explosive emission that possibly develops in avalanche manner, accounting that the current of separate emission centers grows in time as $t^{3/2}$.

Simultaneously, accumulation of ions in the space between SWS ripples occurs. Electrons emitted from the plasma move along the magnetic field lines and their space charge additionally drives accumulation of the ions. In the BWOs with an electric field of $10^5 \div 10^6$ V/cm at the SWS, electrons emitted from one SWS ring can reach another one within one RF period. Since the electron current is space charge limited, it produces a quasi-static field of average value in the order of E_0. In this field, ions move in accelerating manner and fill the gap in few nanoseconds. As a result, quasi-neutral plasma is formed in the gap between the ripples. The space charges of ions and electrons compensate each other in average during RF period. The concentration of plasma grows in time and so does the electron bombardment power.

According to results of simulation using the RZ-version of fully electromagnetic time-dependent PIC-code KARAT [12], for TM_{01} wave with 500 MW initial power propagating in the above specified corrugated waveguide, the power absorption ranges 40% per structure period that

corresponds to $h''\approx 0.16$ см$^{-1}$. The corresponding electron concentration is $n\sim 10^{12}$ см$^{-3}$ (this requires ionization of several cubic microns of substance that is quite typical for the explosive emission).

The growth of plasma concentration and wave losses is limited by the skin effect. Note that this latter can change the dispersion relations of the SWS. Besides, it decreases the effective corrugation depth of SWS and, consequently, the BWO coupling impedance that can also increase the starting current.

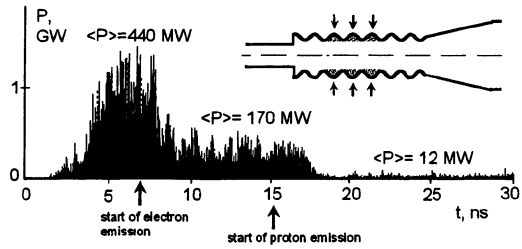

Fig. 4. Simulated waveform of output power from a BWO with electron and ion emission at the SWS

The full-scale time-dependent numerical experiments employing the KARAT code evidenced that combined electron and ion emission from the SWS can substantially decrease the BWO microwave power to the extent of total disappearance of the generation. Figure 4 illustrates the situation where three emitting ripples are placed in the middle of the tube. The starts of electron and proton emission are split in time to separately demonstrate their effects. As is seen, the electron emission visually decreases the microwave power but it does not terminate the generation. In about 3 ns after starting the proton emission (time needed for accumulation of protons in the SWS volume) the microwave power drops to a negligibly low level that is accompanied by destruction of the spectrum and distinctive phase plot of the BWO.

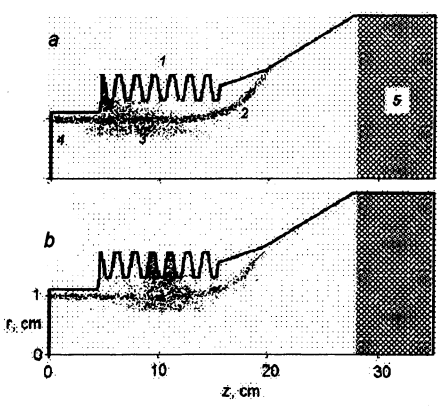

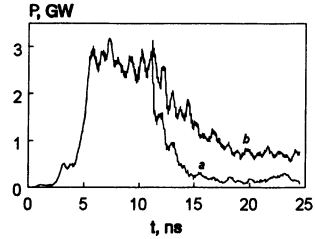

Fig. 5, 6. Simulated BWO configurations and output power waveforms. Particle emission from the SWS surface starts at t=10 ns. *1* - SWS, *2* - driving REB, *3* - proton cloud, *4* - beyond cutoff-neck, *5* – absorber.

We should note that in BWOs optimized in terms of forward traveling wave interaction (especially in that case when the coupling impedance for this interaction is high) the generation is very sensitive to explosive emission in the vicinity of the beyond cutoff-neck (Fig. 5, 6).

Bwo Pulse Lengthening Experiment

In our earlier experiments [3] with a 3-GW X-band relativistic BWO based on electron accelerator SINUS-7 (e-beam pulse duration 45 ns), the microwave pulse width was limited to 6 ns (see the dashed line in Fig. 7). Intense erosion of the SWS surface was observed.

Removal of microprotrusions, dielectric inclusions and oil films from the SWS surface (using its electrochemical polishing and improved vacuum conditions) resulted in the increase of microwave pulse width from 6 ns up to 23 ns at a power level of 3 GW with the pulse energy ~80 J (Fig. 7).

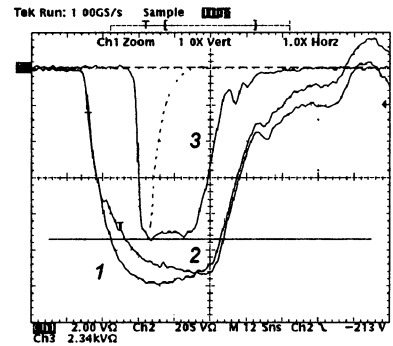

Fig. 7. Waveforms of (*1*) diode voltage, (*2*) e-beam current, and (*3*) the microwave detector signal.

References

1. Zaitsev N. I., et al. Lett. J. Tech. Phys. (Sov.), 1981, **14**, 879.
2. El'chaninov A. S., et al. Lett. J. Tech. Phys. (Sov.), 1981, **19**, 1168.
3. Gunin A. V., et al. Russian Physics Journal, 1996, **12**, 1229.
4. Aleksandrov A. F., et al. Abstr. 4th Symp. High-Current Electronics. Novosibirsk, 1982, 168.
5. Aleksandrov A. F., et al. Relativistic High Frequency Electronics. Issue 3. Gorky, 1983, 219.
6. Mesyats G. A. Proc. Course and Workshop on HPM Generation and Applications. Villa Monastera – Varenna, Italy. 1991, 345.
7. Benford J., Benford G. IEEE Trans. Plasma Sci, 1997, **2**, 311.
8. Kovalev N. F., et al. IEEE Trans. Plasma Sci, 1998, **3**, 246.
9. Loza O. T., Strelkov P. S. Dig. Tech. Papers, Int. Workshop on HPM Generation and Pulse Shortening, Edinburg, UK, 1997, 103.
10. Mesyats G. A. and Proskurovsky D. I. Pulsed Electrical Discharge in Vacuum. Berlin: Springer-Verlag, 1989.
11. Pegel I. V. Russian Physics Journal, 1996, **12**, 1210.
12. Tarakanov V. P. User's Manual for Code KARAT. Springfield: BRA, 1992.

RELATIVISTIC BWO WITH CYCLOTRON SELECTION OF AN ASYMMETRIC WAVE

N.F. Kovalev, N.G. Kolganov, A.V. Palitsin, M.I. Fuchs

Institute of Applied Physics RAS, Nizhny Novgorod

The report presents results of experimental and theoretical investigations of relativistic BWO with cyclotron selection of operating TM_{11} rotating wave. Decompression and cyclotron selection permitted to obtain stable generation of microwave pulses, which have no afterpulse. Cyclotron absorption was described theoretically in self-consistent model. Theoretical model also predict the appearance of specific localized states – "nonlinear Tamm's resonance" in the system of interacting electromagnetic and cyclotron waves.

Introduction

Many consumers properties of relativistic BWO or karcinotron can be approved by choosing higher interacting eigen-modes. First of all, it relates to output power, pulse duration and stability of output radiation parameters. But higher eigen-modes can be employed only if it is possible to provide one-mode generation and to reduce to admissible level reemission and scattering of operating waves on different heterogeneities in electrodynamic system.

The report includes results of investigations of relativistic BWO with the rotating wave of TM_{11} type with additional cyclotron selection [1, 2]. In the experiment operating wave was formed in circular waveguide with not too dip single-threaded helical corrugation. The first backward axial-symmetric harmonic was synchronous with electron beam.

$$\omega - (h(\omega) - \bar{h})v \approx -\frac{\pi}{2}\frac{v}{L}, \qquad (1)$$

where ω – is operating frequency, h – longitudinal wave number, $\bar{h} = 2\pi/d$, d – period of corrugation, L – length of BWO and v – longitudinal velocity of electron. The axial symmetry of synchronous harmonic permits to exclude from synchronism condition (1) azimuthal Doppler amendment. That amendment reduces the efficiency of interaction because of the fibering of electron beam to fractions with different azimuth velocities. Degeneration of the waves rotating in opposite directions is removed by using the corrugation with helical symmetry and by choosing the direction of focusing magnetic field coordinated with corrugation.

BWO was designed and operated in regime:

Accelerating voltage	$U \approx 0.5$ MV
Beam current	$J \approx 2$ kA
Beam diameter	from 2,6 cm to 3,5 cm
Current pulse duration	$T \approx 20$ ns

Experiments

Experiments were held on the setup "Sinus-6", which allowed to implement the designed operating regime, utilizing simplest coaxial diode with field-emission cathode. The setup operated in single pulse regime.

For focusing and formation of electron beam the system of two solenoids was employed, that permitted to verify the idea of BWO operation with magnetic fields slightly less than resonant:

$$H < H_{res} \approx \gamma\beta \frac{mc^2}{e} \frac{2\pi}{d} \approx 6 \div 7 \text{ kOe}, \qquad (2)$$

here γ – relativistic factor; m,e are the electron rest mass and the charge; c – velocity of light; $\beta=v/c$. The formation of the beam in weak magnetic fields is difficult enough problem, that is why the decompression was used [3]. Decompression means the increasing of magnetic field in small region near cathode. Implementing decompression we supposed, that beam quality in the interaction region is slightly improved as a result of decreasing of transverse velocities of electrons.

In the experiment the magnitude of decompression varied for the purpose of adjustment of the beam radius in the interaction region. Experiments were held with the overfall of magnetic field about 4, that is the diameter of emitting edge of cathode and mean diameter of the hollow beam in the interaction space differ almost in 2 times.

Taking into account the polarization, besides the E_{11} mode, 7 another modes can propagate at operating frequency. For the purpose of one mode generation the following means were applied: (i) the choice of diameter of electrodynamic structure, (ii) helical corrugation and smooth transitions to regular regions, (iii) close to resonant magnitude of focusing magnetic field, its direction and choice of the diameter of electron beam.

At first phase of experiment the conditions of E_{11} mode generation were defined by means of choice of the electron beam radius, the current of the beam and the method of collecting of electrons. Out of that conditions, according to spectrum measurements, another modes, for example E_{01}, were exited.

Typical oscillogram of microwave pulses, obtained in optimal conditions, is shown on the Fig. 1. Big pulse is radial polarization, the less one is azimuth polarization. The last one can be made much shorter with approximately the same amplitude. Because of constructional features of two solenoid system, changes of magnetic field were possible only within the limits from 5 to 7 kOe. With the increasing of magnetic field to 7 kOe not significant reduction of power was observed. Later all experiments have been held with the field of 6 kOe. Generation completely disappeared when the direction of magnetic field was changed. This fact testify to excitation of only one E_{11} mode and to absence of another, not BWO's, mechanisms of generation. Pulse duration achieved in some regimes 20 ns and the time of transient processes didn't exceed 3 ns. So short transient process testify of significant exceeding of beam current over starting value.

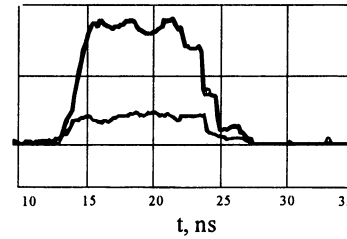

Fig. 1. Oscillogram of microwave pulses (azimuth and radial polarizations)

It is noticeable, that there is no second microwave pulse after the main one even in the case of pulse duration more than 20 ns. In experiments we try to check the idea of cyclotron absorption of second microwave impulse. Since second electron beam has the less energy of electrons, the cyclotron absorption zone shifts to weaker magnetic fields, i.e. in the operating region. Apparently pulse shortening should be explained by the same reason. In our opinion the development of such effect should improve consumers properties of oscillators, especially for radar applications. The generation of the second pulse is undesirable in radiolocation because of reduction of resolution.

As a reflector in the cathode end of elecrodynamic structure axial-symmetric not too high step have been used. Step reflects only a part of radiation (about 0.3–0.5), that permitted in the fist stage of experiments reduce the probability of undesirable feedback due to reflecting and practically exclude phenomena of breakdown. At not too high step E_{11} mode rather badly emitted to rotating H_{11} mode, that is absorbed in the region of insulator. Coefficient of transformation into following H_{11} wave at supercritical reflector:

$$K = \frac{P(H_{11})}{P(E_{11})} \approx 1.7 \frac{k^2}{h(E_{11})h(H_{11})} \left(\frac{R_0 - R}{R_0} \right)^2 \approx 0.5, \qquad (3)$$

where $P(H_{11})$ – the power in through-passing H_{11} mode; $P(E_{11})$ – the power in operating E_{11} mode; $k = \omega/c$; R – radius before reflector; R_0 – radius of reflector; $h(E_{11}), h(H_{11})$ – longitudinal wave numbers of E_{11} and H_{11} modes respectively. Coefficient of transformation, as it follows from the formula, has weak dependence on the frequency, so it didn't cause any inconveniences in measuring of output radiation parameters, except the power of output radiation. Because of uncontrolled magnitude of power loss, output power could be only estimated. Employment of high modes raises the difficult problem of reflecting and maybe transformation of the wave type. Radical solution of the problem can be achieved by using a Bregg reflector.

Theoretical investigations

For the purpose of theoretical description of cyclotron effects in BWO near cyclotron resonance rather simplified model was used. The model takes into account the interaction between the electron beam and one of the eigen waves, existing in the electrodynamic structure. It is supposed that the condition of cyclotron synchronism with fundamental spatial harmonic is fulfilled:

$$\omega \approx \omega_H + h_0 v \tag{4}$$

and cherenkov synchronism with one of the slow harmonic (specifically -1) is fulfilled too (see (1)). Simultaneous fulfillment of both conditions (1),(4) gives the magnitude of resonant magnetic field

$$H_{res} \approx \gamma\beta \frac{mc^2}{e}\frac{2\pi}{d}, \tag{5}$$

that doesn't depend on individual characteristic of eigenmode. Under these conditions we have the self-consistent set of equations (6).

$$\begin{aligned}
\frac{dc}{d\xi} &= -\int_0^{2\pi} (e^{i\varphi} + \alpha\rho e^{i\theta}) d\varphi_0, \\
\frac{d\rho}{d\xi} &= -Re\left(ca\varepsilon e^{-i\theta}\right), \\
\frac{du}{d\xi} &= Re\left(ce^{-i\varphi} + ca\rho e^{-i\theta}\right), \\
\frac{d\theta}{d\xi} &= \delta_2 + 2u(1-\varepsilon) + n\rho^2 + Re\left\{c\frac{\alpha\varepsilon}{\rho} ie^{-i\theta}\right\}, \\
\frac{d\varphi}{d\xi} &= 2u - \delta_1 + \rho^2.
\end{aligned} \tag{6}$$

Here c – amplitude of electromagnetic wave, ρ – transverse momentum of electron, u – energy variable, θ,φ – cyclotron and cherenkov phases respectively, ξ – longitudinal coordinate, $\delta_{1,2}$ – mismatches of cherenkov and cyclotron synchronism respectively, a – coupling coefficient with cyclotron wave, $\varepsilon = \gamma_0^2(1-\frac{h}{k}\beta_{z0})$, $n = \frac{h}{k}$.

First in this model we obtained the typical dependence of output amplitude of electromagnetic wave (C_0) on the mismatch of cyclotron synchronism δ_2, which is proportional the magnitude of the focusing magnetic field. Fig. 2 shows such dependencies, obtained with two different values of parameter α, that define efficiency of cyclotron interaction. Varying radius of electron beam and choosing the direction of magnetic field, we can reduce α for one mode (specifically E_{11}) obtaining the curve of the type 1. In the same time for all other modes the value of α is not small, so we have for them curves of the type 2 with the zone of cyclotron absorption. Obviously, in the regions **a, b** and **c** the generation of one mode dominate. We choose zone **a** to be operating since it is situated in weaker magnetic fields. As we discussed above, it permits to remove second microwave pulse after the main one.

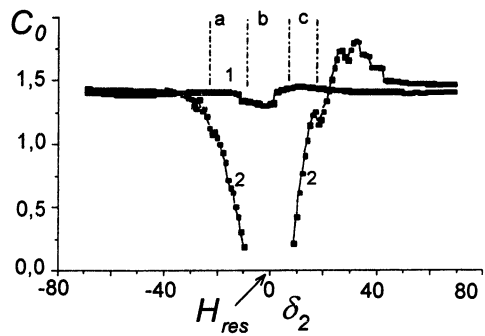

Fig. 2. Dependence of output amplitude of electromagnetic wave C_0 on the mismatch of cyclotron synchronism δ_2; curve 1 - $\alpha = 0{,}03$; curve 2 - $\alpha = 0{,}5$

Theoretical model predicts unexpected solutions for the system without cherenkov interaction but with interacting electromagnetic and cyclotron waves which propagate towards each other. For example, this solution could take place between supercritical reflector and the start of corrugation. Fig. 3 presents amplitude of electromagnetic wave, which is obtained in numerical simulation of boundary problem. Electromagnetic wave propagates from

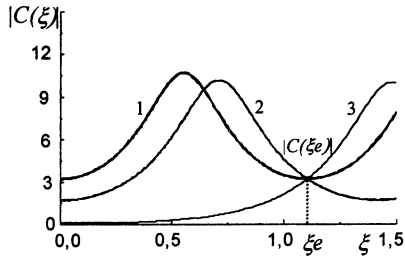

Fig. 3. Dependence of electromagnetic wave amplitude C on longitudinal coordinate ξ

right to left, cyclotron from left to right, so we should set boundary conditions for electromagnetic wave at the right end ($\xi = \xi e$), for cyclotron wave at the left ($\xi = 0$).The solution of such boundary problem is indeterminate, there could be 3 solutions, that are shown in the Fig. 3. We call the curve 1 as a state of "nonlinear Tamm's resonance". The distinction of this state is resonant propagation of electromagnetic wave through the cyclotron interaction space without energy loss, i.e. the amplitudes of electromagnetic wave at the entrance ($\xi = \xi e$) and at the exit ($\xi = 0$) are equal.

Conclusion

In our opinion from all consumers properties of high power relativistic microwave devices the stability and controllability of output radiation are most important. Opportunities that appear with using higher modes, are quite enough to realize stability close to potential barrier. And what is more it is possible simultaneously with reduction of focusing magnetic field, that extremely important in the pulse repetitive regime of generation. Problem of controlling the regime of generation by the external signal also simplifies with using the higher operating modes, because the problem of inputing the signal can be solved comparatively easy.

Acknowledgments

The research described in this publication was made possible in part by Award RP1-243 of the US Civilian Research & Development Foundation for the Independent States of the Former Soviet Union (CRDF) and by Grant № 98-02-17024 of Russian Foundation of the Fundamental Research (RFFR).

References

1. Abubakirov E.B., Belousov V.I., Gintsburg V.A., et. all. Experimental realization of cyclotron-resonance mode selection in relativistic microwave oscillators of cherenkov type // ZhTF Letters, 1983, 9, 9, 533-536 (in Russian).
2. Abubakirov E.B., Kovalev N.F. Cyclotron effects in relativistic microwave devices of cherenkov type // Relativistic microwave electronics, IAP RAS, 7, 1992, 7-21 (in Russian).
3. Abubakirov E.B., Fuchs M.I., Kolganov N.G., Kovalev N.F., Palitsin A.V., Volkov A.B. Reduction of focusing magnetic field in relativistic Cherenkov oscillators // Strong microwaves in plasmas, IAP RAS, 1997, 2, 810-828.

OBSERVATION OF SELF-MODULATION REGIMES IN POWERFUL BWO

N.S. Ginzburg, E.I.Ilyakov, I.S. Kulagin, Yu.V. Novozhilova, A.S. Sergeev, N.I. Zaitsev

Institute of Applied Physics, Nizhny Novgorod, Russia

Self-modulating regimes of generation in X-band BWO of megawatt power level with microwave system in the form of slightly corrugated waveguide was studied theoretically and experimentally. Bifurcation currents corresponding to the oscillation self-excitation, transition to the sinusoidal and then spike self-modulation regimes were in a good agreement with the simulations. The simplification of generation regime under the further current increasing can be explained by the space charge influence.

Introduction

Complex dynamics in backward-wave generators was first studied theoretically in papers [1, 2]. It was shown that as the current exceeds the start value, the regime of stationary single-frequency generation is replaced with the regime of periodic self-modulation, first sinusoidal and then acquiring the shape of a sequence of peaks. As the current grows further, the signal modulation becomes more complicated and loses its periodicity. For the large exceeding of current over threshold generation becomes stochastic. The such sequence of bifurcations was observed experimentally in the non-relativistic BWO with power levels of several milliwatts [3].

This paper is devoted to the theoretical and experimental investigation of self-modulation regimes in BWO with megawatt power level and configuration of the interaction space typical for relativistic BWO [4] (smoothly corrugated waveguide with cut-off narrowing at the cathode end and diffraction output of radiation from the collector end). Obviously, the achievement of chaotic self-modulation in such generators opens prospects to create powerful noise sources operating in the X-band wavelength range.

As a source of electron pulses we used the "Saturn" accelerator based on a magnetron-injection gun with a thermal cathode that allowed formation of beams with duration up to 10 μs, energy of particles up to 300 keV, and current up to 300 A [5].

At the previous stage of experiments on the observation of self-modulation regimes in BWO the lowest mode TE_{11} was chosen as the operating one to avoid the resonance interaction of electron beam with other modes and the problem of mode selection [6]. To provide single mode generation the operating point at dispersion diagram was closed to cut–off frequency in the region of small group velocities. In this region from the one hand the coupling impedance was rather high that was favorable for observation of self-modulation regimes, but from the other hand there were some complications related with spurious reflections from the collector end. These factors resulted in the increasing the electromagnetic field strength inside the interaction space, so the power was limited by RF breakdown at the level 50–100 kW under the pulse duration of about 10 μs.

The main goal of the present stage of the experiments is the achievement of self-modulation regimes in BWO of megawatt power level. The exceeding of operating current over threshold required for the achievement of self-modulation regimes is provided by choice of the E_{01} operating mode having the higher coupling impedance with the electron beam to respect of H_{11} mode. In operating point the group velocity of E_{01} mode was high enough ($0.25\,c$) to ensure the output of radiation energy from the interaction space without strong reflection. The theoretical analysis of two transverse mode competition demonstrated the possibility of single mode self-modulation regime under simultaneous nonlinear suppression of other mode [7].

In the first section of this paper numerical simulation of the self-modulation regime in BWO is carried out in the frame of time domain approach. In the second section the results of experimental observation of self-modulation regimes at E_{01} operating mode are presented. It is shown a good agreement between simulation and experimental results.

1. The numerical simulation of nonstationary processes

Let us consider the BWO model with axially symmetric slightly corrugated slow-wave structure, driven by thin hollow electron beam. Preliminary simulation of multifrequency dynamics in the BWO generator was performed based on the self-consistent system of equations [1], which includes the equation for the field amplitude

$$\frac{\partial A}{\partial \tau} - \frac{\partial A}{\partial \varsigma} = -\frac{J}{\pi}\int_0^{2\pi} \exp(-i\vartheta)\, d\vartheta_0 \qquad (1)$$

and relativistic electron motion equations

$$\frac{\partial \vartheta}{\partial \varsigma} = \frac{1}{\sqrt{1-\gamma^{-2}}} - \frac{1}{\sqrt{1-\gamma_0^{-2}}}, \tag{2}$$

$$\frac{\partial \gamma}{\partial \varsigma} = \mathrm{Re}\left(A(\varsigma,\tau)\exp(i\vartheta) + i\sigma \sum_n f_n \rho_n \exp(i\vartheta) \right). \tag{3}$$

Here $A = eE_z/(mc\omega)$ is the dimensionless resonance field amplitude, $\tau = \omega(t - z/v_0)/(1/\beta_0 + 1/\beta_{gr})$ and $\varsigma = \omega z/c$ are the dimensionless time and longitudinal coordinate respectively, $\vartheta = \omega t - hz$ is the electron phase relative to the synchronous wave, $J = eI|Z|/(2\beta_0^2 mc^2)$, Z is the coupling impedance [8], I is the beam current, γ is the relativistic mass-factor, ω is the frequency of precise synchronism, $\beta_0 = v_0/c$, $\beta_{gr} = v_{gr}/c$, where v_0 is initial velocity of electrons, v_{gr} is group velocity of the wave. The second term in the right-hand part of Eq.(3) describes the Coulomb interaction, $\rho_n = \frac{1}{\pi}\int_0^{2\pi} \exp(-in\vartheta) d\vartheta_0$ is the harmonic of space charge density, $\sigma = \left(Iegc^2\right)/\left(mc^3\omega^2 b\right)$ is the space charge parameter, $f_n = 1 - \exp\left(-2gn(a-b)\right)$ is the coefficient of space charge field reduction due to metallic walls, $g = \left((\omega/v_0)^2 - (\omega/c)^2\right)$ is the transverse wavenumber, a is the mean waveguide radius, b is the electron beam radius. The boundary and initial conditions for equations (1)–(3) have the following form:

$$A|_{\varsigma=l} = 0 \ , \ A|_{\tau=0} = A_0(\tau), \ \ \vartheta|_{\varsigma=0} = \vartheta_0 \in (0,2\pi), \ \ \gamma|_{\varsigma=0} = \gamma_0, \tag{4}$$

where l is dimensionless length of the interaction space.

The numerical simulation was carried out under the different values of electron current for the BWO with parameters closed to the experimental ones. The length of slow-wave structure was 41.5 cm, the average waveguide radius was 1.4 cm, the period of slow-wave structure was 1.7 cm, the electron beam radius was 0.9 cm, the energy of electrons was 150 keV. Impedance 0.9 Ohm at operating frequency 8.7 GHz and start current 6A were found based on the results of [8]. In Fig. 1 the output power temporal dependence, as well as the spectrum of $|A|^2$ at different values of current is shown. Fig. 1a corresponds to sinusoidal-

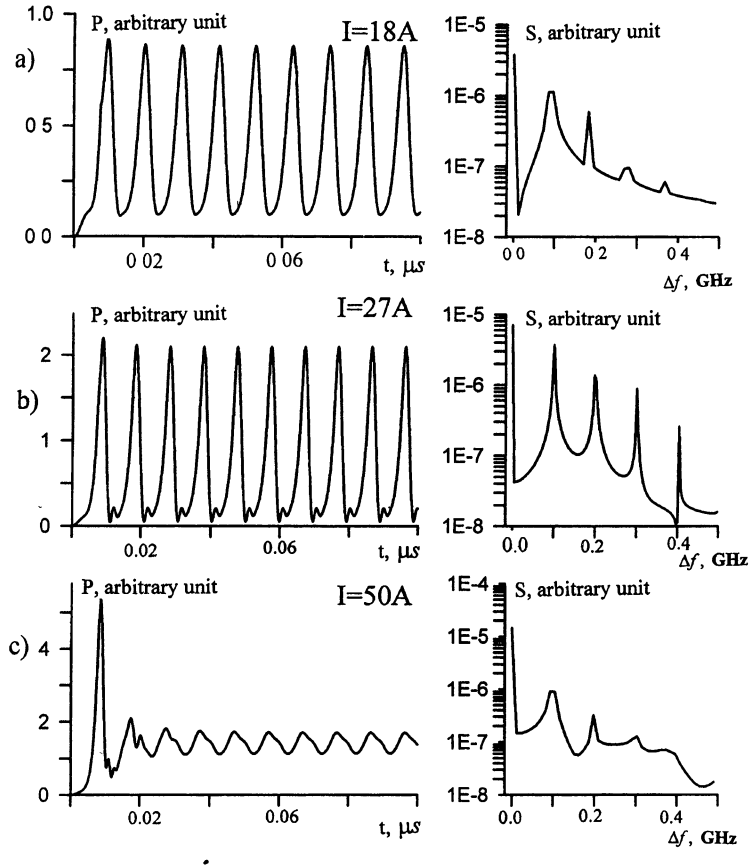

Fig. 1. Evolution of wave amplitude and spectrum with increase of electron current (simulation)

like self-modulation regime under the current 18 A. In fig. 1b the more complicated regime in the form of a periodical sequence of spikes under the current 27 A is presented. It is important to note that the further current increasing for the constant impedance results in the self-modulation suppression due to the space charge influence [1]. As it is seen in Fig 1c for the current 50 A the self-modulation became again close to the sinusoidal one.

Under the group velocity $0.25c$ and drift velocity $0.62c$ self-modulation period is 10 ns. The relative width of the radiation spectrum is 5%.

We simulated also dynamics of BWO with interaction length 61 cm, i.e. one and half time more than the experimental one. The results of simulation showed that the increasing of length should provide possibility to achieve a stochastic self-modulation regime under the current 40 A. The space charge influence in the long BWO has to be less than for short variant.

2. The experimental investigation of self-modulation regimes

In the experiments the output signal was recorded by the digital Tektronix TDS-540A oscilloscope. It allowed storing in memory all the envelope of the high-frequency pulse with total duration up to 10 μs for further analysis of its separate plots. The sections of oscillogramms corresponding to equal accelerating voltages but different values of the operating current are shown in Fig. 2. Radiation was registrated on the collector end of the interaction space. As it is seen from Fig. 2a, at current of 18 A the regime of sinusoidal self-modulation was observed, and as the current increased, the time dependence of the amplitude became more complicated (Fig. 2b). The main period of self-modulation was about 10-11 ns, that corresponded to simulation results. At the current more than 50 A the self-modulation was someway suppressed and acquired sinusoidal form again (Fig. 2c). Based on simulation such suppression can be explained by the space charge influence. In general we believe that experimental results was in a good agreement with the simulations.

There was a high reproducibility of operating regime from pulse to pulse, exclude the part of voltage pulse back front. The radiation pulse asymmetry in the fronts of voltage pulse can be explained by HF breakdown, caused by the bombarding of microwave system by stored positive ions. The duration of radiation pulse became shorter with the increasing of accelerating voltage. Due to this fact it is very probably that radiation power limitation was caused by HF breakdown. The average radiation power in self-modulation regime measured by calorimeter was 0.5 MW under the current 30 A, voltage 150 keV, i.e. electron efficiency amounted to 10 %.

Conclusion

Self-modulation regimes in BWO with megawatt power level have been observed. As the beam current increased from 10 A to 30 A the transitions from stationary regime to deep self-modulation regime took place. In a good agreement with the simulation results the self-modulation period was 10 ns. Under the constant impedance the further

increasing of beam current led to the simplification of generation regime that can be explained by the influence of space charge.

In the part of oscillogram presented in Fig. 2c the self-modulation regime had the periodic character. Nevertheless in the some cases the

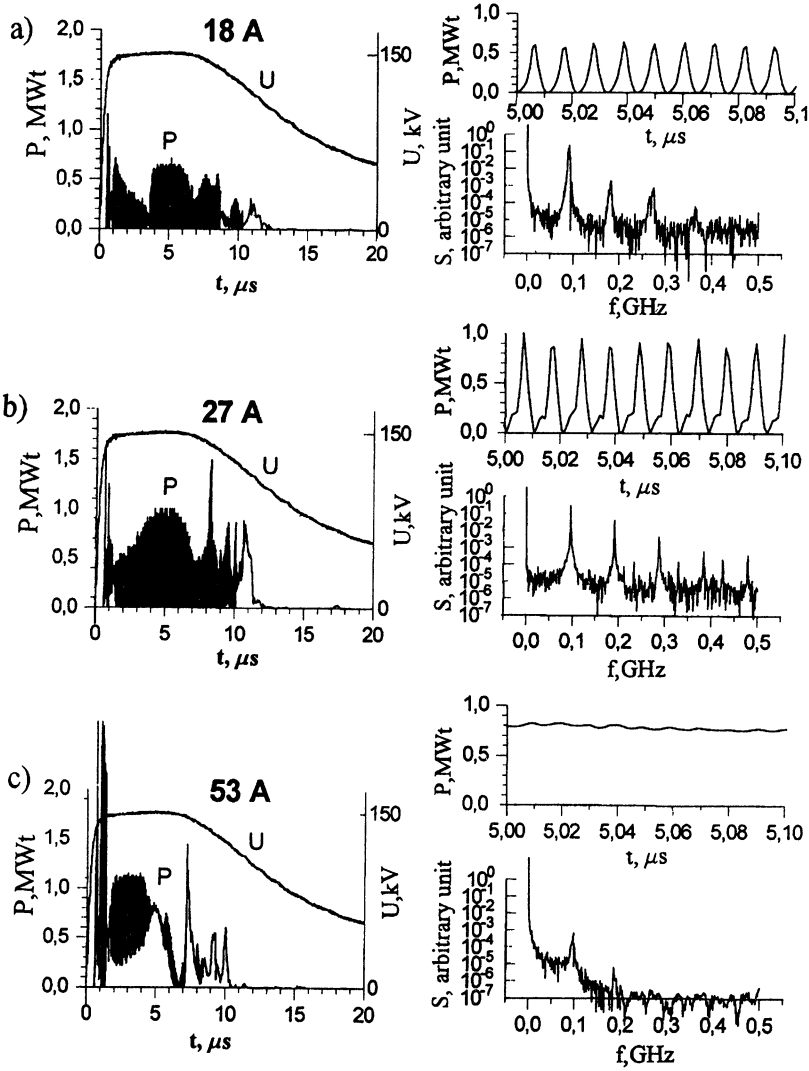

Fig. 2. Experimental oscillograms of output signal amplitude under different electron currents

slight variation of self-modulation spikes profile occurred. However, these variations might be correlated with the changing of accelerating voltage.

At the next stage of experiments we are planing the observation of stochastic regimes in BWO. For this aim on the base of simulation results the length of BWO interaction space will be increased in 1,5 time to respect of the tested model. We also intend to use a special technology for the increasing of microwave system breakdown strength. That can permit us to increase operating voltage, currents and output power. It should be noted that with the voltage growth impedance also increases. All these factors can lead to the increasing up to factor 10–12 the exceeding over the threshold under the simultaneous decreasing of space charge influence.

The work was supported by the Russian Fund for fundamental investigations, grant N 97-02-1761.

References

1. Ginzburg N.S., Kuznetsov S.P., Fedoseeva T.N. Izv.Vuzov. Radiofizika, 1978, **21**, 1037.
2. Ginzburg N.S., Kuznetsov S.P. Relativistic High Frequency Electronics. The Problems of Power and Frequency Enhancement. Gorky; IAP RAS, 1981, 101.
3. Bezruchko B.P., Kuznetsov S.P., Trubetskov D.I. Nonlinear Waves. Turbulence and Stochastics, Gorky, IAP, 1980, 29.
4. Kovalyov N.F., Petelin M.I., Raizer M.D. Pis'ma ZhETF, 1973, **18**, 232.
5. Ilyakov E.V., Zaitsev N.I. et.al. Intense Microwave Pulses III. Proc.SPIE, 1995, **2557**, 457.
6. Ginzburg N.S., Zaitsev N.I., Ilyakov E.V., et. al. Pis'ma ZhTF, 1998, **20**, 66.
7. Ginzburg N.S., Zaitsev N.I., Ilyakov E.V., et. al. Izv.Vuzov. Radiofizika. 1998, **41**, 1565.
8. Kovalyov N.F. Elektronnaya tehnika. Seria 1. HF Electronics, 1978, N 3, 102.

RADIATION SPECTRA OF CHERENKOV PLASMA MASER

P. S. Strelkov, D. K. Ulyanov

General Physics Institute, Moscow, Russia

The results of investigation of the plasma relativistic microwave oscillator in various modes are presented. The possibility of the microwave radiation frequency variation from 4 GHz up to 28 GHz by means of plasma density changing from $3 \cdot 10^{12}$ up to $7 \cdot 10^{13}$ cm^{-3} (at the power level 30÷60 MW) is demonstrated. Relative width of the radiation spectrum at small values of plasma density was 50÷80%, and at major values – 15÷30%.

Introduction

The experiments on the Cherenkov plasma relativistic microwave oscillator (or "Cherenkov plasma maser", CPM) began in 1982 [1]. In [2] the spectrum of full flux of CPM radiation was measured. Both linear and nonlinear theories of Cherenkov plasma relativistic microwave amplifier were developed [3]. In the present work the 7-fold tuning on frequency was obtained, that coincides with calculation. Earlier in [2] such an agreement was not observed. In the rep-rate mode the generation of all microwave frequencies from 4 GHz up to 28 GHz in one burst is possible at power level of 50÷70 MW and electronic efficiency 5%.

This paper is devoted to experimental study of a CPM. The possibility is shown to design a CPM capable to work effectively at lower ($f < 5$ GHz) and higher ($f > 32$ GHz) frequencies. First experiments have shown that a rise of microwave pulse power may be achieved by an increase of electrons energy [4] and preserving the same efficiency.

Experiment

The sketch of the experimental setup is shown in Fig. 1. The accelerator "TEREK-2" generates a high-current REB with the following parameters: electrons energy 500 keV, electron beam current 2÷3 kA, pulse duration of electron current 30 ns. An annular electron beam 4 with the mean radius $r_b = 6$ mm and thickness $\Delta r_b = 1$ mm propagates inside annular plasma 6 with the mean radius $r_p = 7 \div 9$ mm and thickness $\Delta r_p = 1$ mm. Coaxial plasma waveguide where microwaves are generated consists of annular plasma and metal waveguide 7 with the radius $R = 18$ mm. The plasma waveguide is followed by a coaxial emitting

conical horn comprising an exterior 7 and interior 8 cones and a dielectric window 9, through which the radiation is extracted to the atmosphere. The REB and plasma are immersed in a homogeneous longitudinal quasi-steady-state magnetic field ($B = 1.3 \div 2.2$ T) with the duration 6 ms. The plasma is produced in a discharge with a hot ring-shaped cathode [2, 5] in xenon. Gas pressure was $4.5 \cdot 10^{-4}$ Torr. Radius of the plasma is governed by the complementary coil 2.

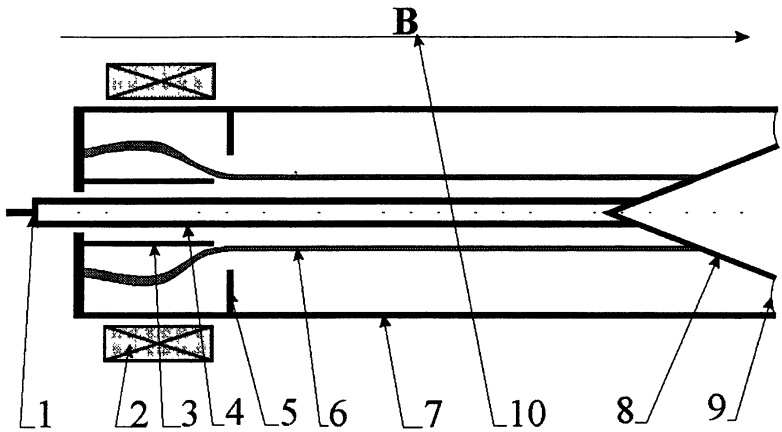

Fig. 1. Cherenkov plasma maser. 1 – cathode, 2 – additional solenoid, 3 – screen, 4 – REB, 5 – diaphragm, 6 – plasma, 7 – metal waveguide, 8 – collector, 9 – dielectric window, 10 – guiding magnetic field

To measure the CPM radiation spectrum the calorimetric spectrometer [2] was used. The total radiation flux energy was measured in several neighboring frequency bands. The boundaries of these bands were defined by the next frequencies: 5.1, 9.3, 12.1, 15.3, 19.5, 24.1, 28.9, 32.4, 38.8 GHz. Typical values of microwave pulse energy E were 1 J with the measurement accuracy 0.05 J.

Results

The dependencies of the total radiation energy on plasma density for several lengths of the plasma waveguide are shown in Fig. 2. The total energy of the REB in one pulse is 30 J (500 keV, 2 kA, 30 ns). Hence, the CPM efficiency in energy is 3%, and the achieved power ~50 MW at the efficiency 5% (the microwave pulse duration 20 ns). With $L = 20$ cm the radiation appears at the threshold value of the plasma density

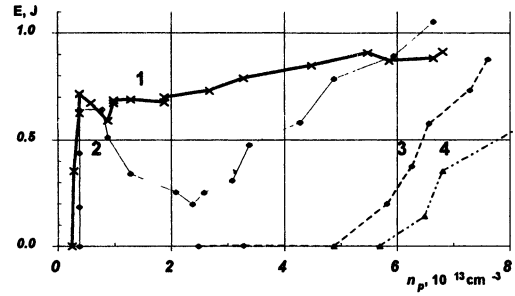

Fig. 2. Microwave pulse energy *vs* plasma density for different interaction lengths [cm]: *1* – 20, *2* – 15, *3* – 12.5, *4* – 10. $B = 2.2$ T, $r_p = 0.9$ cm, $r_b = 0.6$ cm, $p = 4.5 \cdot 10^{-4}$ Torr (xenon)

$2.5 \cdot 10^{12}$ cm^{-3} (*1*, Fig. 2). The device length being decreased, the threshold value of the plasma density grows.

In Fig. 3 similar dependencies $E(n_p)$ for different plasma radii are given. An increase of the gap between the REB and the plasma narrows down the range of plasma densities where the oscillator operates.

The main results of this work are the CPM radiation spectra. The typical spectra for different values of plasma density are shown in Fig. 4. The total energy of a microwave radiation pulse is indicated in each diagram. It follows from our measurements that the spectrum width exceeds the width of the spectrometer bands, $\Delta f > 4$ GHz (Fig. 4).

Several experiments were carried out preserving plasma tube radius $r_p = 0.9$ cm and varying interaction length L and magnetic field B. The obtained results are shown in *Table 1*. Here $f_{\min}$ and $f_{\max}$ are the minimum and the maximum frequencies of microwave radiation, and n_p is

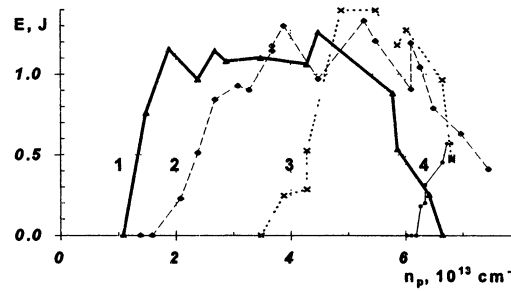

Fig. 3. Microwave pulse energy *vs* plasma density for different plasma radii [cm]: *1* – 16.6, *2* – 18, *3* – 18.8, and *4* – 19.8

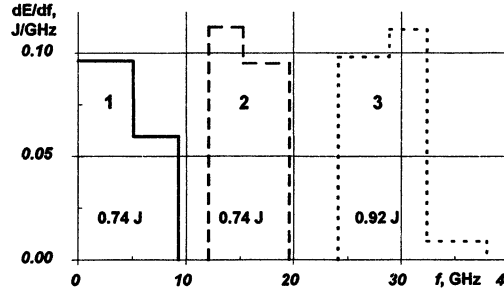

Fig. 4. CPM spectra for different values of plasma density (10^{13} cm^{-3}): *1* – 0.4, *2* – 2.3, *3* – 7.0 (B = 2.2 T, L = 20 cm, r_p = 0.9 cm, r_b = 0.6 cm, $p = 4.5 \cdot 10^{-4}$ Torr)

plasma density, corresponding to the appropriate frequency. The typical bandwidth of oscillations for all sets was ~ 4 GHz.

Two facts follows from this table. First, the minimal microwave frequency grows with L decreasing. Second, the maximal microwave frequency grows with the increase of the magnetic field B.

Comparison of the theoretical and experimental results

Let us compare the dependence of the mean radiation frequency on plasma density for the microwave amplifier in the infinite magnetic field and the experimental dependencies for B = 2.2 T (Fig. 5). Hatching denotes the area where according to calculations the spectral power density exceeds 30% of its peak value. It is seen that in the field of low plasma densities the results of experiments coincide with that of calculations, and for high plasma densities there exists a discrepancy.

Table 1

B, T	L, cm	n_p, $\cdot 10^{13}$ cm^{-3}	f_{min}, GHz	n_p, $\cdot 10^{13}$ cm^{-3}	f_{max}, GHz
1.3	10	1.08	15÷20	6,3	20÷24
	15	0.48	9÷15		
	20	0.25	5÷9		
1.7	20	0.28	5÷9	6,3	24÷32
2.2	20	0.2	0÷9	6,9	24÷32

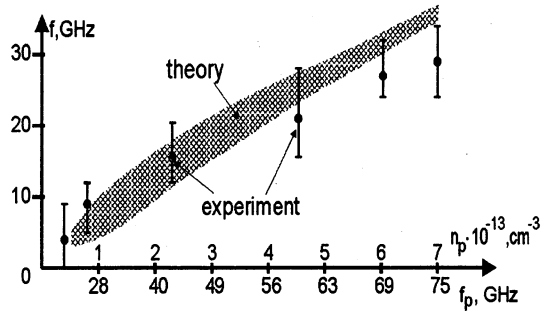

Fig. 5. Mean radiation frequency *vs* plasma density (plasma frequencies $f_p = \omega_p/2\pi$). Dots represent data obtained in experiment ($B = 2.2$ T), hatched area illustrates calculations according to the nonlinear theory

It is possible to explain a discrepancy between the results of calculations and experiments by the fact that in experiment the requirement $\Omega >> \omega_p$ is not valid for high plasma density. In Fig. 5 the measured spectrum widths (vertical segments) are shown. Although the spectrum width were measured roughly, it is possible to state, that for low plasma densities the spectrum widths observed in experiment were approximately equal to theoretically predicted values, and for high plasma densities the former are below the latter.

Agreement of the dependencies of radiation frequency on plasma density $f(n_p)$ obtained experimentally and predicted in theory is the most reliable proof that actually the excited wave is a slow plasma wave which has the lowest radial index and is symmetric over azimuth.

Conclusion

Investigations of the main regimes of the CPM have shown that with the particular geometry and REB parameters the device allows to produce broadband microwave radiation ($\Delta f \sim 4$ GHz). The mean radiation frequency changes from 4 GHz to 28 GHz with the variation of plasma density from $3 \cdot 10^{12}$ to $7 \cdot 10^{13}$ cm^{-3} at practically constant level of power 30÷60 MW (efficiency ~5%). From the engineering standpoint, it is important that this frequency variations can be accomplished during ~30 μs. It is determined by the rate of the plasma density variation [5].

It was proved that the lowest on radial index azimuthally-symmetric mode of the plasma waveguide is excited.

The topmost radiating frequency depends on the magnetic field and the lowest one depends on the interaction length and plasma radius.

High microwave pulse energies (20 J) were obtained in investigation of a CPM driven by a REB with the pulse duration ~1 μs [6]. The pulse duration of microwaves (800 μs) virtually coincided with that of the REB. The maximum pulse power was also about 40 MW.

A study of the CPM at more powerful accelerator (1 MeV, 5 kA, 30 ns) were carried out [4]. Much greater microwave pulse power 450 MW was obtained here.

The authors thank A. A. Rukhadze and O. T. Loza for useful discussions.

The work was carried out with the financial support of the Ministry of Science of Russia ("Unique setup #01-04"), and also the grant of the Russian Foundation of Basic Researches (project # 97-02-16948) and grant «UTS and plasma processes».

References

1. Kuzelev M. V., Mukhametzyanov F. K., Rabinovich M. S. et al, JETP. 1982. V. 54. P. 780.
2. Kuzelev M. V., Loza O. T., Ponomarev A. V. et al., JETP. 1996, № 6. V. 82. P. 1102-1111.
3. Birau M., Krasilnikov M. A., Kuzelev M. V. and Rukhadze A. A. Sov. Phys, Usp. 1997. V. 40.
4. Birau M., Buzzi J.-M., Caillez Y. et al. XXIII ICPIG, Toulouse, France. 1997. V. III. P. 46-47.
5. Loza O. T., Ponomarev A. V., Strelkov P. S. et al. Plasma Physics Rep. 1997. V. 23, № 3. P. 201-208.
6. Loza O. T., Strelkov P. S. and Ivanov I. E. IEEE Trans. on plasma science, Special Issue on high power microwave generation, June 1998. V. 26, № 3. P. 336-339.

INVESTIGATION OF VIRCATORSPECTRUM WITH PLASMA ANODE

A.L.Babkin, E.P.Volkov, A.E.Dubinov, V.S.Zhdanov, V.G.Kornilov, V.D.Selemir, N.V.Stepanov, A.V.Serov, V.G.Suvorov, A.A.Khizhnyakov, V.I.Chelpanov

Russian Federal Nuclear Center, Sarov, 607190, Russia

Investigations of vircator with plasma and mesh anodes on "KOVCHEG" accelerator are described. The accelerator is powered both directly from storage capacitor bank (low-voltage regime), or from inductive storage with plasma open switch (high-voltage regime). Microwave generation in the spectral band of 1...2 GHz is recorded. Microwave spectrum of vircator with plasma anode is shifted to the long-wavelength direction in comparison with spectrum of vircator with mesh anode.

"KOVCHEG" device

Experiments with plasma anode were performed on the accelerator of direct operation "KOVCHEG" [1, 2]. The device (see fig. 1) consists of storage capacitor 1, based on four Marx generators having total capacity of 1.28 μF and power-consuming up to 80 kJ at voltage of up to 350 kV, coaxial transmitting line 2 having inductance of 1 μH, plasma open switch 3, diode section 4, plasma anode unit 5, drift pipe 6 with the diameter of 355 mm and length of 1 m with radiation bend mesh 7 and output window 12.

Graphite planar cathode with the diameter of 160 mm, plasma [2] or mesh anodes were used at the experiments. In the latter case the mesh was set up on the diode side of the plasma anode unit. Distance between the cathode and plasma anode unit cut (diode gap) was changed within the limits of 20...80 mm. During the experiments on investigation of vircator with plasma anode [2] it was found out that intense passing by current forms in this regime. Because of this a significant electric charge, initiating breakdown on the window surface, appears on the output window of the cylinder drift chamber. This shorten the duration of the recorded microwave radiation. We managed to significantly decrease this effect setting bending unit 7 with the reflecting mesh. Radiation output was performed at right angles to axial line of the drift pipe through the window 12.

Current on the input of the transmitting line I_a, diode current I_d, "vircator" current I_V immediately after the anode, passing by current I_{out} on the entrance of radiation bending unit were recorded with Rogovsky coils (8, 9, 10, 11) respectively. Semi-conducting probe was used for recording of bremsstrahlung time dependence.

Generation signal envelope form was recorded with the help of wide-band antenna P6-23A with certified characteristic in 1÷12 GHz frequency range and vacuum diode 6Д13Д, located into standard waveguide R32. Microwave power was recorded with calorimeter having 34 μV/J sensitivity, certified on the wave length of 3 cm, which was located immediately after the output window.

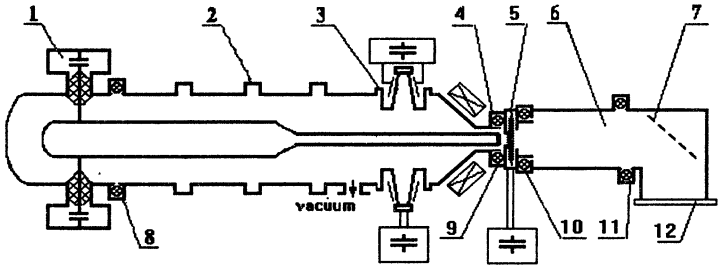

Fig. 1. Schema of KOVCHEG device:
1 – Marx generator, 2 – coaxial transmitting line, 3 – plasma open switch unit, 4 – magneto-insulated anode, 6 – microwave generator (vircator chamber, drift pipe), 7 – radiation bend mesh, 8, 9, 10, 11 – Rogovsky coils, (8 – I_a, 9 – I_d, 10 – I_V, 11 -I_{out}), 12 – radiation output window

At spectral investigations microwave signal was sent to the scope input, which recorded the signal fragment of 5...20 ns duration. Using special software this oscillogram was subject to Fourie-transformation. This allowed to obtain the spectrum of radio signal in the recorded sample.

Experimental results

Vircator with plasma and mesh anodes in the regime of accelerator powering from the inductive storage with plasma open switch.

Accelerator powering from the inductive storage with plasma open switch at the described experimental series allowed to change diode voltage and shorten current front. Plasma generation duration of the open switch t_S and plasma anode t_a before engaging of Marx generators were changed at the experiments.

Fig. 2 shows characteristic signals, obtained with the diode gap of 40. Voltage U_r on the effective load of the inductive generator was obtained with processing of full current I_t oscillogram using Kirhgoff equation.

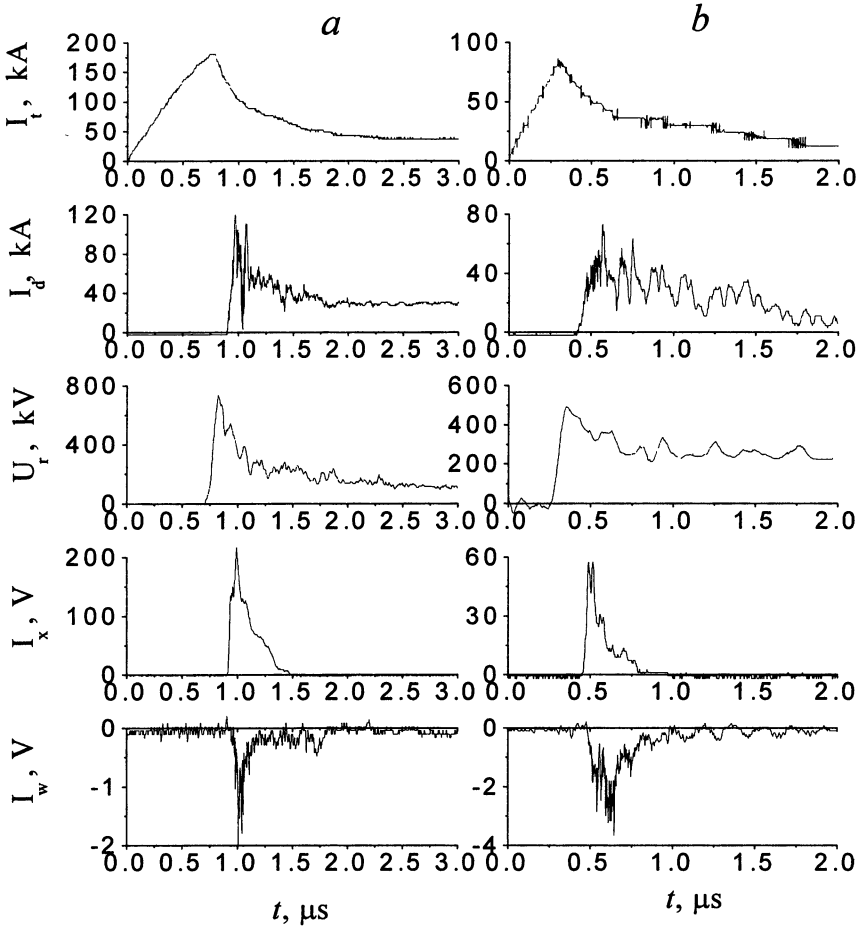

Fig. 2. Signals obtained with 40 mm diode gap:
a– vircator with the mesh anode,
b– vircator with the plasma anode

Since before the moment of current breaking Marx generators are discharged not completely, after high-voltage pulse, generated with inductive storage, the voltage, left on the inductive storage, is applied to the diode. Thus, one can distinguish two phases in the diode operation.

The first one is non-stationary, high-voltage, high-current – phase of inductive storage discharging. Depending on plasma open switch parameters, peak voltage on the diode was changed from 400 to 1200 kV, duration of the inductive storage discharging – 200...300 ns. Smaller values of t_s delay correspond to smaller peak voltage on the diode. Current, transferred to the diode, is approximately 100 kA in its maximum and about 50...40 kA on quazi-stationary stage at 40 mm gap and, respectively, 140 kA and 75 kA at 20 mm gap. Diode front current is 40...60 ns.

On quazi-stationary phase diode current is higher in case of higher peak voltage generation, and at equal conditions on the first phase – for smaller gaps. Voltage on this stage behaves vice versa.

Characteristic peculiarity of the vircator operating regime at powering using peaker was the significant increase (in comparison with direct drive regime) of the diode currents, when microwave generation and smaller current part, recorded in the vircator chamber, were observed. Microwave generation exists during the high-voltage pulse phase only independently of the diode gap value. Generation energy was 8.5 J. Experiments on generation frequency measurement, performed in the directs powering regime with mesh anode and using plasma anode showed, that spectral vircator radiation range of "KOVCHEG" device differs significantly from the certified one for the calorimeter. It is possible to suppose, that recorded energy is underestimated in comparison with actually generated. Comparison of the results in the regimes with the direct drive and with power sharpening shows, that at equal calorimeter display, the duration of antenna signal is 3...5 times higher at the first case, than at the second, i.e. microwave generation power in quazi-stationary regime is lower, than in non-stationary one. Absence of the generation on quazi-stationary stage could be stipulated, possibly, for too high value of the diode current.

Spectral diagnostics experiments

Spectral measurements of the vircator output radiation were performed both at direct accelerator powering (low-voltage regime), and at its powering from the inductive storage (high-voltage regime). In both cases measurements were performed both with mesh and plasma anodes. In the low-voltage regime cathode-anode gap was 40 mm. Fig. 3 shows curves of radio signals and corresponding radiation spectrums for low-

voltage regime. Here and on the other similar diagrams relative units are laid on the ordinate.

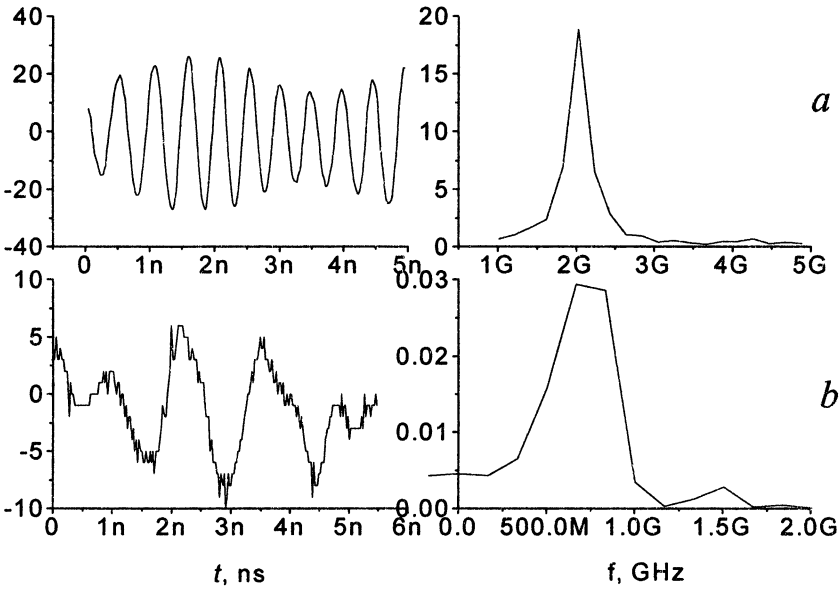

Fig. 3. Radio signals and vircator spectrums in low-voltage regime: *a* – vircator with mesh anode, *b* – vircator with plasma anode

One can see, that noticeable shift of the frequency to the long-wave range is observed in the vircator with plasma anode.

Results of the characteristic pulses for high-voltage regime are presented on Fig. 4. In this regime frequency spectrum of the vircator radiation lies in the range of 1 GHz both with plasma and mesh anode.

The first spectral measurements performed show, that this method allows to estimate microwave radiation spectrum in time interval of minimum 5 ns at any part of the investigated microwave pulse. Having enough scope recorders, it is possible to perform time dependant radiation spectrum measurements during the whole pulse. Spectral measurements in the regime of long-time (microsecond range) pulses should provide with necessary information concerning electron energy, current value, inter-electrode gap dependence on the radiation frequency, since all these parameters are changed.

Further perfection of the method is necessary, but the first results allowed to determine not only frequency range of the vircator radiation,

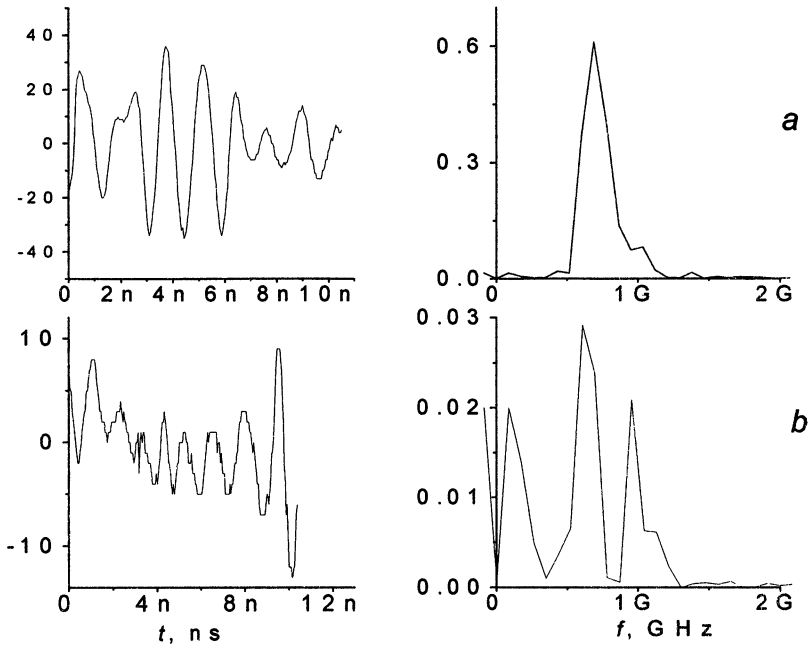

Fig. 4. Characteristic radio signals and vircator spectrums in high – voltage regime:
a – vircator with mesh anode, *b* – vircator with plasma anode

bŭt to detect strong effect of a number of factors on it. Anode plasma happened to be this drastic factor. Spectral results explained sudden decrease of calorimeter display using plasma anode. Characteristic radio signals and vircator spectrums in high-voltage regime.

Discussion

Vircators with relatively low-energy (250...350 keV), and high-energy (0.5...1.2 MeV) electron beam, with mesh and plasma anodes are investigated.

Let us consider the similarities and differences, characterizing each of the vircator operation regimes.

At direct drive (low-voltage regime) increase of the diode current is slow. Microwave generation starts at ~10 kA of the diode current and

ends at $I_d \sim 40$ kA. It seems as if full stachostation of the electron flux in the vircator and generation failure happens at currents of 40 kA. Depending on the diode gap, anode current reaches the value of 40 kA at different time, because of this microwave pulse duration is different. Generation pulses up to 1.5 μs are realized in the direct drive regime.

Preliminary experiments on microwave generation frequency measurements showed, that the vircator radiation spectrum has its maximum on the frequency of ~2 GHz, spectrum width on full width at half length of the intensity of ≈300 MHz at direct drive with mesh anode.

Radiation spectrum is slightly changeable during the generation pulse and almost unchangeable at the diode parameters variation (diode gaps were varied from 20 to 40 mm).

At direct drive with plasma anode maximum of the radiation spectrum was shifted to the frequency range of approximately 1 GHz, though powering conditions and diode gap were almost similar.

In addition to the change of vircator output radiation frequency, application of the plasma anode in low-voltage regime allowed to increase the duration of microwave radiation pulse up to ~ 2.5 μs and eliminate weak element – anode mesh.

The distinction of the vircator in high-voltage regime is, that generation exists 200...250 ns during the high-voltage phase and absents in quazi-stationary phase and at direct drive at currents, higher than 40 kA.

Microwave radiation energy, recorded in high-voltage vircator with mesh anode, was 8.5 J (20 mm gap). On the one hand, short microwave signals duration indicates the significant increase of radiation power, on the other hand – about non-stationary character of the radiation process. In the given regime voltage and current in the diode have relatively short front, improved conditions of the explosive emission and more homogeneous electron beam.

In low-voltage regime vircator currents behind the anode mesh are high, in the order of half of the diode current, and in some cases are equal to it. In high-voltage regime vircator currents are significantly smaller (about 20%) of the diode current both with mesh and plasma anodes.

Geometry of the electron beam, size and evolution of the virtual cathode play important role in radiation formation in the vircator. It was determined, that pinching of the main part of the beam on the one hand,

and electron dispersion and escape to the walls from peripheral beam area on the other hand, is observed.

In high-voltage regime spectral changes showed, that the vircator radiation spectrum both with plasma and mesh anode is shifted to the range of ~1 GHz. Spectrum width is not less than 300 MHz. Spectrums in different experiments have significantly different appearance. Some dependencies of spectral structure on accelerating voltages and beam currents, on plasma anode formation regime are evident. It is not clear why the frequency shifts to the long-wave range at increase of accelerating voltage, especially in high-voltage vircator with mesh anode.

Generation pulse length could be significantly increased in comparison with traditional vircators. Microwave power level in this regime is comparable with the generation energy of the vircator with mesh anode. Experimental investigation shows the necessity of processes study in the system diode-virtual cathode-drift pipe in self-consistent regime taking into account motion of the accelerated fluxes of charged particles in microwave field.

Thus, the perspective of the plasma anode application in vircator systems is shown.

The work is carried out in the frameworks of RFFI project № 99-02-18162.

References

1. Babkin A.L., Chelpanov V.I., Kornilov V.G. et al. Electron Accelerator powered by Inductive Storage Based on Induction Plasma Injectors. Ninth IEEE International Pulsed Power Conference. Albukerque, New Mexico. 1993. V. 2. P. 908-909.
2. A.L.Babkin, V.I.Chelpanov, V.G.Kornilov, et al. Physica Plasmy. 1997. V. 23, № 4. P. 343-349.

VIRCATORS AND VIRTODES

*A.N. Didenko and I.I. Magda**

Russian Academy of Science, Moscow, Russia;
*National Science Center "KhIPT", Kharkov, Ukraine

A modern state of HPM electronics with overcritical current operation regimes is presented as a comparative analysis of a variety of virtual cathode devices. A further progress in vircators is expected in concern with Virtode-like systems – vircators with controlled electromagnetic feedback.

1. Introduction

Essential progress of high-power microwaves (HPM) during last 30 years is a result of successes in the high-current relativistic electron beams (REB) accelerator technologies. On this basis a series of highly effective HPM radiation sources, which use physical principles of non-relativistic devices for both the O- and the M-type had been created. Attempts to decide a problem of radiation power at the expense of beam current increase had come across the existence of a space charge limiting vacuum current J_{SCL} destroying particle motion because of virtual cathode (VC) formation in a drift area.

The high-current charge-neutralized and longitudinally limited electron beam instability resulting in VC formation had been first time treated by Pierce [1]. The effect of self-induction of overcritical current beam and appearance of oscillating particles locked between real and virtual cathodes gave way to a principally new brunch of the HPM electronics, so called VC-systems or vircators. The vircator as a device had been first developed and studied in the USSR at the Institute of Nuclear Physics of the Tomsk Polytechnic University in 1975 [2, 3] and in USA [4].

To compare to magnetron and klystron with their technological upgrade during decades, provided their fluent and successful adaptation to relativistic energies and high currents, vircators has rather short history. The only known non-relativistic and low-current analog of vircator is the Barkhausen - Kurz oscillator - a device where electrons use to oscillate around anode in an area between emissive and reflective cathodes [5].

As it will be shown below a negative result in obtaining of any sufficient efficiency and output radiation power in comparison to vircator is in the nature of this device.

In comparison to conventional HPM relativistic radiation sources vircators have a number of essential advantages. The main is that they are principally high-current and principally intense pulse power devices because their operation is inevitable without an excess of vacuum current limit inaccessible for devices of conventional beam electronics. A simplicity of vircator design together with high output power level (up to 40 GW) and wide tuning frequency band as well as its good adaptivity to various energy storage systems are attractive for a broad application as not expensive and reliable HPM source.

The numerous available data on vircator theory and simulation have shown the possibility to obtain high efficiency levels compared to maximum values for conventional HPM devices. However corresponding experimental results are rather contradictory, as the values on vircator efficiency, obtained in various works, differ more than on 20 times [6]. It is worth mentioning that vircator's potential is not still studied completely. On practice this is chained to difficulties in obtaining electron flows with overcritical current and small velocity spread, and in the field of theory - to complexity in the device linear theory creation because of lack of a small parameter.

To increase a vircator system efficiency and to extend a range of radiation parameter control some progressive vircator configurations had been proposed (reflex triodes, waveguide traveling beam systems, cavity oscillator, reditron, ets). A kind of the traveling beam vircator with a controlled electromagnetic feedback (EMFB) - the Virtode device had been designed and created in the National Science Center "Kharkov Institute of Physics and Technology" in 1989 [7]. From vircators of other type the Virtode differs by its rather large efficiency (up to 17 %) and the possibility of a wide-ranged radiation output power control at the expense of the EMFB conditions variation.

The purpose of the present report is to analyze the role of the EMFB in vircator and to compare various progressive vircator systems on efficiency, spectral characteristics and on conditions of the output radiation parameters control.

2. Vircator system theory

It is general point of view that two mechanisms of electromagnetic generation are realized in vircators. The first one is due to the beam particles flow motion and oscillation around anode in the area cathode - virtual cathode. The second is stipulated by oscillations of the virtual cathode as a whole.

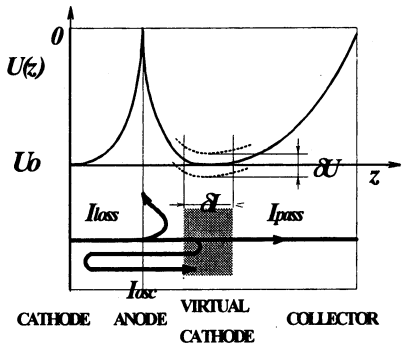

Fig. 1. Currents, potentials and characteristic dimentions of a simplified 1-D vircator model.

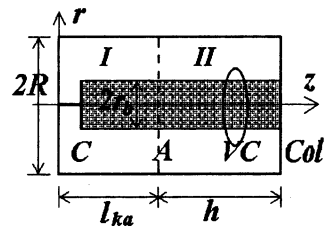

Fig. 2. Simple 2-D model for VC induction in cylindrical resonator of height h; C - cathode, A - transparent anode, Col - collector of REB; I and II - acceleration and drift areas.

The wavelength of the first oscillations is equal approximately to four anode-cathode gap lengths l_{ka}, Fig. 1 and more exactly is

$$\lambda = 6l_{ka}\left(\frac{\gamma_0+1}{\gamma_0-1}\right)^{1/2}\frac{l}{F}, \qquad (1)$$

where $\gamma_0 = E/m_0c^2$ is a relativistic factor, and $1<F<3/2$. So the oscillation frequency is

$$\omega_1 = \frac{c\pi}{3l_{ka}}\left(\frac{\gamma_0-1}{\gamma_0+1}\right)^{1/2}F. \qquad (2)$$

For the second mechanism the oscillation frequency is a function of current density J, and consequently of beam plasma frequency ω_b:

$$\omega_2 \approx 2{,}5\omega_b \approx 20{,}4\pi\,(I_b/\beta\gamma)^{1/2}. \qquad (3)$$

Formula (3) is true for 1-D case, and for 3-D one the coefficient in expression (2) decreases slightly [8].

For the first generation mechanism an oscillation period is $T = 4T_0$,

where $T_0 = l_{ka}/v_0$, $v_0 = (2eU_0/m_0)^{1/2}$, and a gap transit angle is given by small signal theory of reflex klystron

$$\theta = \omega T = 4\pi\, T_0 = 2\pi\,(\kappa - 1/4) = 3/2\pi, \text{ than } \kappa = 1.$$

This means that oscillation frequency is

$$\omega_{osc} = 3/8\pi T_0^{-1} = 3/8\pi v_0\, l_{ka}^{-1} = 3/8\pi\,(2eU_0/m_0)^{1/2} l_{ka}^{-1}. \quad (4)$$

On the other hand, taking into account that the electron density, defined by Child-Langmuir relation, is given by

$$n = \frac{4}{9}\left(\frac{2e}{m_0}\right)^{1/2} \frac{U_0^{3/2}}{4\pi l_{ka}^2}\frac{1}{ev_0},$$

and the plasma electron frequency for the nonrelativistic case is

$$\omega_b = \left(\frac{4\pi ne^2}{m_0}\right)^{1/2} = \left(\frac{4eU_0}{9m_0 l_{ka}^2}\right)^{1/2} = \frac{\sqrt{2}}{3}\left(\frac{2eU_0}{m_0 l_{ka}^2}\right)^{1/2}. \quad (5)$$

Thus, the oscillation frequency corresponding to the first mechanism (4) is equal $2{,}5\omega_b$, i.e. precisely coincides with the oscillation frequency of the second mechanism. Apparently, the cases are possible, where these frequencies do not coincide, but such oscillation modes, when $\omega_1 = \omega_2$, are optimal.

The vircator kinetic theory which takes into account interaction process between beam oscillations and external EDS had been studied in [9]. This approach is based on a solution of the linearized kinetic equation for the distribution function of relativistic electrons, oscillating in an asymmetric potential well.

$$F(r, p_z, t) = N\rho(r, \theta) f(z, p_z, t). \quad (6)$$

Here N is a number of particles per unit length, $\rho(r, \theta)$ is the transverse electrons distribution function normalized per unit, i.e.:

$$\int_s \rho(r, \theta)\, r\, dr\, d\theta \equiv 1.$$

A one-dimensional model of a system, corresponding to variety of real configurations, with the VC located at the axis of a cylindrical resonator with a height h and a radius R, shown in Fig. 2, is used. For description of oscillating electrons motion the following variables - quadrate of the particles oscillation amplitude in stationary conditions a^2, an oscillation frequency Ω and phase $\phi = \Omega t + \phi_0$ are used. The amplitude and phase correspond to the coordinate z and to the momentum p_z, so that $z = l_{ka} + a \sin\phi$, and $p_z = m_0\gamma_0 a^2 \cos\phi$. It is assumed that in gen-

eral case Ω depends on oscillation amplitude. The nonlinearity is stipulated by relativistic effects and the potential well shape deviation from symmetrical parabolic because of high density of the beam current.

In case of the cylindrically symmetric monoenergetic REB with the radius r_b and with the distribution function represented as $f = f_0 + f_1$, where $f_0(a^2) = A\delta(a^2 - a_0^2)/(\pi m_0 \gamma_0 \Omega_0)$, the dispersion relation takes the form:

$$1 + \Lambda A\, c^2 \sum_{k_z} iZ(\omega) \left\{ \frac{l\partial\Omega/\partial(a^2) I_l(k_z a)}{(\omega - l\Omega)^2} + \frac{\partial I_l(k_z a)/\partial(a^2)}{\omega - l\Omega} \right\}_{a=a_0} = 0, \qquad (7)$$

where: $\Lambda = \dfrac{\omega_{be}^2}{2\pi_0 \Omega_0^2}$; $A = \left[1 - \dfrac{1}{2\pi\gamma} \int_0^{2\pi} [\gamma(a_0^2, \varphi) - 1] d\varphi \right]^{-1}$;

$\Omega_0^2 = \Omega(a^2)$; $\gamma = \gamma_0(a^2)$; $Z(\omega)$ is the impedance of a systems corresponding to the high-frequency electromagnetic Z_v^{HF} and coulomb Z_v^C fields:

$$iZ(\omega) = \sum_v iZ_v^{HF} \frac{\omega + i\alpha_v}{\omega_v^2 - \omega^2 - i\alpha_v \omega} + \frac{i}{\omega} Z_v^C,$$

$$iZ_v^{HF} = 16 \left[\varepsilon_M k_\perp^2 r_b^2 l_{ak} \rho_\perp^2 \right] \left[h k^2 R^2 J_n'^2 (k_\perp R) \right]^{-1},$$

$$Z_v^C = -Z_v^{HF} \frac{k_z^2}{k_\perp^2}.$$

Here it is taken into account that $\alpha_v = (1-i)(\omega\omega_v)^{1/2}/Q_v$; $\omega_v = ck = c(k_\perp^2 + k_z^2)^{1/2}$; $k_z = m\pi/h$; $m = 0, 1, 2...$; Q_v is the duty-factor of a resonator at frequency ω_v; $\varepsilon_m = 1/2$ for $m=0$, and $\varepsilon_m = 1$ for $m \neq 0$; l is a number of the resonator eigenmode harmonic, and

$$I_l(kza) = (2\pi)^{-2} \left[\int_0^{2\pi} \frac{\gamma}{c} \dot{z} \cdot \cos(k_z a) \exp(il\varphi) d\varphi \right] \times$$

$$\times \left[\int_0^{2\pi} \frac{\dot{z}}{c\gamma} \cdot \cos(k_z a) \exp(-il\varphi) d\varphi \right],$$

$$\rho_\perp = \int \rho(r,\theta) J_n(k_\perp r) \exp(-in\theta) r dr d\theta = 2(k_\perp r_b)^{-1} J_1(k_\perp r_b),$$

for $n = 0$ and $\rho(r,\theta) =$ const over a beam cross section. For radially homogeneous and rather thin beam, then $J_1(k_\perp r_b) = k_\perp r_b/2$, the transverse distribution function is given by $\rho_\perp = \rho_0 =$ const.

From the expression (7) it follows, that there are two mechanisms for the beam particles grouping in vircator: the first, represented by a term ~ $\partial\Omega ./\partial(a^2)$, is stipulated by the oscillators nonlinearity, and the second ~ $\partial I_l(k_z a) / \partial(a^2)$ is connected to interaction between linear oscillators. In the extremely inhomogeneous vircator fields and under conditions $\partial I_l(k_z a)/\partial(a^2) < 0$, the instability is increased.

The starting conditions may be obtained for a resonant system, when the frequency of a disturbance is in resonance with one of the system eigenfrequencies $\omega \sim l\Omega_0 \sim \omega_v$. Thus, if $(Z_v^C / Z_v^{HF})\, Q_v^{-1} << 1$, the coulomb fields practically does not influence on the instability threshold parameters. In the low-Q systems, on the contrary, a contribution of these fields is essential.

The instability increment for a monochromatic and homogeneous on an angle beam oscillating in the resonator with a rather large Q-factor, $Q_v >> 1$, can be simply obtained for a parabolic potential well approximation $U(z) = U_0 [(z-l_{ka}) / l_{ka}]^2$:

$$\xi = \frac{\sqrt{3}}{4}\frac{\lambda}{\pi R}\left\{\frac{3}{2\gamma_0}\frac{l_{ka}}{\lambda}\frac{R}{h}\frac{J_1^2(k_\perp r)}{J_1^2(k_\perp R)}\right\}^{1/3}\Omega_0 . \qquad (8)$$

Thus the following general conclusions may be possible.

- The increment is in proportion to square root of the beam density n_b.
- The less is the relation of generated wavelength to waveguide (or resonator) radius the less is the increment.
- The less is the beam radius inducing the external EDS the less is the increment.

It is easy to calculate, that for a majority of the vircator parameters, which one may meet in practice, $\xi = (0.1 \ldots 0.01)$. It means, that for a ten-centimeter wavelength a time of the REB instability development is $\tau = \xi^{-1} = (0.5 \ldots 5)$ ns.

The starting conditions for the REB currents, corresponding to the beam instability development, had been obtained for the non-monochromatic beam with the energy spread $\Delta\varepsilon$. An analysis has shown [9], that the start current I_S increases along with the system Q-factor decreasing and with the energy spread increasing, and it appears minimum for harmonics with the minimal wave number, $l = 1$. As the electromagnetic field radiation is accompanied by quasilinear increase of the beam energy spread, the exceeding of the threshold spread value $\Delta\varepsilon$,

which satisfies the condition $I < I_S$, leads to stabilization of the beam instability.

Thus, the start current for the beam with the energy spread $\Delta a^2/a_0^2 = \Delta\varepsilon/\varepsilon$ is

$$I_S = \frac{3\pi}{16}\left(\frac{2\pi R}{\lambda}\right)^2 \frac{r^2}{a_0^2}\left(\frac{a_0^2\Omega_0^2}{c^2}\right)^3\left(\frac{\Delta\varepsilon}{\varepsilon}\right)^2 \frac{hl\phi(Q_v)}{2l_{ka}AQ_v\varepsilon_m I_1(k_z a)} \frac{J_1^2(k_\perp R)}{J_1^2(k_\perp r)} I_0.$$

Taking into account, that for cases, interesting for practice: $a_0\Omega_0/c \cong 1$, $\varepsilon_m = 1$ at $l = 0$, $I_l(k_z a) \cong 1/4$, $J_l^2(k_\perp R) = 1/4$, and also that for enough thin beam $J_1(k_\perp r) = (k_\perp r)/2$, the expression for I_S takes more simple form [10]:

$$I_S = 1.2\left(\frac{\Delta\varepsilon}{\varepsilon}\right)^2 \frac{V_{res}}{V_b}\frac{\phi}{Q_v} I_0, \qquad (9)$$

where V_{res} and V_b are the resonator and the beam volumes, correspondingly. For some cases, interesting for practice, for the resonator and beam parameters $\phi(Q) \sim 2$, $Q_v \sim 10$, $V_{res}/V_b \sim 10^2$, according to (9) one may obtain: $I_S \cong 2.5.10^{-3}\ I_0$ at $\Delta\varepsilon/\varepsilon = 0{,}01$, and $I_S \cong 10^{-2} I_0$ at $\Delta\varepsilon/\varepsilon = 0.02$.

3. Basic VC-system configurations

Conventionally all basic configurations of VC-system are divided on two main groups: reflex triodes (RT) and traveling beam vircators (TBV). Layouts for these basic configurations are shown in Fig. 3,a-d. Every VC- system

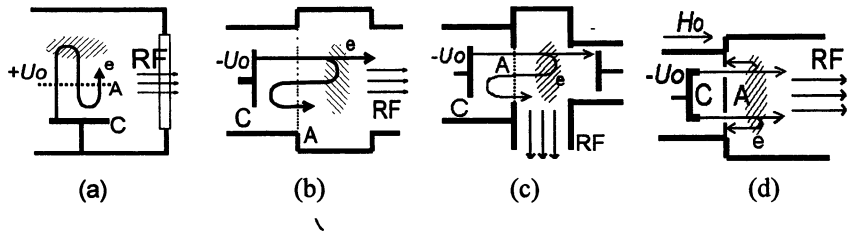

Fig. 3. General view of basic VC-system configurations: a - reflex triode; b - TBV with axial injection; c - TBV with transverse injection; d - Reditron

includes beam transportation channel (by high-current electron emitter, anode block, VC area and beam collector) and variation of EDS. An additional vircator classification reflects means for REB formation and injection into EDS, as well as the EDS peculiarities, determining the system start currents, amplification and conditions for evacuation of the

output electromagnetic radiation. That is why the group of TBV is subdivided on high-Q cavity resonant and low-Q waveguide systems. Apparently the first subgroup is focused on long-pulsed regimes ($\tau > 100$ ns), while another is the best for short and ultra-short pulsed operation mode.

3.1. Traditional types of VC-system

Reflex triode. Concerning to an energy efficiency, the RT appears principally as the most promising VC-system due to the possibility of the 3-D confinement of beam particles, avoiding particle leakage to collector and transport energy losses, Fig. 3,a. The RT would be expected to be more efficient than the traveling beam vircator, insofar as all the beam electrons (injected and reflected) are trapped in the potential well. Ideally, total energy losses for this configuration, consisting of the anode current leakage and the output microwave radiation emission, may be controlled by anode transparency. The anode current losses produce rather strong self-focusing azimuthal magnetic field, providing a radial confinement, whereas the VC high level potential ($U_{vc} \approx U_0$) produces particles trapping in longitudinal direction between real and virtual cathodes. Published experimental and theoretical results demonstrate the RT beam-to-microwave power conversion efficiency exceeds that of the TBV by an order of magnitude.

The second goal of the RT is stipulated to the fact that it is a cavity resonant system. In their reflex motion beam particles in addition to a native beam feedback receive a very strong EMFB from the resonator at some particular frequencies. Thus, the resonant structure is used in order to satisfy two conditions. The first is to provide the resonant frequency of the cavity equal to the frequency of maximum gain for the space-charge instability. The second condition is to provide only one mode with a resonant frequency in the bandwidth where the space-charge instability has significant gain.

An approach, using an analysis of kinetic equation, demonstrates fundamental features of a majority of the resonant VC-systems and allows to interpret the process of the beam particles interaction with EDS [9, 10]. As it had been shown, for system with a high duty-factor (as it is with the resonant cavity TBV or RT) an effect of coulomb fields is negligible, and the space-charge instability grows when the disturbance frequency is in resonance with one of the EDS eigenfrequencies $\omega \sim$

$\sim l\Omega_0 \sim \omega_v$. As it follows from eq. (8), the first condition is satisfied the best for the lowest system harmonic, $l = 1$, corresponding to the space-charge center-of-"mass" oscillations in the VC area. The second may be easily satisfied by the resonant structure design being geometrically adjustable to the frequency of the source.

More precise study [11] has shown a tight correspondence between the space-charge instability excitation mechanism in a variety of VC-systems and the potential well shape. The latter depends on passing beam particles and ions presence in the interaction area, as well as on kind of EDS. A study on advanced RT have shown:

- in contrast to systems operating with currents below vacuum threshold the reflex triodes due to their high level of nonlinearity of the electrons and VC oscillations, which are synchronized with coherent oscillations of an electron flow, can continuously support high interaction and energy conversion efficiency levels between relativistic beam and output radiation;
- the system instability increment is tightly corresponded to a level and shape of potential well nonlinearity;
- the beam particle energy and system geometry optimization results in possibility of the most favorable conditions creation for microwave emission inducing and maintenance at a high frequency band, $\omega = l\Omega_0$ at $l > 1$.

It means that various types of the resonant VC-systems demonstrate a principal difference in starting conditions, increments of instability, and energy efficiency.

Theory analysis of the RT [12] have shown that the microwave feedback could improve an output power by a factor of 40. The first experiments conducted with the RT [3] demonstrated the efficiency about 10 %. In the case of the RT, with a negligible portion of a beam current passing through the virtual cathode, $\omega_b = 0$, and moderate thermal beam spread $\Delta\varepsilon/\varepsilon \sim 4$ - 5 % for a typical REB and cylindrical resonator parameters ($U_0 = 450$ kV, $I_b = 10$ - 14 kA, $r_b = 5$ cm, $R = 30$ cm, $h = 50$ cm, and $Q = 40$ - 60) [9] needed to induce the first resonator harmonic $l = 1$ at $\lambda = 10$ cm, it may be obtained that the system start current and power efficiency, are: $I_s = 2{,}5$ - 5 kA, and $\eta_e = 37$ - 42 %. It needs mentioning that the latter parameter for the electron beam with an initial zero energy spread may exceed 75 %. These estimate data are in a good correspondence with the experiments [13].

The reflex triode has the energy efficiency higher by an order of magnitude, nevertheless it is not free of some problems. These still unsolved problems are: rich spectral composition due to its large cavity volume and the radiation frequency complex dependence on power output, adjusted mostly by the triode anode voltage. In order to narrow its RF spectrum, as a rule, an electromagnetic mode selection is employed with the help of resonator. But this increases the generated pulse duration proportionally to the duty factor [13]. Thus, till the present time the reflex triode is the main candidate for the perspective long-pulsed regime (of 1 mks and more) HPM generator [14].

An important direction in the RT design development is to demonstrate the external signal radiation parameters control. The theoretical and experimental study carried out by the Tomsk group [15], had shown the possibility of the output radiation frequency tuning by means of frequency and amplitude variation of the external signal, injected the into VC-area. The external signal effect has a complex character and appears to be the most efficient when a certain criterion for the amplitudes relation between the signal and accelerating diode fields is fulfilled $E_s/E_{acc} > (f_s - f_0)/f_0^2(\gamma - 1)$. In experiments with the RT generating in 10 cm wavelength band at a 100 - 200 MW power level and at a ratio E_s/E_{acc} = 1/60 - 1/30, the output radiation frequency tuning in the range of 10 % had been obtained.

The recent researches on the electron beam formation in the RT systems allow the Tomsk group [14] to create a facility for the HPM long pulse duration (microwave pulse power - 1.2 GW, efficiency - 12%, and RF pulse duration 1.1 mks). The goal had been obtained by a perfectly shaped high-voltage feeding pulse (sharp front and plate top) and high-voltage diode design. The anode was a specifically formed metal sell, and the cathode was a multi-needle field emission surface.

Axial and transverse beam injection cavity TBV. An extremely developed type of vircators is the TBV Fig. 3, b, c. In contrast to the RT, the devices of this type needs for a collector for a beam passing through the VC area. A VC potential barrier, being lower then an accelerating voltage ($U_{vc} < U_0$), cannot provide complete axial electric field confinement for the supercritical current injected in the interaction area. A sufficiently large portion of the REB current carries the beam energy off a generation circuit resulting principally in lower total system efficiency (by an order of magnitude) in comparison to the RT.

There is a fundamental reason for disadvantages of the axially injected TBV as high-efficiency microwave system. This is large downstream region in comparison to the wavelength. The number of modes available in downstream waveguides or cavities allows many modes to be excited so that as the vircator changes its characteristics because of possible current (voltage) unsteadiness. This breaks the conditions providing the maximum increments in vircator instability mechanism (8). The presence of a large number of resonant modes closely grouped in frequency creates the situation of mode competition that limits the device overall efficiency.

A high-Q resonant structure is to be used to create an electromagnetic feedback and initial cavity field enhancement needed for space-charge instability growth for the selected beam mode. There are a variety of the cavity resonator TBV. They differ on beam injection method and kind and complexity of resonant structure.

As a rule, the injection method is selected to satisfy the condition of a maximum REB power transmitted to and stored by the device resonant system. At the same time the problem of electric strength for the EDS and output vacuum interface is also to be solved. In this case demands for maximal electric strength and optimal vircator system starting conditions result in induction the lowest electromagnetic field modes as the preferable operational EDS modes like this is to be fulfilled for any resonant VC-system.

An axial REB injection into the interaction area is widely used in systems with the cylindrical configuration of the EDS. An azimuthal symmetry of the resonant cavity configuration predicts TM_{011} as the lowest order resonator mode. The most simple are the first vircator systems with axial beam injection into cylindrical waveguide, where extended EDS chamber walls are used as a collector. The coaxial beam and EDS configuration obviously assumes the TM_{01} mode induction in the output waveguide.

In the case of the transverse beam injection systems the conditions for induction a lower TE-modes of rectangular or coaxial cylindrical waveguide are easier. For some transverse injection vircators the EDS contains an intermediate enclosing resonator using slotted wall as frequency filter for the resonator and as mode selector for the output rectangular waveguide [16]. The transverse vircator exhibits similar operational characteristics to the axial vircator. In comparison to the HPM de-

vices with long interaction TBV demonstrates arbitrary low efficiency. It is typically about 2 % for axial and 0.6 % for transverse vircators.

The Reditron [17] is a kind of a traveling beam vircator device, where the specific quality of the "thick" anode with narrow slot together with the external focusing magnetic field promotes a thin separation for the beam particles on trajectories and connects two types of above mentioned particle oscillations, Fig. 3, d. Because of this the BFB takes place only locally close to VC, providing the downstream beam particles bunching in the anode - VC area. As a result the VC oscillations is the only of two vircator operating BFB mechanisms possible for the Reditron device, providing the extremely narrow (of 1 or 2 %) emission spectrum at $\sim 5/2\omega_b$ in the absence of the high-Q resonator.

In addition, as it is stated in [18], the specific quality of the "thick" anode helps to increase the device efficiency by elimination an average VC position shifting. This is due to avoiding the primary REB particles energy scattering, as a result of the two-stream instability excitation under the interaction between the accelerating and reflecting particles in the high-current diode. Nevertheless the Reditron overall milder power performance is a result of a huge particles losses due to the undertaken beam feedback mechanism.

One of recent and promising transverse vircators is the configuration with **radial beam injection into the cylindrical resonant cavity**, which is coaxially oriented to the extracting cylindrical waveguide [19]. From the traditional transverse vircator configuration, it differs by lower starting beam currents and better resonant cavity-to-waveguide matching conditions because of existing mutual mode structure, resulting as it is expected, in higher overall device efficiency.

3.2. Systems with controlled EMFB

Virtode. In recent years a great success in the field of practical assimilation of the HPM technologies, is considered with the appearance of a new type of VC-systems with efficient output control. An alternative approach to the problem of attaining the highest possible efficiency and radiation power in vircator is used in the Virtode configuration, Fig. 4, where the elements creating a high Q-factor resonant circuit within the VC area are basically absent [20, 21].

The principal Virtode configuration, realizing a transverse injection vircator scheme provides the ultra-short pulse (USP) operational regime

and the highest efficiency for lower mode induced in the waveguide EDS. The supercritical REB current is injected into the drift area through a side wall for inducing the fundamental TE_{10} mode of a rectangular waveguide. A strong control on the output parameters is provided at the expense of the EMFB arranged by withdrawal of a portion of the radiation power from the waveguide output into the area of the REB acceleration.

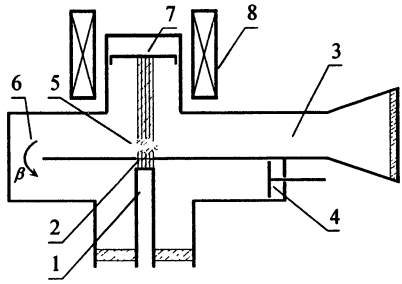

Fig. 4. Schematics of the Virtode: 1) cathode; 2) anode; 3) main wave-guide - output RF circuit; 4) short-circuit piston; 5) VC area; 6) feedback phase reverser; 7) REB current collector; 8) focusing solenoid.

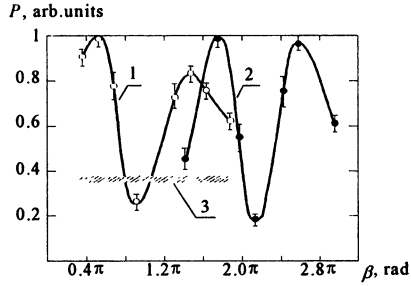

Fig. 5. Emission power as function of the feedback phase for different Virtode tuning conditions at frequency f_0: 1) 4.28 GHz; 2) 4.84 GHz; 3) emission power levels in free oscillation regime (no EMFB).

The goal of the device operation in a control regime is the possibility of a vacuum diode opening ("locked" in the regime of a weak current overcriticality) by means of applying a weak extra voltaging over an acceleration region. The efficiency of such control mechanism in the Virtode is accounted by two factors:

- the diode current high sensitivity to the cathode emission current modulation conditions,
- the EMFB wave-particle interaction takes place at stable particle turning point is diode.

Due to proposed control mechanism the downstream REB current while producing a VC in the interaction area of the EDS, may be preliminary modulated by an appropriate microwave signal injected into the acceleration area. In the Virtode the REB current is premodulated by the feedback signal at a fundamental frequency of the VC oscillations, where the system has maximum gain. This provides high instability increment and total vircator efficiency and narrows the resultant radiation spectrum in contrast to traditional TBV.

The preliminary modulation efficiency in the Virtode can be changed using the assigned phase of the microwave feedback, injected into the acceleration region. The microwave feedback signal phase variation allows to exercise control over a broad-ranged power output with no frequency modification. A movable piston of the feedback circuit makes it possible to alternate a phase of the control microwave signal $U(\beta)$, and due to this the accelerating voltage in the high-current diode esquires a modulating component depending on phase $U = U_0 + U(\beta)$.

An another advantage of the Virtode configuration is obvious from its comparison with the RT. The absence of the microwave energy accumulation in the Virtode device external feedback chain (besides avoiding the danger of the microwave breakdown) results on the VC oscillations stabilization at a certain high-power level due to achieving the threshold level in later time. Thus, the absence of the microwave energy accumulation allows the Virtode to be operated on principally high-power levels, while eliminating the possibility of breakdowns in the electrodynamic structure.

It is known that the time scale for locking the oscillator matched to resonant system by an external signal is determined by the ratio of power levels of a control P_1 and basic P_0 signals:

$$\tau = \frac{Q_L}{4\pi f_0}\left(\frac{P_0}{P_1}\right)^{1/2}, \qquad (10)$$

where Q is the duty-factor of the EDS with the resonant frequency f_0. The possibility of operation at the highest power regimes together with "fast" system response to a control signal may be of great interest for the HPM applications implying the external microwave signal control for the HPM phased arrays operating in the USP regimes [22].

The device produced an intense emission in the range of f_0= 3-5 GHz - the Virtode fundamental emission spectrum, as a result of a transverse excitation of the rectangular waveguide with cross section dimensions of 7.2 × 3.4 cm by the REB current. To obtain an appropriate focusing and transportation to collector for the REB with parameters: energy 450 - 500 keV and current up to 14 kA, a 2 - 6 kG external focusing magnetic field was used as at some kinds of the TBV. The feedback junction provided withdrawal up to 15 % of the radiation output power from the VC area to the REB acceleration gap.

The REB particles dynamics in the vacuum diode was determined by the cooperative effect of the injected microwave fields of EMFB, non-

steady space-charge fields of BFB and quasi-steady-state accelerating field of high-voltage source. The action of these fields resulted in beam premodulation at the VC oscillation frequency. An interference of two signals the phase-varied microwave feedback and the beam feedback (occurred at one and the same fundamental frequency) resulted in dependence of the injection current modulation on the EMFB phase. This mechanism produced an efficient control for the VC oscillations in amplitude and for the output radiation in power.

The characteristic interference envelopes of the radiation output power as a function of the EMFB phase delay $P(\beta)$ shown in Fig. 5 was demonstrated.

It was registered that the central emission frequency $f_C = 1/2(f_{max} + f_{min})$ and tuning frequency band $\Delta f / f_C = 0.37 - 0.52$ were stable and arbitrary spectral width was rather narrow, $\Delta F/f_C \sim 0.1$. The microwave pulse duration was 35 ± 5 ns. The radiation power level being tuned on maximum exceeded the vircator free oscillations power level without EMFB by 5 dB. To compare the generalized performance data for both the autonomous vircator regime (the Virtode operation regime without the EMFB) and the fundamental Virtode regime, they are shown schematically in Fig. 6 as plot *I* and plot *II* correspondingly.

The feedback signal phase β variation by means of feedback junction tuning provided wide-ranged alternation on amplitude of the VC oscillations and accordingly resulted to a general radiation power level control within the limits of 8 dB. A maximum generation power exceeded 500 MW. An efficiency of the Virtode (on power) achieved 17 %.

The passing - oscillating beam current ratio was adjusted by the collector position variation along the beam axis, providing a wide-ranged frequency tuning. An external magnetic field variations produced the device tuning to the maximum power output.

The collector shifting in the drift region because of breaking conditions on the critical current value resulted in a VC central position variation. This mechanism of the beam oscillation mode selection [6] provided tuning on maximum of the beam-mode increment, and consequently the VC emission frequency variation, Fig. 6-*I*. Such a mechanism, regretfully, does not allow the device tuning across a wide frequency band for the fundamental Virtode regime, plot *II*. This can be explained by the necessity of a wide-ranged variations in the relationship between the passing and oscillating components in the structure of the

REB total current. For studied system this ratio can not be done sufficiently high because of limits on injecting beam current.

The validity of a beam-mode selection approach was confirmed in a series of experiments with the Virtode modified by introducing various periodic slow-wave structures (operated in BWO mode) into drift beam area. In created compound EDS the slow-wave structure fields modulated an electron beam at the BWO frequency.

The BWO operational frequencies f_w were selected so that they coincided with or differed from frequencies of the fundamental Virtode oscillations f_0. A coupling efficiency of the electron beam with a periodic structure was controlled by means of a gap variation between the beam and the slow-wave structure internal diameter. Thus, the radiation spectrum of a compound electrodynamic structure contained some or only one frequency, that was determined by a coupling efficiency.

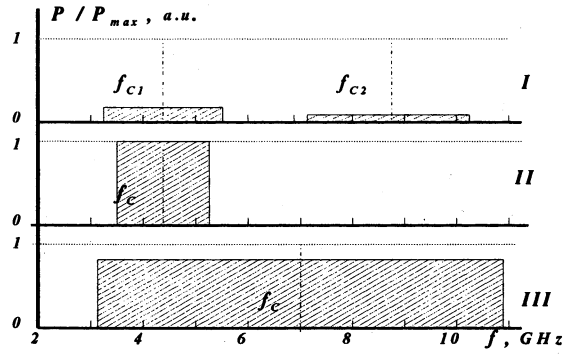

D F/fc	D f/fc	fc, GHz
1)~ 0.11	1)~ 0.52	1)~ 4.3
2)~ 0.07	2)~ 0.37	2)~ 8.7
0.015	0.25-0.3	~ 4.3
0.01-0.02	~ 1	~ 7.0

Fig. 6. Generalized spectral emission parameters of the Virtode, under different experimental conditions: ***I***-autonomous regime (without the EMFB) of device generation; ***II*** - the Virtode fundamental mode; ***III*** - combined system (Virtode-BWO) regime. Shown to the right are:. $\Delta F/fC$ - arbitrary spectral line width, $\Delta f / fC$ - arbitrary tuning frequency band, $fC=1/2(f_{max}+f_{min})$ - central frequency of emission for a given frequency band, and $\Delta f=f_{max}-f_{min}$, - tuning frequency band

In operation of the compound Virtode - BWO electrodynamic structure it is possible to determine three characteristic regimes depending on an interaction efficiency of its main parts by a variety of factors: the axial distance between the Virtode and the BWO, the beam-to-field coupling in BWO, the EMFB/BFB competition in the Virtode, and the microwave power at the BWO output.

A prominent result of the series of the Virtode experiments was a wide-band tuning in the emission frequency. Thus, when a smooth-wall waveguide was used as a drift region for the passing REB for the device tuning with the displacement of the collector, the emission frequency occurred over a range of Δf = 4 - 5.2 GHz. The absolute spectral line width was extremely narrow, ΔF = 60 - 70 MHz. When passing beam induced a variety of periodic slow-wave structure an emission frequency tuning was possible in frequency band Δf = 3.5 - 10 GHz. The results of experimental studies of the emission spectra in the autonomous, basic Virtode, and combined Virtode-BWO stuctures are shown in Fig. 6-*III*.

TBVs with resonant premodulation circuit. A specific position among vircators with preliminary REB modulation is occupied by VC-systems with the external EMFB using resonant quality, as it is with the vircator-klystron, predicted by Sullivan [23] or with the VC oscillator using an effect of a "thick" anode, incorporating resonant cavity, as an intermediate drift and interaction area [24].

a) Vircator-klystron. A new version and system configuration, Fig. 7, of the vircator-klystron for obtaining the supercritical REB current modulation has been proposed and studied in numerical simulations by the Nagaoka University group [23]. The whole system is immersed in an axial magnetic field. An annular electron beam is generated by a foilless diode and is passed through a "thick" anode gap feeding the first cavity. A VC is formed in the drift area behind an anode, representing a coaxial cylindrical resonator with the axial and radial dimensions exceeding operation wavelength. An electron beam collector is placed in the third cavity, which is configured like that of the relativistic klystron amplifier.

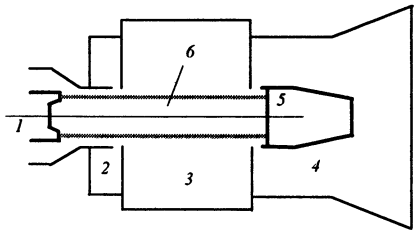

Fig. 7. The vircator-klystron configuration: 1) cathode, 2) input cavity, 3) beam drift area, 4) output coaxial waveguide, 5) passing beam collector, 6) VC region.

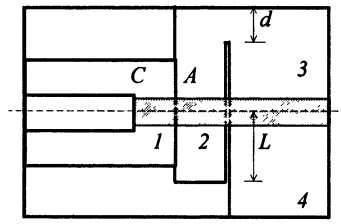

Fig. 8. The TBV with electron beam premodulation configuration: 1) coaxial diode, 2) modulating gap, 3) energy extraction space, 4) microwaves absorber.

The first passive cavity is tuned to the VC oscillation frequency. The most of the electron current is transmitted to the output cavity with the REB current modulation induced by the VC oscillation. The output extraction mechanism from the modulated beam current and its efficiency are supposed to be the same as in the RKA. As it has been found by simulations, if the electron energy of the injected beam is preliminary modulated, large amplitude of the transmitted beam current oscillations can be obtained when the injected current to the space-charge limited current ratio I_{in}/I_{scl} is close to, or even smaller than unity.

As in the klystron, the electron energy of the injected beam is modulated in the bunching cavity, and the microwave energy is extracted in the output cavity from the current modulation of the electron beam. The difference from the klystron is that, in the vircator-klystron, the energy modulation of the electron beam is converted to current modulation due to VC oscillation and that the bunching cavity is energized by the reflected electron beam rather than the external microwave source.

Two-dimensional particle-in-cell simulation results have shown that, within some distance in the direction of beam propagation, the electron beam with the electron energy of 500 keV and current of 3.3 kA is modulated with amplitude up to ~ 57 %. As it had been predicted, the maximum microwave power of ~ 470 MW can be obtained from the electron beam by this modulation mechanism with beam-to-microwave efficiency of ~ 28.5 %.

b) Preliminarily REB modulated TBV. Theoretical study based on a 3-D numerical steady-state experiment, using the electromagnetic PIC code KARAT has been undertaken for a variety of the TBV design operating without an applied focusing magnetic field [24].

Studies of excitation of a simple configuration of rectangular waveguide by transversally injected supercritical electron beam demonstrated some positive effect of wave resonances and the beam current modulation suppression due to the presence of even relatively small energy spread. The passing beam current modulation coefficient (the ratio $\alpha_1 = I_1/I_0$ between the maximum first Fourier harmonic and the constant component) has been chosen as a measure of oscillation efficiency. A rather weak oscillations of VC have been observed for the initial energy spread of 10 - 15%, and the maximum efficiency of microwave emission has not exceed 1-2% (in contrast to 32% efficiency for a monoenergetic beam) even at significant beam currents - two or three times

the critical one. The system microwave emission is poorly self-correlated.

The TBV configuration optimization has been performed to investigate the REB instability regimes and passing beam dynamics in conditions, when the beam current only gently exceeds the critical level. In this regimes, the VC can notably change its current passing capability (from full opening to partial closure) under an external impact. The latter has been suggested to be provided by a resonant circuit, incorporating electromagnetic feedback, that also controls an oscillation frequency.

The Virtode-like TBV configuration, includes a two-sectioned resonant cavity (with modulating and extracting gaps) made from rectangular waveguide and coupled by a rectangular window with aperture *d* through the EMFB path L_{fb}, Fig. 8. It has been assumed that the feedback path is controlled by the reflecting plunger position variation. A radially homogeneous 4 cm diameter electron beam is generated by a planar diode and passes through a transparent foil of a "thick" anode including the modulating gap. A VC is formed in the extracting gap behind an anode. The extracting gap dimensions correspond to the condition of exceeding the characteristic size of one electron cloud - an optimum condition for a beam-to-microwave energy exchange at the fundamental output waveguide TE_{10} mode.

Optimization of the device output radiation parameters done by variation of the EMFB path length have shown: $0.5L_{fb} = L_{opt} = L_{1,2} = \lambda_w/4, 3\lambda_w/4$. It has also been demonstrated that the maximum power corresponds to minimum wave reflections from absorber and generation efficiency decreases monotonously with the increase of the absorption in foils, separating the diode, modulator, and extraction gaps.

In this sense, the system is different from simple VC systems without electromagnetic feedback (vircator-monotron or reflex triode) where optimum foil absorbency is needed for providing a certain beam feedback.

In the regime close to optimum according to the exciting and extraction parameters, the microwave power as well as the system efficiency have expressed maximum of on the injection beam current and waveguide wall size *b*. For a 8.5 kA injection current and a 500 - 700 kV acceleration voltage at the system efficiency exceeding 9 - 10%, there has been an expressed maximum on the output microwave power of 400 MW.

The device frequency tuning is based on a waveguide mode selection mechanism parameter variation. Assuming the phase difference between

the modulating and extracting gaps being independent on oscillation frequency $\varphi = 2\pi L_{fb}/\lambda_w$, one can express the operational frequency as a function of b: $f = f_{cr}\,[1+(\varphi b/\pi L_{fb})^2]^{1/2}$, where $f_{cr} = c/2b$ is a cutoff waveguide frequency. This expression means monotonous frequency tuning over a waveguide frequency band with L_{fb} and b, being limited only by a mode competition process. As it has been shown, at a 1.4 - 1.7 GHz frequency band and a 350 MW average output power the device has exhibited a 5 dB output power variation with parameter b and at a 2.6-3.8 GHz frequency band and a 200 MW power level - a 2.5-3.0 dB output power variation, correspondingly.

4. Comparison between traditional VC-systems and Virtode

On the base of the presented analysis it is useful to compare vircator systems with their low-current and non-relativistic analog - generator with reflective cathode so called Barkhausen - Kurz oscillator. There are some principal differences between these devices.

First of all that is the nature of the reflective cathode, that in the case of the Barkhausen - Kurz oscillator eliminates the parametric amplification regime native to vircator. If the cathode which reflects electrons is driven by an external voltage alternating with the frequency of electron oscillations around anode, the device should work in the mode of amplification. But if the driving voltage is not present, as it is in the case of the Barkhausen - Kurz oscillator, it causes small oscillator efficiency. When the external voltage is however given it might be rather difficult to fulfill the conditions of equality of frequencies. For the vircator this condition is executed automatically because of parametric effect. Thus the device may be regarded as a parametric amplifier which operates in the mode of self-induction.

Another important difference is in the shape of potential well, which in the case of the vircator is principally asymmetric due to relativism and high-current regime. This asymmetry creates conditions for effective particles bunching in external electromagnetic field during short time of their path between cathode and VC needed for obtaining high increments.

At last, the electron flow instability increment should exceed a critical value, when the system parameters variations may be done sufficiently high during one oscillating period. This may be fulfilled only for

the high-current regime native to vircator. Thus, it has to be underlined, that mechanisms of generation of vircators and the Barkhausen - Kurz oscillator differ principally.

Advantages of the Virtode device may demonstrated by comparison with traditional VC-systems - the RT and the TBV in accordance to their basic operational parameters and possibilities to an external signal control. Given the supercritical current systems being associated with one class of HPM devices, one may notice the presence of a strong BFB and EMFB specific for every particular device. Therefore, the complexity and means for providing both kinds of feedback are different for various vircator configurations, detecting their basic features, operation regimes and performance.

The Virtode basic difference from the traditional passing beam vircators is associated with the appearance of principally new control channel, which is based on a strong distributed EMFB occurred between VC area and REB acceleration region. The presence of the EMFB signal in an area of REB formation provides not only the preliminary beam current modulation and the system radiation efficiency increase, but builds up conditions for the system gain control over frequency band given by the EMFB spectral characteristics.

The undertaken experimental study demonstrated the basic advantages of the Virtode as the most promising system for the USP HPM applications:

- The possibility to control the output power of the oscillator based on a passing REB at an efficiency close to the maximum value typical for purely oscillatory regimes.
- The possibility of beam mode selection, as well as good stabilization and the phase and spectrum control.
- A broad-ranged emission parameters variation by means of complex effect of external signal and the system feedback mechanisms, which is especially important for producing microwave devices of a high-power level and USP operation regime.

Theoretical investigation of the Virtode physical model confirmed that the control fields formed in the acceleration area (self-produced and external), essentially influence over the VC dynamics and the device operation on the whole. The radiation output signal and the VC dynamics are the most sensitive to the emission current modulation due to the processes in the acceleration gap. Due to this the possibility for the vircator

system appears to be controlled by means of arbitrary weak signals injected into the particle acceleration area. It was also shown that the external signal variation on amplitude may provide transition between the Virtode stochastic and regular generation regimes. The appropriate amplitude of the injected signal may be amplified in regular regime over a wide frequency range of the original Virtode spectrum.

Being the traveling beam system and possessing adequate output parameters on their absolute value, the Virtode demonstrates an essential (from 5 to 10) magnification on efficiency in comparison to the TBV. At the same time, its efficiency still remains less or comparable to known published data for the RT - the VC-systems with maximum efficiency. There is a simple explanation to this fact, because the Virtode concept has been originally focused to the USP radiation regimes and their applications. To realize just this quality in the Virtode design the role of electromagnetic fields was primary reduced for VC area and, on the contrary, increased for feedback circuit. This was done at the expense of elimination the causes, which promote the microwave field energy accumulation in EDS. The resultant energy extraction efficiency from the beam was reduced in the interaction area, that should decrease the system instability increment.

Conclusion

The represented material contains an analysis of a novel HPM sources, based on supercritical REB current regimes - vircators. A sufficient place in the analysis is denoted to comparison between and traditional schemes of vircators and the Virtode-like -systems on operating mechanisms, efficiency, power and spectral characteristics.

Being based on known practical and theoretical data for the cavity resonant VC-systems one may expect that in case of a high-Q EDS introduction in the Virtode-like configuration, which provides smaller start currents and larger increments, the system overall efficiency improvement may be possible. Thus, such modification of the Virtode as well as the reflex triode configurations are the most promising HPM devices for the long-pulse operation mode.

There are principal limitations on radiated power for microwave devices in conditions of critical levels of an electromagnetic energy loading on mediums and constructional materials, defined by a series of fundamental physical constants and pulse shortening effects. Apparently, this

limit on microwave power is exceeded for modern HPM sources based on REB. Thus, the USP radiation power, which can be extracted from a single-mode EDS does not exceed units, and from a multi-mode EDS - several tens of gigawatts.

The goals for further HPM technologies are focused on producing various methods for the radiation power accumulation and addition for sources with operation mode close to critical. One of the most attractive targets of modern HPM technology is in creation radiation sources with high electrodynamic potential PG based on the ingredient elements emitted in a coherent mode. The system overall gain factor G is in proportion to N^2 for the case of N phased emission modules. Discussion of the phased array ideology application to the high-power USP radiation sources demonstrated the possibility for the synchronized Virtode module to be a base element of the ultra-high-power ($PG = 10^{13}$ - 10^{15} W) sources design and construction [22]. Obviously, this is realizable with a rigid assignment of the phase and narrow spectrum of the control signal which in the case of waveguide EMFB may be provided more easily then for large-volume resonant structures.

References

1. Pierce J.R. Traveling-Wave Tubes, Van Nostrand, New York, 1950.
2. Didenko A.N., Zherlitsyn A.G., Zelenzov V.I., et al. Proc. Int. Conf. on El. Beams Research and Technology. Albuquerque, 1975, 2, p. 424.
3. Didenko A.N., Fomenko G.P., Gleizer I.Z., et al. Proc. 2-nd Int. Top. Conf. on High Power Electron and Ion Beam Research and Technology, Cornell University, Ithaca, NY, 1977, p. 683.
4. Mahaffey R.A., Sprangle P., Golden J., et al. Phys. Rev. Lett. 1977. V. 39. P. 843.
5. Barkhausen H., Kurz K. Phys. Z., 1920, Bd. 21, S. 1.
6. Benford J., and Swegle J. High-Power Microwaves, Artech House, Boston-London, 1992.
7. Gadetski N.P., Magda I.I., Naisteter S.I., et al. Plasma Phys. Rep, 1993, 19. P. 273.
8. Didenko A.N. Doklady Akad. of Sci USSR, 1991, 321, № 4. P. 727.
9. Grigor'ev V.P., Didenko A.N. Radiotekh. Elektron., 1988, 33, № 2. P. 353.
10. Didenko A.N., Zverev B.V. The UHF Energetics, Academy Press of Russia, St-Peterburg, 1995, 293 p.
11. Grigor'ev V.P., Koval T.V. Radiotekh. Elektron. 1990, 35, № 10. P. 2133.
12. Brandt H., Bromborsky A., Burns H., and Kehs A. Proc. 2-nd Int. Top. Conf. on High Power Electron and Ion Beam Research and Technology, 1977. P. 649.
13. Didenko A.N., Arzin A.P., Zerlitsin A.G., et al., in: "Relativistic High-Frequency Electronics", A.V. Gaponov-Grekhov, ed., IAP AS USSR, Gorky. 1984, 4. P. 104.
14. Zerlitsin A.G., Kotlyarevski G.I., Lyakshev A.N., et al. Proc. 11-th Int. Conf. on High Power Electron and Ion Beams "BEAMS '96", Prague, Czech Rep., 1996, 1. P. 492.

15. Grigor'ev V.P., Zherlitsyn A. G., Koval' T. V., et al. Pis'ma Zh. Tekh. Fiz. 1988, 14. P. 2164.
16. Benford J., Price D., Sze H., et al. J. Appl. Phys., 1987, 61. P. 2098.
17. Davis H., Bartsch R., Kwan T. IEEE Trans. Plasma Sci., 1988, 16. P. 192.
18. Davis H., Fulton R., Sherwood E., et al. IEEE Trans. Plasma Sci., 1990, 18. P. 611.
19. Crawford M.T. Ph. D. Dissertation, Texas Tech. University, 1994.
20. Bludov S.P., Gadetski N.P., Kravtsov K.A., et al. Plasma Phys. Rep. 1994, 20, 643.
21. Gadetski N.P., Kravtsov K.A., Magda I.I., et al. Int. Conf. on EMP AMEREM '96, Albuquerque, New Mexico, Abstracts. 1996. P. 79.
22. Magda I.I. and Prokopenko Yu.V. Proc. 11-th Int. Conf. BEAMs '96, Prague, Czech Rep. 1996. P. 422.
23. Jiang W., Masugata K., and Yatsui K. SPIE. 1994, 2154. P. 124.
24. Jiang W., Masugata K., and Yatsui K. Proc. 11-th Int. Conf. BEAMs '96, Prague, Czech Rep. 1996, 1. P. 477.
25. Korovin S.D., Pegel I.V., Polevin S.D., et al. Proc. 12-th Int. Conf. BEAMs '98, Haifa, Israel, 1998.

ACTIVE PULSE COMPRESSION

*A. L. Vikharev, A. M. Gorbachev, O. A. Ivanov, V. A. Isaev, S. V. Kusikov, M. I. Petelin, and J. L. Hirshfield**

Institute of Applied Physics RAS, Nizhny Novgorod, Russia,
* Omega-P, Inc., New Haven, USA

The paper reviews the results in investigation of novel active pulse compressors based on Bragg resonator and different types of plasma switches used for energy extraction in compressors operated in the low-loss TE_{on} modes. An active pulse compressor has been developed that is able to provide output pulses of at least 100 MW power with pulse duration of 100 ns at the X band, and with power gain of 12-15. Variation in phase of compressed output pulse of this active Bragg compressor was measured.

1. INTRODUCTION

The methods of microwave pulse compression have been developed for over two decades. The interest to microwave compressors is connected, primarily, with the necessity to obtain high-power and short-duration pulses in the X-band, which are used in electron-positron supercolliders. This can be achieved by using both passive and active compressors. Up to recently, the object of wider studies was the passive compressor (SLAC energy development-SLED) [1]. Passive compressors do not contain elements with time dependent electrodynamic parameters; but any compressors of the sort implies a special modulation of the primary pulse. This class includes Binary Pulse Compression (BPC) [2], Resonant Delay Lines (SLED-II) [3] and Delay Line Distribution Systems (DLDS) [4]. Passive compressors generally provide peak power multiplication in the range 4-6, with energy efficiency in the range 50-70 %.

In contrast, active pulse compressors have received attention recently [5], on account of the potential they hold for achieving higher peak power multiplication factors. The most widely studied system is a microwave pulse compressor based on storage of microwave energy in cavity and subsequent quick extraction of the energy to a load by a rapid change in the coupling to the load by use of gas switches [6,7]. Best up-to date results obtained are presented in Table 1. These results were obtained with cavities based on oversized waveguides, switches were based on the T-junction. The switched energy storage device most widely studied is shown in Fig.1.

Table 1. The best up-to date results obtained by method of active pulse compression

Frequency, GHz	Power gain	Output power, MW	Pulse duration, ns	Ref.
3	44	70	15	[8]
3	70	100	20	[10]
2.85	23	160	20	[9]
10	50	2.5	8	[10]

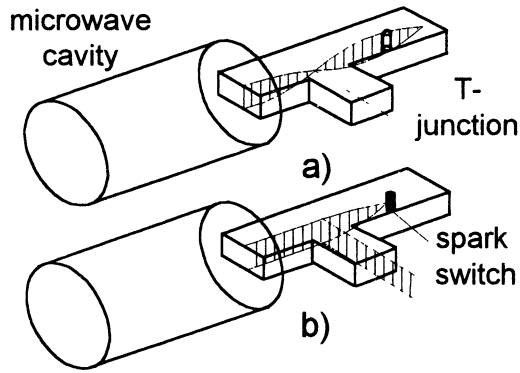

Fig. 1. Switched energy storage and spatial distribution of the electric field during the energy storage cycle (a) and the energy extraction cycle (b)

The simples output switch represent a T-junction of standard single-mode waveguides with a gas discharge gap in one elbows. A standing wave is produced in the storage regime in the T-junction. The node of this wave is situated in the input cross-section of the other arm and therefore the energy does not enter the load. For release of the energy from the store, a plasma is produced at a distance of $\lambda/4$ from the short-circuite and the energy is fed to the load. The switch based on T-junction was successfully used in experiments performed in Tomsk [7], where power gains up to 70 in the single compressor and up to 600 in a three-stage scheme were obtained.

Unfortunately, at the shorter wavelength, such a switch operates much worse. Primarily, this is because the single-mode T-junction has a small cross-section and therefore limits the extracted power. For example, at the atmospheric pressure the power withdrawn from this system in the X-band amount only to a few megawatts [6, 10].

The compressors based on standard waveguides undergo obvious limitations on the carrier frequency, feeding pulse duration and output power. A better performance can be expected with compressors composed of oversize electrodynamic structure and distributed switches. To provide a high power, the pulse compressor should be of a broad cross section and the electric field at the compressor walls should be minimum. From this viewpoint the most attractive seems to use a system with the axial symmetry and operate at TE_{on} modes, which electric field is of ring structure and turns to zero at the metallic walls.

This paper reviews the results in investigation of new type the microwave compressors for operation in the X-band.

2. COMPRESSOR WITH BRAGG REFLECTORS

2.1. Main concept

For operation in the X-band we proposed a new type of the compressor [5,11]. The basic idea consists of using Bragg reflectors in the oversized cylindrical waveguides for storage of microwave energy. A schematic diagram of the compressor is shown in Fig.2.

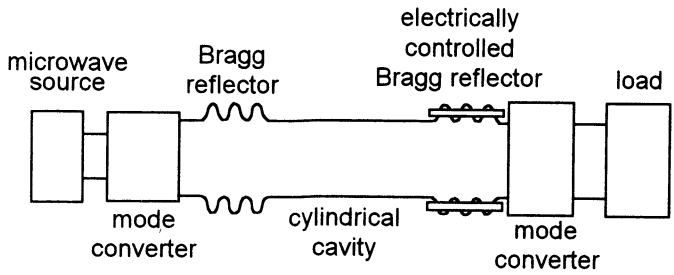

Fig. 2. Schematic layout of microwave pulse compressor with Bragg reflectors

The compressor is the cylindrical cavity limited by Bragg reflectors at both ends. The microwave radiation of the generator is put into the cavity

through one of the Bragg reflector and is put out through the other. Typical frequency characteristic of Bragg reflector is shown in Fig.3.

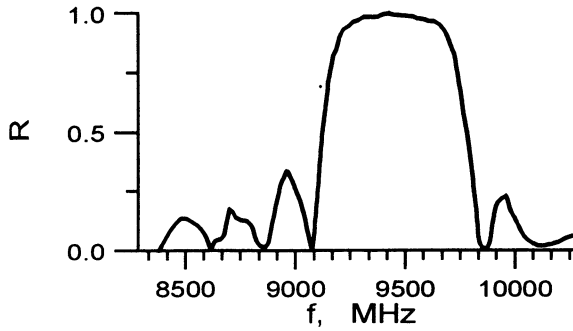

Fig. 3. Typical measured coefficient of reflection for Bragg reflector

The plasma switch placed into the second Bragg reflector is used to switch from the regime of storage of energy to the regime of energy extraction. The compressor operates in the low-loss TE_{0n} mode, the primary microwave generator is coupled to the compressor via a mode convertor.

2.2. Electrically controlled Bragg reflectors

A schematic diagram of the Bragg reflectors with different plasma switches are shown in Fig.4. The plasma switches are made of gas-discharge tubes placed along or inside a periodic structure. The tubes are not switched in the energy storage regime. The plasma in the tubes is produced by supplying a high-voltage pulse to one electrode of the tubes. Provisional results show that the time of switching of such a plasma switch is determined by the propagation velocity of the ionization front in the gas-discharge tube, which, in turn, depends on the high voltage supplied to the tube, the voltage rise velocity, and the gas pressure in the tubes [12]. The experiments show that under 100-150 kV high-voltage pulse of 100 ns duration and gas pressure p=10-100 Torr the velocity of the ionization front in the tubes can reach $V=5\cdot10^9$-10^{10} cm/s. Therefore the time of plasma production in a switch of length ~50 cm can amount to 5-10 ns.

Operation of electrically controlled Bragg reflectors were tested experimentally using low-power microwave radiation. The typical scheme of experiments is shown in Fig.5.

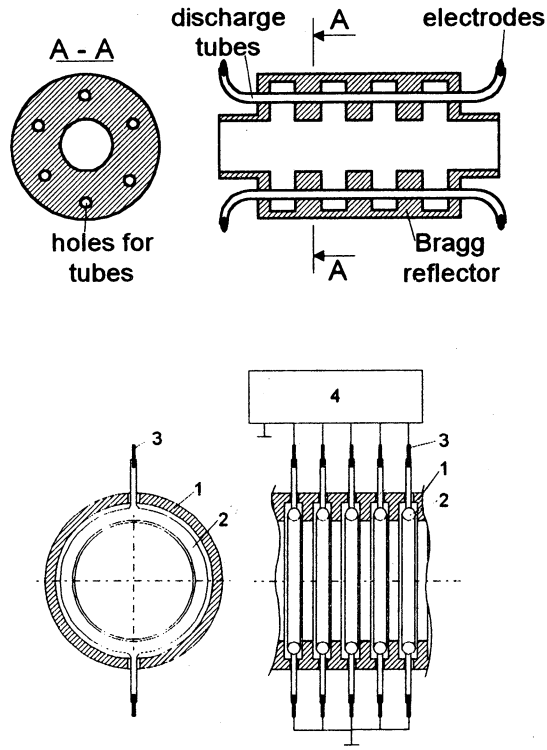

Fig. 4. Electrically controlled Bragg reflectors with tubes placed along and inside a periodic structure: 1- Bragg reflector, 2 -ring-shaped discharge tube, 3 - electrode, 4 - high-voltage pulse generator

When the plasma is produced simultaneously in the tubes, the wave constant in the Bragg reflector is changed at the reflector length, the Bragg reflection conditions are not satisfied and the reflector becomes equivalent to the circular waveguide. In this case transmitted signal (channel II), the signal reflected (channel I) from the plasma switch was registered. Characteristic oscillograms of the transmitted and reflected signals are shown in Fig.6.

Measurements showed good correlation of the moment when the transmitted signal appeared and the decrease in the level of reflected signal. Characteristic time of the front of the transmitted signal at optimal gas pressures in the tubes did not exceed 5-10 ns.

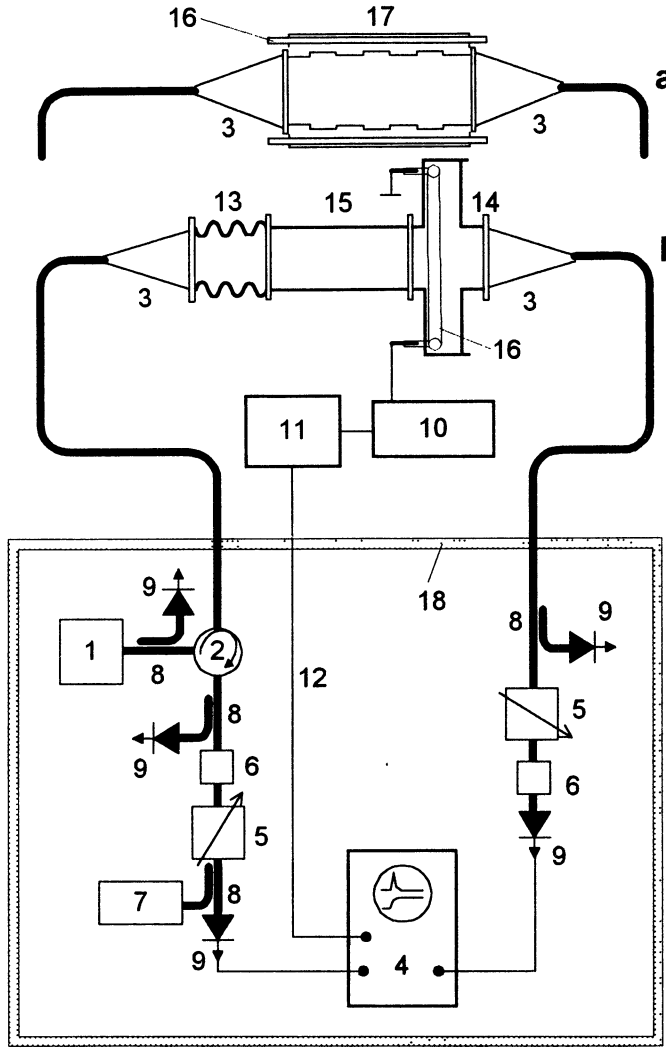

Fig. 5. Schematic diagram of the experimental set-up for measurements of plasma switch (a) and active microwave compressor (b) characteristics: 1 - magnetron, 2 - circulator, 3 - mode converter, 4 - oscilloscope, 5,6 -attenuators, 7 - measure of frequency, 8 - directional coupler, 9 - detector, 10 - high-voltage pulse generator, 11 - synchronizer, 12 - light guide, 13 - input Bragg reflector, 14 - electrically controlled output reflector, 15 - circular waveguide, 16 - discharge tube, 17 - output Bragg reflector, 18 - screen room

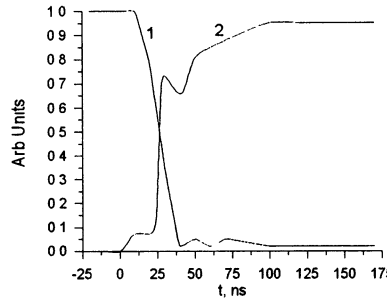

Fig. 6. Characteristic oscillograms of the reflected (1) and transmitted (2) signal of electrically controlled Bragg reflector

2.3. Output reflector based on the step-wise widening of a circular waveguide

Switching a Bragg reflector with a distributed set of gas-discharge tubes requires that the plasma should have high density and a high degree of homogeneity. These requirements can be less strict if the electrodynamic structure of the output reflector has resonance properties, and, consequently, the resonance can be broken by changing parameters of the medium that fills the tube relatively slightly. We realized this method in an axially symmetric microwave compressor operating at the TE_{01}-mode with its output reflector made as a step-wise waveguide widening with a gas discharge tube placed in it. The schemes of the output reflectors with one and two tubes are shown in Fig.7.

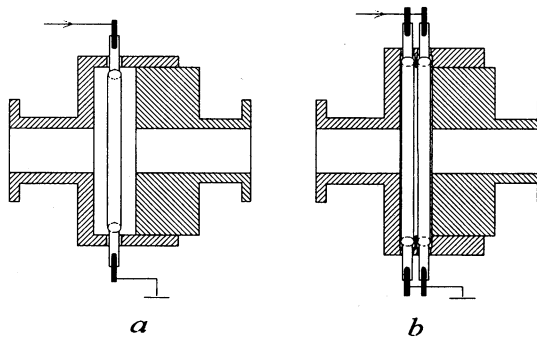

Fig. 7. Electrically controlled output reflectors: a- with one tube; b- with two tubes

The output reflector was made as a cylindrical resonator and was excited by the TE_{0mn}-mode. Inside the resonator, near its wall, a gas-discharge quartz tube shaped as a ring was placed. The length of the output reflector can be changed smoothly by means of an adjustment piston sliding in the wider waveguide. Depending on the length, different axially symmetric modes (TE_{032} or TE_{041}) were excited in the output reflector, and the coefficient of reflection from the reflector at the frequency of f = 11.424 GHz was R = 0.98. The typical frequency characteristic of the output reflector with one quartz tube is shown in Fig.8.

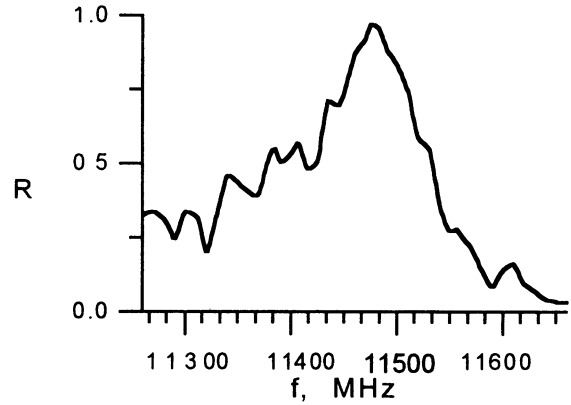

Fig. 8. Measured frequency characteristic of the output reflector with one tube (mode H_{032})

The gas discharge tube was filled with nitrogen in the pressure range p=10-300 Torr. When high-voltage pulses were fed to the electrodes in the quartz tube and plasma appeared there, the eigen frequency shifted to outside of operating frequency and the transmission coefficient grew sharply. As the result, the stored energy was emitted from the resonator as the TE_{01}-mode.

The testing of such a compressor using 100 kW -level microwaves (9.4 GHz) showed that this design is able to provide power gains up to 20 [13]. Experimental results are listed in Table 2. It should be noted that low efficiency in the experiment performed was due to wider spectrum of magnetron generation as compared to the width of the resonator curve characterizing the resonator.

Table2. Experimental results for the compressor with reflector based on a step-wise widening of a circular waveguide

Frequency	9.4 GHz
Operating mode	TE_{01}
Resonator Q-factor	$1.5 \cdot 10^4$
Input power	90 kW
Output power	1.8 MW
Output pulse duration	25 ns
Efficiency	20-30%

2.4. Output reflector with active and passive sections

The experiments performed showed that the power of this microwave compressor is limited by gas self-breakdown in the output reflector. Really, electric fields in this type of the output reflector are still rather high, which makes it impossible to use it to obtain microwave pulses with their output power of the order of 100 MW. Basing on the studies performed we developed a version of a microwave compressor operating at the TE_{01} mode of a circular waveguide, which can produce 100 MW of the output power at the frequency of 11.4 GHz [14]. In this compressor we used resonance output reflector.

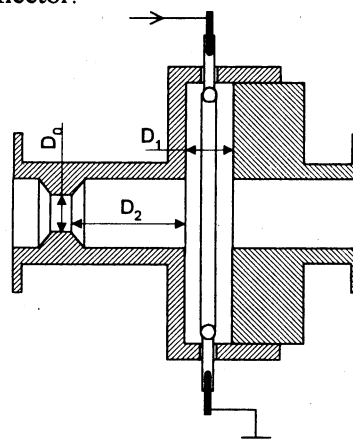

Fig. 9. Electrically controlled output reflector with active and passive sections

The output resonance reflector consists of the active and passive sections. The scheme of the combined output reflector is shown in Fig.9.

The active section is based on a step-wise widening of a circular waveguide. The passive section is a waveguide section with an over-critical narrowing. This passive section makes it possible to reduce intensity of the electric field in the region of gas-discharge tubes in the active section. The experimental studies and numerical modeling showed that the frequency characteristic of the switch has the resonance character Fig.10.

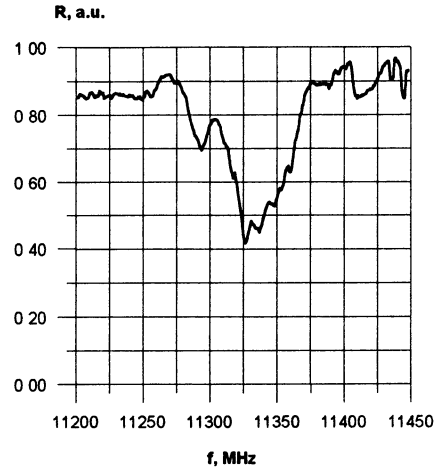

Fig. 10. Measured frequency characteristic of the combined output reflector

When the plasma is formed in gas-discharge tubes situated in the region of waveguide widening, the maximum of the resonance curve shifts to the region of the operating frequency. This provides ejection of the power accumulated in the resonator to the load. It is evident that parameters of the compressed pulse are significantly depending on the value of the transmission coefficient, T, of the switch.. By changing dimensions of the over-critical waveguide narrowing in the passive reflector section one can change the transmission coefficient and, thus, control the amplitude and duration of the compressed pulse. In our experiments the coefficient of reflection from the whole reflector including the passive and active sections was 70 % in regime of energy output.

3. 100 MW ACTIVE BRAGG COMPRESSOR

3.1. Design

The scheme of the compressor which can produce 100 MW of the output power at the frequency of 11.4 GHz is shown in Fig.11. This is an evacuated version made of copper. The compressor consists of mode converters ($TE_{01} \rightarrow TE_{11}^{0}$, $TE_{11}^{0} \rightarrow TE_{01}^{0}$) connected with smooth tapered transitions and a resonator formed by a Bragg reflector, a section of a cylindrical oversized waveguide and an output reflector. The central part of the resonator is a section of an oversized 1m long waveguide 80 mm in diameter, which is equipped with a tapered 400 mm long transition to a narrower waveguide. The diameter of the latter waveguide was 55 mm, and the TE_{01}^{O} mode is the only propagating mode of all the axially symmetric ones.

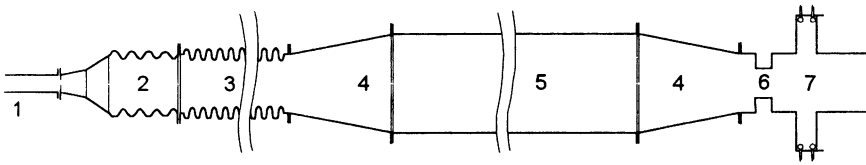

Fig. 11. Schematic diagram of the active Bragg compressor operating at the TE_{01} mode: 1 - input waveguide, 2 - TE_{01}-mode converter, 3 - input Bragg reflector, 4 - smooth tapered transition, 5 - storage cavity, 6 - over-critical narrowing of the waveguide, 7 - output reflector with electrically controlled gas discharge switches

3.2. Low-power test

Operation of the compressor was tested experimentally using low-power microwave radiation. Characteristics of the compressor were measured by the scheme shown in Fig.5. The compressor was tuned in two stages. Initially the output reflector was adjusted in such a way as to provide the match of the maximum of its non-transmission and the operating frequency of the compressor. Then, by changing the length of the cylindrical waveguide the resonator was tuned precisely to the frequency of f_0 = 11.424 GHz by the minimum of the compressor-reflected signal. When a high-voltage pulse was fed in, the microwave power stored in the resonator was emitted from the resonator at the TE_{01}^{O} operating mode.

The efficiency of pulse compression was regulated by changing the length of the step-wise widening of the waveguide. The compression coefficient was determined by the ratio of the power of the compressed pulse, P_p to power P_0 at the compressor input. The compression coefficients obtained in the experiment amounted to k =11-12 at half-width pulse duration τ_p=45-55 ns. Experimental results are presented in Table 3.

Table 3. Experimental results of low-power test

Frequency	11.42 GHz
Operating mode	TE_{01}
Resonator Q-factor	$2.5 \cdot 10^4$
Input pulse duration	1 μs
Power gain	11-12
Output pulse duration	55 ns
Efficiency	50%

Basing on the experimental data compressor efficiency at the pulse excitation regime was found. According to [6] energy accumulation in the resonator is described by the following expression:

$$W(t) = W_0(1 - \exp(-t/2\tau))^2, \quad (1)$$

where $W_0 = (4\beta/(1+\beta))P_0\tau$ is energy accumulated in the resonator in the stationary state, $\beta=Q_0/Q_e$ is coefficient of resonator coupling with the input aperture, Q_0 and Q_e are inherent Q-factor of the resonator and Q-factor of the coupling, $\tau = Q_L/\omega$ is characteristic time of excitation of the loaded resonator with Q-factor $Q_L = Q_0Q_e/(Q_0 + Q_e)$. Total efficiency of pulse compression in the compressor, η, at pulse excitation is determined by expression

$$\eta = \eta_1 \cdot \eta_2, \quad (2)$$

where $\eta_1 = W_p/W_0$ is efficiency of transmission of the accumulated power to the load, $W_p = \int P_p(t)\,dt$ is energy in the compressed pulse, $\eta_2 = W(t)/W_i$ is efficiency of power accumulation in the resonator, and $W_i = P_0t$ is energy at the compressor input to time moment t. The value of τ required for efficiency determination was determined by measuring the loaded Q-factor of the resonator. According to these measurements

$Q=2.5\cdot10^4$ and τ = 300 ns. The value of β determined in the experiment was 2.2. Characteristic oscillogram of the compressed pulse is shown in Fig.12.

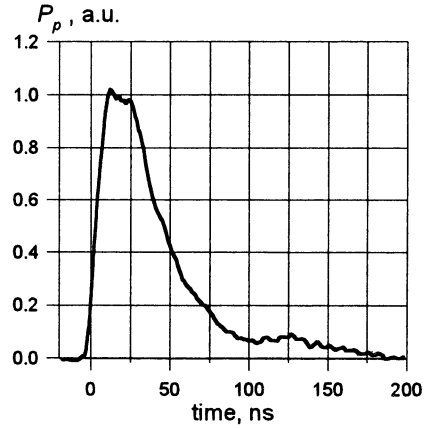

Fig. 12. Envelope of compressed microwave pulse

Efficiency of pulse compression calculated for cases of resonator feeding with pulses of different duration is shown in Fig.13.

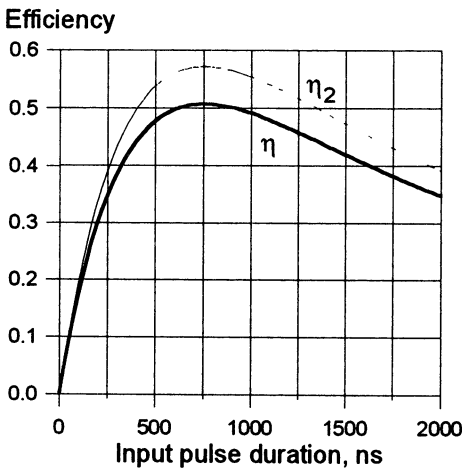

Fig. 13. Total efficiency (η) and efficiency of energy storage in the resonator (η_2) vs input pulse duration

Figure 13 shows the curve for efficiency of power accumulation (upper curve) in the resonator. It is seen from the figure that when

pumping pulses with their duration 1μs are used, the total compression efficiency will be 50%. This efficiency proved to be somewhat lower than the value of efficiency of power accumulation η_2, since energy losses via the Bragg reflector in the regime of output of the compressed pulse. These losses can be eliminated by using the scheme of compressor excitation by means of a 3-dB coupler with a common power input-output element, as shown in Fig.14.

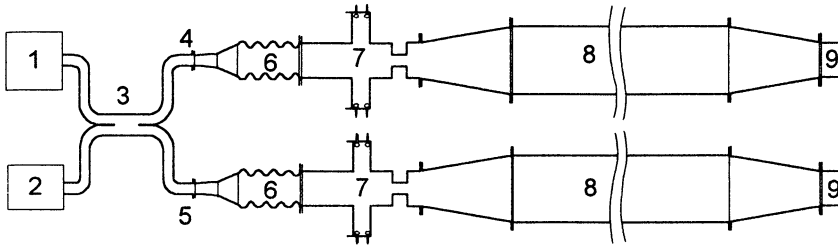

Fig. 14. Schematic diagram of the experimental set-up for composition of microwave pulse from two compressors with a common power input-output element: 1 -microwave generator, 2 - load, 3 - 3dB directional coupler, 4 - first channel of compressor, 5 - second channel of compressor , 6 - TE_{01}-mode converter, 7 - input and output electrically controlled reflector, 8 - storage cavity, 9 - reflector

Thus, the 3-dB coupler makes it possible not only to decouple the generator from the reflected microwave power at the initial stage of energy storage in the resonator, but also to improve efficiency of the existing compressor. When using 3-dB coupler efficiency of the compressor will be close to η_2 The compressor is separated into two equal channels. In this scheme each compressor channel is excited via a reflector, which is both the input reflector and the electrically controlled output one. At the other end of the storage resonator the Bragg reflector is replaced with a simple stopper as a cone.

However realization of the proposed scheme requires phase stability between the initial and compressed pulses and between pulses from each channels.

4. PHASE CORRELATION BETWEEN THE INITIAL AND COMPRESSED PULSES IN THE ACTIVE BRAGG COMPRESSOR

4.1. Measurements

An important point for successful use of active microwave compressors in accelerators of charged particles is the issue of optimizing the shape of the compressed pulse and of phase correlation between the incident and compressed pulses. The use of several microwave compressors controlled by a common initiating generator in linear accelerators supposes that parameters of microwave radiation, i.e. amplitude and frequency (phase) characteristics, are stable (reproducible). The time of functioning of the output reflector, which is determined by duration of breakdown evolution in discharge tubes, is sufficiently shorter than the time of microwave radiation output from the compressor. Hence, one can expect that the phase difference between the primary and compressed pulses will be stable during all the output pulse after it changed fast (in a few nanoseconds) when the compressor switched from the regime of energy storage into the regime of its output.

Phase characteristics of the output compressor radiation were measured experimentally by the usual Mach-Zender interferometric scheme, shown in Fig. 15.

The phase of compressor microwave radiation was compared with the phase of microwave radiation of the generator that fed the compressor. Microwaves from the compressor and generator were mixed in a hybrid junction. The hybrid junction (double T-shaped connection of waveguides) was made a single-unit combination of E- and H- T-joints, the planes of symmetry of which were matched. Branch E (connected to the waveguide at the wide wall) and branch H (at the narrow wall) are always decoupled. The hybrid junction had a rather wide range ~ 15% of operating frequencies.

Microwave radiation of the compressor and the reference radiation branched from the generator by means of a directed coupler with 10 dB isolation were injected into the hybrid junction via side branches. At the H-branch the matched load was installed, and at the E-branch, the detector head (phase detector). Matching and isolation of the side and measuring branches of the hybrid junction were performed by building decoupling

attenuators (with attenuation at least 4dB) and ferrite rectifiers into waveguide lines.

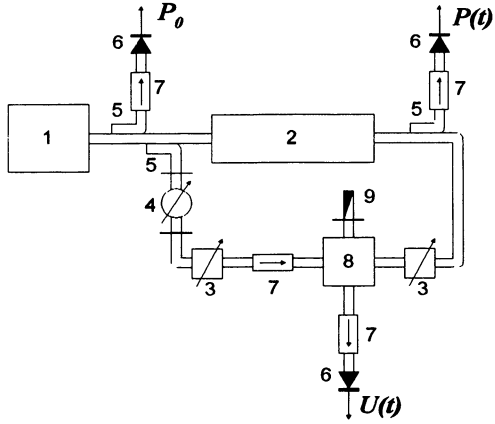

Fig. 15. Schematic diagram of the experimental set-up for measurements of phase characteristics: 1 - microwave generator, 2 - compressor, 3 - attenuator, 4 - phase shifter, 5 - direct coupler, 6 - detector, 7-direction waveguide, 8-magic-T, 9-matched load

Two microwave signals reached the phase detector in E branch: reference signal, $\mathring{A} = \mathring{A}_0 \cdot \cos(\omega_0 t + \varphi_0)$, and measured one, $\mathring{A} = \mathring{A}_{out}(t) \cdot \cos[\omega t + \Delta\varphi(t)]$. The level of those signals was controlled with attenuators and chosen such as to provide operation of the detector at the linear interval of the volt-ampere characteristic. It is known that when using a square-law detector the voltage at the interferometer output is determined by the following ratio:

$$U \propto P_0 + P(t) + 2\sqrt{P_o P(t)} \cos\left[\Delta\varphi(t) + \varphi_0\right], \qquad (3)$$

where P_0 is power of the input reference radiation with constant and known amplitude; radiation frequency is stabilized with relative error below 10^{-5}; $P(t)$ – is power of the output pulse of the compressor; $\Delta\varphi(t)$ is measured variation of the phase of the output radiation; φ_0 is initial phase of measurements changed with a phase rotator from 0 to π. Simultaneous registration of signals at the output of the interferometer, $U(t)$, and of the output microwave pulse of the compressor, $P(t)$, made it possible (at the known amplitude of the reference signal, P_0) to determine phase variation of the output radiation during the whole pulse:

$$\Delta\varphi(t) = \arccos[(C \cdot U(t) - P_0 - P(t))/\, 2(P_0\, P(t))^{1/2}], \qquad (4)$$

where C is factor of proportionality between the voltage at the detector output and the value of microwave power fed to it. The speed of response of the interferometer did not exceed 4 ns and was determined by the transmission band of the microwave line, input circuits of the registering tools and the time constant of the phase detector.

Time dependence of phase difference $\Delta\varphi(t)$ between the input and output radiation and the envelope of the compressed pulse are shown in Fig.16. As seen from the Figures, after the output reflector functions, the radiation phase at the compressor output changes fast to ~30-60°(in a few nanoseconds corresponding to the leading edge of the compressor pulse), and then tunes back smoothly. It is seen that the phase of microwave radiation stays within the 5° variation range for a major part of duration of the compressed output pulse. One must note good recurrence of the shape and amplitude of the compressed microwave pulse of the compressor from pulse to pulse.

4.2. Numerical modeling

Operation of the existing active Bragg compressor at the TE_{01} mode was also modeled numerically by the FDTD method [15]. In numerical calculations parameters and dimensions of the compressor were chosen maximally close to the manufactured compressor.

The time dependencies of the power in the compressed pulse and phase difference $\Delta\varphi(t)$ between the input and output pulses are shown in Fig.17. As seen from the plots of Fig.16 and Fig.17 the calculation results are close to the experimental data.

5. Conclusion

1. A novel active pulse compressor based on Bragg resonator has been developed that is able to provide output pulses of at least 100 MW power with pulse duration of 100 ns at the X band, and with power gain of 12-15. A series of high-power experiments is scheduled that will use the Omega-P/NRL 11.424 GHZ magnicon.
2. The investigations showed that developed active Bragg compressor makes it possible to obtain output pulses with only a slight variation of phase with time.

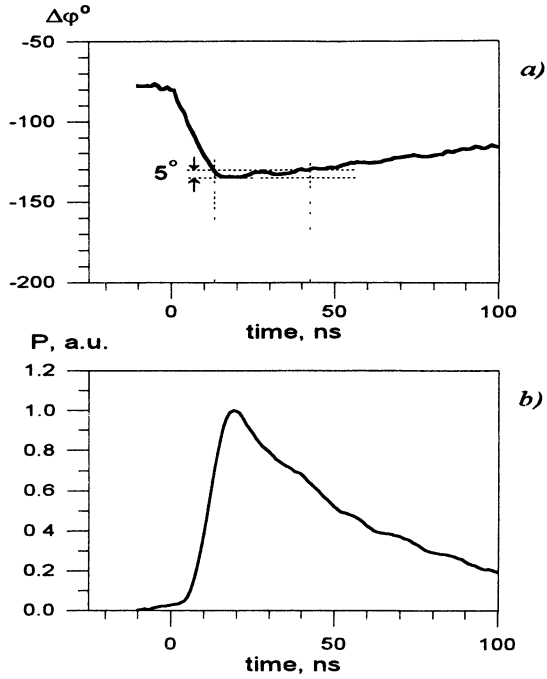

Fig. 16. Time dependence of phase mismatch between the input and output radiation (a) and of power in the compressed pulse (b)

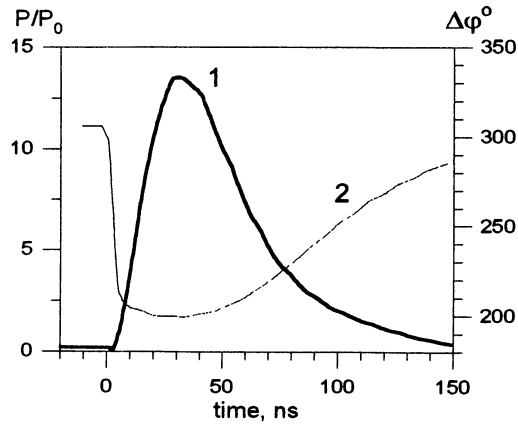

Fig. 17. Time dependence of the power of the compressed pulse (1) normalized to the power of the input signal and phase mismatch (2) between the output and input pulses. The duration of the input pulse is equal to 1μs

Acknowledgment

The authors are grateful for the many useful discussions with Prof. A.G. Litvak, Prof. O.A. Nezhevenko, and Dr. S.H.Gold. Work was supported by Russian Ministry of Science and Technologies and USA Department of Energy under contract DE-FG02-98-ER 82630.

References

1. Farkas Z.D. et al., SLED: A method of doubling SLAC's energy, Proc. 9th Int. Conf. on High Energy Accelerators, 1976, 576; SLAC-PUB-1453.
2. Farkas Z.D., Binary peak power multiplier and its application to linear accelerator design, SLAC-PUB-3694, 1985.
3 Wilson P.B., Farkas Z.D., Ruth R.D., SLED-II: A new method of rf pulse compression, in Proc. of Linear Accl. Conf., Albuquerque, NM, 1990; SLAC-PUB-5330.
4. Mizuno H., Otake Y., A new rf power distribution system for X band linac equivalent to an rf pulse compression scheme of factor 2N, in Proc. 17th Int. Linac Conf. Tsukuba, Japan, 1994; KEK-Preprint-94-112.
5. Petelin M.I., Vikharev A.L., Hirshfield J.L., in Proc of 7th Workshop «Advanced Accelerator Concepts», Lake Tahoe, CA, 1997, **398**, 822.
6. Alvarez R.A , Rev. Sci. Instrum., 1986, **57**, 2481.
7. Yushkov Yu.G., Avgustinovich V.A., Artemenko S.N. et al., in Proc. of the Intern. Workshop «Strong microwaves in plasmas», IAP: Nizhny Novgorod, 1996, **2**, 911.
8. Devyatkov N.D., Didenko A.N., Zamyatin L.Y. et al., Radio Eng. Electronics, 1980, **25**, 1227.
9 Alvarez R., Birx D., Byrne D. et al., Particle Accelerators, 1981, **11, 125**.
10. Avgustinovich V.A., Novikov S.A., Razin S.V., et.el., Radiophisics and Quantum Electron., 1985, **28,** 1347.
11 Vikharev A.L., Kovalev N.F., Petelin M.I., JTP Letters, 1996, **22**, No19, 41.
12. 14.Asinovsky E.I, Vasiljak L.M., Markovets V.V. et. al. Telofizika Visokikh Temperatur, 1983, **21**, 577 (in Russian).
13 Vikharev A.L., Gorbachev A.M., Ivanov O.A. et al., JTP Letters, 1998, **24**, No20, 6.
14 Vikharev A.L., Gorbachev A.M., Ivanov O.A. et al., in Proc. of 8th Workshop «Advanced Accelerator Concepts», Baltimore, Maryland, 1998.
15. Yee K.S., IEEE Trans. Antennas Propagat. 1966, **AP-14**, 302.

RESONANT COMPRESSION OF HIGH-ENERGY MICROWAVE PULSES

V.A. Avgustinovich, S.N. Artemenko, P.Yu. Chumerin, A.N. Didenko, G.P. Fomenko, V.L. Kaminsky, A.I. Mazshenko, S.A. Novikov, A.I. Ryabchikov, I.I. Vintizenko, Yu.G. Yushkov*

Scientific Research Institute of Nuclear Physics, Tomsk, Russia
*Russian Academy of Science, Moscow, Russia

Multimode cavities were used for microwave resonant compression in X- and S-band. The two parallel cavity setup was designed to produce pulses of 100 MW peakpower and 200 ns pulsewidth. The repetitive pulses of 1 GW peakpower and nanosecond pulsewidth were obtained in singlemode compressors using either the industry item 2.5 MW magnetron or the 120 MW relativistic magnetron as a primary microwave source.

1. Introduction

The interest to microwave resonant compressors is caused by the scope for creation of simple and reliable radiation sources producing nanosecond microwave pulses with the peakpower from hundreds of kilowatts to a gigawatt. Singlecavity compressors if used can amplity an output power of any microwave device in X, S or L-band tens or hundreds times per-unit with an according pulsewidth decrease. The efficiency decreases to some degree. But it should be taken into account that well developed commercial microwave tubes having the efficiency over 70% may be used for compressor feeding and so the total efficiency may exceed the efficiency of nanosecond microwave sources with relativistic electron beams. It was reported formerly [1] a compressors containing a single mode cavity with the gaseous insulation can process a limited amount of primary microsecond pulse energy due to reaching critical field strength values in a cavity volume. The output peakpower was below 2...3 MW in X-band and 100...200 MW in S-band. One can increase the resultant power by connecting several compressors in parallel provided the energy extraction is synchronized, or connecting them in series. In first case the feeding microwave power is devided and the workload for each cavity decreases, in second a cavity of each subsequent stage is excited by sorter and shorter pulse and the electrical strength rises at the cost of energy keeping time decrease. The upper limit of stored energy amount in a compressor increases if one employs large volume, and consequently, multimode resonant lines. Though

large volume, and consequently, multimode resonant lines. Though accompanying problems arise and they reside in the working mode separation and design of interference switches for rapid energy extraction.

This paper presents the characteristics of multimode cavities and their designs which offer rapid energy extraction, the experimental results of parallel and series compression, testings of the setup for relativistic magnetron radiation compression all being done to come up to gigawatt output peak power. Demonstration tests of using the compression procedure in radar transmitters are given.

2. Multimode cavities

Schematically the multimode cavity is presented in fig.1.

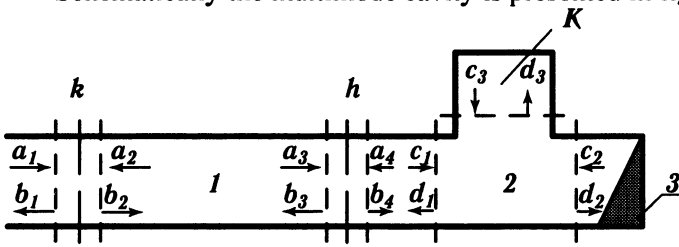

Fig. 1. Schematic of multimode cavity: *1* – multimode storage section; *2* – singlemode waveguide tee coupled through an iris

Normalized wave amplitude denoted herein by letters are related by transition matrix equations at the regions of discontinuity :

$$\begin{vmatrix} b_1 \\ b_2 \end{vmatrix} = \begin{vmatrix} \sqrt{1-k^2} & jk \\ jk & \sqrt{1-k^2} \end{vmatrix} \begin{vmatrix} a_1 \\ a_2 \end{vmatrix}, \qquad \begin{vmatrix} b_3 \\ b_4 \end{vmatrix} = \begin{vmatrix} \sqrt{1-h^2} & jh \\ jh & \sqrt{1-h^2} \end{vmatrix} \begin{vmatrix} a_3 \\ a_4 \end{vmatrix},$$

$$\begin{vmatrix} d_1 \\ d_2 \\ d_3 \end{vmatrix} = \begin{vmatrix} -1/2 & 1/2 & 1/\sqrt{2} \\ 1/2 & -1/2 & 1/\sqrt{2} \\ 1/\sqrt{2} & 1/\sqrt{2} & 0 \end{vmatrix} \begin{vmatrix} c_1 \\ c_2 \\ c_3 \end{vmatrix}$$

where k and h - parameters of cavity coupling to feeding line and interference switch respectively. In regular sections the relationship is defined by corresponding time constants of wave attenuation and phase-shift. Then with due account of wave travelling time along regular sections a wave amplitude value at some moment could be expressed relative to same wave amplitude at the moment differed by double travelling time along the cavity. This leads to approximate differentical equations for variables $b_2(t)$ and $d_2(t)$ defining the transient in a cavity and output

pulse envelope respectively, where t – current time. The field energy in a cavity is determined by

$$W_c = \left| b_2 (t_g) \right|^2 \cdot T_1 / 2,$$

where t_g – input pulsewidth, T_1 – double travelling time along main section. The energy transfered from the cavity to a load is expressed by

$$W = \int_0^\infty \left| d_2 (t) \right|^2 \cdot dt / 2.$$

The energy storing efficiency is $\eta = W_c / P_g \cdot t_g$, total microwave efficiency $\kappa = W / P_g \cdot t_g$ and the power gain.

$$M^2 = \left| d_{2\,max} (t) \right|^2 / a_1^2 .$$

Calculated maximum values of η, κ and M^2 are plotted as functions of t_g and presented in fig.2 and fig.3. In their captions Q_0 – internal Q- factor, τ_1 –compressor output pulsewidth.

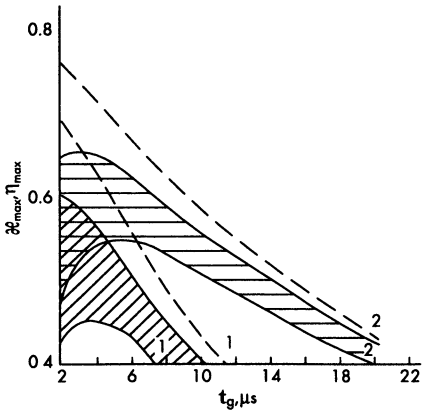

Fig. 2. Plots of storing η_{max} and total κ_{max} efficiency. Cross-hatched area between plots *1* relates to κ_{max}, fixed $Q_0=10^5$ with the upper plot τ_1=80 ns and bottom one τ_1=200 ns; area between plots 2 for $Q_0=1.5\cdot10^5$ and 80 ns$<\tau_1<$ 200 ns. Dashed lines for η_{max} when *1* - $Q_0=10^5$; *2* - $Q_0=1.5\cdot10^5$.

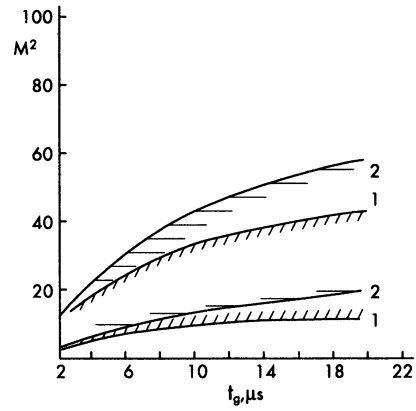

Fig. 3. Power gain M^2 plotted against exciting pulsewidth values. The area *1* between plots relates to $Q_0=10^5$ with the upper plot τ_1=80 ns and botton one τ_1= 200 ns; area between plots *2* for $Q_0=1.5\cdot10^5$ and 80 ns$<\tau_1<$ 200 ns.

The internal Q-factor is dependent on the output interference switch parameters and its coupling to the main section of the cavity. The experimental values of Q_0 plotted as a function of the iris diameter d are presented in fig.4. The working mode was $H_{01(12)}$ of the X-band circular cavity. The fig.4 stands out following particular length values l of the tee input arm: $l = \lambda_w/4$; l is optimum when Q_0 is maximum; l is close to $\lambda_w/2$, but the own resonant frequency is higher when the switch is open (HF, halfwavelength) and l is close to $\lambda_w/2$, but the own resonant frequency is lower (LF, halfwavelength). Corresponding high power tests including switching and energy extraction were run with the pulse magnetron having 60 kW output peak power and 1 μs pulsewidth. The diameter of circular multimode section is 90 mm, coupling hole diameter of the input arm is 9 mm. Output pulse envelopes are presented in fig.5, where a) $l = \lambda_w/2$, LF, b) $l = \lambda_w/4$; c) $l = \lambda_w/2$, HF; d) l - optimum and strong intermode coupling. Maximum power gain was 14 dB and pulsewidth 25 ns at –3 dB power level. The efficiency was up to 0.4 at optimum l and at $l = \lambda_w/2$, HF. One should consider that the electric field strength in the tee is maximum when $l = \lambda_w/2$ and minimum at $l = \lambda_w/4$.

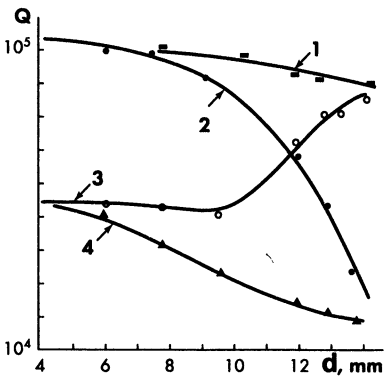

Fig. 4. Storage system Q_0-factor plotted pulse against the iris diameter. *1* - optimum length of the input arm of tee; *2* - quarter wavelength; *3* - HF halfwavelength; *4* – LF - halfwavelength.

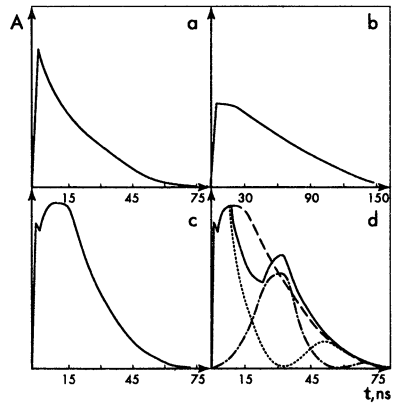

Fig. 5. Output envelopes of X-band multimode compressor.

Data above show that in spite of η high values, the power gain and extraction efficiency stay low with the slow energy extraction in-

herent in conventional compressors having small amount of "main volume – tee" coupling. Multimode cavities are able to accumulate a large quantity of energy. So if the rapid energy extraction was realized then the power gain values would reach several hundreds per-unit and output peakpower several hundreds of megawatts.

One approach to the problem is synchronized extraction through the bunch of single mode interference switches. If it succeeded the total output peakpower P_Σ would increase

$$P_\Sigma \approx NP_1 \approx \kappa N\beta_0 P_g$$

as the pulsewidth decrease. Here P_1 – output power when single switch is used, N – number of switches; β_0 – coupling coefficient of each switch with a main section of cavity; τ - pulsewidth when single switch is used. The extraction through bunch of switches was tested in X-band on the circular cavity. The resonant frequency 9.26 GHz, working mode $H_{01(11)}$ and internal Q-factor $5...6 \cdot 10^4$. Schematically the cavity is shown in fig.6.

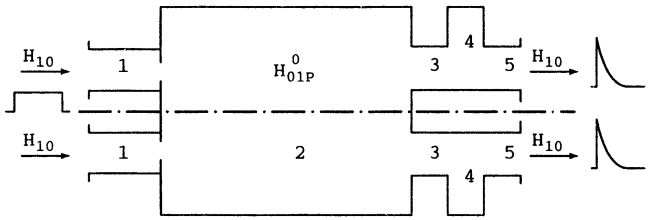

Fig. 6. Circular cavity with multiunit switch output.
1 – input waveguide line; *2* – main multimode section; *3* – input arm of tee; *4* – discharge switch; *5* – output line.

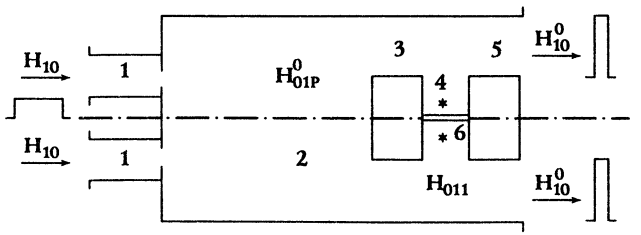

Fig. 7. Circular cavity with coaxial interference switch.
1 – input waveguide line; *2* – main multimode section; *3* – input coaxial line of switch; *4* – radial line; *5* – output coaxial line; *6* – circular discharge region.

Energy extraction was executed coherently through 2 or 4 switches. The shape of output pulses is also shown on the figure. The input microwave power was ~ 50 kW, power gain of each of two channel was about 7...8 dB and the total ~ 11 dB at synchronized extraction. The single channel operation gives 60...80 ns pulsewidth, joint operation of the couple gives total pulsewidth of 30...40 ns. The four switch operation does not differ much from two switch. The increase of switch number involves shortening of output pulsewidth but not rigorously propotional. The channel where the switch was by chance last to be turned on exhibited shortest 5...10 ns pulse with clear amplitude instability.

The operation of the multimode coax switch was tested with the cavity having the cross section diameter 90 mm and length 260 mm. The scheme is presented in fig. 7. The inner conductor of the coax was 45 mm, the width of radial line ~ 24.5 mm, the inner structure rod diameter 6 mm. The internal Q-factor was $4.5 \cdot 10^4$, corresponding estimated maximum power gain at critical coupling ~ 400, at input pulsewidth 1 μs ~ 230. Commuting was due to spontaneous discharges in the radial line 4 in the region of the maximum axial electric field strength. Input power was 140 kW, output power ~ 15...20 MW and output pulsewidth ~ 3 ns at –3 dB level. The power attributed to the travelling wave in the cavity by the end of transient was ~ 30 MW. The storage efficiency was ~ 50%, total microwave efficiency 35...40%. This compressor can produce the output peak power in the range 50...100 MW provided the input power is increased. In S-band the evaluated maximum output poweris 1 GW with short pulsewidth of nanosecond order.

3. Parallel compressionin multimode cavities

The energy extraction from two parallel singlemode cavities and pulse summation was tested with 3-dB coupler circuited into the input line [1]. The case may be an initial microwave source has the peak power far beyond the electric strength possibilities of a single multimode cavity. The problem might be approached by parallel compression. The schemes are presented in fig. 8 and fig. 9.

The cavities of fig. 8 had $H_{11(13)}$ operation mode, 2.8 GHz resonant frequency and were cylindrical of 300 mm diameter and 715 mm length. Fine adjustment of cavity dimentions to the assigned frequency value was brought off by flexing of end plates. The magnetron generator had pulses of 0.8 MW peak power and 3 μs pulsewidth. The internal Q-value

when open. Interference switches were made of waveguides of 72×34 mm^2 cross section as H-plane tees with one arm shorted out. The discharge quartz tube of the switch was being filled with argon at not more than 2 bar. The cavities were filled with nitrogen of 4 bar exceeding pressure. The high-voltage pulse source for triggering switches had variable voltage amplitude 8...16 kV and the pulse risetime about 50 ns. In output summing tee the position of the summing arm tooks account of constant oscillation phase displacement between the cavities. Power gain of each cavity was 10 dB. The summation caused the total power gain decrease of 0.5...1 dB. The total pulsewidth was 60±5 ns while the output pulses of each cavity had pulsewidth of 55±5 ns. The mutual jitter of about 5 ns did not disturb the coherency of summed pulses.

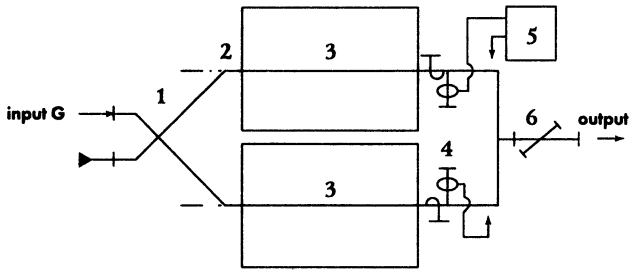

Fig. 8. Schematic of double parallel cavity compressor with H_{11} operational mode: *1* – 3 dB coupler; *2* – input coupling element; *3* - main storage volume; *4* - switching waveguide tee; *5* - high voltage pulse generator; *6* - directional coupler.

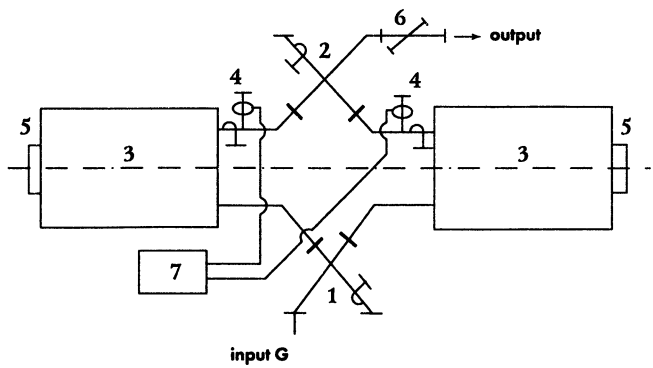

Fig. 9. Schematic of double parallel cavity compressor with H_{01} operational mode: *1* – input 3 dB coupler; *2* – output 3 dB coupling; *3* - main volume; *4* – switching waveguide tee; *5* - choke plunger; 6 - directional coupler; *7* - high voltage generator.

The compressor of fig. 9 had $H_{01(11)}$ operation mode in both cavities.They were cylindrical of 300 mm diameter and 660 mm length. Input and output windows of each cavity were in the same end plate. The cavity had intrinsic Q-value $1.8 \cdot 10^5$, loaded Q_L=3...4·10^4 during storage process and Q_L = 3...4·10^3 during the process of extraction. The resonant frequency of each cavity 2.805 GHz was adjusted by movable choke plunger installed on the end plane lid which did not have coupling windows. Switching came about in argon of exceeding pressure set within the range 1...7 bar. The high voltage for triggering was supplied from the common single source.

The magnetron generator had 2 MW peak power, output pulsewidth of 3 μs and repetition frequency of 50 Hz. The designed optimum input pulsewidth was about 8...9 μs therefore the evaluated power gain of the compressor did not exceed 9 dB for magnetron pulsewidth 3 μs. The measured power gain of each cavity was 8 dB and of the total double cavity system 6.5...7 dB. The pulsewidth of output pulses at -3 dB level was 200...220 ns and 210...230 ns respectively. The single cavity could produce pulses of peak power 12...14 MW when it is fed by 2 MW magnetron and the double cavity compressor 9...9.5 MW with the same total input power. Thus measured power gain values are 1...2 dB less than calculated ones and this can be related to imperfect identity of interfering pulses and reflections in the summing line The mutual jitter of interfering pulses is affected by different conditions as working gas pressure in discharge tubes, composition of gas mixture, working time of continuous operation and so on. The choice of the suitable gas pressure value and gas composition allow to reduce it to several nanoseconds.

It is assumed the power gain will increase up to 11...12 dB for each cavity and 10...11 dB for total system at the pulsewidth 10 μs of input exciting pulses the output pulsewidth being the same about 200 ns. Similar experiments were made in X-band which proved the realiability of the procedure in different bands.

4. Two stage series compression

The setup producing gigawatt nanosecond microwave pulses with the industry issued magnetron driver was developed on the basis of series compression. The scheme is shown in fig. 10. The magnetron driver was a common transmitter of S-band radar. It has 2.5 MW peak power, 3 μs pulsewidth at –3 dB level, the working frequency was tunable within the range (2.79-2.81) GHz, the repetition rate was 400 Hz. The compressor

range (2.79-2.81) GHz, the repetition rate was 400 Hz. The compressor was a resonant load for the magnetron tube and their matching was achieved by the ferrite isolator and by fixing a special length of the waveguide line.

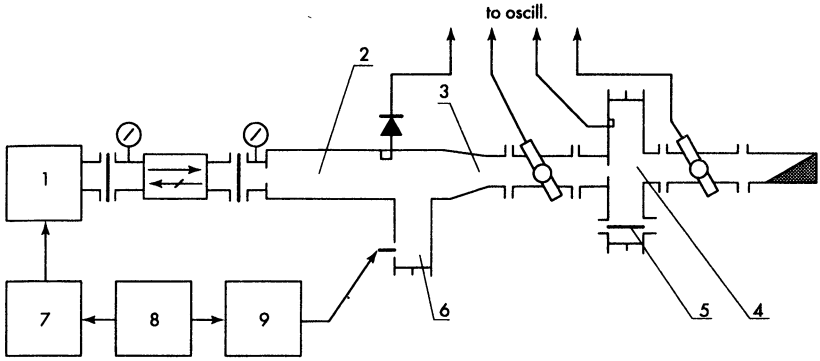

Fig. 10. Two stage series compression scheme.
1- magnetron; *2* - first stage cavity; *3* - circular-rectangular waveguide transition; *4* - second stage cavity; *5* - quartz tube of switch; *6* - short-circuited arm of first stage interference switch; *7* - high voltage magnetron modulator; *8* - controlling generator; *9* - high voltage triggering generator.

When the compressor output peak power exceeds 1 GW the corresponding electrical field strength is within range 300...1000 kV/cm in standard waveguides. Problems of electrical strength are solved using some technical procedures of interior surface treatment and purification of gases or using special design and circuitry of compression systems. In this case the solution of the construction elements insulation problem was the known fact that the electrical strength increases when the time an element or gaseous volume is exposed to electrical field decreases. Particularly this is implemented in the second stage in a two-stage series compression circuit.

Experience has shown that field strength values 100...150 kV/cm are obtained without difficulties. The cheap insulation by gaseous air or nitrogen may be used. The first stage cavity dimentions were chosen to come up to the electrical field strength requirement $E \leq 150$ kV/cm and supply the loaded Q_L value satisfying the equation $\tau = 2\ Q_L / \omega \geq t_g/(3...5)$. The cavity was made from a circular copper waveguide of 90 mm diameter cross section. The measured internal Q-factor was $2 \cdot 10^4$. The calculated first stage cavity length gave the output pulsewidth 11 ns with the power gain 82. The interference switch of the first stage

contained the short circuited section of rectangular waveguide of 3.4×7.2 cm cross section area which is set at right angles to the circular waveguide axis. The microwave gaseous switch was triggered by the additional spark switch lighting the waveguide gap through the hole in the short-circuited section broad wall. The switch operation with the repetion rate 400 Hz was supported by continuous gas circulation in the region of the waveguide gap and triggering gap. Triggering pulses had the voltage up to 10 kV. The second stage cavity was a double waveguide tee with short circuited symmetrical side arms. The waveguide cross section was 3.4×7.2 cm. The internal Q-factor was $9 \cdot 10^3$, power gain 10 and estimated pulsewidth 0.8 ns. The switch included the radio-transparent quartz tube filled with argon at the pressure of 7 bar. It was set at right angles to broad wall planes at the distance $\lambda_w/4$ from the sort-circuit. The switch operated with self-discharges.

The first stage cavity, the second one, waveguide elements and matched load were filled with nitrogen at exceeding pressure. The water cooling was arranged around the ferrite isolator and the load. The pulse output power was measured by the calorimetric meter indicating the average power. The directional coupler calibration and their transmission factor measurement were made when couplers were connected in the output magnetron line with the travelling wave regime.

The envelope of first stage output pulse and second stage output pulse are shown in fig.11,a and fig.11,b respectively. Pulses of the first stage had 150 MW peak power and 11 ns pulsewidth. The second stage increased the peakpower up to 1 GW and decreased the pulsewidth to ~ 1 ns.

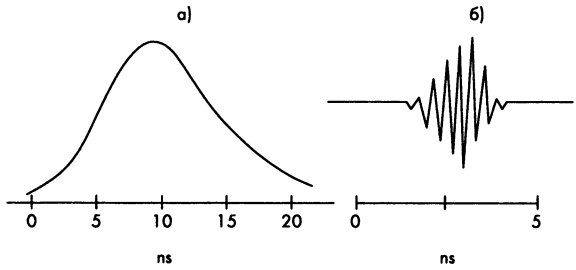

Fig. 11. Output pulses of two stage series compression.
a) output pulse envelope of the first stage cavity;
b) output pulse of the second stage.

5. Compression of relativistic magnetron radiation

Relativistic magnetrons have relatively short pulsewidths, usually about 10^{-7} s, and that does not allow to obtain the high power gain of a compressor. It may be from several per-units to several tens per-units. By the other hand overcoupled storage cavity excited with these pulses has higher efficiencies up to 80% than a critically coupled cavity can provide ≈40% when excited by microsecond pulses. Then it is known a relativistic magnetron has low frequency stability and this is caused by a explosive emission cathode operation and by high current values of several kiloamperes. If the high Q-factor storage cavity of a compressor was connected to a relativistic magnetron it would lead to the frequency control due to frequency pulling.

So the joint operation of a compressor and relativistic magnetron is not obvious as real microwave pulses have amplitude modulation and frequency instability and so the frequency can go beyond the working band of a compressor cavity. The circuits where a magnetron is coupled with a resonant load take ferrite isolators or circulators for a steady operation but they are not developed for a relativistic tube power level so far. The objective was the demonstration of the possibility of microwave compressor joint operation with a relativistic magnetron as a pumping source.

The setup schematic is shown in fig. 12. The S-band relativistic magnetron had the radiation power 120 MW, pulsewidth 120 ns and repetition rate 10 Hz. The magnetron was fed by the LIA type high voltage source supplying the voltage 400 kV and current 4 kA.

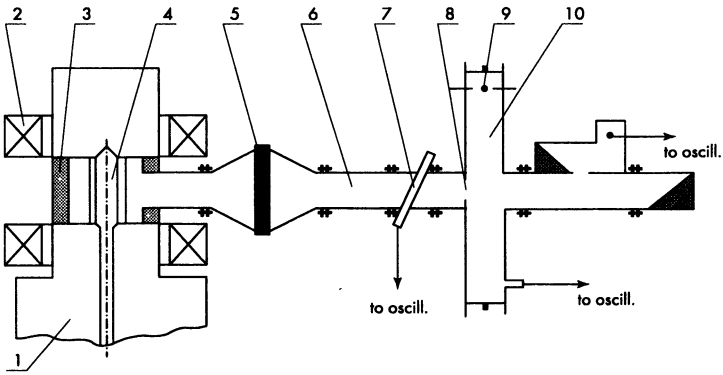

Fig. 12. Compression circuit including the relativistic magnetron as a primary microwave source. *1* - coax high voltage line; *2* - magnet; *3* - anode;*4* - cathode; *5* - dielectric window; *6* - waveguide line; *7* - directional coupler; *8* - input iris; *9* - switch; *10* - storage cavity.

The storage cavity was manufactured from waveguides of the cross section 7.2×3.4 cm and was designed as a double waveguide tee (magic tee) with symmetrical short-circuited side arms. The cavity was excited through the coupling hole in the broad waveguide wall that is in E-plane. The energy was extracted through output in H-plane as soon as the gaseous discharge commutator was switched. It was installed at the quater waveguide wavelength distance from the short-circuiting end plate. The minimum pulsewidth value was detrmined by the double travelling time of a wave propagating with the group velosity along one of side arms. The cavity was over coupled and its loaded Q-factor was about 750, in consequence the excitation period decreased to ~ 120 ns. The interior cavity volume was filled with a gas at 6 bar pressure to ensure the electrical strength. The dielectric window made of lucit had the diameter 250 mm and separated the pressure unit from magnetron evacuated one.

The operation matching of the magnetron and compressor was adjusted experimentally by variation of waveguide line length between the magnetron and excitation hole. The ferrite isolator was tested as a discoupling element as well. The switching of the gaseous commutator was spontaneous when the microwave field reached breakdown level. Output microwave pulses were transmitted to the matched load, the measuring circuit contained the directional coupler, attenuator and wideband oscilloscope.

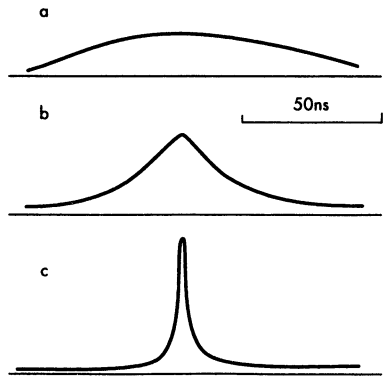

Fig. 13. Microwave pulse envelopes of relativistic magnetron compression setup.

The typical output pulse envelope when the relativistic magnetron operated with a matched load is shown in fig.13,a. Pulses had the

amplitude modulation and the degree of modulation changed from pulse to pulse. The envelope of the pulse demonstrating the field strength variation in the cavity (without stwitching) is shown in fig.13,b. The compressor output pulse in shown in fig.13c, it had 1.1 GW peak power and 5 ns pulsewidth at –3 dB level. Further increase of the parameters is possible with decrease of magnetron output pulse amplitude modulation.

6. Testings in radiolocation experiments

It was proved [2] short nanosecond microwave pulses have some advantages in radar systems. The features of compressors as short pulsewidth range, high output peak power, good repetition rate ability make them very suitable sources to apply in this field.

Testing of radiolocation application of short radiosignals produced by the compression method was run with the radar model containing two separate channels of transmition and receiving. The design of the model contained maximum allowable number of standard item units of industrial radars and so radar model parameters were not specially optimized. The compression setup was connected into the waveguide line between the microwave generator and the transmitting antenna. It contained the waveguide storage cavity, the unit for switch triggering and the circulator to provide steady operation of the microwave generator with a resonant load. The parts of cavity design were the section of overmode circular waveguide of 520 mm length and 58 mm diameter, the tapered transition to 30 mm waveguide diameter and the H-plane tee. The parabolic radio mirror of 3 m diameter with 0.8^0 width of a radiation lobe was used in the transmitting antenna. The receiving antenna was a slot planar array providing the directivity pattern of 7^0 in vertical plane and 4^0 in horizontal.

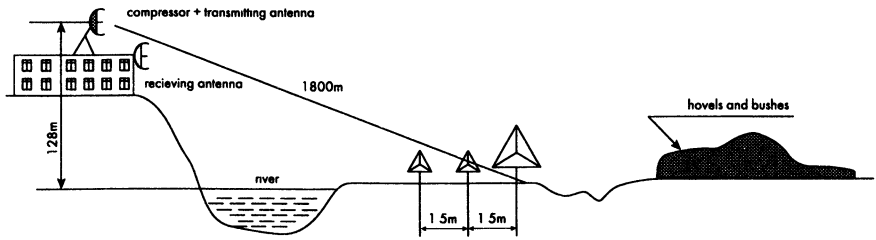

Fig. 14. Scene of radiolocation experiment.

The radar model had following technical parameters: operation wavelength 3 cm; pulsewidth 10 ns; peak power 40 kW; repetiton rate

400 Hz; threshold of receiver sensitivity -95 dB/W; passband of receiving line 150 MHz

The open path was chosen as shown in fig.14. Radiolocation target conditions were established by two corner reflectors of 5 m^2 radar cross section and the one of 500 m^2 all placed on ploughed field at distance of 1800 m. Characteristics of background reflections of the illuminated area were preliminary measured. The first corner reflector 500 m^2 was installed and the ratio signal/background was evaluated with emitting nanosecond and microsecond radiopulses. It was 33 dB and 14 dB respectively. Small corner reflectors were not seen by microsecond sensing pulses but were quite visible under nanosecond pulses. In this case the range resolution appeared to be 1.5 m.

In harmonic radiolocation the receiver takes down a harmonic frequency that of sensing pulse and so only manmade objects having nonlinear current characteristics fall in sight of the radar [3]. In general there is no problem of low ratio "signal response/background clutter" value if elimination of harmonic components in transmitting line is good enough.

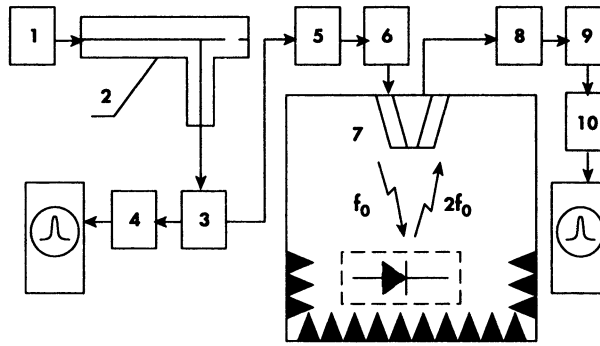

Fig. 15. Schematic of harmonic radar laboratory model.
1 - microwave generator; 2 - coax storage cavity; 3 - directional coupler; 4 - diode units; 5 – low-pass filter; 6 - attenuator; 7 - corkscrew R/T antennas; 8 - pass band filter; 9 - attenuator.

But radar cross section values are very low $10^{-3}...10^{-5}$ m^2 and depend on falling power density P. Therefore the action radius $R \sim P^{1/6}$. A compressor in the harmonic radar transmitter increases the action radius ~ 2.5 times if its power gain close to 20 dB. Relatively low frequencies of a transmitter are preferable as the waves penetrate into soil better and frequencies of receivers are not so high.

The transmitter laboratory model as shown in fig. 15 had peakpower ~ 200 kW, pulsewidth 10 ns and repetition rate 100 Hz. Minimum discernable signal of the receiver was –90 dB/W, center frequency corresponded to second harmonic and objects had radar cross section in the range $10^{-4}...10^{-5}$ m^2. The detection range was proved to be twice as large as one for microsecond pulses. Objects regenerated responses of the same pulsewidth and that allowed to raise a range discrimination to order of a meter.

So this work shows the rapid energy extraction from a multimode cavity is quite feasible and power gain of one cavity could reach several hundreds. Pulses of gigawatt power level was gained using the commercial magnetron as a primary source, the compression of relativistic magnetron was carried out. Testings in radiolocation experiments proved compressors to be suitable and reliable devices for solving some problems.

Acknowledgements

This work has been partially supported by RFBR Grant 97-02-16461 and Thomson Tubes Electronique (France).

The authors are greatful to N. N. Badulin, A. I. Melnikov, A. P. Batsula and E. L. Shoshin for taking part in radiolocation measurements and resolving some diagnostic instrumentation problems.

References

1. Yushkov Yu. G., Avgustinovich V. A. et al. Proc.Intern. Workshop Strong Micro waves in Plasma. Ed.A.G.Litvak. Nizhny Novgorod. 1997. V. 2. P. 911.
2. Bunkin B. V., Gaponov-Grekhov A. V., Mesyats G. A. et al.- Letters to JTF. 1992. V. 18, № 19. P. 61.
3. Kuznetzov A. S., Kutin G. I. Foreign radioelectronics. 1986, № 4. P. 41.

MICROWAVE APPLICATIONS OF GRATINGS

M. I. Petelin

Institute of Applied Physics, Nizhny Novgorod, Russia

Diffraction gratings are sensitive to frequency, polarization and incidence direction of electromagnetic waves. These properties are useful to develop wave beam polarizers, dividers/combiners, pulse compressors, multiplexers, frequency scan antennas, phase and electrically controlled wave switches. At the shortest microwaves, such components are attractive due to spurious mode filtration, low loss and easy cooling.

Introduction

Gratings (Fig. 1) [1, 2] are used, for a very long time, in a number of optical devices: for beam splitting, spectral analysis, pulse compression etc. Now they have become attractive for use at the shortest microwaves as well, especially at high RF powers [3, 4]. This paper represents an attempt to summarize main ideas in the field.

Fig. 1. Wave diffraction by grating

Fundamentals of gratings [1, 2]

Let us remind general properties of the wave diffraction by the infinite ideally conducting grating. As the structure parameters are time-independent, the RF field can be written in the factorized form

$$\mathbf{E} = \mathrm{Re}\left\{\mathbf{E}_\omega(\mathbf{r})e^{i\omega t}\right\},\quad \mathbf{H} = \mathrm{Re}\left\{\mathbf{H}_\omega(\mathbf{r})e^{i\omega t}\right\}. \qquad (1)$$

By analogy, as the grating parameters do not depend on the coordinate z, the RF field complex amplitudes can be factorized as well:

$$\mathbf{E}_\omega(\vec{r}) = \mathbf{E}_0(x, y)e^{-ik_z z},\quad \mathbf{H}_\omega(\vec{r}) = \mathbf{H}_0(x, y)e^{-ik_z z}. \qquad (2)$$

Due to the z-translational symmetry, we deal with a partial case of generalized cylindrical systems where transverse-electric (H) and transverse-magnetic (E) wave modes are independent and described with the Helmholtz equation

$$\frac{\partial^2 \mathrm{K}}{\partial x^2} + \frac{\partial^2 \mathrm{K}}{\partial y^2} + k_\perp^2 \mathrm{K} = 0. \qquad (3)$$

Here $\mathrm{K} = E_{0,z}$ for E modes and $\mathrm{K} = H_{0,z}$ for H modes; correspondingly, at the metallic boundary these functions satisfy the Dirichlet $E_{0,z}\big|_l = 0$ and Neuman $\left.\frac{\partial H_{0,z}}{\partial n}\right|_l = 0$ conditions. The transverse and longitudinal propagators of the wave are Pythagorean related

$$k_z^2 + k_\perp^2 = k^2 \equiv (\omega/c)^2.$$

Transverse components of $\mathbf{E}_0(x, y)$ and $\mathbf{H}_0(x, y)$ are proportional, with coefficients determined by k_z and $k_\perp$, to the gradient of $E_{0,z}(x, y)$ and $H_{0,z}(x, y)$.

Another kind of translational symmetry, namely the grating periodicity in the x-direction, results in the Floquet-Blokh theorem: illuminated with the wave

$$\mathrm{K}_i = exp\left(-ik_{0,x}x + ik_{0,y}y\right), \qquad (4)$$

the grating produces the scattered field

$$\mathrm{K}_S \equiv \mathrm{K} - \mathrm{K}_i = \sum_\alpha C_\alpha \, exp\left(-ik_{\alpha,x}x - ik_{\alpha,y}y\right), \qquad (5)$$

where transverse propagator components satisfy the combination condition

$$k_{\alpha,x} = k_{0,x} + \alpha\chi \tag{6}$$

$$\chi = \frac{2\pi}{d}$$

$$\alpha = 0, \pm 1, \pm 2...$$

and are Pythagorean related

$$(k_{\alpha,x})^2 + (k_{\alpha,y})^2 = k_{\perp}^2. \tag{7}$$

For any incident wave, the number of scattered waves propagating from the grating ($Imk_{\alpha,y} = 0$) is limited (Fig. 2). Higher space harmonics in the sum (5) are exponentially fading in the direction from

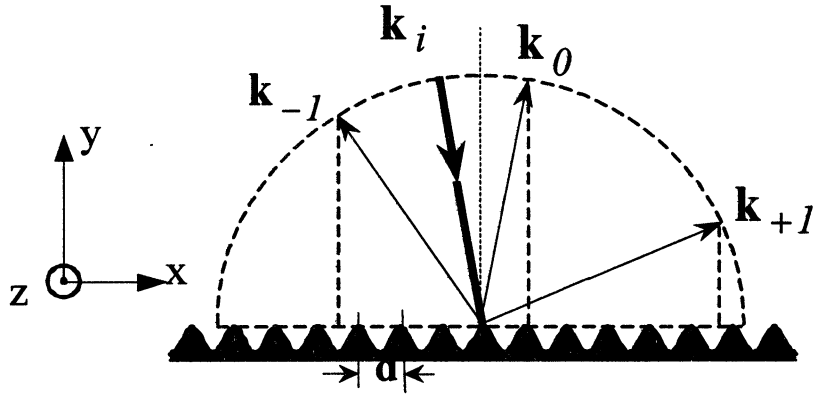

Fig. 2. Ray structure in the plane perpendicular to grooves

the grating. For applications, the number of propagating waves produced by scattering of the incident wave at the grating is the parameter of primary importance.

Dense grating as polarizer

If the grating period d is small compared with the wavelength, or, more exactly, is limited with condition

$$\left(k_{0,x}+k\right)d<2\pi, \tag{8}$$

all the incident wave power is reflected only into the mirror direction $(\alpha=0)$, but the reflection changes the phase shift between E and H waves. The effect can be illustrated with the simplest example shown in Fig. 3 where the E-polarized wave is reflected from the top, and the H-polarized one from the bottom of a dense grating. The E–H phase shift takes place, obviously, for any corrugation profile, in particular, the sinusoidal one which is breakdown-proof and easily cooled.

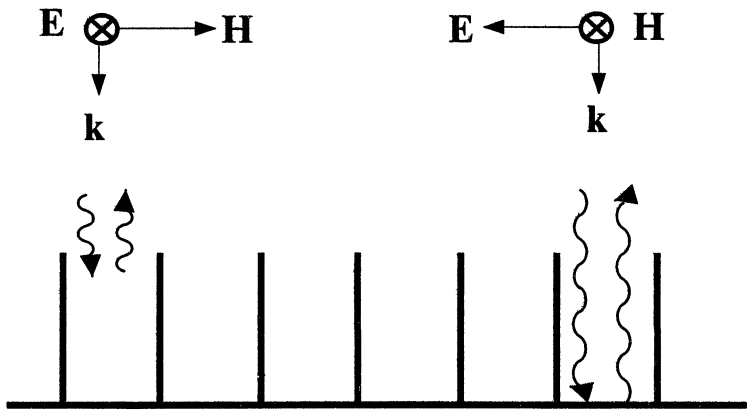

Fig. 3. The simplest example of grating polarizer

So, due to the anisotropy, the dense grating functions as a ***polarizer*** [1, 2], e.g., can 1) convert a linear polarized wave into a circular polarized one or 2) in a linear polarized wave, change the field orientation (in particular, gratings with adiabatically curved grooves are used to convert paraxial wave beams with curve electric field lines into beams of linear polarization [5, 6]).

Rotation of the grating around the axis perpendicular to the corrugated surface provides the wave beam polarization control [7, 8], but within a limited range. A wider control range can be provided with two successive gratings (Fig. 4). Such a steerable ***universal polarizer*** [3, 9, 10] is capable to convert any input wave polarization into any desirable output polarization (for instance, if the input wave is linear polarized, by introducing various combinations of the mirror axis rotation angles, one can obtain the output wave with linear polarization of any direction, left

and right circular polarizations or, in the most general case, any elliptical polarization).

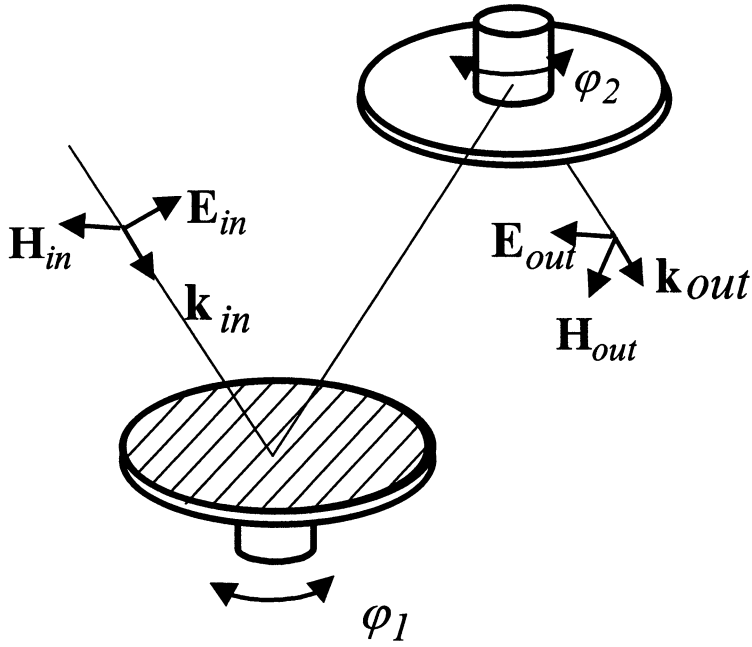

Fig. 4. Universal steerable double-grating polarizer

Gratings with wavelength-commensurable periods

Let us assume that the wave incidence to the grating is oblique and the grating period is chosen to provide only the 0-th order (mirror reflected) wave and the –1-th order (scattered) one (Fig. 1).

If the corrugation depth is small, the –1-th order direction beam power is much less than that of the mirror reflected beam. Such a configuration can be used as a ***directional coupler*** to monitor the RF flow power and to measure the field structure of the RF beam. If the 0-th order beam is reversed, the –1-st order beam is scattered into a conjugated direction; so, the coupler operates as a ***bi-directional*** one [3, 11, 9].

The partial scattering of the incident wave into the –1-th order direction ***couples*** the circulating mode of ***the multi-mirror cavity*** to input and output ***waveguides*** (Fig. 5). Such a cavity [12, 4] can function as a ***resonant ring*** (a plasma reactor or a test bench for various RF components),

as a ***notch filter*** [13] and as a ***pulse compressor*** [12, 4]. Circular cavity with two corrugated mirrors (Fig. 6) can function as a ***component of multiplexers*** (Fig. 7) in long range communication systems and radars with synthesized frequency band [4].

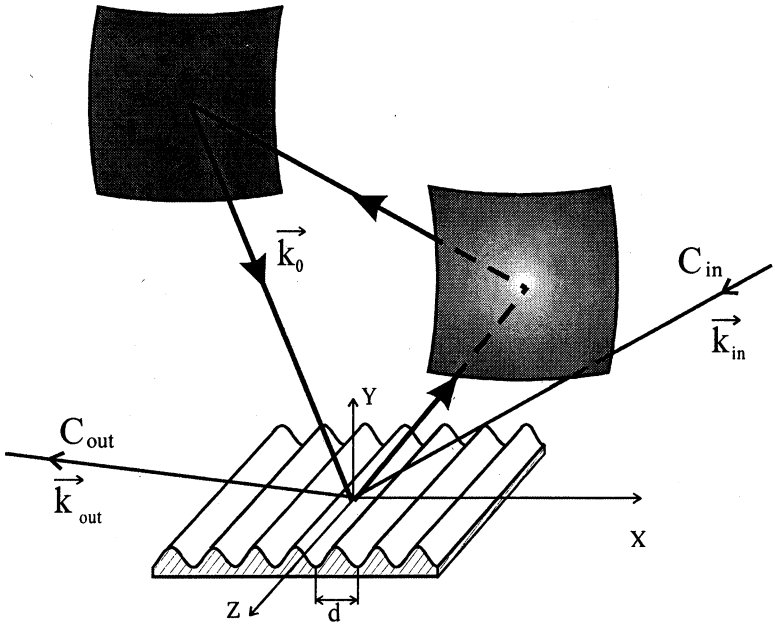

Fig. 5. Circular cavity coupled to input and output wave beams by mirror corrugation

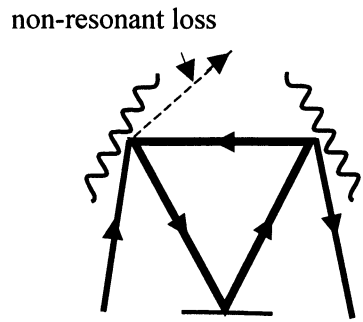

Fig. 6. Cavity with two corrugated mirrors

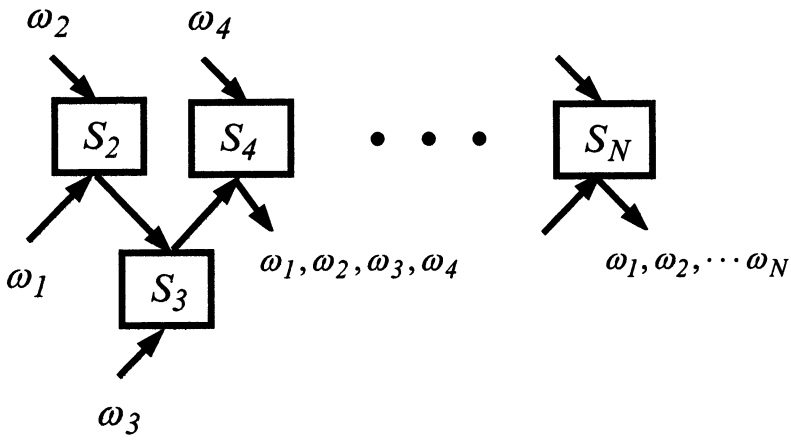

Fig. 7. Multi-resonant multiplexer:
combiner/divider of signals differing in carrier frequencies

With deepening the corrugation, the wave scattering into the –1-st order direction (Fig. 1) saturates, the saturation level depending on the primary wave incidence angle. In the ***anti-mirror reflection*** case (Fig. 8)

$$k_{-1,x} = -k_{0,x}\,, \tag{9}$$

at a proper corrugation depth, the efficiency of RF power conversion into the –1-st order wave is 100% [1] (Fig. 9). The total anti-mirror reflection can be provided, in particular, with the sinusoidal corrugation profile [1, 3, 14], the corrugation depth for E and H modes being different.

A partial anti-mirror reflection (Fig. 9, mode P) can ***enlarge the power capability of dielectric RF windows,*** compared to the conventional resonant matched windows. The resonant window (used to separate, e.g., a vacuum volume from the atmosphere) represents a plate which thickness is equal to any integer number of half-wavelengths in the dielectric. The RF field within the plate represents a superposition of counter-propagating waves. Obviously, that at the same transmitted RF power the RF load on the dielectric would decrease, if the wave propagated only in one direction. The latter condition is, evidently, satisfied if a plane wave is incident from a half-infinite vacuum to a half-infinite dielectric. In this case a part of the incident power is reflected (see the left-hand part of

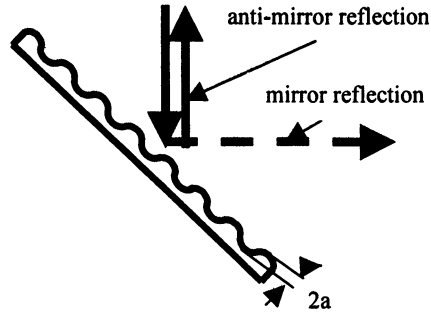

Fig. 8. Wave diffraction under condition that -1^{st} order beam is counter-directional to the incident one

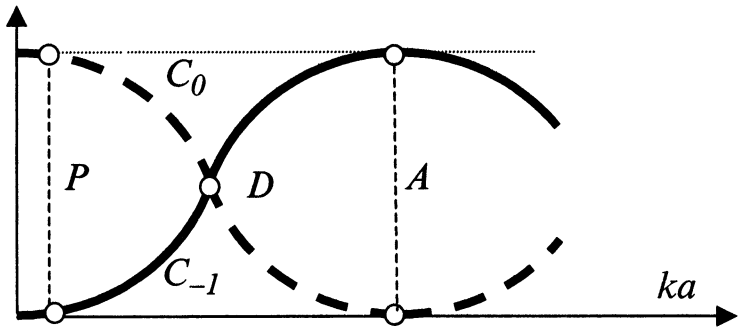

Fig. 9. Performance of grating shown in Fig. 8: P – partial scattering into anti-mirror direction, D – division of power into two halves, A – total anti-mirror reflection

Fig. 10), but the reflection can be compensated by the grating configuration inverse to that shown in Fig. 8 which operates in the partial anti-mirror reflection mode. Basing on the reciprocity theorem, we conclude that a symmetric grating provides the window matching at the right-hand side of Fig. 10. The thickness of such a window can be arbitrary.

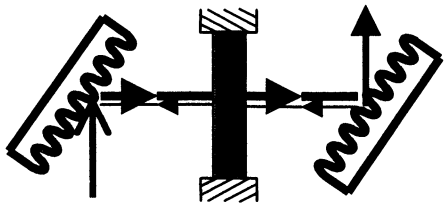

Fig. 10. Travelling wave window with matching anti-mirror reflection gratings

If the anti-mirror reflection grating (Fig. 1) divides the incident wave beam into the 0-th order and the –1-st order beams of equal powers (mode D in Fig. 9), the resulting ***3 dB coupler*** (Fig. 11) is equivalent to the magic T and, so, is capable to operate as a ***phase controlled beam***

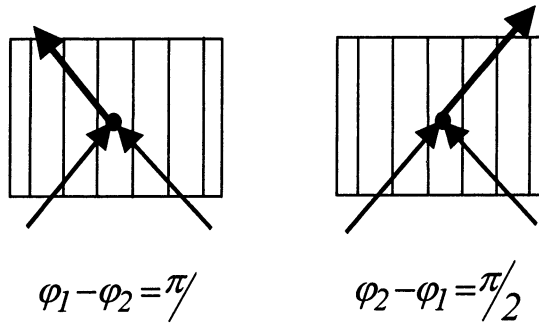

Fig. 11. Top view of phase controlled anti-mirror reflection 3 dB coupler

combiner [4]: by changing the mutual phase shift between two input beam we can change the direction of the output beam. Such phase controlled wave commutators can be used to compose a ***delay line distribution system*** (DLDS, Fig. 12) [4] for particle accelerators. The system provides feeding one accelerating section with one combination of mutually phase locked RF sources, then, after a period of time, feeding a neighboring section with a shifted combination of sources, and so on.

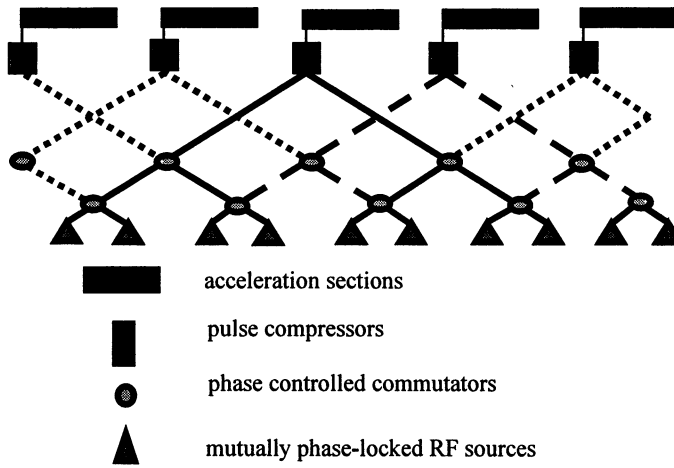

Fig. 12. Delay line distribution system to drive a future $e^- - e^+$ collider

Near to the total anti-mirror reflection (mode A in Fig. 9), the grating (Fig. 1) can operate as a ***frequency scan antenna*** and as a ***multiplexer*** [3, 15]. Combinations of anti-mirror reflection gratings can perform ***compression and decompression of microwave pulses*** [16, 17, 14]. Cavities with anti-mirror reflection gratings (echelettes, Fig. 13) are used in ***frequency tunable microwave generators*** based on the stimulated radiation of intense electron beams [18].

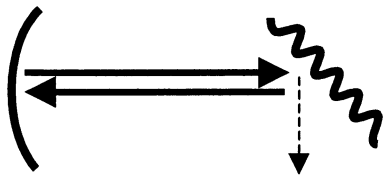

Fig. 13. Open cavity with echelette mirror providing diffraction output of power

Due to the anisotropy, the anti-mirror reflection grating (Fig. 1) can send the E-polarized wave into one (0-th order or –1-st order) direction and the H-polarized wave into another (–1-st order or 0-th order) direction (configurations of wave rays and gratings for these cases being different). Such a polarization ***separator*** [4] combined with a linear-to-circular polarizing grating represents the simplest radar ***antenna duplexer*** (Fig. 14) [4].

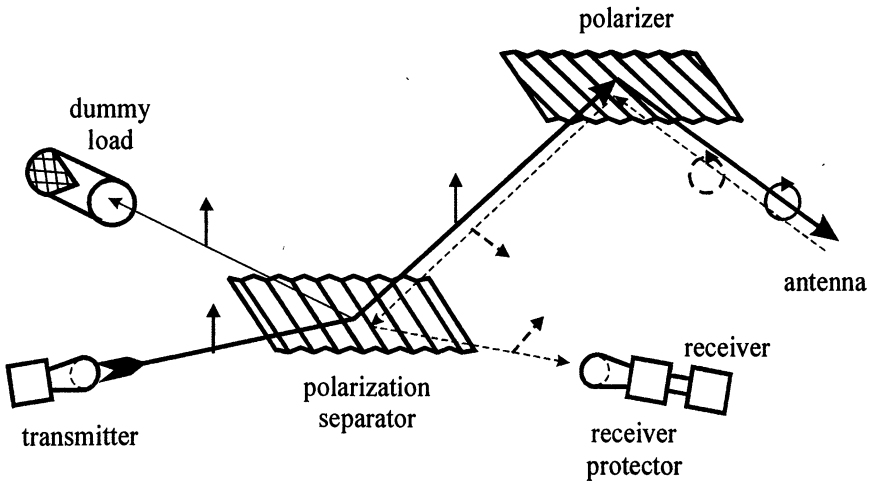

Fig. 14. Antenna duplexer

Gratings with period exceeding the wavelength: wave dividers /combiners

The broader is the ratio of the grating period relative to the wavelength, the larger is the amount of scattered waves. The power distribution between these waves is governed by the equal amount of efficient (linear independent) parameters of the corrugation profile. The inverse process provides ***combining*** any number of ***mutually phase-locked wave beams*** of arbitrary, in particular, equal powers [3].

Conclusion

Gratings can perform most of wave flow control functions similar to those of standard waveguide components used at relatively low frequencies. At the shortest (millimeter and sub-millimeter) microwaves the gratings are advantageous due to lower losses and higher RF power capabilities.

Acknowledgment

The author is grateful to V. Belousov, G. Caryotakis, B. Danly, V. Gregers-Hansen, J. Hirshfeld, W. Kasparek, P. Kolchin, E. Koposova, S. Kuzikov, B. Levush, A. Menegat, O. Nezhevenko, V. Pavelyev, R. Siemann, M. Tai, M. Thumm, S. Vlasov, D. Whittum for encouraging and helpful discussions.

The study was sponsored, in a part, by the Russian Fund for Basic Research, Soros grant 99-02-17781.

References

1. Petit R. (ed.), Electromagnetic theory of gratings, Berlin-Hedelberg-New York: Springer- Verlag, 1980.
2. Shestopalov V.P., Kirilenko A.A., Masalov S.A., Sirenko Yu.K., in *Diffraction gratings*, Kiev, Naukova Dumka, 1986.
3. Belousov V.I., Koposova E.V., Orlova I.M. et al, in *Gyrotrons*, Ed. V.A. Flyagin, Inst Appl. Phys., Gorky, USSR, 1989.
4. Petelin M.I., Caryotakis G., Tolkachev A.A., Kuzikov S.V. et al, in *High Energy Density Microwaves*, Ed R. M. Phillips, 1998 AIP Conference Proceedings 474, Pajaro Dunes, California, Woodbury, NY, 304.
5. Stallard B.W., Byers J.A., Makowski M.A., Int. J. Infrared and Millimeter Waves, 1990, **11**, no.9, 1011.
6. Belousov V.I., Bogdashov A.A., Chirkov A.V., Denisov G.G., Int. J. Infrared and Millimeter Waves, 2000, **21**, no.2.
7. Doane J.L., Int. J. Infrared and Millimeter Waves, 1992, **13**, no.11, 1727.

8. Nagasaki K., Itoh Y., Morioka H., Obiki T., Int. J. Infrared and Millimeter Waves, 1999, **20**, no.5, 823.
9. Thumm M., Kasparek W., Fusion Engineering and Design, 1995, **26**, 291.
10. Alexandrov N.L., Belousov V.I., Bogdashov A.A. et al, in this volume.
11. Henle W., Kasparek W., Kumric H. et al., Proc. EC-7 Joint Workshop, Hefei, China, 1989.
12. Petelin, M.I., Tai, M.L. in Proc. of the IAP Conf. on Pulsed RF Sources for Linear Colliders, Montauk, NY, 1994, 303.
13. Denisov G.G, Kuzikov S.V., Shmelev M.Yu, Proc. 18 Int. Conf. IR and MMW, Essex, 1993, **2104**, 353.
14. Kazakova N.G., Koposova E.V., Petelin M.I., Vlasov S.N., Int. J. Infrared and Millimeter Waves, 1997, **18**, 675.
15. Belousov V.I., Denisov G.G., Peskov N.Yu., Int. J. Infrared and Millimeter Waves, 1991, **12**, 1035.
16. Treacy E.B., IEEE J.Quant. Electr., 1969, **5**, 454.
17. Akhmanov S.A., Vysloukh V.A., Chirkin A.S. Optics of Femtosecond Laser Pulses, AIP, NY, 1992, chapt. 4.
18. Tran M.Q., Cao H., Hogge J.P., Kasparek W., Tran T.M., Paris P.J., J. Appl. Phys., 1993, **73**, 2089.

RESONANCE PROPERTIES OF DIFFRACTION GRIDS MADE OF RODS WITH PERIODIC GAPS

Eungsu Kim, N.F.Kovalev, S.E.Filchenkov

Institute of Applied Physics RAS, Nizhny Novgorod, Russia

The resonance properties of diffraction grids, which have periodical gaps, are introduced. Periodical small gaps in a rod make it possible to control the phase of the reflected wave and even to fully compensate the inductive characteristics of the rod without gaps. At resonance conditions, maximum surface current flows on the rod and evenly radiate all over the angles. And this resonance is not sensitive to the angle of the incident wave.

1. Introduction

Electromagnetic diffraction grids or systematic array of rods are widely used in various applications and in scientific researches. In this report will be investigated only metallic grids, which have the small period compared with wavelength ($\lambda >> D$). The grid, which is drawn in Fig.1, has the characteristics of directional conductivity. So to speak, scattering characteristics are strongly dependent upon the polarization of the incident wave. Specifically, at low frequencies, any kind of grid fully reflects a parallel-polarized wave independently on the diameters of metal rods. But a perpendicular polarized wave is fully transmitted [1]. Fig.2 shows such a characteristic. By additional parallel grids, we can make transmission become high and even to make total transmission at the frequency where we want. And we can also make reflection become high, but by a limited numbers of grids it is impossible to get a total reflection. So it would be very interesting if we could make total reflection by a small modification. But this idea is well described in [2]. A continuous metal rod in a waveguide, even with the big radius compared with waveguide width, can't make a full reflection. But a however thin rod, which has a small gap, totally reflects at a resonance frequency. Just this idea was studied in this report. The characteristics of grids of rods with gaps and one rod, which has periodical gaps as an element of grids, were surveyed. Period of these gaps (d) is very small compared with wavelength as period of rods (D) is. And it will be studied here only $\vec{\mathbf{E}}_{//}$ wave incidence case because just this wave can be reflected greatly under a small period of rods. Partial reflection, not total reflection, is not caused by the poor conductivity of the metal rod, but is

connected with its inductive characteristics. By insertion of small gaps, inductive characteristic may be fully compensated by capacitance of these gaps. The phase of induced current on the rod may be changed over a wide range by the control of this gap geometry.

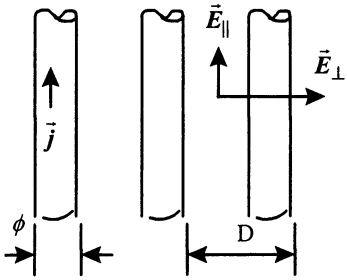

Fig. 1 General diffraction grid

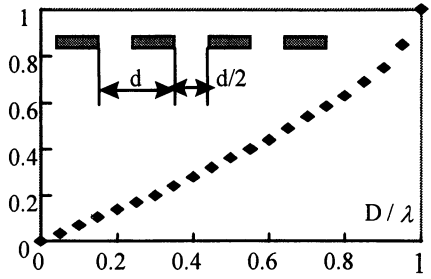

Fig. 2 Transmission characteristics of $\vec{E}_{//}$ wave incidence

2. Experiments

This comparatively simple idea was verified by grid-experiments in a waveguide (fig.3). Wide parallel plate was adopted to get a sufficient capacitance and 30 cm wavelength range was purposely selected. Vivid

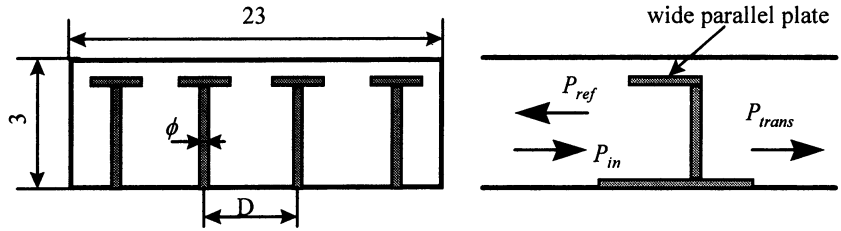

Fig. 3 Rectangular W/G set-up for experiments of grid with small gaps
($\lambda \approx 30$cm, $\phi / D \approx 0.06 \div 0.1$)

resonance curve was observed in the transmission graph fig. 4(a) which shows about $40 \div 50$ [dB] blocking performance at resonance frequency. And it was very easy to control the resonance frequency by changing the gap size or the area of wide parallel plate. As shown in fig. 4(b), the grid angle (γ) was changed from 0° to 60°, but the resonance frequencies varied only in the range of $\pm$ 0.6% of central resonance frequency. And in the near 2.45 GHz band, this grid shows 0.08 [%/cm] change of resonance frequency according to the variation of grid period *D*. Under the conditions described in fig. 4(c), every other rod has one and a half bigger gap size than normal ones. This experiment resulted in shifting of resonance frequency, not in splitting of it as resonator does. And this

resonance was not disappeared even under the inclination and rotation of rods as shown in fig. 4(d), but accompanied by a small change of resonance frequency.

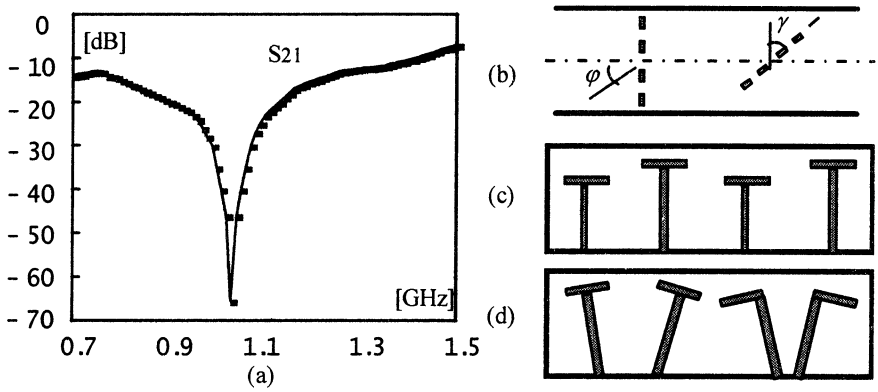

Fig. 4 (a) Transmission curve (experiment) (b) Rotation of grid angle (c) Change of gap sizes. (d) Inclination and rotation of grid.

3. Analysis

The most important result from the grid-experiments is the very weak dependence of resonance frequency upon the angle of incident wave (θ_{inc}) and the period of arrayed rods (D). This tell us that neighboring rods make very weak mutual interactions through their quasi-static fields, and their total effects are determined by their scattered wave. From the experimental results, it is possible to say that resonance phenomena of grids are the characteristics of grid itself. Therefore, most of analysis was devoted to the effective descriptions of scattered wave from one rod. The geometry is shown in fig. 5, where parameters were purposely chosen to make resonance at a wide gap. It is assumed that E-polarization plane wave is incident to the rod, which has a very small period and a diameter compared with the incident wavelength. The characteristics of gaps can be changed by variation of gap size and dielectric properties. It is useful to write the incident plane wave by z-

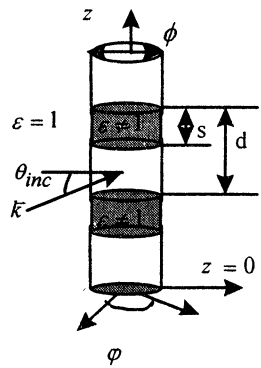

Fig. 5 Geometry of analysis (d = 1cm, ϕ = 0.5cm, λ = 6.28cm, θ_{inc} = 30[deg.])

directional electric type of Hertzian vector potential (1), where Bessel series is used and g_0, h_0 stand for x-, z-directional wave numbers

$$\Pi_z^e = e^{j(g_0 x + h_0 z)} = e^{jh_0 z}\{J_0(g_0 r) + 2\sum_{m=1}^{\infty} j^m J_m(g_0 r)\cos(m\phi)\}. \quad (1)$$

For description of scattered waves, z-directional magnetic type of Hertzian vector potential (2) is used to describe the depolarization phenomena of the scattered waves (m>0), as well as z-directional electric type of Hertzian vector potential (3), where $A_{\pm m}$, $C_{\pm m}$ represent the amplitudes of scattered E and H-wave in case of $i^m H_m^{(2)}(g_0 r)e^{\pm im\phi}e^{ih_0 z}/2$ incident wave

$$\Pi_{\pm m}^{\mu} = \frac{i^m}{2} C_{\pm m} H_m^{(1)}(g_0 r)e^{\pm im\phi}e^{ih_0 z}, \quad (2)$$

$$\Pi_{z,\pm m}^{e} = \frac{i^m}{2}\{H_m^{(2)}(g_0 r) + A_{\pm m} H_m^{(1)}(g_0 r)\}e^{\pm im\phi}e^{ih_0 z}. \quad (3)$$

The unknown coefficients $A_{\pm m}$, $C_{\pm m}$ can be gained by the simplest fields matching method in every m'th harmonics incidence. The fields should satisfy the boundary conditions on the rod surface. Namely, tangential component of total electric fields should be zero on the metal rod surface and tangential component of electric and magnetic fields should be continuous on the gap surfaces. From (2), (3), we can get the scattered wave expressions (4) and (5)

$$\Pi_{\pm m}^{e} = \frac{i^m}{2}(A_{\pm m} - 1)H_m^{(1)}(g_0 r)e^{\pm im\phi}e^{ih_0 z}, \quad (4)$$

$$\Pi_{\pm m}^{m} = \frac{i^m}{2} C_{\pm m} H_m^{(1)}(g_0 r)e^{\pm im\phi}e^{ih_0 z}. \quad (5)$$

But due to the condition $\phi << \lambda$, it is sufficient to consider only first two moments- axis symmetric (m=0) and dipole wave incidence (m=1). Fig. 6 shows the data which were calculated with the chosen parameters described in fig. 5 in case of m=0. When there is no lossy material, the amplitude of reflection coefficient is exactly one and scattering information exists only in the phase of the reflected wave. Fig. 6(a) shows that the phase of reflected wave is changed over a wide range dependently upon the gap size. This shows that there is a good possibility to compensate the inductive phase shift of the reflected wave. The phase of a reflected wave from a continuous rod is indicated by $\overline{A}_0$. As shown

in fig. 6(b), surface current that is proportional to B_0 becomes maximum at resonance. Fig. 6(c) shows the magnitude of the reflection wave when the gaps are filled with different lossy dielectric materials. At some gap condition, the reflection may go to zero.

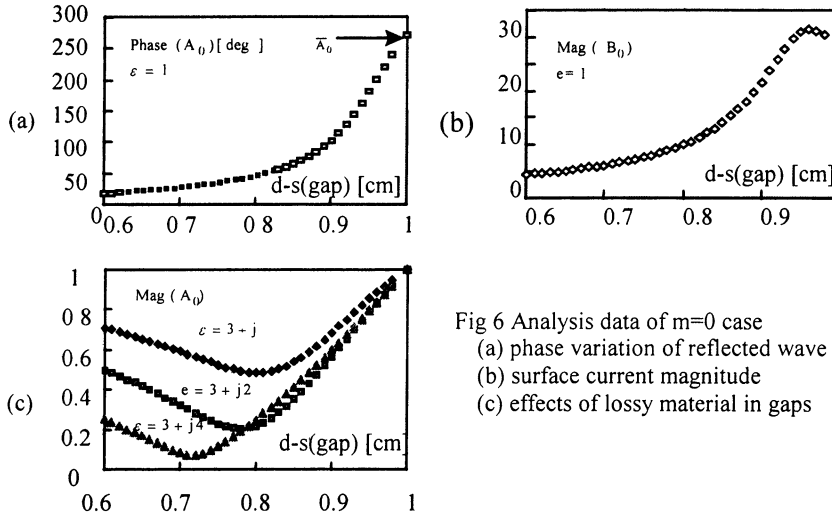

Fig 6 Analysis data of m=0 case
(a) phase variation of reflected wave
(b) surface current magnitude
(c) effects of lossy material in gaps

Fig. 7 shows the data of dipole wave incidence case (m=1), where should be considered depolarization effect, which can always be decreased by the proper choice of the rod radius without losing the resonance. Due to depolarization, the amplitude of E-wave is not exactly equal to one and a very small part radiates through H-wave.

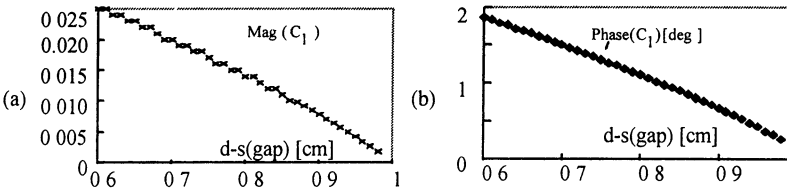

Fig. 7 Analysis data of m=1 case (a) Mag. of H-wave (b) phase variation of H-wave

But the square sum of E-wave and H-wave (C_1) becomes exactly one. Even though the rod diameter is about one tenth of wavelength, the amplitude of H-wave is very small (about 2 % of E-wave). For reference, he phase variation of the reflected E-wave is 2.6 [deg.]. This is about one hundredth of m=0 case, which means that it is difficult to compensate the inductive phase shift. Consequently, any correlation with resonance was not found. From the results of m=0 and m=1 cases, we can get the

solutions of the plane wave incidence case. Potentials (6), (7) from (4) and (5) can be used to find the unknown fields

$$\Pi^e = \frac{1}{2}(A_0 - 1)H_0^{(1)}(g_0 r)e^{ih_0 z} + i(A_1 - 1)H_1^{(1)}(g_0 r)\cos\phi\, e^{ih_0 z}, \quad (6)$$

$$\Pi^m = -C_1 H_1^{(1)}(g_0 r)\sin\phi\, e^{ih_0 z}. \quad (7)$$

Fig. 8(a) shows the directional radiation power density with parameters of gap size. At the resonance gap (s=0.15), radiation power propagates evenly all over the angle and at the same time becomes maximum radiation power density as shown in fig. 8(b). Absence of directional characteristics of radiation power under the resonance gap condition shows the possibility of total reflection of E-wave incidence with arbitrary angle (φ).

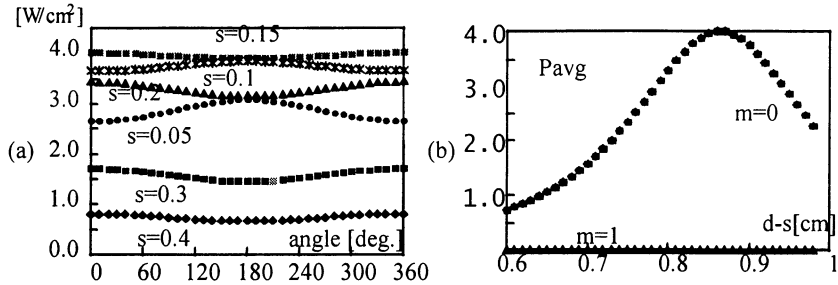

Fig. 8 Plane wave incidence case (a) directional power density of scattered wave (b) averaged power density of scattered wave over angle

4. Conclusion

It is evident that this type of grid is not suitable for the applications in mm wave or shorter wave range. Developed selective screen which used this type of grid shows about 70 [dB] attenuation performance in 10~30 cm wave range and insensitive characteristics to the incident angle. We have plan to develop space filter for radiation diagnosis from the developing high power relativistic microwave generator and to investigate the possibility of application to linear antenna, mode transducer in multi-mode waveguide and spiral waveguide.

References

1. L.A.Vainshtein, Electromagnetic Waves, Moscow: Radio & Comm., 1988, pp. 266-269.
2. N.Marcuvits, Waveguide Handbook, New York: McGraw-Hill, pp. 271-273.

NEW COMPONENTS FOR TE_{01} TRANSMISSION LINES

V.I. Belousov, A.A. Bogdashov, A.V. Chirkov, G.G. Denisov, S.V. Kuzikov

Institute of Applied Physics RAS, Nizhny Novgorod, Russia

New components for TE_{01} transmission line are presented. A new effective method for diminishing diffraction losses in waveguide gaps and miter bends has been developed and successfully applied. Several improved TE_{01} miter bends were designed and tested. Test results showed 10...20 times lower losses than in conventional miter bends. A new quasi-optical TE_{01} - TEM_{00} mode converter is presented. Results of measurements performed at millimeter waves agree well with the design parameters: total conversion efficiency exceeds 90% in the frequency band of 20%.

Introduction

There are many microwave devices operating at the TE_{01} mode of oversized circular waveguides: gyrotrons for plasma experiments and technological applications, low loss transmission lines, rotary joints, etc. Practically in all cases TE_{01} miter bends and TE_{01}-TEM_{00} mode converter are required and they are very important and critical components for applications. The goal of the work presented was improvement of these key components.

Improved miter bend

The miter bend with the plane mirror in the case of oversized waveguide is equivalent to the waveguide gap (Fig.1) [1, 2]. Power losses in the gap of a regular waveguide are:

$$P_{loss} = \frac{2}{\sqrt{\pi}} \cdot \frac{\mu_n^2}{3} \cdot \left(\frac{L}{k \cdot R_w^2} \right)^{3/2}. \qquad (1)$$

Many attempts were undertaken to decrease diffraction losses in the miter bend [2-5]. For example, adiabatic waveguide up-taper was suggested. Another approach based on operating mode transformation into the axis-symmetrical Laguerre-Gaussian wave beam by smooth up-taper and use of the elliptic reflector.

We propose to decrease diffraction losses by surface current diminishing near the gap. Obviously, there is a waveguide mode

superposition corresponding to the minimal surface current at the area where we assume to make the gap. Mode converter is needed to produce the required mode mixture. So, the improved miter bend consists of two symmetric mode converters and flat mirror between them (Fig. 2).

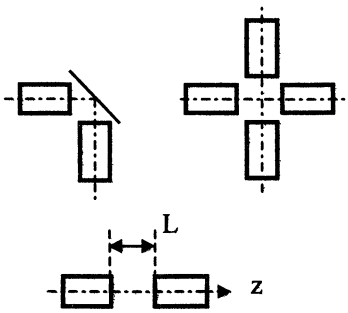

Fig. 1. Conventional miter bend and equivalent waveguide gaps.

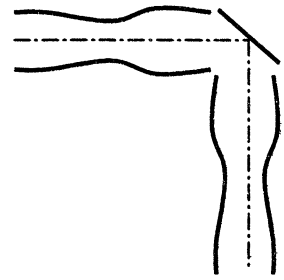

Fig. 2. Improved miter bend scheme.

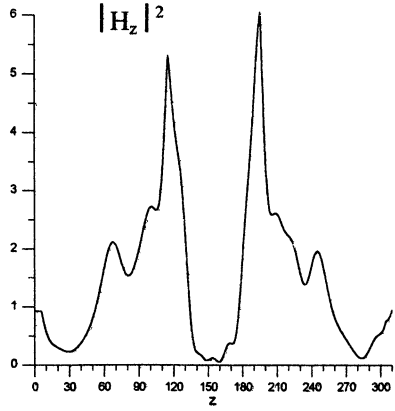

Fig. 3. H_z^2 distribution at the waveguide wall. Position of the gap (miter bend mirror) corresponds to the low field area near z=155 mm.

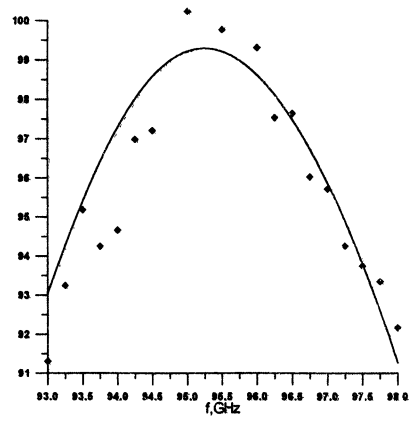

Fig. 4. Calculated (solid curves) and measured (dots) TE_{01} mode transmission coefficient through two gaps versus frequency.

Modified miter bend was designed for frequency 95 GHz and guide diameter 30 mm. Three modes were involved in the optimization procedure. The converter length is approximately 140 mm. The results of optimization are shown in the Fig. 3, 4. Simulated TE_{01} power transmission coefficient is 99.5% (Fig.4) in comparison with 90% for the conventional miter bend (1).

Experimental study of the miter bend

The setup (Fig. 5) includes a microwave oscillator (BWO, 78 - 118 GHz), directional couplers, Marie mode transducer, producing TE_{01} mode in 6 mm diameter waveguide, TE_{01} up-taper to 30 mm waveguide diameter and a miter bend made of Aluminum. The Marie mode transducer provides TE_{01} mode in rather wide frequency band (at least 85 - 100 GHz). The up-taper with a special profile also operates in sufficiently broad band. After the up-taper the measured field structure corresponds to TE_{01} mode with a small (<0.5%) amount of spurious modes. Measurements showed that TE_{01} mode purity at the up-taper output is about 98%. The spurious modes appear in the Marie transducer (1 - 2%).

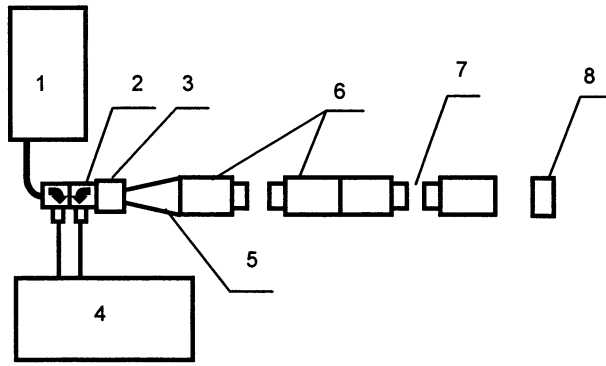

1 Microwave generator f=78...118 GHz
2 Directional coupler and detectors
3 Marie mode transducer
4 Scalar network analyser
5 TE_{01} up-taper Ø6- Ø30mm
6 Miter bend converter
7 Equivalent waveguide gap
8 Selective reflector

Fig. 5. Set-up for measurements of power losses in the mitre bend

The admixture of the wrong modes limited the accuracy of measurements of transmission coefficients as 2%. In the tests the TE_{01}

mode passed the equivalent miter bend gap and reflected back by a special selective mirror for the TE_{01} mode. The latter is a shaped quasi-optical reflector. Its reflection coefficient is more than 99% for TE_{01} mode and relatively small (e.g. 30% for TE_{02}) for all other modes. Measurements showed that the losses 99±1% are in a good agreement with calculations (see Fig. 4).

Two modified miter bends with plane reflectors were manufactured and tested. Experimental results coincide with the ones for waveguide gaps. Reflection coefficient from the miter bend was measured less than 25 dB.

TE_{01}-TEM_{00} mode converter

The converter consists of

- A non-quadratic mirror compensating the TE_{01} phase front appeared due to divergence of the field launching from the waveguide end. Before and after this mirror the field has azimuth polarization;
- Grooved mirror, which transforms azimuth polarization into the linear one;
- The pair of synthesized matching mirrors, which converts the linear polarized wave beam into required TEM_{00} mode.

The scheme of the converter (Fig. 6) has similar features to the one described in [6]. There are two principal differences in the approach to the converter design: 1) the scheme is used for conversion of TE_{01} mode propagating in an oversized waveguide. This makes the paraxial approach adequate; 2) the pair of matching mirrors is synthesized on the base of the iterative method [7-10].

The converter was designed for 95 GHz central frequency and 30 mm diameter of TE_{01} waveguide. Design size of TEM_{00} beam was choosen as 14 mm (half-width at 1/e of intensity). Compensating and grooved mirrors operate better for smaller angles of incidence to the normal, so, they were taken as 15 degrees. For matching mirrors the angle of incidence is 45 degrees. The converter input and output have the same axis.

The azimuth polarized field of the TE_{01} mode is radiated from the waveguide end at a relatively big spatial angle, and after phase compensation by the first mirror azimuth polarized beam comes to the grooved mirror. Grooved mirror turns the polarization of the beam in each point in such a manner that the reflected field has linear polarization.

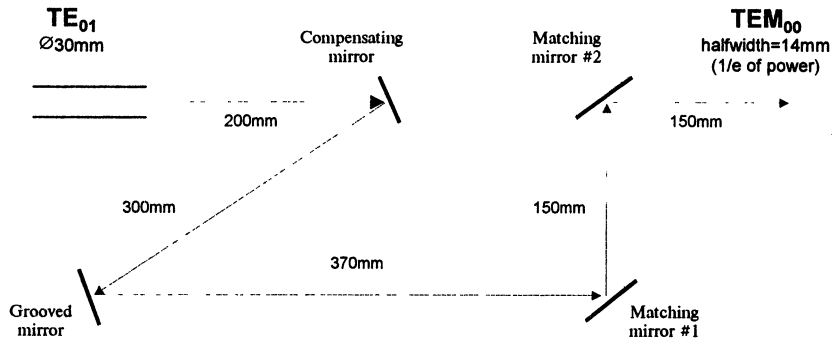

Fig. 6. Scheme of the TE_{01}-TEM_{00} mode converter

Since the radiation of the TE_{01} mode has concentric structure, it is possible to change the polarization vector using confocal parabolic grooves. The grooves transform the initial polarization into the linear one. When the polarization is corrected, it is possible to synthesize [7-10] the required TEM_{00} mode from the linear polarized wave beam.

Experimental study of the converter

The TE_{01} mode was excited using a BWO and Marie transducer. Output intensity patterns were measured in several cross-sections. After that the phase front was reconstructed [8, 10]. The measured patterns of the output beam are in a good agreement with calculations. Gaussian beam content (taking into account amplitude and phase distributions of the measured beam) was found as 96.3 ± 2% (Fig. 7).

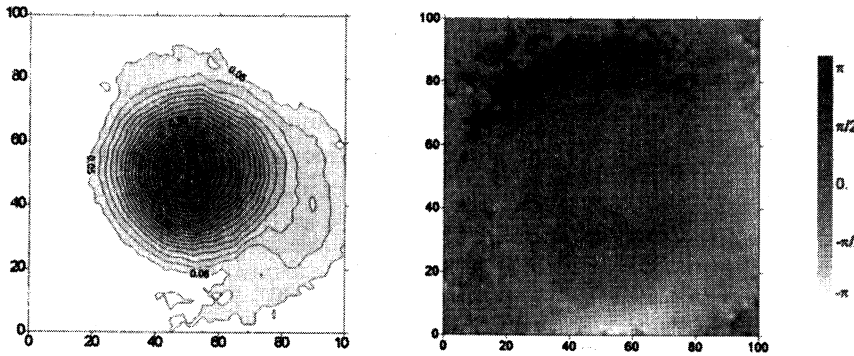

Fig. 7. Measured amplitude a) and reconstructed phase b) patterns at the converter output

Processing of the measured data gives the value of the cross polarization approximately 1.4%, diffraction losses 2% and ohmic losses 0.3...0.5% per mirror. These parameters correspond to the measured aperture of 100 × 100 mm. If a smaller aperture taken (one may filter the output wave beam by a smaller aperture), then the output wave beam parameters will improve. For instance, use of a circular aperture 70 mm of diameter increases the Gaussian content of output wave beam to 98%, and reduces cross polarization to 0.9%. Total efficiency of the converter for the both apertures exceeds 90% in the frequency band 85...105 GHz.

Conclusion

New components for TE_{01} transmission line: low loss miter bend and TE_{01}-TEM_{00} mode converter have been developed and tested successfully. The losses in the modified miter bend are 10...20 times less, than in the conventional one. The mode converter showed total conversion efficiency above 90% in the frequency band 20%. The components are compact and convenient for use.

Acknowledgements

This work is supported by the Small Business Innovation Research Program under contract #N0014-99-0003 and Omega-P, Inc.

References

1. Marcatili E.A., Waveguide Elbow / US Patent 3.090.931.C1.333-98; Filed Mar.8, 1962.
2. Vaganov R.B., Izvestiya VUZ. Radiofizika, **12**, 1969, 630.
3. Doan J.L., Muller G.A., Int. J. Elektronics, **77**, 1994, 489.
4. Katzenelenbaum B.Z., Radiotek. i Elektr., **8**, 1963, 1111.
5. Shapiro M.A., Vlasov S.N., Int. J. Electronics, 1992, vol.72, No 5 and 6, 1127-1133.
6. Stallard B.W., Byers J.A. and Makowski M.A. International Journal of Infrared and Millimeter Waves, 1990, vol. 11, No. 9, p. 1011-1032.
7. Katsenelenbaum B.Z., Semenov V.V. Journal of radiotechnics & electronics, 1967, 2, p. 244-252.
8. Chirkov A.V., Denisov G.G., Aleksandrov N.L. CD-ROM: Proceedings of PIERS'94, ESA-ESTEC, Kluwer academic publishers, The Netherlands, 1994.
9. Bogdashov A.A., Chirkov A.V., Denisov G.G., Vinogradov D.V., Kuftin A.N., Malygin V.I. and Zapevalov V.E. International Journal of Infrared and Millimeter Waves, 1995, vol. 16, No. 4, p. 735-744.
10. Chirkov A.V., Denisov G.G., Aleksandrov N.L. Optics Communications. 1995, vol. 115, p. 449-452.

DEVELOPMENT OF TRANSMISSION LINES FOR MICROWAVE RADIATION OF POWERFUL GYROTRONS

N.L. Alexandrov, V.I. Belousov, A.A. Bogdashov, A.V. Chirkov, G.G. Denisov, S.V. Kuzikov, P.A. Kapustin, D.A. Lukovnikov, V.I. Malygin, Yu.V. Rodin, M.Yu. Shmelyov, D.V. Vinogradov

Institute of Applied Physics RAS, Gycom Ltd.,
Nizhny Novgorod, Russia

A high-power millimeter-wave transmission line has to meet certain requirements, such as: low losses, possibility to measure transmitted and reflected power, to control the polarization of the wave beam, to transform the wave beam into the Gaussian one with required parameters. Additionally, the transmission line should shield the microwave radiation and be compact, as much as possible. A typical transmission line for a gyrotron with a built-in converter consists of a matching optics unit, a meter of transmitted and reflected power, a polarizer, a short quasi-optical mirror line, a corrugated waveguide, a waveguide converter, a barrier window and a mirror launching system into fusion installation vessel. If a gyrotron at the output has a waveguide mode, then additionally it is necessary to use a mode converter. This paper illustrates effective transportation of microwave radiation of a gyrotron with two examples of very different transmission lines: 1 MW / 110 GHz / 2 s for tokamak TdeV (Montreal, Canada) and 200 kW / 28 GHz / CW for tokamak Aditya (Ahmedabad, India). Principal problems and test results for these lines are discussed.

Introduction

Electron cyclotron systems of fusion installations are based on powerful millimeter wave sources – gyrotrons, which can produce now microwave power 0.5 – 1 MW in pulses of several seconds or about 200 kW in the CW regime.

Typical tasks in high power transmission line development are as follows: measurement of gyrotron output wave structure, conversion of gyrotron output wave into the eigenmode of a transmission line, monitoring of transmitted and reflected waves, polarization control, transmission with low losses (long distance), protection systems (arc detectors, reflected signal), microwave screening and cooling (especially for CW radiation) [1].

There are many transmission lines and components for various plasma installations developed at IAP / Gycom during last ten years (1989 – 1999). We may note ECW Transmission lines: T - 10, 15 (83 -

160 GHz / 0.3-0.9 MW / 0.5 s), HL-1 (37, 75 GHz / 0.4 MW / 0.1 s), RTP (110 GHz / 0.5 MW / 0.2 s), TdeV (110 GHz / 1 MW / 2 s), Aditja (28 GHz / 0.2 MW / CW), Textor (110 - 140 GHz / 1 MW / 10 s, under development). We developed different components for ECW transmission lines: W7AS (140 GHz / 0.5 MW / 1-3 s), ASDEX Upgrade (140 GHz / 0.5 MW / 1 s // 0.7 MW / 2 s), Heliotron-E (106 GHz / 0.5 MW / 0.2 s), TCV (82.7 GHz / 0.5 MW / 2 s), JET (140 GHz / 0.5 MW / 0.5 s), FTU (140 GHz / 0.5 MW / 1 s). Several transmission lines for technological gyrotrons (28, 30 GHz / 10 kW / CW) were also developed.

This paper presents the main results on two different transmission lines: 1 MW / 110 GHz / 2 s for tokamak TdeV (Montreal, Canada) and 200 kW / 28 GHz / CW for tokamak "Aditya" (Ahmedabad, India).

110 GHz / 1 MW / 2 s Transmission line for tokamak TdeV

The Gycom 110 GHz gyrotron "Centaur" produces pulses 1 MW / 2 s or 400 kW / 5 s. The output mode of the gyrotron is a Gaussian wave beam (88%) and spurious radiation (12%). The scheme of the transmission line is presented in Fig. 1.

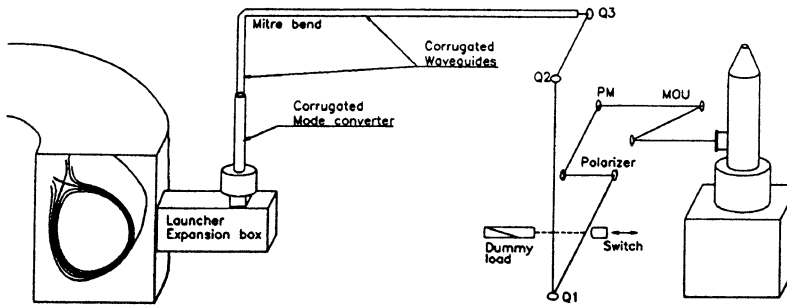

Fig. 1. Scheme of 110 GHz / 1 MW / 2 s transmission line for TdeV

The first component of the transmission line is the Matching Optics Unit (MOU), consisting of two mirrors and a microwave absorbing system on the wall of a metal box (Fig. 2). MOU filters and absorbs the spurious radiation and converts a wave beam to a Gaussian one. The Gaussian mode content at the output of the MOU is near 95%.

The second component of the line is the Meter of Transmitted and Reflected Power and Polarizer (MTP) (Fig. 2). MTP has a quasi-optical directional coupler, which splits the beam in two parts (99% and 1%), in two different directions. The small part (1%, 10 kW) propagates to the next grated mirror, the same like first one, but splits the beam to two parts 99.7% and 0.3%. The greater part (99.7%, ~10 kW) of the power

propagates to the calorimetric load and the smaller part (0.3%, 30 W), to the semiconductor detector. The main microwave power (99%, 1 MW) propagates to the Polarizer, which consists of two grated mirrors and can change the polarization of the wave beam to any polarization (Fig. 2) [2].

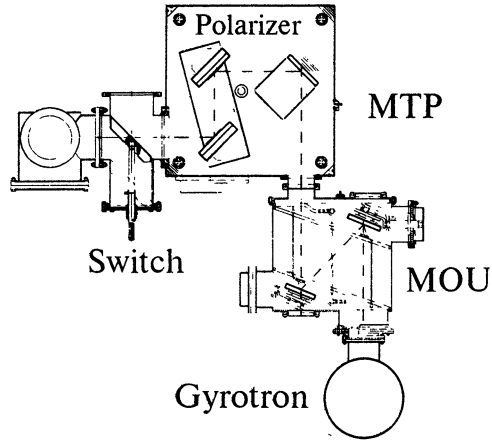

Fig. 2. Gyrotron part of the transmission line

There is a Mirror Switch, installed just after the MTP, to turn the microwave power of the gyrotron to the dummy load (Fig. 2). The next part of the line is a quasi-optical mirror line (three mirrors), that couples the wave beam to the corrugated waveguide. The corrugated waveguide is about 18 m long (I.D. = 88.9 mm), with one miter bend near the tokamak. The corrugated converter is used in the transmission line to flatten the beam distribution at the tokamak window, so as to decrease the maximum amplitude of the power on it by approximately 2.5 times (Fig. 3a) [3].

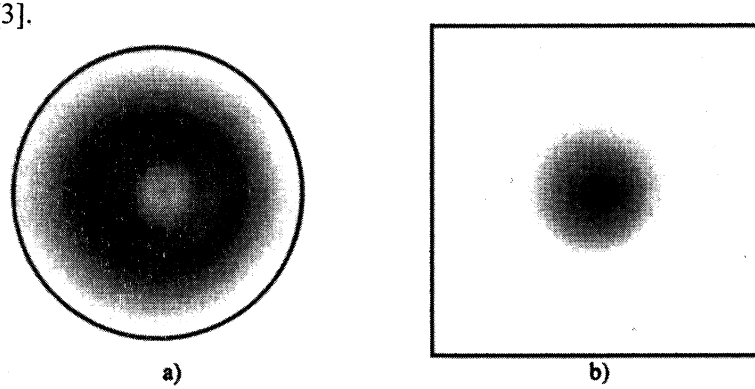

Fig. 3. The distribution of the microwave power at the tokamak window (a) and in plasma (b)

This converter is 1.2 m long and its I.D. = 100 mm. After the barrier window it is necessary to reconvert the wave beam to the Gaussian one (Fig. 3b). The Mirror launching System (two shaped and one flat mirror) in the tokamak port is used for this purpose (Fig. 4).

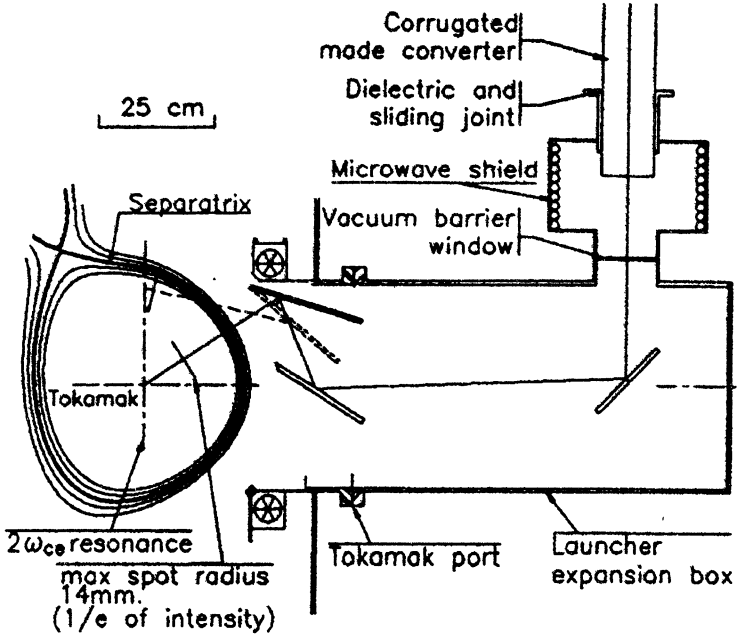

Fig. 4. Mirror launching system into tokamak port

There are some arc-detectors, installed in MOU, in MTP, in the Miter Bend and in the dielectric-sliding joint. There is a microwave shielding of all the transmission line. The high power test of the transmission line was divided into three stages. First of all, MOU and MTP were tested (Fig. 2).

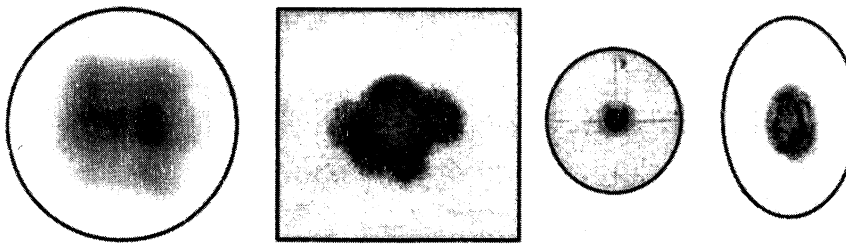

Fig. 5. The distribution of the microwave power at the output flange of the gyrotron "Centaur #2" (infrared measurements) (a), the thermal power patterns on the first mirror of the MOU (b), at the input of the corrugated waveguide (c) and at the miter bend reflector (d)

The microwave power distributions of the wave beam at the output flange of the gyrotron, thermal power patterns on the first mirror of the MOU and at the input of the corrugated waveguide are shown in Fig. 5. During this test the calorimeter load, transmitted and reflected semiconductor detectors in the MTP were calibrated. The total transmission coefficient was about 86%. At the second stage the transmission line from the gyrotron window up to the barrier window of the tokamak was tested. The beam pattern at the reflector of the miter bend is shown in Fig. 5d. The total transmission coefficient was about 81%. Finally a real experiment with the plasma into the tokamak was performed.

28 GHz / 200 kW / CW Transmission line for tokamak "Aditja"

The line is fed by CPI gyrotron which has the TE_{02} output mode. So, the line begins with the mode converter for the TE_{02} mode to a Gaussian wave beam. The drawings of the transmission line are presented in Fig. 6 and 7.

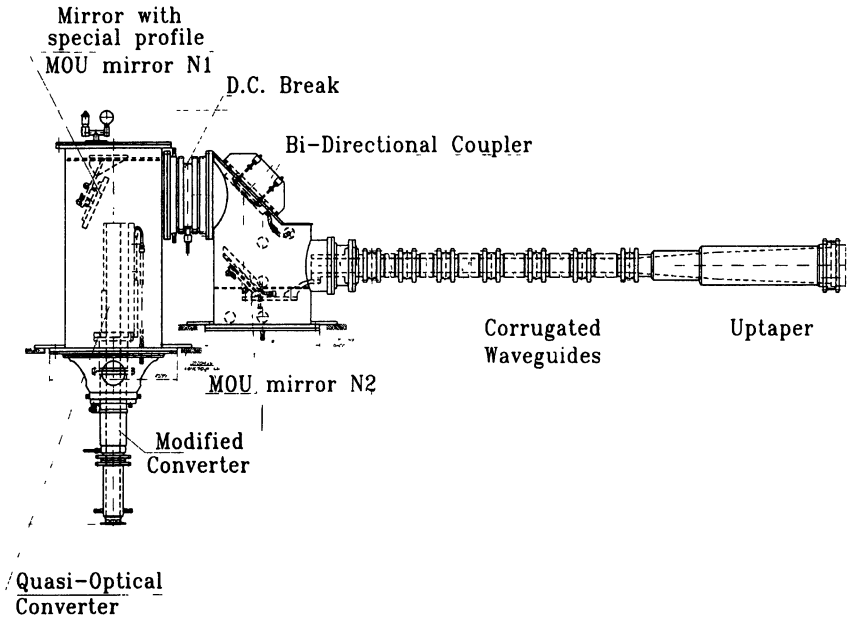

Fig. 6. Gyrotron part of the transmission line

There are bi-directional couples instead of MTP in this line. There is a water-cooling system for mirrors and waveguides. Transmission line is

filled with the fixed nitrogen at 0.5 bar of differential pressure. The modified mode converter and MOU were tested with the low power, using the TE_{02} mode exciter. The efficiency was about 90%.

The transmission line was also tested with a low power. The total losses in transmission line were approximately 20%.

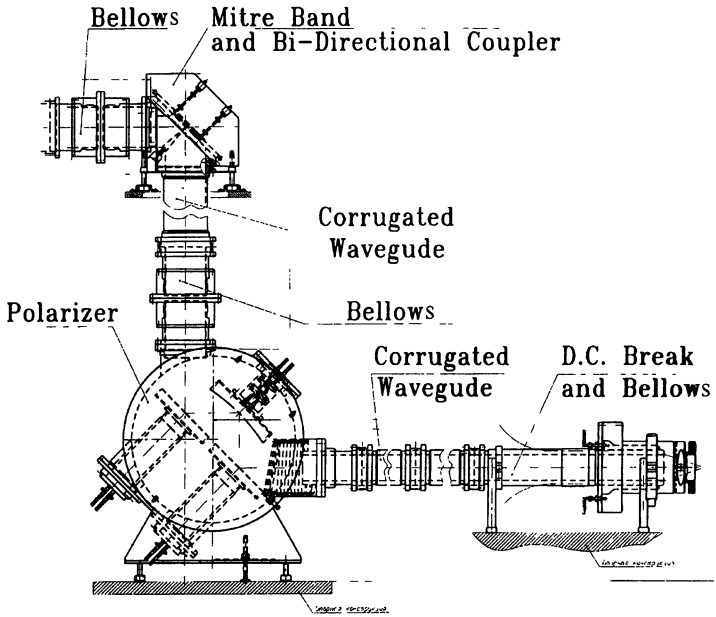

Fig. 7. Tokamak part of the transmission line

Summary

These two transmission lines demonstrate the possibility to transport microwave radiation of a powerful gyrotron for long distances with small power losses. These transmission lines have many important things, which are really needed for fusion installation, for example: monitoring of transmitted and reflected waves, control of the wave beam polarization, protection system and microwave screening.

References

1. Thumm M. and Kasparek W. Fusion Engineering and Design, 1995, 26, 291 – 317.
2. Belousov V.I. at all. Coll. Pap. "Gyrotron", Ed. Flyagin V.A., Inst. Appl. Phys., USSR, Gorky, 1989, 155 - 160.
3. Denisov G.G. at all. Proc. of the tenth Joint Workshop on ECE and ECH, 1997, 569 - 579.

MICROWAVE SYSTEMS BASED ON CONTROLLABLE INTERFERENCE OF PARAXIAL WAVEBEAMS IN OVERSIZED WAVEGUIDES

G.G. Denisov, S.V. Kuzikov

Institute of Applied Physics, Russian Academy of Sciences, Nizhny Novgorod, Russia

There are phenomena of image multiplication and mutual conversion of wavebeams running up in oversized waveguides. The paper discusses on new quasi-optical systems based on these effects. Such systems may be used for plasma fusion transmission lines, millimeter waves sources, RF systems of high-gradient particle accelerators.

Introduction

The phenomena, in which paraxial wavebeams in a waveguide might be repeated or split to several other wavebeams, were described for the first time in [1-2]. Some new phenomena, associated with possibility to operate in time by control of mutual phases in order to obtain necessary variable field structures, have been discovered recently [4, 9-10]. During the last several years many effects of this type were successfully applied for different microwave devices [3-11].

Mathematically, the mentioned phenomena are caused by the fact that phase shifts of waveguide modes representing the given paraxial wavebeams are actually divisible by π at some fixed distances. For example, in a planar metallic waveguide at distances $z=p/q\cdot a^2/\lambda$ the phase shift between modes with transverse indices n and m, respectively, is given by a simple formula:

$$\Delta\varphi_{n,m} = \frac{\pi}{4}\cdot\frac{p}{q}\cdot(n^2 - m^2), \qquad (1)$$

which follows from expressions for propagation constants with assumption of $a/\lambda>>1$ taken into account, where λ is vacuum wavelength, a is waveguide width, and p and q are arbitrary positive integers.

Note that some phenomena of the described nature exist also in waveguides of rectangular, circular, elliptic, and other cross-sections.

Systems Based on Wavebeam Splitting & Recombining

The simplest effect frequently used in microwave devices is actually wavebeam repetition. In rectangular waveguides it occurs: at distance

$z=8\cdot a^2/\lambda$, when all phase shifts are proportional to 2π; and $z=4\cdot a^2/\lambda$, when mutual phases between odd and even modes are proportional to π (all other phase shifts are divisible by 2π). In the second case initial wavebeam distribution is repeated being symmetrically reflected with respect to the waveguide axis.

This property is suggested to be used for wavebeam steering in plasma for ITER tokamak ECRH system [5]. The system allows steering the wavebeam injected into plasma by means of changing the launching angle only (Fig. 1). This makes it possible to exclude rotatable mirrors near the plasma edge. Calculations performed for f=170 GHz show efficiency not less than 95% for angls θ up to $\pm 12°$ and total length of the system ~8 m.

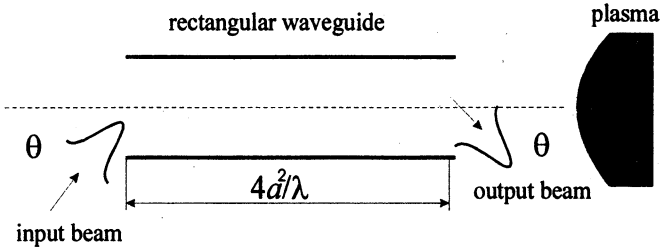

Fig. 1. Steering system scheme

Another application of the mentioned effect is field flattening over a quasi-optical window placed in an oversized waveguide in order to reduce peak RF field intensity [8] (Fig. 2). For wavebeam repetition scheme at =140 GHz peak intensity at circular ∅63.5 mm window is reduced four times.

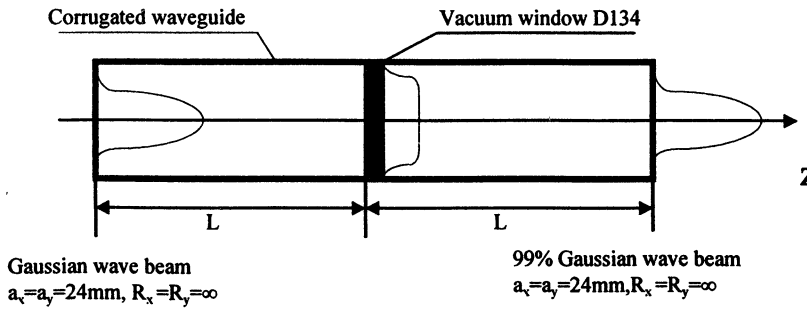

Fig. 2. Scheme of barrier window with field flattening

If the input field distribution is symmetrical, some effects take place at shorter distances. In particular, at distance

$$z=a^2/N\lambda \qquad (2)$$

the wavebeam symmetrical relative to the waveguide axis is divided into N identical wavebeams (Fig. 3).

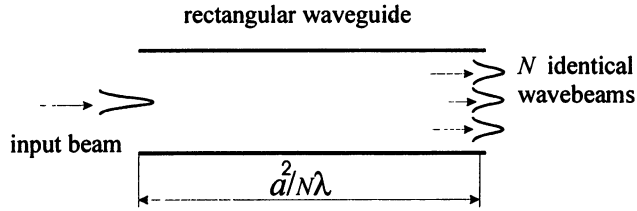

Fig. 3. Symmetrical wavebeam splitting

Splitting of the wavebeam into two wavebeams is helpful to separate the electron beam and microwave radiation in Free Electron Masers [7]. It is possible due to a zero-field region appearing between two split wavebeams. In this device the inverse effect (recombination of two wavebeams into one again) were also used.

The specific effect (Fig. 4), when a non-symmetrically launched wavebeam is split into two not identical parts (85% / 15% at $z=a^2/\lambda$), were successfully applied for quasi-optical input into a high-power FEL amplifier [6].

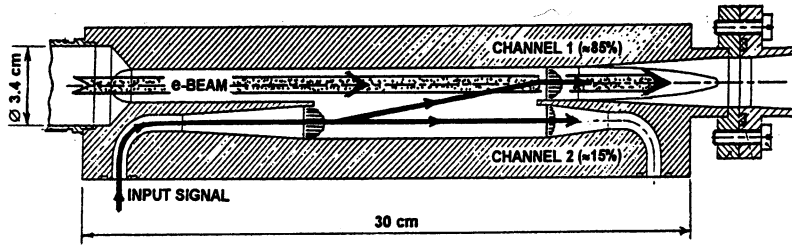

Fig. 4. Quasi-optical input into FEL amplifier

This input applied for the 36.4 GHz amplifier demonstrated unique broad frequency band ~10% where efficiency does not drop lower 82%.

Devices Used Controllable Elements

Some phenomena of the considered type may be applied also in systems, which are to operate with controllable parameters and field structures.

For example, a cavity with tunable Q-factor can be built using combinations of two effects at $z=a^2/2\lambda$ (Fig. 5) [3]. The first effect is the mentioned division of a symmetrical wavebeam into two parts in order to separate electrons and microwaves. The second one is the conversion of these wavebeams into three beams by means of a reflector providing a phase shift between the reflected wavebeams. The quality of the cavity is variable due to variations of power leakage connected with the side wavebeams. This leakage monotonously depends on the phase provided by the reflector.

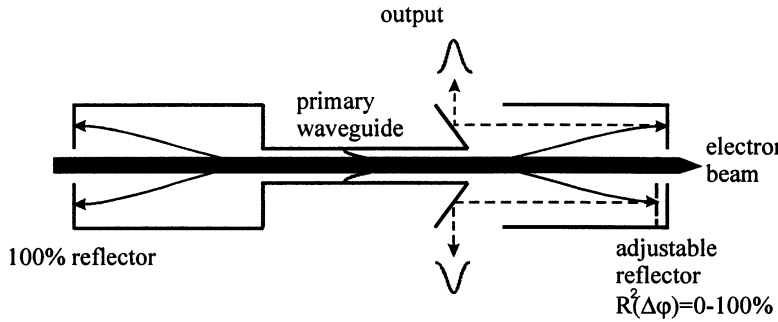

Fig. 5. FEM cavity with controllable Q-factor

The similar effects occur for the non-symmetrical case too. For example, at $z=2a^2/\lambda$ interference of two wavebeams leads to appearance of two other wavebeams in proportion depending on the mutual phase of the incident wavebeams (Fig. 6). According to (1), at this distance mutual phase shifts between odd and even modes are $\pi/2$, and phase shifts between any other modes are 2π. In fact, such system represents a so-called directional coupler, which is an important element of many devices.

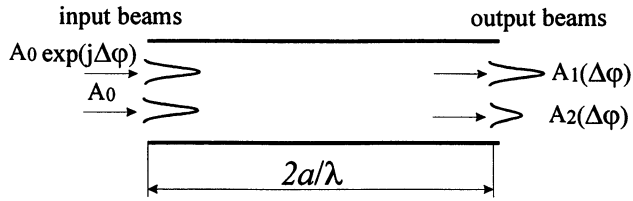

Fig. 6. Quasi-optical directional coupler

In particular, if mutual phase $\Delta\varphi=\pi/2$, then in output one obtains one beam of two times higher power in coparison to powers of each input

beams. If $\Delta\varphi=-\pi/2$, resulting wavebeam is shifted to other side of waveguide unlike the previous case. The considered system can be operated as quasi-optical –3 dB coupler. For ka=40 an efficiency of beams combining reaches 99% [9].

A more general case, when N wavebeams can be recombined into one wavebeam at a place in final cross-section depending on its mutual phases:

$$z=4a^2/N\lambda, \qquad (3)$$

seems promising for so-called Delay Line Distribution Systems. These systems are being elaborated now for acceleration of charged particles in future linear colliders. Its would be based on microwave amplifiers with electrically controlled phases.

In Fig. 7 the so-called four-channel coupler is shown. This component allows to combine powers from four amplifiers and feed consequently four independent consumers by means of operation in time by input mutual phases.

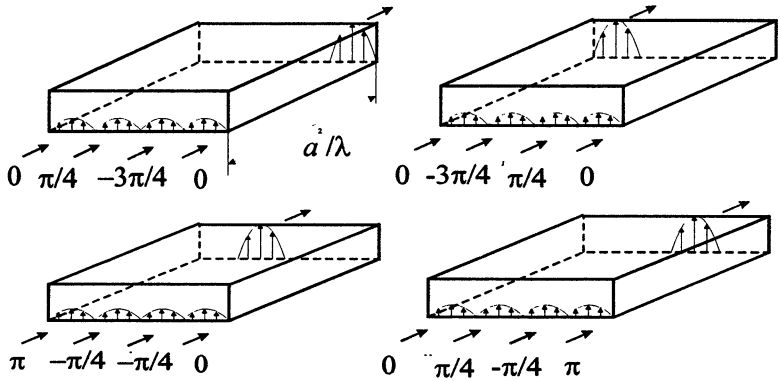

Fig. 7. Quasi-optical four-channel coupler

For a waveguide with width ka=100 an efficiency of the considered four-channel coupler exceeds 98% [9].

An attractive feature of such systems is that RF feeding of accelerating structures can be organized with power compression using electrically proof oversized waveguides only [9-11].

The systems like four-channel coupler seem perspective for radars where it is neccesary to operate frequently by characteristics of microwaves in time. In particular, one can provide fast scanning of radiation pattern. For example, multi-channel coupler, fed by several sources with controllable phases, forms the output wavebeam in different

positions depending on current mutual phases, and this obtained beam is reflected by parabolic mirror in different angle directions (Fig. 8).

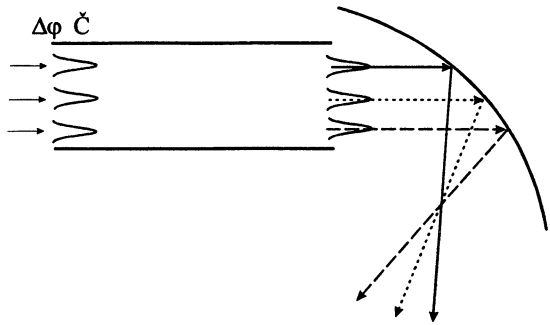

Fig. 8. Antenna system with controllable radiation pattern

Note that effects used in multi-channel coupler exist in 3D systems too which can be more convinient for radars. One of such versions of four-channel coupler, based on a waveguide with impedance corrugation of top and bottom walls, is shown in Fig. 9a. Resulting wavebeam appears here in one of four possible positions in output (these positions are separated by dashed lines). For a waveguide with ka=69 an efficiency of power combining reaches 99% [9].

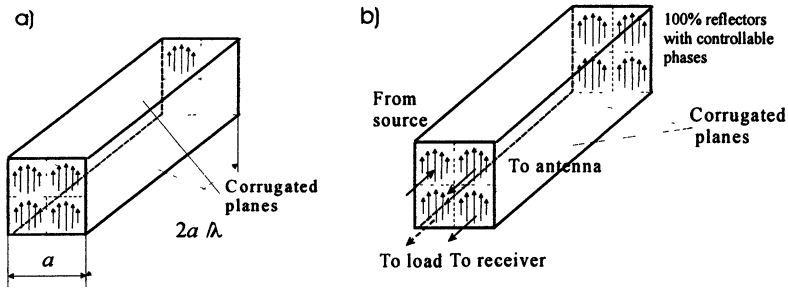

Fig. 9. Systems based on 3D couplers: four-channel combiner (a), duplexer (b)

The described device can be used also as a duplexer, if one applies electrical reflectors provided controllable phases of reflection (Fig. 9b). Such switchable reflectors are eloborated now basing on properties of silicon to change their reflectivity under illuminating its by intensive laser radiation [11]. So, the system allows to feed the only transmitting/receiving antenna providing protection of sensible receiver from irradiation of powerful source.

Conclusion

The systems based on the considered phenomena are simple, efficient, and broad-band. The new mentioned effects allow either electrical or mechanical real-time control of different regimes. The systems, based on the described phenomena, are very attractive for many applications.

References

1. Rivlin L.A. et al. Izv. VUZov, Radiophizika, 1968, Vol. 11, No. 4, p.572. (in Russian).
2. Semenov and Rivlin L.A., 1981, Laser Focus Feb. 1981, p. 82-84.
3. Verhoeven A.G. et al. The FOM-Fusion-FEM as a tunable ECRH source. Proc. of the Int. Workshop Strong Microwaves in Plasmas, Nizhny Novgorod, 1994, Vol.2, p. 616-631.
4. Denisov G.G. et al. Microwave Systems Based on the Effect of Image Multiplication in Oversized Waveguides. Conference Digest of 18-th Int. Conf. on Infrared and Millimeter Waves, 6-10 Sept. 1993, University of Essex, Colchester, United Kingdom, Vol. 2104, p. 485-486.
5. Chirkov A.V., Denisov G.G., Kasparek W., Wagner D. Simulation and Experimental Study of a Wavebeam Remote Steering System. Conference Digest of 23rd Int. Conf. on Infrared and Millimeter Waves, 7-11 Sept. 1998, University of Essex, Colchester, United Kingdom, p. 250-251.
6. Kaminsky A.K. et al. 36.4 GHz FEL-Amplifier Driven by Linear Induction Accelerators. Proceeding of FEL98 Conference, August 16-21, 1998, WE-3-20.
7. Abramovich A. et al. First operation of the Israel Tandem Electrostatic Accelerator Free-Electron Laser. Proceedings of the 19th International FEL Conference, August 18-22, China, 1997, p. 16-20.
8. Denisov G.G. et al. Calculations and Experiments on HE_{11} Mode Excitation by Paraxial Wavebeams. Proc. of 10th Electron-Cyclotron Emission and Electron-Cyclotron Heating Conf., 6-11 April 1997, Ameland, p. 569-580.
9. Kuzikov S.V. Wavebeam Multiplication Phenomena to RF Power Distribution Systems of High-Energy Linear Accelerators. International Journal of Infrared and Millimeter Waves, Vol. 19, No.11, 1998. P. 1523-1539.
10. Kuzikov S.V. Quasi-Optical RF Power Distribution Systems of Future Linear Accelerators, Abstracts of 17th International Conference on High Energy Accelerators, Dubna, 1998, p.25.
11. Petelin M.I., Tolkachev A.A., Kuzikov S.V. et al, Quasi-Optical Components for MMW Fed Radars and Particle Accelerators, RF98 Workshop, October 5-9, 1998, hosted by SLAC (in print).

DEVELOPMENT OF 1 MW OUTPUT POWER LEVEL GYROTRONS FOR FUSION SYSTEMS

G.G. Denisov

Institute of Applied Physics Russian Academy of Sciences,
GYCOM Ltd, Nizhny Novgorod, Russia

The paper presents the latest results of development of 1 MW power level gyrotrons for future fusion installations. These applications require a very long pulse of microwaves (10...1000 s) or CW tube operation at frequencies 110...170 GHz. The distinctive features of modern gyrotrons, the main problems of elaborating powerful gyrotrons, highlights of gyrotron development in the last 3-4 years and future perspectives are discussed.

Introduction

Gyrotrons are the most advanced high-power sources of millimeter wavelength radiation [1–4]. They have been used for many years in electron-cyclotron-wave (ECW) systems of many existing fusion installations. Typically modern gyrotrons produce power of 0.5...0.8 MW in pulses of 2–3 seconds, or lower power in longer pulses (e.g. 300–400 kW in pulses up to 10–15 seconds). For the next generation of fusion installations, such as ITER or W7-X the ECW systems based on gyrotrons capable to produce 1MW/CW radiation are considered. Definitely, such gyrotrons with enhanced performance are very interesting also for the use also at existing installations.

Main problems of elaborating high-frequency CW gyrotrons are associated with attainment of the megawatt RF power level. A modern millimeter wave gyrotron consists of an electron gun, which forms an electron beam with helical trajectories of particles (typical gun voltage is 70...90 kV, current 30...40 A, pitch factor 1.2...1.4), electron beam tunnel, an oversized cavity operating at a high-order mode, quasi-optical mode converter, output window and collector. At the megawatt power level many of gyrotron subassemblies (cavity, window, collector) have to operate at thermal loads close to their limits. There are principal problems to provide high efficiency of the device and absence of parasitic instabilities in the tube in high power regimes of gyrotron operation. The problem of matching the gyrotron output beam of the megawatt power level and the following transmission line proved to be a quite serious problem. And the most acute problem in the recent years was gyrotron window development.

Analyzing the gyrotron development during the last three-four years one may notice that several principal steps were made in development of the megawatt power gyrotrons:

- efficient and stable gyrotron operation was demonstrated at very high order volume modes (e.g. $TE_{25\,10}$). Operation at such modes allows one to solve the problem of thermal cavity loading;
- demonstration of the depressed collector in high power gyrotrons. This point gives a great move in solving gyrotron collector and power supply problems;
- gyrotron windows made of artificial diamond discs were developed. They are still very expensive but, no doubts, they will help to solve the very old and painful problem of barrier windows.
- successful use of gyrotrons in plasma experiments.

These points form a very reliable basement for elaboration of MW/CW tube and bring optimism to gyrotron developers and users.

High-Order Operating Modes in Gyrotrons

Gyrotrons are capable to produce a very high average power because they operate at very high volume modes of cavities formed by sections of slightly irregular waveguides. Practically every year gyrotron developers show higher and higher gyrotron operating modes. Ten years ago $TE_{15\,4}$ (fifteen azimuth and four radial variations) seemed to be a very high gyrotron mode. Several years ago $TE_{22\,6}$, mode was a favorite mode for gyrotron developers. In the last years extremely high-order modes $TE_{25\,10}$, $TE_{31\,8}$ were successfully used in gyrotrons [24, 25]. Cavity for the latter modes is approximately twenty wavelengths in diameter. Figure 1 gives an idea about the field structure of such a high mode.

The main reason to use large size cavities is the problem of thermal loading on the cavity wall. Specific power absorbed in the cavity with radius R_C, length L_C, Ohmic and diffraction Q factors is:

$$\Delta P/\Delta S = P_{out}\cdot(Q_{diff}/Q_{ohm})\cdot(R_C\cdot L_C)^{-1},\ Q_{ohm} = (R_C/\delta)(1 - m^2/\nu^2),$$

where $k\cdot R_C = \nu_{m.p}$, $k = \omega/c = 2\pi/\lambda$, $\nu_{m.p}$ is corresponding Bessel function root, m is azimuth index, and δ is skin depth.

The specific power is limited for gyrotron cavity configuration and technology as $\Delta P/\Delta S < (\Delta P/\Delta S)_{crit} = 2–3$ kW/cm^2 and power enhancement is strictly linked with cavity size increase. Typical diffraction Q-factor for fusion gyrotrons is 1000–1500. Ohmic quality depending on the cavity size and wavelength is of the order of 50000, so several per cent of power

(tens kilowatt) is dissipated in the cavity. This power and its density require very advanced cooling systems for gyrotron cavities.

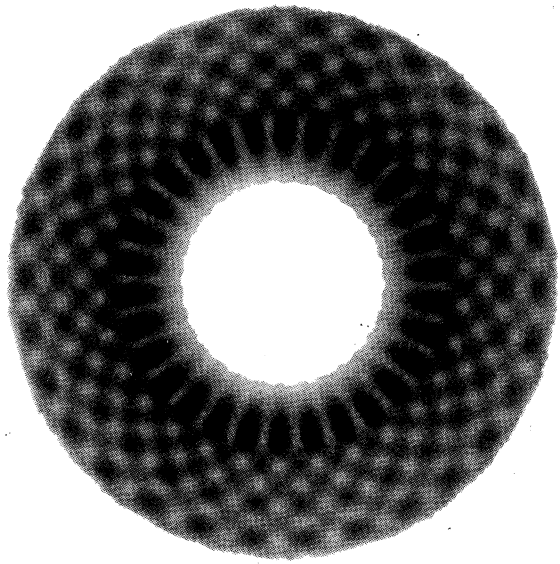

Fig. 1. Relatively "low" (ν=29.907) gyrotron operating mode: $TE_{15\,4}$. Transverse electric field $|E_{\perp}|^2$

The use of very high-order modes in gyrotrons brings some principal problems. The main problem is stable and efficient gyrotron operation. Recent calculations and experiments give a feeling that operating modes with indexes 60–70 are near the limit for gyrotron operation with acceptable efficiency (not less than 30 % without collector energy recovery) in sufficient (not extremely small) area of the magnetic field and voltage. We can illustrate how the problem arises accordingly to the increase of the cavity size. Let us consider two 1 MW gyrotrons with optimized cavities [7]. If one takes the $TE_{19.5}$ operating mode, then (see Fig. 2) practically any initial combination of amplitudes of the operating and the most dangerous parasitic modes comes after some time to the chosen mode. The situation for the $TE_{31.8}$ operating mode is quite different (Fig. 3): very small area of initial amplitudes results in the single-mode and efficient operation of the gyrotron.

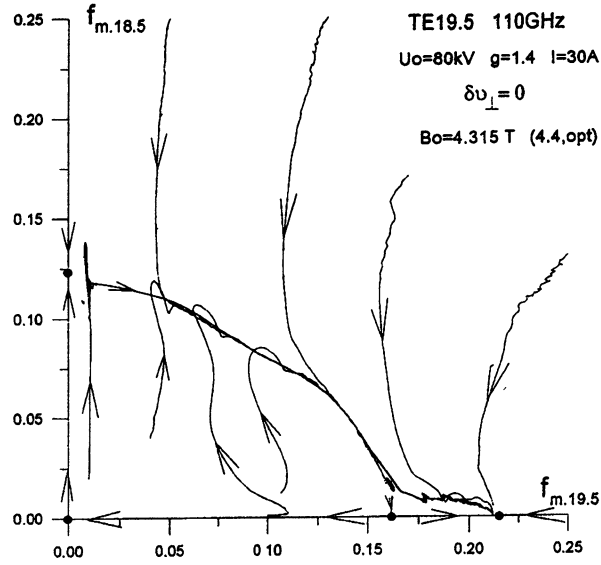

Fig. 2. Oscillations of modes versus initial amplitudes. Magnetic field and voltage are optimized for efficient oscillations of $TE_{19\,5}$ operating mode

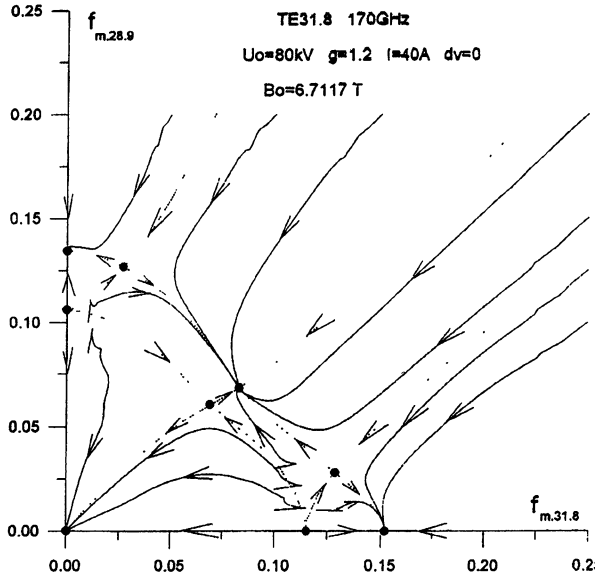

Fig. 3. Oscillations of modes versus initial amplitudes. Magnetic field and voltage are optimized for efficient oscillations of $TE_{31\,8}$ operating mode

A further increase of cavity size requires additional ways of mode discrimination. One of the tested ways is the use of a coaxial insert into the cavity. Such an insert of a proper diameter and shape makes diffraction quality of some parasitic modes lower. The insert has diameter a bit less than the caustic diameter of the chosen operating mode and does not disturb it but makes less diffraction quality of modes with smaller caustics. Rather sophisticated methods [28–30] based on optimization of the insert profile and surface impedance resulted already in successful gyrotron operation at modes with extremely high transverse indexes as $TE_{28\,16}$ and $TE_{31\,17}$, (cavity diameter $\varnothing_C \approx 30\lambda$). Calculations show that this way is promising and for further steps in the cavity size.

Scheme of Modern Gyrotron

Gyrotrons for fusion systems are developed by several companies and institutions [1–4]. The scheme of the most advanced gyrotrons are similar for all companies and presented on Fig. 4. There are also similar definitions of gyrotron sub-assemblies. We shall enumerate them and indicate critical points and principles of component development.

Electron gun and beam tunnel is intended to form an intense electron beam with design parameters. The goals of optimization are maximal transverse energy $(V_\perp/V)^2$, small velocity spread $(\Delta V_\perp/V_\perp)$ and prevention of instabilities in a beam tunnel. This component is usually optimized thoroughly on the base of special codes [5, 6]. Typical electron beam parameters of megawatt gyrotrons are presented on Figs. 5, 6.

Cavity sizes and its quality factor depend on electron beam parameters. A very critical parameter is the thermal loading of the cavity. There are some contradictions in providing simultaneously high gyrotron efficiency and relatively low specific Ohmic losses. The compromise is achieved in numerical optimization of cavity/electron beam parameters and very often the parameter choice is checked in a so-called short-pulse gyrotron prototype. In the experiment with a short-pulse tube (e.g. 100 microseconds pulse duration) the regimes of efficient gyrotron operation are found compared with the simulated predictions. The short pulse tests give also information whether the gyrotron mode converter works properly.

Quasi-optical mode converter [8–10] transforms a high-order operating mode into a paraxial wave beam with linear polarization and separates electron and wave beams. The electron beam goes to the collector and the wave beam usually comes out of the tube in the direction

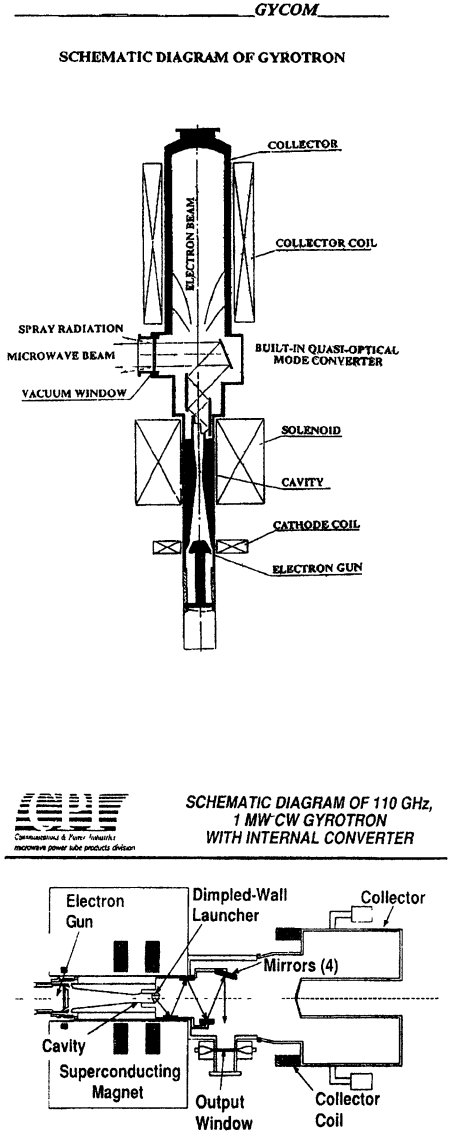

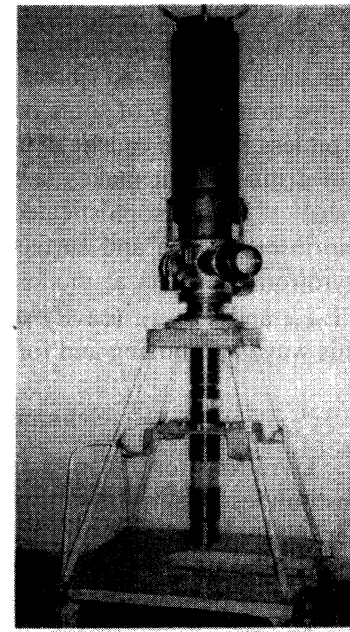

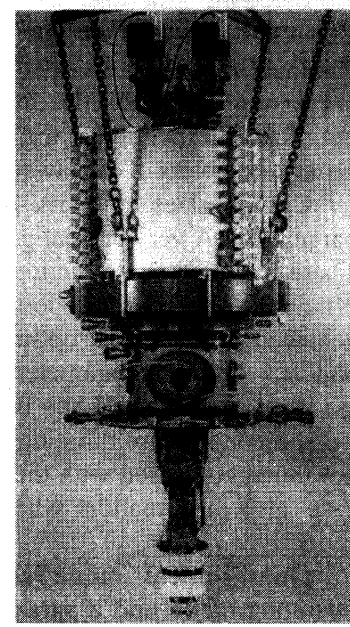

Fig. 4. General scheme and appearance of megawatt gyrotrons: GYCOM and CPI

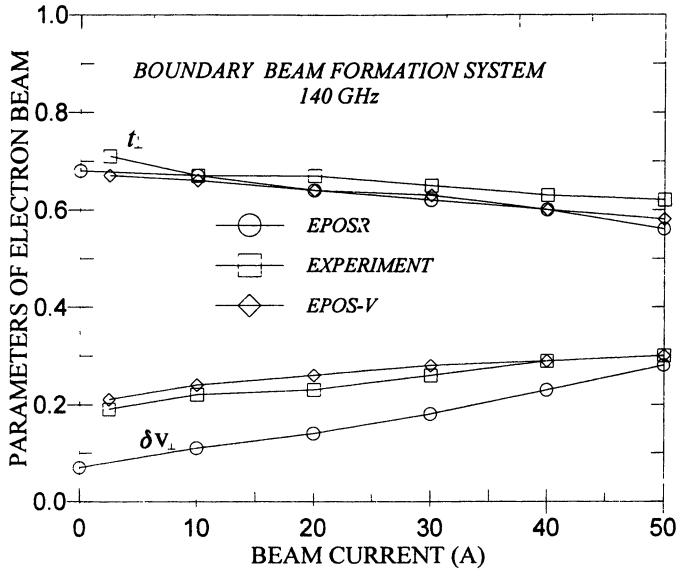

Fig. 5. Velocity spread $\delta v_\perp$ and relative oscillatory energy of electrons $t_\perp$ as a function of beam current

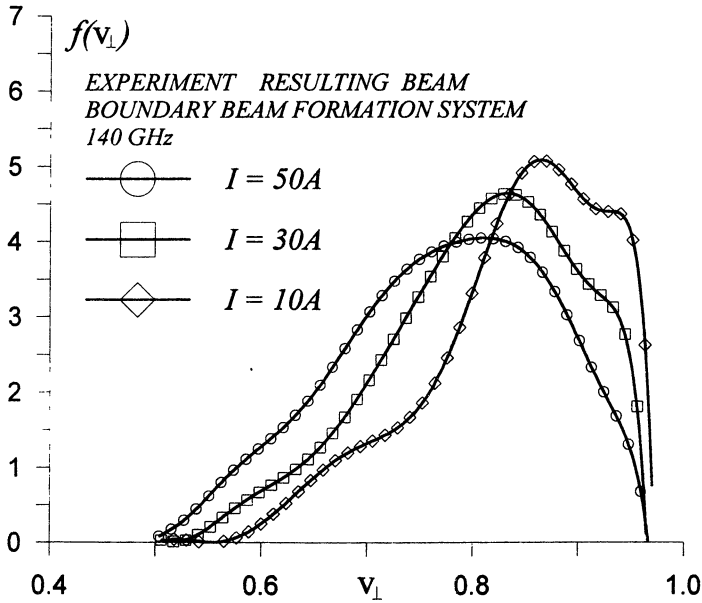

Fig. 6. Oscillatory velocity distribution function at various currents (experiment, resulting beam)

perpendicular to the magnet axis. This separation gives the possibility to solve collector and window problems practically independently. The mode converter consists of a special irregular cut ending waveguide up-taper from the cavity, quasi-parabolic reflector and one or two specially shaped mirrors. Sometimes more mirrors are applied to transmit the wave beam inside the magnet. The converter forms an optimal spatial field structure over the window surface: the flattened distribution for long pulse gyrotrons with ceramics (BN) windows, where thermal conductivity of window material is relatively low, or Gaussian distribution (optimal for wave beam transmission) for diamond windows.

The mode converter is an open mirror line and there are diffraction losses inside a gyrotron. For the megawatt tube the acceptable level of these losses is 3...5 %. There are methods to provide so low diffraction losses: pre-shaping of the wavebeam before its launching from the guide cut [9], and synthesis of the quasi-optical reflectors [10, 11]. By the first method the field of the operating wave is shaped (by means of small irregularities of up-taper) even before its radiation from the cut. The shaped beam has weak fields at the cut edges (lower diffraction) and a nearly Gaussian angle spectrum. The second method allows one to synthesize a desired field structure of paraxial wavebeams (see Fig. 7).

In fact, the mode converter ends outside the tube. The output wave beam before its use practically in all cases passes through so-called **matching optics** which adjust the beam to the following transmission line. To do this accurate wavebeam measurements are needed. High-power beams structure measurements may be performed by means of infrared camera recorded thermal traces of the beam passing through thin dielectric films [35]. Having measured intensity distributions one can perform phase front retrieval [12] and after that mirror synthesis for the beam conditioning. The matching optics unit includes at least two mirrors, which align the angle and position of the beam at the input of transmission guide.

Electrons after separation from the wave beam come to a **collector**, which is the biggest part of a megawatt gyrotron (Fig. 4). A tremendous power (2–3 MW) is to be dissipated on the collector surface. This results in huge water consumption of 20–30 l/s. The collector has large diameter 200–300 mm and length of about 1 meter. For some gyrotrons electron beam sweeping is applied to distribute it over collector surface. Magnetic field guiding the electrons is weak at the collector area and consequently it is rather sensitive with respect to stray magnetic fields (from

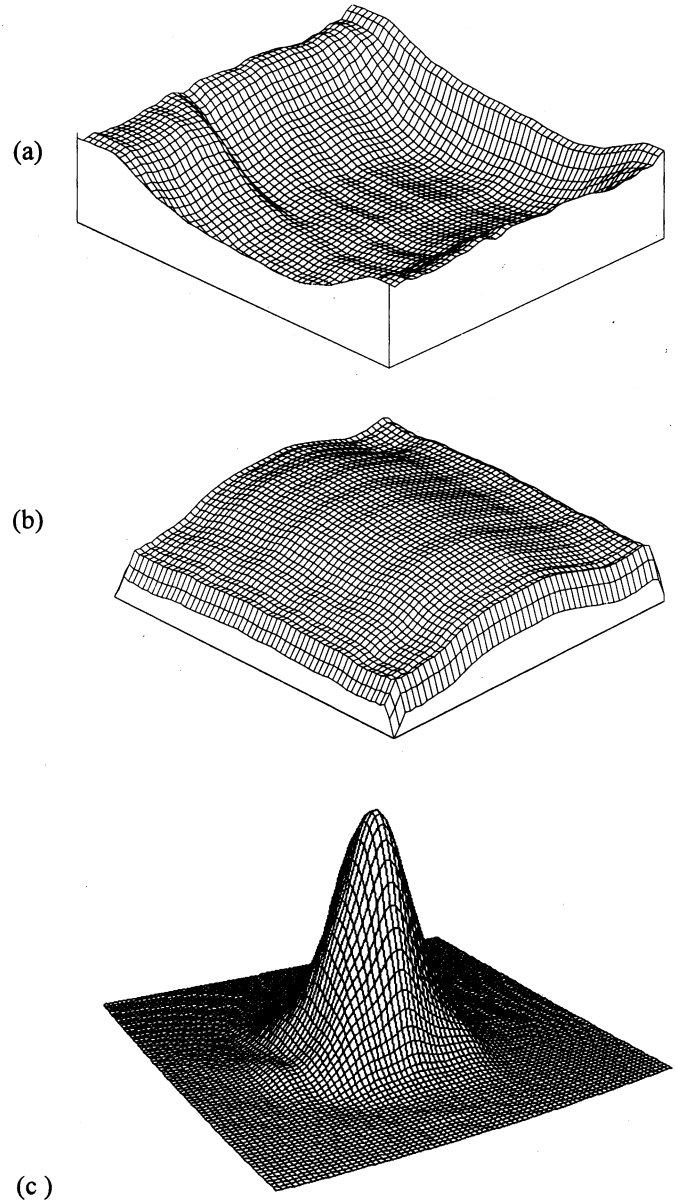

Fig. 7. Typical surface (a, b) of shaped mirrors inside a gyrotron: 170 GHz GYCOM gyrotron (mirror #1: 120x135x1.44mm, mirror #2: 90x93x1.93mm). Field intensity (c) of the output beam at the gyrotron window

neighboring gyrotrons, tokamak or stellarators). A principal step in gyrotron development was demonstration of possibility of electron energy recovery in collectors with potential depression. This point is discussed below.

Microwaves leave the tube through a **barrier window**. For pulse gyroton operation up to several second pulse duration the windows are made of ceramics as BN or SiN. The ceramics windows are convenient in use, however, because of low thermal conductivity pulse duration is limited (1MW/110GHz/2s) and average transmitted power does not exceed 100–200 kW. Ceramics windows at extreme parameters of operation withstand temperatures higher than 1000° C [18, 23]. Even in such conditions they operate quite reliably.

There were many concepts to develop CW window capable to transmit megawatt power microwaves. Here we mention only a sapphire window at cryo-temperatures [2, 34] , a distributed window [19] and a window based on silicon disks [18]. Now all these concepts lost in competition with windows on the base of artificial (produced by CVD technology) diamonds.

Gyrotron consists of many large, complicated and precise sub-assemblies mentioned and their mechanical assembling, brazing and welding parts, and finally baking out the tube are very serious operations on the way of tube fabrication.

We shall not discuss development problems of external gyrotron sub-assemblies such as gyrotron magnets and power supply though they are very important.

Depressed Collectors in High Power Gyrotrons

The possibility of energy recovery of electrons in gyrotrons was discussed for the first time many year ago [13]. The problem was not very acute for gyrotrons with moderate average power (kilowatts) and, of course, short pulse tubes, where efficiency enhancement of the tube with a depressed collector is compensated by more complicated tube design with an additional insulator and an additional power supply unit. The problem showed up itself when the development of megawatt power, CW gyrotrons for ITER began. Extraordinary power dissipated at the collector (and corresponding water flows) and strict requirement to over-total efficiency of the tube bring back depressed collectors to consideration.

Along with efficiency enhancement (for real tubes efficiency increase is about 1.5 times) there are obvious but very impressive drop in the

power dissipated on the collector. So the efficiency increase from 33 % to 50 % makes the dissipated power two times lower: 1 MW instead 2 MW for the megawatt power output. It is reasonable to stress that the main (high current) power supply operate at lower voltage and, also, the electron beam with lower energy causes significantly lower intensity of X-rays.

The return to depressed collectors for megawatt power gyrotrons in the experiment was very impressive. Practically simultaneously several groups demonstrated essential efficiency enhancement [31–33, 14]. Nowadays gyrotron efficiency of 50 % seems to be more a routine than a record. The situation is illustrated by results of long pulse gyrotron development at Nizhny Novgorod branch of GYCOM [14].

The developed CPD gyrotron scheme (see Fig. 8) implies the use of insulated anode-cavity block with the positive potential to the ground fed by low power source, gyrotron body and collector are grounded. Cathode is fed by high power source with the negative potential to the ground. Such gyrotrons have relatively simple design. Most of them can be installed in the cryomagnet with the warm bore diameter 140–160 mm. There is relatively free proportion between anode and cathode voltages. This means that such a type of power supply gives a possibility of output power modulation by anode low current supply.

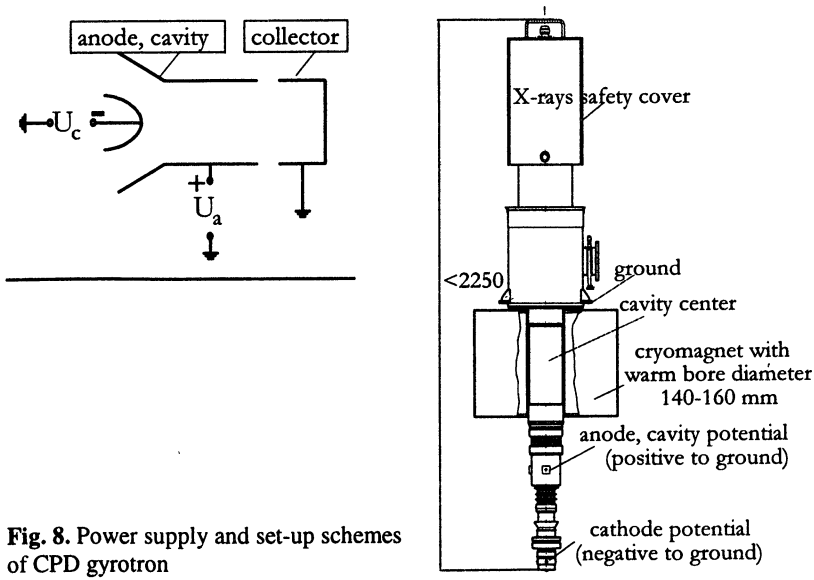

Fig. 8. Power supply and set-up schemes of CPD gyrotron

The series of CPD gyrotrons was produced and tested in the period 1996–1999. Below the experimental results for long pulse (1...3 s) gyrotrons are presented. 140 GHz gyrotron was produced in 1996, 82.7 GHz – in 1997. 70 and 84 GHz gyrotrons were tested in 1999. 84 GHz tube is prototype of 1 MW CW gyrotron.

Experimental regimes with maximum power and efficiency are presented in the tables 1, 2. The 84 GHz gyrotron maximum power was obtained at the total beam voltage risen up to 87.5 kV, in this case the gyrotron operates quite reliable. The maximum depression voltage and maximum gain of efficiency took place in the 70 GHz tube. The high value of 55 % efficiency in 82.7 GHz tube was obtained also due to the high "natural" efficiency of the gyrotron without depressed collector.

All these tubes showed stable and reliable behavior during operation. Microwave power was predictably controlled by voltage and electron beam current (see, for example, Fig. 9).

Table 1. Gyrotrons regimes with maximum output power

	70 GHz	82.7 GHz	84 GHz	140 GHz
Total voltage U_{beam}	78.5 kV	75.5 kV	87.5 kV	72.5 kV
Cathode voltage U_{cath}	- 49.5 kV	-50 kV	-60 kV	-52.5 kV
Beam current I_{beam}	28.5 A	24.5 A	31 A	33.5 A
Output power P_{out}	**680 kW**	**650 kW**	**875 kW**	**880 kW**
Efficiency η	48 %	53 %	47 %	50 %
Pulse duration τ	3 s	3 s	2 s	1 s

Table 2. Gyrotron regimes with maximum efficiency

	70 GHz	82.7 GHz	84 GHz	140 GHz
Total voltage U_{beam}	78.5 kV	75.5 kV	82 kV	72.5 kV
Cathode voltage U_{cath}	-49.5 kV	-50 kV	-53 kV	-52.5 kV
Beam current I_{beam}	22 A	21.5 A	28.5 A	29.5 A
Output power P_{out}	583 kW	591 kW	745 kW	790 kW
Efficiency η	**53.5 %**	**55 %**	**49.3 %**	**51 %**
Pulse duration τ	3 s	3 s	2 s	1 s

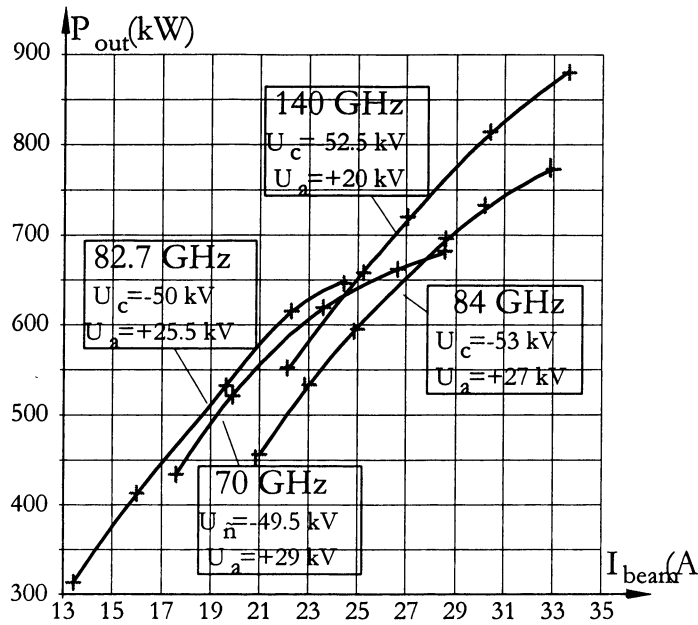

Fig. 9. Output power P_{out} of CPD gyrotrons versus electron beam current

CVD Diamond Windows for Gyrotrons

A diamond disc has the following outstanding combination of features:

- thermal conductivity of the CVD diamond discs is close to the conductivity of natural diamonds and very high (about four times higher than for copper) for a very wide temperature range,
- low losses of microwaves. Loss tangent less than 10^{-5} at millimeter waves was demonstrated for several discs,
- extremely high mechanical properties. For example, the disc of 1.5 mm thickness and 100 mm diameter can withstand several bars of gas pressure.

The properties of artificial diamond discs were improved essentially during last years. The discs with diameter about 100 mm, thickness 1.5–2 mm, loss tangent $(1–3)\cdot10^{-5}$ at short millimeter waves, thermal conductivity 20 W/cmK are available now. They are still very expensive, but in fact the window based on an artificial diamond nowadays is the only window version which solves the problem of a megawatt CW

window [15–18, 20, 21]. Calculations show that the windows based on the best discs are capable to transmit even 2–3 MW power.

Diamond discs allow one to use the window with edge cooling by water at room temperature. This fact is a principal point which makes use of gyrotrons much more comfortable as compared with previous window schemes operating at cryogenic temperatures or using some sophisticated (and sometimes even dangerous) coolants.

There are several manufactures of diamond discs: De Beers holds the major positions, other groups and companies, which are trying to produce cheaper discs, do not yet play essential role on the market. One more company (besides De Beers) from Russia "Digascron" produces CVD discs of very high quality [21]. Russian discs (Fig. 10, 11) have up to now limited diameter (less than 65 mm) and thickness (less than 1.5 mm).

Figures 10, 12 give an idea about microwave properties of the discs. It is necessary to note that a very extensive study of electrical, mechanical and heat properties of CVD discs is carryed out at FZK and their paper content a lot of information [16, 20].

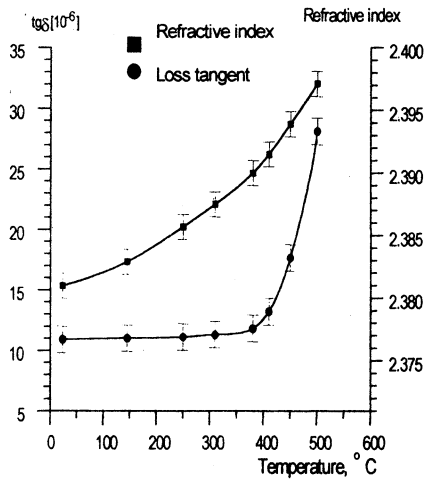

Fig. 10. Dielectric properties of Russian CVD disc versus temperature.

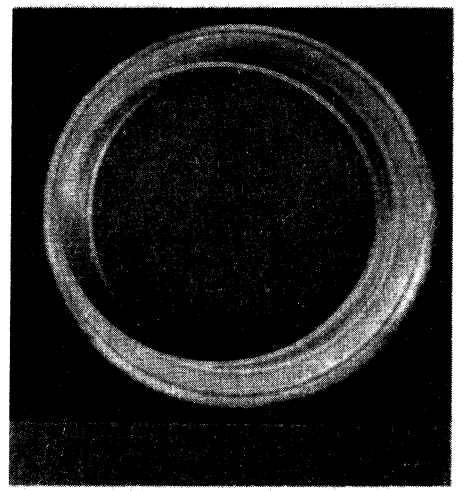

Fig. 11. Russian diamond disc brazed to copper pipe with high temperature alloy.

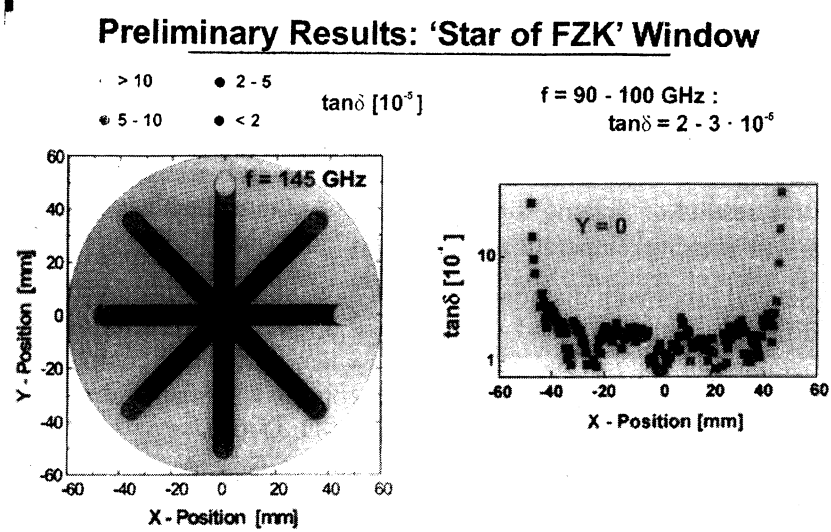

Fig. 12. Map of losses for "Star of FZK" (∅120mm)

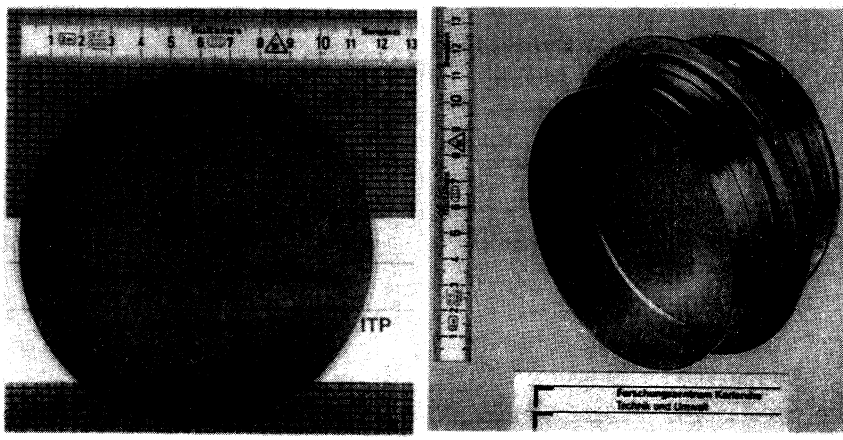

Fig. 13. Disc "Star of FZK": "free" and brazed

Diamond discs for gyrotron windows have to be brazed to metal constructions with a high temperature alloy in order the tube can pass the process of baking out. This is a difficult problem because diamond and metal parts have very different thermal expansion. There is a way to braze the diamond discs on the base of Aluminum. This kind of brazing limits the maximal temperature of baking out as 400–450°C, however the main part of the brazed discs made in such a way. High temperature brazing is now also under development in several groups. There are positive results of brazing diamond discs of 60mm diameter to copper cuffs with melting temperature of the alloy 750°C.

Several tubes with diamond windows have been fabricated and tested by different institutions and companies [26, 27]. Test results are very encouraging in spite of natural problems when a new key component is implemented in a tube (Figs. 14). Some gyrotrons with diamond windows are already used at plasma installations (DIII-D, JT-60).

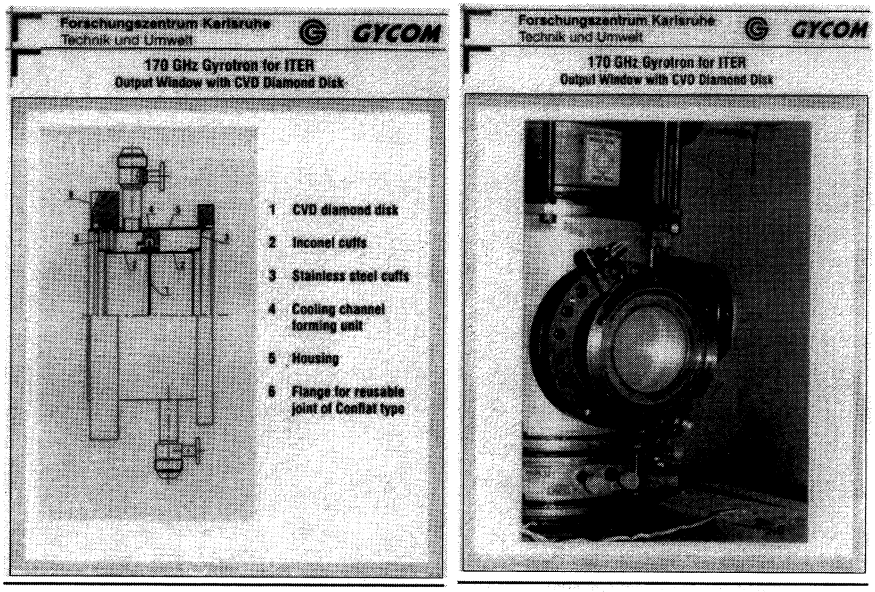

Fig. 14. Scheme and photo of the gyrotron output unit

Use of gyrotrons at fusion installations

Ten years ago there were very few fusion installations where gyrotron complexes were used for plasma parameters control. There were no installations, which exploited megawatt power level gyrotrons. Since that time the situation has changed dramatically. Now practically each fusion installation has a gyrotron complex. Last experimental campaigns on many toroidal devices and especially results on MHD stabilization and ECCD at discharges with internal barrier at Asdex-UG and sophisticated experimental ECH schemes at stellarator W-7AS have demonstrated conversion of ECH and ECCD systems based on gyrotrons into a routine instrument for fusion experiments. The progress became possible due to industrial production of reliable gyrotrons in the entire millimeter wave band with the power $\geq$ 500 kW and a few second pulse duration.

Perspectives

Megawatt power CW gyrotron at millimeter wavelengths is feasible. Definitely it will be demonstrated in a few years. For the next round of gyrotron development there are two more demands and two directions: development of multi-megawatt microwave power source and frequency tunable megawatt gyrotrons. The work on these extremely ambitious and difficult problems is carrying out. Projects of multi-megawatt coaxial gyrotrons and step-frequency-tunable gyrotrons are now at the stage of studying short pulse prototypes. There are plans for next year to test at GYCOM an industrial version of long pulse 2 MW coaxial gyrotron with a depressed collector.

Last achievements with CVD diamond output windows and model experiments with coaxial gyrotrons, in principal, make it possible to consider the 5 MW coaxial gyrotrons at the frequencies up to 170 GHz. Now discussions on such a gyrotron look similar to the discussion on 1MW/CW gyrotron ten years ago.

Acknowledgments

The author is very grateful to his colleagues for discussions and valuable help in preparing the paper.

References

1. Felch K.L., Danly B.G., Jory H.R. et al. Characteristics and Applications of Fast-Wave Gyro-devices. Proceedings of IEEE, 1999. V. 87, № 5, p.752-781.
2. Thumm M. State-of-the-Art of High power Gyro-Devices and Free Electron Masers. Update 1998. Forschungcentrum Karlsruhe, Germany, 1999.
3. Litvak A.G., Alikaev V.V. Denisov G.G., Zapevalov V.E., Kurbatov V.I., Myasnikov V.E. , Flyagin V.A. Development of 1 MW output power level gyrotron for ITER ECRH system. 17th IAEA Fusion Energy Conference. Yokohama, Japan, 19-24 October 1998 IAEA-F1-CN-69/FTP/24.
4. Goldenberg A.L., Denisov G.G., Zapevalov V.E. et al. Cyclotron Resonance Masers: State of the Art. Radiophys. And Quantum Electronics. 1996, **39**, p.423-446.
5. Kuftin A.N., Lygin V.K., Tsimring Sh.E., and Zapevalov V.E. 1992, Int. J. Electronics, 72(5-6), 1145-1151.
6. Kuftin A.N., Lygin V.K., Manuilov V.N. et al. Advanced numerical and experimental investigation for gyrotron helical electron beams. Int.J.Infrared and Millimeter Waves. 1999. V. 20, № 3, p. 361-282.
7. Moiseev M.A., Nemirovskaya L.L., Zapevalov V.E., Zavolsky N.A. Int.J.IR&MM Waves, 1997. V. 18, № 11. P. 2177.
8. Vlasov S.N., Zagryadskaya L.I., Petelin M.I. Transformation of a whispering gallery mode, propagating in a circular waveguide, into a beam of waves. Radio Eng. Electron. Phys. 1975. V. 20, № 10, p. 14-17.
9. Denisov G.G., Kuftin A.N., Malygin V.I., et al. 110 GHz gyrotron with a built-in high -efficiency converter. Int.J.Electronics, 1992. V. 72, № 5-6, p. 1079-1091.
10. Katsenelenbaum B.Z. and Semenov V.V. Synthesis of the phase correctors forming arequired field. J.Radiotechnics and Electronics, 1967, № 12, p. 244-252.
11. Bogdashov A.A., Chirkov A.V., Denisov G.G. et al. Mirror synthesis for gyrotron quasi-optical mode converters, Int. Journal of Infrared and Millimeter Waves, 1995. V. 16, № 4, p.735-744.
12. Aleksandrov N.L., Denisov G.G., Chirkov A.V. 3D wavebeam field reconstruction from intesity measurements in a few cross-sections, Optics Communication, 1995. V. 115, p. 449-452.
13. Fix A.Sh., Flyagin V.A., Goldenberg A.L. et al. Int.J.Electronics, The problems of increase in power, efficiency and frequency of gyrotrons for plasma investigations. 1984. V. 57, № 6, p. 821-826.
14. Kurbatov V.I., Malygin S.A., Orlov V.B., Solujanova E.A., Tai E.M. 70-140 GHz 1 MW gyrotrons on their way to CW operation, this book.

15. Hiedinger R., Sporl R., Thumm M. el al. CVD diamond windows for High power gyrotrons. Procedings of 23rd Int. Conf. Infrared and Millimeter Waves, Sept. 1998, p. 223-224.

16. Thumm M. Development of output windows for high-power long-pulse gyrotrons and EC wave applications. Int.J.Infrared and Millimeter Waves, 1998, **19**, p. 3-14.

17. Kasugai A., Sakamoto K., Takashi K., et al. Chemical vapor deposition diamond for high-power and long-pulse millimeter wave transmission. Rev. Scientific Instruments, **69**, 2160-2165.

18. Alikaev V.V., Khmara D.V., Khmara V.A. et al. Output Power Windows of GYCOM Gyrotrons and their Prospectiv. ITG Conf. Displays and Vacuum Electronics. Garmisch-Patenkirchen, Germany. 1998, p. 357-362.

19. Moeller C.P., Doane J.L., DiMartino M. A vacuum window for 1MW CW 110 GHz gyrotron. Conf.Digest 19th Int.Conf. on Infrared and MM Waves, 1994, Sendai, p. 279-280.

20. Sporl R., Schwab R., Heidinger R., Parshin V.V. CVD Diamond for High Power Gyrotrons: Characterisation of Dielectric Properties. ITG Conf. Displays and Vacuum Electronics. Garmisch-Patenkirchen, Germany. 1998, p. 369-374.

21. Parshin V., Ralchenko V. and Konov V. Diamond for High-Power Gyrotron Window. The 23th Int. Conf. on IR & MM Waves. Colchester, England, 1998.

22. Myasnikov V.E., et all. Long-pulse operation of 110 GHz/1MW gyrotron, 22 Int. Conf. on IR&MM Waves. 1997, p. 102-103.

23. Myasnikov V.E., Agapova M.V., Alikaev V.V. el al. Megawatt power level long-pulse 110 and 140GHz gyrotrons. Proc, 3rd Int Workshop on Strong Microwaves in Plasmas, Nizhny Novgorod, 1996. V. 2, p. 577-598.

24. Denisov G.G., Flyagin V.A., Kuftin V.A. et al. Development of the prototype170 GHz, 1MW gyrotron for ITER at IAP. Proc, 3rd Int Workshop on Strong Microwaves in Plasmas, Nizhny Novgorod, 1996. V. 2, p. 717-722.

25. Sakamoto K., Kasugai A., Takashi K. et al. Stable single-mode oscillation with high-order mode at 1MW, 170 GHz Gyrotron. J.of Physical Society of Japan, **65**, 1888-1890.

26. Sakamoto K., Kasugai A., Tsuneoka M. et al. Development of high-power gyrotron with a diamond window. Proc.23rd Int. Conf.Infrared and MM Waves, Sept 1998, p. 363-364.

27. Felch K., Borchard P., Caufman S., et al. Status report on a 110 GHz, 1 MW gyrotron with a diamond window. Proc.23rd Int. Conf.Infrared and MM Waves, Sept 1998, p. 367-368.

28. Vlasov S.N., Zagryadskya L.I., Orlova I.M. Open coaxial resonators for gyrotrons. Radio Eng.Electron.Phys. 1976, **21**, p. 96-102.

29. Flyagin V.A., Khizhnyak V.I., Kuftin, A.N. et al. Investigation of coaxial gyrotrons at IAP RAS. Conf. Digest 22nd Int.Conf on Infrared and MM Waves.1997, Wintergreen, USA, p.112-113.

30. Thumm.M., Braz O., Dammertz G. et al. Experimental results of 1.5MW coaxial cavity gyrotrons in the frequency range 115-170 GHz. Proc.3rd Int.Workshop on strong Microwaves in Plasmas. Nizhny Novgorod. 1997. V. 2, p. 614-633.

31. Sakamoto K., Tsuneoka M., Kasugai A., et al. Major improvement of gyrotron efficiency with beam energy recovery. Phys. Rev. Lett., **73**, 3532-3535.

32. Piosczyk B., Iatrou C.T., Dammertz G., Thumm M. Operation of gyrotrons with single-stage depressed collector. Conf.Digest 20th Int.Conf.on Infared and Millimeter Waves, 1995, Orlando, p. 491-492.

33. Glyavin M.Yu., Kuftin A.N., Venedictov N.P., Zapevalov V.E. Experimental investigation of a 110GHz/1MW gyrotron with one-step depressed collector. Int.J.Infrared and Millimeter Waves, 1997, **18**, p. 2129-2136.

34. Alberti S., Braz O., Garin P. et al. Long-pulse operation of a 0.5 MW - 118 GHz gyrotron with cryogenic window. Proc.21st Conf. on Infrared and Millimeter Waves, 1996, Berlin, AF1.

35. Kuznetsov S.O., Malygin V.I. Determination of gyrotron wave beam parameters. Int.J.of Infrared and Millimeter Waves, 1991. V. 12, № 11, p.1241-1252.

CONTENTS OF VOLUME 2

NONLINEAR PROCESSES IN PLASMAS (THEORY AND MICROWAVE EXPERIMENTS)

DEVELOPMENT OF HIGH-POWER MICROWAVE SOURCES

STRONG MICROWAVES IN PLASMAS

PROCEEDINGS
OF THE INTERNATIONAL WORKSHOP

In two volumes

Volume 2

License № ЛР 040840 of 22.08.97.

Institute of Applied Physics,
Russian Academy of Sciences

46 Ul'yanov Street, 603600 Nizhny Novgorod, Russia

Printed by Printing House № 2, "Nauka" Publishers,
6 Shubinsky Pereulok, 121099 Moscow